A Fluvial Perspective on the Role of Sulfide Oxidation in the Global Carbon Cycle

Thesis by
Preston Cosslett Kemeny

In Partial Fulfillment of the
Requirements for the Degree of
Doctor of Philosophy

CALIFORNIA INSTITUTE OF TECHNOLOGY
Pasadena, California

2022
(Defended May 10th, 2022)

To isotopes, a language of nature we are still learning to read,
and their potential to help us write a better future.

© 2022

Preston Cosslett Kemeny
ORCID: 0000-0003-1693-4142

All rights reserved except where otherwise noted

Acknowledgments

I am foremost grateful to Jess Adkins and Woodward Fischer for generously sharing their expertise, time, and resources throughout my years at Caltech. Membership in their research groups has been extremely rewarding. Many fruitful interactions with John Eiler, Alex Sessions, and Josh West also contributed to the ideas in this thesis, as have several excellent fieldtrips and arguments with Joe Kirschvink, Mike Lamb, and Francois Tissot. Outside of Caltech, Mark Torres has been an exceptional mentor, collaborator, and friend, while Sylvia Dee and Tony Wang have provided invaluable guidance. I am also grateful to Daniel Sigman, John Higgins, Gerta Keller, and Jonathan Heiles for inspiring my interests in isotope biogeochemistry and climate-life interactions.

I would like to thank Nathan Dalleska, Grecia Lopez, John Magyar, Jared Marske, Nami Kitchen, Jonathan Treffkorn, Sam Webb, and Fenfang Wu for providing laboratory assistance, as well as Tim Pyles, Issaku Kohl, and Ben Byerly for sharing their mass spectrometry expertise. Many thanks are also due to Mark Garcia, Kacey Gibson, Janice Grancich, Nora Oshima, and Leilani Rivera-Dotson for keeping the department running. I am grateful to Kitty Cahalan for coordinating outreach at local schools, Brian Brophy for supporting the improv group, and Ernie Mercado for providing research-nourishing burritos.

I am indebted to Caltech's many graduate students and postdoctoral scholars. I would specifically like to thank Dan Johnson for our weekly discussions on isotopes and Earth History, Usha Lingappa for her camaraderie and encouragement, and Alex Phillips for her critiques of my figures and writings. I am additionally thankful for the friendship of, among many others, Elizabeth Bailey, Makayla Betts, Jennifer Buz, Austin Chadwick, Gray Chadwick, Elle Chimiak, Antoine Cremiere, Madison Douglas, Yoni Goldsmith, Alistair Hayden, Miquela Ingalls, Gen Li, Max Lloyd, Peter Martin, Paula Mateo, Kyle Metcalfe, John Naviaux, Frankie Pavia, Ted Present, Kevin Roback, Daniela Osorio Rodriguez, Uri Ryb, Daan Speth, Nithya Thiagarajan, and Lewis Ward. My early years at Caltech benefited from strong friendships with Bradley Gorsline, Matt Gwin, and Nikita Klimovich. In the latter years, connections with Paul Fanto, Alexa McCall, and Stephen Wood helped to sustain me through the pandemic.

This dissertation was generously funded through the Cohan-Jacobs & Stein Families Fellowship from the Fannie and John Hertz Foundation and through the National Defense Science and Engineering Graduate Fellowship. I would like to thank the donors, staff, and fellows who make the Hertz Foundation possible.

To Mom and Dad, thank you for everything. To Malcolm and Schuyler, thank you for many adorable photos of Chloe and Brooke, who I hope may one day skim this thesis and envision themselves as geologists. Many thanks as well to Sabrina and Dovid for opening their home and to Chris and Gulden for their encouragement. I would also like to thank my grandparents, Nana, Boobah, and Gran, as well as my Uncle Bob, who passed away before this thesis was completed and are deeply missed.

Lastly, this work was only possible with the support and love of Celeste Ritter Labedz and Tethys Mega Ojala Kemeny. Thank you both for reminding me to enjoy each day.

Abstract

This thesis contains an introduction and five studies on the role of sulfide oxidation in regulating the relationship between chemical weathering and climate. Chapter I provides an overview of the key question — what stabilizes the global carbon cycle? — and motivates the specific questions addressed in each subsequent chapter. Chapter II describes a new numerical tool for inverting observations of dissolved river chemistry for information about chemical weathering reactions. Chapters III, IV, and V describe observations from field sites in Iceland, Nepal, and Alaska that address the fidelity of fluvial sulfur isotope ratios, the role of sulfide oxidation in Cenozoic cooling, and sulfur dynamics within permafrost landscapes, respectively. Using the tools and lessons of the preceding chapters, Chapter VI quantifies the impact of global chemical weathering on the concentration of atmospheric carbon dioxide.

Published Content and Contributions

Chapter II

Kemeny, P.C. and Torres, M.A., 2021. Presentation and applications of Mixing Elements ANd Dissolved Isotopes in Rivers (MEANDIR), a customizable MATLAB model for Monte Carlo inversion of dissolved river chemistry. *American Journal of Science*, 321(5), pp.579-642. doi: 10.2475/05.2021.03.

P.C.K. designed the study, coded the MEANDIR model, and wrote the manuscript.

Chapter III

Kemeny, P.C., Torres, M.A., Lamb, M.P., Webb, S.M., Dalleska, N., Cole, T., Hou, Y., Marske, J., Adkins, J.F. and Fischer, W.W., 2021. Organic sulfur fluxes and geomorphic control of sulfur isotope ratios in rivers. *Earth and Planetary Science Letters*, 562, p.116838. doi: 10.1016/j.epsl.2021.116838.

P.C.K. designed the study in collaboration with senior authors, led sample collection, measured the samples, conducted the analysis, and wrote the manuscript.

Chapter IV

Kemeny, P.C., Lopez, G.I., Dalleska, N.F., Torres, M., Burke, A., Bhatt, M.P., West, A.J., Hartmann, J. and Adkins, J.F., 2021. Sulfate sulfur isotopes and major ion chemistry reveal that pyrite oxidation counteracts CO_2 drawdown from silicate weathering in the Langtang-Trisuli-Narayani River system, Nepal Himalaya. *Geochimica et Cosmochimica Acta*, 294, pp.43-69. doi: 10.1016/j.gca.2020.11.009.

P.C.K. designed the study in collaboration with senior authors, measured the samples, conducted the analysis, and wrote the manuscript.

Table of Contents

Acknowledgments iii
Abstract iv
Published Content and Contributions v
Table of Contents vi
List of Tables ix
List of Figures x

Chapter I: Introduction to Sulfide Oxidation and its Role in the Relationship Between Weathering and Climate 1

1: Overview 2
2: The role of sulfide oxidation 4
3: Guiding questions and context 9
4: Looking down the river 12
5: Figures 18
6: References 20

Chapter II: Presentation and Applications of Mixing Elements ANd Dissolved Isotopes in Rivers (MEANDIR), a Customizable MATLAB Model for Monte Carlo Inversion of Dissolved River Chemistry 24

1: Abstract 25
2: Introduction to MEANDIR 26
3: Mathematics of MEANDIR 31
4: Applications of MEANDIR 89
5: Conclusions 108
6: Code availability and data sources 109
7: Acknowledgments 110
8: Figures 111
9: Tables 123
10: References 136
11: MEANDIR user guide 144

Chapter III: Organic Sulfur Fluxes and Geomorphic Control of Sulfur Isotope Ratios in Rivers 154

1: Abstract 155
2: Introduction 156
3: Methods 159
4: Results 169
5: Discussion 171
6: Conclusions 181

7: Data statement 183
8: Acknowledgments 184
9: Figures 185
10: References 196
11: Supplementary text 202
12: Supplementary figures 213
13: Supplementary tables 228
14: Supplementary references 230

Chapter IV: Sulfate Sulfur Isotopes and Major Ion Chemistry Reveal that Pyrite Oxidation Counteracts CO_2 Drawdown from Silicate Weathering in the Langtang-Trisuli-Narayani River System, Nepal Himalaya 233

1: Abstract 234
2: Introduction 235
3: Methods 242
4: Results 257
5: Discussion 263
6: Conclusions 282
7: Data availability 283
8: Acknowledgments 284
9: Figures 285
10: Tables 299
11: References 300
12: Supplementary text 313
13: Supplementary figures 331
14: Supplementary tables 349
15: Supplementary references 350

Chapter V: Permafrost Degradation and Sulfide Oxidation in the Koyukuk River, AK . 355

1: Abstract 356
2: Introduction 357
3: Methods 359
4: Results 374
5: Discussion 379
6: Conclusions 390
7: Acknowledgments 391
8: Figures 392
9: Tables 403
10: References 405
11: Supplementary figures 413
12: Supplementary tables 430

Chapter VI: Global River Chemistry Constrains Crustal Sulfide $^{34}S/^{32}S$ and ΔALK/ΔDIC of Inorganic Weathering 431

1: Abstract 432
2: Introduction 433
3: The $\delta^{34}S$ of global excess SO_4^{2-} is between -6.2‰ and 1.0‰ 434
4: Accounting for anthropogenic inputs 437
5: Crustal sulfide $\delta^{34}S$ constrains the global sulfur cycle 439
6: The timescale-dependent interpretation of f_{pyr} 442
7: Sulfide oxidation and the global carbon cycle 444
8: Conclusions 446
9: Acknowledgments 448
10: Methods 449
11: Figures 451
12: Tables 454
13: References 455
14: Supplementary text 459
15: Supplementary figures 469

List of Tables

Chapter II: Presentation and Applications of Mixing Elements ANd Dissolved Isotopes in Rivers (MEANDIR), a Customizable MATLAB Model for Monte Carlo Inversion of Dissolved River Chemistry

1: Summary of choices during construction of inversion models 123
2: Variables used throughout the text 124
3: Subscripts and superscripts on variables used throughout the text 125
4: Example end-member ratios for new normalizations 126
5: Inversion scenarios using data from Gaillardet et al. (1999) 127
6: Inversion scenarios using data from Burke et al. (2018) 128
7: End-members for Gaillardet et al. (1999), Burke et al. (2018) inversions 129
8: Inversion scenarios using data from Torres et al. (2016) 130
9: End-members for Torres et al. (2016) inversions 131
10: Inversion scenarios using data from Gíslason et al. (1996) 132
11: End-members for Gíslason et al. (1996) inversions 133
12: Inversion scenarios using data from Horan et al. (2019) 134
13: End-members for Horan et al. (2019) inversions 135

Chapter III: Organic Sulfur Fluxes and Geomorphic Control of Sulfur Isotope Ratios in Rivers

S1: End-member distributions for Monte Carlo inversion model 228
S2: Dissolved chemistry of repeat river water samples across field seasons 229

Chapter IV: Sulfate Sulfur Isotopes and Major Ion Chemistry Reveal that Pyrite Oxidation Counteracts CO_2 Drawdown from Silicate Weathering in the Langtang-Trisuli-Narayani River System, Nepal Himalaya

1: Inversion end-member means and uncertainty 299

S1: Precision of ion chromatography measurements 349

Chapter V: Permafrost Degradation and Sulfide Oxidation in the Koyukuk River, AK

1: Parameters for Monte Carlo binary mixing model 403
2: End-member distributions for Monte Carlo inversion model 404

S1: Precision and accuracy of ion chromatography measurements 430

Chapter VI: Global River Chemistry Constrains Crustal Sulfide $^{34}S/^{32}S$ and $\Delta ALK/\Delta DIC$ of Inorganic Weathering

1: Inversion end-member distributions 454

List of Figures

Chapter I: Introduction to Sulfide Oxidation and its Role in the Relationship Between Weathering and Climate

1: Cross plot of alkalinity and dissolved inorganic carbon with relevant processes 18
2: Schematic of alkalinity and dissolved inorganic carbon reservoirs 19

Chapter II: Presentation and Applications of Mixing Elements ANd Dissolved Isotopes in Rivers (MEANDIR), a Customizable MATLAB Model for Monte Carlo Inversion of Dissolved River Chemistry

1: Architecture of MEANDIR 111
2: Sensitivity analysis..... 112
3: Comparison of median fractional contributions..... 114
4: Distributions of fraction of reconstructed river observations..... 116
5: Inversion-constrained end-member chemistry 117
6: Influence of including bicarbonate in inversion..... 118
7: Example of constraining the chemical composition of secondary clay..... 119
8: Influence of different inversion methods on R, Z, calculated $\delta^{34}S$..... 120
9: Simultaneous quantification of R, Z, C for Mackenzie River basin..... 122

Chapter III: Organic Sulfur Fluxes and Geomorphic Control of Sulfur Isotope Ratios in Rivers

1: Schematic of the global sulfur cycle..... 185
2: Elevation maps with indicated sampling locations 186
3: Cation and anion ternary diagrams..... 187
4: $\delta^{34}S_{SO4}$, $[SO_4^{2-}]$, and Cl^-/SO_4^{2-} of river water samples 188
5: Sediment $\delta^{34}S$ on map, against 1/S and ^{14}C content..... 189
6: Observations and spectral fitting of synchrotron measurements 190
7: Spatial structure of $[SO_4^{2-}]$ and $\delta^{34}S_{SO4}$ 191
8: Geomorphic analyses..... 192
9: River channel long profile 194
10: Relationships among sediment S speciation, $\delta^{34}S$, ^{14}C content, 1/S, C/S 195

S1: Drone images of the Efri Haukadalsá catchment..... 213
S2: Field photographs of the Efri Haukadalsá catchment..... 214
S3: Satellite images of the Efri Haukadalsá catchment..... 215
S4: $[Ca^{2+}]$, $[Mg^{2+}]$, $[Na^+]$, $[K^+]$ determinations 216
S5: Synchrotron analysis of vegetation cross section..... 217
S6: Seasonality in precipitation, wind speed at Ásgarður and Stykkishólmur 218
S7: Seasonality in precipitation chemistry at Íráfoss and Stórhöfði 219
S8: Sulfur mixing, $\delta^{34}S_{SO4}$ against Cl^-/SO_4^{2-} with inversion end-members..... 220
S9: Seasonal $\delta^{34}S_{SO4}$ and Cl^-/SO_4^{2-} in Hvítá, Olfusa, Thjorsa, Sog Rivers..... 221
S10: Inversion results for the fractional contributions of end-members..... 222

S11: Inversion results with and without carbonate for variable precipitation 223
S12: Extended geomorphic analysis 224
S13: [Ca^{2+}], [Mg^{2+}], [Na^{+}], [K^{+}], [Σ^{+}], and [Cl^{-}] Efri Haukadalsá maps 225
S14: $\delta^{34}S_{SO4}$ of Efri Haukadalsá samples collected on single day 226
S15: Rayleigh model calculations 227

Chapter IV: Sulfate Sulfur Isotopes and Major Ion Chemistry Reveal that Pyrite Oxidation Counteracts CO_2 Drawdown from Silicate Weathering in the Langtang-Trisuli-Narayani River System, Nepal Himalaya

1: Sample locations and geologic map of the Langtang-Trisuli-Narayani 285
2: Cation and anion ternary diagrams 286
3: Timeseries of river dissolved chemistry 287
4: River water $\delta^{34}S_{SO4}$, [SO_4^{2-}], and Cl^{-}/SO_4^{2-} 288
5: Principal component analysis biplot and factor scores 289
6: Elemental and isotopic mixing diagrams 290
7: Fractional contributions of end-members to dissolved load 291
8: FeS_2-derived SO_4^{2-}/Σ^{+}, $\delta^{34}S_{FeS2}$ values, lithologic fractions 292
9: FeS_2 weathering fraction against carbonate weathering fraction 293
10: R and Z regression on synthetic hydrograph 295
11: Schematic of seasonal weathering cycle 296
12: FeS_2 and carbonate weathering across the Ganges catchment 297

S1: Comparison of major ion chemistry in this study and Bhatt et al. (2018) 331
S2: [Ca^{2+}], [Mg^{2+}], [Na^{+}], and [K^{+}] before and after sample acidification 332
S3: [Cl^{-}] and Cl^{-}/Σ^{+} in samples from the Lirung Glacier catchment 333
S4: Dissolved chemistry of springs in the Narayani River system 334
S5: Major ions chemistry of Himalayan precipitation 335
S6: Chemical indicators of anthropogenic pollution 336
S7: Derivation of synthetic discharge curve 337
S8: Impacts of secondary carbonate precipitation on Ca^{2+}/Σ^{+} and SO_4^{2-}/Σ^{+} 338
S9: Sulfur isotope mixing plots 339
S10: Cumulative distribution functions for fractional contributions 340
S11: R and Z by month of sample collection, with regression 341
S12: R and Z by location of sample collection, with regression 342
S13: Inversion-constrained $\delta^{34}S_{FeS2}$ against catchment lithology 343
S14: Seasonality of R and Z in prior data from Narayani catchment 344
S15: R against Z when inversion includes an evaporite end-member 345
S16: R against Z when inversion includes a spring end-member 346
S17: R against Z when inversion excludes K^{+} and Cl^{-} 347
S18: R against Z using a simple forward model 348

Chapter V: Permafrost Degradation and Sulfide Oxidation in the Koyukuk River, AK

1: Site context and sampling map 392
2: Major ion chemistry and mixing diagrams 393
3: Sulfur and oxygen isotope ratios in SO_4^{2-} and H_2O 394
4: Sedimentary sulfur chemistry 395
5: Sulfate sulfur isotope mixing diagrams 396
6: XANES results on floodplain and suspended sediment 397
7: DIC concentration and $^{13}C/^{12}C$ ratio 398
8: Carbon cycle impacts of weathering in the Koyukuk 399
9: Temporal changes in the major ion chemistry of the Koyukuk River 400
10: Temporal changes in the major ion chemistry of the Yukon River 401
11: Schematic of seasonal and long-term changes in major ion chemistry 402

S1: Drone images of the Koyukuk catchment 413
S2: Water $^{18}O/^{16}O$ and D/H isotope ratios 415
S3: Sulfur isotope mixing diagrams 416
S4: Sedimentary sulfur and carbon isotope ratios 417
S5: Transect of pore fluid $^{34}S/^{32}S$ isotope ratios 418
S6: Median end-member fractional contributions for inversion without degassing 419
S7: Median end-member fractional contributions for inversion with degassing 420
S8: Inversion-constrained end-member chemistry 421
S9: Comparison of inversion results with and without CO_2 degassing 422
S10: Concentration-discharge relationships for the Koyukuk River at Hughes 423
S11: Monthly discharge for timeseries data from the Yukon River at Pilot Station 424
S12: Discharge, Ca^{2+}, Mg^{2+}, and SO_4^{2-} for the Yukon River at Pilot Station 425
S13: Discharge, Ca^{2+}, Mg^{2+}, and SO_4^{2-} for the Yukon River at Stevens Village 426
S14: Discharge, Ca^{2+}, Mg^{2+}, and SO_4^{2-} for the Yukon River at Eagle 427
S15: Discharge, Ca^{2+}, Mg^{2+}, and SO_4^{2-} for the Tanana River at Nenana 428
S16: Discharge, Ca^{2+}, Mg^{2+}, and SO_4^{2-} for the Porcupine River at Fort Yukon 429

Chapter VI: Global River Chemistry Constrains Crustal Sulfide $^{34}S/^{32}S$ and ΔALK/ΔDIC of Inorganic Weathering

1: Inversion-constrained $\delta^{34}S$ of excess SO_4^{2-} 451
2: Implications of inversion results for the global sulfur cycle 452
3: FeS_2 weathering fraction against carbonate weathering fraction 453

S1: Dissolved ion chemistry for river water samples from Burke et al. (2018) 469
S2: Inversion model MEANDIR 470
S3: Excess SO_4^{2-} and its $^{34}S/^{32}S$ ratio 471
S4: Fractional contribution of each river to global excess SO_4^{2-} 472
S5: SO_4^{2-} $\delta^{34}S$ and excess SO_4^{2-} $\delta^{34}S$ against Na^+/Cl^- 473
S6: Impacts of anthropogenic SO_4^{2-} on calculated $\delta^{34}S$ of crustal sulfide 474
S7: Sensitivity of results to the chemical composition of the evaporite end-member. 475
S8: Sensitivity of results to the isotopic composition of anthropogenic SO_4^{2-} 476
S9: R, Z, and ΔALK/ΔDIC for individual river water samples 477
S10: Precipitation treatment impacts Cl^- and SO_4^{2-} contributions, excess SO_4^{2-} $\delta^{34}S$. 478
S11: Precipitation treatment impacts global excess SO_4^{2-} $\delta^{34}S$, reduced data 479
S12: Precipitation treatment impacts global excess SO_4^{2-} $\delta^{34}S$, all data 480
S13: Precipitation treatment impacts sample R and Z values 481
S14: Crustal sulfide $\delta^{34}S$ and f_{mantle} in sulfur model with one sulfide reservoir 482
S15: Crustal sulfide $\delta^{34}S$ and f_{mantle} in sulfur model with two sulfide reservoirs..... 484
S16: f_{mantle} and $^{34}\Delta_{shallow}$ in sulfur model with two sulfide reservoirs 486

Chapter I

Introduction to Sulfide Oxidation and its Role in the Relationship Between Weathering and Climate

Preston Cosslett Kemeny[1]

[1] Division of Geological and Planetary Sciences, California Institute of Technology, Pasadena, CA, USA

I.1: Overview

How is a habitable planet maintained, not just today, but throughout the coevolution of life with climate? Over the last 4.5 billon years Earth's atmospheric, oceanic, and lithospheric reservoirs have undergone major chemical transformations due to both the evolution of life and the abiotic processes of planetary development. Likewise, life itself has survived geologic time by influencing and responding to its environment. To understand the persistence of habitability, it is thus critical to resolve the amplifying and mitigating biogeochemical feedbacks that couple the global biosphere with inorganic chemical reservoirs. Understanding these connections is important because elucidating the interwoven nature of biogeochemical cycles, including how the cascading temporal scales of geologic time are manifest in modern environmental processes, provides critical context for predicting and responding to the impacts of anthropogenic climate change.

The chemical and physical processes that break down and dissolve rock, called weathering, are feedbacks in the Earth system which contribute to the maintenance of planetary habitability. This thesis is focused around one component of weathering, sulfide oxidation, which removes alkalinity from the ocean-atmosphere system and complicates the canonical view of weathering as a temperature-dependent stabilizing feedback. The research in this dissertation quantifies the amount and controls of sulfide oxidation by applying multiple analytical techniques to river water and sediment samples from Iceland, Nepal, and Alaska, and by developing and applying numerical techniques to existing data.

Each chapter of this thesis addresses a different component of chemical weathering and sulfide oxidation. The remainder of Chapter I presents background and motivation on chemical weathering, frames subsequent chapters within the larger context of research on

the global carbon and sulfur cycles, and concludes with speculations regarding how emerging biogeochemical tools may improve future studies of river chemistry. Second, Chapter II reviews and extends numerical methods for converting measurements of river chemistry into information about chemical weathering and climate, culminating in a new open-access tool called MEANDIR for performing flexible river inversion calculations. Chapters III, IV, and V describe three studies of modern river systems oriented towards understanding sulfide oxidation in the present, past, and future, respectively. Chapter III uses observations from an Icelandic catchment to evaluate whether fluvial sulfate sulfur isotope ratios faithfully record the isotopic composition of weathering lithologies or are overwritten by biological processes. Chapter IV quantifies sulfide oxidation in the Nepal Himalaya to expand on prior work evaluating the impact of silicate weathering and mountain building on Cenozoic climate. Chapter V uses new water and sediment samples from the Koyukuk River in Alaska to evaluate whether sulfide oxidation secondary to permafrost degradation is a positive feedback on anthropogenic climate change. Lastly, Chapter VI constrains the amount of sulfide oxidation globally and the isotopic ratio of crustal sulfide using an existing dataset of river chemistry and sulfate sulfur isotope ratios.

In summary, this dissertation investigates numerical methods for quantifying weathering using the chemistry of rivers, the fidelity of fluvial sulfate sulfur isotope ratios, the impact of sulfide oxidation on atmospheric carbon dioxide across the geologic past and the anthropogenic future, and the amount and isotopic character of global sulfide oxidation. These projects collectively emphasize that sulfide oxidation, as a substantial flux in the biogeochemical cycles of sulfur, carbon, and alkalinity, has a moderating role in the relationship between weathering and climate.

I.2: The role of sulfide oxidation

I.2.1: The need for feedbacks in the global carbon cycle

The atmospheric concentration of carbon dioxide (pCO_2) is regulated by the relative abundance of dissolved inorganic carbon (DIC) and alkalinity (ALK) in the coupled ocean-atmosphere system (Fig. I-1). DIC reflects the total amount of carbon while ALK regulates, in conjunction with ocean circulation and biology, how carbon is partitioned between the ocean and atmosphere. The modern system contains slightly more ALK than DIC, resulting in a relatively alkaline ocean that stores approximately sixty time more carbon than the atmosphere (Sarmiento and Gruber, 2006). If the ocean-atmosphere system had a lower ALK/DIC ratio, seawater pH would decrease and carbon would partition into the atmosphere (Fig. I-1). Conversely, seawater would become more alkaline and pCO_2 would decline at a higher ALK/DIC ratio. It is notable that modern pCO_2 is relatively insensitive to equal changes in ALK and DIC.

The outgassing of CO_2 from the solid Earth through volcanic and metamorphic processes constitutes a source of DIC to the ocean-atmosphere system without a source of ALK (Figs. I-1 and I-2). On the removal side, carbon leaves the ocean-atmosphere system through the burial of organic matter (C_{org}) and calcium carbonate ($CaCO_3$), the latter of which removes twice as much ALK as DIC. The amount of CO_2 in Earth's atmosphere is very sensitive to imbalances between these input and output fluxes; even minor differences will repartition nearly all DIC into the atmosphere or ocean in only a few million years (Myr; Kerrick and Caldeira, 1999). However, paleoenvironmental records indicate that atmospheric CO_2 levels have been largely equable over the preceding hundreds of millions of years. These observations require the existence of biogeochemical feedbacks that

balance inputs and outputs of ALK and DIC to sustain moderate pCO_2 and perpetuate planetary habitability (Berner and Caldeira, 1997). Chemical weathering is commonly invoked as one such feedback that, through the temperature dependence of silicate mineral weathering, forces outputs of DIC into balance with inputs from volcanic and metamorphic degassing (Walker et al., 1981).

I.2.2: Silicate weathering as a temperature-dependent stabilizing feedback

Chemical weathering reactions can be viewed as the neutralization of environmental acids on alkaline minerals. The weathering of silicate minerals, often represented by wollastonite ($CaSiO_3$), results in the addition of cations, ALK, and silica to rivers (Eq. I-1). The weathering of carbonate minerals, represented by calcium carbonate ($CaCO_3$), likewise results in addition of cations and ALK to rivers (Eq. I-2). Over timescales shorter than the 5-10 thousand year (kyr) timescale of carbonate compensation (Archer et al., 1997), weathering of silicate and carbonate lithologies sources more ALK than DIC to the ocean-atmosphere system and results in lower concentrations of atmospheric CO_2 (Fig. I-1).

$$\frac{1}{2}CaSiO_3 + H^+ \rightarrow \frac{1}{2}Ca^{2+} + \frac{1}{2}SiO_2 + \frac{1}{2}H_2O \quad \text{(I-1)}$$

$$\frac{1}{2}CaCO_3 + H^+ \rightarrow \frac{1}{2}Ca^{2+} + \frac{1}{2}H_2CO_3 \quad \text{(I-2)}$$

Weathering products are transported to the ocean where production of $CaCO_3$ consumes Ca^{2+}, DIC, and ALK (Eq. I-3). In the case of carbonate mineral weathering, the formation of $CaCO_3$ reverses the original reaction and results in no net changes to marine

chemistry or ocean-atmosphere ALK or DIC. In the case of silicate mineral weathering, where ALK production by weathering is commonly set equal to ALK consumption through $CaCO_3$ formation, the net reaction removes DIC (Eq. I-4; Urey, 1952).

$$\frac{1}{2}Ca^{2+} + \frac{1}{2}H_2CO_3 \rightarrow H^+ + \frac{1}{2}CaCO_3 \quad \text{(I-3)}$$

$$CaSiO_3 + CO_2 \rightarrow CaCO_3 + SiO_2 \quad \text{(I-4)}$$

The conversion of silicate minerals to carbonate minerals is commonly viewed as a temperature-dependent stabilizing feedback on pCO_2 (Walker et al., 1981). Within this framework, elevated global temperature due to higher pCO_2 enhances silicate weathering, the production of ALK, and the removal of DIC through $CaCO_3$ burial (Eq. I-4). Conversely, lower pCO_2 decreases global temperature, ALK production, and removal of DIC, allowing CO_2 to accumulate until equilibrium between ALK production and consumption is restored. Changes in the sensitivity of ALK production to temperature allow for shifts in the equilibrium pCO_2 value, as indicated by the geologic record (Witkowski et al., 2018).

I.2.3: Sulfide oxidation removes alkalinity and increases pCO_2

A major role for sulfide oxidation in weathering systems was identified in early studies of river chemistry (Rabinovich and Grinenko, 1979; Stallard and Edmond, 1983). However, interest in the impact of sulfide oxidation on pCO_2 has only recently been rekindled due to observations of abundant sulfide-derived sulfate in regional and global analyses (Calmels et al., 2007; Torres et al., 2016; Burke et al., 2018). In general, the

oxidation of sulfide minerals removes ALK from the ocean-atmosphere system without impacting DIC (Eq. I-5). In detail, however, this statement is only true when partner cations in the original mineral form secondary phases rather than entering solution, such as when pyrite (FeS_2) oxidizes to sulfate (SO_4^{2-}) and hematite (Fe_2O_3). Oxidation of a compound like calcium sulfide does not remove ALK because both SO_4^{2-} and Ca^{2+} are soluble in oxic solutions. When sulfide oxidation removes ALK without impacting DIC, pCO_2 rises over the timescale for ALK to be restored; the ~10 Myr residence time of modern SO_4^{2-} is often taken as the duration over which changes in pCO_2 are manifest (Burke et al., 2018).

$$\frac{1}{4}FeS_2 + \frac{15}{16}O_2 + \frac{1}{2}H_2O \rightarrow H^+ + \frac{1}{2}SO_4^{2-} + \frac{1}{8}Fe_2O_3 \quad \text{(I-5)}$$

Marine SO_4^{2-} is principally output from the ocean through formation of evaporite minerals and microbial sulfate reduction (Rees, 1970). The formation of evaporite minerals does not impact ALK or DIC directly but may alter them indirectly by lowering the concentration of marine Ca^{2+} and SO_4^{2-} (Shields and Mills, 2021). Microbial sulfate reduction, which depends on parameters such as sedimentation rate and the availability of organic carbon, directly restores ALK and DIC to the ocean-atmosphere system (Figs. I-1 and I-2). The net impact of sulfide oxidation on pCO_2 thus depends on its difference from sulfate reduction rather than on the absolute magnitude of either process. If the sulfur cycle were in steady-state such that ALK lost during sulfide oxidation balanced ALK gained in sediment, rivers would contain abundant sulfide-derived SO_4^{2-} that may exceed silicate-derived cations but sulfide oxidation would not, in a global sense, be altering pCO_2.

These considerations stress that the impact of sulfide oxidation on pCO_2 is deeply intertwined with the accumulation of SO_4^{2-} in seawater and has dynamics analogous but opposite to those of silicate-derived Na^+ and K^+. Like SO_4^{2-}, the monovalent cations impact pCO_2 based on differences between weathering sources and sedimentary sinks. Moreover, is it notable that prior studies have often excluded silicate-derived Na^+ and K^+ when quantifying the impact of weathering on pCO_2 through the assumption that these cations are removed from seawater during reverse weathering reactions. Following this convention, it might be reasonable to assume steady-state in the global sulfur cycle and that sulfide-derived SO_4^{2-} does not impact pCO_2.

On the supply side, the balance between sulfide oxidation and silicate weathering depends on erosion rate. Because sulfide oxidation is a transport-limited process that requires exposure of fresh minerals within the oxidative weathering zone (Calmels et al., 2007), sulfide oxidation will increase during periods of mountain building and abate during times of tectonic quiescence. However, the exposure of fresh mineral phases also encourages silicate weathering. Based on prior work (Torres et al., 2016) and research in this thesis, it seems that sulfide oxidation often exceeds silicate weathering in mountainous environments. Conversely, floodplains primarily host silicate weathering (Lupker et al., 2012). As a result, once floodplains have developed and river dissolved load is predominantly derived from lowland settings, ALK gained through silicate weathering will likely exceed ALK lost through sulfide oxidation. However, it is critical to appreciate that the impact of such supply-side dynamics on pCO_2 depends on both marine output processes and, through them, the timescale under consideration.

I.3: Guiding questions and context

This section provides a motivating question for each chapter in the thesis and summarizes how the projects fit within the larger body of research on river chemistry.

Chapter II: How do we use dissolved river chemistry to quantify weathering?

This chapter reports the development of an open-access numerical tool for apportioning dissolved river chemistry among contributions from weathering end-members (Kemeny and Torres, 2021). The tool is called Mixing Elements ANd Dissolved Isotopes in Rivers (MEANDIR; https://github.com/PrestonCosslettKemeny/MEANDIR). Although river inversion calculations have been applied extensively over the past thirty years, pioneered by Négrel et al. (1993) and famously employed by Gaillardet et al. (1999), no prior studies have provided a full discussion of their underlying mathematics nor how choices during model construction impact results. The first contribution of this work is to synthesize and explain the mathematics of river inversion, and the second is to extend existing numerical methods to quantify processes like sulfide oxidation, petrogenic organic carbon oxidation, and the formation of secondary phases with isotopic fractionation.

Chapter III: Is fluvial SO_4^{2-} $\delta^{34}S$ altered by biological processes?

Prior studies interpreted downstream increases in river SO_4^{2-} $\delta^{34}S$ as reflecting isotopic distillation due to microbial sulfate reduction (Turchyn et al., 2013; Hemingway et al., 2020). If fractionating sulfur transformation are widespread, quantifications of sulfide oxidation and the fraction of river SO_4^{2-} output as sulfide in marine sediment would be biased to lower values (Fike et al., 2015; Burke et al., 2018). However, the identification

of non-conservative sulfur cycling processes in river catchments is often complicated by the presence of multiple weathering lithologies with unknown $\delta^{34}S$ values. This chapter explores the influence of sulfur cycling on river SO_4^{2-} $\delta^{34}S$ using geochemical observations from a small catchment in Iceland with isotopically constrained bedrock. The data indicate that the primary control on SO_4^{2-} $\delta^{34}S$ is not biological activity, but instead that geomorphic regime modulates the supply of sulfide into the weathering zone (Burt et al., 2021).

Chapter IV: Did sulfide oxidation stabilize Cenozoic pCO_2?

Decades of literature have debated the role of mountain building in modulating pCO_2 (Raymo et al., 1998; Raymo and Ruddiman, 1992). Within this debate, silicate weathering of the Himalaya has featured prominently due to the apparent coherence between Cenozoic cooling and the collision of India with Eurasia (Zachos et al., 2001). However, even moderate imbalances between carbon inputs and outputs due to increases in silicate weathering following Himalayan uplift could have repartitioned all CO_2 from the atmosphere into the ocean within only a few Myr (Kerrick and Caldeira, 1999). This chapter evaluates one potential solution to the conundrum, proposed in Torres et al. (2014), which is that sulfide oxidation countered silicate weathering to stabilize Cenozoic pCO_2. Using measurements of major ion chemistry and SO_4^{2-} $\delta^{34}S$ in seasonal water samples from the Nepal Himalaya, this chapter shows that ALK loss due to sulfide oxidation exceeds ALK gain from silicate weathering in upstream catchments but not in the Ganges floodplain (Kemeny et al., 2021a). While sulfide oxidation may thus extend the duration over which silicate weathering could be elevated without catastrophic pCO_2 drawdown, another mechanism may still be necessary to ensure stability of the Cenozoic carbon cycle.

Chapter V: Does permafrost sulfide oxidation positively feedback on climate change?

The melting of previously frozen ground due to anthropogenic climate change induces large chemical fluxes. Previously, much attention has been directed to quantifying the oxidation of aged organic carbon and changes in silicate weathering due to permafrost degradation. However, few studies have considered sulfide oxidation secondary to permafrost degradation (Toohey et al., 2016; Zolkos et al., 2018). This chapter reports observations of dissolved chemistry, SO_4^{2-} $\delta^{34}S$ and $\delta^{18}O$, and sediment $\delta^{34}S$ from the Koyukuk River in Alaska. Elevated ratios of SO_4^{2-}/Cl^- with moderate SO_4^{2-} $\delta^{34}S$ values indicate abundant sulfide oxidation, and timeseries data from the Yukon at Pilot Station show increasing SO_4^{2-} and Ca^{2+} concentrations suggestive of increased sulfide oxidation over the preceding decades. This sulfide could be sourced from either melting permafrost or anthropogenic mining activities. Overall, the exposure and oxidation of sulfide phases by melting permafrost may be an important feedback on anthropogenic climate change.

Chapter VI: What is the ALK/DIC of global weathering and the $\delta^{34}S$ of crustal sulfide?

Burke et al. (2018) used a compilation of global river chemistry to show that approximately one third of global river SO_4^{2-} derives from sulfide oxidation. This chapter extends that analysis by showing that the $\delta^{34}S$ of crustal sulfide is generally heavier than expected on the basis of a 1-input 2-output mass balance model of the global sulfur cycle, and that the fraction of river SO_4^{2-} output as sulfide in marine sediment may be larger than previously calculated. Moreover, this work finds that ALK removed from the ocean-atmosphere system during sulfide oxidation does not fully compensate for ALK sourced during silicate weathering, meaning that chemical weathering results in lower pCO_2 values.

I.4: Looking down the river

The major element and isotope chemistry of river water and suspended sediment are valuable tools for studying the role of weathering in planetary habitability. However, several component of this research would benefit from additional constraints, perspectives, and technologies. This section highlights a few such areas.

I.4.1: Quantifying meteoric inputs through Cl^- critical values

A recurring challenge in the interpretation of river chemistry is the need to account for inputs from meteoric precipitation. There are two primary approaches to this problem. The first method is to define an end-member based on observations of precipitation chemistry and include that end-member within inversion calculations. One issue with this treatment is that, without a strong chemical distinction between precipitation and additional end-members that source Cl^-, such as an evaporite, the inversion may not be able to distinguish among end-member contributions. The second approach is to employ values of Cl^- critical that define the maximum amount of river Cl^- that can be attributed to meteoric inputs, which can be calculated as the concentration of Cl^- in precipitation scaled by the ratio of precipitation to catchment discharge (Gaillardet et al., 1997). Where defined, Cl^- critical values help to allocate the river Cl^- budget and reduce uncertainty in end-member contributions. Unlike the first approach, however, calculating Cl^- critical values requires approximating the degree of evapotranspiration within each catchment. Future research to constrain Cl^- critical values would help to reduce uncertainty in the allocation of the river Cl^- budget and, in turn, reduce uncertainty in the contributions of weathering end-members to river dissolved load.

I.4.2: The need to constrain anthropogenic inputs

A major challenge in studying river chemistry is quantifying and correcting for solutes derived from anthropogenic pollution, which enter rivers both directly and through atmospheric deposition. In general, the community of river geochemists currently lacks strong constraints on either the total amount of anthropogenic SO_4^{2-} in rivers or its range of $^{34}S/^{32}S$ ratios (Berner, 1971; Meybeck, 2003). Common estimates for anthropogenic SO_4^{2-} derive from considering differences in the SO_4^{2-}/Cl^- ratios between polluted and unpolluted rivers, but these comparisons often do not account for how lithologic and erosional context may contribute to observed differences. In the future, improved constraints on anthropogenic SO_4^{2-} may be possible through atmospheric modeling. By accounting for known anthropogenic emissions, models have the potential to quantity the dry deposition of SO_4^{2-} and the incorporation of pollutant SO_4^{2-} into precipitation. Such analyses are particularly critical for improving the interpretation of SO_4^{2-} concentration and SO_4^{2-} $\delta^{34}S$ values in river systems that integrate over vast spatial scales.

I.4.3: Interconnections and emergent behavior in biogeochemical cycles

A conventional view of biogeochemistry focuses on the movements of individual elements; that is, we commonly refer to "the carbon cycle" or "the nitrogen cycle." However, environmental variables such as pCO_2 typically respond to the interactions and emergent dynamics of multiple elemental cycles rather than to any one elemental flux. In a recent example of such interactions, Maffre et al. (2021) argued that sulfide oxidation can result in lower pCO_2 due to a feedback where reduced marine dissolved oxygen concentration results in enhanced burial of organic matter. More broadly, when considering

environmental variables such as seawater pH or the availability of electron donors for microbial metabolisms, the relevant fluxes are protons and electrons. Recasting conventional views of the major elemental cycles into "the proton cycle" and "the electron cycle," as constrained through isotopic ratios, may provide powerful new insights into controls on habitability.

I.4.4: Emerging tools in mass spectrometry

Isotope ratios are important tools for quantifying and diagnosing biogeochemical processes. While several analytical techniques are employed in this thesis, emerging isotopic technologies may revolutionize how we measure isotopic structures and interpret fluvial chemistry. This section addresses existing analytical infrastructure for measuring isotopic ratios and how emerging techniques could improve upon the work in this thesis.

This dissertation includes observations of isotope ratios measured by elemental analyzer isotope ratio mass spectrometry (EA-IRMS) and multi-collector inductively coupled plasma mass spectrometry (MC-ICP-MS). Although many differences distinguish these techniques, they share the fundamental similarity of applying electromagnetic fields to physically separate ion beams. The instruments then record the impact of the ion beams on detectors and the ratio of beam intensities is interpreted as isotopic information. This type of mass spectrometer is broadly known as a sector instrument and has historically been a core technology for isotope analysis. The abilities of such instruments, however, are regulated by their geometry and electromagnetic stability; a stronger magnet, a larger mass spectrometer, or improved electronics all increase ion separation efficiency and the instrument's ability to resolve isotopologues. As a result, sector instruments have become

increasingly large as isotope geochemists have sought higher precision, lower sample requirements, and rarer isotopic forms. However, this tendency towards larger instruments is unsustainable. While certain improvements may extend the lifetime of the approach, such as implementation of cryogenic cooling or hosting ever-larger instruments within shared facilities, it is not clear that further investments in sector instrumentation will continue to expand measurement possibilities. Although sector instruments will always have an important role in geochemical research, the analytical frontier is rapidly shifting.

A second type of mass spectrometer, broadly known as spectroscopy instruments, do not physically separate ion beams. These instruments instead determine isotopic ratios by quantifying the extent to which known wavelengths of light are absorbed by different isotopologues. Spectroscopy instruments do not require large electromagnets and so are attractive for fieldwork and spacecraft missions. However, spectroscopy is a relatively inflexible technique because the instruments rely on absorptions arising from chemical physics and not on the physical impacts of ions. Spectroscopic approaches will continue to grow over the coming decade, but likely to miniaturize measurements already possible through sector instrumentation rather than to enable fundamentally new measurements. There remains great potential in this work, particularly for out-of-lab deployments, for prohibitively expensive measurements such as ^{14}C activity, and for analytes where absorptions are known and optimized such as H_2O, CO_2, and CH_4.

A final and emerging method for measuring isotopic ratios is orbitrap mass spectrometry (Eiler et al., 2017). Instead of physically separating ion beams or relying on the chemical parameters of isotopologues, orbitrap instruments construct mass spectra through a Fourier transformation of the current produced by confined ions. As a result,

orbitrap mass spectrometers have extraordinary mass resolution that can resolve isotopologues which might never be physically separated. Second, orbitrap instruments with electrospray ionization can preserve the isotopic ordering of dissolved oxyanions during analysis (Neubauer et al., 2020). The conservation of isotopic information is different than plasma ionization, where molecules are blown apart before entering the mass spectrometer, or electron-bombardment ionization, which is primarily a technique for gas-phase molecules. However, orbitrap mass spectrometry also carries substantial new complexity. There are important and open questions regarding how to avoid or correct for ionic interactions within the analyzer, as well as how to convert the results of a spectral analysis into international isotopic notation. Looking forward, it might be possible to address several of these challenges by combining orbitrap analysis with sector instrumentation. It seems likely that, within the next decade, commercial entities will sell mass spectrometers bearing an electrospray source, a magnetic sector, and two or three orbitrap mass analyzers.

Several chapters of this thesis report and interpret measurements of river SO_4^{2-} $\delta^{34}S$. However, this dissertation contains only a handful of SO_4^{2-} $\delta^{18}O$ values and zero measurements of $\Delta^{33}S$ or $\Delta^{17}O$. These omissions generally reflect that the sample requirements of relevant techniques exceed what is available for dilute river water. For example, $\delta^{18}O$ can only be measured on samples with sufficient SO_4^{2-} for the precipitation, recovery, and combustion of barite. Furthermore, we do not report observations of the ^{34}S-^{18}O or ^{18}O-^{18}O clumped isotopologues of SO_4^{2-} because methods to make those measurements, even using conventional mass spectrometers, are still under development. These limitations are unfortunate because determining the full isotopic structure of SO_4^{2-}

would strongly constrain the provenance of dissolved SO_4^{2-} and fluvial sulfur transformations. Based on initial results from Neubauer et al. (2020), it appears that orbitrap mass spectrometry can simultaneously resolve the major, minor, and clumped isotopic forms of SO_4^{2-} using only a few nanomole of analyte. It seems extremely likely that, within the coming years, orbitrap analysis will supplant MC-ICP-MS determinations of SO_4^{2-} $\delta^{34}S$ and expand the realm of SO_4^{2-} isotope analysis. Coupled with new measurements of organic molecules, this technology may revolutionize how we quantify the role of fluvial processes in regulating atmospheric CO_2.

I.5: Figures

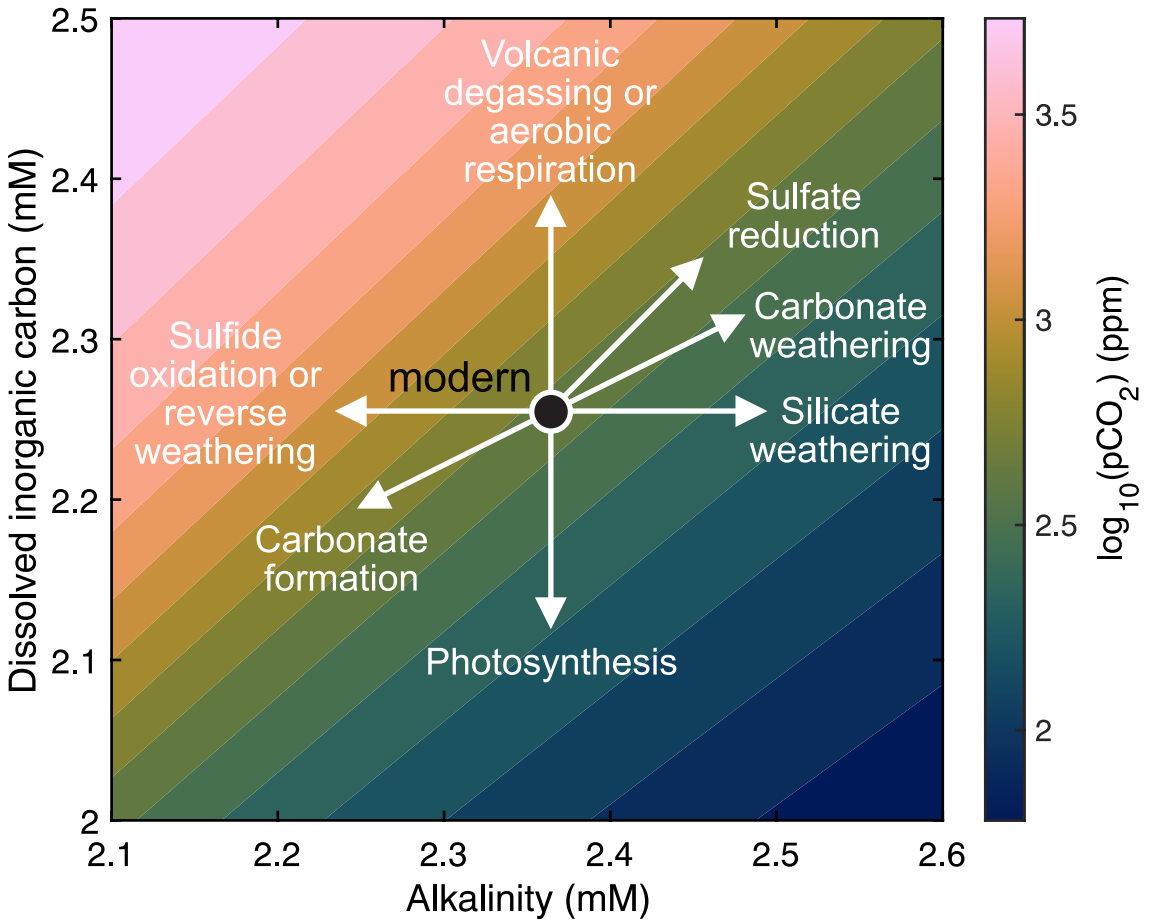

Fig. I-1: The abundance of atmospheric carbon dioxide (pCO_2) is modulated by dissolved inorganic carbon (DIC) and alkalinity (ALK) in the ocean-atmosphere system. Note that slopes of pCO_2 contours are approximately 1:1 near the modern values for ALK and DIC. Silicate weathering, carbonate weathering, and photosynthesis decrease pCO_2, while volcanic degassing, aerobic respiration, carbonate formation, reverse weathering, and sulfide oxidation increase pCO_2. Sulfide oxidation results in higher pCO_2 for the duration over which product SO_4^{2-} remains in seawater. Calculations of pCO_2 from ALK and DIC were performed in CO2SYS (Lewis and Wallace, 1998) using the mean ocean parameters of Sarmiento and Gruber (2006).

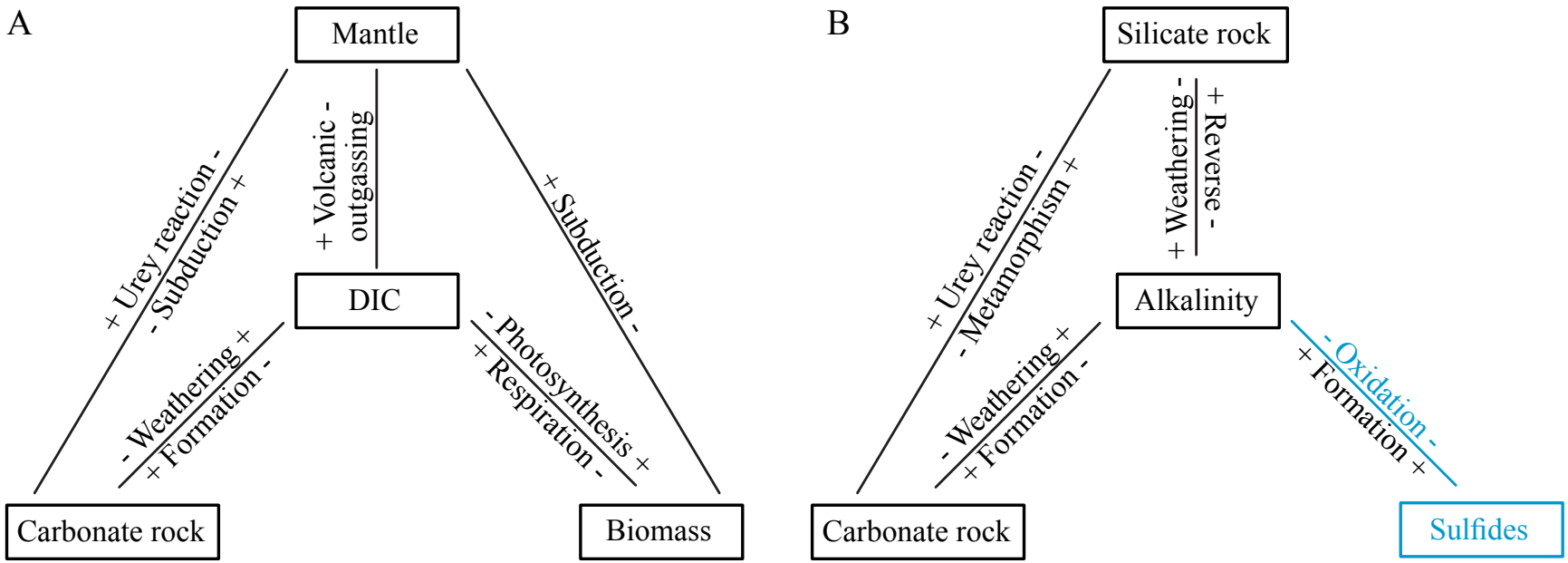

Fig. I-2: Schematic of major reservoirs and processes impacting ocean-atmosphere dissolved inorganic carbon (DIC) and alkalinity (ALK). Boxes indicate reservoirs and lines indicate processes where + and – indicate increases or decreases in reservoir size. For example, photosynthesis decreases ocean-atmosphere DIC and increases the amount of biomass, while sulfide oxidation decreases both ocean-atmosphere ALK and the amount of sulfide. (A) DIC enters the ocean-atmosphere system through volcanic and metamorphic degassing, carbonate rock weathering, and biomass respiration, and is removed through carbonate precipitation and photosynthesis. (B) ALK in the ocean-atmosphere system is increased through silicate weathering, carbonate weathering, and sulfide formation, and is removed through reverse weathering, carbonate burial, and sulfide oxidation. Sulfide oxidation, the focus of the research in this thesis, is highlighted in blue. Sulfide oxidation is seen as a component of the global carbon cycle separate from the standard Urey reaction, which represents the conversion of mantle DIC and silicate alkalinity into carbonate rock.

I.6: References

Archer, D., Kheshgi, H. and Maier-Reimer, E., 1997. Multiple timescales for neutralization of fossil fuel CO_2. *Geophysical Research Letters*, 24(4), pp.405-408. https://doi.org/10.1029/97GL00168.

Berner, R.A., 1971. Worldwide sulfur pollution of rivers. *Journal of Geophysical Research*, 76(27), pp.6597-6600. https://doi.org/10.1029/JC076i027p06597.

Burke, A., Present, T.M., Paris, G., Rae, E.C., Sandilands, B.H., Gaillardet, J., Peucker-Ehrenbrink, B., Fischer, W.W., McClelland, J.W., Spencer, R.G. and Voss, B.M., 2018. Sulfur isotopes in rivers: Insights into global weathering budgets, pyrite oxidation, and the modern sulfur cycle. *Earth and Planetary Science Letters*, 496, pp.168-177. https://doi.org/10.1016/j.epsl.2018.05.022.

Burt, E.I., Bill, M., Conrad, M.E., Quispe, A.J.C., Christensen, J.N., Hilton, R.G., Dellinger, M. and West, A.J., 2021. Conservative transport of dissolved sulfate across the Rio Madre de Dios floodplain in Peru. *Geology*, 49(9), pp.1064-1068. https://doi.org/10.1130/G48997.1.

Calmels, D., Gaillardet, J., Brenot, A. and France-Lanord, C., 2007. Sustained sulfide oxidation by physical erosion processes in the Mackenzie River basin: Climatic perspectives. *Geology*, 35(11), pp.1003-1006. https://doi.org/10.1130/G24132A.1.

Eiler, J., Cesar, J., Chimiak, L., Dallas, B., Grice, K., Griep-Raming, J., Juchelka, D., Kitchen, N., Lloyd, M., Makarov, A. and Robins, R., 2017. Analysis of molecular isotopic structures at high precision and accuracy by Orbitrap mass spectrometry. *International Journal of Mass Spectrometry*, 422, pp.126-142. https://doi.org/10.1016/j.ijms.2017.10.002.

Fike, D.A., Bradley, A.S. and Rose, C.V., 2015. Rethinking the ancient sulfur cycle. *Annual Review of Earth and Planetary Sciences*, 43, pp.593-622. https://doi.org/10.1146/annurev-earth-060313-054802.

Gaillardet, J., Dupre, B., Allegre, C.J. and Négrel, P., 1997. Chemical and physical denudation in the Amazon River Basin. *Chemical geology*, 142(3-4), pp.141-173. https://doi.org/10.1016/S0009-2541(97)00074-0.

Gaillardet, J., Dupré, B., Louvat, P. and Allegre, C.J., 1999. Global silicate weathering and CO_2 consumption rates deduced from the chemistry of large rivers. *Chemical Geology*, 159(1-4), pp.3-30. https://doi.org/10.1016/S0009-2541(99)00031-5.

Hemingway, J.D., Olson, H., Turchyn, A.V., Tipper, E.T., Bickle, M.J. and Johnston, D.T., 2020. Triple oxygen isotope insight into terrestrial pyrite oxidation. *Proceedings of the National Academy of Sciences*, 117(14), pp.7650-7657. https://doi.org/10.1073/pnas.1917518117.

Kemeny, P.C., Lopez, G.I., Dalleska, N.F., Torres, M., Burke, A., Bhatt, M.P., West, A.J., Hartmann, J. and Adkins, J.F., 2021a. Sulfate sulfur isotopes and major ion chemistry reveal that pyrite oxidation counteracts CO_2 drawdown from silicate weathering in the Langtang-Trisuli-Narayani River system, Nepal Himalaya. *Geochimica et Cosmochimica Acta*, 294, pp.43-69. https://doi.org/10.1016/j.gca.2020.11.009.

Kemeny, P.C., Torres, M.A., Lamb, M.P., Webb, S.M., Dalleska, N., Cole, T., Hou, Y., Marske, J., Adkins, J.F. and Fischer, W.W., 2021b. Organic sulfur fluxes and geomorphic control of sulfur isotope ratios in rivers. *Earth and Planetary Science Letters*, 562, p.116838. https://doi.org/10.1016/j.epsl.2021.116838.

Kemeny, P.C. and Torres, M.A., 2021. Presentation and applications of mixing elements and dissolved isotopes in rivers (MEANDIR), a customizable MATLAB model for Monte Carlo inversion of dissolved river chemistry. *American Journal of Science*, 321(5), pp.579-642. https://doi.org/10.2475/05.2021.03.

Lewis, E.R. and Wallace, D.W.R., 1998. Program developed for CO_2 system calculations (No. cdiac: CDIAC-105). Environmental System Science Data Infrastructure for a Virtual Ecosystem. https://doi.org/10.15485/1464255.

Lupker, M., France-Lanord, C., Galy, V., Lavé, J., Gaillardet, J., Gajurel, A.P., Guilmette, C., Rahman, M., Singh, S.K. and Sinha, R., 2012. Predominant floodplain over mountain weathering of Himalayan sediments (Ganga basin). *Geochimica et Cosmochimica Acta*, 84, pp.410-432. https://doi.org/10.1016/j.gca.2012.02.001.

Maffre, P., Swanson-Hysell, N.L. and Goddéris, Y., 2021. Limited carbon cycle response to increased sulfide weathering due to oxygen feedback. *Geophysical Research Letters*, 48(19), p.e2021GL094589. https://doi.org/10.1029/2021GL094589.

Meybeck, M., 2003. Global occurrence of major elements in rivers. *Treatise on Geochemistry*, 5, p.605. https://doi.org/10.1016/B0-08-043751-6/05164-1.

Neubauer, C., Crémière, A., Wang, X.T., Thiagarajan, N., Sessions, A.L., Adkins, J.F., Dalleska, N.F., Turchyn, A.V., Clegg, J.A., Moradian, A. and Sweredoski, M.J., 2020. Stable isotope analysis of intact oxyanions using electrospray quadrupole-orbitrap mass spectrometry. *Analytical Chemistry*, 92(4), pp.3077-3085. https://doi.org/10.1021/acs.analchem.9b04486.

Négrel, P., Allègre, C.J., Dupré, B. and Lewin, E., 1993. Erosion sources determined by inversion of major and trace element ratios and strontium isotopic ratios in river water: The Congo Basin case. *Earth and Planetary Science Letters*, 120(1-2), pp.59-76. https://doi.org/10.1016/0012-821X(93)90023-3.

Raymo, M.E., Ruddiman, W.F. and Froelich, P.N., 1988. Influence of late Cenozoic mountain building on ocean geochemical cycles. *Geology*, 16(7), pp.649-653. https://doi.org/10.1130/0091-7613(1988)016<0649:IOLCMB>2.3.CO;2.

Raymo, M.E. and Ruddiman, W.F., 1992. Tectonic forcing of late Cenozoic climate. *Nature*, 359(6391), pp.117-122. https://doi.org/10.1038/359117a0.

Rees, C.E., 1970. The sulphur isotope balance of the ocean: An improved model. *Earth and Planetary Science Letters*, 7(4), pp.366-370. https://doi.org/10.1016/0012-821X(69)90051-X.

Sarmiento, J.L. and Gruber, N., 2006. Ocean Biogeochemical Dynamics. Princeton University Press. https://doi.org/10.2307/j.ctt3fgxqx.

Shields, G.A. and Mills, B.J., 2021. Evaporite weathering and deposition as a long-term climate forcing mechanism. *Geology*, 49(3), pp.299-303. https://doi.org/10.1130/G48146.1.

Toohey, R.C., Herman-Mercer, N.M., Schuster, P.F., Mutter, E.A. and Koch, J.C., 2016. Multidecadal increases in the Yukon River Basin of chemical fluxes as indicators of changing flowpaths, groundwater, and permafrost. *Geophysical Research Letters*, 43(23), pp.12-120. https://doi.org/10.1002/2016GL070817.

Torres, M.A., West, A.J. and Li, G., 2014. Sulphide oxidation and carbonate dissolution as a source of CO_2 over geological timescales. *Nature*, 507(7492), pp.346-349. https://doi.org/10.1038/nature13030.

Torres, M.A., West, A.J., Clark, K.E., Paris, G., Bouchez, J., Ponton, C., Feakins, S.J., Galy, V. and Adkins, J.F., 2016. The acid and alkalinity budgets of weathering in the Andes–Amazon system: Insights into the erosional control of global biogeochemical cycles. *Earth and Planetary Science Letters*, 450, pp.381-391. https://doi.org/10.1016/j.epsl.2016.06.012.

Turchyn, A.V., Tipper, E.T., Galy, A., Lo, J.K. and Bickle, M.J., 2013. Isotope evidence for secondary sulfide precipitation along the Marsyandi River, Nepal, Himalayas. *Earth and Planetary Science Letters*, 374, pp.36-46. https://doi.org/10.1016/j.epsl.2013.04.033.

Urey, H.C., 1952. On the early chemical history of the earth and the origin of life. *Proceedings of the National Academy of Sciences of the United States of America*, 38(4), p.351. https://doi.org/10.1073/pnas.38.4.351.

Witkowski, C.R., Weijers, J.W., Blais, B., Schouten, S. and Sinninghe Damsté, J.S., 2018. Molecular fossils from phytoplankton reveal secular pCO_2 trend over the Phanerozoic. *Science Advances*, 4(11), p.eaat4556. https://doi.org/10.1126/sciadv.aat4556.

Zachos, J., Pagani, M., Sloan, L., Thomas, E. and Billups, K., 2001. Trends, rhythms, and aberrations in global climate 65 Ma to present. *Science*, 292(5517), pp.686-693. https://doi.org/10.1126/science.1059412.

Zolkos, S., Tank, S.E. and Kokelj, S.V., 2018. Mineral weathering and the permafrost carbon-climate feedback. *Geophysical Research Letters*, 45(18), pp.9623-9632. https://doi.org/10.1029/2018GL078748.

Chapter II

Presentation and Applications of Mixing Elements ANd Dissolved Isotopes in Rivers (MEANDIR), a Customizable MATLAB Model for Monte Carlo Inversion of Dissolved River Chemistry

Preston Cosslett Kemeny[1], Mark A. Torres[2]

[1] Division of Geological and Planetary Sciences, California Institute of Technology, Pasadena, CA, USA
[2] Department of Earth, Environmental and Planetary Sciences, Rice University, Houston, TX, USA

Keywords: River inversion, river geochemistry, chemical weathering, sulfide oxidation, petrogenic organic carbon, RZC, pCO_2

Kemeny, P.C. and Torres, M.A., 2021. Presentation and applications of mixing elements and dissolved isotopes in rivers (MEANDIR), a customizable MATLAB model for Monte Carlo inversion of dissolved river chemistry. *American Journal of Science*, 321(5), pp.579-642. https://doi.org/10.2475/05.2021.03.

II.1: Abstract

The dissolved chemistry of rivers has been extensively studied to elucidate physical and climatic controls of chemical weathering at local to global spatial scales, as well as the impacts of chemical weathering on climate over short to geologic temporal scales. Within this effort, mixing models with Monte Carlo uncertainty propagation are a common tool for inverting measurements of dissolved river chemistry to distinguish among contributions from end-members with distinct elemental and/or isotopic compositions. However, the methods underlying prior river inversion models have typically been opaque. Here we present Mixing Elements ANd Dissolved Isotopes in Rivers (MEANDIR), a set of MATLAB scripts that enable highly customizable inversion of dissolved river chemistry with Monte Carlo propagation of uncertainty. First, we present an overview of the mathematics underlying MEANDIR. This overview includes, among other topics, derivation of equations for mass balance, implementation of chlorine critical values, construction of cost functions, normalization to the sum of dissolved variables, quantification of river sulfate sourced from pyrite oxidation, resolution of petrogenic organic carbon oxidation, representation of secondary phase formation with isotopic fractionation, and calculation of the impact of weathering on atmospheric carbon dioxide. Second, we apply MEANDIR to five previously published datasets to demonstrate the sensitivity of results to parameter choices. We invert data from two global compilations of river chemistry (Gaillardet et al., 1999; Burke et al., 2018), the major element chemistry and sulfate sulfur isotope ratios of rivers in the Peruvian Amazon (Torres et al., 2016), the major element chemistry of Icelandic rivers (Gíslason et al., 1996), and the major and trace element chemistry of water samples from the Mackenzie River (Horan et al., 2019). MEANDIR and its user guide are freely available online.

II.2: Introduction to MEANDIR

Chemical weathering modulates the partial pressure of atmospheric carbon dioxide (CO_2) by sourcing alkalinity (ALK) and dissolved inorganic carbon (DIC) to the coupled ocean-atmosphere system (Gaillardet et al., 1999). Although silicate weathering is generally thought to regulate atmospheric CO_2 over geologic timescales (Urey, 1952; Walker et al., 1981), recent efforts have shown that the negative ALK flux from sulfide oxidation can also substantially impact CO_2 over the duration for which seawater sulfate (SO_4^{2-}) concentrations remain elevated (Spence and Telmer, 2005; Lerman et al., 2007; Calmels et al., 2007; Torres et al., 2016; Burke et al., 2018). Similarly, the oxidation of petrogenic organic carbon (C_{org}) exerts a major influence on atmospheric CO_2 by adding DIC into the ocean-atmosphere system (France-Lanord and Derry, 1997; Bolton et al., 2006; Bouchez et al., 2010; Horan et al., 2019). Because the impact of weathering on the global carbon cycle depends on mineralogy, the relative importance of acids, and petrogenic carbon fluxes, it is crucial to quantitatively constrain the prevalence and controls of different mechanisms of chemical denudation.

The primary tool for quantifying chemical weathering is measurement of the concentrations ($[Ca^{2+}]$, $[Mg^{2+}]$, $[Sr^{2+}]$, $[Na^{+}]$, $[K^{+}]$, $[Cl^{-}]$, $[SO_4^{2-}]$, [Si], etc.) and isotopic ratios ($^{87}Sr/^{86}Sr$, $^{34}S/^{32}S$, $^{44}Ca/^{40}Ca$, $^{30}Si/^{28}Si$, etc.) of elements dissolved in river water (Stallard and Edmond, 1983; Négrel et al., 1993; Gaillardet et al., 1999; Moon et al., 2014; Burke et al., 2018). By inverting the relative abundance of dissolved variables with knowledge of weathering lithologies, researchers model the provenance of each constituent and the associated weathering fluxes of ALK and DIC (Négrel et al., 1993; Gaillardet et al., 1999). One common form of such inversions takes a Monte Carlo approach to propagation

of uncertainty, in which the chemical composition of end-members and samples is varied throughout the calculation in order to constrain the range of possible results. However, Monte Carlo inversion models are subject to many assumptions that alter both the results and the efficiency with which they are attained. As river inversion models expand in scope to utilize large new data sets, such as Hartmann et al. (2014), it becomes increasingly important to use efficient, reliable schemes for calculating the fractional contributions of weathering lithologies. Although the nuances of inverting river dissolved load may seem esoteric, these calculations are critical for quantifying the fluxes of ALK and DIC from carbonate and silicate weathering, which are used to calibrate models of the global carbon cycle (Li and Elderfield, 2013; Caves et al., 2016).

Here we introduce Mixing Elements ANd Dissolved Isotopes in Rivers (MEANDIR), a customizable set of MATLAB scripts for inverting the dissolved chemistry of rivers for the fractional contributions of end-members and for constraining the chemical and isotopic compositions of those end-members (Fig. II-1). The required inputs to MEANDIR are measurements of major or trace element concentrations and isotope ratios, a user-defined set of initial end-member chemical compositions, and choices for how to perform the inversion. In turn, MEANDIR inverts the dissolved observations for the fractional contributions of each end-member to the budget of each dissolved variable; this attribution includes solute sources such as silicate weathering and atmospheric deposition, as well as solute sinks such as the formation of isotopically fractionated secondary phases. By isolating successful simulations following user-defined criteria, the model constrains the chemical composition of each end-member. Moreover, when a pollution end-member is well-defined, MEANDIR is capable of modeling the contributions of anthropogenic

inputs to dissolved river data (Berner, 1971). MEANDIR can also utilize a novel normalization strategy to model chemical processes as independent end-members, including sulfide oxidation, organic carbon oxidation, and CO_2 exchange between the atmosphere and river. Furthermore, MEANDIR quantifies the ratio of changes in ALK to changes in DIC associated with chemical weathering upstream of a water sampling site.

MEANDIR allows users to select among different data normalizations, variable combinations of observations and end-members, different types of precipitation corrections, and several standard or custom cost functions for performing the inversion. MEANDIR currently supports inversion of the following variables, where brackets represent concentration and δ represents the normalized isotopic ratio ($R_{sample}/R_{standard}$-1, where R is an isotopic ratio, and δ is typically reported in ‰) following standard conventions: [ALK], [DIC], $[Ca^{2+}]$, $[Mg^{2+}]$, $[Na^{+}]$, $[K^{+}]$, $[Sr^{2+}]$, $[HCO_3^-]$, $[Cl^-]$, $[SO_4^{2-}]$, $[NO_3^-]$, $[PO_4^{3-}]$, [Si], [Ge], $[Li^+]$, $[F^-]$, [Fe], [B], [Re], [Mo], [Os], δ^7Li, HCO_3^- or DIC δ^{13}C and normalized $^{14}C/^{12}C$ ratio, SO_4^{2-} δ^{34}S and δ^{18}O, δ^{26}Mg, δ^{30}Si, $\delta^{44/40}$Ca and $\delta^{44/42}$Ca, δ^{56}Fe, $^{87}Sr/^{86}Sr$, δ^{98}Mo, and $^{187}Os/^{188}Os$. Additional dissolved constituents can be added to the model or can utilize the slot of an otherwise unused variable.

The fundamental mass balance equation for river inversion models has been presented previously (Négrel et al., 1993; Gaillardet et al., 1999; Moon et al., 2016; Torres et al., 2016; Burke et al., 2018), but few detailed discussions or line-by-line calculations have been published. Existing calculations are also mostly written in code, such as the MATLAB files of Torres et al. (2016) and the Python files of Hemingway et al. (2020), rather than being written symbolically. Overall, methods previously used to invert observations of dissolved river chemistry are relatively opaque and difficult to modify for

new applications. A major goal of our work in this article is thus to provide a flexible tool to the geochemical community for inverting observations of dissolved river chemistry, as well as to describe the choices inherent in river inversion models and clarify how the decisions during model construction impact results.

An extensive literature exists on the mathematics of numerical inversion, including published models for treating geochemical data (Pisias et al., 2013), quantification of uncertainty in source partitioning (Phillips and Gregg, 2001; 2003; Parnell et al., 2010), the selection of end-members (Dunlea and Murray, 2015), and the statistics of data with sum equal to 1 (known as a "unit-sum" constraint or, more broadly, "compositional" data; Miesch, 1976; Aitchison, 1983). However, no dedicated tool exists for customizable inversion of dissolved river chemistry and the problems that naturally arise during such calculations. Unlike MEANDIR, existing tools are not constructed to quantify the fraction of carbonate weathering relative to sulfuric acid weathering (Torres et al., 2016), or to constrain the chemical composition of secondary phases formed with isotopic fractionation. Although the mathematics underlying river inversion have been established for decades, MEANDIR is a new and useful tool because it is tailored to address the issues typically encountered by river geochemists inverting observations of dissolved chemistry. MEANDIR is freely available online, commented, and accompanied by a user guide, making the code substantially more accessible than prior inversion models. We readily acknowledge that ample opportunity remains to improve MEANDIR, such as through implementation of Markov Chain methods, programs for identification of end-members based on raw chemical observations, and refactoring to improve efficiency and readability. We hope such improvements may be implemented in future releases.

In this article, we first present the mathematics of MEANDIR, beginning with the derivation of the fundamental mass balance equations. We then test the performance of MEANDIR using several previously published datasets. We apply the model to two global compilations of dissolved river chemistry (Gaillardet et al., 1999; Burke et al., 2018), river data from Iceland (Gíslason et al., 1996), river data from the Peruvian Amazon (Torres et al., 2016), and river data from the Mackenzie River basin (Horan et al., 2019). We explore the sensitivity of model results to the variable or combination of variables used for normalization (for example, dividing all solute observations by the amount of Na^+ or the sum of dissolved cations), the distribution of possible end-member chemistry, the cost function of the inversion, and whether all samples use the same end-member selections. We also demonstrate the ability of MEANDIR to quantify the loss of dissolved constituents into secondary phases such as clays, validate different approaches for calculating the $\delta^{34}S$ of river SO_4^{2-} derived from the oxidation of pyrite (FeS_2) (Torres et al., 2016; Burke et al., 2018; Hemingway et al., 2020; Kemeny et al., 2021a), and extend a formalism previously defined in Torres et al. (2016) to account for oxidation of petrogenic organic carbon.

II.3: Mathematics of MEANDIR

II.3.1: Overview

This section is concerned with the mathematics of river mixing models utilizing Monte Carlo propagation of uncertainty. We attempt to present existing inversion methods and extend those quantitative frameworks for novel applications. Table II-1 summarizes the key points of this section. After deriving the mass balance equations that underlie MEANDIR, we discuss three core components of river inversions: selection of end-members, construction of a cost function, and selection of successful simulations. We identify many additional complexities: normalizing to the sum of cations or sum of other dissolved variables (including SO_4^{2-}, ALK, and DIC), accounting for Cl^- from meteoric precipitation, quantifying the formation and chemistry of secondary phases formed with isotopic fractionation, calculating the fractions of river SO_4^{2-} sourced from oxidation of FeS_2 and DIC sourced from oxidation of petrogenic C_{org}, including HCO_3^- in the inversion, and calculating the impacts of carbonate weathering, sulfuric acid weathering, and organic carbon oxidation on atmospheric CO_2. Each of these components is discussed below and several are demonstrated in the text by applying MEANDIR to published datasets. The variables, superscripts, and subscripts used throughout this article are summarized in Tables II-2 and II-3.

II.3.2: Mass balance equations

We first consider inversion of a single river water sample with known end-member chemistry. The number of moles (χ) of an element in a river water sample is the sum of contributions from n distinct end-members (Eq. II-1; Négrel et al., 1993). End-members in

our formalism are indexed by s between 1 and n, where s refers to a source or sink; χ is given the superscript s to refer to the sth end-member and the superscript riv to indicate a river water sample. To indicate that the chosen χ is merely one dissolved variable from a set of k observations, χ is given a subscript i between 1 and k to refer to the ith variable. When the ith variable is a dissolved element, χ_i^{riv} indicates the number of moles of the ith variable in a sample of river water and χ_i^s indicates the number of moles of the ith variable derived from the sth end-member (Eq. II-1). In general, we will use rectangular brackets to indicate expressions within summations.

$$\chi_i^{riv} = \Sigma_s^n[\chi_i^s] \tag{II-1}$$

For isotopic variables, each contribution is weighted by the corresponding isotopic composition (Eq. II-2). When the ith variable is an isotopic observation, we represent the isotopic information of the sth end-member as ${}^A R_i^s$ where R represents an isotopic ratio, i takes on the relevant element or molecule for the given isotopic system, and A represents the cardinal mass of the heavier isotope. For example, ${}^{34}R_{SO_4^{2-}}^{riv}$ refers to the ${}^{34}S/{}^{32}S$ ratio of river SO_4^{2-}, and ${}^{44}R_{Ca^{2+}}^s$ refers to the ${}^{44}Ca/{}^{40}Ca$ ratio of Ca^{2+} released by the sth end-member. Note that in all equations ${}^A R_i^s$ should formally refer to the isotopic mass fraction, but here we use the isotopic ratio for simplicity.

$$\chi_i^{riv} \cdot {}^A R_i^{riv} = \Sigma_s^n\left[\chi_i^s \cdot {}^A R_i^s\right] \tag{II-2}$$

Solute observations are typically measurements of abundance normalized by liquid volume (μM or mg/L), while measurements of solids are typically abundance normalized by mass (ppm or wt%). The two sets of measurements are made comparable through molar ratios. One dissolved variable, or a combination of variables, will thus serve as a "normalization variable" in order to generate a set of molar ratios from measurements of dissolved concentrations or the relative mass abundances in solid end-members. We indicate the normalization variable with the subscript norm. Although commonly $\chi_{norm} = \chi_{Na^+}$ (Négrel et al., 1993), alternative choices are possible and discussed extensively later in this article.

The contribution of the sth end-member to χ_i^{riv} (Eq. II-3) or to $\chi_i^{riv} \cdot {}^{A}R_i^{riv}$ (Eq. II-4) is found by scaling χ_{norm}^s by the ratio χ_i^s/χ_{norm}^s or the ratio $(\chi_i^s \cdot {}^{A}R_i^s)/\chi_{norm}^s$. In turn, we can define f_i^s as the fractional contribution of the sth end-member to the ith variable either for elemental (Eq. II-5) or isotopic information (Eq. II-6). The ratios $\chi_i^{riv}/\chi_{norm}^{riv}$ or $\left(\chi_i^{riv} \cdot {}^{A}R_i^{riv}\right)/\chi_{norm}^{riv}$ can then be expressed as the sums of fractional contributions from each of n end-members to χ_{norm}^{riv} multiplied by the corresponding χ_i^s/χ_{norm}^s (Eq. II-7) or $\left(\chi_i^s \cdot {}^{A}R_i^s\right)/\chi_{norm}^s$ (Eq. II-8) of each end-member.

$$\chi_i^{riv} = \Sigma_s^n \left[\chi_{norm}^s \left(\frac{\chi_i^s}{\chi_{norm}^s}\right)\right] \tag{II-3}$$

$$\chi_i^{riv} \cdot {}^{A}R_i^{riv} = \Sigma_s^n \left[\chi_{norm}^s \left(\frac{\chi_i^s \cdot {}^{A}R_i^s}{\chi_{norm}^s}\right)\right] \tag{II-4}$$

$$f_i^s = \frac{\chi_i^s}{\chi_i^{riv}} \tag{II-5}$$

$$f_i^s = \frac{\chi_i^s \cdot {}^{A}R_i^s}{\chi_i^{riv} \cdot {}^{A}R_i^{riv}} \tag{II-6}$$

$$\frac{\chi_i^{riv}}{\chi_{norm}^{riv}} = \frac{\Sigma_s^n\left[\chi_{norm}^s\left(\frac{\chi_i^s}{\chi_{norm}^s}\right)\right]}{\chi_{norm}^{riv}} = \Sigma_s^n\left[\left(\frac{\chi_{norm}^s}{\chi_{norm}^{riv}}\right)\left(\frac{\chi_i^s}{\chi_{norm}^s}\right)\right] = \Sigma_s^n\left[f_{norm}^s\left(\frac{\chi_i^s}{\chi_{norm}^s}\right)\right] \quad \text{(II-7)}$$

$$\left(\frac{\chi_i^{riv\cdot {}^A R_i^{riv}}}{\chi_{norm}^{riv}}\right) = \frac{\Sigma_s^n\left[\chi_{norm}^s\left(\frac{\chi_i^{s\cdot {}^A R_i^s}}{\chi_{norm}^s}\right)\right]}{\chi_{norm}^{riv}} = \Sigma_s^n\left[\left(\frac{\chi_{norm}^s}{\chi_{norm}^{riv}}\right)\left(\frac{\chi_i^{s\cdot {}^A R_i^s}}{\chi_{norm}^s}\right)\right] = \Sigma_s^n\left[f_{norm}^s\left(\frac{\chi_i^{s\cdot {}^A R_i^s}}{\chi_{norm}^s}\right)\right] \quad \text{(II-8)}$$

A single sample defines k linear equations that can be written in matrix form as $\mathbf{b} = \mathbf{A} \cdot \mathbf{f}$. The ith position of the observation vector $\mathbf{b}$ (size k x 1) is either a normalized elemental concentration or the normalized product of an element and its isotopic ratio (Eq. II-9). Matrix $\mathbf{A}$ (size k x n) is defined to contain the end-member elemental or isotopic compositions, using the same χ_{norm} as used in $\mathbf{b}$ (Eq. II-10). The solution vector $\mathbf{f}$ (size n x 1) contains the fractional contributions from each end-member to the normalization variable (the f_{norm}^s values) for the sample described in $\mathbf{b}$ with end-member matrix $\mathbf{A}$ (Eq. II-11).

$$\mathbf{b}(i) = \left(\frac{\chi_i^{riv}}{\chi_{norm}^{riv}}\right) \text{ or } \mathbf{b}(i) = \left(\frac{\chi_i^{riv\cdot {}^A R_i^{riv}}}{\chi_{norm}^{riv}}\right) \quad \text{(II-9)}$$

$$\mathbf{A}(i,s) = \left(\frac{\chi_i^s}{\chi_{norm}^s}\right) \text{ or } \mathbf{A}(i,s) = \left(\frac{\chi_i^{s\cdot {}^A R_i^s}}{\chi_{norm}^s}\right) \quad \text{(II-10)}$$

$$\mathbf{f}(s) = f_{norm}^s \quad \text{(II-11)}$$

Generic (Eq. II-12) and specific (Eq. II-13) examples of the equation $\mathbf{b} = \mathbf{A} \cdot \mathbf{f}$ are given below for three dissolved concentrations and one isotope ratio (indexed by i_1, i_2, i_3, with the isotopic ratio on the i_3 variable, or Na^+, Cl^-, Ca^{2+}, and $^{44}Ca/^{40}Ca$) and three end-members (indexed by s_1, s_2, and s_3, or carbonate (carb), silicate (slct), and precipitation (prec)) where $\chi_{norm} = \chi_{Na^+}$. Note that, because one of the dissolved variables is equal to

the normalization variable, the corresponding equation simplifies to $1 = \Sigma_s^n\left[f_{Na^+}^s\right] = \Sigma_s^n[f_{norm}^s]$ (first row of Eq. II-13). We stress that this equation results from our starting point of fundamental mass balance and is not taken axiomatically; not all choices of χ_{norm} lead directly to an equation comparable to $1 = \Sigma_s^n[f_{norm}^s]$. For example, when normalization is to the sum of dissolved variables instead of a single dissolved variable, an equation of this type does not appear without summing multiple normalized mass balance equations.

$$\begin{bmatrix} \left(\frac{\chi_{i_1}^{riv}}{\chi_{norm}^{riv}}\right) \\ \left(\frac{\chi_{i_2}^{riv}}{\chi_{norm}^{riv}}\right) \\ \left(\frac{\chi_{i_3}^{riv}}{\chi_{norm}^{riv}}\right) \\ \left(\frac{\chi_{i_3}^{riv} \cdot {}^{A}R_{i_3}^{riv}}{\chi_{norm}^{riv}}\right) \end{bmatrix} = \begin{bmatrix} \left(\frac{\chi_{i_1}^{s_1}}{\chi_{norm}^{s_1}}\right) & \left(\frac{\chi_{i_1}^{s_2}}{\chi_{norm}^{s_2}}\right) & \left(\frac{\chi_{i_1}^{s_3}}{\chi_{norm}^{s_3}}\right) \\ \left(\frac{\chi_{i_2}^{s_1}}{\chi_{norm}^{s_1}}\right) & \left(\frac{\chi_{i_2}^{s_2}}{\chi_{norm}^{s_2}}\right) & \left(\frac{\chi_{i_2}^{s_3}}{\chi_{norm}^{s_3}}\right) \\ \left(\frac{\chi_{i_3}^{s_1}}{\chi_{norm}^{s_1}}\right) & \left(\frac{\chi_{i_3}^{s_2}}{\chi_{norm}^{s_2}}\right) & \left(\frac{\chi_{i_3}^{s_3}}{\chi_{norm}^{s_3}}\right) \\ \left(\frac{\chi_{i_3}^{s_1} \cdot {}^{A}R_{i_3}^{s_1}}{\chi_{norm}^{s_1}}\right) & \left(\frac{\chi_{i_3}^{s_2} \cdot {}^{A}R_{i_3}^{s_2}}{\chi_{norm}^{s_2}}\right) & \left(\frac{\chi_{i_3}^{s_3} \cdot {}^{A}R_{i_3}^{s_3}}{\chi_{norm}^{s_3}}\right) \end{bmatrix} \begin{bmatrix} f_{norm}^{s_1} \\ f_{norm}^{s_2} \\ f_{norm}^{s_3} \end{bmatrix} \quad \text{(II-12)}$$

$$\begin{bmatrix} \left(\frac{\chi_{Na^+}^{riv}}{\chi_{Na^+}^{riv}}\right) = 1 \\ \left(\frac{\chi_{Cl^-}^{riv}}{\chi_{Na^+}^{riv}}\right) \\ \left(\frac{\chi_{Ca^{2+}}^{riv}}{\chi_{Na^+}^{riv}}\right) \\ \left(\frac{\chi_{Ca^{2+}}^{riv} \cdot {}^{44}R_{Ca^{2+}}^{riv}}{\chi_{Na^+}^{riv}}\right) \end{bmatrix} = \begin{bmatrix} \left(\frac{\chi_{Na^+}^{carb}}{\chi_{Na^+}^{carb}}\right) = 1 & \left(\frac{\chi_{Na^+}^{slct}}{\chi_{Na^+}^{slct}}\right) = 1 & \left(\frac{\chi_{Na^+}^{prec}}{\chi_{Na^+}^{prec}}\right) = 1 \\ \left(\frac{\chi_{Cl^-}^{carb}}{\chi_{Na^+}^{carb}}\right) & \left(\frac{\chi_{Cl^-}^{slct}}{\chi_{Na^+}^{slct}}\right) & \left(\frac{\chi_{Cl^-}^{prec}}{\chi_{Na^+}^{prec}}\right) \\ \left(\frac{\chi_{Ca^{2+}}^{carb}}{\chi_{Na^+}^{carb}}\right) & \left(\frac{\chi_{Ca^{2+}}^{slct}}{\chi_{Na^+}^{slct}}\right) & \left(\frac{\chi_{Ca^{2+}}^{prec}}{\chi_{Na^+}^{prec}}\right) \\ \left(\frac{\chi_{Ca^{2+}}^{carb} \cdot {}^{44}R_{Ca^{2+}}^{carb}}{\chi_{Na^+}^{carb}}\right) & \left(\frac{\chi_{Ca^{2+}}^{slct} \cdot {}^{44}R_{Ca^{2+}}^{slct}}{\chi_{Na^+}^{slct}}\right) & \left(\frac{\chi_{Ca^{2+}}^{prec} \cdot {}^{44}R_{Ca^{2+}}^{prec}}{\chi_{Na^+}^{prec}}\right) \end{bmatrix} \begin{bmatrix} f_{Na^+}^{carb} \\ f_{Na^+}^{slct} \\ f_{Na^+}^{prec} \end{bmatrix} \quad \text{(II-13)}$$

The system of equations defined by $\mathbf{b} = \mathbf{A} \cdot \mathbf{f}$ is solved by optimizing a cost function to minimize the misfit of inversion results from observations. In turn, the inversion-constrained f_{norm}^s values are scaled to reach end-member contributions to the other variables. For elemental observations these values are reached through multiplication

with χ_i^s/χ_{norm}^s and division by $\chi_i^{riv}/\chi_{norm}^{riv}$ (Eq. II-14). In the case of isotopes, values are reached through multiplication with $(\chi_i^s \cdot {}^A R_i^s)/\chi_{norm}^s$ and division by $(\chi_i^{riv} \cdot {}^A R_i^{riv})/\chi_{norm}^{riv}$ (Eq. II-15).

$$f_i^s = \frac{\chi_i^s}{\chi_i^{riv}} = \left(\frac{\chi_i^s}{\chi_i^{riv}}\right)\left(\frac{f_{norm}^s \cdot \chi_{norm}^{riv}}{\chi_{norm}^s}\right) = f_{norm}^s \frac{\left(\frac{\chi_i^s}{\chi_{norm}^s}\right)}{\left(\frac{\chi_i^{riv}}{\chi_{norm}^{riv}}\right)} \quad \text{(II-14)}$$

$$f_i^s = \frac{\chi_i^s \cdot {}^A R_i^s}{\chi_i^{riv} \cdot {}^A R_i^{riv}} = \left(\frac{\chi_i^s \cdot {}^A R_i^s}{\chi_i^{riv} \cdot {}^A R_i^{riv}}\right)\left(\frac{f_{norm}^s \cdot \chi_{norm}^{riv}}{\chi_{norm}^s}\right) = f_{norm}^s \frac{\left(\frac{\chi_i^s \cdot {}^A R_i^s}{\chi_{norm}^s}\right)}{\left(\frac{\chi_i^{riv} \cdot {}^A R_i^{riv}}{\chi_{norm}^{riv}}\right)} \quad \text{(II-15)}$$

II.3.3: Monte Carlo propagation of uncertainty

The preceding discussion focused on a single instance of inverting a single river water sample with known values of end-member χ_i^s/χ_{norm}^s and ${}^A R_i^s$. However, due to the lithological heterogeneity of most river catchments, it is common to employ a Monte Carlo approach to account for the uncertainty in end-member chemical composition. Although in principle one could address uncertainty propagation analytically, and indeed quantifying the uncertainty associated with mixing is analytically tractable in certain cases (Genereux, 1998; He et al., 2020), a Monte Carlo approach generally provides much more flexibility. The Monte Carlo formulation implemented in MEANDIR allows end-members to have different types of chemical distributions while also being subject to solution constraints. The uncertainty due to both of these conditions may be very difficult or impossible to solve analytically.

Application of a Monte Carlo technique entails repeatedly re-defining the entries of the end-member chemical matrix **A** and repeatedly inverting the mass balance equations

for each sample. Prior river inversion models have commonly defined the entries of **A** as having either uniform or normal distributions of possible values. On each inversion instance, a value from each distribution is selected for use in the calculation. MEANDIR currently performs this repeated re-definition of **A** without knowledge of prior results, but implementation of more complex methods for selecting end-member chemistry could be implemented in future releases. MEANDIR can also repeatedly re-define entries of **b**, allowing the model to account for analytical error associated with measurements of dissolved chemistry.

The output of Monte Carlo river mixing models is two sets of distributions for each sample: one set consists of separate distributions of the fraction of each dissolved variable from each end-member (f_i^s values), and the second set consists of separate distributions of the normalized elemental (χ_i^s/χ_{norm}^s) or isotopic $\left({}^{A}R_i^s\right)$ ratios of each end-member. The nature of these two sets of distributions depends on user choices regarding the selection of successful results. For example, when each river water sample uses the same selections from end-member distributions, the distributions describing inversion-constrained end-member chemistry converge. The fundamental problem of river inversion is how to generate these two sets of distributions for each sample using measurements of dissolved chemistry, the analytical error of those measurements, and an initial set of end-member distributions. Once determined, analysis of the inversion-constrained distributions of fractional contributions and end-member chemistry can provide information on chemical weathering upstream of the river water sampling site.

The application of Monte Carlo techniques to river mixing produces many sets of results. Throughout this article we will use “simulation” to refer to the set of results arising

from an individual instance of calculating fractional contributions from river observations (one single solution to the equation $\mathbf{b} = \mathbf{A} \cdot \mathbf{f}$) and "scenario" to distinguish among inversions conducted on different river data, end-members, or model parameters.

II.3.4: Selection of end-members

MEANDIR requires a user-defined number of end-members with defined chemical distributions, although exceptions to the latter condition arise when end-member ratios are set relative to sample chemistry or through fractionation factors. Previously, selection of the number of end-members has relied mostly on lithologic context. Prior work has often included a carbonate lithology and a silicate lithology, where the chemistry of the latter is informed by fluorescence measurements or acid digestions of local bedrock and/or suspended sediment. Additionally, most studies have included an end-member with non-zero $\chi^s_{Cl^-}/\chi^s_{norm}$, typically called either precipitation or evaporite.

An alternative approach for quantifying the number of end-members is Principal Component Analysis (PCA), which is a statistical technique that identifies combinations of variables that minimize variance. Following PCA, a scree test can help inform the user of the number of significant components, which approximates the number of unique sources of variance. Identification of the number of significant components can thus help to identify the number of end-members contributing to the observed river chemistry (Christophersen and Hooper, 1992; Négrel et al., 1993). Importantly, however, when performing PCA on ratios or data subject to a unit-sum constraint, the effects of auto-correlation and closure may require data transformations prior to analysis (Aitchison, 1983).

It is possible to uniquely deconvolve k variables among contributions from n linearly independent end-members when $k = n$. However, this condition does not constrain end-member contributions to be positive and negative contributions are typically unphysical, although exceptions arise when modeling the formation of secondary phases. In an overdetermined system where $k > n$, the system of equations has excess information for constraining fractional contributions to measured dissolved chemistry. In this case exact agreement between end-members and observations is unlikely due to both analytical error and the chemical heterogeneity of bedrock. Conversely, in an under-constrained system where $k < n$, multiple combinations of end-member contributions may explain observations equally well. The number of independent end-members should generally not greatly exceed the number of observations, but can be less than or equal to the number of observations.

In addition to defining the number of end-members, users must also define the allowable ranges in end-member chemical composition. The spread associated with the composition of an end-member, which is used in the Monte Carlo analysis, is typically described as either uniform or normal. In either case, concern is warranted regarding how the structure of the initial distribution may influence the distribution of end-member chemistry in successful simulations. When end-member uncertainty is described with a uniform distribution over a positive domain, no negative end-member ratios are possible and MEANDIR selects end-member ratios from the user-defined distributions. Conversely, when the chemical range of an end-member is described as a normal distribution, a subset of the possible values are likely to be negative. For example, if selecting values from the normal distribution $\mu \pm \mu$, approximately 16% of selections will be negative. If

independently selecting multiple ratios for multiple end-members, many sets of values are likely to contain at least 1 negative term. A similar challenge occurs when selecting end-member ratios subject to a unit-sum constraint, such as when normalizing to the sum of cations; in this case, values greater than 1 are a common, but unphysical, outcome of selecting values from normal distributions. To address these problems, when the user defines end-member uncertainty to be distributed normally, MEANDIR selects end-member chemical ratios from truncated normal distributions. When the normalization is to a dissolved concentration such as χ_{Na^+}, distributions are bound on the lower side at 0. When normalization is to the sum of dissolved variables, ratios with a variable in the numerator constituent to the denominator are bounded between 0 and 1. Notably, the lower truncation is not applied when end-members ratio are allowed to be negative, which can occur when modeling FeS_2 oxidation. Furthermore, an additional constraint from charge balance occurs when all major cations and anions are included in the inversion. In most cases an inversion including $\chi^{riv}_{Ca^{2+}}$, $\chi^{riv}_{Mg^{2+}}$, $\chi^{riv}_{Na^+}$, $\chi^{riv}_{K^+}$, $\chi^{riv}_{SO_4^{2-}}$, $\chi^{riv}_{Cl^-}$, and $\chi^{riv}_{HCO_3^-}$ will represent most of the positive and negative charge in solution. In this case, the sum of an end-member's normalized cation ratios should equal the sum of its normalized anion ratios.

An additional question is whether separate river samples should use the exact same set of end-member values or if samples should be treated independently. For river waters from the same location, such as a time series, it may be appropriate to evaluate all samples using the same set of end-member compositions. However, if there are large seasonal changes in the source of river water, it can be more appropriate to evaluate each sample independently. MEANDIR can run simulations where all samples use independently drawn end-member chemical ratios or where all samples use the same set of end-member ratios.

II.3.5: Cost functions

The equation $\mathbf{b} = \mathbf{A} \cdot \mathbf{f}$ (Eqs. II-9, II-10, and II-11) is solved through optimization of a cost function, indicated as $c(\mathbf{f})$. That is, MEANDIR solves for the vector $\mathbf{f}$ that minimizes a function $c(\mathbf{f})$ given the current end-member matrix $\mathbf{A}$ and observations vector $\mathbf{b}$. Least-squares optimization in MATLAB can be called using the command mldivide, and the command lsqnonneg returns a non-negative least-squares solution. Both of these programs optimize a cost function for absolute misfit between observations and inversion results (Eq. II-16; where subscripts on b, A, and f indicate positions within the relevant vectors or matrix), while lsqnonneg also constrains fractional contributions to be positive. The functions mldivide and lsqnonneg are both available for use in MEANDIR. However, MEANDIR can also solve the equation $\mathbf{b} = \mathbf{A} \cdot \mathbf{f}$ through optimization of custom cost functions. An important custom function, further discussed below, is one that evaluates the proportional misfit between observations and reconstructed river chemistry (Eq. II-17).

$$c(\mathbf{f}) = \sqrt{\Sigma_i^k \left[\Upsilon_i \left(\Sigma_s^n \left[A_{i,s} f_s \right] - b_i \right)^2 \right]} \tag{II-16}$$

$$c(\mathbf{f}) = \sqrt{\Sigma_i^k \left[\Upsilon_i \left(\frac{\Sigma_s^n [A_{i,s} f_s] - b_i}{b_i} \right)^2 \right]} \tag{II-17}$$

The results of river inversion reflect the choice of cost function. For example, if a water sample has $\chi^{riv}_{Ca^{2+}} / \chi^{riv}_{Na^+} = 10$ and $\chi^{riv}_{K^+} / \chi^{riv}_{Na^+} = 1$, an absolute cost function would assign the same cost to a simulation generating $\chi^{riv}_{Ca^{2+}} / \chi^{riv}_{Na^+} = 11$ and $\chi^{riv}_{K^+} / \chi^{riv}_{Na^+} = 1$ as a simulation generating $\chi^{riv}_{Ca^{2+}} / \chi^{riv}_{Na^+} = 10$ and $\chi^{riv}_{K^+} / \chi^{riv}_{Na^+} = 2$. In both cases one ratio

contributes a misfit of 0 and the other contributes a misfit of 1, and these two scenarios would result in the same evaluation of an absolute cost function (Eq. II-16). However, the two scenarios are different in proportional cost (Eq. II-17), where the difference between model results and observations are compared to the observations. The first simulation generates a 10% proportional misfit for $\chi^{riv}_{Ca^{2+}}/\chi^{riv}_{Na^{+}}$ and no misfit for $\chi^{riv}_{K^{+}}/\chi^{riv}_{Na^{+}}$, while the latter generates no misfit for $\chi^{riv}_{Ca^{2+}}/\chi^{riv}_{Na^{+}}$ and a 100% proportional misfit for $\chi^{riv}_{K^{+}}/\chi^{riv}_{Na^{+}}$.

The results of the proportional cost function could be reached using the absolute cost function by including weighting terms, indicated as values contained within the vector $\boldsymbol{\Upsilon}$ (size k x 1) (Eqs. II-16 and II-17). Continuing the above example, the results of the relative cost function could be attained using the absolute cost function by including a weighting term of 10 on the ratio of $\chi^{riv}_{K^{+}}/\chi^{riv}_{Na^{+}}$ and a weighting term of 1 on $\chi^{riv}_{Ca^{2+}}/\chi^{riv}_{Na^{+}}$. In other words, the difference between the absolute and relative cost functions can be partially negated through the use of appropriate weights.

Isotopic ratios introduce an important complication to these considerations. For data reported in δ notation, where 0‰ means having an isotopic ratio equal to international reference materials, proportional misfit is less meaningful than absolute misfit. That is, a difference of 1‰ in δ units between observations and model results should incur the same cost if that difference occurs when the observed value is 0‰ or 20‰. We note that this expectation assumes linearity in δ values, which is generally appropriate at Earth's surface conditions for isotopic systems heavier than hydrogen. Where the 0‰ observation would have infinite proportional misfit as evaluated with a relative cost function (Eq. II-17), fractional misfit for the 20‰ case would be merely 5%.

We identify two main approaches for addressing the reference frame problem associated with δ notation. The first approach, which we do not recommend, is to use an absolute cost function for the isotopic data in δ notation while using a proportional cost function for variables describing normalized elemental abundances. The second mechanism, which we do recommend, is to convert δ notation to isotopic ratios prior to inversion in order to remove the reference frame that defines 0‰. When considering isotopic ratios, rather than δ notation, proportional differences between observations and inversion results become meaningful. Because isotopic data are often reported in δ notation, MEANDIR is able to convert user-supplied δ values to isotopic ratios for inversion with a proportional cost function (Eq. II-17), and then convert the results back to δ notation for ease of analysis. MEANDIR comes equipped with defined values for the isotopic ratios of common reference materials in order to perform the conversion from δ notation to isotopic ratios (Moore and Machlan, 1972; Baertschi, 1976; Chang and Li, 1990; Taylor et al., 1992; Qi et al., 1997; Ding et al., 2001; Valkiers et al., 2005; Bizzarro et al., 2011; Brand et al., 2014; Mayer and Wiser, 2014; Daëron et al., 2016), but users can easily modify these values to reflect the specific reference materials underlying their isotopic measurements.

In summary, MEANDIR allows users to specify whether the cost function should be the built-in functions mldivide or lsqnonneg or should be a user-defined function with weighting terms. In general, we recommend that inversions use a proportional cost function for chemical observations to ensure that variables at low relative abundance are faithfully reconstructed. When inverting isotopic information, we likewise recommend using a proportional cost function for isotopic ratios but, if required, an absolute cost function for

data in δ notation. To balance these competing demands the default optimization in MEANDIR is to minimize a mixed cost function that combines absolute and proportional misfit (Eq. II-18), but where each dissolved variable only contributes to one of the two terms (indicated through the vector **ω**, which only contains values of 1 or 0).

$$c(\mathbf{f}) = \sqrt{\Sigma_i^k \left[(\xi_i Y_i) \left(\omega_i \left(\Sigma_s^n \left[A_{i,s} f_s \right] - b_i \right)^2 + (1 - \omega_i) \left(\frac{\Sigma_s^n \left[A_{i,s} f_s \right] - b_i}{b_i} \right)^2 \right) \right]} \quad \text{(II-18)}$$

Initial values for the optimization can be set equal to the output of the built-in absolute cost functions or set uniformly equal to 1 divided by the number of end-members. Moreover, MEANDIR allows for only a subset of dissolved variables to be included in the cost function evaluation. This serves the purpose of allowing degenerate variables, such as $\chi_{HCO_3^-}^{riv}$ when calculated through charge balance, to be included in the inversion without impacting evaluation of the cost function. To allow observations to be excluded from the cost function, the vector **ξ** contains values of only 0 or 1 (Eq. II-18). Lastly, the use of custom cost functions also allows users to supply custom optimization criteria. For example, MEANDIR could bound end-member fractional contributions between arbitrary ranges or constrain the contributions of certain end-members to be negative.

II.3.6: Selection of successful simulations

Misfit between inversion results and river observations occurs when the chemical composition of end-members is unable to generate sample observations. As discussed above, when dissolved chemistry is normalized to χ_{Na^+} the mass balance equation for $\chi_{Na^+}^{riv}$

simplifies to $1 = \Sigma_s^n\left[f_{Na^+}^s\right]$ (Eq. II-13). However, in inversions that are over-constrained or with inappropriate end-members, in many results $1 \neq \Sigma_s^n\left[f_{Na^+}^s\right]$; rather, $\Sigma_s^n\left[f_{Na^+}^s\right]$ will equal a value that, in conjunction with the other equations being inverted, optimizes the relevant cost function (Eq. II-18). This example demonstrates that, even though the equations given to the inversion are derived from mass balance, simulations may return results that are offset from observations. The user is thus left with either a set of results that require sub-sampling prior to analysis or the implementation of a quality test during each simulation.

A first solution to the problem of low-quality fits is to accept a fraction of all simulations with the lowest misfit between results and observations (Torres et al., 2016). However, this approach does not guarantee that the isolated subset of simulations is a reasonable match to observations. The additional question arises of whether simulations should be culled at the level of each individual river sample or across the entire sample suite. MEANDIR is able to run calculations of this type, in which only a small fraction of simulations with lowest misfit from observations are retained. Based on user selection, MEANDIR can isolate this best fitting fraction at the level of either an individual sample or the entire sample set.

A second solution to the problem of low-quality fits is to accept simulations based on the magnitude of misfit from observations, rather than on misfit relative to other results. One important approach to this problem is to only accept simulations that meet a criterion in which all variables are modeled within a desired precision. We call this approach "sample matching" because the condition for a simulation to count as successful is whether the result recreates sample observations. Analytical error during quantification of major ion concentrations is typically about 5%, so forcing model results to match observations of

dissolved concentrations within about 15% (3σ) would include ~99% of likely values. Notably, if the inversion model already accounts for analytical error when defining the vector **b** of river observations, allowing for misfit between model results and observations may still be required. The sample matching approach ensures that only simulations with acceptable misfit between inversion results and observations are kept while allowing simulations with high misfit to be removed efficiently during the calculation.

The 15% sample matching criteria described above is equivalent to the condition that, for a non-isotopic variable, $0.85 \leq \Sigma_s^n[f_i^s] \leq 1.15$. However, for isotopic information the individual f_i^s values reference the ratio of the product of concentration and isotopic ratio (Eq. II-6), so bounding the sum of such terms between 85% and 115% does not guarantee robust consistency between inversion results and isotopic observations. Rather, MEANDIR accomplishes sample matching for isotopic data by evaluating whether the absolute difference between sample observations and model-reconstructed isotope value is within user-defined limits. This condition can be expressed as whether $\text{diff}_i^{low} \leq {}^{A}R_i^{riv} - \Sigma_s^n[f_i^s \cdot {}^{A}R_i^s]/\Sigma_s^n[f_i^s] \leq \text{diff}_i^{high}$ given user-supplied values of diff_i^{low} and diff_i^{high} as permissible differences. For example, if an inversion included data on both $\chi_{SO_4^{2-}}^{riv}$ and ${}^{34}R_{SO_4^{2-}}^{riv}$, users could specify to only accept simulation results that recreate between 85% and 115% of $\chi_{SO_4^{2-}}^{riv}$ and recreate within ±1‰ of the $\delta^{34}S$ value corresponding to ${}^{34}R_{SO_4^{2-}}^{riv}$.

II.3.7: Defining the fraction of $\chi_{Cl^-}^{riv}$ from precipitation ($\chi_{Cl^-\,critical}^{riv}$ values)

Quantifying the sources of $\chi_{Cl^-}^{riv}$ is important for separating the components of river chemistry that derive from chemical weathering from those derived from cyclic salts. $\chi_{Cl^-}^{riv}$

is often attributed to either precipitation or evaporite dissolution (Galy and France-Lanord, 1999), with a subset of studies also accounting for inputs from hot springs (Tipper et al., 2006) and anthropogenic pollution (Burke et al., 2018). When inverting data with multiple possible sources for $\chi^{riv}_{Cl^-}$, one approach is to first define how much $\chi^{riv}_{Cl^-}$ can be attributed to precipitation, often called "Cl^- critical" and here indicated as $\chi^{riv}_{Cl^-\,critical}$. These values can be derived from the Cl^- concentration of precipitation scaled by a factor reflecting the ratio of precipitation to discharge within a river basin (Gaillardet et al., 1999). When $\chi^{riv}_{Cl^-\,critical} \geq \chi^{riv}_{Cl^-}$, precipitation provides 100% of $\chi^{riv}_{Cl^-}$ (Eq. II-19, where the subscript "prec" indicates the end-member representing meteoric precipitation). In turn, other end-members with non-zero normalized $\chi^{s}_{Cl^-}$ ratios must then have zero fractional contribution to the normalization variable. When $\chi^{riv}_{Cl^-\,critical} < \chi^{riv}_{Cl^-}$, precipitation does not fully account for $\chi^{riv}_{Cl^-}$ and additional Cl^--bearing end-members make contributions to dissolved chemistry (Eq. II-20). Note that Equations II-19 and II-20 are specific instances of Equation II-14.

$$\chi^{riv}_{Cl^-\,critical} \geq \chi^{riv}_{Cl^-}: f^{prec}_{Cl^-} = 1, f^{prec}_{i} = \frac{\left(\frac{\chi^{prec}_{i}}{\chi^{prec}_{Cl^-}}\right)}{\left(\frac{\chi^{riv}_{i}}{\chi^{riv}_{Cl^-}}\right)} \tag{II-19}$$

$$\chi^{riv}_{Cl^-\,critical} < \chi^{riv}_{Cl^-}: f^{prec}_{Cl^-} = \frac{\chi^{riv}_{Cl^-\,critical}}{\chi^{riv}_{Cl^-}}, f^{prec}_{i} = f^{prec}_{Cl^-}\frac{\left(\frac{\chi^{prec}_{i}}{\chi^{prec}_{Cl^-}}\right)}{\left(\frac{\chi^{riv}_{i}}{\chi^{riv}_{Cl^-}}\right)} \tag{II-20}$$

Precipitation also sources dissolved variables other than Cl^-, and the chemistry of the river water sample must be manually adjusted to reflect these additional inputs when correcting $\chi^{riv}_{Cl^-}$ with $\chi^{riv}_{Cl^-\,critical}$ values. Mathematically, the vector **b** must be updated (Eqs.

II-21 and II-22), the matrix **A** should no longer have a column for precipitation, and the vector **f** should no longer have a row for precipitation.

$$\mathbf{b}(\mathrm{i}) = \left(\frac{\chi_{\mathrm{i}}^{\mathrm{riv}}}{\chi_{\mathrm{norm}}^{\mathrm{riv}}}\right) - \mathrm{f}_{\mathrm{norm}}^{\mathrm{prec}} \left(\frac{\chi_{\mathrm{i}}^{\mathrm{prec}}}{\chi_{\mathrm{norm}}^{\mathrm{prec}}}\right) \quad \text{(II-21)}$$

$$\mathbf{b}(\mathrm{i}) = \left(\frac{\chi_{\mathrm{i}}^{\mathrm{riv}} \cdot {}^{\mathrm{A}}\mathrm{R}_{\mathrm{i}}^{\mathrm{riv}}}{\chi_{\mathrm{norm}}^{\mathrm{riv}}}\right) - \mathrm{f}_{\mathrm{norm}}^{\mathrm{prec}} \left(\frac{\chi_{\mathrm{i}}^{\mathrm{prec}} \cdot {}^{\mathrm{A}}\mathrm{R}_{\mathrm{i}}^{\mathrm{prec}}}{\chi_{\mathrm{norm}}^{\mathrm{prec}}}\right) \quad \text{(II-22)}$$

The application of $\chi_{\mathrm{Cl^-\ critical}}^{\mathrm{riv}}$ values becomes difficult when $\chi_{\mathrm{Cl^-}}^{\mathrm{riv}}$ and $\chi_{\mathrm{Cl^-\ critical}}^{\mathrm{riv}}$ are sufficiently large relative to other dissolved variables that removal of $\chi_{\mathrm{Cl^-\ critical}}^{\mathrm{riv}}$ from the water sample causes element ratios to become negative (Eq. II-21). A first solution to this problem is to remove from the river sample as much $\chi_{\mathrm{Cl^-}}^{\mathrm{riv}}$ as possible without causing other ratios to attain negative values. However, if the limiting variable is an observation such as $\chi_{\mathrm{Ca^{2+}}}^{\mathrm{riv}}$, most of the remaining end-members are likely to source this constituent and it becomes difficult to find a solution that faithfully reconstructs dissolved chemistry. Moreover, if precipitation is the only source of $\chi_{\mathrm{Cl^-}}^{\mathrm{riv}}$, removal of only a fraction of $\chi_{\mathrm{Cl^-}}^{\mathrm{riv}}$ will not satisfy sample matching requirements. Instead, the solution implemented in MEANDIR is to continuously re-select the chemical composition of the precipitation end-member until removal of the specified $\chi_{\mathrm{Cl^-\ critical}}^{\mathrm{riv}}$ would not produce negative ratios for the other observations. After the inversion, comparison of the initial and inversion-constrained distributions of normalized $\chi_{\mathrm{Cl^-}}^{\mathrm{prec}}$ ratios can guide decisions on whether the chosen values of $\chi_{\mathrm{Cl^-\ critical}}^{\mathrm{riv}}$ resulted in reasonable changes to the precipitation end-member. Note that additional complexity arises when using $\chi_{\mathrm{Cl^-\ critical}}^{\mathrm{riv}}$ values in simulations that also account for the formation of secondary phases. In this case, removal of the specified amount of

$\chi^{riv}_{Cl^-\,critical}$ resulting in negative values could be a meaningful result reflecting uptake into secondary phases. As a result, MEANDIR does not continuously re-draw the end-member compositions when using $\chi^{riv}_{Cl^-\,critical}$ values and also quantifying secondary phase formation.

Overall, MEANDIR allows the user to choose whether $\chi^{riv}_{Cl^-\,critical}$ values are used in the inversion. When $\chi^{riv}_{Cl^-\,critical}$ values are used, MEANDIR sets the contribution of the precipitation end-member and precipitation is removed from the inversion. Notably, Cl^- is not removed entirely from the inversion unless $\chi^{riv}_{Cl^-} \leq \chi^{riv}_{Cl^-\,critical}$, in which case precipitation accounts for 100% of the observed value. When $\chi^{riv}_{Cl^-\,critical}$ values are not used, $\chi^{riv}_{Cl^-}$ is treated like any other dissolved variables and precipitation is treated like any other end-member.

II.3.8: Mineralogical constraints on the evaporite end-member

Inversion models frequently include an evaporite end-member capable of sourcing $\chi^{riv}_{Cl^-}$ and other dissolved variables to river water. As a simple case, the chemical ratios characterizing such an evaporite could simply reflect user-defined distributions. However, it is also possible to limit the allowable composition of an evaporite end-member by imposing mineralogical constraints. In particular, evaporites are often considered to reflect a stoichiometric combination of gypsum ($CaSO_4 \cdot 2H_2O$) and halite (NaCl), with secondary contributions from additional phases such as epsomite ($MgSO_4 \cdot 7H_2O$) and sylvite (KCl). To reflect this mineral composition, MEANDIR is able to impose an optional constraint on an evaporite end-member that the mole contribution of SO_4^{2-} must equal the sum of contributions from Ca^{2+}, Mg^{2+}, and Sr^{2+} (Eq. II-23), while the molar contribution of Cl^-

must equal the contribution of all other cations (Eq. II-24). We generally recommend applying this mineralogical constraint when quantifying the contributions from an evaporite end-member. Indeed, we apply the constraint during most of the inversion scenarios discussed below for data from Gaillardet et al. (1999) and Burke et al. (2018).

$$\chi_{SO_4^{2-}}^{evap} = \chi_{Ca^{2+}}^{evap} + \chi_{Mg^{2+}}^{evap} + \chi_{Sr^{2+}}^{evap} \quad \text{(II-23)}$$

$$\chi_{Cl^-}^{evap} = \chi_{Na^+}^{evap} + \chi_{K^+}^{evap} + \text{other cations} \quad \text{(II-24)}$$

II.3.9: Normalization with the sum of cations (χ_{Σ^+})

χ_{Na^+} is commonly used as χ_{norm} even though some common end-members, such as carbonate, do not contain substantial Na^+ (Négrel et al., 1993; Gaillardet et al., 1999). This problem has previously been addressed by using high ratios of $\chi_{Ca^{2+}}^{carb}/\chi_{Na^+}^{carb}$, such as 60 ± 30 (Burke et al., 2018), but this approach still allows for simulation results where carbonate provides a meaningful fraction of $\chi_{Na^+}^{riv}$. An alternative approach is to instead normalize to the charge-weighted sum of cations (χ_{Σ^+}), which removes the need for a common element among all end-members and allows lithologies such as carbonate to be represented stoichiometrically (Eq. II-25; Torres et al., 2016). That is, when normalizing with χ_{Σ^+}, the carbonate end-member can have $\chi_{Na^+}^{carb}/\chi_{\Sigma^+}^{carb} = 0$ and $2\chi_{Ca^{2+}}^{carb}/\chi_{\Sigma^+}^{carb} = 1$ (the factor of 2 reflects that χ_{Σ^+} is defined in units of charge-equivalent moles, while $\chi_{Ca^{2+}}$ is defined in units of moles, and the conversion factor is 2 because that value is the charge of dissolved Ca^{2+}). Although the specific example of χ_{Σ^+} in Eq. II-25 considers $\chi_{Ca^{2+}}$, $\chi_{Mg^{2+}}$, χ_{Na^+}, and χ_{K^+}, the mathematics underlying normalization by χ_{Σ^+} are similar regardless of which cations are included. That is, χ_{Σ^+} could also include χ_{Li^+} or $\chi_{Sr^{2+}}$, when available,

or not include χ_{K^+}. We stress that normalizing to χ_{Σ^+} does not introduce new information into the inversion but is merely a restatement of measured quantities that allows for improved representation of end-members.

$$\chi_{\Sigma^+} = 2\chi_{Ca^{2+}} + 2\chi_{Mg^{2+}} + \chi_{Na^+} + \chi_{K^+} \tag{II-25}$$

Analogous to normalization with a single dissolved variable such as χ_{Na^+}, the ratio $\alpha_i\chi_i^{riv}/\chi_{\Sigma^+}^{riv}$ equals the sum of the end-member $\alpha_i\chi_i^s/\chi_{\Sigma^+}^s$ scaled by fractional contributions to $\chi_{\Sigma^+}^{riv}$ (Eq. II-26, where α_i is a factor to convert between units of moles and charge for the ith dissolved variable and s and s' independently index the same list of length n containing all end-members). Observations of dissolved river chemistry normalized with $\chi_{\Sigma^+}^{riv}$ again define a series of k linear equations where the solution vector **f** contains $f_{\Sigma^+}^s$ values (Eq. II-26).

$$\left(\frac{\alpha_i\chi_i^{riv}}{\chi_{\Sigma^+}^{riv}}\right) = \left(\frac{\alpha_i\chi_i^{riv}}{2\chi_{Ca^{2+}}^{riv} + 2\chi_{Mg^{2+}}^{riv} + \chi_{Na^+}^{riv} + \chi_{K^+}^{riv}}\right)$$

$$= \alpha_i\left(\frac{\Sigma_s^n[\chi_i^s]}{\Sigma_{s\prime}^n\left[2\chi_{Ca^{2+}}^{s\prime}\right] + \Sigma_{s\prime}^n\left[2\chi_{Mg^{2+}}^{s\prime}\right] + \Sigma_{s\prime}^n\left[\chi_{Na^+}^{s\prime}\right] + \Sigma_{s\prime}^n\left[\chi_{K^+}^{s\prime}\right]}\right)$$

$$= \alpha_i\Sigma_s^n\left[\frac{\chi_i^s}{\Sigma_{s\prime}^n\left[2\chi_{Ca^{2+}}^{s\prime} + 2\chi_{Mg^{2+}}^{s\prime} + \chi_{Na^+}^{s\prime} + \chi_{K^+}^{s\prime}\right]}\right]$$

$$= \alpha_i\Sigma_s^n\left[\left(\frac{\chi_i^s}{\Sigma_{s\prime}^n\left[2\chi_{Ca^{2+}}^{s\prime} + 2\chi_{Mg^{2+}}^{s\prime} + \chi_{Na^+}^{s\prime} + \chi_{K^+}^{s\prime}\right]}\right)\left(\frac{2\chi_{Ca^{2+}}^s + 2\chi_{Mg^{2+}}^s + \chi_{Na^+}^s + \chi_{K^+}^s}{2\chi_{Ca^{2+}}^s + 2\chi_{Mg^{2+}}^s + \chi_{Na^+}^s + \chi_{K^+}^s}\right)\right]$$

$$= \alpha_i\Sigma_s^n\left[\left(\frac{2\chi_{Ca^{2+}}^s + 2\chi_{Mg^{2+}}^s + \chi_{Na^+}^s + \chi_{K^+}^s}{\Sigma_{s\prime}^n\left[2\chi_{Ca^{2+}}^{s\prime} + 2\chi_{Mg^{2+}}^{s\prime} + \chi_{Na^+}^{s\prime} + \chi_{K^+}^{s\prime}\right]}\right)\left(\frac{\chi_i^s}{2\chi_{Ca^{2+}}^s + 2\chi_{Mg^{2+}}^s + \chi_{Na^+}^s + \chi_{K^+}^s}\right)\right]$$

$$= \Sigma_s^n \left[f_{\Sigma^+}^s \left(\frac{\alpha_i \chi_i^s}{\chi_{\Sigma^+}^s} \right) \right] \quad \text{(II-26)}$$

Normalization with χ_{Σ^+} does not simply result in the equation $1 = \Sigma_s^n \left[f_{\Sigma^+}^s \right]$. This is different from normalization with χ_{Na^+}, where the equation $1 = \Sigma_s^n \left[f_{Na^+}^s \right]$ resulted naturally from the mass balance equation corresponding to the variable χ_{Na^+} (Eq. II-13). However, the equation $1 = \Sigma_s^n \left[f_{\Sigma^+}^s \right]$ can be reached as the sum of mass balance equations for the individual variables normalized by $\chi_{\Sigma^+}^{riv}$ (Eq. II-27). Including the equation $1 = \Sigma_s^n \left[f_{\Sigma^+}^s \right]$ in the inversion is thus degenerate when the mass balance equations for all the elements contributing to χ_{Σ^+} are included. Stated another way, an inversion consisting of concentration data for $\chi_{Na^+}^{riv}$, $\chi_{K^+}^{riv}$, $\chi_{Ca^{2+}}^{riv}$, and $\chi_{Mg^{2+}}^{riv}$ yields a maximum of 4 mixing equations for inversion regardless of whether normalizing the data by one element (χ_{Na^+}) or the sum of all the major cations (χ_{Σ^+}).

$$1 = \left(\frac{2\chi_{Ca^{2+}}^{riv}}{\chi_{\Sigma^+}^{riv}} \right) + \left(\frac{2\chi_{Mg^{2+}}^{riv}}{\chi_{\Sigma^+}^{riv}} \right) + \left(\frac{\chi_{Na^+}^{riv}}{\chi_{\Sigma^+}^{riv}} \right) + \left(\frac{\chi_{K^+}^{riv}}{\chi_{\Sigma^+}^{riv}} \right)$$

$$= \Sigma_s^n \left[f_{\Sigma^+}^s \left(\frac{2\chi_{Ca^{2+}}^s}{\chi_{\Sigma^+}^s} \right) \right] + \Sigma_s^n \left[f_{\Sigma^+}^s \left(\frac{2\chi_{Mg^{2+}}^s}{\chi_{\Sigma^+}^s} \right) \right] + \Sigma_s^n \left[f_{\Sigma^+}^s \left(\frac{\chi_{Na^+}^s}{\chi_{\Sigma^+}^s} \right) \right] + \Sigma_s^n \left[f_{\Sigma^+}^s \left(\frac{\chi_{K^+}^s}{\chi_{\Sigma^+}^s} \right) \right]$$

$$= \Sigma_s^n \left[f_{\Sigma^+}^s \left(\frac{2\chi_{Ca^{2+}}^s + 2\chi_{Mg^{2+}}^s + \chi_{Na^+}^s + \chi_{K^+}^s}{\chi_{\Sigma^+}^s} \right) \right] = \Sigma_s^n \left[f_{\Sigma^+}^s \right] \quad \text{(II-27)}$$

When $\chi_{norm} = \chi_{\Sigma^+}$, the set of river water ratios will be internally consistent when the denominator $\chi_{\Sigma^+}^{riv}$ is calculated using the values of $\chi_{Ca^{2+}}^{riv}$, $\chi_{Mg^{2+}}^{riv}$, $\chi_{Na^+}^{riv}$, $\chi_{K^+}^{riv}$, $\chi_{Sr^{2+}}^{riv}$, etc. in the numerators of each ratio. However, ensuring internal consistency is more challenging

when selecting end-member ratios from user-defined distributions. If all $\alpha_i\chi_i^s/\chi_{\Sigma+}^s$ ratios are selected from given distributions, the resulting set of values will not necessarily sum to unity and would define an internally inconsistent end-member. For example, when $\chi_{\Sigma+}$ includes $\chi_{Ca^{2+}}$, $\chi_{Mg^{2+}}$, χ_{Na^+}, and χ_{K^+}, only three of the four $\chi_{\Sigma+}$-normalized ratios can be selected independently from user-supplied end-member distributions before the fourth is uniquely defined. It is convenient to select a number of $\alpha_i\chi_i^s/\chi_{\Sigma+}^s$ ratios from their respective distributions equal to 1 less than the number of cations constituent to $\chi_{\Sigma+}$ and calculate the final ratio by difference from 1 to ensure the internal consistency of the end-member. In general, the ratio calculated by mass balance should be that with the largest expected $\alpha_i\chi_i^s/\chi_{\Sigma+}^s$ value.

An additional constraint from charge balance occurs when all major cations and anions are included in the inversion. In this case, the sum of cation ratios normalized with $\chi_{\Sigma+}$ must equal the sum of the anion ratios normalized with $\chi_{\Sigma+}$ (Eq. II-28). Similar to ensuring the internal consistency of each end-member by selecting one $\alpha_i\chi_i^s/\chi_{\Sigma+}^s$ ratio to be calculated from the other selections, charge balance is attained by defining a second $\alpha_i\chi_i^s/\chi_{\Sigma+}^s$ ratio for each end-member to be calculated from the other selections.

$$1 = \frac{2\chi_{Ca^{2+}}}{\chi_{\Sigma+}} + \frac{2\chi_{Mg^{2+}}}{\chi_{\Sigma+}} + \frac{\chi_{Na^+}}{\chi_{\Sigma+}} + \frac{\chi_{K^+}}{\chi_{\Sigma+}} = \frac{2\chi_{SO_4^{2-}}}{\chi_{\Sigma+}} + \frac{\chi_{Cl^-}}{\chi_{\Sigma+}} + \frac{\chi_{HCO_3^-}}{\chi_{\Sigma+}} \qquad \text{(II-28)}$$

When normalizing with $\chi_{\Sigma+}$, the user inputs to MEANDIR which elements should be included in the normalization variable and provides end-member distributions for $\alpha_i\chi_i^s/\chi_{\Sigma+}^s$. Furthermore, the user specifies which of the constituent variables should be

calculated through mass balance to ensure the internal consistency of each end-member. When all cations and anions are included in the inversion, the user also selects which variable for each end-member should be calculated through charge balance. MEANDIR does not currently allow the ratio calculated by charge balance to have its numerator constituent to the normalization variable; if the normalization is the sum of $2\chi_{Ca^{2+}}$, $2\chi_{Mg^{2+}}$, and $\chi_{Na^{+}}$, neither $\chi_{Ca^{2+}}$, $\chi_{Mg^{2+}}$, or $\chi_{Na^{+}}$ could be used to ensure charge balance.

II.3.10: Modeling the formation of secondary phases with isotopic fractionation

The formation of secondary clays and calcite is common in river systems (Gíslason et al., 1996; Jacobson et al., 2002; Bickle et al., 2015, 2018). While end-members in river mixing models typically source dissolved constituents to solution and contribute positively to river dissolved load, secondary phases can be viewed as end-members that remove dissolved constituents from solution and contribute negatively to river dissolved load. In MEANDIR, the formation of secondary phases is represented as end-members that make negative contributions to the normalization variable ($\chi^{s}_{norm} < 0, f^{s}_{norm} < 0$). As a result, in inversions including the formation of secondary phases the sum of fractional contributions from primary end-members may exceed the upper boundary of the user-defined range for sample matching while the sum of fractional contributions from all end-members will still fall within the user-defined criteria.

Robust quantification of secondary phase formation requires that secondary products are chemically distinct from the primary lithologies. Secondary clays are often distinct from bedrock and form with isotopic fractionation, suggesting that river mixing models should be able to accurately quantify clay formation. Likewise, MEANDIR can be

used to quantify the formation of secondary carbonate if there is a chemical distinction relative to the weathering end-members. In the absence of a chemical or isotopic signal to differentiate primary from secondary carbonate, such as $\chi^{s}_{Ca^{2+}}/\chi^{s}_{Mg^{2+}}$ or $^{44}Ca/^{40}Ca$, formation of secondary calcite is difficult to separate from a scenario with less gross carbonate weathering.

Modeling river isotopic ratios in the presence of a secondary solute sink requires approaches for both stable isotopic systems, where secondary phases can have different isotopic compositions relative to primary minerals, and radiogenic isotopic systems, where isotopic fractionation is relatively small such that secondary phases can have a similar isotopic composition to the weighted sum of all solute sources. For example, secondary silicate minerals tend to have lower $\delta^{30}Si$ values relative to all primary mineral sources and the magnitude of the isotopic offset tends to vary with the amount of the total Si supply that is incorporated into secondary minerals (Bouchez et al., 2013). Conversely, mass-dependent fractionation in systems such as $^{87}Sr/^{86}Sr$ may be much smaller than radiogenic variations among the sources of Sr^{2+} to river water (de Souza et al., 2010), leading the $^{87}Sr/^{86}Sr$ ratio of clays to approximately match the Sr isotope ratio of sources to the river.

To address these complexities MEANDIR allows users to define the elemental or isotopic composition of secondary end-members relative to the measured values of individual samples or with fractionation relative to sources of the relevant element from all other end-members. For example, rather than setting distributions for the isotopic ratio of a clay end-member prior to inversion, MEANDIR can define the clay $^{87}Sr/^{86}Sr$ ratio to equal the $^{87}Sr/^{86}Sr$ ratio in each river water sample or to equal the $^{87}Sr/^{86}Sr$ ratio of all weathering sources. Similarly, MEANDIR can set the clay end-member to have a $^{30}Si/^{28}Si$

ratio pulled from a uniform distribution corresponding to 1‰ to 2‰ lower than the sample δ^{30}Si value, or to have its $^{30}Si/^{28}Si$ ratio equal to a value fractionated relative to weathering inputs. As with pre-defined chemical distributions, users can select if the isotopic composition of a secondary end-member should have a normal, uniform, or log-uniform distribution of fractionation factors or of values offset from the observed value.

The isotopic composition of secondary phases formed with fractionation depends on the contribution and isotopic composition of all other end-members in the inversion. The isotopic composition of a secondary phase thus cannot be set prior to inversion because it depends on the inversion results. This is fundamentally different from weathering end-members, where user-defined end-member distributions are selected prior to inversion. MEANDIR addresses this problem by employing the optimization process to iteratively re-define the isotopic value of secondary end-members while also solving for fractional contributions, allowing for the representation of isotopic fractionation during the formation of secondary phases.

MEANDIR's treatment of fractionation utilizes a user-supplied fractionation factor (Δ_i) or distribution of fractionation factors that set the degree of isotopic discrimination during secondary phase formation (Eq. II-29, where we use the superscript s^{second} to refer to a generic secondary phase such as a clay, and negative values of Δ_i reflect isotope effects favoring the movement of the light isotope to the secondary phase). In turn, the isotopic difference between the river and the contribution-weighted isotopic composition of sources is equal to the fractionation factor scaled by fractional uptake into the secondary phase (Eq. II-30; Bouchez et al., 2013). Rearranging these equations yields an expression for the isotopic composition of the secondary phase (Eq. II-31) as a function of the fractional

contributions of each end-member (Eq. II-32). MEANDIR is able to account for fractionation during the formation of secondary phases by repeatedly applying Eq. II-32 during the optimization process to continuously re-define the isotopic composition of secondary phases based on the active values for the fractional contributions. In considering Eqs. II-29 to II-32, recall that $f_i^{s^{second}}$ is negative when there is net formation of a secondary phase, and that a negative value of Δ_i favors movement of the lighter isotope to the secondary phase.

$$ {}^{A}R_i^{s^{second}} - {}^{A}R_i^{riv} = \Delta_i \tag{II-29}$$

$$ {}^{A}R_i^{riv} - {}^{A}R_i^{source} = \left(\frac{f_i^{s^{second}}}{\Sigma_{s_i^{source}}^{n_i^{source}} \left[f_i^{s_i^{source}} \right]} \right) \Delta_i \tag{II-30}$$

$$ {}^{A}R_i^{s^{second}} = \left({}^{A}R_i^{source} + \Delta_i \right) + \left(\frac{f_i^{s^{second}}}{\Sigma_{s_i^{source}}^{n_i^{source}} \left[f_i^{s_i^{source}} \right]} \right) \Delta_i \tag{II-31}$$

$$ {}^{A}R_i^{s^{second}} = \left(\frac{\Sigma_{s_i^{source}}^{n_i^{source}} \left[f_i^{s_i^{source}} \cdot {}^{A}R_i^{s_i^{source}} \right]}{\Sigma_{s_i^{source}}^{n_i^{source}} \left[f_i^{s_i^{source}} \right]} + \Delta_i \right) + \left(\frac{f_i^{s^{second}}}{\Sigma_{s_i^{source}}^{n_i^{source}} \left[f_i^{s_i^{source}} \right]} \right) \Delta_i \tag{II-32}$$

In summary, MEANDIR quantifies the formation of secondary phases by allowing the fractional contributions from those end-members to be negative. Moreover, MEANDIR provides three mechanisms for regulating the isotopic composition of secondary phases. First, users can simply set a desired distribution of values. Second, users can define the isotopic composition of the secondary phase relative to the observed value for each river water sample. However, because the water chemistry reconstructed by MEANDIR may not perfectly match observations, this approach does not guarantee agreement between

model-constructed river chemistry and the isotopic value of the secondary phase. For example, when setting the $^{87}Sr/^{86}Sr$ ratio of a secondary phase equal to the sample ratio, the $^{87}Sr/^{86}Sr$ ratio of the secondary phase may differ from the inversion-constructed $^{87}Sr/^{86}Sr$ ratio of river water. Conversely, in the final method users can define a fractionation factor that sets the isotopic offset of secondary phases from the sources of the corresponding element. For the same example, if the fractionation factor is set to zero, the $^{87}Sr/^{86}Sr$ ratio of the secondary phase would match the reconstructed value of river water chemistry, but both would likely be offset from the actual measured value. Although all three approaches have their uses depending on the specific isotopic system and environment under consideration, we generally recommend the final treatment when seeking an internally consistent method for quantifying the formation of secondary phases with or without isotopic fractionation.

II.3.11: Sulfide oxidation

FeS_2 oxidation consumes ALK and increases both the concentration of marine SO_4^{2-} and atmospheric pCO_2. Currently, the river inversion literature contains two main approaches for calculating the fraction of $\chi^{riv}_{SO_4^{2-}}$ derived from FeS_2 oxidation, both of which can be implemented in MEANDIR (Torres et al., 2016; Burke et al., 2018; Hemingway et al., 2020; Kemeny et al., 2021a). After discussing these two techniques, later in this text we present a third, improved method for quantifying the fraction of $\chi^{riv}_{SO_4^{2-}}$ derived from FeS_2 oxidation and evaluate the mutual consistency of the three approaches.

Burke et al. (2018) quantified $\chi^{riv}_{SO_4^{2-}}$ which could not be attributed to precipitation, evaporites, carbonates, or silicates and called this quantity "excess SO_4^{2-}" (in our notation, $\chi^{riv}_{excess\ SO_4^{2-}}$) (Eq. II-33), which is proposed to mainly derive from FeS_2 oxidation and anthropogenic inputs. When quantifying FeS_2 oxidation this way the inversion must first calculate the fractional contributions of end-members using the non-SO_4^{2-} variables and, after the inversion is complete, each $\chi^{s}_{SO_4^{2-}}$ value can be calculated to then compute $\chi^{riv}_{excess\ SO_4^{2-}}$. In this approach $\chi^{riv}_{SO_4^{2-}}$ values should not be included directly in the inversion; if they are the second term of Eq. II-33 $\left(\Sigma^{n}_{s}\left[\chi^{s}_{SO_4^{2-}}\right]\right)$ will be optimized to equal the first term of Eq. II-33 ($\chi^{riv}_{SO_4^{2-}}$) and leave $\chi^{riv}_{excess\ SO_4^{2-}}$ as the residual of the optimization. Likewise, ${}^{34}R^{riv}_{excess\ SO_4^{2-}}$ is calculated following inversion from ${}^{34}R^{riv}_{SO_4^{2-}}$ and each ${}^{34}R^{s}_{SO_4^{2-}}$ values (Eq. II-34).

$$\chi^{riv}_{excess\ SO_4^{2-}} = \chi^{riv}_{SO_4^{2-}} - \Sigma^{n}_{s}\left[\chi^{s}_{SO_4^{2-}}\right] \quad \text{(II-33)}$$

$${}^{34}R^{riv}_{excess\ SO_4^{2-}} = \frac{\left(\chi^{riv}_{SO_4^{2-}} \cdot {}^{34}R^{riv}_{SO_4^{2-}}\right) - \Sigma^{n}_{s}\left[\chi^{s}_{SO_4^{2-}} \cdot {}^{34}R^{s}_{SO_4^{2-}}\right]}{\chi^{riv}_{SO_4^{2-}} - \Sigma^{n}_{s}\left[\chi^{s}_{SO_4^{2-}}\right]} \quad \text{(II-34)}$$

An advantage of the Burke et al. (2018) treatment is that, because it solves for the total amount and isotopic composition of $\chi^{riv}_{excess\ SO_4^{2-}}$ after the inversion is complete, it does not incur computational expense from testing values of normalized $\chi^{s}_{SO_4^{2-}}$ or ${}^{34}R^{s}_{SO_4^{2-}}$. Second, this treatment allows for identification of $\chi^{riv}_{SO_4^{2-}}$ in excess of conservative mixing without explicitly assuming its source, leaving open the interpretation of $\chi^{riv}_{excess\ SO_4^{2-}}$.

Conversely, by not explicitly connecting sources of SO_4^{2-} with carbonate or silicate weathering, this method does not easily resolve the relative fractions of carbonate or silicate weathering driven with H_2SO_4. This approach also allows the inversion to over-predict measured $\chi^{riv}_{SO_4^{2-}}$, resulting in negative values of $\chi^{riv}_{excess\ SO_4^{2-}}$.

A second approach, used in Torres et al. (2016), Hemingway et al. (2020), and Kemeny et al. (2021a), assigns a value for normalized SO_4^{2-} to a subset of end-members that do not contain structural SO_4^{2-}. In this case, the normalized ratios do not reflect SO_4^{2-} sourced from the lithology itself, but instead reflect SO_4^{2-} released into solution when H_2SO_4 formed through FeS_2 oxidation weathers the corresponding end-member. In our notation we reference this type of FeS_2-derived SO_4^{2-} as "$FeS_2\ SO_4^{2-}$." For example, a silicate rock without structural SO_4^{2-} would have $2\chi^{slct}_{SO_4^{2-}}/\chi^{slct}_{\Sigma^+} = 0$, while a silicate rock where 50% of weathering is done by H_2SO_4 would have $2\chi^{slct}_{FeS_2\ SO_4^{2-}}/\chi^{slct}_{\Sigma^+} = 0.5$. Following inversion, ${}^{34}R_{FeS_2\ SO_4^{2-}}$ is calculated from ${}^{34}R^{riv}_{SO_4^{2-}}$ and ${}^{34}R^{s}_{SO_4^{2-}}$ (Eqs. II-35 and II-36, where $s_{FeS_2\ SO_4^{2-}}$ indexes a list of length $n_{FeS_2\ SO_4^{2-}}$ containing end-members where SO_4^{2-} reflects FeS_2 oxidation and $s_{SO_4^{2-}}$ indexes a list of length $n_{SO_4^{2-}}$ containing end-members where SO_4^{2-} reflects non-FeS_2-derived SO_4^{2-}). Unlike the inversion scheme of Burke et al. (2018), this approach constrains the normalized $\chi^{s}_{FeS_2\ SO_4^{2}}$ ratios for each end-member and prevents negative values of $\chi^{riv}_{excess\ SO_4^{2-}}$. However, as shown below, this approach can result in problematic behavior at low values of $2\chi^{riv}_{SO_4^{2-}}/\chi^{riv}_{\Sigma^+}$.

$$\chi^{riv}_{FeS_2\ SO_4^{2-}} = \Sigma^{n_{FeS_2\ SO_4^{2-}}}_{s_{FeS_2\ SO_4^{2-}}} \left[\chi^{s_{FeS_2\ SO_4^{2-}}}_{FeS_2\ SO_4^{2-}}\right] \quad \text{(II-35)}$$

$$^{34}R^{riv}_{FeS_2\ SO_4^{2-}} = \frac{\left(\chi^{riv}_{SO_4^{2-}} \cdot {}^{34}R^{riv}_{SO_4^{2-}}\right) - \Sigma^{n}_{s\ SO_4^{2-}}\left[{}^{s}_{SO_4^{2-}} \cdot {}^{34}R^{s}_{SO_4^{2-}}\right]}{\Sigma^{n}_{s\ FeS_2\ SO_4^{2-}}\left[\chi^{s}_{FeS_2\ SO_4^{2-}}\right]} \quad \text{(II-36)}$$

In Torres et al. (2016) the silicate and carbonate end-members had well-defined values of $^{34}R^{s}_{FeS_2\ SO_4^{2-}}$ in addition to normalized $\chi^{s}_{FeS_2\ SO_4^{2-}}$ ratios. This choice was motivated by actual measurements of FeS_2 $\delta^{34}S$ such that the inclusion of sulfur isotope ratios added new constraint to the inversion. When FeS_2 $\delta^{34}S$ has not been measured, including $\delta^{34}S$ in the inversion merely adds computational expense to isolate the subset of simulations that select the correct $^{34}R^{s}_{FeS_2\ SO_4^{2-}}$ value to generate $^{34}R^{riv}_{SO_4^{2-}}$ given a successful combination of normalized $\chi^{s}_{FeS_2\ SO_4^{2-}}$ values. In this case, it is more efficient to instead calculate the $\delta^{34}S$ of FeS_2-derived SO_4^{2-} after the inversion is complete (Kemeny et al., 2021a).

II.3.12: Including $\chi^{riv}_{HCO_3^-}$ in inversions

Quantifying sources of $\chi^{riv}_{HCO_3^-}$ and interpreting $^{13}R^{riv}_{HCO_3^-}$ are recalcitrant problems in river geochemistry. In part, this difficulty reflects that the non-conservative behavior of $\chi^{riv}_{HCO_3^-}$, the specific methods used to determine $\chi^{riv}_{HCO_3^-}$, and the numerical approaches to quantifying sources of $\chi^{riv}_{HCO_3^-}$ each engender substantial confusion. Each of these problems is briefly discussed below. Later in this article, we present a method of river inversion focused on quantifying sources of χ^{riv}_{ALK} and χ^{riv}_{DIC} rather than $\chi^{riv}_{HCO_3^-}$.

In-situ $\chi^{riv}_{HCO_3^-}$ is determined by in-situ χ^{riv}_{ALK} and in-situ χ^{riv}_{DIC}. As processes such as carbonate weathering, degassing, and aquatic respiration alter χ^{riv}_{DIC}, or processes such as

FeS_2 oxidation or weathering alter χ^{riv}_{ALK}, the value of $\chi^{riv}_{HCO_3^-}$ does not change linearly. That is, due to the speciation dynamics of dissolved CO_2, $\chi^{riv}_{HCO_3^-}$ is not a weighted linear combination of lithologic and atmospheric sources reflecting the integrated history of upstream chemical processes. The non-linearity of $\chi^{riv}_{HCO_3^-}$ may present substantial complexity when using linear algebra to model its sources, although there are also situations in which the error is likely to be negligible. In contrast, χ^{riv}_{ALK} and χ^{riv}_{DIC} do mix linearly. Moreover, χ^{riv}_{ALK} and χ^{riv}_{DIC} are often the quantities actually measured during research on river systems and later used to infer $\chi^{riv}_{HCO_3^-}$. While χ^{riv}_{ALK}, χ^{riv}_{DIC}, and $\chi^{riv}_{HCO_3^-}$ are occasionally viewed as interchangeable, and indeed one can sometimes be used as an approximation for the others, their mutual distinctions become important when using MEANDIR to model processes such as FeS_2 oxidation and CO_2 degassing across the river-atmosphere boundary; FeS_2 oxidation impacts χ^{riv}_{ALK}, CO_2 degassing impacts χ^{riv}_{DIC}, and both alter $\chi^{riv}_{HCO_3^-}$.

Quantification of $\chi^{riv}_{HCO_3^-}$ often occurs either through measurement of χ^{riv}_{ALK} or through calculation by charge balance. In the former case, it is typical to assume that $\chi^{riv}_{HCO_3^-}$ equals χ^{riv}_{ALK}, which is generally an appropriate assumption for rivers near circumneutral pH and without substantial organic matter content. In the case of charge balance, $\chi^{riv}_{HCO_3^-}$ is quantified as the difference between the charge-equivalent sum of conservative cations and conservative anions. When $\chi^{riv}_{HCO_3^-}$ is determined through charge balance, it only provides new information for the inversion when the constituent measurements are not all included in the inversion. For example, if $\chi_{Ca^{2+}}$, $\chi_{Mg^{2+}}$, χ_{Na^+}, χ_{K^+}, $\chi_{SO_4^{2-}}$, and χ_{Cl^-} are all included in the inversion, the mass balance equation for $\chi^{riv}_{HCO_3^-}$ would be degenerate with a linear

combination of the other equations. Notably, including a degenerate equation in the inversion can result in a different answer than in an inversion with only linearly independent information because the additional equation still contributes to the cost function. Indeed, it can be useful to include $\chi^{\mathrm{riv}}_{\mathrm{HCO_3^-}}$ in inversions to ensure that results match the value of $\chi^{\mathrm{riv}}_{\mathrm{HCO_3^-}}$ to within a user-specified range for sample matching. MEANDIR thus allows the user to include the constraint that inversion results should recreate $\chi^{\mathrm{riv}}_{\mathrm{HCO_3^-}}$ within a specified range, but not include the misfit of $\chi^{\mathrm{riv}}_{\mathrm{HCO_3^-}}/\chi^{\mathrm{riv}}_{\Sigma^+}$ when evaluating the cost function.

Analogous to $\mathrm{FeS_2}$ oxidation and weathering with $\mathrm{H_2SO_4}$, the addition of $\mathrm{HCO_3^-}$ to rivers from weathering with $\mathrm{H_2CO_3}$ is often reflected within the end-member values of $\chi^{\mathrm{s}}_{\mathrm{HCO_3^-}}/\chi^{\mathrm{s}}_{\Sigma^+}$. For silicate, $\chi^{\mathrm{slct}}_{\mathrm{HCO_3^-}}$ entirely reflects $\mathrm{HCO_3^-}$ sourced from the deprotonation of atmospheric $\mathrm{CO_2}$. For carbonate, $\chi^{\mathrm{carb}}_{\mathrm{HCO_3^-}}$ has previously represented the combination of structural $\mathrm{CO_3^{2-}}$ and atmospheric $\mathrm{CO_2}$. Recent work has explicitly separated the weathering of carbonate and silicate end-members with carbonic or sulfuric acid (Blattmann et al., 2019). In this case, each end-member reflects a single lithology being weathered with a single acid. Rather than having an end-member for each type of lithology with variable $\chi^{\mathrm{s}}_{\mathrm{HCO_3^-}}/\chi^{\mathrm{s}}_{\Sigma^+}$ and $2\chi^{\mathrm{s}}_{\mathrm{FeS_2\ SO_4^{2-}}}/\chi^{\mathrm{s}}_{\Sigma^+}$, the explicit separation requires two end-members for each type of lithology where each has fixed ratios for $\chi^{\mathrm{s}}_{\mathrm{HCO_3^-}}/\chi^{\mathrm{s}}_{\Sigma^+}$ and $2\chi^{\mathrm{s}}_{\mathrm{FeS_2\ SO_4^{2-}}}/\chi^{\mathrm{s}}_{\Sigma^+}$. Below, we compare results when using variable or fixed ratios of $\chi^{\mathrm{s}}_{\mathrm{HCO_3^-}}/\chi^{\mathrm{s}}_{\Sigma^+}$.

Overall, MEANDIR is able to invert observations of $\chi^{\mathrm{riv}}_{\mathrm{HCO_3^-}}$, $^{13}\mathrm{R}^{\mathrm{riv}}_{\mathrm{HCO_3^-}}$, and $^{14}\mathrm{R}^{\mathrm{riv}}_{\mathrm{HCO_3^-}}$ for the fractional contributions of end-members by assuming linear behavior of user-defined end-member ratios. Furthermore, MEANDIR is able to invert observations of $\chi^{\mathrm{riv}}_{\mathrm{ALK}}$

and χ_{DIC}^{riv}, as well as measurements of $^{13}R_{DIC}^{riv}$ and $^{14}R_{DIC}^{riv}$. While MEANDIR represents a step forward in inverting observations of dissolved CO_2, studies of $^{13}R_{DIC}^{riv}$ and $^{13}R_{HCO_3^-}^{riv}$ may continue to be hindered by fractionation during degassing and the continued re-equilibration among dissolved CO_2 species. Although it is possible that degassing could be approximated using the approach MEANDIR takes to model isotopic fractionation during secondary phase formation, along with a deliberate choice of normalization variable, this idea has not been independently tested and may not capture important complexities that are explicitly resolved in purpose-built models of river gas exchange (Polsenaere and Abril, 2012).

II.3.13: Writing chemical weathering reactions with DIC as HCO_3^- or H_2CO_3

The geochemical literature on river inversion contains competing standards of how to write the basic chemical reactions for weathering of carbonate and silicate minerals with H_2CO_3 and H_2SO_4. The different equations matter because they generate variable expectations for carbonate $2\chi_{FeS_2\ SO_4^{2-}}^{carb}/\chi_{\Sigma^+}^{carb}$ and impede comparison across studies attempting to quantify the role of FeS_2 oxidation in the long-term carbon cycle. The difference in weathering equations results from whether reactions are written with chemical species at the circumneutral pH of most rivers or at the carbonic acid equivalence point (Zeebe and Wolf-Gladrow, 2001). More broadly, these different equations reflect differing opinions on the importance of DIC degassing during downstream transport.

When written at ambient conditions with DIC in the form of HCO_3^- (Eqs. II-37 to II-40), carbonate weathering is constrained to have $\chi_{HCO_3^-}^{carb}/\chi_{\Sigma^+}^{carb}$ between 0.5 and 1 (Eqs. II-37 and II-38) and silicate weathering is constrained to have $\chi_{HCO_3^-}^{slct}/\chi_{\Sigma^+}^{slct}$ between 0 and

1 (Eqs. II-39 and II-40). Similarly, the carbonate end-member $2\chi^{carb}_{FeS_2\ SO_4^{2-}}/\chi^{carb}_{\Sigma^+}$ is bounded between 0 (Eq. II-37) and 0.5 (Eq. II-38), while silicate $2\chi^{slct}_{FeS_2\ SO_4^{2-}}/\chi^{slct}_{\Sigma^+}$ is bounded between 0 (Eq. II-39) and 1 (Eq. II-40).

$$\frac{1}{2}CaCO_3 + \frac{1}{2}CO_2 + \frac{1}{2}H_2O \rightarrow \frac{1}{2}Ca^{2+} + HCO_3^- \quad \text{(II-37)}$$

$$\frac{1}{2}CaCO_3 + \frac{1}{8}FeS_2 + \frac{15}{32}O_2 + \frac{1}{4}H_2O \rightarrow \frac{1}{2}Ca^{2+} + \frac{1}{2}HCO_3^- + \frac{1}{4}SO_4^{2-} + \frac{1}{16}Fe_2O_3 \quad \text{(II-38)}$$

$$\frac{1}{2}CaSiO_3 + CO_2 + \frac{1}{2}H_2O \rightarrow \frac{1}{2}Ca^{2+} + \frac{1}{2}SiO_2 + HCO_3^- \quad \text{(II-39)}$$

$$\frac{1}{2}CaSiO_3 + \frac{1}{4}FeS_2 + \frac{15}{16}O_2 \rightarrow \frac{1}{2}Ca^{2+} + \frac{1}{2}SiO_2 + \frac{1}{2}SO_4^{2-} + \frac{1}{8}Fe_2O_3 \quad \text{(II-40)}$$

When written at the carbonic acid equivalence point (Eqs. II-41 to II-44), both carbonate $2\chi^{carb}_{FeS_2\ SO_4^{2-}}/\chi^{carb}_{\Sigma^+}$ and silicate $2\chi^{slct}_{FeS_2\ SO_4^{2-}}/\chi^{slct}_{\Sigma^+}$ are bounded between 0 (Eqs. II-41 and II-43) and 1 (Eqs. II-42 and II-44). The higher value for carbonate $2\chi^{carb}_{FeS_2\ SO_4^{2-}}/\chi^{carb}_{\Sigma^+}$ in this second set of equations occurs because DIC from the carbonate mineral is now written as the uncharged species H_2CO_3, not as the charged species HCO_3^-. As a result, the positive charge of $\chi^{carb}_{Ca^{2+}}$ is compensated by the negative charge of $\chi^{carb}_{FeS_2\ SO_4^{2-}}$ and not the negative charge of $\chi^{carb}_{HCO_3^-}$. Because weathering of silicate minerals with sulfuric acid does not result in release of HCO_3^-, Eqs. II-40 and II-44 are identical.

$$\frac{1}{2}CaCO_3 + H^+ \rightarrow \frac{1}{2}Ca^{2+} + \frac{1}{2}H_2CO_3 \quad \text{(II-41)}$$

$$\frac{1}{2}CaCO_3 + \frac{1}{4}FeS_2 + \frac{15}{16}O_2 + \frac{1}{2}H_2O \rightarrow \frac{1}{2}Ca^{2+} + \frac{1}{2}H_2CO_3 + \frac{1}{2}SO_4^{2-} + \frac{1}{8}Fe_2O_3 \quad \text{(II-42)}$$

$$\frac{1}{2}CaSiO_3 + H^+ \rightarrow \frac{1}{2}Ca^{2+} + \frac{1}{2}SiO_2 + \frac{1}{2}H_2O \quad \text{(II-43)}$$

$$\frac{1}{2}\mathrm{CaSiO_3} + \frac{1}{4}\mathrm{FeS_2} + \frac{15}{16}\mathrm{O_2} \rightarrow \frac{1}{2}\mathrm{Ca^{2+}} + \frac{1}{2}\mathrm{SiO_2} + \frac{1}{2}\mathrm{SO_4^{2-}} + \frac{1}{8}\mathrm{Fe_2O_3} \qquad \text{(II-44)}$$

There are thus two common sets of values for $2\chi^{\mathrm{carb}}_{\mathrm{FeS_2}\ \mathrm{SO_4^{2-}}}/\chi^{\mathrm{carb}}_{\Sigma^+}$ that differ only in the choice of whether DIC released during weathering is written as $\mathrm{H_2CO_3}$ or $\mathrm{HCO_3^-}$. Moreover, while both sets of weathering reactions predict that $2\chi^{\mathrm{riv}}_{\mathrm{SO_4^{2-}}}/\chi^{\mathrm{riv}}_{\Sigma^+} \leq 1$, natural waters with $2\chi^{\mathrm{riv}}_{\mathrm{SO_4^{2-}}}/\chi^{\mathrm{riv}}_{\Sigma^+} > 1$ have been reported (Torres et al., 2016). As an extreme example, $2\chi^{\mathrm{riv}}_{\mathrm{SO_4^{2-}}}$ can substantially exceed $\chi^{\mathrm{riv}}_{\Sigma^+}$ in acid mine drainage (Hubbard et al., 2009). These observations show that $\mathrm{FeS_2}$ oxidation can proceed without weathering of either carbonate or silicate lithologies, and that neither set of equations (Eqs. II-37 to II-40, II-41 to II-44) fully captures relevant weathering dynamics. As described below, MEANDIR begins to address this problem by explicitly separating the production and consumption of ALK, rather than explicitly tying together the source of acid and the weathering lithology; this new framework allows MEANDIR to model river waters where $2\chi^{\mathrm{riv}}_{\mathrm{SO_4^{2-}}}/\chi^{\mathrm{riv}}_{\Sigma^+} > 1$.

II.3.14: Oxidation of $\mathrm{FeS_2}$ and $\mathrm{C_{org}}$ as independent end-members

The preceding sections discussed normalization to χ_{Σ^+}, accounting for $\chi^{\mathrm{riv}}_{\mathrm{SO_4^{2-}}}$ sourced from $\mathrm{FeS_2}$ oxidation, including $\chi^{\mathrm{riv}}_{\mathrm{HCO_3^-}}$ in the inversion, and the different forms of chemical weathering reactions. In this section, we extend prior techniques to propose a new normalization strategy that allows for direct representation of $\mathrm{FeS_2}$ oxidation, $\mathrm{C_{org}}$ oxidation, and $\mathrm{CO_2}$ degassing as independent end-members decoupled from chemical weathering of lithologic end-members. The development underlying our approach is the inclusion of additional dissolved constituents into the normalization variable, such as

$\chi^{riv}_{SO_4^{2-}}$, χ^{riv}_{ALK}, or χ^{riv}_{DIC}. Similar to how normalization by χ_{Σ^+} rather than χ_{Na^+} allows a carbonate end-member to become stoichiometric, normalization to additional sums of variables enables representation of new end-member and processes that have previously eluded direct quantification. The myriad applications of our new method include disentangling contributions to $\chi^{riv}_{SO_4^{2-}}$ from multiple FeS_2 end-members with distinct $\delta^{34}S$ values and apportioning χ^{riv}_{DIC} between carbonate weathering, atmospheric CO_2, and petrogenic C_{org} oxidation. Example end-member compositions for several prior and new normalizations are given in Table II-4.

II.3.14.1: Normalization with arbitrary sum of dissolved variables

We first derive the basic mass balance equations of normalization with an arbitrary sum of dissolved constituents (Eq. II-45, with i_{norm} indexing a list of length k_{norm} containing all variables included in the normalization χ_{norm}, and Eq. II-46, where s and s′ independently index the same list of length n containing all end-members in the inversion). The derivation of the general equation follows the logic of our earlier derivation for the specific case of normalization with χ_{Σ^+} (Eq. II-26). As before, normalization with an arbitrary sum of dissolved variables generates a series of k linear equations that can be written as $\mathbf{b} = \mathbf{A} \cdot \mathbf{f}$ where each equation is of the form $\alpha_i\chi_i^{riv}/\chi_{norm}^{riv} = \Sigma_s^n \left[f_{norm}^s \left(\frac{\alpha_i\chi_i^s}{\chi_{norm}^s}\right)\right]$ (Eq. II-46).

$$\chi_{norm} = \Sigma_{i_{norm}}^{k_{norm}} \left[\alpha_{i_{norm}}\chi_{i_{norm}}\right] \quad \text{(II-45)}$$

$$\frac{\alpha_i \chi_i^{riv}}{\chi_{norm}^{riv}} = \frac{\Sigma_s^n[\alpha_i \chi_i^s]}{\Sigma_{i_{norm}}^{k_{norm}}[\alpha_{i_{norm}} \chi_{i_{norm}}^{riv}]} = \Sigma_s^n \left[\frac{\alpha_i \chi_i^s}{\Sigma_{i_{norm}}^{k_{norm}} \left[\Sigma_{s'}^n [\alpha_{i_{norm}} \chi_{i_{norm}}^{s'}] \right]} \right]$$

$$= \Sigma_s^n \left[\left(\frac{\Sigma_{i_{norm}}^{k_{norm}} [\alpha_{i_{norm}} \chi_{i_{norm}}^s]}{\Sigma_{s'}^n \left[\Sigma_{i_{norm}}^{k_{norm}} [\alpha_{i_{norm}} \chi_{i_{norm}}^{s'}] \right]} \right) \left(\frac{\alpha_i \chi_i^s}{\Sigma_{i_{norm}}^{k_{norm}} [\alpha_{i_{norm}} \chi_{i_{norm}}^s]} \right) \right] = \Sigma_s^n \left[f_{norm}^s \left(\frac{\alpha_i \chi_i^s}{\chi_{norm}^s} \right) \right]$$

(II-46)

MEANDIR can normalize river data to arbitrary sums of dissolved constituents in order to best fit the requirements of individual studies. As described below, a very general choice of normalization is the sum of χ_{Σ^+}, χ_{ALK}, and χ_{DIC}, as this normalization allows for quantification of most end-members of interest and can include arbitrary sources of weathering acids.

II.3.14.2: Normalization to $\chi_{\Sigma^+ + SO_4^{2-}}$ and $\chi_{\Sigma^+ + ALK}$

Modeling FeS_2 oxidation as an independent end-member is untenable when normalizing with χ_{Na^+} or χ_{Σ^+} because FeS_2 oxidation alone does not generate cations (Eq. II-47). For this reason, SO_4^{2-} from FeS_2 oxidation has previously been included in the chemical composition of weathering end-members as values of $\chi^s_{FeS_2\ SO_4^{2-}}$ (Torres et al., 2016). However, because FeS_2 oxidation is a source of SO_4^{2-} and a sink of ALK (Eq. II-47), including $\chi_{SO_4^{2-}}$ or χ_{ALK} in χ_{norm} allows FeS_2 oxidation to be modeled as an end-member independent of weathering lithology. Examples of such normalizations are the sum of $\chi^s_{\Sigma^+}$ and $2\chi^s_{SO_4^{2-}}$ ($\chi^s_{\Sigma^+ + SO_4^{2-}}$; Eq. II-48) or $\chi^s_{\Sigma^+}$ and χ^s_{ALK} ($\chi^s_{\Sigma^+ + ALK}$; Eq. II-49).

$$\frac{1}{4} FeS_2 + \frac{15}{16} O_2 + \frac{1}{2} H_2O \rightarrow \frac{1}{2} SO_4^{2-} + H^+ + \frac{1}{8} Fe_2O_3 \qquad \text{(II-47)}$$

$$\chi^{s}_{\Sigma^+ + SO_4^{2-}} = 2\chi^{s}_{Ca^{2+}} + 2\chi^{s}_{Mg^{2+}} + \chi^{s}_{Na^+} + \chi^{s}_{K^+} + 2\chi^{s}_{SO_4^{2-}} \quad \text{(II-48)}$$

$$\chi^{s}_{\Sigma^+ + ALK} = 2\chi^{s}_{Ca^{2+}} + 2\chi^{s}_{Mg^{2+}} + \chi^{s}_{Na^+} + \chi^{s}_{K^+} + \chi^{s}_{ALK} \quad \text{(II-49)}$$

When normalizing to $\chi_{\Sigma^+ + SO_4^{2-}}$, the end-member for FeS_2 oxidation has $2\chi^{FeS_2\ ox.}_{SO_4^{2-}}/\chi^{FeS_2\ ox.}_{\Sigma^+ + SO_4^{2-}} = 1$ and all normalized cation ratios equal to zero. Note that, in the expression $\chi^{FeS_2\ ox.}_{SO_4^{2-}}$, FeS_2 oxidation is now written as a superscript on χ to indicate its status as an end-member that sources SO_4^{2-} to the river. Assuming that the carbonate and silicate end-members do not contain structural SO_4^{2-} ($\chi^{s}_{SO_4^{2-}} = 0$), these end-members have $2\chi^{s}_{SO_4^{2-}}/\chi^{s}_{\Sigma^+ + SO_4^{2-}} = 0$ and the same cation ratios as when normalizing with χ_{Σ^+}: $2\chi^{slct}_{Ca^{2+}}/\chi^{slct}_{\Sigma^+ + SO_4^{2-}} = 2\chi^{slct}_{Ca^{2+}}/\chi^{slct}_{\Sigma^+}$. For end-members that source SO_4^{2-}, like evaporite or precipitation, cation ratios normalized with $\chi_{\Sigma^+ + SO_4^{2-}}$ are decreased relative to normalization by χ_{Σ^+} because $\chi^{s}_{SO_4^{2-}}$ is included in the denominator of the ratio: $2\chi^{evap}_{Ca^{2+}}/\chi^{evap}_{\Sigma^+ + SO_4^{2-}} < 2\chi^{evap}_{Ca^{2+}}/\chi^{evap}_{\Sigma^+}$ (Table II-4).

When normalizing to $\chi^{s}_{\Sigma^+ + ALK}$, FeS_2 oxidation has $2\chi^{FeS_2\ ox.}_{SO_4^{2-}}/\chi^{FeS_2\ ox.}_{\Sigma^+ + ALK} = -1$, $\chi^{FeS_2\ ox.}_{ALK}/\chi^{FeS_2\ ox.}_{\Sigma^+ + ALK} = 1$, and all other normalized non-isotopic ratios equal to zero. Similarly, because carbonate and silicate weathering source ALK, $2\chi^{carb}_{Ca^{2+}}/\chi^{carb}_{\Sigma^+ + ALK} < 2\chi^{carb}_{Ca^{2+}}/\chi^{carb}_{\Sigma^+}$ and $2\chi^{slct}_{Ca^{2+}}/\chi^{slct}_{\Sigma^+ + ALK} < 2\chi^{slct}_{Ca^{2+}}/\chi^{slct}_{\Sigma^+}$. The normalization with $\chi_{\Sigma^+ + ALK}$ is more general than normalization with $\chi_{\Sigma^+ + SO_4^{2-}}$ because it allows for representation of any acid source or sink. For example, a process such as NH_3 oxidation could not be directly modeled when $\chi_{norm} = \chi_{\Sigma^+ + SO_4^{2-}}$ because neither $\chi_{NO_3^-}$ nor χ_{ALK} are in the normalization variable. Conversely, NH_3 oxidation can be included in a model normalized to $\chi_{\Sigma^+ + ALK}$.

Analogous to FeS_2 oxidation, the end-member for NH_3 oxidation would have $\chi^{\mathrm{NH_3\ ox.}}_{NO_3^-}/\chi^{\mathrm{NH_3\ ox.}}_{\Sigma^+ + \mathrm{ALK}} = -1$, $\chi^{\mathrm{NH_3\ ox.}}_{\mathrm{ALK}}/\chi^{\mathrm{NH_3\ ox.}}_{\Sigma^+ + \mathrm{ALK}} = 1$, and all other non-isotopic normalized ratios equal to zero.

Normalization with $\chi_{\Sigma^+ + SO_4^{2-}}$ or $\chi_{\Sigma^+ + \mathrm{ALK}}$ entails a constraint on the normalized ratios to achieve internal consistency (Eqs. II-50 and II-51). As in the case of $\chi_{\mathrm{norm}} = \chi_{\Sigma^+}$, the requirement for internal consistency is satisfied by selecting a single ratio with a numerator constituent to the normalization variable to be solved using the other end-member selections.

$$1 = \frac{2\chi^{s}_{Ca^{2+}}}{\chi^{s}_{\Sigma^+ + SO_4^{2-}}} + \frac{2\chi^{s}_{Mg^{2+}}}{\chi^{s}_{\Sigma^+ + SO_4^{2-}}} + \frac{\chi^{s}_{Na^{+}}}{\chi^{s}_{\Sigma^+ + SO_4^{2-}}} + \frac{\chi^{s}_{K^{+}}}{\chi^{s}_{\Sigma^+ + SO_4^{2-}}} + \frac{2\chi^{s}_{SO_4^{2-}}}{\chi^{s}_{\Sigma^+ + SO_4^{2-}}} \qquad \text{(II-50)}$$

$$1 = \frac{2\chi^{s}_{Ca^{2+}}}{\chi^{s}_{\Sigma^+ + \mathrm{ALK}}} + \frac{2\chi^{s}_{Mg^{2+}}}{\chi^{s}_{\Sigma^+ + \mathrm{ALK}}} + \frac{\chi^{s}_{Na^{+}}}{\chi^{s}_{\Sigma^+ + \mathrm{ALK}}} + \frac{\chi^{s}_{K^{+}}}{\chi^{s}_{\Sigma^+ + \mathrm{ALK}}} + \frac{\chi^{s}_{\mathrm{ALK}}}{\chi^{s}_{\Sigma^+ + \mathrm{ALK}}} \qquad \text{(II-51)}$$

The preceding discussion focused on explicitly representing FeS_2 oxidation as an independent end-member during river inversion. However, the same equations can be used to represent any external source of $\chi^{\mathrm{riv}}_{SO_4^{2-}}$, including inputs of SO_4^{2-} from anthropogenic pollution or from the biosphere. An independent end-member sourcing $\chi^{\mathrm{riv}}_{SO_4^{2-}}$ not attributable to evaporites or precipitation functions very similarly to excess SO_4^{2-} (Burke et al., 2018). To distinguish the quantification of $\chi^{\mathrm{riv}}_{\mathrm{excess}\ SO_4^{2-}}$, where $\chi^{\mathrm{riv}}_{SO_4^{2-}}$ is not included in the inversion, from an independent SO_4^{2-}-bearing end-member, where $\chi^{\mathrm{riv}}_{SO_4^{2-}}$ is included in the inversion, we call the latter "other SO_4^{2-}." Because such "other SO_4^{2-}" derives from the "other" end-member, moles of other SO_4^{2-} are indicated in our notation as $\chi^{\mathrm{other}}_{SO_4^{2-}}$; note

the superscript for "other" in contrast to the subscript for "excess SO_4^{2-}," marking the former as an end-member in the inversion. An advantage of quantifying $\chi^{other}_{SO_4^{2-}}$ rather than $\chi^{riv}_{excess\ SO_4^{2-}}$ is that, while $\chi^{riv}_{excess\ SO_4^{2-}}$ can attain negative values, $\chi^{other}_{SO_4^{2-}}$ can be constrained to have a minimum value of zero by setting limits on the contribution of the "other" end-member.

As with the quantification of $\chi^{riv}_{excess\ SO_4^{2-}}$, the $\delta^{34}S$ of $\chi^{other}_{SO_4^{2-}}$ can be calculated from inversion results. For each successful simulation result, MEANDIR calculates a range of possible values for ${}^{34}R^{other}_{SO_4^{2-}}$ based on possible values for ${}^{34}R^{s}_{SO_4^{2-}}$ (Eq. II-52). That is, when $\delta^{34}S$ is not explicitly included in the inversion, the possible $\delta^{34}S$ ranges for all end-members can be accounted for by performing a second Monte Carlo simulation on each successful set of $\chi^{s_{SO_4^{2-}}}_{SO_4^{2-}}$ values.

$$ {}^{34}R^{other}_{SO_4^{2-}} = \frac{\left(\chi^{riv}_{SO_4^{2-}} \cdot {}^{34}R^{riv}_{SO_4^{2-}}\right) - \Sigma_{s}^{n_{SO_4^{2-}}} \left[\chi^{s_{SO_4^{2-}}}_{SO_4^{2-}} \cdot {}^{34}R^{s_{SO_4^{2-}}}_{SO_4^{2-}}\right]}{\chi^{other}_{SO_4^{2-}}} \qquad \text{(II-52)} $$

II.3.14.3: Normalization to $\chi_{\Sigma^+ + DIC}$

The oxidation of petrogenic organic carbon has an important role in chemical weathering budgets (Bolton et al., 2006; Bouchez et al., 2010; Horan et al., 2019; Hilton and West, 2020). Including C_{org} oxidation in inversion models allows for quantification of DIC impacts from C_{org} oxidation which, along with quantification of ALK sinks from FeS_2 oxidation and sources from chemical weathering, enables assessing the influence of weathering systems on atmospheric CO_2. Including C_{org} oxidation in inversion models

would be beneficial when employing tracers like $^{13}R^{riv}_{DIC}$ or χ^{riv}_{Re} as these variables are influenced by weathering of multiple lithologies in addition to C_{org} oxidation (Horan et al., 2019). However, there has been limited success in representing petrogenic organic carbon oxidation directly in river inversion models. Like FeS_2 oxidation, the lack of prior explicit C_{org} representation partially reflects that the oxidation of C_{org} does not source cations to river water, and cannot be included as an independent end-member when normalizing to χ_{Na^+} or χ_{Σ^+} (Eq. II-53). Instead, including χ_{DIC} in χ_{norm} enables the direct representation of C_{org} oxidation. One such example is the sum of $\chi^s_{\Sigma^+}$ and χ^s_{DIC} ($\chi^s_{\Sigma^+ + DIC}$; Eqs. II-54 and II-55).

$$CH_2O + O_2 \rightarrow H_2CO_3 \tag{II-53}$$

$$\chi^s_{\Sigma^+ + DIC} = 2\chi^s_{Ca^{2+}} + 2\chi^s_{Mg^{2+}} + \chi^s_{Na^+} + \chi^s_{K^+} + \chi^s_{DIC} \tag{II-54}$$

$$1 = \frac{2\chi^s_{Ca^{2+}}}{\chi^s_{\Sigma^+ + DIC}} + \frac{2\chi^s_{Mg^{2+}}}{\chi^s_{\Sigma^+ + DIC}} + \frac{\chi^s_{Na^+}}{\chi^s_{\Sigma^+ + DIC}} + \frac{\chi^s_{K^+}}{\chi^s_{\Sigma^+ + DIC}} + \frac{\chi^s_{DIC}}{\chi^s_{\Sigma^+ + DIC}} \tag{II-55}$$

Setting $\chi_{norm} = \chi_{\Sigma^+ + DIC}$ also enables representation of CO_2 exchange between the river and atmosphere. By allowing end-members for atmospheric CO_2 or C_{org} oxidation to have either positive or negative fractional contributions to $\chi^{riv}_{\Sigma^+ + DIC}$, MEANDIR allows the former process to represent net gas exchange across the river/atmosphere boundary and the latter process to represent net uptake or release of DIC through oxidation or fixation of organic carbon. Because the end-members for both C_{org} oxidation and atmospheric CO_2 have $\chi^s_{DIC}/\chi^s_{\Sigma^+ + DIC} = 1$ and all dissolved cations ratios equal to zero, distinguishing their relative influence on river water requires characteristic values for $^{13}R^s_{DIC}$, $^{14}R^s_{DIC}$, or trace

metal ratios. Silicate weathering has $\chi^{\mathrm{slct}}_{\mathrm{DIC}}/\chi^{\mathrm{slct}}_{\Sigma^+ + \mathrm{DIC}} = 0$, while carbonate weathering has $\chi^{\mathrm{carb}}_{\mathrm{DIC}}/\chi^{\mathrm{carb}}_{\Sigma^+ + \mathrm{DIC}} = 1/3$ as it sources 1 mole of DIC per two charge-equivalent moles of cations (Table II-4).

The preceding discussion highlights the utility of including χ_{Σ^+}, χ_{ALK}, and χ_{DIC} in χ_{norm}. Inclusion of χ_{Σ^+} enables representation of end-members such as evaporites that only source conservative ions, inclusion of χ_{ALK} allows representation of end-members such as FeS_2 oxidation that alter $\chi^{\mathrm{riv}}_{\mathrm{ALK}}$, and inclusion of χ_{DIC} allow representation of end-members such as C_{org} oxidation that alter $\chi^{\mathrm{riv}}_{\mathrm{DIC}}$. A highly generic choice of normalization variable is thus the sum of χ_{Σ^+}, χ_{ALK}, and χ_{DIC} ($\chi^{\mathrm{s}}_{\Sigma^+ + \mathrm{ALK} + \mathrm{DIC}}$; Eq. II-56), with an associated normalization constraint (Eq. II-57). Below, we use this normalization with the data of Horan et al. (2019) to simultaneously constrain the fraction of $\chi^{\mathrm{riv}}_{SO_4^{2-}}$ derived from FeS_2 oxidation and $\chi^{\mathrm{riv}}_{\mathrm{DIC}}$ derived from petrogenic C_{org} oxidation.

$$\chi^{\mathrm{s}}_{\Sigma^+ + \mathrm{ALK} + \mathrm{DIC}} = 2\chi^{\mathrm{s}}_{Ca^{2+}} + 2\chi^{\mathrm{s}}_{Mg^{2+}} + \chi^{\mathrm{s}}_{Na^+} + \chi^{\mathrm{s}}_{K^+} + \chi^{\mathrm{s}}_{\mathrm{ALK}} + \chi^{\mathrm{s}}_{\mathrm{DIC}} \quad \text{(II-56)}$$

$$1 = \frac{2\chi^{\mathrm{s}}_{Ca^{2+}}}{\chi^{\mathrm{s}}_{\Sigma^+ + \mathrm{ALK} + \mathrm{DIC}}} + \frac{2\chi^{\mathrm{s}}_{Mg^{2+}}}{\chi^{\mathrm{s}}_{\Sigma^+ + \mathrm{ALK} + \mathrm{DIC}}} + \frac{\chi^{\mathrm{s}}_{Na^+}}{\chi^{\mathrm{s}}_{\Sigma^+ + \mathrm{ALK} + \mathrm{DIC}}} + \frac{\chi^{\mathrm{s}}_{K^+}}{\chi^{\mathrm{s}}_{\Sigma^+ + \mathrm{ALK} + \mathrm{DIC}}} + \frac{\chi^{\mathrm{s}}_{\mathrm{ALK}}}{\chi^{\mathrm{s}}_{\Sigma^+ + \mathrm{ALK} + \mathrm{DIC}}} + \frac{\chi^{\mathrm{s}}_{\mathrm{DIC}}}{\chi^{\mathrm{s}}_{\Sigma^+ + \mathrm{ALK} + \mathrm{DIC}}} \quad \text{(II-57)}$$

II.3.14.4: Charge balance when normalizing to sums of dissolved variables

An additional constraint from charge balance occurs when all cations and anions are explicitly included in the inversion model. Practically, this would occur when all major conservative cations and anions are measured and either $\chi^{\mathrm{s}}_{HCO_3^-}$ or $\chi^{\mathrm{s}}_{\mathrm{ALK}}$ is included in the inversion (Eq. II-58). Each term in the charge balance equation can then be normalized

(Eq. II-59), and a specific equation for charge balance found by substitution and simplification using the internal consistency of end-members (Eqs. II-60 to II-63). In MEANDIR, these equations are solved by selecting one ratio with numerator constituent to the normalization and one ratio with numerator external to the normalization to calculate using the other ratios drawn from user-defined distributions.

$$2\chi^{s}_{Ca^{2+}} + 2\chi^{s}_{Mg^{2+}} + \chi^{s}_{Na^{+}} + \chi^{s}_{K^{+}} = 2\chi^{s}_{SO_4^{2-}} + \chi^{s}_{Cl^{-}} + \chi^{s}_{ALK} \quad \text{(II-58)}$$

$$\left(\frac{2\chi^{s}_{Ca^{2+}}}{\chi^{s}_{norm}} + \frac{2\chi^{s}_{Mg^{2+}}}{\chi^{s}_{norm}} + \frac{\chi^{s}_{Na^{+}}}{\chi^{s}_{norm}} + \frac{\chi^{s}_{K^{+}}}{\chi^{s}_{norm}}\right) = \left(\frac{2\chi^{s}_{SO_4^{2-}}}{\chi^{s}_{norm}} + \frac{\chi^{s}_{Cl^{-}}}{\chi^{s}_{norm}} + \frac{\chi^{s}_{ALK}}{\chi^{s}_{norm}}\right) \quad \text{(II-59)}$$

$$\left(\frac{2\chi^{s}_{Ca^{2+}}}{\chi^{s}_{\Sigma^{+}+SO_4^{2-}}} + \frac{2\chi^{s}_{Mg^{2+}}}{\chi^{s}_{\Sigma^{+}+SO_4^{2-}}} + \frac{\chi^{s}_{Na^{+}}}{\chi^{s}_{\Sigma^{+}+SO_4^{2-}}} + \frac{\chi^{s}_{K^{+}}}{\chi^{s}_{\Sigma^{+}+SO_4^{2-}}} + \frac{2\chi^{s}_{SO_4^{2-}}}{\chi^{s}_{\Sigma^{+}+SO_4^{2-}}}\right)$$

$$= \left(2\left(\frac{2\chi^{s}_{SO_4^{2-}}}{\chi^{s}_{\Sigma^{+}+SO_4^{2-}}}\right) + \frac{\chi^{s}_{Cl^{-}}}{\chi^{s}_{\Sigma^{+}+SO_4^{2-}}} + \frac{\chi^{s}_{ALK}}{\chi^{s}_{\Sigma^{+}+SO_4^{2-}}}\right) = 1 \quad \text{(II-60)}$$

$$\left(\frac{2\chi^{s}_{Ca^{2+}}}{\chi^{s}_{\Sigma^{+}+ALK}} + \frac{2\chi^{s}_{Mg^{2+}}}{\chi^{s}_{\Sigma^{+}+ALK}} + \frac{\chi^{s}_{Na^{+}}}{\chi^{s}_{\Sigma^{+}+ALK}} + \frac{\chi^{s}_{K^{+}}}{\chi^{s}_{\Sigma^{+}+ALK}} + \frac{\chi^{s}_{ALK}}{\chi^{s}_{\Sigma^{+}+ALK}}\right)$$

$$= \left(\frac{2\chi^{s}_{SO_4^{2-}}}{\chi^{s}_{\Sigma^{+}+ALK}} + \frac{\chi^{s}_{Cl^{-}}}{\chi^{s}_{\Sigma^{+}+ALK}} + 2\left(\frac{\chi^{s}_{ALK}}{\chi^{s}_{\Sigma^{+}+ALK}}\right)\right) = 1 \quad \text{(II-61)}$$

$$\left(\frac{2\chi^{s}_{Ca^{2+}}}{\chi^{s}_{\Sigma^{+}+DIC}} + \frac{2\chi^{s}_{Mg^{2+}}}{\chi^{s}_{\Sigma^{+}+DIC}} + \frac{\chi^{s}_{Na^{+}}}{\chi^{s}_{\Sigma^{+}+DIC}} + \frac{\chi^{s}_{K^{+}}}{\chi^{s}_{\Sigma^{+}+DIC}} + \frac{\chi^{s}_{DIC}}{\chi^{s}_{\Sigma^{+}+DIC}}\right)$$

$$= \left(\frac{2\chi^{s}_{SO_4^{2-}}}{\chi^{s}_{\Sigma^{+}+DIC}} + \frac{\chi^{s}_{Cl^{-}}}{\chi^{s}_{\Sigma^{+}+DIC}} + \frac{\chi^{s}_{ALK}}{\chi^{s}_{\Sigma^{+}+DIC}} + \frac{\chi^{s}_{DIC}}{\chi^{s}_{\Sigma^{+}+DIC}}\right) = 1 \quad \text{(II-62)}$$

$$\left(\frac{2\chi^{s}_{Ca^{2+}}}{\chi^{s}_{\Sigma^{+}+ALK+DIC}} + \frac{2\chi^{s}_{Mg^{2+}}}{\chi^{s}_{\Sigma^{+}+ALK+DIC}} + \frac{\chi^{s}_{Na^{+}}}{\chi^{s}_{\Sigma^{+}+ALK+DIC}} + \frac{\chi^{s}_{K^{+}}}{\chi^{s}_{\Sigma^{+}+ALK+DIC}} + \frac{\chi^{s}_{ALK}}{\chi^{s}_{\Sigma^{+}+ALK+DIC}} + \frac{\chi^{s}_{DIC}}{\chi^{s}_{\Sigma^{+}+ALK+DIC}}\right)$$

$$= \left(\frac{2\chi^{s}_{SO_4^{2-}}}{\chi^{s}_{\Sigma^{+}+ALK+DIC}} + \frac{\chi^{s}_{Cl^{-}}}{\chi^{s}_{\Sigma^{+}+ALK+DIC}} + 2\left(\frac{\chi^{s}_{ALK}}{\chi^{s}_{\Sigma^{+}+ALK+DIC}}\right) + \frac{\chi^{s}_{DIC}}{\chi^{s}_{\Sigma^{+}+ALK+DIC}}\right) = 1 \quad \text{(II-63)}$$

II.3.15: Calculation of R, Z, Y, W, and C

II.3.15.1: Definition of R, Z, Y, W, C and calculation of χ_{ALK}/χ_{DIC}

Prior work has quantified the impact of chemical weathering on the global carbon cycle by considering the relative fractions of carbonate weathering (R) and sulfuric acid weathering (Z) (Torres et al., 2016). Below, we update the formalism of Torres et al. (2016) to define a variable C that reflects the net effect of organic carbon production and oxidation. We also define the variable Y to represent the fraction of $\chi^{riv}_{SO_4^{2-}}$ sourced from FeS_2 oxidation and the variable W to represent the ratio of $\chi^{riv}_{SO_4^{2-}}$ sourced from FeS_2 oxidation relative to χ^{riv}_{norm}. Variables Y and W have previously been used without formal definition (Torres et al., 2016; Kemeny et al., 2021a). We note that defining the carbonate weathering fraction with the variable R is the second definition of R, which is defined earlier in this text as an isotopic ratio (Table II-2). Unfortunately, the symbol R is already established as representing both isotopic ratios and carbonate weathering fraction. Although not ideal, the two uses of R are generally distinguishable by context.

The weathering of carbonate and silicate rock can be written as generic H^+ consuming reactions (Eqs. II-41 and II-43), while H^+ for weathering can be sourced from H_2SO_4 following FeS_2 oxidation (Eq. II-47). Similarly, carbonate weathering and C_{org} oxidation source DIC (Eq. II-53). To represent the net effect of chemical weathering in a river catchment, we consider the weighted sums of carbonate weathering, silicate weathering, FeS_2 oxidation, and net C_{org} oxidation (Eq. II-64). The variables ϕ and β are taken to represent the alkalinity released by carbonate weathering and silicate weathering, respectively, the variable γ is taken to represent the alkalinity consumed through FeS_2 oxidation, and the variable θ is taken to represent the DIC released through net C_{org}

oxidation (Eq. II-64; Table II-2). Because the aggregate chemical weathering reaction is written at the carbonic acid equivalence point, the net effect of the reaction on ALK is the factor on H^+ ($\phi + \beta - \gamma$) and the net effect on DIC is the factor on H_2CO_3 ($\frac{1}{2}\phi + \theta$) (Eq. II-64).

$$(\phi + \beta - \gamma)H^+ + \left(\frac{1}{2}\phi\right)CaCO_3 + \left(\frac{1}{2}\beta\right)CaSiO_3 + \left(\frac{1}{4}\gamma\right)FeS_2 + \left(\frac{15}{16}\gamma + \theta\right)O_2 + (\theta)CH_2O + \left(\frac{1}{2}\gamma - \frac{1}{2}\beta\right)H_2O \rightarrow \left(\frac{1}{2}\phi + \frac{1}{2}\beta\right)Ca^{2+} + \left(\frac{1}{2}\phi + \theta\right)H_2CO_3 + \left(\frac{1}{2}\beta\right)SiO_2 + \left(\frac{1}{2}\gamma\right)SO_4^{2-} + \left(\frac{1}{8}\gamma\right)Fe_2O_3 \quad \text{(II-64)}$$

The condition $\theta < 0$ is a possible scenario reflecting net biomass generation in excess of organic carbon oxidation. However, given that biospheric C_{org} is typically exported as a solid phase, quantifying the overall θ value for a watershed system may be complicated as solutes and particulates obey different concentration-discharge relationships (Torres et al., 2015; Turowski et al., 2016), biospheric C_{org} export may be highly episodic (West et al., 2011), and biospheric C_{org} fluxes are rapidly degraded in downstream settings such as floodplains (Scheingross et al., 2021) and near-shore marine environments (Blair and Aller, 2012). As MEANDIR focuses on solutes, in this work we limit our use of θ to chemical weathering processes. This approach captures useful information on offsets in silicate weathering due to petrogenic organic carbon oxidation but does not capture every terrestrial process that affects atmospheric pCO_2.

We define the variable R as the ratio of alkalinity released during carbonate weathering to alkalinity released during carbonate and silicate weathering (Eq. II-65). We

define the variable Z as the ratio of alkalinity consumed during sulfide oxidation relative to alkalinity released during carbonate and silicate weathering (Eq. II-66). We define the variable C as DIC released during oxidation of organic matter relative to alkalinity released during carbonate and silicate weathering (Eq. II-67). The normalization for C is chosen to match the normalization of R and Z. Although alternative choices for the normalization of C are possible, the normalization matching R and Z is useful. With these definitions, the net χ_{ALK}/χ_{DIC} of a weathering system is a simple function of R, Z, and C (Eq. II-68). At a non-zero value of χ_{ALK}/χ_{DIC} the variables R, Z, and C form the plane $1/\left(\frac{\chi_{ALK}}{\chi_{DIC}}\right) = R/2 + Z/\left(\frac{\chi_{ALK}}{\chi_{DIC}}\right) + C$. That is, accounting for organic carbon oxidation alters the relationships among R, Z, and χ_{ALK}/χ_{DIC} that were established in Torres et al. (2016).

$$R = \frac{\phi}{\phi+\beta} \tag{II-65}$$

$$Z = \frac{\gamma}{\phi+\beta} \tag{II-66}$$

$$C = \frac{\theta}{\phi+\beta} \tag{II-67}$$

$$\frac{\chi_{ALK}}{\chi_{DIC}} = \frac{(\phi+\beta-\gamma)}{\left(\frac{1}{2}\phi+\theta\right)} = \frac{\frac{(\phi+\beta-\gamma)}{(\phi+\beta)}}{\frac{\left(\frac{1}{2}\phi+\theta\right)}{\phi+\beta}} = \frac{2(1-Z)}{R+2C} \tag{II-68}$$

II.3.15.2: Calculating R, Z, Y, W, and C from inversion results

The carbonate weathering fraction R can be calculated in several ways. First, when χ_{ALK}^{riv} is included in the inversion, R is equal to the ratio of ALK from carbonate weathering to ALK from carbonate and silicate weathering (R_{ALK}; Eq. II-69, where s_{carb} indexes the list of length n_{carb} containing all carbonate end-member, and s_{weath} indexes the list of

length n_{weath} containing all weathering end-members). R is also calculated as the charge-equivalent cation contributions of carbonate end-members relative to the sum of charge-equivalent contributions from all weathering end-members ($R_{i_{RZC}\ldots k_{RZC}}$; Eq. II-70, where i_{RZC} indexes the list of length k_{RZC} containing the cations used to calculate the denominators of R, Z, and C, and $\alpha_{i_{RZC}}$ is the charge of the relevant variable). We use the subscript $i_{RZC} \ldots k_{RZC}$ on R to indicate which observations are in the calculation; as discussed below, this is in response to disagreement regarding whether χ_{Na^+} and χ_{K^+} should be included in R, and thus whether the denominator of R reflects the total alkalinity released from all carbonate and silicate sources. As argued below, it is our opinion that the list indexed by i_{RZC} should generally include all cations sourced to the river from weathering, including χ_{Na^+} and χ_{K^+}.

$$R_{ALK} = \frac{\Sigma_{s_{carb}}^{n_{carb}}\left[\chi_{ALK}^{s_{carb}}\right]}{\Sigma_{s_{weath}}^{n_{weath}}\left[\chi_{ALK}^{s_{weath}}\right]} \tag{II-69}$$

$$R_{i_{RZC}\ldots k_{RZC}} = \frac{\Sigma_{s_{carb}}^{n_{carb}}\left[\Sigma_{i_{RZC}}^{k_{RZC}}\left[\alpha_{i_{RZC}}\chi_{i_{RZC}}^{s_{carb}}\right]\right]}{\Sigma_{s_{weath}}^{n_{weath}}\left[\Sigma_{i_{RZC}}^{k_{RZC}}\left[\alpha_{i_{RZC}}\chi_{i_{RZC}}^{s_{weath}}\right]\right]} \tag{II-70}$$

Examples of R_{ALK} (Eq. II-71) and $R_{i_{RZC}\ldots k_{RZC}}$ (Eqs. II-72 and II-73) are given for an inversion including χ_{ALK}, $\chi_{Ca^{2+}}$, $\chi_{Mg^{2+}}$, χ_{Na^+}, and χ_{Cl^-} with four end-members: calcite (calc), dolomite (dolo), silicate (slct), and precipitation (prec). Only $\chi_{Ca^{2+}}$ and $\chi_{Mg^{2+}}$ contribute to R in Eq. II-72 ($R_{Ca,Mg}$), while in Eq. II-73 the calculation also includes χ_{Na^+} ($R_{Ca,Mg,Na}$).

$$R_{ALK} = \frac{\chi_{ALK}^{calc} + \chi_{ALK}^{dolo}}{\chi_{ALK}^{calc} + \chi_{ALK}^{dolo} + \chi_{ALK}^{slct}} \quad \text{(II-71)}$$

$$R_{Ca,Mg} = \frac{2\chi_{Ca^{2+}}^{calc} + 2\chi_{Ca^{2+}}^{dolo} + 2\chi_{Mg^{2+}}^{dolo}}{2\chi_{Ca^{2+}}^{calc} + 2\chi_{Ca^{2+}}^{dolo} + 2\chi_{Mg^{2+}}^{dolo} + 2\chi_{Ca^{2+}}^{slct} + 2\chi_{Mg^{2+}}^{slct}} \quad \text{(II-72)}$$

$$R_{Ca,Mg,Na} = \frac{2\chi_{Ca^{2+}}^{calc} + 2\chi_{Ca^{2+}}^{dolo} + 2\chi_{Mg^{2+}}^{dolo}}{2\chi_{Ca^{2+}}^{calc} + 2\chi_{Ca^{2+}}^{dolo} + 2\chi_{Mg^{2+}}^{dolo} + 2\chi_{Ca^{2+}}^{slct} + 2\chi_{Mg^{2+}}^{slct} + \chi_{Na^{+}}^{slct}} \quad \text{(II-73)}$$

Calculation of the sulfuric acid weathering fraction Z depends on how FeS_2 oxidation is represented. When FeS_2 is treated as a stand-alone end-member, Z can be calculated as the alkalinity consumed during FeS_2 oxidation relative to alkalinity released during chemical weathering ($Z_{ALK}^{FeS_2\ ox.\ ALK}$; Eq. II-74) or as the charge-equivalent $\chi_{SO_4^{2-}}^{FeS_2\ ox.}$ relative to cations sourced from weathering end-members ($Z_{i_{RZC}\ldots k_{RZC}}^{FeS_2\ ox.\ SO_4^{2-}}$; Eq. II-75). When attributing $\chi_{excess\ SO_4^{2-}}^{riv}$ to FeS_2 oxidation, Z is the charge-equivalent ratio of $\chi_{excess\ SO_4^{2-}}^{riv}$ to the charge-equivalent sum of cation contributions from all weathering end-members ($Z_{i_{RZC}\ldots k_{RZC}}^{excess\ SO_4^{2-}}$; Eq. II-76). When values of $\chi_{FeS_2\ SO_4^{2-}}^{s}$ are constrained, Z is calculated as the ratio of the sum of FeS_2-derived SO_4^{2-} contributions relative to cations sourced from weathering end-members ($Z_{i_{RZC}\ldots k_{RZC}}^{FeS_2\ SO_4^{2-}}$; Eq. II-77, where $s_{FeS_2\ SO_4^{2-}}$ indexes the list of length $n_{FeS_2\ SO_4^{2-}}$ containing end-members weathered by H_2SO_4).

$$Z_{ALK}^{FeS_2\ ox.\ ALK} = \frac{-\chi_{ALK}^{FeS_2\ ox.}}{\Sigma_{s_{weath}}^{n_{weath}}\left[\chi_{ALK}^{s_{weath}}\right]} \quad \text{(II-74)}$$

$$Z_{i_{RZC}\ldots k_{RZC}}^{FeS_2\ ox.\ SO_4^{2-}} = \frac{2\chi_{SO_4^{2-}}^{FeS_2\ ox.}}{\Sigma_{s_{weath}}^{n_{weath}}\left[\Sigma_{i_{RZC}}^{k_{RZC}}\left[\alpha_{i_{RZC}}\chi_{i_{RZC}}^{s_{weath}}\right]\right]} \quad \text{(II-75)}$$

$$Z_{i_{RZC}\ldots k_{RZC}}^{excess\ SO_4^{2-}} = \frac{2\chi_{excess\ SO_4^{2-}}^{riv}}{\Sigma_{s_{weath}}^{n_{weath}}\left[\Sigma_{i_{RZC}}^{k_{RZC}}\left[\alpha_{i_{RZC}}\chi_{i_{RZC}}^{s_{weath}}\right]\right]} \quad \text{(II-76)}$$

$$Z_{i_{RZC}\ldots k_{RZC}}^{FeS_2\ SO_4^{2-}} = \frac{\Sigma_{s_{FeS_2\ SO_4^{2-}}}^{n_{FeS_2\ SO_4^{2-}}}\left[2\chi_{FeS_2\ SO_4^{2-}}^{s_{FeS_2\ SO_4^{2-}}}\right]}{\Sigma_{s_{weath}}^{n_{weath}}\left[\Sigma_{i_{RZC}}^{k_{RZC}}\left[\alpha_{i_{RZC}}\chi_{i_{RZC}}^{s_{weath}}\right]\right]} \quad \text{(II-77)}$$

For the example given above, but also including SO_4^{2-} and FeS_2 oxidation, the sulfuric acid weathering fraction is given for inversions when FeS_2 is explicitly included as an end-member in the inversion (Eqs. II-78 and II-79) or when quantifying FeS_2 oxidation with $\chi_{excess\ SO_4^{2-}}^{riv}$ (Eq. II-80) or with $\chi_{FeS_2\ SO_4^{2-}}^{s}$ values (Eq. II-81).

$$Z_{ALK}^{FeS_2\ ox.\ ALK} = \frac{-\chi_{ALK}^{FeS_2\ ox.}}{\chi_{ALK}^{carb}+\chi_{ALK}^{dolo}+\chi_{ALK}^{slct}} \quad \text{(II-78)}$$

$$Z_{Ca,Mg,Na}^{FeS_2\ ox.\ SO_4^{2-}} = \frac{2\chi_{SO_4^{2-}}^{FeS_2\ ox.}}{2\chi_{Ca^{2+}}^{calc}+2\chi_{Ca^{2+}}^{dolo}+2\chi_{Mg^{2+}}^{dolo}+2\chi_{Ca^{2+}}^{slct}+2\chi_{Mg^{2+}}^{slct}+\chi_{Na^{+}}^{slct}} \quad \text{(II-79)}$$

$$Z_{Ca,Mg,Na}^{excess\ SO_4^{2-}} = \frac{2\chi_{excess\ SO_4^{2-}}^{riv}}{2\chi_{Ca^{2+}}^{calc}+2\chi_{Ca^{2+}}^{dolo}+2\chi_{Mg^{2+}}^{dolo}+2\chi_{Ca^{2+}}^{slct}+2\chi_{Mg^{2+}}^{slct}+\chi_{Na^{+}}^{slct}} \quad \text{(II-80)}$$

$$Z_{Ca,Mg,Na}^{FeS_2\ SO_4^{2-}} = \frac{2\chi_{FeS_2\ SO_4^{2-}}^{carb}+2\chi_{FeS_2\ SO_4^{2-}}^{dolo}+2\chi_{FeS_2\ SO_4^{2-}}^{slct}}{2\chi_{Ca^{2+}}^{calc}+2\chi_{Ca^{2+}}^{dolo}+2\chi_{Mg^{2+}}^{dolo}+2\chi_{Ca^{2+}}^{slct}+2\chi_{Mg^{2+}}^{slct}+\chi_{Na^{+}}^{slct}} \quad \text{(II-81)}$$

Two variables related to Z are the charge-equivalent ratio of FeS_2-derived SO_4^{2-} to $\chi^{riv}_{SO_4^{2-}}$ (Eqs. II-82 to II-85) and to χ^{riv}_{norm} (Eqs. II-86 to II-89), which we define as Y and W, respectively. These ratios have been used in prior publications to evaluate the importance of FeS_2 oxidation relative to dissolved SO_4^{2-} and the sum of cations (Torres et al., 2016; Kemeny et al., 2021a) and are reported among the results of MEANDIR.

$$Y^{FeS_2\ ox.\ ALK} = \frac{-\chi^{FeS_2\ ox.}_{ALK}}{2\chi^{riv}_{SO_4^{2-}}} \tag{II-82}$$

$$Y^{FeS_2\ ox.\ SO_4^{2-}} = \frac{\chi^{FeS_2\ ox.}_{SO_4^{2-}}}{\chi^{riv}_{SO_4^{2-}}} \tag{II-83}$$

$$Y^{excess\ SO_4^{2-}} = \frac{\chi^{riv}_{excess\ SO_4^{2-}}}{\chi^{riv}_{SO_4^{2-}}} \tag{II-84}$$

$$Y^{FeS_2\ SO_4^{2-}} = \frac{\Sigma^{n}_{s_{FeS_2\ SO_4^{2-}}}\left[{}^{s}\chi_{FeS_2\ SO_4^{2-}}\right]}{\chi^{riv}_{SO_4^{2-}}} \tag{II-85}$$

$$W^{FeS_2\ ox.\ ALK} = \frac{-\chi^{FeS_2\ ox.}_{ALK}}{\chi^{riv}_{norm}} \tag{II-86}$$

$$W^{FeS_2\ ox.\ SO_4^{2-}} = \frac{2\chi^{FeS_2\ ox.}_{SO_4^{2-}}}{\chi^{riv}_{norm}} \tag{II-87}$$

$$W^{excess\ SO_4^{2-}} = \frac{2\chi^{riv}_{excess\ SO_4^{2-}}}{\chi^{riv}_{norm}} \tag{II-88}$$

$$W^{FeS_2\ SO_4^{2-}} = \frac{\Sigma^{n}_{s_{FeS_2\ SO_4^{2-}}}\left[2\,{}^{s}\chi_{FeS_2\ SO_4^{2-}}\right]}{\chi^{riv}_{norm}} \tag{II-89}$$

When C_{org} oxidation is treated as a stand-alone end-member, the organic carbon weathering fraction C is calculated as $\chi_{DIC}^{C_{org}\ ox.}$ relative to charge-equivalent cations sourced from weathering end-members (Eqs. II-90 and II-91).

$$C_{i_{RZC}\ldots k_{RZC}} = \frac{\chi_{DIC}^{C_{org}\ ox.}}{\Sigma_{s_{weath}}^{n_{weath}}\left[\Sigma_{i_{RZC}}^{k_{RZC}}\left[\alpha_{i_{RZC}}\chi_{i_{RZC}}^{s_{weath}}\right]\right]} \quad \text{(II-90)}$$

$$C_{Ca,Mg,Na} = \frac{\chi_{DIC}^{C_{org}\ ox.}}{2\chi_{Ca^{2+}}^{carb}+2\chi_{Ca^{2+}}^{dolo}+2\chi_{Mg^{2+}}^{dolo}+2\chi_{Ca^{2+}}^{slct}+2\chi_{Mg^{2+}}^{slct}+\chi_{Na^{+}}^{slct}} \quad \text{(II-91)}$$

II.3.15.3: R, Z, Y, W, and C values accounting for secondary phase formation

The formation of secondary phases removes solutes from river water and reduces each term in the summations that underlie calculation of R, Z, Y, W, and C. In the presence of secondary phases, we thus need to distinguish between gross (${}^{g}R$, ${}^{g}Z$, ${}^{g}C$) and net (${}^{n}R$, ${}^{n}Z$, ${}^{n}C$) weathering variables, both of which are reported in the results of MEANDIR. To calculate the net weathering parameters, we assume that the formation of secondary phases removes solutes in proportion to the fraction in which they are sourced from primary end-members.

As an example, consider a case where a carbonate end-member and a silicate end-member are the only sources to $\chi_{Ca^{2+}}^{riv}$ and $\chi_{Na^{+}}^{riv}$ and there is formation of a single secondary phase that uptakes both Ca^{2+} and Na^{+}. If the carbonate and silicate end-members contribute equally to $\chi_{Ca^{2+}}^{riv}$, MEANDIR will calculate that half the Ca^{2+} taken up into the secondary phase derives from the carbonate end-member and the remaining half derives from the silicate end-member. In this case, the gross values of $\chi_{Ca^{2+}}^{carb}$ and $\chi_{Ca^{2+}}^{slct}$ are reduced

by the same amount to reach net values. Conversely, if the gross $\chi^{carb}_{Ca^{2+}} = 2\chi^{slct}_{Ca^{2+}}$, then the net values of $\chi^{carb}_{Ca^{2+}}$ and $\chi^{slct}_{Ca^{2+}}$ are reached after removing twice as much from the gross value of $\chi^{carb}_{Ca^{2+}}$ as from that of $\chi^{slct}_{Ca^{2+}}$. If we assume that the carbonate end-member does not contain Na^+, the net value of $\chi^{slct}_{Na^+}$ is found by subtracting the full amount of Na^+ taken up into the secondary phase from the gross value of $\chi^{slct}_{Na^+}$. If the gross ratio of Na^+ to Ca^{2+} released from the carbonate and silicate end-members is different than the ratio of Na^+ to Ca^{2+} in the secondary phase, the net and gross values of R will be different. Below, we give a generalized mathematical treatment of these effects from secondary phase formation on contributions to R, Z, Y, W, and C.

We initially consider the effect of two secondary phases referenced with the superscripts s_1^{second} and s_2^{second}. When considering the net contribution of solute i_{RZC} from end-member s, the net value ${}^{n}\chi^{s}_{i_{RZC}}$ is calculated by scaling the gross value ${}^{g}\chi^{s}_{i_{RZC}}$ by one plus the ratio of the uptake into secondary phases, $\chi^{s_1^{second}}_{i_{RZC}}$ and $\chi^{s_2^{second}}_{i_{RZC}}$, to the sum of all sources of i_{RZC}, indexed by $s^{source}_{i_{RZC}}$ over a list of length $n^{source}_{i_{RZC}}$ (Eq. II-92). In turn, the terms for secondary uptake are aggregated into a sum over $s^{sink}_{i_{RZC}}$ indexing a list of length $n^{sink}_{i_{RZC}}$ containing all end-members that uptake solute i_{RZC} from river water. To account for secondary phase formation each gross term in the calculation of R, Z, Y, W, and C must be multiplied by the sum of 1 and the ratio of all solute sinks to all solute sources (Eq. II-93 for ${}^{n}R_{i_{RZC}\ldots k_{RZC}}$ and Eq. II-94 for ${}^{n}Z^{FeS_2\ SO_4^{2-}}_{i_{RZC}\ldots k_{RZC}}$). In MEANDIR, the individual gross terms of Y, W, and C are likewise modified to reach net values.

$$
{}^{n}\chi^{s}_{i_{RZC}} = {}^{g}\chi^{s}_{i_{RZC}} \left(1 + \left(\frac{\chi^{s_1^{second}}_{i_{RZC}}}{\Sigma^{n_{i_{RZC}}^{source}}_{s_{i_{RZC}}^{source}} \left[{}^{g}\chi_{i_{RZC}}^{s_{i_{RZC}}^{source}} \right]} \right) + \left(\frac{\chi^{s_2^{second}}_{i_{RZC}}}{\Sigma^{n_{i_{RZC}}^{source}}_{s_{i_{RZC}}^{source}} \left[{}^{g}\chi_{i_{RZC}}^{s_{i_{RZC}}^{source}} \right]} \right) + \cdots \right)
$$

$$
= {}^{g}\chi^{s}_{i_{RZC}} \left(1 + \frac{\Sigma^{n_{i_{RZC}}^{sink}}_{s_{i_{RZC}}^{sink}} \left[\chi_{i_{RZC}}^{s_{i_{RZC}}^{sink}} \right]}{\Sigma^{n_{i_{RZC}}^{source}}_{s_{i_{RZC}}^{source}} \left[{}^{g}\chi_{i_{RZC}}^{s_{i_{RZC}}^{source}} \right]} \right) \tag{II-92}
$$

$$
{}^{n}R_{i_{RZC} \ldots k_{RZC}} = \frac{\Sigma^{n_{carb}}_{s_{carb}} \left[\Sigma^{k_{RZC}}_{i_{RZC}} \left[\alpha_{i_{RZC}} \left({}^{g}\chi_{i_{RZC}}^{s_{carb}} \right) \left(1 + \frac{\Sigma^{n_{i_{RZC}}^{sink}}_{s_{i_{RZC}}^{sink}} \left[\chi_{i_{RZC}}^{s_{i_{RZC}}^{sink}} \right]}{\Sigma^{n_{i_{RZC}}^{source}}_{s_{i_{RZC}}^{source}} \left[{}^{g}\chi_{i_{RZC}}^{s_{i_{RZC}}^{source}} \right]} \right) \right] \right]}{\Sigma^{n_{weath}}_{s_{weath}} \left[\Sigma^{k_{RZC}}_{i_{RZC}} \left[\alpha_{i_{RZC}} \left({}^{g}\chi_{i_{RZC}}^{s_{weath}} \right) \left(1 + \frac{\Sigma^{n_{i_{RZC}}^{sink}}_{s_{i_{RZC}}^{sink}} \left[\chi_{i_{RZC}}^{s_{i_{RZC}}^{sink}} \right]}{\Sigma^{n_{i_{RZC}}^{source}}_{s_{i_{RZC}}^{source}} \left[{}^{g}\chi_{i_{RZC}}^{s_{i_{RZC}}^{source}} \right]} \right) \right] \right]} \tag{II-93}
$$

$$
{}^{n}Z^{FeS_2\ SO_4^{2-}}_{i_{RZC} \ldots k_{RZC}} = \frac{\Sigma^{n_{FeS_2\ SO_4^{2-}}}_{s_{FeS_2\ SO_4^{2-}}} \left[2\ {}^{g}\chi^{s_{FeS_2\ SO_4^{2-}}}_{FeS_2\ SO_4^{2-}} \left(1 + \frac{\Sigma^{n_{SO_4^{2-}}^{sink}}_{s_{SO_4^{2-}}^{sink}} \left[\chi_{SO_4^{2-}}^{s_{SO_4^{2-}}^{sink}} \right]}{\Sigma^{n_{SO_4^{2-}}^{source}}_{s_{SO_4^{2-}}^{source}} \left[{}^{g}\chi_{SO_4^{2-}}^{s_{SO_4^{2-}}^{source}} \right]} \right) \right]}{\Sigma^{n_{weath}}_{s_{weath}} \left[\Sigma^{k_{RZC}}_{i_{RZC}} \left[\alpha_{i_{RZC}} \left({}^{g}\chi_{i_{RZC}}^{s_{weath}} \right) \left(1 + \frac{\Sigma^{n_{i_{RZC}}^{sink}}_{s_{i_{RZC}}^{sink}} \left[\chi_{i_{RZC}}^{s_{i_{RZC}}^{sink}} \right]}{\Sigma^{n_{i_{RZC}}^{source}}_{s_{i_{RZC}}^{source}} \left[{}^{g}\chi_{i_{RZC}}^{s_{i_{RZC}}^{source}} \right]} \right) \right] \right]} \tag{II-94}
$$

II.3.15.4: R, Z, Y, W, and C with scaled values

A final complexity in calculating R, Z, Y, W, and C arises in the case of systematic difference between inversion results and river observations. In general, the composition of a river sample calculated using the inversion model results may not exactly match river observations. In a case where the model results consistently under-predict observed $\chi^{riv}_{Na^+}$ $\left(\Sigma^{n}_{s}\left[f^{s}_{Na^+}\right] < 1\right)$ and over-predict observed $\chi^{riv}_{Ca^{2+}}$ $\left(\Sigma^{n}_{s}\left[f^{s}_{Ca^{2+}}\right] > 1\right)$ in a sample, the

calculated value of R will likely be different compared to a case where both $\chi^{riv}_{Na^+}$ and $\chi^{riv}_{Ca^{2+}}$ are reconstructed more accurately. To enforce the condition that fractional contributions should sum to 1, even when the results of the cost function optimization do not meet that criteria, it is formally possible to normalize each fractional contribution to the sum of all fractional contributions during the calculation of weathering parameters (Eqs. II-95 to II-97, where s indexes the list of length n containing all end-members). We refer to this normalization as the "scaled" value of a parameter. That is, the calculation of scaled weathering parameters ($_{sc}$R, $_{sc}$Z, $_{sc}$Y, $_{sc}$W, and $_{sc}$C) adapts the inversion results to better recreate sample observations. Results with and without scaling will be very similar if MEANDIR is able to fit observations well and converge to the same value when observations are perfectly reconstructed ($\Sigma_s^n[f_i^s] = 1$). In general, we urge caution in using scaled parameters as these derived variables are a modified version of the inversion results and are not natural solutions to the mixing model.

$$ {}^{n}_{sc}\chi^{s}_{i_{RZC}} = \frac{{}^{n}\chi^{s}_{i_{RZC}}}{\Sigma_s^n\left[f^s_{i_{RZC}}\right]} = \frac{{}^{g}\chi^{s}_{i_{RZC}}}{\Sigma_s^n\left[f^s_{i_{RZC}}\right]}\left(1 + \frac{\Sigma^{n^{sink}_{i_{RZC}}}_{s^{sink}_{i_{RZC}}}\left[{}^{s^{sink}_{i_{RZC}}}\chi_{i_{RZC}}\right]}{\Sigma^{n^{source}_{i_{RZC}}}_{s^{source}_{i_{RZC}}}\left[{}^{s^{source}_{i_{RZC}}}\chi_{i_{RZC}}\right]}\right) \tag{II-95} $$

$$ {}^{n}_{sc}R_{i_{RZC}\ldots k_{RZC}} = \frac{\Sigma^{n_{carb}}_{s_{carb}}\left[\Sigma^{k_{RZC}}_{i_{RZC}}\left[\alpha_{i_{RZC}}\left(\frac{{}^{g}\chi^{s_{carb}}_{i_{RZC}}}{\Sigma_s^n\left[f^s_{i_{RZC}}\right]}\right)\left(1+\frac{\Sigma^{n^{sink}_{i_{RZC}}}_{s^{sink}_{i_{RZC}}}\left[{}^{s^{sink}_{i_{RZC}}}\chi_{i_{RZC}}\right]}{\Sigma^{n^{source}_{i_{RZC}}}_{s^{source}_{i_{RZC}}}\left[{}^{s^{source}_{i_{RZC}}}\chi_{i_{RZC}}\right]}\right)\right]\right]}{\Sigma^{n_{weath}}_{s_{weath}}\left[\Sigma^{k_{RZC}}_{i_{RZC}}\left[\alpha_{i_{RZC}}\left(\frac{{}^{g}\chi^{s_{weath}}_{i_{RZC}}}{\Sigma_s^n\left[f^s_{i_{RZC}}\right]}\right)\left(1+\frac{\Sigma^{n^{sink}_{i_{RZC}}}_{s^{sink}_{i_{RZC}}}\left[{}^{s^{sink}_{i_{RZC}}}\chi_{i_{RZC}}\right]}{\Sigma^{n^{source}_{i_{RZC}}}_{s^{source}_{i_{RZC}}}\left[{}^{s^{source}_{i_{RZC}}}\chi_{i_{RZC}}\right]}\right)\right]\right]} \tag{II-96} $$

$$ {}^{n}_{sc}Z^{FeS_2\ SO_4^{2-}}_{i_{RZC}\ldots k_{RZC}} = \frac{\Sigma^{{}^{n}FeS_2\ SO_4^{2-}}_{{}^{s}FeS_2\ SO_4^{2-}}\left[\left(\frac{2\ {}^{g}\chi^{{}^{s}FeS_2\ SO_4^{2-}}_{FeS_2\ SO_4^{2-}}}{\Sigma^{n}_{s}\left[f^{s}_{SO_4^{2-}}\right]}\right)\left(1+\frac{\Sigma^{{}^{n}sink}_{{}^{s}sink}\left[{}^{s}\chi^{{}^{s}sink}_{SO_4^{2-}}\right]}{\Sigma^{{}^{n}source}_{{}^{s}source}\left[{}^{s}g_{\chi^{{}^{s}source}_{SO_4^{2-}}}\right]}\right)\right]}{\Sigma^{{}^{n}weath}_{{}^{s}weath}\left[\Sigma^{k_{RZC}}_{i_{RZC}}\left[\alpha_{i_{RZC}}\left(\frac{{}^{g}\chi^{{}^{s}weath}_{i_{RZC}}}{\Sigma^{n}_{s}\left[f^{s}_{i_{RZC}}\right]}\right)\left(1+\frac{\Sigma^{{}^{n}sink}_{{}^{s}sink}\left[{}^{s}\chi^{{}^{s}sink}_{i_{RZC}}\right]}{\Sigma^{{}^{n}source}_{{}^{s}source}\left[{}^{s}g_{\chi^{{}^{s}source}_{i_{RZC}}}\right]}\right)\right]\right]} \quad \text{(II-97)} $$

In summary, MEANDIR calculates four different values of R, Z, Y, W, and C reflecting net or gross fluxes and with or without scaling to the sum of all fractional contributions. In the absence of secondary phase formation, the net and gross parameters are equal. For most applications, we recommend using the net weathering parameters derived without scaling (Eqs. II-93 and II-94).

II.3.15.5: Including $\chi^{slct}_{Na^+}$ and $\chi^{slct}_{K^+}$ in R and Z

Researchers disagree on the appropriate role of $\chi^{slct}_{Na^+}$ and $\chi^{slct}_{K^+}$ when using river chemistry to study the carbon cycle. In part, this argument reflects the need to distinguish between the drawdown of atmospheric CO_2 and the drawdown of DIC. Below, we argue that $\chi^{slct}_{Na^+}$ and $\chi^{slct}_{K^+}$ can be partially neglected or excluded when quantifying the removal of DIC from the ocean-atmosphere system but should be included when quantifying the impact of chemical denudation on the concentration of atmospheric CO_2. Because R and Z capture dynamics relating to the latter, we suggest that $\chi^{slct}_{Na^+}$ and $\chi^{slct}_{K^+}$ should be included in the weathering parameters discussed above. Note, however, that MEANDIR calculates R and Z based on user-supplied criteria and is agnostic to the opinion of its authors.

Regardless of which elements are included, the denominators of R, Z, and C should all be calculated using the same cations.

The common argument against including $\chi^{slct}_{Na^+}$ and $\chi^{slct}_{K^+}$ in calculations of carbon drawdown is that, because alkali cations are removed from seawater during reverse weathering, $\chi^{slct}_{Na^+}$ and $\chi^{slct}_{K^+}$ do not contribute to loss of carbon during burial of marine $CaCO_3$. In the same framework, $\chi^{slct}_{Mg^{2+}}$ is often considered interchangeable with $\chi^{slct}_{Ca^{2+}}$ despite that Mg-bearing carbonate is not directly precipitated in the modern ocean. Rather, the principal loss of marine Mg^{2+} is through hydrothermal vent circulation, which entails both Mg^{2+}-Ca^{2+} exchange and reverse weathering reactions (Edmond et al., 1979a, 1979b). It is worth noting that fully including or excluding $\chi^{slct}_{Na^+}$ and $\chi^{slct}_{K^+}$ in calculations of carbon drawdown lacks historical precedent. For example, Gaillardet et al. (1999) report results for different combinations of cations, while Galy and France-Lanord (1999) assume that 30% of $\chi^{slct}_{Na^+}$ and 20% of $\chi^{slct}_{K^+}$ can be included in their calculations due to the participation of these ions in exchange reactions that ultimately liberate Ca^{2+}. Overall, we largely agree with the practice of using $\chi^{slct}_{Ca^{2+}}$ and fractions of $\chi^{slct}_{Mg^{2+}}$, $\chi^{slct}_{Na^+}$ and $\chi^{slct}_{K^+}$ to quantify DIC removal from the ocean-atmosphere system.

Conversely, because atmospheric pCO_2 is set by the balance between marine ALK and DIC, accounting for the impacts of weathering on atmospheric carbon dioxide requires considering $\chi^{slct}_{Na^+}$ and $\chi^{slct}_{K^+}$. The role of $\chi^{slct}_{Na^+}$ and $\chi^{slct}_{K^+}$ in impacting pCO_2 is analogous but opposite to that of $\chi^{riv}_{SO_4^{2-}}$ derived from FeS_2 oxidation; the three fluxes alter pCO_2 through repartitioning of carbon between the ocean and atmosphere without altering total ocean-atmosphere DIC. However, like FeS_2 oxidation, $\chi^{slct}_{Na^+}$ and $\chi^{slct}_{K^+}$ only impact

pCO_2 if their inputs to seawater are out of balance with their loss terms. Leaving $\chi_{Na^+}^{slct}$ and $\chi_{K^+}^{slct}$ out of R and Z is effectively assuming steady-state in the biogeochemical cycles of Na^+ and K^+, akin to setting $Z = 0$ by assuming steady-state in the global biogeochemical cycle of SO_4^{2-}. Whether or not to include $\chi_{Na^+}^{slct}$ and $\chi_{K^+}^{slct}$ in R and Z is thus a question of whether the seawater concentrations of Na^+ and K^+ are assumed to be changing. As it is common to study the role of weathering in response to geologic perturbations to the carbon cycle, such as the Paleocene Eocene Thermal Maximum, it may be particularly important to account for non-steady-state behavior in global biogeochemical cycles. Our opinion is that, when using the R-Z-C space to quantify the impacts of weathering on pCO_2, $\chi_{Na^+}^{slct}$ and $\chi_{K^+}^{slct}$ should be included in the weathering parameters so that they reflect the actual χ_{ALK}/χ_{DIC} of the weathering system itself and not an assumption of marine processes. Lastly, including Na^+ and K^+ captures the maximum alkalinity generated through chemical weathering and is more conservative than leaving them out when evaluating the impacts of FeS_2 oxidation and C_{org} oxidation on pCO_2.

II.4: Applications of MEANDIR

II.4.1: Overview of inversion scenarios

We present selected results from inversion of five previously published river chemistry datasets to demonstrate the functionality of MEANDIR and its sensitivity to parameter choices (Tables II-5 to II-13). The first dataset is a global compilation of major element concentrations from Gaillardet et al. (1999), the second dataset is the major element chemistry of global river water samples from Burke et al. (2018), the third is the major element chemistry and SO_4^{2-} $\delta^{34}S$ values of river water samples from the Peruvian Amazon reported in Torres et al. (2016), the fourth is the major element chemistry of Icelandic rivers from Gíslason et al. (1996), and the fifth is the major and trace element chemistry of Mackenzie River water samples from Horan et al. (2019). The scenarios are indexed alphanumerically by the initials of the first author on the article underlying each data source: JG for Gaillardet et al. (1999), AB for Burke et al. (2018), MT for Torres et al. (2016), SG for Gíslason et al. (1996), and KH for Horan et al. (2019). For a given data source, scenario numbering follows the order in which results are presented in the text. We consider results from 28 different inversion scenarios across these five datasets: 12 JG scenarios (Tables II-5 and II-7), 6 AB scenarios (Tables II-6 and II-7), 7 MT scenarios (Tables II-8 and II-9), 1 SG scenario (Tables II-10 and II-11), and 2 KH scenarios (Tables II-12 and II-13). Relevant inversion parameters and end-member chemical compositions are tabulated for all scenarios (Tables II-5 to II-13), and the full suite of inversion parameters are included in the MEANDIR download.

Scenarios JG-1 through JG-8 and JG-2c through JG-5c operate on the global dataset of Gaillardet et al. (1999) (Tables II-5 and II-7). Scenario JG-1 describes a large inversion

that accepts nearly all simulation results, with other parameter selections reflecting our favored settings, in order to perform sensitivity testing. Scenario JG-2 describes a modified inversion in which only a subset of results are kept, and most scenarios reflect a change of only one or two parameters from scenario JG-2. Scenario JG-3 uses uniform distributions for end-member chemistry and scenario JG-4 normalizes observations and end-members with χ_{Na^+} rather than χ_{Σ^+}. Scenario JG-5 solves each combination of observations and end-members using a constrained optimization of absolute misfit rather than proportional misfit. Scenarios JG-2 through JG-5 are also evaluated using $\chi^{riv}_{Cl^-\,critical}$ values, in which case the scenario number is appended with "c." Because $\chi^{riv}_{Cl^-\,critical}$ values are not available in the original publication (Gaillardet et al., 1999), we instead select $\chi^{riv}_{Cl^-\,critical}$ values for each sample that are a random fraction of $\chi^{riv}_{Cl^-}$. This is merely for demonstration purposes; simulations with randomly selected $\chi^{riv}_{Cl^-\,critical}$ values are not used to reach conclusions regarding controls on weathering or its influence on climate. The criteria for a single simulation to count as successful in scenarios JG-2 through JG-5 and JG-2c through JG-5c is that the sum of fractional contributions from all end-members to each dissolved variable is between 85% and 115%. Conversely, in scenario JG-6 all samples are presented with the same end-members and all results are temporarily accepted. At the conclusion of the inversion, the 1% of simulations with lowest misfit between observations and model results, as evaluated across all samples, are retained for additional analysis. Scenarios JG-7 and JG-8 differ from scenario JG-3 by including $\chi^{riv}_{HCO_3^-}$ in the inversion. Scenario JG-7 uses end-members where $\chi^{s}_{HCO_3^-}/\chi^{s}_{\Sigma^+}$ ratios are drawn from distributions, while scenario JG-8 uses end-members with fixed ratios of $\chi^{s}_{HCO_3^-}/\chi^{s}_{\Sigma^+}$ (Blattmann et al., 2019).

Scenarios AB-1 through AB-6 invert the river chemistry dataset of Burke et al. (2018) (Tables II-6 and II-7). Scenarios AB-1, AB-2, and AB-3 differ by whether $\chi^{\mathrm{riv}}_{\mathrm{HCO_3^-}}$ is included or excluded from the inversion and cost function. Scenario AB-4 quantifies Z with $\chi^{\mathrm{riv}}_{\mathrm{excess\ SO_4^{2-}}}$ and does not include $\chi^{\mathrm{riv}}_{\mathrm{SO_4^{2-}}}$ in the inversion, and scenario AB-5 uses an independent end-member to quantify $\chi^{\mathrm{other}}_{\mathrm{SO_4^{2-}}}$. Notably, the AB-5 scenario uses our novel normalization where χ_{norm} includes $\chi_{\mathrm{SO_4^{2-}}}$. Scenario AB-6 is identical to AB-1 except that the carbonate and silicate end-members are constrained to have $\chi^{\mathrm{S}}_{\mathrm{FeS_2\ SO_4^{2-}}}/\chi^{\mathrm{S}}_{\Sigma+}$ ratios ranging from 0 to 0.15 instead of from 0 to 1, which we find impacts the inversion-constrained value of the median carbonate weathering fraction.

Scenarios MT-1 through MT-7 operate on the dataset of water samples presented in Torres et al. (2016) (Tables II-8 and II-9). Scenario MT-1 is the default scenario for these inversions, and scenarios MT-2 and MT-4 differ by optimizing to absolute misfit rather than proportional misfit. Similar to scenario JG-6, in scenarios MT-3 and MT-4 all samples are presented with the same end-members and all results are temporarily accepted. At the conclusion of the inversion, the 1% of simulations with lowest misfit between observations and model results, but in this case evaluated at the level of each individual sample, are retained for additional analysis. Scenario MT-5 is identical to MT-1 except that it has ~1000 successful simulations for each sample. Scenario MT-6 differs from scenario MT-5 by calculating Z from excess $\mathrm{SO_4^{2-}}$ rather than including $\chi^{\mathrm{riv}}_{\mathrm{SO_4^{2-}}}$ directly in the inversion, and scenario MT-7 treats $\mathrm{FeS_2}$ oxidation as an independent end-member. As in AB-5, in MT-7 the normalization includes $\chi_{\mathrm{SO_4^{2-}}}$. We compare estimates for the $\delta^{34}\mathrm{S}$ of lithologic $\mathrm{FeS_2}$ across scenarios MT-5, MT-6, and MG-7 and, through comparison to

measured bedrock $\delta^{34}S$ values reported in Torres et al. (2016), validate the application of river inversion models for constraining bedrock sulfur isotope composition.

Scenario SG-1 operates on the dataset of Icelandic river water samples from Gíslason et al. (1996) (Tables II-10 and II-11). The only solute sources in this inversion are meteoric precipitation and basalt weathering, and we consider one solute sink due to the formation of secondary clay. Our analysis focuses on using MEANDIR to quantify the chemical composition of the secondary clay end-member. We compare inversion results with observations of Icelandic clay chemistry from Moulton et al. (2000) and Thorpe et al. (2019).

Scenarios KH-1 and KH-2 invert water samples from the Mackenzie River reported in Horan et al. (2019) (Tables II-12 and II-13). Our analysis uses $\chi^{\mathrm{riv}}_{\Sigma^+}$, $\chi^{\mathrm{riv}}_{SO_4^{2-}}$, and $\chi^{\mathrm{riv}}_{\mathrm{Re}}$ to simultaneously quantify chemical weathering, FeS_2 oxidation, and C_{org} oxidation, respectively. The normalized χ_{Re} ratios for organic carbon oxidation are derived from the text of Horan et al. (2019), while the ratios for the FeS_2 and silicate end-members are estimated from Figure 4B of that same work. KH-1 is normalized to $\chi_{\Sigma^+ + \mathrm{ALK} + \mathrm{DIC}}$ and KH-2 is normalized to $\chi_{\Sigma^+ + SO_4^{2-} + \mathrm{DIC}}$, but the scenarios are otherwise identical. The results of KH-1 and KH-2 are extremely similar despite the different normalizations. We only show results for KH-1 but for completeness also present the inversion parameters for KH-2 (Tables II-12 and II-13). Given that KH-1 and KH-2 are intended merely as proof-of-concept that MEANDIR can use new normalizations to quantify FeS_2 oxidation and C_{org} oxidation as independent end-members, we make several simplifying assumptions in these scenarios. First, we assume that no evaporites are present in the sampled catchments. Second, we allow the silicate and carbonate end-members to take on a wide range of

possible chemical compositions. Third, we assume that river χ^{riv}_{ALK} and χ^{riv}_{DIC} are equal to $\chi^{riv}_{HCO_3^-}$. Although this assumption is less than ideal, the dearth of existing χ^{riv}_{Re} measurements limits the number of datasets where quantification of C_{org} oxidation can be demonstrated. Fourth, unlike the full analysis of Horan et al. (2019), our analysis does not account for the production or burial of modern organic carbon. That is, our inversion is based only on the river water chemistry and does not consider carbon burial in floodplains or marine sediments.

II.4.2: Sensitivity of results to sample matching or lowest misfit fraction

The sensitivity of model results to changes in the fraction of retained simulations is demonstrated using scenario JG-1, an inversion of the data from Gaillardet et al. (1999) where nearly all simulation results are initially accepted (Fig. II-2; Table II-5). We calculate changes in the median fractional contribution of the carbonate end-member to $\chi^{riv}_{Ca^{2+}}$, $f^{carb}_{Ca^{2+}}$, resulting from either changing the permissible fractional difference between inversion results and observations or from considering only a fraction of simulations with the lowest misfit between inversion results and observations. Overall, imposing a selection criterion based on either sample matching or lowest misfit fraction generates large changes in the median value of $f^{carb}_{Ca^{2+}}$ (Fig. II-2A). For the Rhone River sample, which was selected as an example for illustrative purposes, the median value of $f^{carb}_{Ca^{2+}}$ shifts from 0.26 to 0.86 when constraining results to only those simulations that reconstruct between 85% and 118% of all river observations (Fig. II-2B). Likewise, the median value of $f^{carb}_{Ca^{2+}}$ shifts from 0.26 to 0.94 when only retaining the 5% of simulations with lowest misfit between inversion results and observations (Fig. II-2C). These 60-68% absolute changes in the

inversion-constrained contribution of the carbonate end-member to $\chi^{riv}_{Ca^{2+}}$ would have substantial implications for the interpretation of inversion results.

Across most samples from Gaillardet et al. (1999), the median value of $f^{carb}_{Ca^{2+}}$ increases and the inversion-constrained range in $f^{carb}_{Ca^{2+}}$ (95th – 5th percentile) decreases with more stringent selection criteria (Figs. II-2D, E, H, and I). Moreover, the inversion-constrained range of carbonate $2\chi^{carb}_{Ca^{2+}}/\chi^{carb}_{\Sigma^{+}}$ also generally decreases with tighter sample matching criteria (Fig. II-2G) or with a lower fraction of retained simulations (Fig. II-2K).

To constrain the sensitivity of inversion results to the number of successful simulations, we also quantify changes in the fractional contribution of the carbonate end-member with changes in the number of simulations satisfying an imposed sample matching criteria (Figs. II-2M and N). These results, generated from scenario JG-2, show relatively little change in the median $f^{carb}_{Ca^{2+}}$ value or range in $f^{carb}_{Ca^{2+}}$ (95th – 5th percentile range of the inversion-constrained distribution) after about 100 successful simulations.

This sensitivity analysis demonstrates that inversion results change drastically when removing simulations that either fail to recreate river observations or have high misfit from observations. However, the results of JG-1 appear only minimally sensitive to small changes in the specific values of success criteria. For example, results are qualitatively similar when sample matching criteria are 75-133% or 80-125%. Likewise, results are qualitatively similar when retaining the 2% or 5% of simulations with lowest misfit between model results and observations. In MEANDIR, the choice of how to subsample inversion results is left to the user.

II.4.3: Median fractional contributions to dissolved variables

Values of f_i^s for carbonate, silicate, and evaporite end-members show different sensitivities to common choices for inversion parameters (Fig. II-3). For all dissolved variables, the fractional contributions of the carbonate and silicate end-members are relatively consistent among scenario JG-2 and either scenario JG-3 (uniform end-member distributions; Figs. II-3A and B), scenario JG-4 (χ_{Na+} normalization; Figs. II-3E and F) or scenario JG-5 (absolute cost function; Figs. II-3I and J). For these scenarios the agreement of median fractional contributions from silicate and carbonate end-members is often within 10% and frequently within 25% (Fig. II-3 gray shading). For any individual sample the differences in the median f_i^{carb} or f_i^{slct} values between scenarios tend to be smaller or comparable to the range in simulation results. Conversely, the fractional differences among median evaporite contributions tend to be larger (Figs. II-3C, G, and K). In particular, values of $f_{Na^+}^{evap}$ and $f_{Cl^-}^{evap}$ in scenario JG-5 are generally lower than in scenario JG-2 (Fig. II-3K), with the difference taken up by higher values of $f_{Na^+}^{prec}$ and $f_{Cl^-}^{prec}$. The disagreement of $f_{Na^+}^{evap}$ and $f_{Cl^-}^{evap}$ among JG-2 and the other scenarios reflects that simulations satisfying sample matching criteria can be found when the majority of $\chi_{Cl^-}^{riv}$ is sourced from either evaporite or from precipitation, such that changes in the scenario parameters alter which end-member is calculated to make the larger contribution to river dissolved load. Lacking a robust chemical basis for differentiating precipitation from evaporites, the inversion-constrained median $f_{Na^+}^{evap}$ and $f_{Cl^-}^{evap}$ values can easily shift. In general, identification of a chemical tracer distinguishing precipitation from evaporite inputs would greatly aid inversion models.

Applying values of $\chi^{riv}_{Cl^-\ critical}$ addresses this problem by explicitly assigning $f^{prec}_{Cl^-}$, which also uniquely defines $f^{evap}_{Cl^-}$ because in these scenarios only the precipitation and evaporite end-members have non-zero values of $\chi^{s}_{Cl^-}$ (Table II-7). When $\chi^{riv}_{Cl^-\ critical}$ values are implemented, the four scenarios are in stronger agreement for the fraction of each element sourced from each end-member (Figs. II-3D, H, and L). $\chi^{riv}_{Cl^-\ critical}$ values are thus a valuable tool for partitioning $\chi^{riv}_{Cl^-}$ between precipitation and evaporite end-members.

II.4.4: Distributions of the sum of fractional contributions in successful simulations

Inversion models can produce results that only poorly recreate observations of river dissolved load. To demonstrate the problem, we consider distributions of the sum of inversion-constrained fractional contributions from all end-members ($\Sigma^{n}_{s}[f^{s}_{i}]$) (Fig. II-4). In the case that inversion results perfectly match observations, the sum of fractional contributions from all end-members would equal 100%. In scenario MT-1 (relative cost function) and scenario MT-2 (absolute cost function) distributions of $\Sigma^{n}_{s}\left[f^{s}_{Ca^{2+}}\right]$ (Fig. II-4A), $\Sigma^{n}_{s}\left[f^{s}_{Mg^{2+}}\right]$ (Fig. II-4B), $\Sigma^{n}_{s}\left[f^{s}_{Na^{+}}\right]$ (Fig. II-4C), and $\Sigma^{n}_{s}[f^{s}_{Cl^-}]$ (Fig. II-4D) are all constrained between 85% and 115%. Within this range, however, more values of $\Sigma^{n}_{s}\left[f^{s}_{Ca^{2+}}\right]$ and $\Sigma^{n}_{s}\left[f^{s}_{Mg^{2+}}\right]$ are close to 100% in scenario MT-2 than in scenario MT-1 (Figs. II-4A and B). The distribution of $\Sigma^{n}_{s}\left[f^{s}_{Na^{+}}\right]$ is similar for the two scenarios (Fig. II-4C), and the distribution of $\Sigma^{n}_{s}[f^{s}_{Cl^-}]$ in scenario MT-1 has more values close to 100% than in MT-2 (Fig. II-4D).

These differences reflect whether the scenario uses a cost function based on absolute misfit or relative misfit. In the former case, variables with higher normalized

values are reconstructed with higher proportional fits than variables with lower normalized values. In the latter case, variables with low normalized ratios exert a relatively stronger influence on the cost function and equalize proportional misfit across observations. Because most samples have $\chi^{riv}_{Ca^{2+}} > \chi^{riv}_{Na^{+}} > \chi^{riv}_{Cl^{-}}$, results from scenario MT-2 have $\Sigma^{n}_{s}\left[f^{s}_{Ca^{2+}}\right]$ values near 100% but a large range in $\Sigma^{n}_{s}[f^{s}_{Cl^{-}}]$ values. Following the same logic, we would expect results from scenario MT-1 to show similar ranges in $\Sigma^{n}_{s}\left[f^{s}_{Ca^{2+}}\right]$ and $\Sigma^{n}_{s}[f^{s}_{Cl^{-}}]$. However, the results of MT-1 instead show that $\Sigma^{n}_{s}[f^{s}_{Cl^{-}}]$ values are typically closer to 100% than values of $\Sigma^{n}_{s}\left[f^{s}_{Ca^{2+}}\right]$ in the same scenario (Figs. II-4A and D). This difference from expectations potentially reflects that, while $\chi^{riv}_{Cl^{-}}$ is sourced from only a single end-member in scenarios MT-1 through MT-4, multiple end-members contribute to $\chi^{riv}_{Ca^{2+}}$ and may introduce additional variability to $\Sigma^{n}_{s}\left[f^{s}_{Ca^{2+}}\right]$.

Successful results in scenarios MT-3 (relative cost function) and MT-4 (absolute cost function) are the 1% of simulations for each sample with the lowest misfit between model results and observations, without the explicit sample matching requirement of scenarios MT-1 and MT-2. In scenario MT-3 several samples have values for $\Sigma^{n}_{s}\left[f^{s}_{Ca^{2+}}\right]$, $\Sigma^{n}_{s}\left[f^{s}_{Mg^{2+}}\right]$, and $\Sigma^{n}_{s}\left[f^{s}_{Na^{+}}\right]$ substantially offset from 100% while values of $\Sigma^{n}_{s}[f^{s}_{Cl^{-}}]$ are close to 100%. Conversely, in scenario MT-4 most results have values for $\Sigma^{n}_{s}\left[f^{s}_{Ca^{2+}}\right]$, $\Sigma^{n}_{s}\left[f^{s}_{Mg^{2+}}\right]$, and $\Sigma^{n}_{s}\left[f^{s}_{Na^{+}}\right]$ near 100% while very few values of $\Sigma^{n}_{s}[f^{s}_{Cl^{-}}]$ are close to 100% (Fig. II-4D). These results are similar to those from MT-1 and MT-2, where the scenario using a proportional cost function is better able to recreate variables at low relative abundance.

Overall, this analysis demonstrates that selecting a small fraction of simulations with the lowest misfit between results and observations does not necessarily produce

results consistent with dissolved river chemistry. Rather, using explicit sample matching criteria produces results consistent with observations, and using a proportional cost function helps to model observations at low relative abundance. For most applications, MT-1 (sample matching with relative misfit) is thus our favored choice among the four scenarios considered in this section.

II.4.5: Distributions of constrained end-member chemistry

The distributions of end-member chemical ratios in successful inversions can differ substantially from the initial distributions (Fig. II-5). To demonstrate these changes we consider the initial and final distributions of $2\chi^{carb}_{Mg^{2+}}/\chi^{carb}_{\Sigma^+}$ and $2\chi^{carb}_{Mg^{2+}}/\chi^{carb}_{Na^+}$ in inversions of the global river data of Gaillardet et al. (1999) (scenarios JG-2, JG-3, JG-4, and JG-6) (Figs. II-5A to F) and distributions of $2\chi^{dolo}_{Mg^{2+}}/\chi^{dolo}_{\Sigma^+}$ and $2\chi^{dolo}_{SO_4^{2-}}/\chi^{dolo}_{\Sigma^+}$ in inversions of the river samples of Torres et al. (2016) (scenario MT-1 and MT-3) (Figs. II-5G to I). Regardless of whether the initial distribution of end-member chemistry is normal (Fig. II-5A), uniform (Fig. II-5B), or normalized with χ_{Na^+} rather than χ_{Σ^+} (Fig. II-5D), the final distributions are typically distinct from the initial distributions. Moreover, inversion-constrained distributions of end-member chemistry can be relatively insensitive to whether the initial distribution is normal or uniform; on a percentile-percentile cross plot of $2\chi^{carb}_{Mg^{2+}}/\chi^{carb}_{\Sigma^+}$ in scenarios JG-2 and JG-3, most of the point density occurs close to a 1:1 line (Fig. II-5C). However, we note that the shape of the initial end-member distribution may have a larger impact on the final end-member distributions when only accepting a fraction of simulations with lowest misfit because the distributions of misfit may differ between the various scenarios. We also consider results when each sample is presented

with the same set of end-members and the best 1% of simulations, as evaluated across all samples, is retained (Fig. II-5E). In this case the distributions of end-member chemistry collapse to a single set of values. There are then large differences between this final distribution and those in a scenario where each sample defines its own distribution of end-member chemical ratios (Fig. II-5F).

In the river water samples of Torres et al. (2016), inversion-constrained $2\chi^{\mathrm{dolo}}_{\mathrm{Mg^{2+}}}/\chi^{\mathrm{dolo}}_{\Sigma^+}$ (Fig. II-5G) and $2\chi^{\mathrm{dolo}}_{\mathrm{SO_4^{2-}}}/\chi^{\mathrm{dolo}}_{\Sigma^+}$ (Fig. II-5H) identify chemical gradients across sampling site. Median $2\chi^{\mathrm{dolo}}_{\mathrm{SO_4^{2-}}}/\chi^{\mathrm{dolo}}_{\Sigma^+}$ values are higher in samples from Mountain-1 and Mountain-2 than in samples from the Mountain-Front, which in turn are higher than in samples from the Foreland-floodplain. These results demonstrate that, when there are large chemical gradients across the sampling region, inversion-constrained distributions can be used to interrogate spatial changes in the composition of weathering lithologies. Lastly, comparison of end-member chemistry in scenarios MT-1 and MT-3 suggest minimal sensitivity to whether results are subsampled on the basis of sample matching or lowest misfit fraction (Fig. II-5I).

II.4.6: Including $\chi^{\mathrm{riv}}_{\mathrm{HCO_3^-}}$ in river inversion models

Inversion-constrained distributions of R are similar between scenario JG-7, where $\chi^{\mathrm{carb}}_{\mathrm{HCO_3^-}}/\chi^{\mathrm{carb}}_{\Sigma^+}$ and $\chi^{\mathrm{slct}}_{\mathrm{HCO_3^-}}/\chi^{\mathrm{slct}}_{\Sigma^+}$ take on variable values, and JG-8, where two carbonate and two silicate end-members each have fixed $\chi^{\mathrm{s}}_{\mathrm{HCO_3^-}}/\chi^{\mathrm{s}}_{\Sigma^+}$ ratios (Fig. II-6A; Table II-5). In general, including $\chi^{\mathrm{riv}}_{\mathrm{HCO_3^-}}$ in the inversion, such as in JG-7, has only a small impact on R when compared to an inversion without $\chi^{\mathrm{riv}}_{\mathrm{HCO_3^-}}$, such as JG-3 (Fig. II-6B). Likewise, results

of scenarios AB-1 and AB-2 also indicate that R is generally insensitive to inclusion of $\chi^{riv}_{HCO_3^-}$ (Fig. II-6C). However, samples with particularly low or high values of $\chi^{riv}_{HCO_3^-}/\chi^{riv}_{\Sigma^+}$ may display changes in R when $\chi^{riv}_{HCO_3^-}$ is included in the inversion. For example, two to three samples from Gaillardet et al. (1999) plot with lower values of R and three samples from Burke et al. (2019) plot at higher values of R when accounting for $\chi^{riv}_{HCO_3^-}$ (Figs. II-6B and C). Notably, the samples showing these changes exhibit large ranges in simulation results. One possible reason for the shifted distribution of R is that scenarios JG-3 and AB-1, where $\chi^{riv}_{HCO_3^-}$ is not included in the inversions, do not require MEANDIR to generate results within 15% of $\chi^{riv}_{HCO_3^-}$ in order to meet the sample matching criteria. When $\chi^{riv}_{HCO_3^-}$ is included in the inversion, as in JG-7 and AB-2, samples with low $\chi^{riv}_{HCO_3^-}/\chi^{riv}_{\Sigma^+}$ can be inconsistent with majority carbonate input and require a larger influence from silicate weathering while samples with high $\chi^{riv}_{HCO_3^-}/\chi^{riv}_{\Sigma^+}$ require additional carbonate inputs. Our results demonstrate that including $\chi^{riv}_{HCO_3^-}$ generally does not change results, but that doing so may add meaningful constraint for samples with particularly high or low values of $\chi^{riv}_{HCO_3^-}/\chi^{riv}_{\Sigma^+}$.

In the samples of Burke et al. (2018), $\chi^{riv}_{HCO_3^-}$ is calculated by charge balance using reported major element concentrations. As discussed above, including $\chi^{riv}_{HCO_3^-}$ derived from charge balance accounts to adding degenerate information into the inversion when all constituent mass balance equations are also included. Users of MEANDIR can decide whether to exclude model misfit of $\chi^{riv}_{HCO_3^-}$ from the cost function. For scenarios AB-2 and AB-3, R values are similar when $\chi^{riv}_{HCO_3^-}$ is included or excluded from the cost function (Fig. II-6D).

II.4.7: Quantifying formation of secondary phases

Icelandic river water samples from Gíslason et al. (1996) are elevated in $2\chi^{riv}_{Ca^{2+}}/\chi^{riv}_{\Sigma^+}$ and $\chi^{riv}_{Na^+}/\chi^{riv}_{\Sigma^+}$ relative to expectations from conservative mixing between basalt and precipitation (Fig. II-7A). Multiple explanations of this discrepancy exist, including variable bedrock chemistry and seasonal changes in the chemistry of precipitation, but a substantial role for clay formation is supported by numerous studies across isotopic systems (Georg et al., 2007; Vigier et al., 2009; Hindshaw et al., 2013; Kemeny et al., 2021b). Assuming basalt and precipitation are the sole solute sources, we use MEANDIR to determine the chemical composition of the secondary clay phase that would be necessary to produce the river observations. We then compare this calculated value to solid-phase measurements of clay-rich soil/sediment samples from Iceland as a test of MEANDIR's ability to simulate clay formation.

MEANDIR finds that the river observations of Gíslason et al. (1996) can be generated through formation of a secondary clay with low median $\chi^{clay}_{Na^+}/\chi^{clay}_{\Sigma^+}$ (Figs. II-7B and C). The inversion-constrained distribution of $2\chi^{clay}_{Mg^{2+}}/\chi^{clay}_{\Sigma^+}$(Fig. II-7B, blue) is elevated from $2\chi^{clay}_{Ca^{2+}}/\chi^{clay}_{\Sigma^+}$ (Fig. II-7B, yellow), which is elevated from $\chi^{clay}_{Na^+}/\chi^{clay}_{\Sigma^+}$ (Fig. II-7B, red). The average median value of $2\chi^{clay}_{Ca^{2+}}/\chi^{clay}_{\Sigma^+}$ is 0.34, $2\chi^{clay}_{Mg^{2+}}/\chi^{clay}_{\Sigma^+}$ is 0.57, and $\chi^{clay}_{Na^+}/\chi^{clay}_{\Sigma^+}$ is 7% (Fig. II-7C). Despite the initial distribution of the clay end-member in scenario SG-1 being quite general (Table II-11), the chemical composition of the inversion-constrained secondary product is consistent with observations of Icelandic clay chemistry. Moulton et al. (2000) report $2\chi^{clay}_{Ca^{2+}}/\chi^{clay}_{\Sigma^+}$ of 0.44, $2\chi^{clay}_{Mg^{2+}}/\chi^{clay}_{\Sigma^+}$ of 0.44, and $\chi^{clay}_{Na^+}/\chi^{clay}_{\Sigma^+}$ of 12% for the finest fraction of soils from Skorradalur (uncorrected for possible Cl^- contributions;

Stefánsson and Gíslason (2001)), and Thorpe et al. (2019) report $2\chi^{clay}_{Ca^{2+}}/\chi^{clay}_{\Sigma^+}$ ranging from 0.43 to 0.58, $2\chi^{clay}_{Mg^{2+}}/\chi^{clay}_{\Sigma^+}$ ranging from 0.32 to 0.49, and $\chi^{clay}_{Na^+}/\chi^{clay}_{\Sigma^+}$ ranging from 0.08 to 0.10 in the < 2 μm fraction of Hvítá River sediments (Fig. II-7C, shaded patches). MEANDIR's prediction of a low $\chi^{clay}_{Na^+}/\chi^{clay}_{\Sigma^+}$ ratio and elevated ratios of $2\chi^{clay}_{Ca^{2+}}/\chi^{clay}_{\Sigma^+}$ and $2\chi^{clay}_{Mg^{2+}}/\chi^{clay}_{\Sigma^+}$ approximately match these observations. Moreover, the accuracy of the SG-1 scenario could be improved by including the constraints from Moulton et al. (2000) or Thorpe et al. (2019) in the pre-defined chemical ranges of the secondary phase. However, in many applications secondary phase formation is expected while direct observational constraints of those phases are unavailable. Our results demonstrate that MEANDIR can generate reasonably accurate results for the chemistry of secondary clays even in the absence of direct observational constraints.

II.4.8: Quantifying FeS_2 oxidation

We evaluate the mutual consistency of three techniques for quantifying the fraction of $\chi^{riv}_{SO_4^{2-}}$ sourced from FeS_2 oxidation. The three techniques are quantifying $\chi^{riv}_{SO_4^{2-}}$ not attributable to evaporites and precipitation ($\chi^{riv}_{excess\ SO_4^{2-}}$, or the "excess SO_4^{2-}" approach; Burke et al., 2018), combining FeS_2 oxidation and end-member weathering ($2\chi^{s}_{FeS_2\ SO_4^{2-}}/\chi^{s}_{\Sigma+}$ values, or the "SO_4^{2-} in end-members" approach; Torres et al., 2016), and using an independent end-member to represent FeS_2 oxidation ($\chi^{FeS_2\ ox.}_{SO_4^{2-}}$) or inputs of other SO_4^{2-} ($\chi^{other}_{SO_4^{2-}}$) (the "independent SO_4^{2-}-bearing end-member" or "other SO_4^{2-}" approach) (Fig. II-8). We compare results for scenarios AB-1, AB-4, AB-5, and AB-6 using the data

of Burke et al. (2018) and scenarios MT-5, MT-6, and MT-7 using the data of Torres et al. (2016). In the latter scenarios we also consider the $^{34}S/^{32}S$ ratio of the oxidized FeS_2.

For the data of Burke et al. (2018), values of the carbonate weathering fraction R are in mutual agreement for scenarios AB-4 (excess SO_4^{2-}) and AB-5 (independent SO_4^{2-}-bearing end-member) (Fig. II-8A). As expected, higher values of R occur at higher values of $2\chi^{riv}_{Ca^{2+}}/\chi^{riv}_{Na^{+}}$. Conversely, R values disagree between scenarios AB-5 (independent SO_4^{2-}-bearing end-member) and AB-1 (SO_4^{2-} in end-members) in a subset of samples with low values of $2\chi^{riv}_{SO_4^{2-}}/\left(2\chi^{riv}_{Ca^{2+}} + 2\chi^{riv}_{Mg^{2+}} + \chi^{riv}_{Na^{+}}\right)$ (Fig. II-8B). Median values of R in scenario AB-1 do not increase coherently with $2\chi^{riv}_{Ca^{2+}}/\chi^{riv}_{Na^{+}}$, suggesting a previously unrecognized complexity that arises from combining SO_4^{2-} sources with weathering. The inversion results for the discrepant samples in scenario AB-1 tend to have many simulations where silicate inputs dominate over carbonate inputs, with either a long tail to high values of R or even a second mode at elevated values of R. About 25% to 50% of simulations for these samples predict very strong dominance of either silicate or carbonate inputs.

We hypothesize that the differences in R between AB-1 and AB-5 arise from the low ratios of $2\chi^{riv}_{SO_4^{2-}}/\left(2\chi^{riv}_{Ca^{2+}} + 2\chi^{riv}_{Mg^{2+}} + \chi^{riv}_{Na^{+}}\right)$ in the problematic samples. Because successful simulations for these samples in AB-1 requires MEANDIR to select a low $2\chi^{s}_{FeS_2\ SO_4^{2-}}/\chi^{s}_{\Sigma^{+}}$ ratio for either the carbonate or silicate end-members, but the inversion is unlikely to select low $2\chi^{s}_{FeS_2\ SO_4^{2-}}/\chi^{s}_{\Sigma^{+}}$ ratios for both end-members, successful model results have a tendency to be dominated by only one weathering lithology. For samples where the required combination of ratios is more likely to occur for the silicate end-member

than the carbonate end-member, MEANDIR finds that the median value of R reflects silicate inputs. As a result, for some samples the median value of R in AB-1 disagrees with that of AB-5 and with $2\chi^{riv}_{Ca^{2+}}/\chi^{riv}_{Na^{+}}$. We test the existence of such a statistical artifact in scenario AB-1 by considering an additional scenario, AB-6, which is identical to AB-1 except the silicate and carbonate end-members are limited to have $2\chi^{s}_{FeS_2\ SO_4^{2-}}/\chi^{s}_{\Sigma^{+}}$ ratios between 0 and 0.15 rather than between 0 and 1 (Table II-7). This smaller range allows the inversion model to more often select two low values of $2\chi^{s}_{FeS_2\ SO_4^{2-}}/\chi^{s}_{\Sigma^{+}}$. For the problematic samples, the median R values in AB-6 are a stronger match to those of AB-5 than the median R values of scenario AB-1 (Fig. II-8C). However, note that the reduced range of $2\chi^{s}_{FeS_2\ SO_4^{2-}}/\chi^{s}_{\Sigma^{+}}$ in AB-6 forces the precipitation and evaporite end-members to source $\chi^{riv}_{SO_4^{2-}}$ that is attributed to FeS_2 oxidation in AB-1, resulting in large reductions to the inversion-constrained median values of Z.

These results demonstrate that, for samples with low ratios of $2\chi^{riv}_{SO_4^{2-}}/\chi^{riv}_{\Sigma^{+}}$, inversion models that combine FeS_2 oxidation with weathering can be subject to probabilistic influences reflecting the likelihood of selecting a required combination of end-member chemical ratios. In contrast, when quantifying $\chi^{riv}_{excess\ SO_4^{2-}}$ or $\chi^{other}_{SO_4^{2-}}$, the inversion is not constrained by selecting low ratios of $2\chi^{s}_{FeS_2\ SO_4^{2-}}/\chi^{s}_{\Sigma^{+}}$ and results are in stronger agreement with expectations from $2\chi^{riv}_{Ca^{2+}}/\chi^{riv}_{Na^{+}}$ (Fig. II-8A). Our comparison thus shows that it is preferable to treat FeS_2 oxidation independent of weathering. This result also stresses the importance of considering the full range of model results, as opposed to only the median of the inversion-constrained distributions.

In the data of Torres et al. (2016), scenario MT-5 (SO_4^{2-} in end-members), scenario MT-6 (excess SO_4^{2-}), and scenario MT-7 (other SO_4^{2-}) all return similar values for R and Z (Fig. II-8D). The major difference among the three scenarios is that samples with the highest values of Z in scenarios MT-6 and MT-7 have lower values of Z in scenario MT-5. This downward shift reflects that, in scenario MT-5, it is impossible to attain Z values substantially above 1 because the carbonate and silicate end-members are limited to have $2\chi^{S}_{FeS_2\ SO_4^{2-}}/\chi^{S}_{\Sigma^+}$ values between 0 and 1. However, Z > 1 is a possible outcome in scenarios MT-6 and MT-7. We note that the inversion approach used in scenario MT-5 could be modified to have end-member $2\chi^{S}_{FeS_2\ SO_4^{2-}}/\chi^{S}_{\Sigma^+}$ values exceed 1, if motivated by observations of $2\chi^{riv}_{SO_4^{2-}}/\chi^{riv}_{\Sigma^+}$>1. That is, charge equivalent $\chi^{riv}_{SO_4^{2-}}$ exceeding $\chi^{riv}_{\Sigma^+}$ is sometimes observed in natural waters and need not reflect analytical error if, for example, the samples also have low pH values or high iron concentrations where $\chi^{riv}_{\Sigma^+}$ only includes alkali and alkaline earth cations.

Calculated values of FeS_2 $\delta^{34}S$ agree strongly among scenarios MT-5, MT-6, and MT-7 (Fig. II-8E). Overall, despite observed values not being used to constrain the inversion, the calculated values of FeS_2 $\delta^{34}S$ are generally in agreement with measured bedrock $\delta^{34}S$. MEANDIR predicts values of FeS_2 $\delta^{34}S$ ranging from -4.8‰ to 7.0‰, reaching values approximately 6‰ higher than the measured range of -5‰ to 1‰ (Torres et al., 2016). Notably, most of the samples with FeS_2 $\delta^{34}S$ values higher than the measured range are from the Foreland-floodplain and may include sedimentary inputs that are not resolved in the inversion model.

II.4.9: Quantifying petrogenic C_{org} oxidation

FeS_2 and C_{org} oxidation have important roles in chemical weathering and the global carbon cycle (Torres et al., 2016; Horan et al., 2019). Using normalizations to $\chi_{\Sigma^+ + ALK + DIC}$ and $\chi_{\Sigma^+ + SO_4^{2-} + DIC}$, as well as the R-Z framework extended to include C, we simultaneously evaluate conventional silicate weathering, FeS_2 oxidation, and C_{org} oxidation in the catchment of the Mackenzie River using the data of Horan et al. (2019). In particular, the Horan et al. (2019) dataset includes measurements of χ_{Re}^{riv} that enable quantification of C_{org} oxidation. To do so, we define a C_{org} oxidation end-member with a well-defined ratio of $\chi_{Re}^{C_{org}\ ox.}/\chi_{\Sigma^+ + SO_4^{2-} + DIC}^{C_{org}\ ox.}$ (Table II-13).

Model results indicate dominance of carbonate weathering over silicate weathering in the Mackenzie River (Fig. II-9), with substantial H_2SO_4 weathering (Calmels et al., 2007). Values of C range from 0% to 43%. The χ_{ALK}/χ_{DIC} associated with chemical weathering in the catchment upstream of each sample is calculated from R, Z, and C (Fig. II-9, with indicated planes for $\chi_{ALK}/\chi_{DIC} = 1$ and $\chi_{ALK}/\chi_{DIC} = 2$). All river water samples represent weathering systems with $\chi_{ALK}/\chi_{DIC} < 2$, indicating that weathering in the sampled catchments increases pCO_2 on timescales longer than marine carbonate burial. Moreover, several samples have $\chi_{ALK}/\chi_{DIC} < 1$, indicating weathering that results in instantaneous pCO_2 increase. Notably, our inversion does not constrain C_{org} production or burial, nor the cation or nitrogen fluxes associated with biomass cycling, meaning that it does not capture the full carbon cycle budget of the Mackenzie River. This caveat is important because accounting for C_{org} burial in the floodplain or marine sediments may alter the direction of how weathering in this system impacts atmospheric CO_2 (Horan et al.,

2019). Regardless, our inversion demonstrates the ability of MEANDIR to quantify petrogenic C_{org} oxidation and FeS_2 oxidation from χ^{riv}_{Re} and $\chi^{riv}_{SO_4^{2-}}$ (Hilton et al., 2014).

II.5: Conclusions

Here we present Mixing Elements ANd Dissolved Isotopes in Rivers (MEANDIR), a set of MATLAB scripts for performing highly customizable inversion of river dissolved chemistry with Monte Carlo propagation of uncertainty. After introducing the mathematics underlying MEANDIR, we evaluate its performance using five previously published datasets (Gíslason et al., 1996; Gaillardet et al., 1999; Torres et al., 2016; Burke et al., 2018; Horan et al., 2019). Among others results, we evaluate the sensitivity of river inversion to the choice of cost function, review and compare multiple methods for the quantification of FeS_2 oxidation, extend an existing formalism to account for the oxidation of petrogenic organic carbon, and introduce a new normalization method. MEANDIR is available online for ongoing critique and development.

II.6: Code availability and data sources

Mixing Elements ANd Dissolved Isotopes in Rivers (MEANDIR) and its user guide are available at https://github.com/PrestonCosslettKemeny/MEANDIR. The data analyzed in this study come from Table 1 of Gíslason et al., (1996), Table 1 of Gaillardet et al. (1999), the supplementary materials of Torres et al. (2016) and Burke et al. (2018), and Table 2 of Horan et al. (2019).

II.7: Acknowledgments

P.C.K. is supported by The Fannie and John Hertz Foundation Cohan/Jacobs and Stein Families Fellowship. M.A.T. gratefully acknowledges support from the Alfred. P. Sloan Foundation. Both authors thank J. Adkins for comments on an early draft of this article and A. Phillips for advice on the design of figures. We are grateful to J. Bouchez, A. Bufe, and an anonymous referee for thoughtful reviews.

II.8: Figures

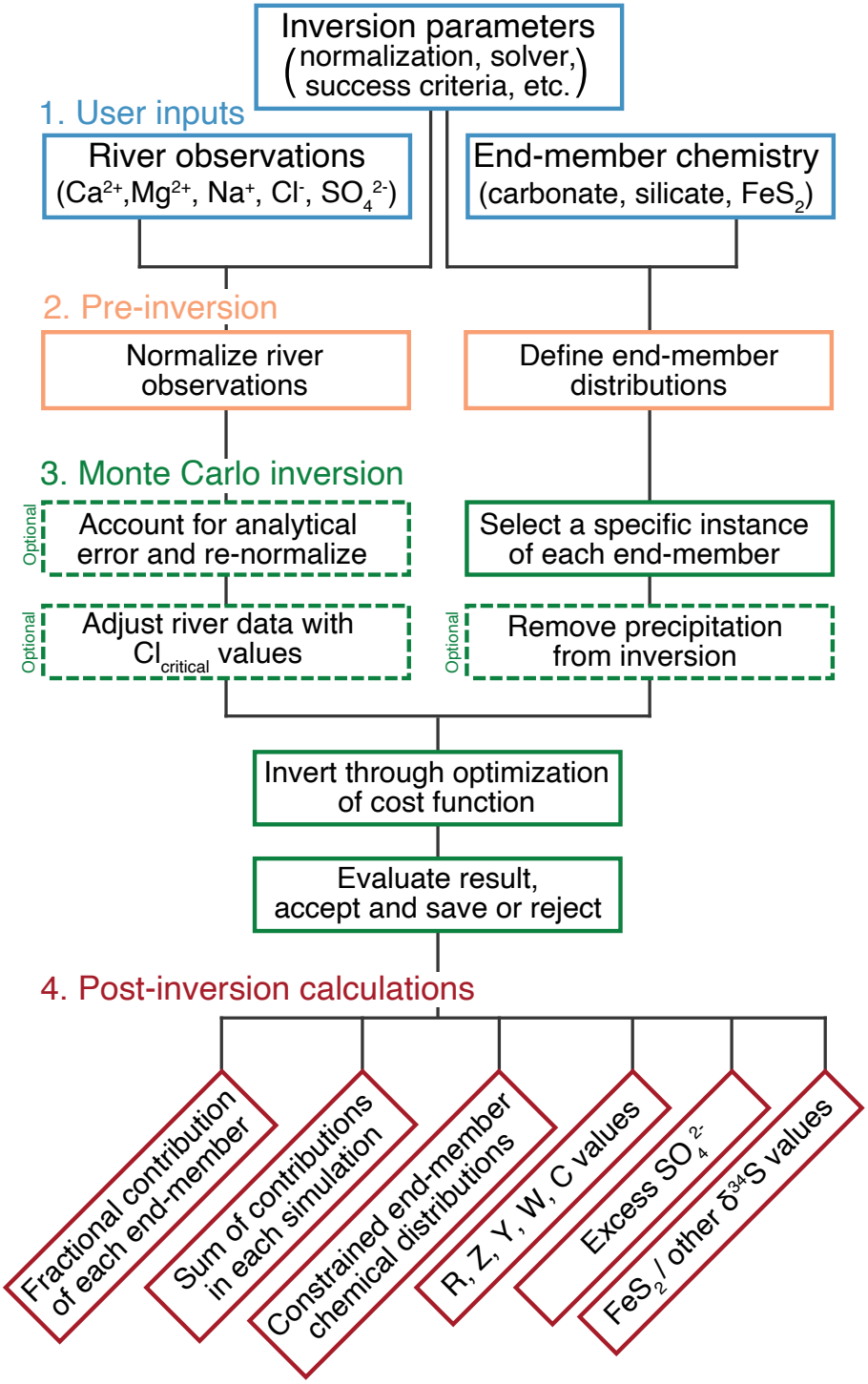

Fig. II-1: Architecture of MEANDIR. Users supply observations of dissolved river chemistry, choices for how to perform the inversion, and the chemical composition of end-members (blue boxes). MEANDIR then prepares inputs (orange boxes), conducts the Monte Carlo inversion (green boxes), and calculates variables of interest (red boxes). Many of these steps are highly customizable to suit the needs of individual datasets and research questions.

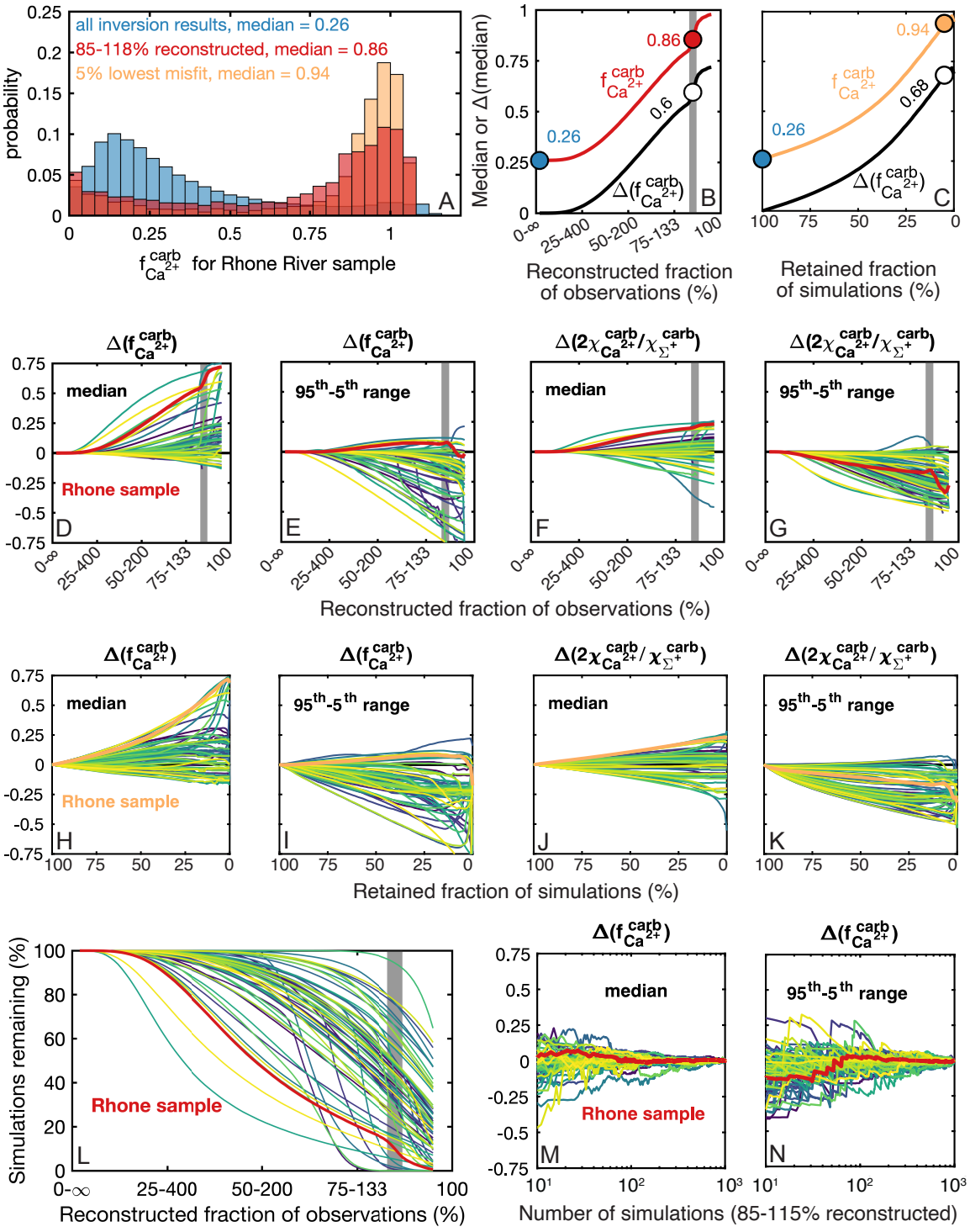
all inversion results, median = 0.26
85-118% reconstructed, median = 0.86
5% lowest misfit, median = 0.94
probability
A
Median or Δ(median)
0.86
0.26
0.6
B
Reconstructed fraction of observations (%)
0.94
0.68
C
Retained fraction of simulations (%)
median
Rhone sample
D
95th-5th range
E
F
G
H
I
J
K
Simulations remaining (%)
L
M
N
Number of simulations (85-115% reconstructed)

Fig. II-2: Sensitivity analysis based on (A-L) scenario JG-1 and (M, N) scenario JG-2. Overall, this analysis shows that the inversion results change when isolating the simulations that reconstruct observations to within a specified fraction or which have low misfit from observations, but that the results are only minimally sensitive to small changes in the specific constraints imposed. (A) Distributions of $f_{Ca^{2+}}^{carb}$, the fraction of $\chi_{Ca^{2+}}^{riv}$ from the carbonate end-member, for a sample from the Rhone River. Results are plotted for all simulations (blue distribution), results where 85-118% of all observations ($\chi_{Ca^{2+}}^{riv}$, $\chi_{Mg^{2+}}^{riv}$, $\chi_{Na^{+}}^{riv}$, $\chi_{Cl^{-}}^{riv}$) are reconstructed (red distribution), and results for the 5% of simulations with the lowest misfit between model results and observations (orange distribution). (B) Median of the $f_{Ca^{2+}}^{carb}$ distribution and change in the median of the $f_{Ca^{2+}}^{carb}$ distribution ($\Delta f_{Ca^{2+}}^{carb}$) when only retaining results where all observations are reconstructed within the indicated range of fractions. (C) Median of the $f_{Ca^{2+}}^{carb}$ distribution and change in the median of the $f_{Ca^{2+}}^{carb}$ distribution when only retaining the indicated fraction of simulations with lowest misfit between inversion results and river observations. (D-G) Results where all observations are reconstructed within the indicated range of fractions. (H-K) Results when only retaining the indicated fraction of simulations with lowest misfit between model results and river observations. (D, H) Change in the median $f_{Ca^{2+}}^{carb}$, (E, I) 95th-5th percentile range in $f_{Ca^{2+}}^{carb}$, (F, J) median $\chi_{Ca^{2+}}^{carb}/\chi_{\Sigma^{+}}^{carb}$, and (G, K) 95th-5th percentile range in $\chi_{Ca^{2+}}^{carb}/\chi_{\Sigma^{+}}^{carb}$. (L) The fraction of simulations remaining when only retaining results where all observations are reconstructed within the indicated range of fractions. For all samples, fewer simulations are retained as the imposed constraint tightens. Change in the (M) median of $f_{Ca^{2+}}^{carb}$ and (N) change in the 95th-5th percentile of $f_{Ca^{2+}}^{carb}$ with increasing number of simulations, where all simulations reconstruct between 85% and 115% of each observation. Values in (M) and (N) are given relative to the values at 1000 successful simulations. The sample from the Rhone River is highlighted (D-G, L-N) in red or (H-K) in orange. The grey vertical bar (B, D – G, L) is centered at sample matching criteria of 85-118%, very similar to the 85-115% criteria used in most of the scenarios in this analysis. All data underlying these inversion results are from Gaillardet et al. (1999).

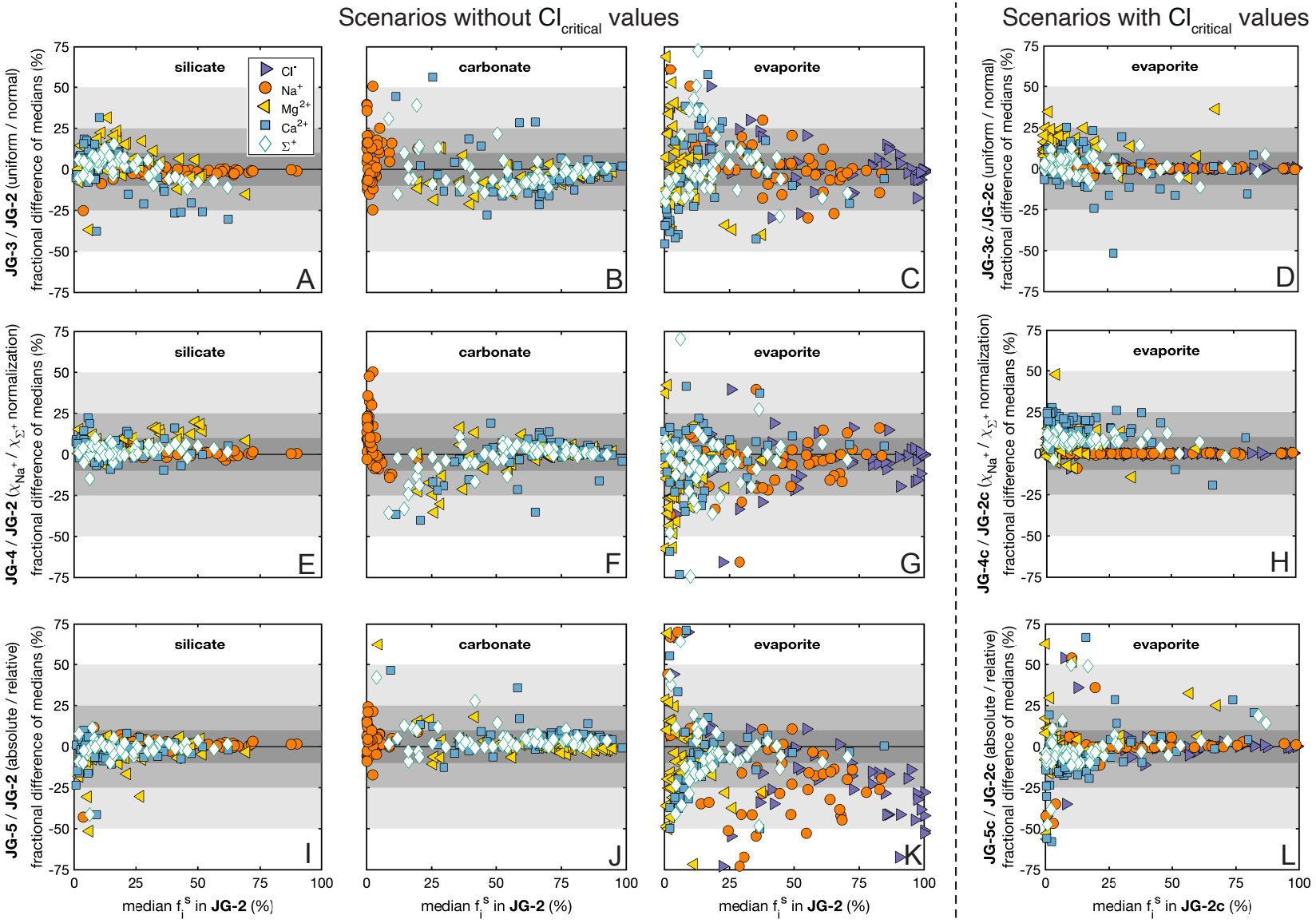
Scenarios without Cl critical values
Scenarios with Cl critical values
silicate
carbonate
evaporite
Cl-
Na+
Mg2+
Ca2+
Σ+
JG-3 / JG-2 (uniform / normal)
JG-4 / JG-2 (χNa+ / χΣ+ normalization)
JG-5 / JG-2 (absolute / relative)
JG-3c / JG-2c (uniform / normal)
JG-4c / JG-2c (χNa+ / χΣ+ normalization)
JG-5c / JG-2c (absolute / relative)
fractional difference of medians (%)
median fi S in JG-2 (%)
median fi S in JG-2c (%)
A
B
C
D
E
F
G
H
I
J
K
L

Fig. II-3: Comparison of median fractional contributions in scenarios JG-3 and JG-3c (uniform end-member distributions), JG-4 and JG-4c (normalization to χ_{Na^+}), JG-5 and JG-5c (absolute cost function) relative to scenarios JG-2 and JG-2c (normal end-member distribution, normalization to χ_{Σ^+}, relative cost function) for the (A, E, I) silicate, (B, F, J) carbonate, and (C, D, G, H, K, L) evaporite end-members. Median contributions are plotted for $\chi^{riv}_{Cl^-}$ (purple right-pointing triangles), $\chi^{riv}_{Na^+}$ (orange circles), $\chi^{riv}_{Mg^{2+}}$ (yellow left-pointing triangles), $\chi^{riv}_{Ca^{2+}}$ (blue square), and $\chi^{riv}_{\Sigma^+}$ (green diamonds), in scenarios without (A-C, E-G, I-K) $\chi^{riv}_{Cl^-\,critical}$ values and (D, H, L) with $\chi^{riv}_{Cl^-\,critical}$ values. Overall, median f_i^{carb} and f_i^{slct} values are similar across scenarios while median f_i^{evap} values are only similar when comparing observations inverted using $\chi^{riv}_{Cl^-\,critical}$ values. Samples are plotted when either of the two median f_i^s values exceed 0.1%. Shading indicates proportional differences of 10%, 25%, and 50%. All data underlying these inversion results are from Gaillardet et al. (1999).

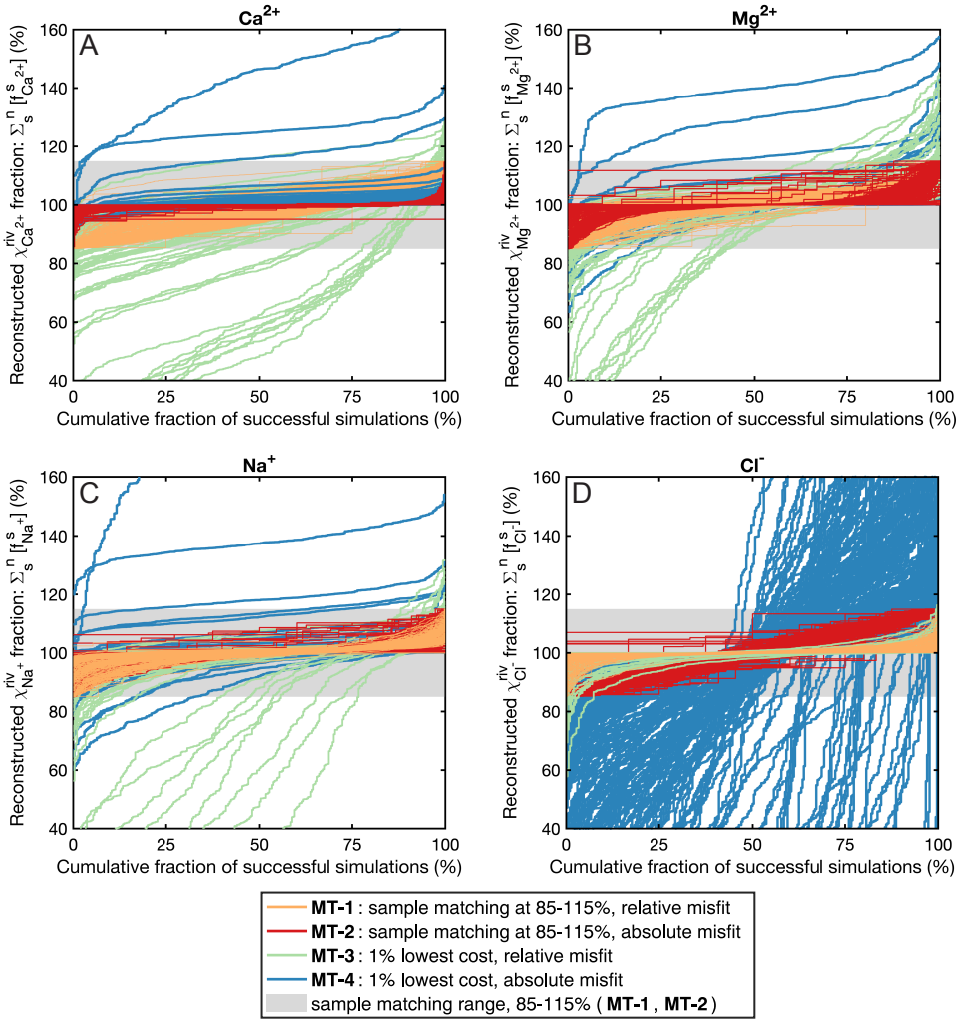

Fig. II-4: Distributions of the fraction of reconstructed river observations. Each curve shows the cumulative distribution, for a single sample in one of four color-coded scenarios, of the summed fractional contributions from all end-members in accepted simulations. (A) $\Sigma_s^n[f_{Ca^{2+}}^s]$, (B) $\Sigma_s^n\left[f_{Mg^{2+}}^s\right]$, (C) $\Sigma_s^n[f_{Na^+}^s]$, and (D) $\Sigma_s^n[f_{Cl^-}^s]$. Results are shown for scenario MT-1 (orange, default scenario using relative cost function), MT-2 (red, using an absolute cost function), MT-3 (green, best 1% of simulations solved with a relative cost function) and MT-4 (blue, best 1% of simulations solved with an absolute cost function). Scenarios MT-1 and MT-2 are constrained to reconstruct between 85% and 115% of all observations (gray shaded region), while scenarios MT-3 and MT-4 are not constrained to generate results within a particular fraction of observed values. In MT-3 and MT-4 the lack of explicit sample matching criteria allows for results that disagree with observations; this misfit is exemplified by the wide range of $\Sigma_s^n[f_{Cl^-}^s]$ values in MT-4. Most samples in scenario MT-1 have 300 successful simulations, 75% of samples in MT-2 have at least 100 successful simulations, and all samples in scenarios MT-3 and MT-4 have 300 successful simulations (1% of 30,000 simulations). In all scenarios the fractional contribution of each end-member to χ_{norm} is constrained between 0 and 1. All data underlying these inversion results are from Torres et al. (2016).

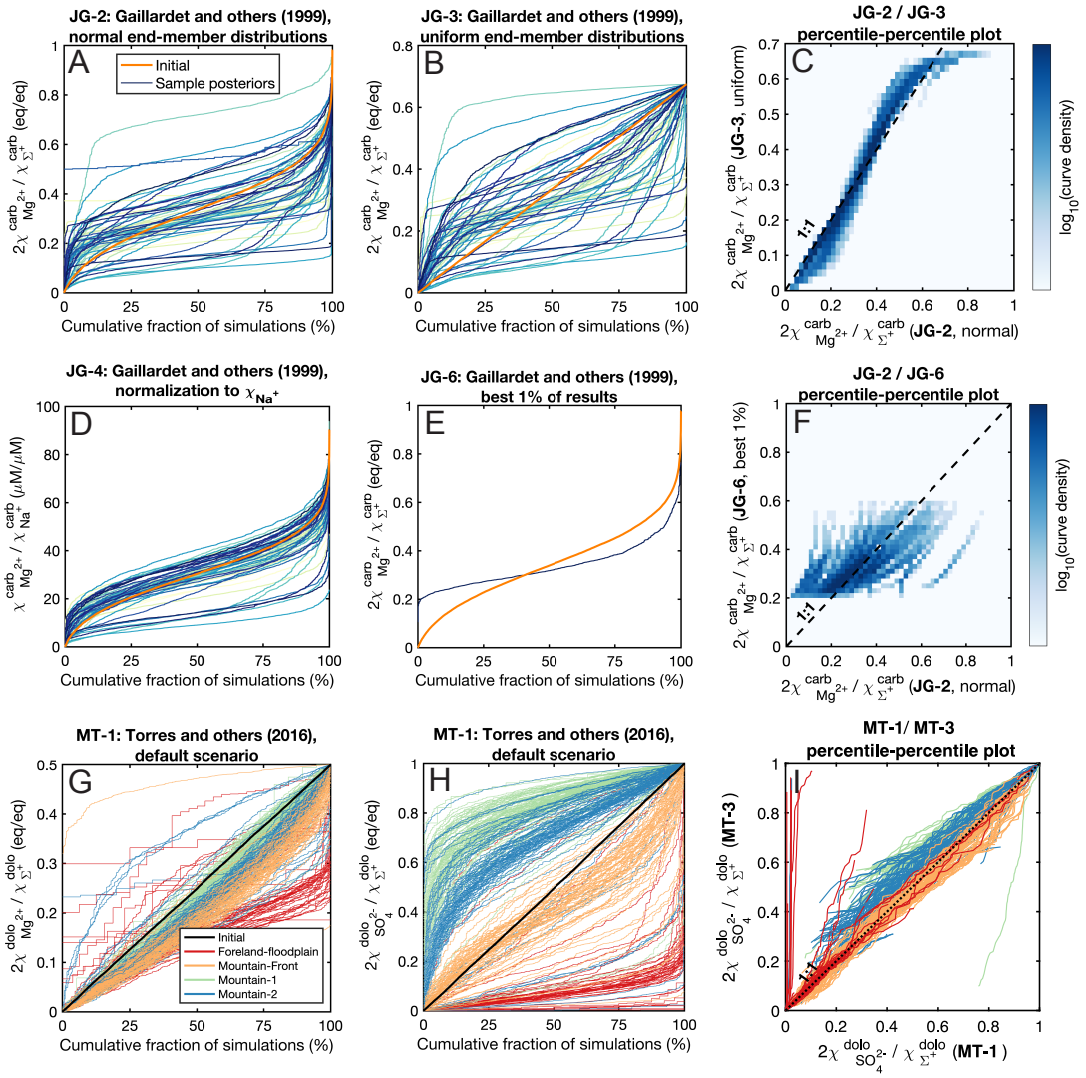

Fig. II-5: Inversion-constrained end-member chemistry calculated using the data from (A-F) Gaillardet et al. (1999) or (G-I) Torres et al. (2016). In (A, B, D, E, G, H) each curve shows the cumulative distribution, for a single sample, of either $2\chi^{carb}_{Mg^{2+}}/\chi^{carb}_{\Sigma^+}$, $2\chi^{carb}_{Mg^{2+}}/\chi^{carb}_{Na^+}$, $2\chi^{dolo}_{Mg^{2+}}/\chi^{dolo}_{\Sigma^+}$, or $2\chi^{dolo}_{SO_4^{2-}}/\chi^{dolo}_{\Sigma^+}$. In (A, B, D) different colors reflect individual samples, and in (G, H) samples are color-coded by site of collection. (A) The distributions of end-member chemistry in successful simulations of scenario JG-2 differ from the initial distribution. Differences are also found for (B) scenario JG-3 (uniform end-member distributions) and (D) scenario JG-4 (normalization to χ_{Na^+}). (E) In scenario JG-6 (best 1% of simulation results, as evaluated across all samples), the final distribution is a set of values distinct from the initial distribution. (C, F) Curve density of percentile-percentile plots for the results of scenarios JG-2, JG-3, and JG-6. The curve density is elevated near the 1:1 line when comparing (C) JG-2 and JG-3 but is away from 1:1 line when comparing (F) JG-2 and JG-6. (G, H) In the data from Peru, the distributions of $2\chi^{dolo}_{Mg^{2+}}/\chi^{dolo}_{\Sigma^+}$ and $2\chi^{dolo}_{SO_4^{2-}}/\chi^{dolo}_{\Sigma^+}$ in successful simulations coherently vary with sampling location. (I) Distributions of inversion-constrained end-member ratios are similar in scenarios MT-1 and MT-3.

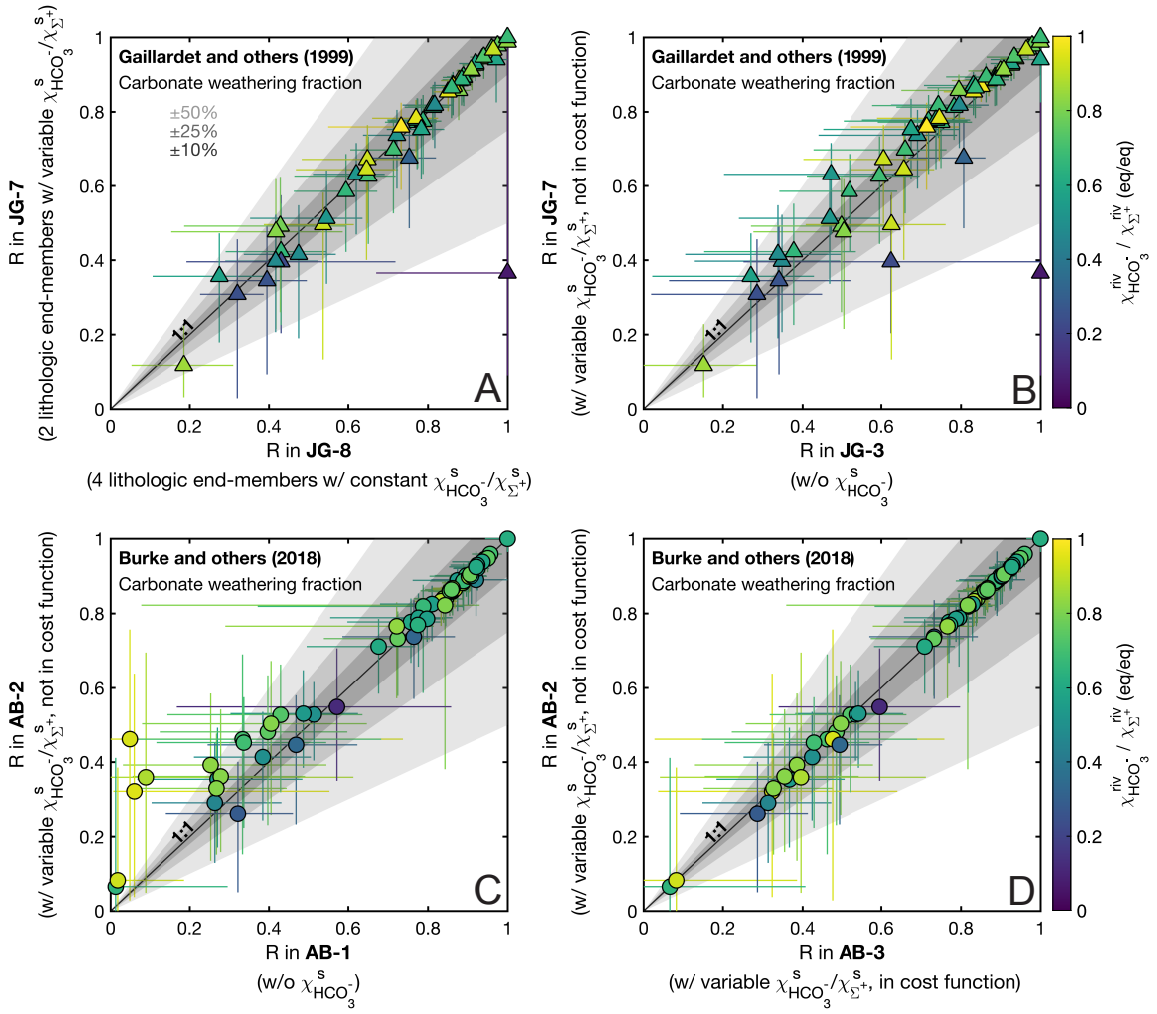

Fig. II-6: Carbonate weathering fraction (R) when including $\chi^{riv}_{HCO_3^-}$ in inversions of data from (A, B) Gaillardet et al. (1999) and (C, D) Burke et al. (2018). (A) R is similar when calculated using two end-members with variable $\chi^{s}_{HCO_3^-}/\chi^{s}_{\Sigma^+}$ ratios or when calculated using 4 end-members with fixed $\chi^{s}_{HCO_3^-}/\chi^{s}_{\Sigma^+}$ ratios (Blattmann et al., 2019). (B, C) R is generally similar with and without $\chi^{riv}_{HCO_3^-}$. At particularly high or low ratios of $\chi^{riv}_{HCO_3^-}/\chi^{riv}_{\Sigma^+}$, including $\chi^{riv}_{HCO_3^-}$ in the inversion results in higher values of R in samples with elevated ratios and lower values of R in samples with lower ratios. (D) R is similar when $\chi^{riv}_{HCO_3^-}/\chi^{riv}_{\Sigma^+}$ is included or excluded from the cost function. Plotted points are the medians of accepted simulations, error bars extend from the 25th to 75th percentiles of accepted results, and shading indicates proportional differences of 10%, 25%, and 50%.

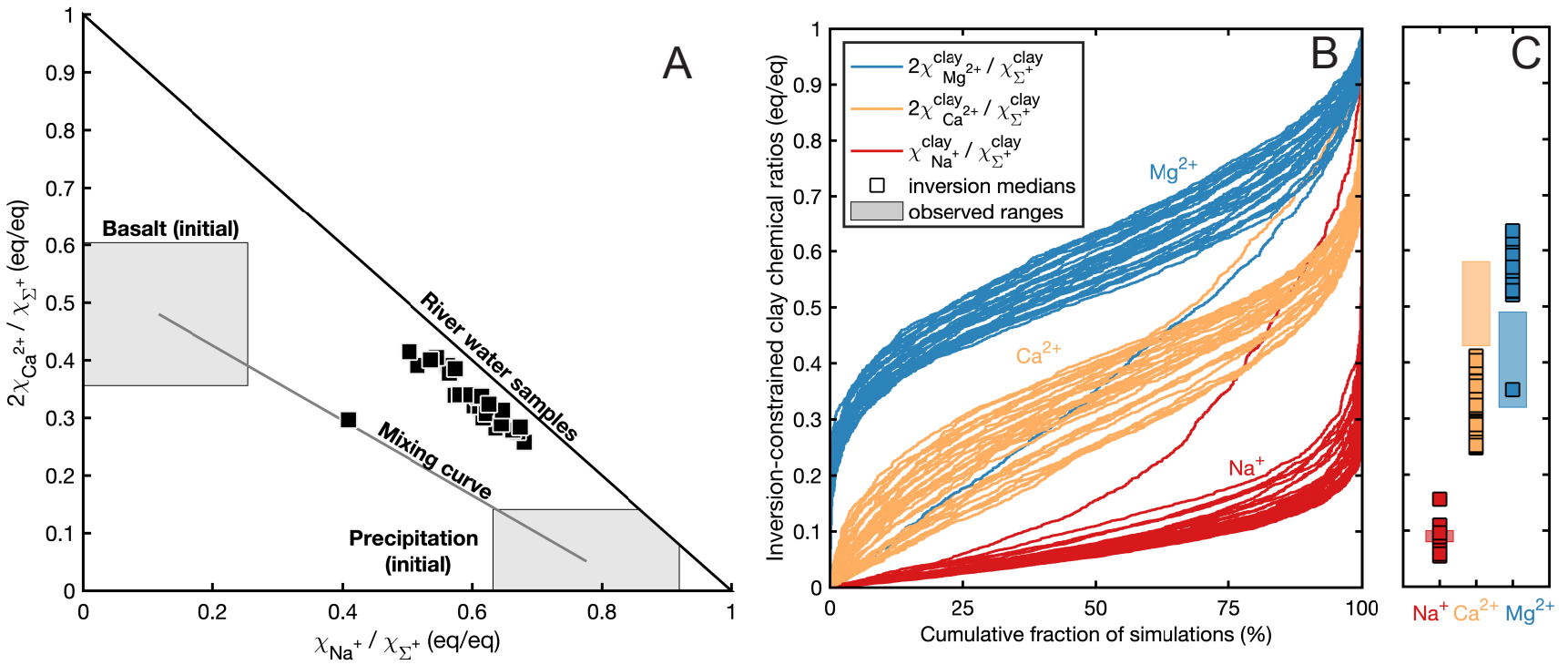

Fig. II-7: Constraining the chemical composition of secondary clay. (A) Observations of $2\chi^{riv}_{Ca^{2+}} / \chi^{riv}_{\Sigma^+}$ and $\chi^{riv}_{Na^+} / \chi^{riv}_{\Sigma^+}$ in Icelandic river water samples from Gíslason et al. (1996). River water is depleted in $2\chi^{riv}_{Mg^{2+}} / \chi^{riv}_{\Sigma^+}$ relative to the mixing of basalt and precipitation, which has previously been attributed to the formation of secondary clays. Shaded regions for basalt and precipitation are centered on the mean of the initial distributions and extend two standard deviations. (B) Inversion-constrained clay chemistry based on the same river data (scenario SG-1). Each curve shows the cumulative distribution, for a single sample, of inversion-constrained $2\chi^{clay}_{Mg^{2+}} / \chi^{clay}_{\Sigma^+}$ (blue), $2\chi^{clay}_{Ca^{2+}} / \chi^{clay}_{\Sigma^+}$ (yellow), or $\chi^{clay}_{Na^+} / \chi^{clay}_{\Sigma^+}$ (red). (C) The median of each inversion-constrained distribution (squares). Shaded regions indicate the range of clay observations from Thorpe et al. (2019).

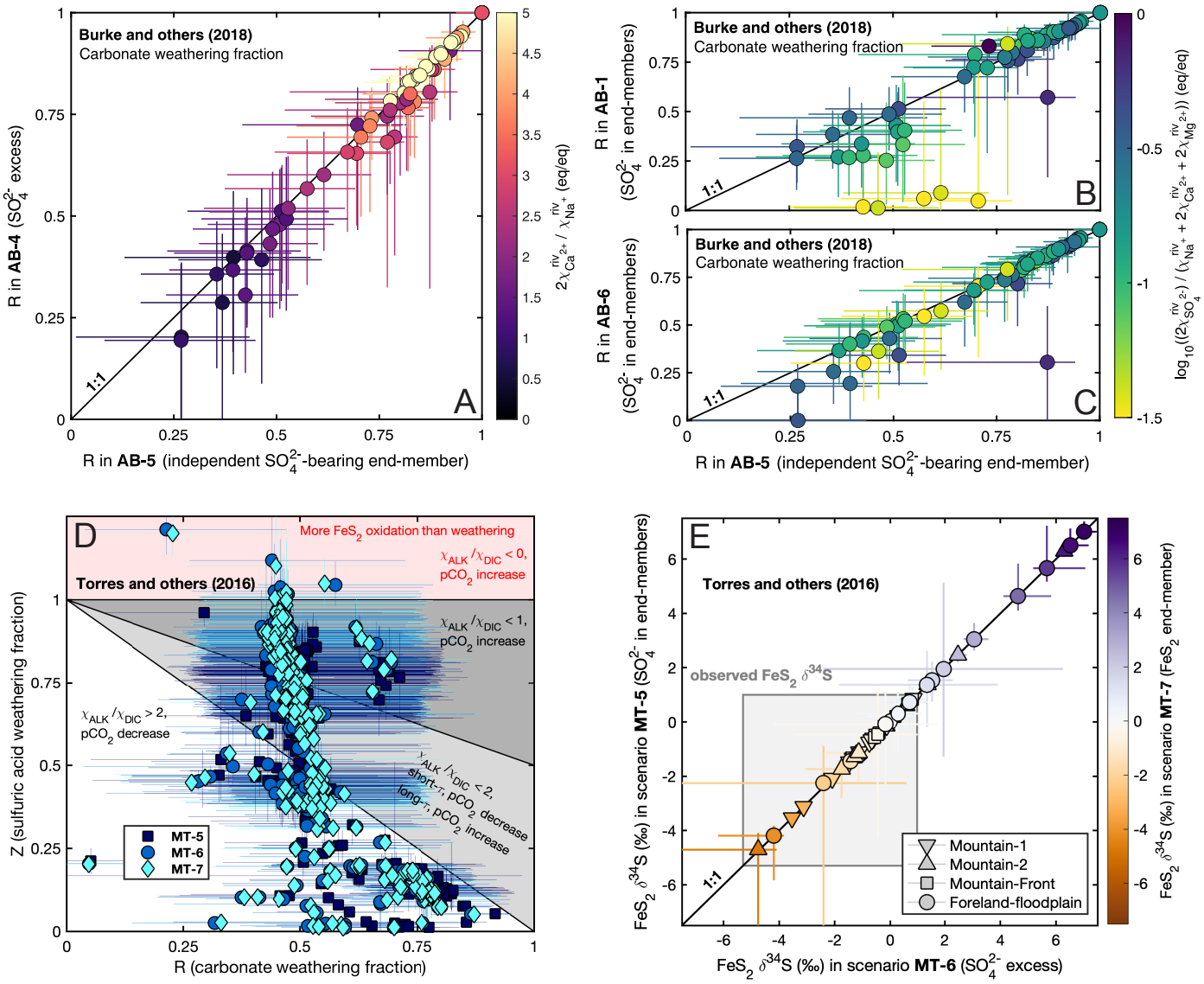
A
Burke and others (2018)
Carbonate weathering fraction
1:1
R in AB-4 (SO_4^{2-} excess)
R in AB-5 (independent SO_4^{2-}-bearing end-member)
$2\chi_{Ca^{2+}}^{riv} / \chi_{Na^+}^{riv}$ (eq/eq)
B
R in AB-1 (SO_4^{2-} in end-members)
C
R in AB-6 (SO_4^{2-} in end-members)
$\log_{10}((2\chi_{SO_4^{2-}}^{riv}) / (\chi_{Na^+}^{riv} + 2\chi_{Ca^{2+}}^{riv} + 2\chi_{Mg^{2+}}^{riv}))$ (eq/eq)
D
Torres and others (2016)
More FeS_2 oxidation than weathering
$\chi_{ALK}/\chi_{DIC} < 0$, pCO_2 increase
$\chi_{ALK}/\chi_{DIC} < 1$, pCO_2 increase
$\chi_{ALK}/\chi_{DIC} > 2$, pCO_2 decrease
$\chi_{ALK}/\chi_{DIC} < 2$, short-$\tau$, pCO_2 decrease
long-τ, pCO_2 increase
MT-5
MT-6
MT-7
Z (sulfuric acid weathering fraction)
R (carbonate weathering fraction)
E
Torres and others (2016)
observed FeS_2 $\delta^{34}S$
Mountain-1
Mountain-2
Mountain-Front
Foreland-floodplain
FeS_2 $\delta^{34}S$ (‰) in scenario MT-5 (SO_4^{2-} in end-members)
FeS_2 $\delta^{34}S$ (‰) in scenario MT-6 (SO_4^{2-} excess)
FeS_2 $\delta^{34}S$ (‰) in scenario MT-7 (FeS_2 end-member)

Fig. II-8: Influence of different inversion methods on the carbonate weathering fraction R, the sulfuric acid weathering fraction Z, and the $^{34}S/^{32}S$ ratio of $\chi^{riv}_{SO_4^{2-}}$ derived from FeS_2 oxidation, excess SO_4^{2-}, or from other SO_4^{2-}. (A) R values in scenarios AB-4 and AB-5 are in mutual agreement and increase coherently with increasing ratios of $2\chi^{riv}_{Ca^{2+}}/\chi^{riv}_{Na^+}$. (B) R values at low $(2\chi^{riv}_{SO_4^{2-}})/(2\chi^{riv}_{Ca^{2+}}+2\chi^{riv}_{Mg^{2+}}+\chi^{riv}_{Na^+})$ disagree between scenarios AB-1 and AB-5, which we interpret as reflecting a probabilistic artifact arising during the inversion of AB-1. (C) When the carbonate and silicate end-members have a reduced range of possible $2\chi^{s}_{FeS_2\ SO_4^{2-}}/\chi^{s}_{\Sigma^+}$ ratios, as in scenario AB-6, R values in samples with low ratios of $\chi^{riv}_{SO_4^{2-}}$ are in much stronger agreement with R values from AB-5. (D) R and Z values are in mutual agreement for scenarios MT-5 (dark blue squares), MT-6 (blue circles) and MT-7 (light blue diamonds). Note that $Z > 1$ is a natural outcome of MT-6 and MT-7, but not MT-5 (where $2\chi^{s}_{FeS_2\ SO_4^{2-}}/\chi^{s}_{\Sigma^+} \leq 1$). (E) The derived isotopic composition of FeS_2 is very similar among scenarios MT-5, MT-6 and MT-7. Moreover, the lower range of the inversion-constrained values match observations of FeS_2 $\delta^{34}S$ (Torres et al., 2016). Samples with values of FeS_2 $\delta^{34}S$ higher than the observed range are predominantly from the Foreland-floodplain and may reflect inputs of sedimentary lithologies that are not included in the inversion, such as evaporites. Notably, observed values of FeS_2 $\delta^{34}S$ were not included in the inversion to constrain the possible range of FeS_2 $\delta^{34}S$ values. Plotted points are the medians of accepted inversion results and error bars extend from the (A, B, C) 25th to 75th percentiles of accepted results or the (D, E) 5th to 95th percentiles of accepted results.

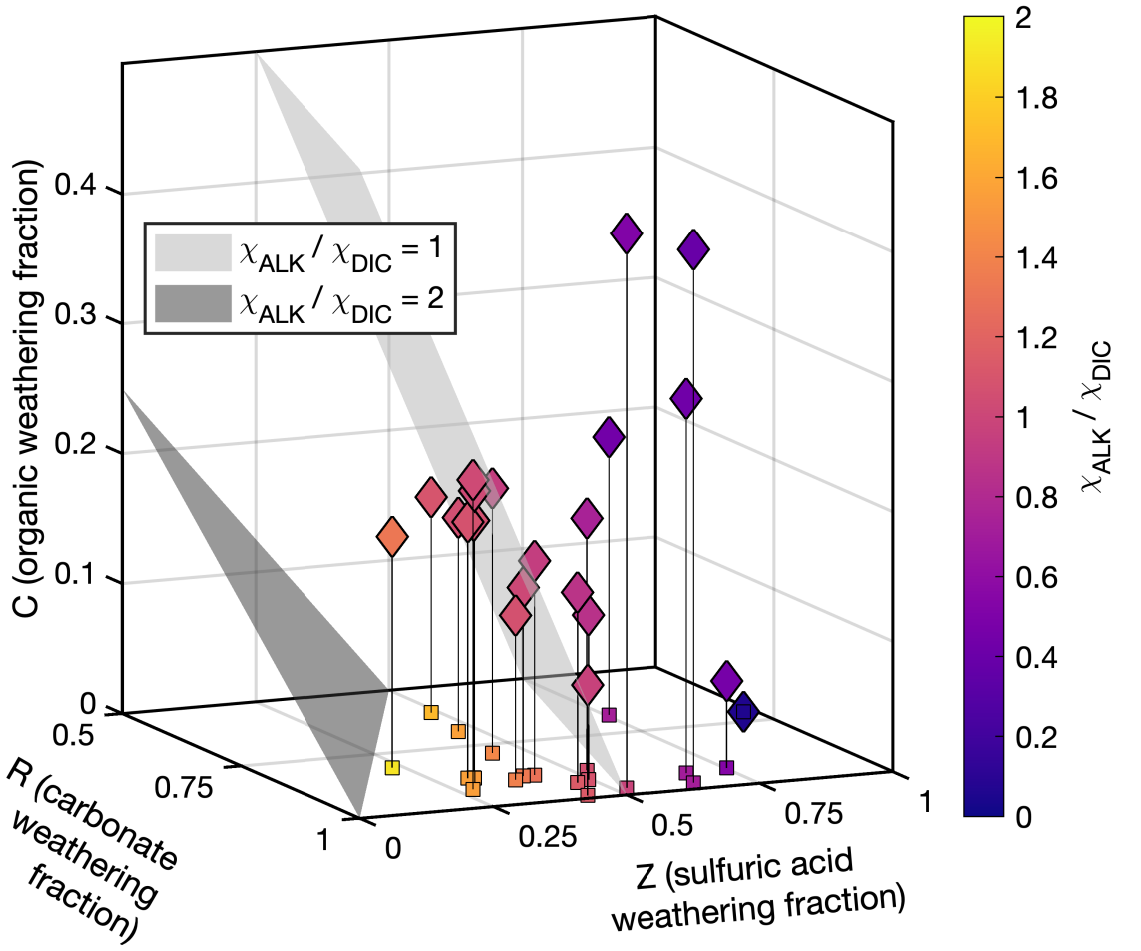

Fig. II-9: Results for the simultaneous quantification of silicate weathering, carbonate weathering, precipitation inputs, FeS_2 oxidation, C_{org} oxidation, and gas exchange in the Mackenzie River basin. Carbonate weathering fraction (R), sulfuric acid weathering fraction (Z), and organic carbon oxidation relative to weathering alkalinity (C) color-coded by χ_{ALK}/χ_{DIC}, with indicated planes for $\chi_{ALK}/\chi_{DIC} = 1$ and $\chi_{ALK}/\chi_{DIC} = 2$. All river water samples have $\chi_{ALK}/\chi_{DIC} < 2$, indicating that chemical weathering upstream of these sample sites increases atmospheric CO_2 over timescales longer than carbonate burial. Vertical lines connect results accounting for non-zero C (diamonds) with results only considering the R-Z plane (squares); note the lower χ_{ALK}/χ_{DIC} ratios of the calculation accounting for C_{org} oxidation. Plotted points are the medians of accepted inversion results. All data underlying this inversion are from Horan et al. (2019).

II.9: Tables

Table II-1: Summary of choices during construction of inversion models. For some categories (for example, normalization) all variables must use the same selection, while in other categories (for example, cost function) each variable has an independent selection.

Topic	Parameter choice	Pros	Cons
Normalization	Na^+	Intuitive, values exist from prior studies	End-members must all contain Na^+
	Σ^+ $(+ALK,\ DIC,\ SO_4^{2-})$	End-members not required to contain same element, model FeS_2 ox. or C_{org} ox. directly	Unintuitive, imposes unit-sum constraint on end-member ratios
End-member distribution	Normal	Generate more simulations near expected values for each end-member	Must trim distributions to avoid unphysical values (for example, Ca^{2+}/Na^+ ratios < 0)
	Uniform	Low impact on posterior distribution	Unlikely to represent natural data
Precipitation correction	Cl^- critical	Constrains precipitation contribution	Cl^- critical values often unavailable
	Precipitation as an end-member	Treats precipitation the same way as any other end-member in the inversion	Generally difficult to distinguish precipitation from evaporite or hot springs
Cost function	Absolute misfit	Can fit variables with value of 0, is useful when modeling isotopic ratios in δ notation	Hard to fit at low abundances, although partially alleviated with weighting terms
	Relative misfit	Better fit at low abundances, isotope ratios	Likely a worse fit to total charge
Culling simulation results	By sample matching	Guarantees results match observations within user-specific criteria	May be impossible to achieve desired precision for user-supplied end-members
	By fraction with lowest misfit	Ensures model results are found and minimizes total error	Model-constructed chemistry may differ from observations, sensitive to cost function
Using $\mathbf{HCO_3^-}$ in inversion	From titration	Independent data constrains the inversion	Should be viewed as ALK, not HCO_3^-
	From charge balance	Ensures results match river observations	Typically degenerate with other equations
Quantifying $\mathbf{FeS_2}$ oxidation	SO_4^{2-} excess	Non-specific to origin of excess SO_4^{2-}	Can predict negative values of excess SO_4^{2-}
	End-member SO_4^{2-}	Constrains lithologic weathering fractions	Results subject to statistical influence
	FeS_2 ox. end-member	Constrains FeS_2 oxidation directly	Requires relatively complex normalization
Secondary phases	Negative fractional contributions	Enables estimates for chemical composition of secondary phases, with fractionation	Secondary phases must be chemically or isotopically distinct from primary phases
Calculating **R**, **Z**, **C**	Include Na^+, K^+	Reflects full alkalinity of weathering	Not all Na^+ and K^+ contribute to DIC loss
	Do not include Na^+, K^+	Accounts for reverse weathering when calculating DIC loss	Assumes Na^+ and K^+ in steady-state when evaluating effects of weathering on pCO_2

Table II-2: Variables used throughout the text.

Variable	Description
$\boldsymbol{\chi}$	Number of moles
$^{A}\mathbf{R}$	Isotopic ratio, where A is the cardinal mass of the heavy isotope
$\mathbf{f}$	Fraction of river observation
$\mathbf{A}$	Matrix of end-member chemistry
$\mathbf{f}$	Vector of fractional contributions
$\mathbf{b}$	Vector of river observations
$\boldsymbol{\alpha}$	Factor converting concentration to charge equivalents
$\boldsymbol{\Delta}$	Fractionation of river water and secondary phase (negative means secondary products are enriched in the lighter isotope)
$\boldsymbol{\Upsilon}$	Weighting terms in the cost function
$\boldsymbol{\omega}$	Vector of 0 and 1 controlling absolute or relative cost function
$\boldsymbol{\xi}$	Vector of 0 and 1 controlling if variable is in cost function
$\boldsymbol{\phi}$	Alkalinity released through carbonate weathering
$\boldsymbol{\beta}$	Alkalinity released through silicate weathering
$\boldsymbol{\gamma}$	Alkalinity consumed through FeS_2 oxidation
$\boldsymbol{\theta}$	Dissolved inorganic carbon released through C_{org} oxidation
$\mathbf{R}$	Carbonate weathering fraction
$\mathbf{Z}$	Sulfuric acid weathering fraction
$\mathbf{Y}$	Fraction of river SO_4^{2-} from FeS_2 oxidation
$\mathbf{W}$	SO_4^{2-} from FeS_2 oxidation relative to normalization variable
$\mathbf{C}$	Organic weathering fraction

Table II-3: Subscripts and superscripts on variables used throughout the text.

Subscripts	Description
$\mathbf{i}$	Generic dissolved observation, ranges from 1 to k
$\mathbf{i_1}$, $\mathbf{i_2}$, $\mathbf{i_3}$	Example of three dissolved observations
$\mathbf{i_{norm}}$	A single variable contributing to normalization, ranges from 1 to k_{norm}
$\mathbf{i_{RZC}}$	A single variable in the denominator of R, Z, C, ranges from 1 to k_{RZC}
$\mathbf{i_{RZC}}$ ... $\mathbf{k_{RZC}}$	List of variables in denominator of R, Z, C. For example, Ca^{2+}, Mg^{2+}, Na^{+}
norm	Normalization, either an individual variable or sum of variables
$\mathbf{\Sigma^+}$	Charge-equivalent sum of cations, typically Ca^{2+}, Mg^{2+}, Na^{+}, and K^{+}
$\mathbf{Cl^-}$ **critical**	Cl^- attributable to precipitation
excess $\mathbf{SO_4^{2-}}$	SO_4^{2-} in excess of mixing (calculated without SO_4^{2-} in inversion)
$\mathbf{FeS_2}$ $\mathbf{SO_4^{2-}}$	SO_4^{2-} from end-members representing FeS_2 oxidation
sc (left-hand)	Scaled values after normalizing by the sum of all fractional contributions
Superscripts	**Description**
riv	Sample of river water
$\mathbf{s}$	Generic inversion end-member (a source or sink), ranges from 1 to n
$\mathbf{s_1}$, $\mathbf{s_2}$, $\mathbf{s_3}$	Example of three end-members
$\mathbf{s'}$	Generic inversion end-member (a source or sink), ranges from 1 to n, used when equations require independent summations over end-members
$\mathbf{s^{second}}$	End-member representing a secondary phase, such as clay
$\mathbf{s_i^{source}}$	End-member sources of the variable i, ranges from 1 to n_i^{source}
$\mathbf{s_{FeS_2\ SO_4^{2-}}}$	End-member source of FeS_2-derived SO_4^{2-}, ranges 1 to $n_{FeS_2\ SO_4^{2-}}$
$\mathbf{s_{SO_4^{2-}}}$	End-member source of non-FeS_2-derived SO_4^{2-}, ranges 1 to $n_{SO_4^{2-}}$
$\mathbf{s_{carb}}$	Carbonate end-member, ranges from 1 to n_{carb}
$\mathbf{s_{weath}}$	Weathering end-member, ranges from 1 to n_{weath}
$\mathbf{s_{i_{RZC}}^{source}}$	End-member sources of the variable i_{RZC}, ranges from 1 to $n_{i_{RZC}}^{source}$
$\mathbf{s_{i_{RZC}}^{sink}}$	End-member sinks of the variable i_{RZC}, ranges from 1 to $n_{i_{RZC}}^{sink}$
source	Gross input from primary end-members (not including secondary phases)
other	The 'other' end-member, which sources SO_4^{2-} to river water
$\mathbf{FeS_2\ ox.\ ALK}$	On Z, Y, W, means numerator from FeS_2 end-member, ALK
$\mathbf{FeS_2\ ox.\ SO_4^{2-}}$	On Z, Y, W, means numerator from FeS_2 end-member, SO_4^{2-}
excess $\mathbf{SO_4^{2-}}$	On Z, Y, W, means numerator from river excess SO_4^{2-}
$\mathbf{FeS_2}$ $\mathbf{SO_4^{2-}}$	On Z, Y, W, means numerator from end-members weathered with H_2SO_4
g (left-hand)	Gross (not accounting for formation of secondary phases)
n (left-hand)	Net (accounting for formation of secondary phases)

Table II-4: Example end-member ratios for normalization to χ_{Na^+}, χ_{Σ^+}, $\chi_{\Sigma^+ + ALK + DIC}$, and $\chi_{\Sigma^+ + SO_4^{2-} + DIC}$. All normalized ratios are given for the same arbitrary, but realistic, carbonate, dolomite, silicate and evaporite end-members. See Tables II-7, 9, 11, and 13 for the end-member ratios used in the scenarios discussed in the text.

-	Carbonate	Dolomite	Silicate	Evaporite	FeS_2 ox.	C_{org} ox.
Normalization with $\boldsymbol{\chi_{Na^+}}$ ($\boldsymbol{\mu M/\mu M}$)						
$\boldsymbol{\chi^s_{Ca^{2+}}}$	-	-	0.30	0.375	-	-
$\boldsymbol{\chi^s_{Mg^{2+}}}$	-	-	0.20	0.375	-	-
$\boldsymbol{\chi^s_{Na^+}}$	-	-	1.00	1.00	-	-
$\boldsymbol{\chi^s_{SO_4^{2-}}}$	-	-	0.00	0.75	-	-
$\boldsymbol{\chi^s_{Cl^-}}$	-	-	0.00	1.00	-	-
$\boldsymbol{\chi^s_{ALK}}$	-	-	2.00	0.00	-	-
$\boldsymbol{\chi^s_{DIC}}$	-	-	0.00	0.00	-	-
Normalization with $\boldsymbol{\chi_{\Sigma^+}}$ (eq/eq)						
$\boldsymbol{2\chi^s_{Ca^{2+}}}$	1.00	0.50	0.30	0.30	-	-
$\boldsymbol{2\chi^s_{Mg^{2+}}}$	0.00	0.50	0.20	0.30	-	-
$\boldsymbol{\chi^s_{Na^+}}$	0.00	0.00	0.50	0.40	-	-
$\boldsymbol{2\chi^s_{SO_4^{2-}}}$	0.00	0.00	0.00	0.60	-	-
$\boldsymbol{\chi^s_{Cl^-}}$	0.00	0.00	0.00	0.40	-	-
$\boldsymbol{\chi^s_{ALK}}$	1.00	1.00	1.00	0.00	-	-
$\boldsymbol{\chi^s_{DIC}}$	0.50	0.50	0.00	0.00	-	-
Normalization with $\boldsymbol{\chi_{\Sigma^+ + ALK + DIC}}$ (eq/eq)						
$\boldsymbol{2\chi^s_{Ca^{2+}}}$	0.40	0.20	0.15	0.30	0.00	0.00
$\boldsymbol{2\chi^s_{Mg^{2+}}}$	0.00	0.20	0.10	0.30	0.00	0.00
$\boldsymbol{\chi^s_{Na^+}}$	0.00	0.00	0.25	0.40	0.00	0.00
$\boldsymbol{2\chi^s_{SO_4^{2-}}}$	0.00	0.00	0.00	0.60	-1.00	0.00
$\boldsymbol{\chi^s_{Cl^-}}$	0.00	0.00	0.00	0.40	0.00	0.00
$\boldsymbol{\chi^s_{ALK}}$	0.40	0.40	0.50	0.00	1.00	0.00
$\boldsymbol{\chi^s_{DIC}}$	0.20	0.20	0.00	0.00	0.00	1.00
Normalization with $\boldsymbol{\chi_{\Sigma^+ + SO_4^{2-} + DIC}}$ (eq/eq)						
$\boldsymbol{2\chi^s_{Ca^{2+}}}$	0.66	0.33	0.30	0.1875	0.00	0.00
$\boldsymbol{2\chi^s_{Mg^{2+}}}$	0.00	0.33	0.20	0.1875	0.00	0.00
$\boldsymbol{\chi^s_{Na^+}}$	0.00	0.00	0.50	0.25	0.00	0.00
$\boldsymbol{2\chi^s_{SO_4^{2-}}}$	0.00	0.00	0.00	0.375	1.00	0.00
$\boldsymbol{\chi^s_{Cl^-}}$	0.00	0.00	0.00	0.25	0.00	0.00
$\boldsymbol{\chi^s_{ALK}}$	0.66	0.66	1.00	0.00	-1.00	0.00
$\boldsymbol{\chi^s_{DIC}}$	0.33	0.33	0.00	0.00	0.00	1.00

Table II-5: Summary of river inversion scenarios using data from Gaillardet et al. (1999). When evaluated using values of $\chi^{riv}_{Cl^-\,critical}$, scenarios are appended with the letter "c." Blank entries indicate the parameter is unchanged from the default case (JG-1). Nearly all model results are accepted in scenario JG-1, which is used for sensitivity testing (Fig. II-2), while in other scenarios only a subset of simulation results are accepted based on either sample matching (JG-2 through JG-5, JG-7, JG8) or lowest misfit fraction (JG-6). In all scenarios except JG-8 the inversion end-members are precipitation, carbonate, silicate, and evaporite (stoichiometrically constrained). Scenario JG-7 has variable $\chi_{HCO_3^-}/\chi_{\Sigma^+}$ ratios, while scenario JG-8 has two silicate and two carbonate end-members with fixed ratios of $\chi_{HCO_3^-}/\chi_{\Sigma^+}$. Entries in the successful simulations row are the 25th percentile of the number of accepted simulations across all samples in the scenario.

	Inversion scenarios using data from Gaillardet et al. (1999)							
Parameters	**Default: JG-1**	**JG-2(c)**	**JG-3(c)**	**JG-4(c)**	**JG-5(c)**	**JG-6**	**JG-7**	**JG-8**
Variables	$\chi_{Ca^{2+}}$, $\chi_{Mg^{2+}}$, χ_{Na^+}, χ_{Cl^-}						$+\chi_{HCO_3^-}$	$+\chi_{HCO_3^-}$
Reconstructed observations	10^{-4} - 10^4 % (sensitivity testing)	85-115%	85-115%	85-115%	85-115%	N/A	85-115%	85-115%
Normalization	$\chi_{Ca^{2+}}+\chi_{Mg^{2+}}+\chi_{Na^+}$			χ_{Na^+}				
EM distribution	normal		uniform				uniform	uniform
Cost function	relative				absolute			
Cull solutions	sample matching					1%, all samples		
$\mathbf{SO_4^{2-}}$ treatment	$\chi_{SO_4^{2-}}$ not included							
Max attempted simulations	10^5	10^6 ($3\cdot10^5$)	10^6 ($3\cdot10^5$)	10^6 ($3\cdot10^5$)	10^6 ($3\cdot10^5$)	10^5	10^6	10^6
Successful simulations (25th)	10^5	10^3 (10^3)	10^3 (10^3)	10^3 (10^3)	10^3 (10^3)	10^3	10^3	10^3
End-member distributions	$\chi_{HCO_3^-}$ not in the inversion						$\chi_{HCO_3^-}/\chi_{\Sigma^+}$ variable	$\chi_{HCO_3^-}/\chi_{\Sigma^+}$ fixed

Table II-6: Summary of river inversion scenarios using the global river data of Burke et al. (2018). Blank entries indicate the parameter is unchanged from the default case (AB-1), while entries of "Variables" (AB-2, AB-3, AB-4), "Normalization" (AB-5), or "SO_4^{2-} treatment" (AB-4, AB-5) are modifications to the default values. Scenarios AB-2 and AB-3 differ by whether the misfit of model results from calculated $\chi^{riv}_{HCO_3^-}/\chi^{riv}_{\Sigma^+}$ is included in the cost function. In scenario AB-6, the carbonate and silicate end-members have smaller ranges for $\chi_{FeS_2\ SO_4^{2-}}/\chi_{\Sigma^+}$, which we find impacts the inversion-constrained median values of carbonate weathering fraction (R). Inversion end-members are precipitation, silicate, carbonate, and evaporite (stoichiometrically constrained) and scenario AB-5 contains an additional end-member representing other SO_4^{2-}. Entries in the successful simulations row are the 25th percentile of the number of accepted simulations across all samples in the scenario.

Inversion scenarios using data from Burke et al. (2018)						
Parameters	**Default: AB-1**	**AB-2**	**AB-3**	**AB-4**	**AB-5**	**AB-6**
Variables	$\chi_{Ca^{2+}}, \chi_{Mg^{2+}}, \chi_{Na^+}, \chi_{Cl^-}, \chi_{SO_4^{2-}}$	$^{+}\chi_{HCO_3^-}$, not in cost function	$^{+}\chi_{HCO_3^-}$, in cost function	$^{-}\chi_{SO_4^{2-}}$		
Reconstructed observations	85-115%					
Normalization	$\chi_{Ca^{2+}}{}^{+}\chi_{Mg^{2+}}{}^{+}\chi_{Na^+}$				$^{+}\chi_{SO_4^{2-}}$	
EM distribution	uniform					
Cost function	relative					
Cull solutions	sample matching					
$\mathbf{SO_4^{2-}}$ treatment	in end-members			excess	other	
Max attempted simulations	10^6					
Successful simulations (25th)	10^3					
End-member distributions	$\chi_{FeS_2\ SO_4^{2-}}/\chi_{\Sigma^+}$ ranges from 0 to 1					$\chi_{FeS_2\ SO_4^{2-}}/\chi_{\Sigma^+}$ ranges from 0 to 0.15

Table II-7: Summary of end-members for inversion of data from Gaillardet et al. (1999) and Burke et al. (2018). Ratios are given as the mean and standard deviation of normal distributions for variables normalized to χ_{Σ^+} or χ_{Na^+}, as well as the minimum and maximum values of uniform distributions normalized to χ_{Σ^+} or $\chi_{\Sigma^+ + SO_4^{2-}}$. Na^+-normalized values are from Burke et al. (2018), and values normalized to χ_{Σ^+} or $\chi_{\Sigma^+ + SO_4^{2-}}$ were calculated by Monte Carlo simulation from the Na^+-normalized distributions. All scenarios have $\chi_{Cl^-}^{evap} = \chi_{Na^+}^{evap}$ and all scenarios including $\chi_{SO_4^{2-}}$ have $\chi_{SO_4^{2-}}^{evap} = \chi_{Ca^{2+}}^{evap} + \chi_{Mg^{2+}}^{evap}$.

End-members for inverting data from Gaillardet et al. (1999) and Burke et al. (2018): JG-1 through JG-8 and AB-1 through AB-6						
Notes	**Ratio**	**Precipitation**	**Carbonate**	**Silicate**	**Evaporite**	**Other**
Scenarios JG-1, 2, 2c, 5, 5c, and 6. Ratios are relative to sum $\boldsymbol{\chi_{Ca^{2+}}}$, $\boldsymbol{\chi_{Mg^{2+}}}$, $\boldsymbol{\chi_{Na^+}}$ in eq/eq.	$2\chi_{Ca^{2+}}$	0.036±0.015	0.663±0.173	0.315±0.138	0.454±0.183	–
	$2\chi_{Mg^{2+}}$	0.174±0.013	0.332±0.172	0.226±0.120	0.088±0.064	–
	χ_{Na^+}	0.790±0.017	0.005±0.004	0.443±0.117	0.447±0.155	–
	χ_{Cl^-}	0.908±0.082	0.000±0.000	0.000±0.000	0.437±0.184	–
	$2\chi_{SO_4^{2-}}$	0.095±0.016	0.001±0.001	0.017±0.007	0.342±0.226	–
Scenarios JG-3, 3c, 7, 8, AB-1, 2, 3, 4, 6. Ratios relative to sum of $\boldsymbol{\chi_{Ca^{2+}}}$, $\boldsymbol{\chi_{Mg^{2+}}}$, and $\boldsymbol{\chi_{Na^+}}$ in eq/eq. In AB-6, some $\boldsymbol{\chi_{FeS_2\ SO_4^{2-}}}$ ratios are lower (0-0.15).	$2\chi_{Ca^{2+}}$	0.006–0.066	0.317–1.000	0.039–0.591	0.088–0.820	–
	$2\chi_{Mg^{2+}}$	0.148–0.200	0.000–0.675	0.000–0.466	0.000–0.216	–
	χ_{Na^+}	0.756–0.824	0.000–0.013	0.209–0.677	0.137–0.757	–
	χ_{Cl^-}	0.744–1.072	0.000–0.000	0.000–0.000	0.069–0.805	–
	$\chi_{HCO_3^-}$	0.000–0.000	0.500–1.000	0.000–1.000	0.000–0.000	–
	$2\chi_{SO_4^{2-}}$	0.063–0.127	0.000–0.003	0.003–0.031	0.000–0.794	–
	$\delta^{34}S$	15–20‰	10–30‰	0–5‰	10–30‰	–
	$\chi_{FeS_2\ SO_4^{2-}}$	0.000–0.000 (0.00–0.00)	0.000–1.000 (0.00–0.15)	0.000–1.000 (0.00–0.15)	0.000–0.000 (0.00–0.00)	–
Scenarios JG-4, 4c. Ratios relative to $\boldsymbol{\chi_{Na^+}}$ in μM/μM.	$\chi_{Ca^{2+}}$	0.023±0.010	60.00±30.00	0.350±0.250	0.500±0.500	–
	$\chi_{Mg^{2+}}$	0.110±0.010	30.00±15.00	0.250±0.200	0.100±0.080	–
	χ_{Na^+}	1.000±0.000	1.000±0000	1.000±0.000	1.000±0.000	–
	χ_{Cl^-}	1.150±0.100	0.000±0000	0.000±0.000	1.000±0.200	–
	$\chi_{SO_4^{2-}}$	0.060±0.010	0.060±0.030	0.019±0.005	0.400±0.200	–
Scenario AB-5. Ratios relative to sum of $\boldsymbol{\chi_{Ca^{2+}}}$, $\boldsymbol{\chi_{Mg^{2+}}}$, $\boldsymbol{\chi_{Na^+}}$, and $\boldsymbol{\chi_{SO_4^{2-}}}$ in eq/eq.	$2\chi_{Ca^{2+}}$	0.005–0.061	0.317–1.000	0.039–0.591	0.012–0.660	0
	$2\chi_{Mg^{2+}}$	0.133–0.185	0.000–0.675	0.000–0.466	0.000–0.159	0
	χ_{Na^+}	0.685–0.757	0.000–0.013	0.209–0.677	0.128–0.520	0
	χ_{Cl^-}	0.680–0.980	0.000–0.000	0.000–0.000	0.078–0.562	0
	$2\chi_{SO_4^{2-}}$	0.061–0.113	0.000–0.000	0.000–0.000	0.031–0.479	1
	$\delta^{34}S$	15–20‰	–	–	10–30‰	–

Table II-8: Summary of river inversion scenarios using data from Torres et al. (2016). Blank entries indicate the parameter is unchanged from the default case (MT-1). In scenarios MT-3 and MT-4, the 1% of 30,000 simulations with lowest cost function evaluation are retained for additional analysis. Note that MT-5 is identical to MT-1 except that it has more successful simulations. Inversion end-members are precipitation, dolomite, silicate, and shale, and scenario MT-7 contains an additional end-member representing FeS_2 oxidation. $\chi^{riv}_{Cl^-}$ is not corrected using values of $\chi^{riv}_{Cl^-\,critical}$. In simulations MT-1 through MT-5, FeS_2 oxidation is included within the lithologic end-members. In MT-6, FeS_2 oxidation is diagnosed following the approach of Burke et al. (2018). In MT-7, FeS_2 oxidation is an independent end-member. Entries in the successful simulations row are the 25th percentile of the number of accepted simulations across all samples in the scenario.

Inversion scenarios using data from Torres et al. (2016)							
Parameters	**Default: MT-1**	**MT-2**	**MT-3**	**MT-4**	**MT-5**	**MT-6**	**MT-7**
Variables	$\chi_{Ca^{2+}}, \chi_{Mg^{2+}}, \chi_{Sr^{2+}}, \chi_{Na^+}, \chi_{Cl^-}, \chi_{SO_4^{2-}}$					$-\chi_{SO_4^{2-}}$	
Reconstructed observations	85-115%		N/A	N/A			
Normalization	$\chi_{Ca^{2+}}+\chi_{Mg^{2+}}+\chi_{Na^+}+\chi_{Sr^{2+}}$						$+\chi_{SO_4^{2-}}$
EM distribution	uniform						
Cost function	relative	absolute		absolute			
Cull solutions	sample matching		1%, each sample	1%, each sample			
$\mathbf{SO_4^{2-}}$ treatment	in end-members					excess	other
Max attempted simulations	$3 \cdot 10^5$		$3 \cdot 10^4$	$3 \cdot 10^4$	$4 \cdot 10^5$	$4 \cdot 10^5$	$4 \cdot 10^5$
Successful simulations (25th)	$3 \cdot 10^2$	10^2			10^3	10^3	10^3

Table II-9: Summary of inversion end-members for Torres et al. (2016). Chemical ratios normalized to the sum of $\chi_{Ca^{2+}}$, $\chi_{Mg^{2+}}$, $\chi_{Na^{+}}$, and $\chi_{Sr^{2+}}$ are after Torres et al. (2016). Ratios including $\chi_{SO_4^{2-}}$ in the normalization were reached through Monte Carlo simulation of the data normalized to $\chi_{\Sigma^{+}}$. For all scenarios the isotopic composition of the FeS_2 end-member is constrained through inversion.

End-members for inverting data of Torres et al. (2016): MT-1 through MT-7						
Notes	**Ratio**	**Precipitation**	**Dolomite**	**Silicate**	**Shale**	**FeS_2**
Scenarios MT-1, 2, 3, 4, 5, 6. Ratios relative to sum of $\boldsymbol{\chi_{Ca^{2+}}}$, $\boldsymbol{\chi_{Mg^{2+}}}$, $\boldsymbol{\chi_{Na^{+}}}$, and $\boldsymbol{\chi_{Sr^{2+}}}$ in eq/eq.	$2\chi_{Ca^{2+}}$	0.200 – 0.650	0.500 – 1.000	0.030 – 0.400	0.030 – 0.300	–
	$2\chi_{Mg^{2+}}$	0.100 – 0.200	0.000 – 0.500	0.003 – 0.030	0.450 – 0.600	–
	$10^3 \cdot 2\chi_{Sr^{2+}}$	0.050 – 5.000	1.000 – 9.000	0.500 – 2.500	0.500 – 2.500	–
	$\chi_{Na^{+}}$	0.050 – 0.430	0.000 – 0.000	0.500 – 0.800	0.100 – 0.200	–
	$\chi_{Cl^{-}}$	0.060 – 0.500	0.000 – 0.000	0.000 – 0.000	0.000 – 0.000	–
	$2\chi_{SO_4^{2-}}$	0.060 – 0.400	0.000 – 0.000	0.000 – 0.000	0.000 – 0.000	–
	$\chi_{FeS_2\ SO_4^{2-}}$	0.000 – 0.000	0.000 – 1.000	0.000 – 1.000	0.000 – 1.000	–
	$\delta^{34}S$	-5‰ – 9‰	calculated	calculated	calculated	–
Scenario MT-7. Ratios relative to sum of $\boldsymbol{\chi_{Ca^{2+}}}$, $\boldsymbol{\chi_{Mg^{2+}}}$, $\boldsymbol{\chi_{Na^{+}}}$, $\boldsymbol{\chi_{Sr^{2+}}}$, and $\boldsymbol{\chi_{SO_4^{2-}}}$ in eq/eq.	$2\chi_{Ca^{2+}}$	0.212 – 0.600	0.500 – 1.000	0.030 – 0.400	0.030 – 0.300	0
	$2\chi_{Mg^{2+}}$	0.065 – 0.221	0.000 – 0.500	0.003 – 0.030	0.450 – 0.600	0
	$10^3 \cdot 2\chi_{Sr^{2+}}$	0.000 – 6.000	1.000 – 9.000	0.500 – 2.500	0.500 – 2.500	0
	$\chi_{Na^{+}}$	0.045 – 0.413	0.000 – 0.000	0.500 – 0.800	0.100 – 0.200	0
	$\chi_{Cl^{-}}$	0.000 – 0.549	0.000 – 0.000	0.000 – 0.000	0.000 – 0.000	0
	$2\chi_{SO_4^{2-}}$	0.050 – 0.390	0.000 – 0.000	0.000 – 0.000	0.000 – 0.000	1
	$\delta^{34}S$	-5‰ – 9‰	-	-	-	calculated

Table II-10: Summary of inversion scenario for the data of Gíslason et al. (1996). The inversion end-members are basalt, meteoric precipitation, and secondary clay formation ("clay"). Entries in the successful simulations row are the 25th percentile of the number of accepted simulations across all samples in the scenario.

Inversion scenario using data from Gíslason et al. (1996)	
Parameters	**SG-1**
Variables	$\chi_{Ca^{2+}}, \chi_{Mg^{2+}}, \chi_{Na^{+}}, \chi_{Cl^{-}}$
Reconstructed observations	85-115%
Normalization	$\chi_{Ca^{2+}} + \chi_{Mg^{2+}} + \chi_{Na^{+}}$
EM distribution	normal
Cost function	relative
Cull solutions	sample matching
$\mathbf{SO_4^{2-}}$ treatment	$\chi_{SO_4^{2-}}$ not included
Max attempted simulations	10^6
Successful simulations (25th)	10^3

Table II-11: Summary of inversion end-members for Gíslason et al. (1996). Ratios are given as the mean and standard deviation of normal distributions normalized to χ_{Σ^+}. The chemistry of precipitation is calculated from observations at the Íráfoss meteorological station collected as part of the European Monitoring and Evaluation Programme under the Convention on Long-range Transboundary Air Pollution, but with reduced variability in normalized $\chi_{Cl^-}^{prec}$. The chemical composition of basalt is calculated from observations in Torssander (1989), Gíslason et al. (1996), and Moulton et al. (2000). The chemistry of the secondary clay is intentionally general for comparison of inversion-constrained values to the observations of Moulton et al. (2000) and Thorpe et al. (2019).

End-members for inverting data of Gíslason et al. (1996): SG-1				
Notes	**Ratio**	**Precipitation**	**Basalt**	**Clay**
Scenario SG-1. Ratios relative to sum of $\boldsymbol{\chi_{Ca^{2+}}}$, $\boldsymbol{\chi_{Mg^{2+}}}$, and $\boldsymbol{\chi_{Na^+}}$ in eq/eq.	$2\chi_{Ca^{2+}}$	0.051 ± 0.045	0.480 ± 0.062	0.500 ± 0.500
	$2\chi_{Mg^{2+}}$	0.173 ± 0.024	0.393 ± 0.111	0.500 ± 0.500
	χ_{Na^+}	0.776 ± 0.072	0.116 ± 0.069	0.500 ± 0.500
	χ_{Cl^-}	0.910 ± 0.150	0.000 ± 0.000	0.000 ± 0.000
	$2\chi_{SO_4^{2-}}$	0.122 ± 0.108	0.000 ± 0.000	0.000 ± 0.000

Table II-12: Summary of river inversion scenarios using data from Horan et al. (2019). Blank entries indicate the parameter is unchanged from the default case (KH-1). The inversion end-members are precipitation, dolomite, silicate, FeS_2 oxidation, C_{org} oxidation, and atmospheric gas exchange. Entries in the successful simulations row are the 25th percentile of the number of accepted simulations across all samples in the scenario.

Inversion scenarios using data from Horan et al. (2019)		
Parameters	**Default: KH-1**	**KH-2**
Variables	$\chi_{Ca^{2+}}$, $\chi_{Mg^{2+}}$, $\chi_{Na^{+}}$, $\chi_{Cl^{-}}$, $\chi_{SO_4^{2-}}$, χ_{Re}, χ_{ALK}, χ_{DIC}	
Reconstructed observations	85-115%	
Normalization	$\chi_{Ca^{2+}}+\chi_{Mg^{2+}}+\chi_{Na^{+}}+\chi_{ALK}+\chi_{DIC}$	- χ_{ALK}, $+\chi_{SO_4^{2-}}$
EM distribution	uniform	
Cost function	relative	
Cull solutions	sample matching	
$\mathbf{SO_4^{2-}}$ treatment	other	
Max attempted simulations	10^6	
Successful simulations (25th)	10^3	

Table II-13: Inversion end-members for Horan et al. (2019). Values are the ranges for uniform distributions normalized to $\chi_{\Sigma^+ + ALK + DIC}$ or $\chi_{\Sigma^+ + SO_4^{2-} + DIC}$. Precipitation is calculated from the Na^+-normalized precipitation end-member in Burke et al. (2018). The carbonate and silicate end-members are generic. Negative values for the FeS_2 end-member reflects that FeS_2 oxidation increases $\chi^{riv}_{SO_4^{2-}}$ and χ^{riv}_{Re} while decreasing χ^{riv}_{ALK}. The C_{org} χ_{Re}/χ_{DIC} ratio is from Horan et al. (2019); we estimated normalized χ_{Re} for the FeS_2 and silicate end-members using the $[Re]/[SO_4^{2-}]$ and [Re]/[Na] ranges plotted for the 'sulfides' and 'silicates' regions in Figure 4b of that work. MEANDIR samples the normalized Re distributions as log-uniform distributions. These assignments for relative χ_{Re} abundance should be viewed only as approximations meant to illustrate MEANDIR's ability to quantify C_{org} oxidation.

End-members for inverting data of Horan et al. (2019): KH-1 and KH-2							
Notes	**Ratio**	**Precipitation**	**Carbonate**	**Silicate**	**FeS_2**	**C_{org}**	**Atmosphere**
Scenario KH-1. Ratios relative to sum of $\boldsymbol{\chi_{Ca^{2+}}}$, $\boldsymbol{\chi_{Mg^{2+}}}$, $\boldsymbol{\chi_{Na^+}}$, $\boldsymbol{\chi_{ALK}}$, and $\boldsymbol{\chi_{DIC}}$ in eq/eq.	$2\chi_{Ca^{2+}}$	0.008 – 0.060	0.20 – 0.40	0.05 – 0.25	0.0 – 0.0	00 – 00	0.0 – 0.0
	$2\chi_{Mg^{2+}}$	0.122 – 0.190	0.00 – 0.20	0.05 – 0.25	0.0 – 0.0	00 – 00	0.0 – 0.0
	χ_{Na^+}	0.586 – 0.830	0.00 – 0.00	0.05 – 0.25	0.0 – 0.0	00 – 00	0.0 – 0.0
	χ_{Cl^-}	0.564 – 0.972	0.00 – 0.00	0.00 – 0.00	0.0 – 0.0	00 – 00	0.0 – 0.0
	$2\chi_{SO_4^{2-}}$	0.050 – 0.114	0.00 – 0.00	0.00 – 0.00	-1.0 – -1.0	00 – 00	0.0 – 0.0
	$\chi_{Re} \cdot 10^9$	0.000 – 0.000	0.00 – 0.00	0.10 – 7.50	-1.0 – -0.2	25 – 37	0.0 – 0.0
	χ_{ALK}	0.000 – 0.122	0.40 – 0.40	0.50 – 0.50	1.0 – 1.0	00 – 00	0.0 – 0.0
	χ_{DIC}	0.000 – 0.122	0.20 – 0.20	0.00 – 0.00	0.0 – 0.0	01 – 01	1.0 – 1.0
Scenario KH-2. Ratios relative to sum of $\boldsymbol{\chi_{Ca^{2+}}}$, $\boldsymbol{\chi_{Mg^{2+}}}$, $\boldsymbol{\chi_{Na^+}}$, $\boldsymbol{\chi_{SO_4^{2-}}}$, and $\boldsymbol{\chi_{DIC}}$ in eq/eq.	$2\chi_{Ca^{2+}}$	0.007 – 0.059	0.33 – 0.66	0.10 – 0.50	0.0 – 0.0	00 – 00	0.0 – 0.0
	$2\chi_{Mg^{2+}}$	0.126 – 0.178	0.00 – 0.33	0.10 – 0.50	0.0 – 0.0	00 – 00	0.0 – 0.0
	χ_{Na^+}	0.618 – 0.750	0.00 – 0.00	0.10 – 0.50	0.0 – 0.0	00 – 00	0.0 – 0.0
	χ_{Cl^-}	0.598 – 0.886	0.00 – 0.00	0.00 – 0.00	0.0 – 0.0	00 – 00	0.0 – 0.0
	$2\chi_{SO_4^{2-}}$	0.054 – 0.106	0.00 – 0.00	0.00 – 0.00	1.0 – 1.0	00 – 00	0.0 – 0.0
	$\chi_{Re} \cdot 10^9$	0.000 – 0.000	0.00 – 0.00	0.20 – 15.0	0.2 – 1.0	25 – 37	0.0 – 0.0
	χ_{ALK}	0.000 – 0.126	0.66 – 0.66	1.00 – 1.00	-1.0 – -1.0	00 – 00	0.0 – 0.0
	χ_{DIC}	0.000 – 0.126	0.33 – 0.33	0.00 – 0.00	0.0 – 0.0	01 – 01	1.0 – 1.0

II.10: References

Aitchison, J., 1983. Principal component analysis of compositional data. *Biometrika*, 70(1), pp.57-65. https://doi.org/10.1093/biomet/70.1.57.

Baertschi, P., 1976. Absolute ^{18}O content of standard mean ocean water. *Earth and Planetary Science Letters*, 31(3), pp.341-344. https://doi.org/10.1016/0012-821X(76)90115-1.

Berner, R.A., 1971. Worldwide sulfur pollution of rivers. *Journal of Geophysical Research*, 76(27), pp.6597-6600. https://doi.org/10.1029/JC076i027p06597.

Bickle, M.J., Tipper, E.D., Galy, A., Chapman, H. and Harris, N., 2015. On discrimination between carbonate and silicate inputs to Himalayan rivers. *American Journal of Science*, 315(2), pp.120-166. https://doi.org/10.2475/02.2015.02.

Bickle, M.J., Chapman, H.J., Tipper, E., Galy, A., Christina, L. and Ahmad, T., 2018. Chemical weathering outputs from the flood plain of the Ganga. *Geochimica et Cosmochimica Acta*, 225, pp.146-175. https://doi.org/10.1016/j.gca.2018.01.003.

Bizzarro, M., Paton, C., Larsen, K., Schiller, M., Trinquier, A. and Ulfbeck, D., 2011. High-precision Mg-isotope measurements of terrestrial and extraterrestrial material by HR-MC-ICPMS—implications for the relative and absolute Mg-isotope composition of the bulk silicate Earth. *Journal of Analytical Atomic Spectrometry*, 26(3), pp.565-577. https://doi.org/10.1039/C0JA00190B.

Blair, N.E. and Aller, R.C., 2012. The fate of terrestrial organic carbon in the marine environment. *Annual Review of Marine Science*, 4, pp.401-423. https://doi.org/10.1146/annurev-marine-120709-142717.

Blattmann, T.M., Wang, S.L., Lupker, M., Märki, L., Haghipour, N., Wacker, L., Chung, L.H., Bernasconi, S.M., Plötze, M. and Eglinton, T.I., 2019. Sulphuric acid-mediated weathering on Taiwan buffers geological atmospheric carbon sinks. *Scientific Reports*, 9(1), pp.1-8. https://doi.org/10.1038/s41598-019-39272-5.

Bolton, E.W., Berner, R.A. and Petsch, S.T., 2006. The weathering of sedimentary organic matter as a control on atmospheric O_2: II. Theoretical modeling. *American Journal of Science*, 306(8), pp.575-615. https://doi.org/10.2475/08.2006.01.

Bouchez, J., Beyssac, O., Galy, V., Gaillardet, J., France-Lanord, C., Maurice, L. and Moreira-Turcq, P., 2010. Oxidation of petrogenic organic carbon in the Amazon floodplain as a source of atmospheric CO_2. *Geology*, 38(3), pp.255-258. https://doi.org/10.1130/G30608.1.

Bouchez, J., Von Blanckenburg, F. and Schuessler, J.A., 2013. Modeling novel stable isotope ratios in the weathering zone. *American Journal of Science*, 313(4), pp.267-308. https://doi.org/10.2475/04.2013.01.

Brand, W.A., Coplen, T.B., Vogl, J., Rosner, M. and Prohaska, T., 2014. Assessment of international reference materials for isotope-ratio analysis (IUPAC Technical Report). *Pure and Applied Chemistry*, 86(3), pp.425-467. https://doi.org/10.1515/pac-2013-1023.

Burke, A., Present, T.M., Paris, G., Rae, E.C., Sandilands, B.H., Gaillardet, J., Peucker-Ehrenbrink, B., Fischer, W.W., McClelland, J.W., Spencer, R.G. and Voss, B.M., 2018. Sulfur isotopes in rivers: Insights into global weathering budgets, pyrite oxidation, and the modern sulfur cycle. *Earth and Planetary Science Letters*, 496, pp.168-177. https://doi.org/10.1016/j.epsl.2018.05.022.

Calmels, D., Gaillardet, J., Brenot, A. and France-Lanord, C., 2007. Sustained sulfide oxidation by physical erosion processes in the Mackenzie River basin: Climatic perspectives. *Geology*, 35(11), pp.1003-1006. https://doi.org/10.1130/G24132A.1.

Caves, J.K., Jost, A.B., Lau, K.V. and Maher, K., 2016. Cenozoic carbon cycle imbalances and a variable weathering feedback. *Earth and Planetary Science Letters*, 450, pp.152-163. https://doi.org/10.1016/j.epsl.2016.06.035.

Chang, T., and Li, W, 1990. A calibrated measurement of the atomic weight of carbon. *Chinese Science Bulletin*, (4), pp.290-296.

Christophersen, N. and Hooper, R.P., 1992. Multivariate analysis of stream water chemical data: The use of principal components analysis for the end-member mixing problem. *Water Resources Research*, 28(1), pp.99-107. https://doi.org/10.1029/91WR02518.

Daëron, M., Blamart, D., Peral, M. and Affek, H.P., 2016. Absolute isotopic abundance ratios and the accuracy of Δ^{47} measurements. *Chemical Geology*, 442, pp.83-96. https://doi.org/10.1016/j.chemgeo.2016.08.014.

de Souza, G.F., Reynolds, B.C., Kiczka, M. and Bourdon, B., 2010. Evidence for mass-dependent isotopic fractionation of strontium in a glaciated granitic watershed. *Geochimica et Cosmochimica Acta*, 74(9), pp.2596-2614. https://doi.org/10.1016/j.gca.2010.02.012.

Ding, T., Valkiers, S., Kipphardt, H., De Bievre, P., Taylor, P.D.P., Gonfiantini, R. and Krouse, R., 2001. Calibrated sulfur isotope abundance ratios of three IAEA sulfur isotope reference materials and V-CDT with a reassessment of the atomic weight of sulfur. *Geochimica et Cosmochimica Acta*, 65(15), pp.2433-2437. https://doi.org/10.1016/S0016-7037(01)00611-1.

Dunlea, A.G. and Murray, R.W., 2015. Optimization of end-members used in multiple linear regression geochemical mixing models. *Geochemistry, Geophysics, Geosystems*, 16(11), pp.4021-4027. https://doi.org/10.1002/2015GC006132.

Edmond, J.M., Measures, C., McDuff, R.E., Chan, L.H., Collier, R., Grant, B., Gordon, L.I. and Corliss, J.B., 1979a. Ridge crest hydrothermal activity and the balances of the major and minor elements in the ocean: The Galapagos data. *Earth and Planetary Science Letters*, 46(1), pp.1-18. https://doi.org/10.1016/0012-821X(79)90061-X.

Edmond, J.M., Corliss, J.B. and Gordon, L.I., 1979b. Ridge Crest-Hydrothermal Metamorphism at the Galapagos Spreading Center and Reverse Weathering. *Deep Drilling Results in the Atlantic Ocean: Ocean Crust*, 2, pp.383-390.

France-Lanord, C. and Derry, L.A., 1997. Organic carbon burial forcing of the carbon cycle from Himalayan erosion. *Nature*, 390(6655), pp.65-67. https://doi.org/10.1038/36324.

Gaillardet, J., Dupré, B., Louvat, P. and Allegre, C.J., 1999. Global silicate weathering and CO_2 consumption rates deduced from the chemistry of large rivers. *Chemical Geology*, 159(1-4), pp.3-30. https://doi.org/10.1016/S0009-2541(99)00031-5.

Galy, A. and France-Lanord, C., 1999. Weathering processes in the Ganges–Brahmaputra basin and the riverine alkalinity budget. *Chemical Geology*, 159(1-4), pp.31-60. https://doi.org/10.1016/S0009-2541(99)00033-9.

Genereux, D., 1998. Quantifying uncertainty in tracer-based hydrograph separations. *Water Resources Research*, 34(4), pp.915-919. https://doi.org/10.1029/98WR00010.

Georg, R.B., Reynolds, B.C., West, A.J., Burton, K.W. and Halliday, A.N., 2007. Silicon isotope variations accompanying basalt weathering in Iceland. *Earth and Planetary Science Letters*, 261(3-4), pp.476-490. https://doi.org/10.1016/j.epsl.2007.07.004.

Gíslason, S.R., Arnorsson, S. and Armannsson, H., 1996. Chemical weathering of basalt in Southwest Iceland; effects of runoff, age of rocks and vegetative/glacial cover. *American Journal of Science*, 296(8), pp.837-907. https://doi.org/10.2475/ajs.296.8.837.

Hartmann, J., Lauerwald, R. and Moosdorf, N., 2014. A brief overview of the GLObal RIver CHemistry Database, GLORICH. *Procedia Earth and Planetary Science*, 10, pp.23-27. https://doi.org/10.1016/j.proeps.2014.08.005.

He, Z., Unger-Shayesteh, K., Vorogushyn, S., Weise, S.M., Duethmann, D., Kalashnikova, O., Gafurov, A. and Merz, B., 2020. Comparing Bayesian and traditional end-member mixing approaches for hydrograph separation in a glacierized basin. *Hydrology and Earth System Sciences*, 24(6), pp.3289-3309. https://doi.org/10.5194/hess-24-3289-2020.

Hemingway, J.D., Olson, H., Turchyn, A.V., Tipper, E.T., Bickle, M.J. and Johnston, D.T., 2020. Triple oxygen isotope insight into terrestrial pyrite oxidation. *Proceedings of the National Academy of Sciences*, 117(14), pp.7650-7657. https://doi.org/10.1073/pnas.1917518117.

Hilton, R.G., Gaillardet, J., Calmels, D. and Birck, J.L., 2014. Geological respiration of a mountain belt revealed by the trace element rhenium. *Earth and Planetary Science Letters*, 403, pp.27-36. https://doi.org/10.1016/j.epsl.2014.06.021.

Hilton, R.G. and West, A.J., 2020. Mountains, erosion and the carbon cycle. *Nature Reviews Earth & Environment*, 1(6), pp.284-299. https://doi.org/10.1038/s43017-020-0058-6.

Hindshaw, R.S., Bourdon, B., von Strandmann, P.A.P., Vigier, N. and Burton, K.W., 2013. The stable calcium isotopic composition of rivers draining basaltic catchments in Iceland. *Earth and Planetary Science Letters*, 374, pp.173-184. https://doi.org/10.1016/j.epsl.2013.05.038.

Horan, K., Hilton, R.G., Dellinger, M., Tipper, E., Galy, V., Calmels, D., Selby, D., Gaillardet, J., Ottley, C.J., Parsons, D.R. and Burton, K.W., 2019. Carbon dioxide emissions by rock organic carbon oxidation and the net geochemical carbon budget of the Mackenzie River Basin. *American Journal of Science*, 319(6), pp.473-499. https://doi.org/10.2475/06.2019.02.

Hubbard, C.G., Black, S. and Coleman, M.L., 2009. Aqueous geochemistry and oxygen isotope compositions of acid mine drainage from the Río Tinto, SW Spain, highlight inconsistencies in current models. *Chemical Geology*, 265(3-4), pp.321-334. https://doi.org/10.1016/j.chemgeo.2009.04.009.

Jacobson, A.D., Blum, J.D. and Walter, L.M., 2002. Reconciling the elemental and Sr isotope composition of Himalayan weathering fluxes: Insights from the carbonate geochemistry of stream waters. *Geochimica et Cosmochimica Acta*, 66(19), pp.3417-3429. https://doi.org/10.1016/S0016-7037(02)00951-1.

Kemeny, P.C., Lopez, G.I., Dalleska, N.F., Torres, M., Burke, A., Bhatt, M.P., West, A.J., Hartmann, J. and Adkins, J.F., 2021a. Sulfate sulfur isotopes and major ion chemistry reveal that pyrite oxidation counteracts CO_2 drawdown from silicate weathering in the Langtang-Trisuli-Narayani River system, Nepal Himalaya. *Geochimica et Cosmochimica Acta*, 294, pp.43-69. https://doi.org/10.1016/j.gca.2020.11.009.

Kemeny, P.C., Torres, M.A., Lamb, M.P., Webb, S.M., Dalleska, N., Cole, T., Hou, Y., Marske, J., Adkins, J.F. and Fischer, W.W., 2021b. Organic sulfur fluxes and geomorphic control of sulfur isotope ratios in rivers. *Earth and Planetary Science Letters*, 562, p.116838. https://doi.org/10.1016/j.epsl.2021.116838.

Lerman, A., Wu, L. and Mackenzie, F.T., 2007. CO_2 and H_2SO_4 consumption in weathering and material transport to the ocean, and their role in the global carbon balance. *Marine Chemistry*, 106(1-2), pp.326-350. https://doi.org/10.1016/j.marchem.2006.04.004.

Li, G. and Elderfield, H., 2013. Evolution of carbon cycle over the past 100 million years. *Geochimica et Cosmochimica Acta*, 103, pp.11-25. https://doi.org/10.1016/j.gca.2012.10.014.

Mayer, A.J. and Wieser, M.E., 2014. The absolute isotopic composition and atomic weight of molybdenum in SRM 3134 using an isotopic double-spike. *Journal of Analytical Atomic Spectrometry*, 29(1), pp.85-94. https://doi.org/10.1039/C3JA50164G.

Miesch, A.T., 1976. Q-mode factor analysis of compositional data. *Computers & Geosciences*, 1(3), pp.147-159. https://doi.org/10.1016/0098-3004(76)90003-0.

Moon, S., Chamberlain, C.P. and Hilley, G.E., 2014. New estimates of silicate weathering rates and their uncertainties in global rivers. *Geochimica et Cosmochimica Acta*, 134, pp.257-274. https://doi.org/10.1016/j.gca.2014.02.033.

Moore, L.J. and Machlan, L.A., 1972. High-accuracy determination of calcium in blood serum by isotope dilution mass spectrometry. *Analytical Chemistry*, 44(14), pp.2291-2296. https://doi.org/10.1021/ac60322a014.

Moulton, K.L., West, J. and Berner, R.A., 2000. Solute flux and mineral mass balance approaches to the quantification of plant effects on silicate weathering. *American Journal of Science*, 300(7), pp.539-570. https://doi.org/10.2475/ajs.300.7.539.

Négrel, P., Allègre, C.J., Dupré, B. and Lewin, E., 1993. Erosion sources determined by inversion of major and trace element ratios and strontium isotopic ratios in river water: the Congo Basin case. *Earth and Planetary Science Letters*, 120(1-2), pp.59-76. https://doi.org/10.1016/0012-821X(93)90023-3.

Parnell, A.C., Inger, R., Bearhop, S. and Jackson, A.L., 2010. Source partitioning using stable isotopes: Coping with too much variation. *PloS One*, 5(3), p.e9672. https://doi.org/10.1371/journal.pone.0009672.

Phillips, D.L. and Gregg, J.W., 2001. Uncertainty in source partitioning using stable isotopes. *Oecologia*, 127(2), pp.171-179. https://doi.org/10.1007/s004420000578.

Phillips, D.L. and Gregg, J.W., 2003. Source partitioning using stable isotopes: Coping with too many sources. *Oecologia*, 136(2), pp.261-269. https://doi.org/10.1007/s00442-003-1218-3.

Pisias, N.G., Murray, R.W. and Scudder, R.P., 2013. Multivariate statistical analysis and partitioning of sedimentary geochemical data sets: General principles and specific MATLAB scripts. *Geochemistry, Geophysics, Geosystems*, 14(10), pp.4015-4020. https://doi.org/10.1002/ggge.20247.

Polsenaere, P. and Abril, G., 2012. Modelling CO_2 degassing from small acidic rivers using water pCO_2, DIC and $\delta^{13}C$-DIC data. *Geochimica et Cosmochimica Acta*, 91, pp.220-239. https://doi.org/10.1016/j.gca.2012.05.030.

Qi, H.P., Taylor, P.D.P., Berglund, M. and De Bièvre, P., 1997. Calibrated measurements of the isotopic composition and atomic weight of the natural Li isotopic reference material IRMM-016. *International Journal of Mass Spectrometry and Ion Processes*, 171(1-3), pp.263-268. https://doi.org/10.1016/S0168-1176(97)00125-0.

Scheingross, J.S., Repasch, M.N., Hovius, N., Sachse, D., Lupker, M., Fuchs, M., Halevy, I., Gröcke, D.R., Golombek, N.Y., Haghipour, N. and Eglinton, T.I., 2021. The fate of fluvially-deposited organic carbon during transient floodplain storage. *Earth and Planetary Science Letters*, 561, p.116822. https://doi.org/10.1016/j.epsl.2021.116822.

Spence, J. and Telmer, K., 2005. The role of sulfur in chemical weathering and atmospheric CO_2 fluxes: Evidence from major ions, $\delta^{13}C_{DIC}$, and $\delta^{34}S_{SO4}$ in rivers of the Canadian Cordillera. *Geochimica et Cosmochimica Acta*, 69(23), pp.5441-5458. https://doi.org/10.1016/j.gca.2005.07.011.

Stallard, R.F. and Edmond, J.M., 1983. Geochemistry of the Amazon: 2. The influence of geology and weathering environment on the dissolved load. *Journal of Geophysical Research: Oceans*, 88(C14), pp.9671-9688. https://doi.org/10.1029/JC088iC14p09671.

Stefánsson, A. and Gíslason, S.R., 2001. Chemical weathering of basalts, Southwest Iceland: Effect of rock crystallinity and secondary minerals on chemical fluxes to the ocean. *American Journal of Science*, 301(6), pp.513-556. https://doi.org/10.2475/ajs.301.6.513.

Taylor, P.D.P., Maeck, R. and De Bièvre, P., 1992. Determination of the absolute isotopic composition and atomic weight of a reference sample of natural iron. *International Journal of Mass Spectrometry and Ion Processes*, 121(1-2), pp.111-125. https://doi.org/10.1016/0168-1176(92)80075-C.

Thorpe, M.T., Hurowitz, J.A. and Dehouck, E., 2019. Sediment geochemistry and mineralogy from a glacial terrain river system in southwest Iceland. *Geochimica et Cosmochimica Acta*, 263, pp.140-166. https://doi.org/10.1016/j.gca.2019.08.003.

Tipper, E.T., Bickle, M.J., Galy, A., West, A.J., Pomiès, C. and Chapman, H.J., 2006. The short term climatic sensitivity of carbonate and silicate weathering fluxes: Insight from seasonal variations in river chemistry. *Geochimica et Cosmochimica Acta*, 70(11), pp.2737-2754. https://doi.org/10.1016/j.gca.2006.03.005.

Torres, M.A., West, A.J. and Clark, K.E., 2015. Geomorphic regime modulates hydrologic control of chemical weathering in the Andes–Amazon. *Geochimica et Cosmochimica Acta*, 166, pp.105-128. https://doi.org/10.1016/j.gca.2015.06.007.

Torres, M.A., West, A.J., Clark, K.E., Paris, G., Bouchez, J., Ponton, C., Feakins, S.J., Galy, V. and Adkins, J.F., 2016. The acid and alkalinity budgets of weathering in the Andes–Amazon system: Insights into the erosional control of global biogeochemical cycles. *Earth and Planetary Science Letters*, 450, pp.381-391. https://doi.org/10.1016/j.epsl.2016.06.012.

Turowski, J.M., Hilton, R.G. and Sparkes, R., 2016. Decadal carbon discharge by a mountain stream is dominated by coarse organic matter. *Geology*, 44(1), pp.27-30. https://doi.org/10.1130/G37192.1.

Urey, H.C., 1952. On the early chemical history of the earth and the origin of life. *Proceedings of the National Academy of Sciences of the United States of America*, 38(4), p.351. https://doi.org/10.1073/pnas.38.4.351.

Valkiers, S., Ding, T., Inkret, M., Rußе, K. and Taylor, P., 2005. Silicon isotope amount ratios and molar masses for two silicon isotope reference materials: IRMM-018a and NBS28. *International Journal of Mass Spectrometry*, 242(2-3), pp.319-321. https://doi.org/10.1016/j.ijms.2004.11.027.

Vigier, N., Gislason, S.R., Burton, K.W., Millot, R. and Mokadem, F., 2009. The relationship between riverine lithium isotope composition and silicate weathering rates in Iceland. *Earth and Planetary Science Letters*, 287(3-4), pp.434-441. https://doi.org/10.1016/j.epsl.2009.08.026.

Walker, J.C., Hays, P.B. and Kasting, J.F., 1981. A negative feedback mechanism for the long-term stabilization of Earth's surface temperature. *Journal of Geophysical Research: Oceans*, 86(C10), pp.9776-9782. https://doi.org/10.1029/JC086iC10p09776.

West, A.J., Lin, C.W., Lin, T.C., Hilton, R.G., Liu, S.H., Chang, C.T., Lin, K.C., Galy, A., Sparkes, R.B. and Hovius, N., 2011. Mobilization and transport of coarse woody debris to the oceans triggered by an extreme tropical storm. *Limnology and oceanography*, 56(1), pp.77-85. https://doi.org/10.4319/lo.2011.56.1.0077.

Zeebe, R.E. and Wolf-Gladrow, D., 2001. CO_2 in seawater: Equilibrium, kinetics, isotopes (No. 65). Gulf Professional Publishing.

II.11: MEANDIR user guide

II.11.1: Introduction

This guide explains the organization and use of Mixing Elements ANd Dissolved Isotopes in Rivers (MEANDIR). The goal of this guide is to allow researchers to invert dissolved river chemistry with basic understanding and relative ease, rather than to provide an exhaustive report of the 40 MATLAB files and 4 excel worksheets comprising the model. This guide thus contains sections on required user inputs, inversion variables, and a brief model walk-though. File names are given in blue, variables names in green, and text values in purple. For those interested in deeper understanding, the model is commented and the header of each file provides a summary of its function. Lastly, feel free to contact Preston Cosslett Kemeny with any questions.

II.11.2: Required user inputs

MEANDIR requires four user inputs: a scenario name, observations of dissolved river chemistry, inversion end-members, and parameters for how to perform the inversion. MEANDIR defines these inputs in two MATLAB scripts (MEANDIR_Master, MEANDIR_FindScenarioParameters) and two excel spreadsheets (MyDefaultRiverDataSpreadsheet, MEANDIR_UserEntries). Note that the workbook MEANDIR_UserEntries contains three spreadsheets for defining end-members and conversion factors, but that only the end-members sheet will generally require modifications.

II.11.2.1: Scenario name

MEANDIR_Master is the master script of the model. The only required input in this script is the vector ScenarioList, which is defined near the top of MEANDIR_Master. The model will progress sequentially through entries of ScenarioList and treat each entry as a unique experiment with separate results. The default value of ScenarioList is MyDefaultScenario (line 24). If inverting only one dataset, we recommend starting with this default value. Upon download, MyDefaultScenario is configured to run a short inversion similar to scenario JG-2 (Tables II-5 and II-7).

II.11.2.2: Scenario parameters

Users set inversion variables in MEANDIR_FindScenarioParameters. The first part of this script is an *if* statement that searches for the current entry of ScenarioList. Once found, each of 44 variables is defined (see section 3 of this guide). The two parameters Riverdatasource and EMdatasource identify the river data and end-members for the inversion, respectively, and are always required. However, for most scenarios many of the other variables are optional. After defining variables, tests within MEANDIR_FindScenarioParameters attempt to identify common mistakes. Upon download, MEANDIR_FindScenarioParameters contains the full inversion information for all 28 scenarios reported in the main manuscript, plus an entry for MyDefaultScenario. Users can define new scenarios, such as MyDefaultScenario2, by expanding the primary *if* statement of MEANDIR_FindScenarioParameters.

II.11.2.3: River observations

Having found Riverdatasource in MEANDIR_FindScenarioParameters, MEANDIR_Master calls MEANDIR_ReadRiverDataIntoMatlab to match Riverdatasource with instructions on reading the dissolved chemical observations from an excel spreadsheet. The default Riverdatasource is MyDefaultRiverData, which imports MyDefaultRiverDataSpreadsheet using MEANDIR_StandardInput. Upon download, MyDefaultRiverDataSpreadsheet contains the observations from Gaillardet et al. (1999). If inverting a single dataset, simply populate MyDefaultRiverDataSpreadsheet with new data and leave ScenarioList = {'MyDefaultScenario'} and Riverdatasource = 'MyDefaultRiverData'. Note that the error of dissolved chemistry should be given as 1σ absolute errors in the data spreadsheet. Missing data can be left blank for individual samples, but a given sample will only be inverted if all variables for the inversion have values in the spreadsheet. For inputting multiple sets of data, the simplest way to enter the second set of observations into MEANDIR is to copy the spreadsheet MyDefaultRiverDataSpreadsheet, save it under a new name such as MyDefaultRiverDataSpreadsheet2, and put the second set of data in the relevant columns. Then, add a new section to the *if* loop of MEANDIR_ReadRiverDataIntoMatlab to evaluate whether or not Riverdatasource is equal to a new value, such as MyDefaultRiverData2. Within the new portion of the loop, copy code from the existing section but give the name MyDefaultRiverDataSpreadsheet2 to xlsread. The river observations are read into the structure variable river within the field observations. MEANDIR_ReadRiverDataIntoMatlab also converts concentrations into charge equivalents using conversion factors from the sheet MEANDIR_conc2equi within MEANDIR_UserEntries, as indicated in the names of the variables Ex. river.observations.Ca_conc and river.observations.Ca_equi give sample Ca^{2+} in μM and equivalents, respectively.

II.11.2.4: End-member chemical distributions

The MEANDIR_Endmembers sheet of the excel workbook MEANDIR_UserEntries defines the elemental and isotopic compositions of end-members. End-members are organized within groups, identified in column A, and the group name should match EMdatasource. Column B identifies the distribution of end-member chemistry (normal, uniform, log-uniform), column C is the active variable, column D is the desired normalization (almost always Na or SumObs), and column E is the type of entry (mean, minimum, etc.). The workbook then constructs a name for the variable in column F. If an entry of F says False, that end-member distribution will not be read correctly into MEANDIR. All columns after F correspond to end-members. The first row gives a long name of each end-member and the second row is an abbreviated name used to identify each end-member in the inversion. Additional end-members are added simply by populating new columns of the spreadsheet. Note that using $\chi^{riv}_{Cl^-\ critical}$ values requires defining a prec end-member and combining FeS_2 oxidation with rock weathering requires defining a pyri end-member. To define an end-member distribution relative to individual samples, enter sample#X. For example, when an end-member should equal the sample measurement, enter sample#0. To define an end-member as fractionated relative to the inputs from other end-members, the entry should say frac#X where X is the desired fractionation factor Δ (Eqs. II-29 to II-32). For example, when an end-member should equal the inputs from all

other end-members, enter frac#0 to represent no fractionation. Entering the code EM = MEANDIR_ReadEndMembersIntoMatlab reads the end-members into the structure EM; for example, EM.AB18_JG99_Na_normal.carb.NOR_MenCaNa would return the mean Ca^{2+}/Na^{+} ratio of the carbonate end-member in the end-member group AB18_JG99_Na_normal. If a new end-member does not appear in EM, check that the first and second rows of the spreadsheet contain names without special characters. If the chemistry of the end-members is missing, confirm that the variable names in column F of MEANDIR_Endmembers match expectations. After the scenario is complete, the relevant entries of EM are also saved within the EndMembers field of river.

II.11.2.5: Model results

The output structure river contains information on model inputs, the full distributions of end-member fractional contributions, inversion-constrained elemental and isotopic end-member ratios, and weathering variables. Much of the results are condensed into metrics such as the median and $5^{th}/25^{th}/75^{th}/95^{th}$ percentiles, although raw inversion results are also available within most subfields. Some of the following fields are saved for each scenario:

- settings: User-selected inversion parameters
- info: Some variables (name, latitude, etc.) and overview of results
- observations: User-reported river data (information from the spreadsheet)
- model_variable: Data used in the scenario (in same units as EMUnits)
- RiverMatrix: Matrix of river observation ratios
- InvertedRiverValues: Data used in simulations (model_variable if AdjustRiverObs = 0)
- fractionation: Fractionation factors used in the simulations
- inversionmatrix: End-member matrices used in the simulations
- reconstructed: Simulation-constructed sample chemistry
- fraction: Fractional contributions from each end-member to each variable
- misfit: Simulation misfits, both cost function and model-observation
- massbalance: Sum of fractional contributions from end-members
- EndMembers: Inversion-constrained composition of each end-member
- RZCWY: Calculated values of R, Z, Y, W, and C for each sample
- calculated_other_d34S: Calculated $\delta^{34}S$ of the other and/or FeS_2 end-member
- ExcessSO4: The fractional and absolute amount of excess SO_4^{2-}

II.11.3: Model variables

MEANDIR_FindScenarioParameters defines 44 variables divided among 5 groups: (1) river observations, (2) general settings, (3) end-member variables, (4) Cl^- correction, and (5) calculating R, Z, Y, W, and C. Below, we briefly describe each of these variables.

II.11.3.1: River observations and normalization

(1) Riverdatasource: Keyword identifying the source of river data to be inverted. Input as a string. Ex. Riverdatasource = 'JG99RiverData' could correspond to Gaillardet et al. (1999). As described above, the default for the 'MyDefaultScenario' scenario is that Riverdatasource = 'MyDefaultRiverData'.

(2) AdjustRiverObs: Whether or not river measurements should be adjusted to reflect analytical uncertainty. Can be either 0 or 1. If 1, on each simulation river chemistry is drawn from a normal distribution with the mean and standard deviation defined in the data spreadsheet. That is, river dissolved load is modified to reflect user-given analytical error. Ex. AdjustRiverObs = 1.

(3) ObsList: Variables included in the mixing model. Inputs given as strings within a cell. Ex. ObsList = {'Na','Cl','Ca','Mg','K','SO4', 'd34S'} would include observations of $\chi^{riv}_{Na^+}$, $\chi^{riv}_{Cl^-}$, $\chi^{riv}_{Ca^{2+}}$, $\chi^{riv}_{Mg^{2+}}$, $\chi^{riv}_{K^+}$, $\chi^{riv}_{SO_4^{2-}}$, and ${}^{34}R^{riv}_{SO_4^{2-}}$ in the inversion. Altering the entries of ObsList modifies the variables included in the inversion. MEANDIR can identify the following dissolved observations: ALK, DIC, Ca, Mg, Na, K, Sr, Cl, SO4, NO3, PO4, Si, Ge, Li, F, B, Re, Mo, Os, HCO3, d7Li, d13C, d18O, d26Mg, d30Si, d34S, d42Ca, d44Ca, Sr8786, d98Mo, Os8788, and Fmod. Additional observations can be added to MEANDIR or use the place of an otherwise unused variable.

(4) CostFunType: Whether or not each variable in ObsList should be evaluated with a relative cost function or absolute cost function. Options are rel and abs. Ex. CostFunType ={'rel','rel','rel','rel'} would use a relative cost function for the four observations in ObsList. CostFunType serves the purpose of the vector $\boldsymbol{\omega}$ in Eq. II-18.

(5) WeightingList: Weighting terms for cost function. Ex. WeightingList = [1 1 1 1] would multiply the misfit between model results and observations for each of four observations in ObsList by 1. WeightingList serves the purpose of the vector $\boldsymbol{\Upsilon}$ in Eqs. II-16, II-17, and II-18.

(6) ErrorCutMinMB: When IterateOver equals Samples, ErrorCutMinMB sets the minimum fraction of concentration observations, or the maximum allowable negative offset for isotopic observations, for a simulation to count as successful. Ex. ErrorCutMinMB = [85 85 85 -2] when ObsList = {'Na','Cl','SO4', 'd34S'} defines the success criteria as simulations where >85% of $\chi^{riv}_{Na^+}$, $\chi^{riv}_{Cl^-}$, and $\chi^{riv}_{SO_4^{-2}}$ are recreated and where the model-constructed $\delta^{34}S$ value is >2‰ lower than the measurement. This vector thus sets the lower boundary of sample matching criteria. When IterateOver equals End-members, all values of ErrorCutMinMB are set equal to $-1x10^{10}$.

(7) ErrorCutMaxMB: When IterateOver equals Samples, ErrorCutMaxMB sets the maximum fraction of concentration observations, or the maximum allowable positive offset for isotopic observations, for a simulation to count as successful. Ex. ErrorCutMaxMB = [115 115 115 3] when ObsList = {'Na','Cl','SO4', 'd34S'} defines the success criteria as simulations where <115% of $\chi^{riv}_{Na^+}$, $\chi^{riv}_{Cl^-}$, and $\chi^{riv}_{SO_4^{-2}}$ are recreated and where the model-constructed $\delta^{34}S$ value is <3‰ higher than the measurement. This vector thus sets the upper boundary of sample matching criteria. When IterateOver equals End-members, all values of ErrorCutMinMB are set equal to $1x10^{10}$.

(8) nCFList: Variables in ObsList that should not be included in the cost function but should be reconstructed by the model. Ex. nCFList = {'HCO3'}. nCFList serves the purpose

of the vector ξ in Eq. II-18, and its role is demonstrated in the comparison of AB-2 and AB-3 (Fig. II-6D). nCFList will often be empty.

(9) ConvertDelta2RList: Isotopic variables in δ notation to be converted into isotopic ratios for inversion, typically to allow meaningful evaluation with a proportional cost function. Inversion results are converted back to δ notation for ease of interpretation. Ex. ConvertDelta2RList = {'d34S'} would convert $\delta^{34}S$ values to $^{34}S/^{32}S$ ratios prior to inversion. Values to convert from δ notation to ratios are in MEANDIR_DeltaNotationToR within MEANDIR_UserEntries.

(10) AllIonsExplicitlyResolved: Indicates if all major cations and anions are included in ObsList. Values are 1 or 0. If 1, ListChargeClosure ensures that the sum of normalized positive charge equals the sum of normalized negative charge. Ex. AllIonsExplicitlyResolved = 1.

(11) ObsInNormalization: Variables in the normalization. Entries can include cations, anions, and neutral species. Ex. ObsInNormalization = {'Ca','Mg','Na'}. To ensure internal consistency of end-members, one ratio contributing to the normalization variable is solved using other entries.

(12) ImposeNormalizationCheck: Whether to impose a constraint that the sum of fractional contributions to the normalization variable must be between the lowest non-isotopic value of ErrorCutMinMB and highest non-isotopic value of ErrorCutMaxMB. Values are 0 or 1. Ex. ImposeNormalizationCheck = 1.

II.11.3.2: Simulation settings

(13) Solver: The numerical technique used to invert each simulation. Options are: mldivide, lsqnonneg, mldivide_optimize, lsqnonneg_optimize, and optimize. The choice mldivide refers to standard least squares inversion and lsqnonneg is a non-negative least squares inversion, both of which optimize absolute cost functions. When followed by _optimize, the solver is a constrained optimization using the first solver's result as the initial condition. Depending on the values of CostFunType, mldivide_optimize, lsqnonneg_optimize, and optimize can optimize for either absolute or proportional misfit. If Solver equals optimize the model uses an initial condition of equal fractional contributions from each of the end-members. Input as a string. Ex. Solver = 'mldivide_optimize'. See Fig. II-4 for comparison of the different solvers.

(14) IterateOver: Options are Samples and End-members. If equal to Samples, each sample is treated fully independently. If End-members, all samples are inverted using the same end-members. MEANDIR supports parallel processing at two mutually exclusive locations within MEANDIR_Master. The first location is a loop from 1 to the number of iterations (lines 176 and 177 of MEANDIR_Master). When IterateOver equals End-members, the code will run faster when this loop is set to be *parfor*. The second location is a loop from 1 to the number of samples (lines 215 and 216 of MEANDIR_Master). When IterateOver equals Samples, the code will run faster when this second loop is set to *parfor*. Moreover,

when IterateOver equals Samples, the code will generate a transparency error if the first loop is *parfor* and the second loop is *for*. Input as a string. Ex. IterateOver = 'End-members'.

(15) maxiterations: When IterateOver equals Samples, this is maximum number of simulations attempted per sample. Define as a number. Ex. maxiterations = 10000. If IterateOver equals End-members, MEANDIR sets maxiterations to equal 1.

(16) maxsuccess: When IterateOver equals Samples, this is the desired number of successful simulations for each sample. MEANDIR stops testing each sample when this number of successful simulations is found or the maximum number of simulations is reached. Input as number. Ex. maxsuccess = 500. If IterateOver equals End-members, MEANDIR sets maxsuccess to equal 1.

(17) numberiterations: When IterateOver equals End-members, numberiterations is the number of iterations to be performed. Because this number of simulations will be stored and later subsampled, large values can cause MEANDIR to run slowly. Input as a number. Ex. numberiterations = 10000. If IterateOver equals Samples, MEANDIR sets numberiterations to equal 1.

(18) MisfitCuts: When IterateOver equals End-members, this fraction of samples with lowest misfit will be kept (in units of %). Input as a number. Ex. MisfitCuts = 1 keeps the 1% of simulations with lowest misfit between models results and observations. MisfitCuts = 100 will keep all results. If IterateOver equals Samples, MEANDIR sets MisfitCuts to equal NaN.

(19) CullOn: When IterateOver equals End-members, this is whether inversion results should be cut to the lowest MisfitCuts fraction based on misfit at the level of each individual samples or the entire sample set. Values are EachSample or AllSample. Input as string. Ex. CullOn = 'AllSample'.

(20) saveuncutdata: When IterateOver equals End-members, this variable controls if all results are saved (in addition to the fraction defined by MisfitCuts) in a different subfield. Value is 0 or 1. Ex. saveuncutdata = 0. This is useful for evaluating the impact of culling the model results, but can result in very large files.

II.11.3.3: End-member variables

(21) EMdatasource: Identifies the end-member group (column A of MEANDIR_Endmembers in MEANDIR_UserEntries). Input as string. Ex. EMdatasource = 'AB18_JG99_SumObs_normal'.

(22) EMList0: End-members to be included in the inversion. Each end-member is identified using the code from row 2 of the MEANDIR_Endmembers spreadsheet. Input as strings within a cell. Ex. EMList0 = {'prec','carb','dolo','slct','biot','clay'} will include six end-members in the inversion.

(23) MinFractionalContribution: For constrained optimization, this is the list of minimum fractional contributions from each end-member to the normalization, corresponding to entries of EMList0. Ex. MinFractionalContribution = [0 0 0 -inf] constrains optimization to have a minimum contribution of 0 from each of the first three end-members and no minimum from the fourth (contributions outside the range of 0 to 1 may be required when modeling secondary phase formation).

(24) MaxFractionalContribution: For constrained optimization, the list of maximum fractional contributions from each end-member to the normalization, corresponding to entries of EMList0. Ex. MaxFractionalContribution = [inf inf inf 0] constrains optimization to have no maximum contribution from the first three end-member and a maximum contribution of 0 from the last entry.

(25) ListNormClosure: When normalizing to the sum of variables, define the variable for each end-member that will be calculated by mass balance to ensure internal consistency. This variable will often be the most abundant cation for that end-member. Inputs given as strings corresponding to each entry of EMList0. Ex. ListNormClosure = {'Na','Ca','Cl','Ca'}.

(26) ListChargeClosure: When AllIonsExplicitlyResolved equals 1, this vector lists the variable for each end-member solved through charge balance. Often, this is the anion at highest abundance. Inputs as strings corresponding to EMList0 entries. Ex. ListChargeClosure ={'Cl','SO4','HCO3'}.

(27) EMUnits: Whether end-member chemistry is given as concentration ratios or charge-equivalent ratios. Must be conc or equi. Input given as string. Ex. EMUnits = 'equi'.

(28) EMsources: End-members that count as sources of dissolved variables. Without secondary phases, EMsources is typically equal to EMList0. Ex. EMsources = {'prec','bslt', 'carb','htsp'}.

(29) EMsinks: End-members that count as sinks of dissolved variables, such as clays and other secondary phases. EMsinks is often empty or only contains one entry. Ex. EMsinks = {'clay'}.

(30) EndMembersWithNegativeRatios: List of end-members where chemical ratios may be negative. Be careful to account for these selections relative to MinFractionalContribution and MinFractionalContribution. Ex. EndMembersWithNegativeRatios = {'pyri'}.

(31) CoupleFeS2SO4intoEM: List of end-members where SO_4^{2-} values are overwritten by the pyri end-member. Input given as strings in a cell. Ex. CoupleFeS2SO4intoEM = {'carb','slct'}. Note that end-member SO_4^{2-} values are overwritten by the distribution of FeS2SO4 values in end-member pyri.

(32) CoupleFeS2d34SintoEM: List of end-members where SO_4^{2-} $\delta^{34}S$ values are overwritten by the pyri end-member. Input given as strings in a cell. Ex. CoupleFeS2d34SintoEM = {'carb', 'slct'}. Note that end-member SO_4^{2-} δ^{34} values are overwritten by the distribution of FeS2d34S values in end-member pyri.

(33) RecordFullFeS2Distribution: Whether or not to record the full distributions of calculated other $\delta^{34}S$ and FeS_2 $\delta^{34}S$ when $\delta^{34}S$ is not in the inversion. Either 0 or 1. Ex. RecordFullFeS2Distribution = 0. Recording the full distribution will result in larger file sizes.

(34) BalanceEvaporite: Whether or not evaporite $SO_4^{2-} = Ca^{2+} + Mg^{2+} + Sr^{2+}$ and evaporite $Cl^- = Na^+ + K^+$. Either 0 or 1. Ex. BalanceEvaporite = 1.

II.11.3.4: Cl^- and precipitation

(35) PrecProcessing: Whether to use values of $\chi^{riv}_{Cl^-\,critical}$. Options are ClCrit or EndMember. If ClCrit, $\chi^{riv}_{Cl^-\,critical}$ are subtracted from $\chi^{riv}_{Cl^-}$ and other measurements are corrected by precipitation ratios. If PrecProcessing equals EndMember, no special correction is made. Only used if prec is included in EMList0. Input is given as a string. Ex. PrecProcessing = 'ClCrit'.

(36) ClCriticalValuesGiven: Indicates whether or not $\chi^{riv}_{Cl^-\,critical}$ values are provided. Only used if prec is included in EMList0. Must be either 0 or 1. If $\chi^{riv}_{Cl^-\,critical}$ values are known, this value should be 1. If PrecProcessing is ClCrit but ClCriticalValuesGiven equals 0, 100% of river Cl^- will be subtracted (MEANDIR will assume that $\chi^{riv}_{Cl^-\,critical} = \chi^{riv}_{Cl^-}$). Ex. ClCriticalValuesGiven = 0.

II.11.3.5: Weathering parameters

(37) CalculateRZCWY: Whether or not MEANDIR should calculate R, Z, C, W, and Y. Options are: 0 or 1. Ex. CalculateRZCWY = 1 will attempt the calculations.

(38) R_Numerator_EMList: End-members that contribute to the numerator of R (carbonate end-members). Inputs given as strings in a cell. Ex. R_Numerator_EMList = {'carb','dolo'}.

(39) R_Numerator_IonList: Ions that contribute to the numerator of R. Inputs given as strings contained within a cell. Ex. R_Numerator_IonList = {'Na','Ca','Mg'}.

(40) Z_NumeratorType: How the numerator of Z is calculated. Values are ZfromSO4excess, ZfromriverSO4, ZfromEM, or Znotcalculated. If ZfromSO4excess, the Z numerator is SO_4^{2-} in the river sample not attributable to end-members. If ZfromriverSO4, the Z numerator is SO_4^{2-} in the river. If ZfromEM, the Z numerator is SO_4^{2-} derived from end-members listed in Z_Numerator_EMList. If Znotcalculated, Z is not calculated. Ex. Z_NumeratorType = {'ZfromEM'}.

(41) Z_Numerator_EMList: End-members that contribute to the numerator of Z. Use if Z_NumeratorType is ZfromEM. Input given as strings contained within a cell. Ex. Z_Numerator_EMList = {'carb', 'slct'} or Z_Numerator_EMList = {'pyri'.}

(42) C_Numerator_EMList: End-members that contribute to the numerator of C (organic carbon end-members). Inputs given as strings in a cell. Ex. C_Numerator_EMList = {'corg'}.

(43) RZC_Denominator_EMList: End-members that contribute to the denominator of R, Z, and C (all weathering end-members). Ex. RZC_Denominator_EMList = {'carb','dolo','slct','biot'}.

(44) RZC_Denominator_IonList: Ions that contribute to the denominator of R, Z, and C. Ex. RZC_Denominator_IonList = {'Na','Ca','Mg','K'}. Our opinion is that this vector should contain all inverted cations, but there is debate in the literature on whether or not Na^+ and K^+ should be included.

II.11.4: Model walk-through

MEANDIR defines inversion parameters in MEANDIR_FindScenarioParameters, uses MEANDIR_ReadEndMembersIntoMatlab to identify inversion end-members, and calls on MEANDIR_ReadRiverDataIntoMatlab to find river data. These steps, which entail most of the user involvement in the inversion, were our focus in the preceding text. We now briefly summarize the remainder of MEANDIR_Master.

II.11.4.1: Define the river water matrix

MEANDIR_GenerateRiverMatrix generates the matrix RiverMatrix0 containing normalized river observations. The rows of RiverMatrix0 correspond to the normalized elemental or isotopic ratios and columns correspond to samples.

II.11.4.2: Define the end-member distributions

MEANDIR_makeEMdistributions generates an array of probability distributions for end-member chemistry, as well as multiple additional arrays encoding information on which end-members are defined relative to samples and which end-members are defined through fractionation relative to the inputs from other end-members.

II.11.4.3: Initiate primary model loop

MEANDIR then initiates a loop to either iterate over samples or over end-member values. MEANDIR supports parallel processing at two locations: lines 176/177, and lines 215/216.

II.11.4.4: Adjust observations accounting for analytical error

If AdjustRiverObs equals 1, MEANDIR_AdjustRiverDataForAnalyticalError modifies observations of river chemistry and recalculates the normalization. In this case river observations are pulled from normal distributions with user-supplied means and standard deviations, the latter of which should be given in the data spreadsheets as 1σ

absolute errors. MEANDIR_AdjustRiverDataForAnalyticalError is called but does not alter the river observations if AdjustRiverObs equals 0.

II.11.4.5: Calculate end-members

MEANDIR_PullEndMemberRatios calculates an internally consistent set of end-member values. MEANDIR_PullEndMemberRatios will attempt to generate a viable set of end-members up to maxtrycount times per function call (default value is 500).

II.11.4.6: Correct river data for precipitation

If PrecProcessing is ClCrit and EMList0 contains prec, MEANDIR_ClCriticalCorrection adjusts river observations for inputs from precipitation using values of $\chi^{riv}_{Cl^-\ critical}$. If the removal of the specified amount of Cl^- would cause another element to become negative, the end-member matrix is regenerated up to maxredefinition times per simulation (default value is 100).

II.11.4.7: Perform river inversion

MEANDIR_InvertActiveSimulation sets the initial conditions of optimization and defines MEANDIR_CostFunction as an optimization problem for fmincon.

II.11.4.8: Evaluate inversion results

MEANDIR_EvaluateInversionInstance evaluates if the simulation generated results that meet user-supplied criteria for success. If IterateOver equals Samples, results are only saved if they satisfy the values defined in ErrorCutMinMB and ErrorCutMaxMB. If IterateOver equals End-Members, nearly all simulations are saved at this step.

II.11.4.9: Unpack results

Following the inversion, MEANDIR_UnpackInversionResults aggregates the inversion results for subsequent calculations.

II.11.4.10: Cull results

If IterateOver equals End-Members, MEANDIR_CalculateCullDatabyMisfit isolates the fraction of simulations with lowest misfit as set by MisfitCuts.

II.11.4.11: Calculations and saving

MEANDIR calculates and saves variables of interest into subfields of the variable river. Relevant programs include MEANDIR_CalculateMassBalance, MEANDIR_SaveFractionalContributions, MEANDIR_SaveInvertedRiverValues, MEANDIR_SaveFractionations, MEANDIR_CalculateReconstructedObservations, MEANDIR_CalculateExcessSO4, MEANDIR_CalculateOther_d34S, MEANDIR_CalculateEndMemberValues, and MEANDIR_CalculateRZCWY.

Chapter III

Organic Sulfur Fluxes and Geomorphic Control of Sulfur Isotope Ratios in Rivers

Preston Cosslett Kemeny[1], Mark A. Torres[2], Michael P. Lamb[1], Samuel M. Webb[3], Nathan F. Dalleska[1], Trevor Cole[2], Yi Hou[2], Jared Marske[1], Jess F. Adkins[1], Woodward W. Fischer[1]

[1] Division of Geological and Planetary Sciences, California Institute of Technology, Pasadena, CA, USA
[2] Department of Earth, Environmental, and Planetary Sciences, Rice University, Houston, TX, USA
[3] Stanford Synchrotron Radiation Lightsource, SLAC National Accelerator Laboratory, Menlo Park, CA, USA

Highlights:

- Sulfur cycle observations from Iceland with a focus on the Efri Haukadalsá catchment
- Dissolved $\delta^{34}S_{SO4}$ and Cl^-/SO_4^{2-} indicated mixing of basalt and precipitation
- Pyrite oxidation was focused in V-shaped, fluvially incising tributaries
- XANES identified varied organic sulfur moieties from floodplain sulfur cycling
- Organic sulfur flux was < 10% dissolved SO_4^{2-} flux, had minimal impact on $\delta^{34}S_{SO4}$

Keywords: Chemical weathering, pyrite oxidation, sulfur isotopes, XANES, Iceland

Kemeny, P.C., Torres, M.A., Lamb, M.P., Webb, S.M., Dalleska, N., Cole, T., Hou, Y., Marske, J., Adkins, J.F. and Fischer, W.W., 2021. Organic sulfur fluxes and geomorphic control of sulfur isotope ratios in rivers. *Earth and Planetary Science Letters*, 562, p.116838. https://doi.org/10.1016/j.epsl.2021.116838.

III.1: Abstract

Pyrite oxidation plays a critical role in the relationship between weathering and climate, and its impact on the global carbon cycle has previously been constrained through inversion models utilizing observations of river sulfate (SO_4^{2-}) and its $^{34}S/^{32}S$ isotope ratio ($\delta^{34}S_{SO4}$). However, measurements from some rivers have suggested that $\delta^{34}S_{SO4}$ can be substantially impacted by processes such as microbial sulfate reduction and/or sulfur assimilation and cycling, rather than simply reflecting a weighted mixture of lithologic sulfur sources. To study the prevalence and controls on SO_4^{2-} transformations, we measured dissolved major element concentrations and $\delta^{34}S_{SO4}$ in river water samples from throughout western Iceland. Our analyses focused on samples from a small catchment hosting the Efri Haukadalsá river, a system with relatively uniform and isotopically constrained basaltic bedrock. We also measured sediment $\delta^{34}S$ and sulfur speciation using sulfur K-edge X-ray absorption spectroscopy on sediment and vegetation samples from this catchment. Values of dissolved $\delta^{34}S_{SO4}$ in the Efri Haukadalsá ranged from 2.5‰ to 23.7‰ and had a linear relationship with Cl^-/SO_4^{2-} ratios, indicating that SO_4^{2-} predominantly derived from basalt weathering and meteoric precipitation. The lower $\delta^{34}S_{SO4}$ values were found in fluvial valleys with V-shaped cross sections, while higher values of $\delta^{34}S_{SO4}$ occurred in U-shaped, glacially eroded valleys with thick alluvial fills blanketing the valley floor. Spectroscopic observations identified organic sulfur phases in suspended river sediment, floodplain deposits, and vegetation. Mass balance calculations quantified the organic sulfur flux as less than 10% of SO_4^{2-} export, and sediment $\delta^{34}S$ values were comparable to river $\delta^{34}S_{SO4}$. We interpreted these isotopic and chemical patterns as reflecting differences in the availability of unweathered bedrock across the Efri Haukadalsá catchment, with V-shaped valleys having greater access to fresh sulfide-bearing minerals than alluviated U-shaped valleys; this interpretation is in contrast to one in which the elevated $\delta^{34}S_{SO4}$ values reflect fractionation during sulfur transformations along alluvial reaches. These results validated the application of river inversion models for constraining weathering fluxes and affirmed that pyrite oxidation globally, even in the presence of river sulfur cycling, modulates the abundance of atmospheric carbon dioxide.

III.2: Introduction

Chemical weathering regulates the concentration of atmospheric carbon dioxide (CO_2) by sourcing alkalinity and dissolved inorganic carbon into the coupled ocean-atmosphere system (Walker et al. 1981). While weathering of silicate minerals was previously thought to largely control atmospheric CO_2 over geologic timescale, studies have now also demonstrated that ubiquitous oxidation of pyrite (FeS_2) to sulfuric acid removes alkalinity from the ocean-atmosphere system and partially compensates for CO_2 drawdown associated with silicate weathering (Calmels et al., 2007; Torres et al., 2014, 2016; Burke et al., 2018; Kemeny et al., 2021). Quantifying the climatic and lithologic controls of FeS_2 oxidation during weathering have thus emerged as important questions in study of the global carbon, sulfur, and alkalinity cycles.

Quantifying the role of FeS_2 oxidation during weathering requires apportioning measurements of river sulfate (SO_4^{2-}) between multiple sources such as meteoric precipitation, evaporite dissolution, and hydrothermal fluids (Gaillardet et al., 1999; Burke et al., 2018). This attribution often relies on inversion models that assume dissolved river chemistry reflects conservative mixing of a limited number of end-members with constrained elemental and isotopic compositions. However, researchers have suggested that microbial sulfate reduction (MSR) and SO_4^{2-} assimilation may alter the abundance and/or $^{34}S/^{32}S$ isotope ratio of fluvial SO_4^{2-} ($\delta^{34}S_{SO4}$) during transport (Fig. III-1). Evidence of MSR impacting $\delta^{34}S_{SO4}$ comes from the Marsyandi River in the Nepal Himalaya, where researchers found coherent relationships among the concentration of sulfate ($[SO_4^{2-}]$), the value of $\delta^{34}S_{SO4}$, and the major and minor oxygen isotope ratios of SO_4^{2-} (Turchyn et al., 2013; Hemingway et al., 2020). More broadly, sulfur is an important nutrient for the

terrestrial biosphere (Kertesz and Mirleau, 2004) and sulfur cycling associated with plant uptake and growth or the recycling of plant-derived biomass within soils and the rhizosphere might engender small but meaningful isotopic fractionations (Trust and Fry, 1992; Tcherkez and Tea, 2013). If biological transformations lead to substantial changes in $\delta^{34}S_{SO4}$ then $^{34}S/^{32}S$ isotope ratios may not faithfully record weathering processes, affecting estimates of FeS_2 oxidation.

Microbial sulfate reduction is expected to increase residual river $\delta^{34}S_{SO4}$ to values above the primary lithologic sources of sulfur. Were such a process widespread, this increase would force river inversion models to calculate larger contributions from high-$\delta^{34}S$ end-members such as evaporites and meteoric precipitation, with the effect of underestimating the importance of terrestrial FeS_2 oxidation. Moreover, measurements of river $\delta^{34}S_{SO4}$ form an important boundary condition for global isotope mass balance models involving the sulfur cycle and its connections to carbon cycling and atmospheric dioxygen (Kump and Garrels, 1986). If values of river $\delta^{34}S_{SO4}$ are elevated due to microbial activity these models may be systematically biased towards reconstructing lower fractions of FeS_2 burial across geologic time.

Evaluating the importance of in-catchment sulfur cycling requires quantifying the relative export and storage of organic and inorganic sulfur. Export of inorganic sulfur as species other than SO_4^{2-}, such as detrital minerals or gaseous H_2S, is unexpected in oxygenated surface environments based on both theoretical calculations of mineral oxidation kinetics (Johnson et al., 2014) and direct observations of atmospheric gases (Andreae et al. 1990). The greater stability of organosulfur species (Xia et al., 1998) suggests that particulate and dissolved organic phases may provide a reduced sulfur flux,

yet direct observations are currently lacking. Identifying sulfur transformations from existing dissolved data is complicated by the presence of multiple weathering lithologies in most catchments, each of which may carry a variable range of $\delta^{34}S$ values (Calmels et al., 2007; Kemeny et al., 2021).

In this work, we studied weathering, sediment transport, and sulfur cycling in river catchments of western Iceland. Due to the catchments' relatively uniform basaltic bedrock lithology, fluvial sulfur transformations were expected to be easier to diagnose than in catchments containing diverse lithologies. Our approach was further bolstered by previous work on the $^{34}S/^{32}S$ isotope ratio of Icelandic rocks (Sakai et al., 1980; Torssander, 1989; Hildebrand and Torssander, 1998; Stefánsson et al., 2015) and prior measurements of $\delta^{34}S_{SO4}$ in Icelandic rivers (Gislason and Torssander 2006, Robinson et al. 2009).

III.3: Methods

III.3.1: Field sites

River water and sediment samples were collected from the Efri Haukadalsá river catchment and surrounding region during two field campaigns in August 2016 and July-August 2019 (Figs. III-2, III-S1, III-S2, and III-S3 for drone imagery and field photographs; III.11.1). Carbon analyses from the 2016 field season, including ^{14}C dates, $\delta^{13}C$ measurements, and estimates of the amount of alluvial fill in the catchment, were previously reported in Torres et al. (2020).

The Efri Haukadalsá is a meandering river constructing a prograding delta as it drains into lake Haukadalsvatn (Fig. III-2C). A sediment core from Haukadalsvatn containing glacial dropstones and marine mollusk shells below finely laminated lacustrine sediment indicated that the catchment deglaciated ~13 ka and was only briefly marine before reflecting the deposits from the active fluvial-deltaic-lacustrine source-to-sink system (Geirsdóttir et al., 2009). The 170 km^2 Efri Haukadalsá catchment does not currently contain glaciers. The catchment lies within late Miocene (5.3-11 Ma) basaltic and intermediate extrusive rocks, although a small exposure of silicic rock is reported in the headwaters of tributary 3 (Fig. III-2; Hjartarson and Sæmundsson, 2014). The Efri Haukadalsá catchment is far from Iceland's primary hydrothermal axis and current volcanic or hydrothermal inputs are expected to be negligible; no visual indicators of hydrothermal activity were observed. The presence of calcite and zeolites in vugs suggests that some basalt beds may have previously been hydrothermally altered, although such features could also have formed through groundwater influences. Porosity is largely sealed in this region due to secondary mineralization, causing surface runoff to dominate over

groundwater flow (Gislason et al., 1996). Vegetation in the catchment is currently dominated by grasses and sedges, but site names indicate that the region was previously forested (Geirsdóttir et al., 2009).

The Efri Haukadalsá is alluvial for much of its length, but with bedrock exposures in some tributaries, and is mostly gravel-bedded, but with a transition to sand-bedding near Haukadalsvatn (Torres et al., 2020). The lower section of the mainstem Efri Haukadalsá has a U-shaped cross section and the channel is alluvial in this lower valley, meandering across a floodplain approximately 600-800 m wide (Fig. III-2C). This channel and floodplain material are part of a relatively thick alluvial fill that is likely the result of fluvial and lacustrine deposition following deglaciation (Geirsdóttir et al., 2009; Torres et al., 2020). Several steep tributaries branch from the lower section of the Efri Haukadalsá mainstem. Tributaries 1 and 2 enter the mainstem near Lake Haukadalsvatn and upstream of the lower reach, respectively (Figs. III-2C and III-S1). A major split in the Efri Haukadalsá occurs about halfway upstream, after which both branches curve in parallel toward the southeast. The lower branch of the split, tributary 3, is a hanging valley off the mainstem, separated by a steep knickzone. On the basis of dissolved chemistry, we calculated that tributary 3 supplied 26±7% (2σ) of the water flow downstream of the confluence. Tributaries 1, 2, and 3 tended to have only a thin cover of sediment, typical of bedrock rivers, and lacked the thick alluvial fill of the lower mainstem valley. In the upper branch of the split, there is a moraine along tributary 5 (Fig. III-2C, pink outline). Two bedrock knickpoints occur in the Efri Haukadalsá mainstem, the first near the confluence with tributary 3 and the second near the site of sediment input from the moraine. Emergent springs with conspicuous iron oxide deposits were identified throughout the catchment,

which we refer to as “Fe springs” (Fig. III-S2F). River water samples were classified on the basis of either location (mainstem, tributary, lake), notable geomorphologic features (draining the moraine), or visual indicators of chemistry (Fe springs).

Thirty-two additional water samples from outside of the Efri Haukadalsá catchment were collected during the 2016 field campaign (Fig. III-2B) which we refer to as “NW rivers,” and seven additional water samples from five sites along the Hvítá river and its tributaries were sampled from a catchment draining the Langjökull and Eiríksjökull glaciers during the 2019 field season (Fig. III-2D). The former sampling sites were more coastal than the Efri Haukadalsá and included catchments with increased exposures of felsic lithologies (Gislason et al., 1996; Hjartarson and Sæmundsson, 2014); this shift in underlying lithology is expected to impact dissolved ion concentrations but have little impact on $\delta^{34}S_{SO4}$ (Torssander, 1989). The catchment of the Hvítá river includes mafic and intermediate lithologies (Gislason et al., 1996).

III.3.2: Sample collection

In August of 2016, water samples were collected directly from the rivers in single-use syringes and passed through 0.2 μm nylon porosity filters into two 15 ml sampling tubes. Syringes were rinsed with river water and containers with eluate prior to collection, and one split was acidified with concentrated high-purity HNO_3 dispensed from a FEP dropper bottle. Precipitation was collected into a bowl approximately 35 km south of Haukadalsvatn during six rain events; this sampling site was further inland than the Efri Haukadalsá catchment and located about 200 m from Route 1. Precipitation samples were

processed in the same fashion as the river samples. Two rain events were sampled twice, with one of each sampling lacking an acidified split.

In August 2019, most river water samples were filtered through a 0.22 μm porosity nylon syringe filter into two eluate-rinsed 50 ml sampling tubes, one of which was acidified with high-purity HNO_3. Several river samples were collected in duplicate using a motorized peristaltic pump, a polypropylene 142 mm filter holder, and 0.2 μm porosity nitrocellulose mixed ester filter; no chemical differences were discernible between the methods. In 2019, a single rain sample was collected from the field site using an HDPE funnel atop an upright HDPE container, and was not acidified due to low collected volume. Two samples of seasonal snow were collected from tributary 7 in the catchment headwaters of the Efri Haukadalsá (Fig. III-2C), as well as one sample of ice from Langjökull glacier. We did not determine [SO_4^{2-}] for these snow and ice samples due to analytical detection limits and did not measure $\delta^{34}S_{SO4}$. For comparison, prior measurements of $\delta^{34}S$ and Cl^-/SO_4^{2-} in ice from Langjökull glacier were digitized from Figure 7 of Gislason and Torssander (2006).

Suspended sediment, deposited sediment, and vegetation samples were also collected from the Efri Haukadalsá catchment. Suspended sediment was sampled in 2016 through large-volume (~30-80 L) filtrations using 0.3 μm pre-combusted Glass Fiber Filters and was given the sample prefix "LHWS" (Fig. III-2C, purple pentagons). Floodplain deposits were logged and sampled with hand auger or by river cut-bank exposures, with multiple depths sampled from within each stratigraphic section (Fig. III-2C, red triangles). Deposit sites were given the sample prefix "LHSS" and were lyophilized and homogenized prior to isotopic or synchrotron analysis (Torres et al., 2020). All filter

samples were stored frozen, and lyophilized and homogenized sediment samples were stored at room temperature. Additionally, five vegetation samples, given the sample prefix "LHVS," were collected from the Efri Haukadalsá catchment in 2019 (Fig. III-2C, green diamonds). After being lyophilized, a subset of each vegetation sample was ground in liquid nitrogen using a pre-combusted mortar and pestle cleaned between samples with quartz abrasive and organic solvent.

III.3.3: Ion chromatography

The dissolved concentrations of major cations and anions were quantified in the Environmental Analysis Center at the California Institute of Technology. A Dionex ICS-2000 with CG12A guard column (2 mm x 50 mm), CS12A separator column (2 mm x 250 mm), and 20 mM isocratic methanesulfonic eluent was used to quantify [Ca^{2+}], [Mg^{2+}], [Na^{+}], and [K^{+}]. A Dionex ISC-3000 with AG29 guard column (2 mm x 50 mm), AS29 separator column (2 mm x 250 mm), and 4.5 mM / 2.5 mM Na_2CO_3 / $NaHCO_3$ isocratic eluent was used to quantify [SO_4^{2-}] and [Cl^{-}]. All chromatography measurements were made with suppressed conductivity detection. Precision was quantified through repeated measurements of MAURI-09 and CRANBERRY-05 from Environment and Climate Change Canada. The relative standard deviation was better than 4.1% (1σ) for all elements other than Ca^{2+}, which was 6.7% (1σ) for MAURI-09. No SO_4^{2-} data were available for three snow/ice samples due to detection limits, and no cation data were available for the two rain samples lacking acidified splits (Fig. III-S4; III.11.2). The concentration of HCO_3^{-} was calculated by charge balance.

III.3.4: MC-ICP-MS measurements of $\delta^{34}S_{SO4}$

River water and precipitation $\delta^{34}S_{SO4}$ values were measured by Multicollector Inductively Coupled Plasma Mass Spectrometry (MC-ICP-MS) at the California Institute of Technology following an adapted method of Paris et al. (2013). Briefly, SO_4^{2-} was isolated using AG 1-X8 analytical grade 100-200 mesh chloride form anion-exchange resin, matrix matched to an in-house Na_2SO_4 standard, and measured with sample-standard bracketing. Outlier $^{34}S/^{32}S$ determinations were identified statistically (>3σ) and visually when associated with substantial loss of signal intensity and removed from the analysis, as were entire sets of measurement cycles following large changes in mass biasing. The average blank of column chromatography was 0.4 nmol SO_4^{2-}, and we report $\delta^{34}S_{SO4}$ values calculated from the mean of blank-corrected $^{34}S/^{32}S$ ratios. Consistency standards included seawater ($\delta^{34}S_{SO4}$=20.9±0.5‰; 2σ, n=50 aggregating measurements of natural seawater and IAPSO seawater) and the in-house reference material Switzer Falls ($\delta^{34}S_{SO4}$=4.2±0.4‰; 2σ, n=56) (Burke et al., 2018). The standard deviation of the distribution of error-normalized deviations ranged from 2.0 to 9.5 across 11 analytical sessions (John and Adkins, 2010). The $^{34}S/^{32}S$ ratio was measured at least twice on all 121 river water and precipitation samples. Furthermore, 44 samples were processed through column chromatography at least twice; for the 38 of these samples measured only twice, the mean of two times the absolute difference in $\delta^{34}S_{SO4}$ between the two determinations was 0.5‰. We report error as the larger of either the reproducibility of consistency standards or the standard deviation of replicate blank-corrected $^{34}S/^{32}S$ determinations.

III.3.5: EA-IRMS measurements of deposit $\delta^{34}S$

The $\delta^{34}S$ value of 20 deposit samples was measured using a Thermo Flash Elemental Analyzer coupled through a Conflo-IV interface to a Thermo Delta V isotope ratio mass spectrometer. Most samples were burned in the presence of V_2O_5 and $^{34}S/^{32}S$ ratios were corrected for the capsule blank. Measurements were calibrated to the VCDT scale using IAEA-S1 and IAEA-S2. For samples measured once (7/20), we assigned error as the precision of replicate $\delta^{34}S$ determinations on sample LHSS-07, 137 cm ($2\sigma = 0.8‰$, n = 10), which is the sample with the most measurements. For samples measured multiple times (13/20), we assigned error as the larger of either the standard deviation of replicate $\delta^{34}S$ values or the reproducibility of sample LHSS-07, 137 cm. We compared sediment $\delta^{34}S$ values with previously published observations (Torres et al., 2020) of $\delta^{13}C$ and fraction modern ($(^{14}C/^{12}C)_{sample}/(^{14}C/^{12}C)_{standard}$, corrected for mass-dependent stable isotope fractionation using measured $^{13}C/^{12}C$).

III.3.6: X-ray Absorption Near Edge Structure spectroscopy

X-ray Absorption Near Edge Structure (XANES) spectroscopy measurements across the sulfur K-edge using an X-ray microprobe provided micron-scale information on the electronic structure and redox state of sulfur in our solid phase samples. XANES measurements were conducted on suspended sediment, deposit samples, and vegetation samples at beamline 14-3 of the Stanford Synchrotron Radiation Lightsource at the SLAC National Accelerator Laboratory. The X-ray microprobe beam was focused to ~5 μm using K-B mirrors and calibrated to define the first pre-edge feature of sodium thiosulfate at 2472.02 eV. Subsamples of filters with suspended sediment were directly attached to

sampling trays, while deposit samples and vegetation samples were typically prepared by inverting homogenized powders onto tape. Most samples were initially mapped at or above the sulfur K-edge at 20-25 μm resolution to identify sulfur-rich regions, which were then mapped at 5 μm resolution and multiple energies characteristic of the resonances of specific sulfur species. Principle Component Analysis within the high-resolution map region identified points of interest for sampling chemical diversity, which were selected for collection of complete X-ray absorption spectra. Because this method characterized the spectral diversity of a sample, the data should not be viewed as a random survey. During the measurements we identified an oxidized sulfur blank on the filters used to sample suspended sediment, but testing revealed that the blank was highly soluble and was likely removed during sample collection (III.11.3; Torres et al., 2020).

Replicate X-ray absorption spectra were averaged and baseline corrected using the SIXPACK software package (Webb, 2005). Several averaged spectra (18/184) displayed high noise relative to the maximum fluorescence, interpreted as low sulfur abundance, and were excluded from subsequent analysis. Remaining spectra (166/184) were fit between 2470 eV and 2490 eV to spectra of standard materials containing thiol, disulfide, sulfoxide, sulfonate, and sulfate from the ID 21 database of the European Synchrotron Radiation Facility (Bohic et al., 2008). Fitting was done in MATLAB as an optimization to minimize proportional misfit, where fractional contributions were constrained to be positive but with an unconstrained sum, and the optimization utilized a normalized fluorescence threshold of 0.1 (Prietzel et al., 2011; Manceau and Nagy, 2012). We quantified speciation as the fit of each reference spectra normalized to the sum of all contributions, and defined a statistic, $F_{reduced}$, as the sum of fractional contributions from the thiol, disulfide, and sulfoxide

moieties. This statistic integrated the relative abundance of organic sulfur (S_{org}) species that are particularly reactive in the presence of dioxygen and other high-potential redox species in the environment (e.g. manganese oxides).

After aggregating data in the software package SMAK (Webb, 2011), maps of $F_{reduced}$ values were generated in MATLAB through pixel-by-pixel fitting of multiple-energy maps to the same ID 21 standards. The fitting was conducted on pixels with more than 5 counts at an incident energy at or above the sulfur K-edge, and responses of 0 counts for any incident energy were removed prior to fitting. This pixel-by-pixel fitting was validated through comparison with $F_{reduced}$ values derived from complete spectra. By characterizing the sulfur speciation at each pixel of regions mapped with multiple incident energies, we generated a single $F_{reduced}$ value representative of each mapped region. However, because suspended sediment samples were not homogenized prior to synchrotron analysis, mapped regions for these samples were not necessarily representative of the bulk sample.

III.3.7: Geomorphic analyses

We used Digital Elevation Models (DEM) to quantify the topographic form of the Efri Haukadalsá catchment in order to evaluate relationships between landscape morphology and river $\delta^{34}S_{SO4}$. DEMs were acquired from the Icelandic Land Survey (10m resolution, EPSG 3057 referenced to the GRS 1980 ellipsoid) and Polar Geospatial Center (Arctic DEM Mosaic, 2m resolution, EPSG 3413 referenced to WGS84 ellipsoid). Using TopoToolbox in MATLAB (Schwanghart and Kuhn, 2010) we used the Arctic DEM to generate 405 cross sections at approximately constant spacing throughout the Efri

Haukadalsá catchment and conducted three different analyses. The first and second analyses were based on quantitative fitting of models to represent the shape of each valley cross section. In the first analysis, we fit each cross section topography by constraining the variable *r*, which determined the valley shape from U-shaped to V-shaped, and the variable *a*, which aligned the valley center, to minimize the function $f(r,a)=(|x-a|^r-y)^2$, where *x* represented horizontal distance and *y* represented elevation (Allen et al., 2018). We performed this fitting both for raw elevation data and after trimming each cross section so that the two sides reached approximately the same elevation, and in both cases the elevation data were normalized to range from 0 to 1 prior to fitting. We reported the mean and range of the shape parameter, *r*, for the two data reductions. In the second analysis, we identified a central point in each cross section and isolated the continuous section on either side of this point that was neither flat nor decreasing in elevation. We then independently fit each side of the valley to a power law by constraining the variables *a*, *b*, and *c* to minimize the function $f(a,b,c)=(ax^b+c-y)^2$, and reported the mean of the two *b* values (Fig. III-S12; III.11.6). In the third analysis each cross section was, in a random order, visually inspected and manually assigned to one of five categories: U-shaped with flat bottom, U-shaped with rounded bottom, V-shaped, V-in-U, and N/A. This classification was done in triplicate and the three sets of classifications were mutually consistent. We compared $\delta^{34}S_{SO4}$ and $[SO_4^{2-}]$ to the mean power law exponents *r* and *b* and the fraction of V-shaped cross sections upstream of each sampling site. All three geomorphic analyses yielded similar relationships.

III.4: Results

Ternary diagrams of cation and anion concentrations characterized the dissolved chemistry of samples (Fig. III-3). The ion Ca^{2+} comprised between 23% and 60% of the cation charge in river waters, Na^{+} sourced 19% to 68%, Mg^{2+} was 7% to 36%, and K^{+} made up only 1% to 2%, as charge equivalent ratios (Fig. III-3A). Samples from NW Iceland, which tended to be from locations closer to the coast than samples from the Efri Haukadalsá, were enriched in $(Na^{+}+K^{+})/\Sigma^{+}$ relative to samples from the Efri Haukadalsá ($\Sigma^{+}=2*Ca^{2+}+2*Mg^{2+}+Na^{+}+K^{+}$). Within the Efri Haukadalsá, a subset of tributaries and samples near the moraine and Fe springs were relatively depleted in $(Na^{+}+K^{+})/\Sigma^{+}$ and enriched in Ca^{+}/Σ^{+}. Overall, samples had lower values of Mg^{2+}/Σ^{+} than expected from conservative mixing between basalt weathering and annually-integrated precipitation, consistent with prior observations (Gislason et al., 1996). Summertime precipitation samples and ice samples formed an array between high Ca^{+}/Σ^{+} and high $(Na^{+}+K^{+})/\Sigma^{+}$ with low Mg^{2+}/Σ^{+}.

The anions HCO_3^{-} and Cl^{-} dominated the anion budget of river water samples (Fig. III-3B). The ion Cl^{-} accounted for 10% to 44% of anion charge, with higher fractions in samples from NW Iceland, and HCO_3^{-} constituted between 49% and 87% of charge. Except in a single sample from outside of the Efri Haukadalsá catchment, SO_4^{2-}/Σ^{+} was between 1% and 12% in all river samples. The anion SO_4^{2-} comprised a larger fraction of the charge budget in precipitation than in river water.

Values of $\delta^{34}S_{SO4}$ ranged from 0.6‰ to 23.7‰ in all river water samples and ranged from 2.5‰ to 23.7‰ in samples from the Efri Haukadalsá (Fig. III-4). Measured $\delta^{34}S_{SO4}$ in precipitation ranged from 6.2‰ to 18.1‰ (Fig. III-4A). In samples from the Efri

Haukadalsá, $\delta^{34}S_{SO4}$ values increased with $1/SO_4^{2-}$ (Fig. III-4B). Moreover, measurements of $\delta^{34}S_{SO4}$ values fell along linear arrays when plotted against Cl^-/SO_4^{2-} (Fig. III-4C). Repeat sampling of the Efri Haukadalsá indicated that river $\delta^{34}S_{SO4}$ was largely constant in time (Table III-S2; III.11.8); conversely, we identified slight temporal changes in the dissolved chemistry of Haukadalsvatn (III.11.9).

The sulfur content of floodplain deposits ranged from 0.025 wt.% to 1.01 wt.% and sediment $\delta^{34}S$ values ranged from 11.1‰ to 17.8‰ (Fig. III-5). With the exception of the organic carbon-rich site LHSS-07 and the site LHSS-04, sediment $\delta^{34}S$ values were relatively constant at a single location while sulfur contents were variable across samples (Figs. III-5A and B). At LHSS-07, sulfur contents were relatively uniform across samples while $\delta^{34}S$ values ranged from 12.6‰ to 17.8‰. Sediment $\delta^{34}S$ values were poorly correlated with ^{14}C abundance and only weakly related to $\delta^{13}C$ values (Fig. III-5C).

X-ray absorption spectra revealed a range of organic sulfur moities in suspended sediment, deposit samples, and vegetation (Fig. III-6A). Flourscence peaks corresponding to organic disulfide (e.g. oxidized glutathione), thiol, sulfoxide, sulfonate, and sulfate moities were observed across vegetation, suspended sediment, and deposit samples (Fig. III-6B).

III.5: Discussion

III.5.1: Source of ions to river water

The linear trend defined by $\delta^{34}S_{SO4}$ and Cl^-/SO_4^{2-} (Fig. III-4C) was consistent with two end-member mixing, where SO_4^{2-} in the Efri Haukadalsá was predominantly sourced from a low-$\delta^{34}S$, low Cl^-/SO_4^{2-} end-member and a high-$\delta^{34}S$, high Cl^-/SO_4^{2-} end-member. We proposed that the low-$^{34}S/^{32}S$ end-member was basalt and the high-$^{34}S/^{32}S$ end-member was annually-integrated precipitation, where the latter reflected the sum of distinct summertime and wintertime meteoric inputs (III.11.4; Torssander, 1989; Gislason et al., 1996; Moulton et al., 2000; Gislason and Torssander, 2006, Bern et al., 2015).

The $\delta^{34}S$ value of Icelandic basalt ranges from approximately -2‰ to 2.5‰ with a mean value of -0.5±2.4‰ (2σ) (Sakai et al., 1980; Torssander, 1989; Hildebrand and Torssander, 1998). The $\delta^{34}S$ of rhyolite is 1-2‰ higher than basalt and with lower sulfur abundance (Torssander, 1989). The sulfur content of Icelandic basalt is approximately 150±160 ppm (1σ) (Sakai et al., 1980; Torssander, 1989) and the chlorine content is approximately 235±140 ppm (1σ) (Sigvaldason and Óskarsson, 1976), giving an expected Cl^-/SO_4^{2-} molar ratio of approximately 1.4.

We calculated a molar Cl^-/SO_4^{2-} ratio of 14.9 and $\delta^{34}S_{SO4}$ value of 18.5‰ for annually-integrated precipitation based on our samples of summer precipitation, prior observations of precipitation chemistry at the Íráfoss meteorological station, and prior observations of precipitation intensity at the Ásgarður and Stykkishólm meteorological stations (Figs. III-2A, B, III-S6 to III-S9; III.11.4). Approximately 70-80% of this annual precipitation was estimated to fall outside of the summer months with Cl^-/Na^+, Cl^-/Ca^{2+}, Cl^-/Mg^{2+}, and Cl^-/SO_4^{2-} ratios similar to seawater. The remaining fraction of annual

precipitation was estimated to fall from May through August with decreased Cl^-/SO_4^{2-} and Cl^-/Ca^{2+} ratios compared to seawater values (Figs. III-S6 to III-S9; III.11.4).

A river mixing model with Monte Carlo error propagation confirmed that dissolved SO_4^{2-} was predominantly sourced from basalt and wintertime precipitation, with a secondary contribution from summertime precipitation (Figs. III-S10 and III-S11; III.11.5). Allowing for formation of a secondary phase with relatively low Na^+/Σ^+ and elevated Ca^{2+}/Σ^+ and Mg^{2+}/Σ^+ ratios recreated our observations of dissolved cation ratios. The results of our inversion model were thus consistent with prior observations of secondary clay formation in Icelandic catchments (Gislason et al., 1996; Thorpe et al., 2019).

III.5.2: Catchment geometry regulated pyrite oxidation

The fraction of SO_4^{2-} sourced from basalt or from seasonal precipitation in river water samples from the Efri Haukadalsá displayed spatial structure linked to landscape processes (Figs. III-7 and III-S13; III.11.7). Overall, $[SO_4^{2-}]$ was low (Fig. III-7A) and $\delta^{34}S_{SO4}$ values were high (Fig. III-7B) in samples from the catchment headwaters and the upper mainstem river, implying that precipitation was the dominant source of SO_4^{2-} to these samples. Conversely, water samples from tributaries 1, 2, and 3 had high values of $[SO_4^{2-}]$ and low values of $\delta^{34}S_{SO4}$, reflecting that basalt weathering was the dominant source of SO_4^{2-} to these samples. Samples from the lower mainstem river had intermediate $[SO_4^{2-}]$ and $\delta^{34}S_{SO4}$ values reflecting a mixture of water derived from the headwaters and from the tributaries.

Values of [SO_4^{2-}] and $\delta^{34}S_{SO4}$ were related to the geometry of valley cross sections upstream of each sampling site (Figs. III-7 and III-8). In the mainstem lower valley, downstream of the confluence with tributary 3, cross sections were U-shaped (Figs. III-7D, E, III-8A, F, and III-S12; III.11.6), reflecting glacial erosion, with a flat floor defined by postglacial floodplain alluvium. In these reaches the valley bottom has been substantially filled with alluvium, reflecting the progradation and aggradation of the fluvial-deltaic-lacustrine system as it adjusts to the bedrock topography left by glaciation (Torres et al., 2020). Satellite and drone imagery revealed that the river is meandering through its floodplain deposits in this region, with little connection to bedrock on the steep valley walls (Figs. III-S1, III-S2, and III-S3; III.11.1). Above the first knickzone (Fig. III-9) the valley cross sections again resembled glacially carved valleys, but with a more parabolic valley floor suggesting less sediment accumulation (Figs. III-7F and G). We interpreted that SO_4^{2-} in these sites was dominantly sourced from precipitation because bedrock is not exposed on the riverbed, there is likely little fresh FeS_2 in the floodplain deposits, and the floodplain disconnects the river from hillslope bedrock sources. Although the isotopic composition of dissolved SO_4^{2-} in the lower valley was lower than precipitation, the ^{34}S-depletion is explained by mixing of SO_4^{2-} with high-$\delta^{34}S_{SO4}$ values from the upper section of the catchment with SO_4^{2-} with low-$\delta^{34}S_{SO4}$ values from tributaries 1, 2, and 3.

In contrast to the U-shaped valleys, the cross sections of tributary 1 (Fig. III-7I), tributary 2 (Fig. III-7J), and tributary 3 (Fig. III-7K) displayed evidence for fluvial bedrock incision. For tributary 1, the river topographic profile was very steep (Fig. III-9), and the valley was strongly V-shaped (Figs. III-7I, III-8A, and F), suggesting fluvial incision into bedrock. For tributary 3 (Fig. III-8K), the V-shaped portion of the profile was occasionally

within a larger U-shaped cross section, indicative of fluvial incision following the glacial carving of the valley (Montgomery and Korup, 2011), and there was a prominent bedrock knickzone in the lower portion of the valley. Satellite imagery and field photography showed that the V-shaped valley walls have some landslide scarring and deposits that extend to the valley floor, indicating active bedrock erosion and delivery of rock to the riverbed (Fig. III-S3; III.11.1). Within these incising reaches, $\delta^{34}S_{SO4}$ values indicated that SO_4^{2-} was dominantly sourced from fresh basalt, a pattern consistent with exposure of fresh minerals as the rivers erode into unweathered bedrock. Overall, lower $\delta^{34}S_{SO4}$ values were associated with higher fractions of V-shaped cross sections (Fig. III-8K) and lower power law exponents (Figs. III-8L and III-S12; III.11.6); these observations partially led us to conclude that landscape morphology exerted the primary control on dissolved $\delta^{34}S_{SO4}$.

Above their knickzones, the upper mainstem valley and tributary 3 had similar elevation profiles (Fig. III-9) and drainage areas, raising the question of why the two valleys had different cross-sectional geometries. Our results suggested, despite that Iceland was covered by an ice sheet during the last glacial maximum (Gudmundsson, 1997), that tributary 3 and the other V-shaped valleys were not shaped by glaciers to the same degree as the main valley. The orientation of the primary U-shaped valley in the Efri Haukadalsá catchment was interpreted to show ice flow was locally to the southwest, whereas some of the V-shaped tributaries were approximately orthogonal to this direction (Fig. III-7). We proposed that the orientation of the V-shaped fluvial valleys sheltered them from ice flow and led to the preservation of their shape despite glaciation (Montgomery and Korup, 2011; Lajeunesse, 2014). Following deglaciation, these valleys maintained their steep valley walls and bedrock floors, allowing for continued bedrock incision and hillslope-channel

coupling. In contrast, we interpreted that the valleys oriented parallel to the ice flow experienced major glacial erosion and were cut down such that less eroded tributaries became hanging tributaries (Fig. III-9; MacGregor et al., 2000). The low valley-floor gradients and undulating bedrock topography with overdeepenings are typical of glacial valleys (MacGregor et al., 2000), and this disequilibrium with the fluvial system has led to interglacial fluvial and lacustrine aggradation, wide and flat valley floors, and a disconnect between bedrock sources and fluvial transport and weathering (Church and Ryder, 1972).

The physical abrasion associated with glacial erosion generates fine-grained sediment susceptible to rapid weathering (Vance et al., 2009). In a granitic landscape, the initial weathering pulse from deglaciation was previously shown to source strontium with elevated $^{87}Sr/^{86}Sr$ isotope ratios (Blum and Erel, 1995). Using a similar argument, the deglaciation at ~10 ka is expected to have generated large quantities of fine-grained sediment with fresh surface area throughout western Iceland, as evidenced by the moraine at tributary 5. In the short-term, weathering of such material could generate low-$\delta^{34}S_{SO4}$ values due to FeS_2 oxidation. However, values of $\delta^{34}S_{SO4}$ in water samples near the moraine in the catchment of the Efri Haukadalsá were elevated from that of unweathered bedrock and dominantly reflected SO_4^{2-} inputs from seasonal precipitation (Fig. III-7). This observation suggested that FeS_2 in this fine-grained glacial sediment had already undergone oxidation in less than 10 kyr, which is comparable to the timescale for decay of the $^{87}Sr/^{86}Sr$ ratio sourced from glacial granitoid soils (Blum and Erel, 1995). Overall, when considering controls on $\delta^{34}S_{SO4}$ values and the role of glaciation in supplying FeS_2 for oxidative weathering, it was thus useful to consider the role of fluvial alluviation in disconnecting bedrock sources in formerly glaciated valleys, the persistence of some V-

shaped valleys that maintain active bedrock incision, and the prior weathering of existing deposits such as moraines.

III.5.3: Relative abundance and isotopic ramifications of organic sulfur phases

We calculated the relative flux of organic and inorganic sulfur in two ways; the first method was based on observed carbon fluxes, and the second on sediment accumulation rate. Measurements of carbon concentration in suspended sediment ranged from 40 μg/L to 300 μg/L, with a mean value of 120±90 μg/L (n=11) (Torres et al., 2020). Using a C/S mass ratio of 35, the mean value we measured in deposit samples, and taking a characteristic river [SO_4^{2-}] of 10 μM, the flux of organic sulfur in the Efri Haukadalsá was calculated as 1.1±1.6% (2σ) of the dissolved SO_4^{2-} flux. However, this estimate was biased to low values because our sampling was during summer when the river stage was relatively low and particle transport is expected to have been similarly low.

The second calculation relied on observations from the Haukadalsvatn sediment core (Geirsdóttir et al., 2009). Using a sediment accumulation rate of 5280 m^3/yr (Torres et al., 2020), a sediment density of 2 g/cm^3, a C/S mass ratio of 35, and an organic carbon fraction of 2 wt% (Geirsdóttir et al., 2009), we calculated that $1.9x10^5$ moles of S_{org} were transported annually as river suspended load. Taking river [SO_4^{2-}] equal to 10 μM and scaling by discharge, we calculated that 4.3% of the sulfur flux occurred within organic phases. It is likely that this estimate was also biased to lower values by not accounting for the storage of particulate sulfur within the floodplain. While the magnitude of this underestimate is subject to assumption of porosity, sediment stored within the catchment could be 2-3 times the mass stored in the lake (Torres et al., 2020). On the basis of these

two calculations, we concluded that flux of S_{org} in the Efri Haukadalsá was less than ~10% of the dissolved SO_4^{2-} flux. Globally, approximately 6% of non-anthropogenic river sulfur occurs within organic phases; the relative flux of S_{org} in the Efri Haukadalsá was thus comparable to the global value despite the lack of sedimentary lithologies in the catchment (Galy et al., 2015; Burke et al., 2018).

The removal of 10% SO_4^{2-} to organic phases could have exerted an influence on the Cl^-/SO_4^{2-} ratio of river water and, if removed through a fractionating process, dissolved $\delta^{34}S_{SO4}$. As a simple model, we considered whether or not the Cl^-/SO_4^{2-} and $\delta^{34}S_{SO4}$ of river water samples could reflect mixing of basalt and annually-integrated precipitation followed by fractional consumption according to a Rayleigh model (Fig. III-S15; III.11.10). For this calculation we optimized for the end-member mixing fraction and isotope fractionation that best fit observations under the assumption that 10% of initial SO_4^{2-} was consumed, and then calculated the $\delta^{34}S$ of the reaction product. Although the calculated isotope fractionations were dependent on the choice of precipitation end-member, for most samples the required fractionation was more positive than expected for MSR (Fig. III-S15; III.11.10). Moreover, for isotope effects offset from zero but elevated from MSR expectations, the product sulfur would have a median $\delta^{34}S$ value much lower than measured sediment $\delta^{34}S$ values (Figs. III-5 and III-S15; III.11.10). These calculations thus indicated that, for the range in sediment $\delta^{34}S$ to largely match river water $\delta^{34}S_{SO4}$, the generation of S_{org} occurred with minimal sulfur isotope fractionation.

The overall assimilation of SO_4^{2-} by plants has a fractionation of only about 1.5‰ (Trust and Fry, 1992), although plant metabolites exhibit substantial isotopic variations (Tcherkez and Tea, 2013). Our results were consistent with this magnitude of fractionation

and led us to conclude that the observed S_{org} phases were generated through SO_4^{2-} assimilation and subsequent reduction within biomass. These findings were largely consistent with those of Yi-Balan et al. (2014), who identified only a moderate offset in the $\delta^{34}S$ of organic biomass from SO_4^{2-} inputs in the Luquillo Critical Zone Observatory. Moreover, in previous work Zhu et al. (2016) found that the isotopic composition of humic acids extracted from Yangtze River sediment were similar to dissolved $\delta^{34}S_{SO4}$. Our results indicated that the sulfur isotopic composition of particles deposited in river catchments may, in general, not be systematically offset from river $\delta^{34}S_{SO4}$ values. Notably, this hypothesis should be further tested in tropical rivers with elevated organic carbon loading.

III.5.4: Sulfur cycling during floodplain storage

X-ray absorption spectra revealed a substantial range in the relative contributions of thiol, disulfide, sulfoxide, sulfonate, and sulfate to suspended sediment, deposit samples, and vegetation (Fig. III-6C). On average, the fractional sum of contributions from reduced sulfur moieties ($F_{reduced}$) to deposit samples was similar between deposit samples stored within the floodplain (25.1±51.6%, 2σ) and sediment suspended in the river (28.9±17.3%, 2σ). One sample from LHSS-07 at 25 cm depth, a horizon with elevated organic carbon content, appeared as an outlier from other deposit samples by showing a large contribution from disulfide (Fig. III-6). Moreover, multiple-energy maps indicated that a wide diversity of sulfur speciation was present across spatial scales (Torres et al., 2020). These observations were consistent with prior observations of organic sulfur phases within natural soils (Xia et al., 1998; Solomon et al., 2011; Prietzel et al., 2011).

The mean $F_{reduced}$ value in vegetation samples was 56.2±16.8% (2σ). This value was consistent with results of Jalilehvand (2005), who measured X-ray absorption spectra at the sulfur K-edge on plant leaves from northern California. Redox imaging of photosynthetic tissues of grasses and sedges from the Efri Haukadalsá catchment identified spatial diversity in sulfur speciation. For example, the outer photosynthetic mesophyll tissue of sample LHVS19-01 was S-rich and relatively reduced, while the inner parts richer in vasculature were lower in sulfur content and more oxidized (Fig. III-S5; III.11.3).

The relative abundances of disulfide, sulfoxide, and sulfate were similar across suspended sediment, deposit samples, and vegetation (Fig. III-6D). However, large changes were identified in the relative contributions of thiol and sulfonate moieties between the different materials. Thiols were abundant in vegetation, while sulfonate moieties were rare. Conversely, suspended sediment and deposit samples displayed abundant sulfonate but only a small contribution from thiols. Prior studies have observed a similar abundance of sulfonate species in soils, suggesting it is a recalcitrant form of organic sulfur capable of resisting long-term oxidation compared to more reactive species (Autry and Fitzgerald, 1990; Solomon et al., 2011).

If S_{org} in deposit and suspended sediment was mostly derived from plant material, as suggested by the similarity of sediment $\delta^{34}S$ and dissolved $\delta^{34}S_{SO4}$, our observations indicated that the processes of generating, transporting, and storing sediment involved net conversion of thiols into sulfonates. However, we did not recover a positive relationship between ^{14}C abundance in sediment and the fractional contribution of reduced moieties to X-ray absorption spectra (Fig. III-10). For both deposit and suspended samples, older sediment was associated with higher $F_{reduced}$ values (Figs. III-10A and B) and a lower

fractional contribution from sulfonate specifically (Figs. III-10C and D), patterns opposite of expectations if the aging process generated sulfonate from thiol.

Boye et al. (2017) suggested that carbon-bearing phases with redox states above a thermodynamic threshold were preferentially oxidized within anaerobic settings while reduced carbon-bearing phases were preferentially stored in floodplains. Our data displayed older ^{14}C ages associated with carbon that had a more reduced organic sulfur speciation in sediment (Fig. III-10) and suggested that a similar explanation may pertain to our sulfur observations. In this case, the oxidized phases such as sulfonate would have been preferentially lost from the floodplain. We observed that the 1/S and C/S ratios of samples were not clearly correlated with ^{14}C age, suggesting that, under this interpretation, carbon and sulfur would have been preferentially oxidized at similar rates through time (Figs. III-10E and F). However, because the radiocarbon content of sediment reflects a complex mixture of time-dependent physical reworking processes and the addition of newly fixed C_{org}, we stress that ^{14}C content only approximately represents deposit age (Torres et al., 2017; 2020).

III.6: Conclusions

We have studied the major ion chemistry, $\delta^{34}S_{SO4}$, and speciation of sulfur in river water, sediment, and vegetation samples from the Efri Haukadalsá catchment of western Iceland, as well as the dissolved chemistry of river water samples from around NW Iceland and the Hvítá catchment. We found that dissolved anion chemistry reflected mixing of products generated from basalt weathering and seasonal precipitation, while dissolved cation chemistry also reflected influences of clay formation. In the catchment of the Efri Haukadalsá, fluxes of organic sulfur in suspended sediment constituted less than approximately 10% of the dissolved flux of SO_4^{2-}. X-ray absorption spectroscopy of suspended sediment, deposit samples, and vegetation identified a range of reduced sulfur compounds, with sediment enriched in sulfonate and depleted in thiol relative to vegetation. Because the $\delta^{34}S$ of deposit samples was similar to that of dissolved SO_4^{2-}, we concluded that organic phases did not require formation through MSR and more likely were generated through SO_4^{2-} assimilation and reduction within biomass. Overall, biological processes exerted only a minimal influence on $\delta^{34}S_{SO4}$ values in the Efri Haukadalsá. Rather, landscape morphology exerted the primary control on the $^{34}S/^{32}S$ ratio of river SO_4^{2-}. Glacially eroded, U-shaped valleys with bedrock floor overdeepenings that have been partially or completely filled through fluvial sedimentation lacked fresh bedrock exposure and had $\delta^{34}S_{SO4}$ values reflecting meteoric inputs. In contrast, V-shaped valleys had lower $\delta^{34}S_{SO4}$ values reflecting the continued exposure and weathering of fresh bedrock. We interpreted these differences in valley shape, alluviation, and $\delta^{34}S_{SO4}$ as reflecting contrasting patterns of ice-flow and development of fluvial drainage networks resulting from topographic disequilibrium across glacial-interglacial cycles. Overall, our

results emphasized the tight linkages between pyrite oxidation and geomorphic processes. This work has indicated that, even in the presence of organic sulfur fluxes, inversion models of dissolved river chemistry can be used to reconstruct the fractional contributions of lithologic end-members to river SO_4^{2-}. This research thus validated the application of river inversion models for constraining the impact of pyrite oxidation on the global carbon cycle.

III.7: Data statement

Data from this article on major ion concentrations, river water and precipitation $\delta^{34}S_{SO4}$ values, sediment $\delta^{34}S$ and $F_{reduced}$ values, and vegetation $F_{reduced}$ values are available as supplementary material.

III.8: Acknowledgments

P.C.K. is supported by the The Fannie and John Hertz Foundation Cohan-Jacobs and Stein Families Fellowship. This research was conducted with government support under and awarded by DoD, Air Force Office of Scientific Research, National Defense Science and Engineering Graduate (NDSEG) Fellowship, 32 CFR 168a (P.C.K.). M.A.T. gratefully acknowledges support from the Alfred P. Sloan Foundation. This research was supported by the Discovery Fund (to W.W.F. and M.P.L.) at the California Institute of Technology, and this work was partially support by the US National Science Foundation through grants 1349858 and 1834492. Use of the Stanford Synchrotron Radiation Lightsource, SLAC National Accelerator Laboratory, is supported by the U.S. Department of Energy, Office of Science, Office of Basic Energy Sciences under Contract No. DE-AC02-76SF00515. We acknowledge DEMs provided by the Polar Geospatial Center under NSF-OPP awards 1043681, 1559691, and 1542736. We gratefully acknowledge A.J. West for loaning sampling equipment, A. Sessions, F. Wu, and A. Phillips for assistance with EA-IRMS measurements, G. Lopez, T. Present, and D. Johnson for assistance with MC-ICP-MS measurements, N. Edwards, S. Bone, and C. Roach for assistance with synchrotron measurements at SLAC, and A. Phillips and P. Mateo for advice on figure design. We thank Louis Derry and two anonymous referees for their constructive comments.

III.9: Figures

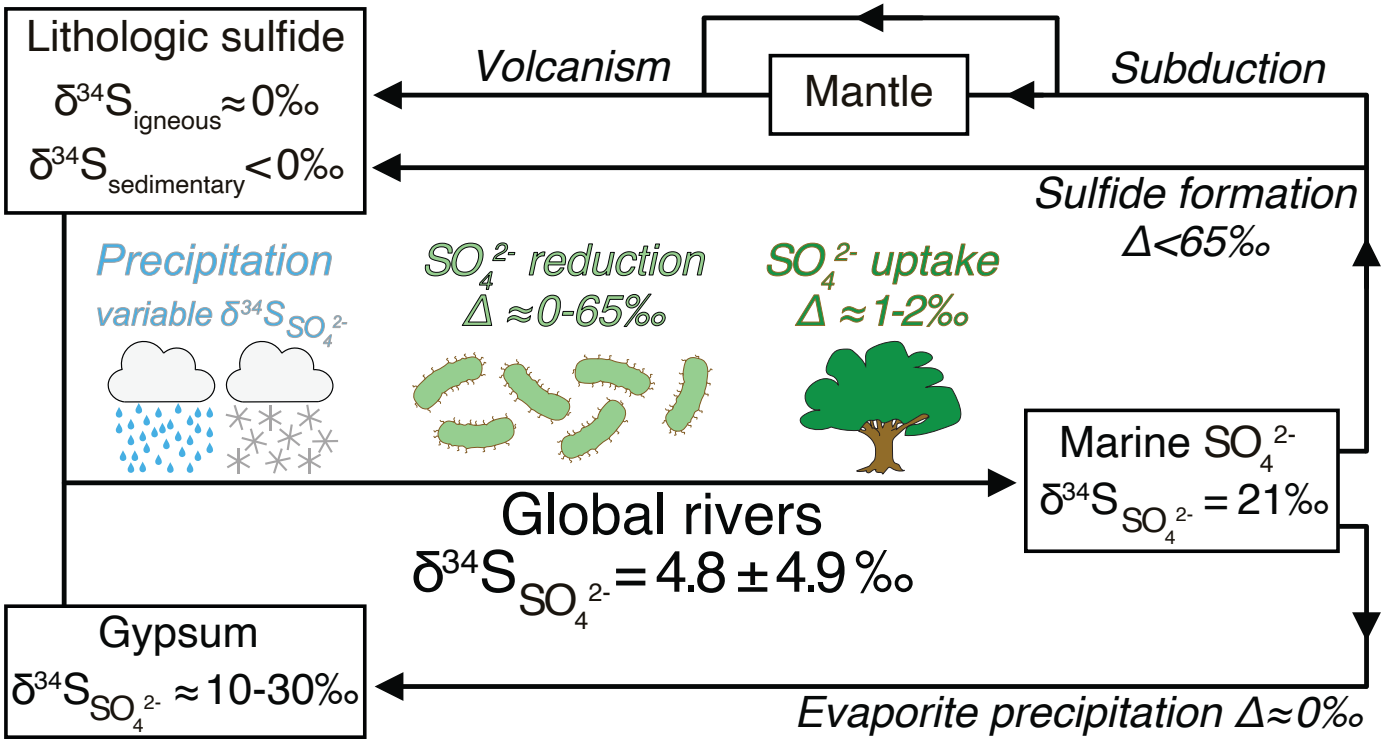

Fig. III-1: Schematic of the global sulfur cycle. River $[SO_4^{2-}]$ and $\delta^{34}S_{SO4}$ have been used to quantify chemical weathering reactions and the associated biogeochemical fluxes of alkalinity and dissolved inorganic carbon in rivers globally. Additionally, river $[SO_4^{2-}]$ and $\delta^{34}S_{SO4}$ have been used to constrain the abundance and $^{34}S/^{32}S$ ratio of SO_4^{2-} input to seawater, which are key parameters in biogeochemical models interpreting geologic records of $\delta^{34}S$ and $\delta^{13}C$ (Kump and Garrels, 1986). However, rivers may host fractionating processes such as dissimilatory microbial SO_4^{2-} reduction or SO_4^{2-} assimilation that could bias the results of river inversion calculations and biogeochemical models. The given range of river $\delta^{34}S_{SO4}$ values is from Burke et al. (2018), gypsum $\delta^{34}S$ was assumed to span the $^{34}S/^{32}S$ range of Phanerozoic evaporites, the $\delta^{34}S$ of igneous sulfide was assumed to match bulk terrestrial sulfur, and the range of fractionations associated with MSR was estimated from laboratory culture studies.

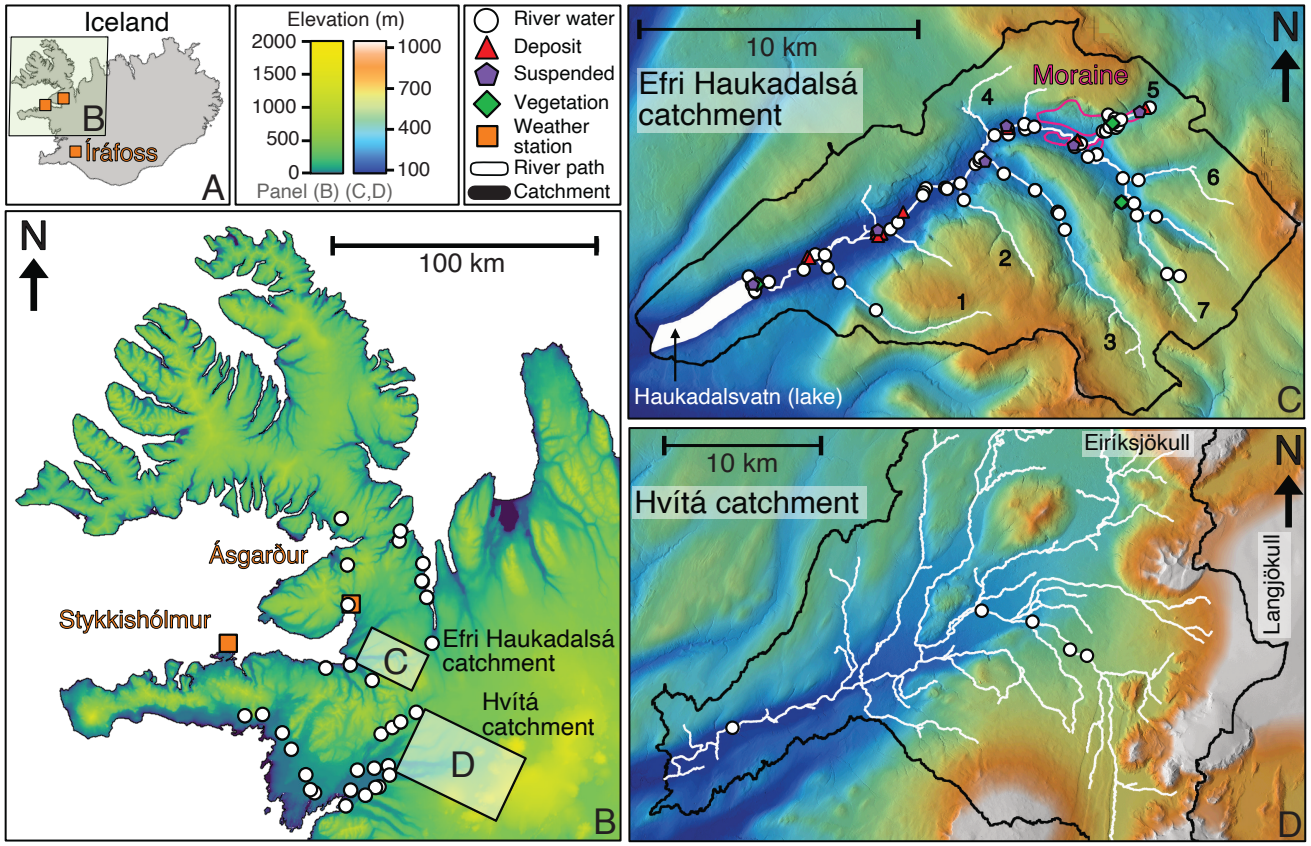

Fig. III-2: Sampling sites. (A) Iceland with indicated study region and relevant meteorological stations (orange squares). Coastline data were sourced from the European Environment Agency in EPSG 3035. (B) Western Iceland with river water sampling locations (white circles). Boxed regions show the Efri Haukadalsá catchment and the Hvítá catchment. Elevation data were sourced from the Icelandic Land Survey in EPSG 3057. (C) The Efri Haukadalsá catchment with indicated sampling locations for river water samples (white circles), deposit samples (red triangles), suspended sediment samples (purple pentagons), and vegetation samples (green diamonds, locations approximate). The location of a moraine is indicated. Tributaries are numbered following Torres et al. (2020). (D) The Hvítá catchment with indicated sampling locations. Elevation data for the Efri Haukadalsá and Hvítá catchments were sourced from the Polar Geospatial Center in EPSG 3413. Note that the north arrow rotates between panels due to change of projection.

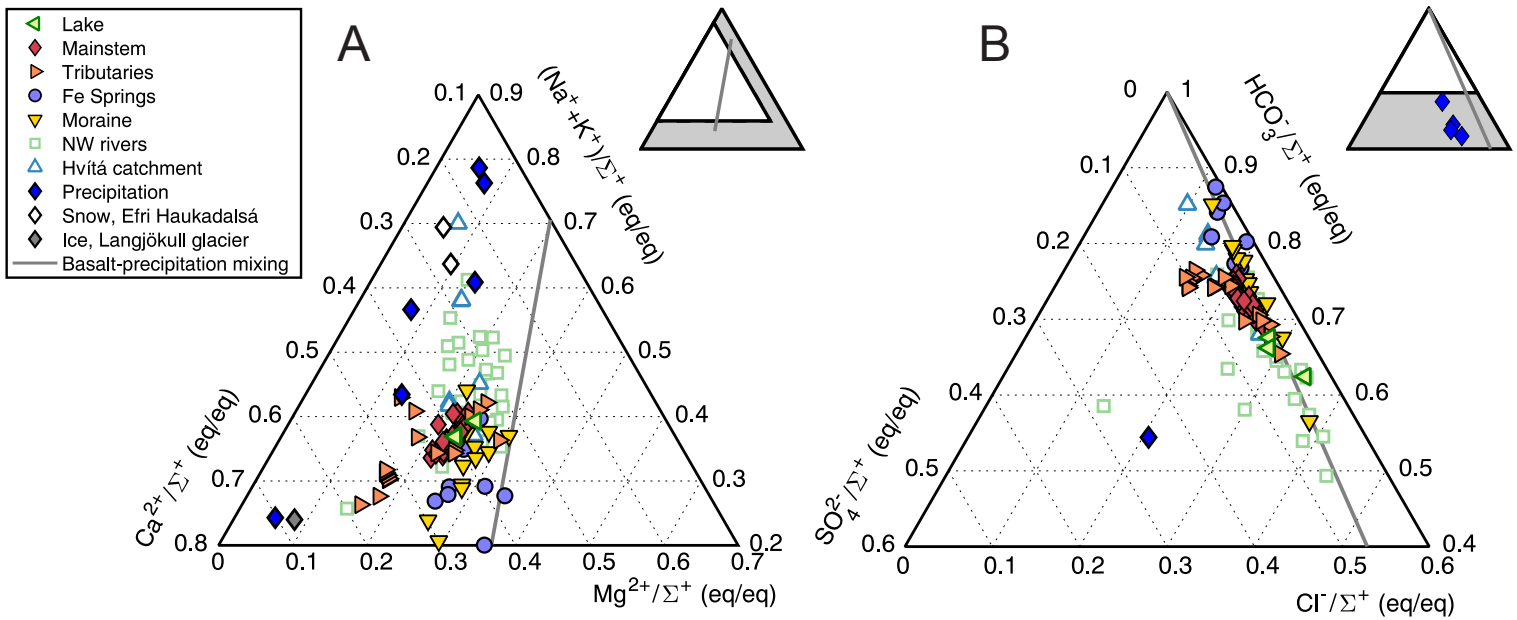

Fig. III-3: Cation and anion ternary diagrams. Plotted data are ratios of charge-equivalent concentrations uncorrected for Cl^- inputs from precipitation, and the plotted regions are subsets of the full parameter space (as indicated in the schematic to the top-right above each panel: filled white triangles are plotted areas and the grey triangles indicate the full space). (A) Cation ternary diagram of Ca^{2+}-Mg^{2+}-Na^++K^+ for all samples. River waters from the Efri Haukadalsá tended to have higher Ca^{2+}/Σ^+ and lower $(Na^+ + K^+)/\Sigma^+$ than samples from NW Iceland or from the Hvítá catchment. All river water samples plotted away from a mixing line between basalt and annually-integrated precipitation (grey line), indicating depletion in Mg^{2+}/Σ^+ relative to two-component mixing. As previously suggested (Gislason et al., 1996) and supported by inversion modeling with Monte Carlo error propagation (Figs. III-S10 and III-S11; III.11.5), we attributed this depletion to the formation of secondary clays. Three precipitation samples lacking measurements of Σ^+ were not plotted. (B) Anion ternary diagram of SO_4^{2-}-Cl^--HCO_3^- for all samples. The anion HCO_3^-, quantified through charge balance, was the dominant anion in solution. The ion Cl^- was the second most abundant anion and samples from NW Iceland were enriched in Cl^-/Σ^+ relative to samples from the Efri Haukadalsá, consistent with their elevated values of $(Na^+ + K^+)/\Sigma^+$. Most samples had $SO_4^{2-}/\Sigma^+ < 12\%$ (eq/eq). The anion SO_4^{2-} comprised a larger fraction of charge in precipitation samples (blue diamonds in top-right schematic). One precipitation sample with $(Cl^- + SO_4^{2-})/\Sigma^+ > 1$ was not plotted. The anion data were largely consistent with mixing between basalt and annually-integrated precipitation.

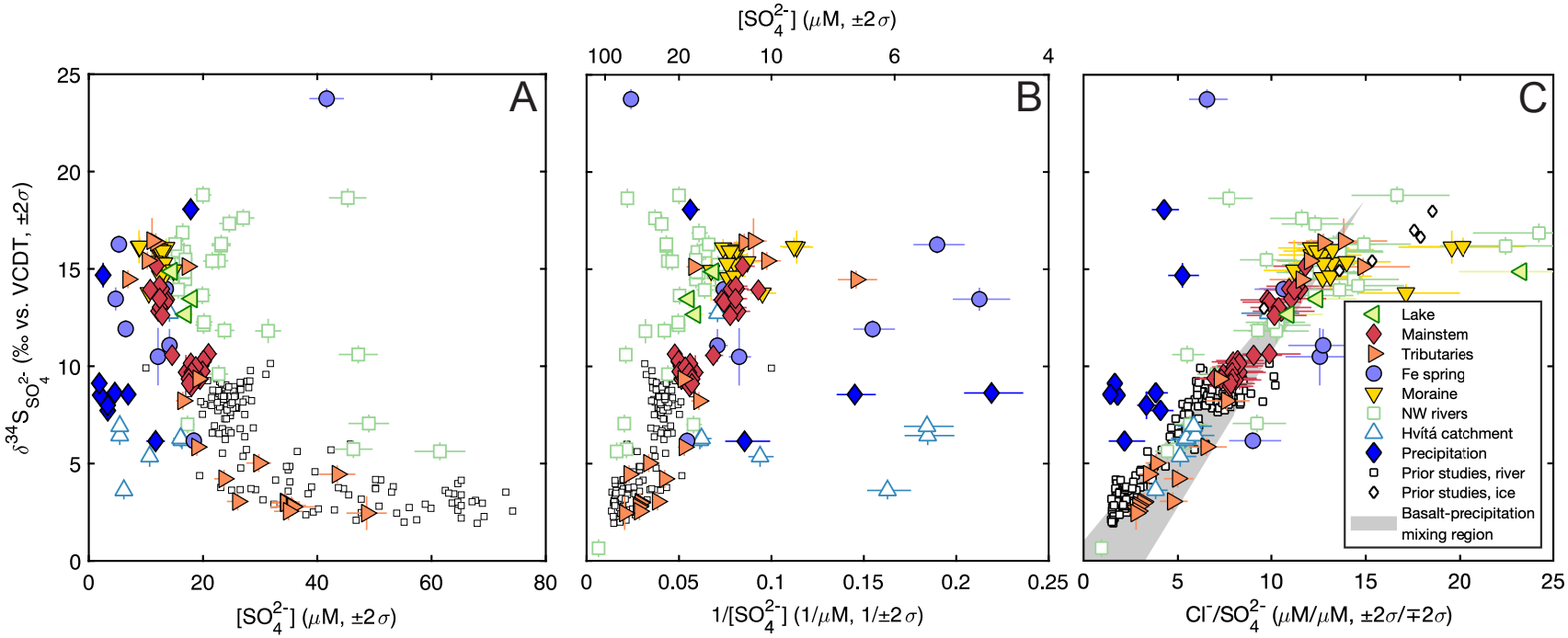

Fig. III-4: $\delta^{34}S_{SO4}$, $[SO_4^{2-}]$, and Cl^-/SO_4^{2-} of river water samples. (A) $\delta^{34}S_{SO4}$ decreased with increasing $[SO_4^{2-}]$. (B) $\delta^{34}S_{SO4}$ was linear with $1/SO_4^{2-}$, excluding samples from Fe springs. (C) $\delta^{34}S_{SO4}$ against Cl^-/SO_4^{2-}. The data were well described by mixing between a low-$\delta^{34}S$ end-member and a high-$\delta^{34}S$ end-member, proposed to be basalt and precipitation, respectively. Note that the end-members of the mixing line (grey) were independently constrained and not fit through our river water measurements. The plotted basalt end-member had $\delta^{34}S$ ranging from -2‰ to 1‰ and Cl^-/SO_4^{2-} between 0 and 2 (Sakai et al., 1980; Torssander, 1989). The precipitation end-member had $\delta^{34}S_{SO4}$ derived from our observations and the precipitation intensity recorded at the Ásgarður and Stykkishólm meteorological stations, and Cl^-/SO_4^{2-} based on the observed chemistry of precipitation at the Íráfoss meteorological station (III.11.4). Several precipitation samples are out of the plotting range in (B) and three Fe springs samples with elevated Cl^-/SO_4^{2-} ratios are out of range in (C). Prior observations of river $\delta^{34}S_{SO4}$ and Langjökull $\delta^{34}S$ are from Gislason and Torssander (2006).

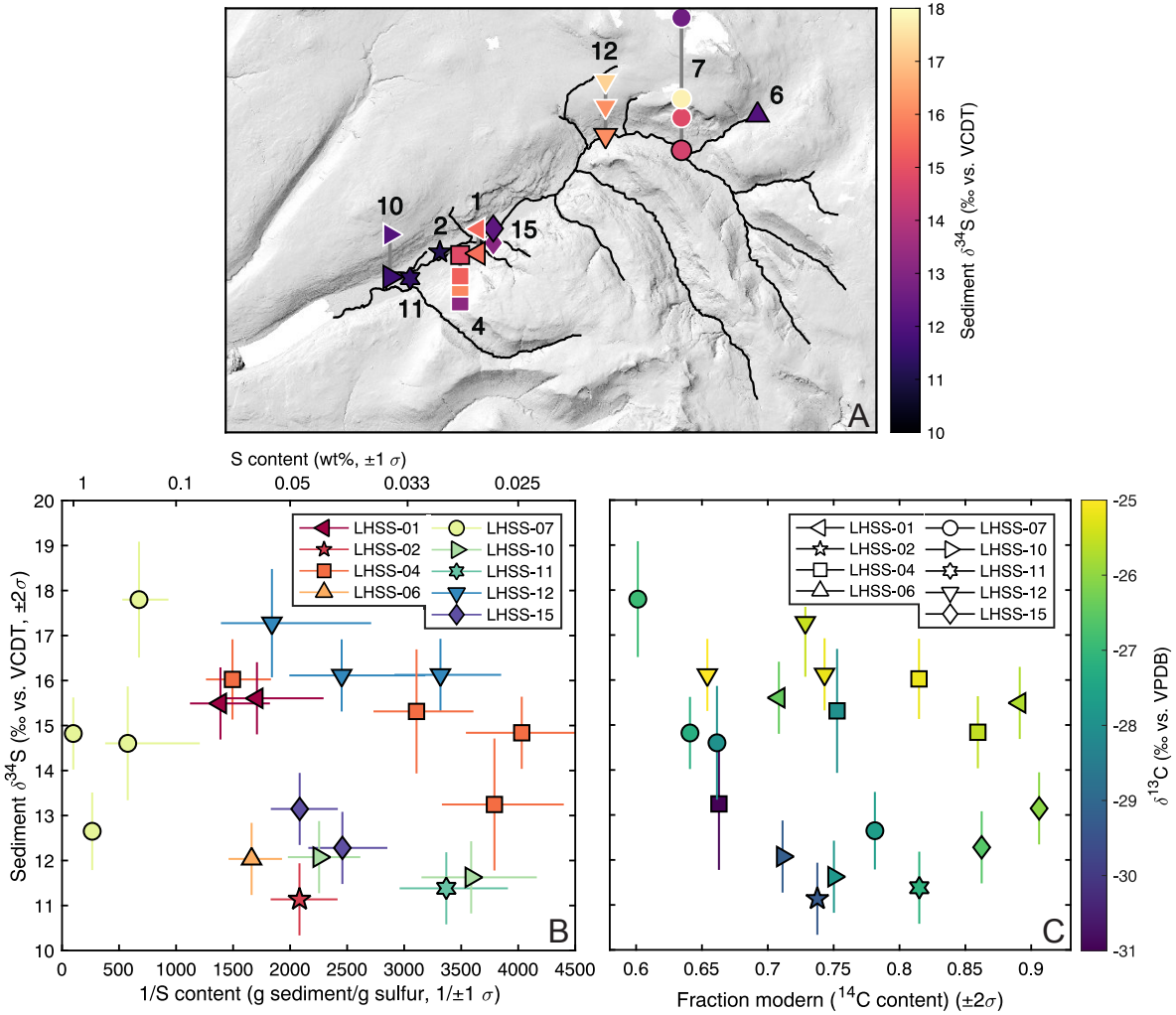

III-5: Sediment $\delta^{34}S$. (A) $^{34}S/^{32}S$ isotope ratio by sampling location. Numbers refer to sediment sampling sites, which are coded by plotting symbol, and multiple points per symbol reflect vertical sampling. Markers with black edges indicate the ground surface or river surface; markers with white edges below these indicate depth below surface, while markers with white edges above these indicate height above the river. Points that would otherwise overlap are partially offset from one another; true sampling locations are plotted in Fig. III-2C. (B) Sediment $^{34}S/^{32}S$ ratio against inverse sulfur content. Except for LHSS-07 and LHSS-04, samples from the same site generally had similar $\delta^{34}S$ values but variable sulfur abundances. At LHSS-07, all samples had high sulfur abundances but variable $^{34}S/^{32}S$ ratios. (C) Sediment $\delta^{34}S$ against fraction modern (^{14}C content) color-coded by $\delta^{13}C$. There was no clear relationship between sediment $\delta^{34}S$ value and ^{14}C content. The fraction modern of the sample from the moraine (LHSS-06) had a value of 0.27 and is not plotted.

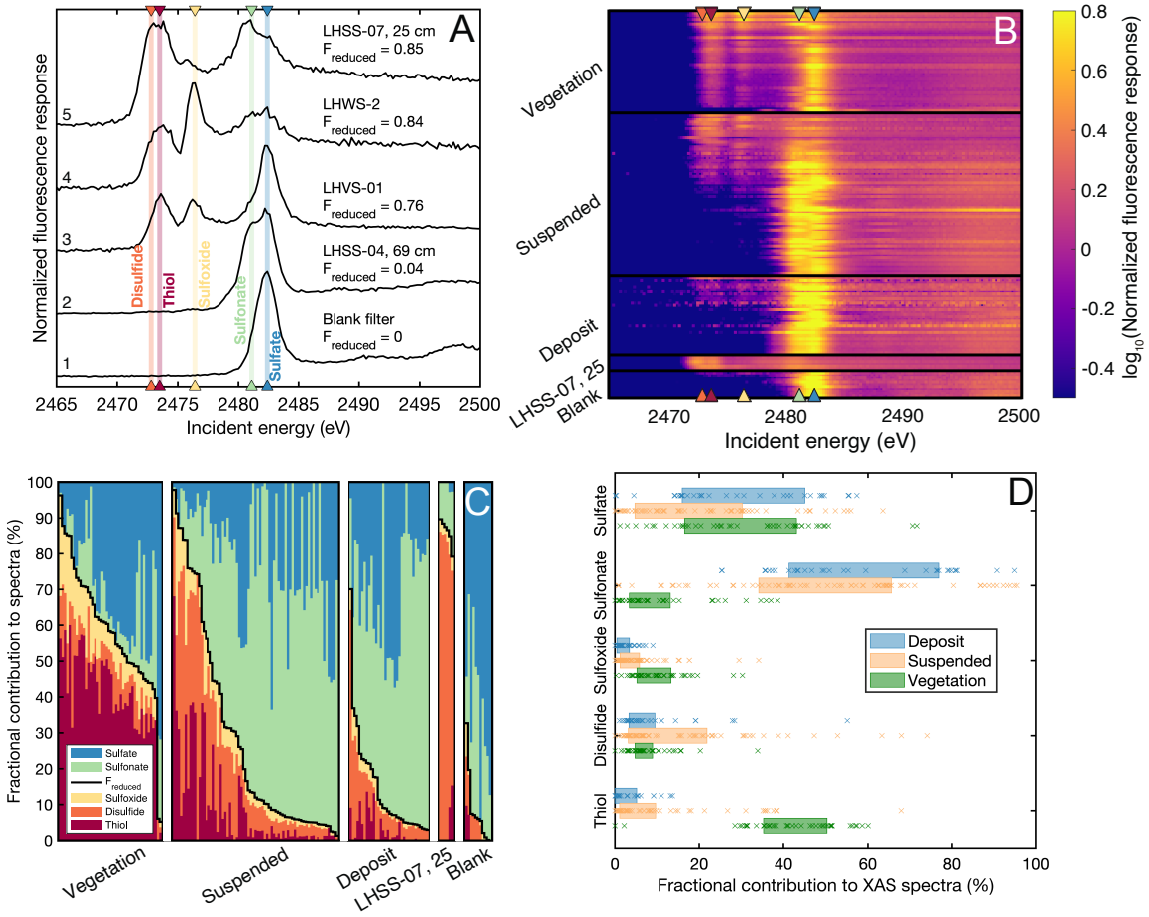

Fig. III-6: X-ray spectroscopy results and fitting. XANES identified reduced and oxidized sulfur moieties in suspended sediment, deposit sediment, and vegetation samples. (A) Example X-ray absorption spectra from (1) blank filter, (2, 5) deposit samples, (3) vegetation, and (4) suspended sediment. The statistics $F_{reduced}$ quantified the contribution of thiol, disulfide, and sulfoxide to each spectra relative to the contributions of all moieties. (B) Top-down view of X-ray absorption spectra. Within each category, spectra are organized with higher $F_{reduced}$ values at the top to lower $F_{reduced}$ values at the bottom. The spectra showed peaks at incident energies characteristic of the resonances for reduced sulfur phases such as disulfide, thiol, and sulfoxide. (C) Stacked bar chart showing the fractional contributions of sulfate, sulfonate, sulfoxide, disulfide, and thiol to spectra collected on vegetation, suspended sediment, deposit samples, and blank filters. (D) Fractional contributions arranged by moiety. Thiols made a large contribution to spectra collected on vegetation, while sulfonates made a large contribution to the spectra collected on suspended sediment and deposit samples. Shaded boxes extend from the 25th to 75th percentiles of results.

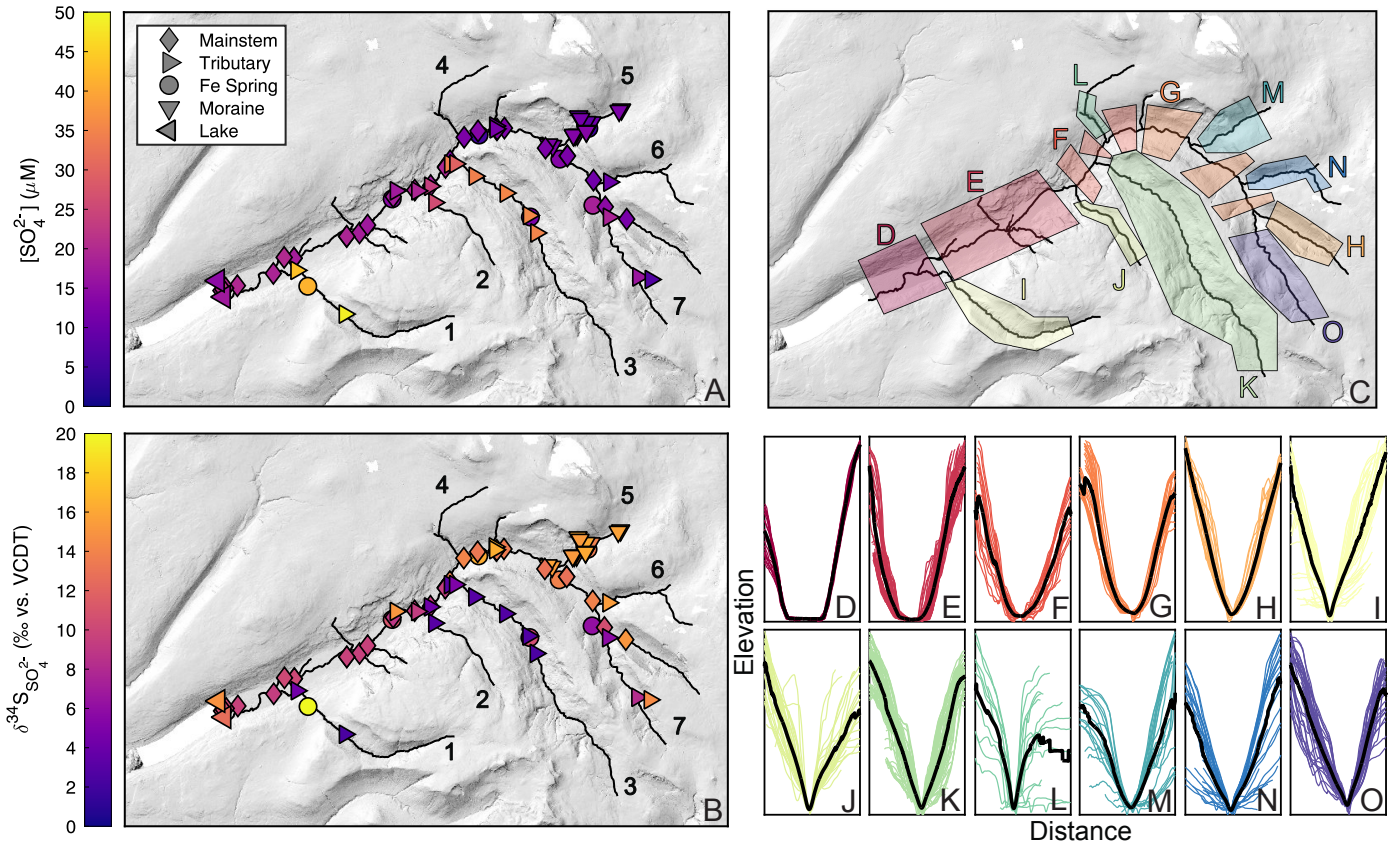

Fig. III-7: Spatial structure of $[SO_4^{2-}]$ and $\delta^{34}S_{SO4}$. Maps of (A) $[SO_4^{2-}]$ and (B) $\delta^{34}S_{SO4}$. Values of $[SO_4^{2-}]$ were elevated and $\delta^{34}S_{SO4}$ values were low in samples from tributaries 1, 2 and 3, while values of $[SO_4^{2-}]$ were low and $\delta^{34}S_{SO4}$ values were elevated in samples from the upper section of the mainstem river. In the lower section of the mainstem, SO_4^{2-} and $\delta^{34}S_{SO4}$ had intermediate values. (C) Shaded regions indicate the locations of cross sections show in (D)-(O), where thin colored lines are individual elevation profiles and black lines are averaged cross sections. Averaged cross sections in regions (D)-(H) appeared dominantly U-shaped, consistent with alluviation and higher $\delta^{34}S_{SO4}$ values. Regions (I)-(O) appeared dominantly V-shaped, consistent with fluvial incision and lower $\delta^{34}S_{SO4}$ values. Cross sections in (D)–(O) are presented after both horizontal and vertical alignment.

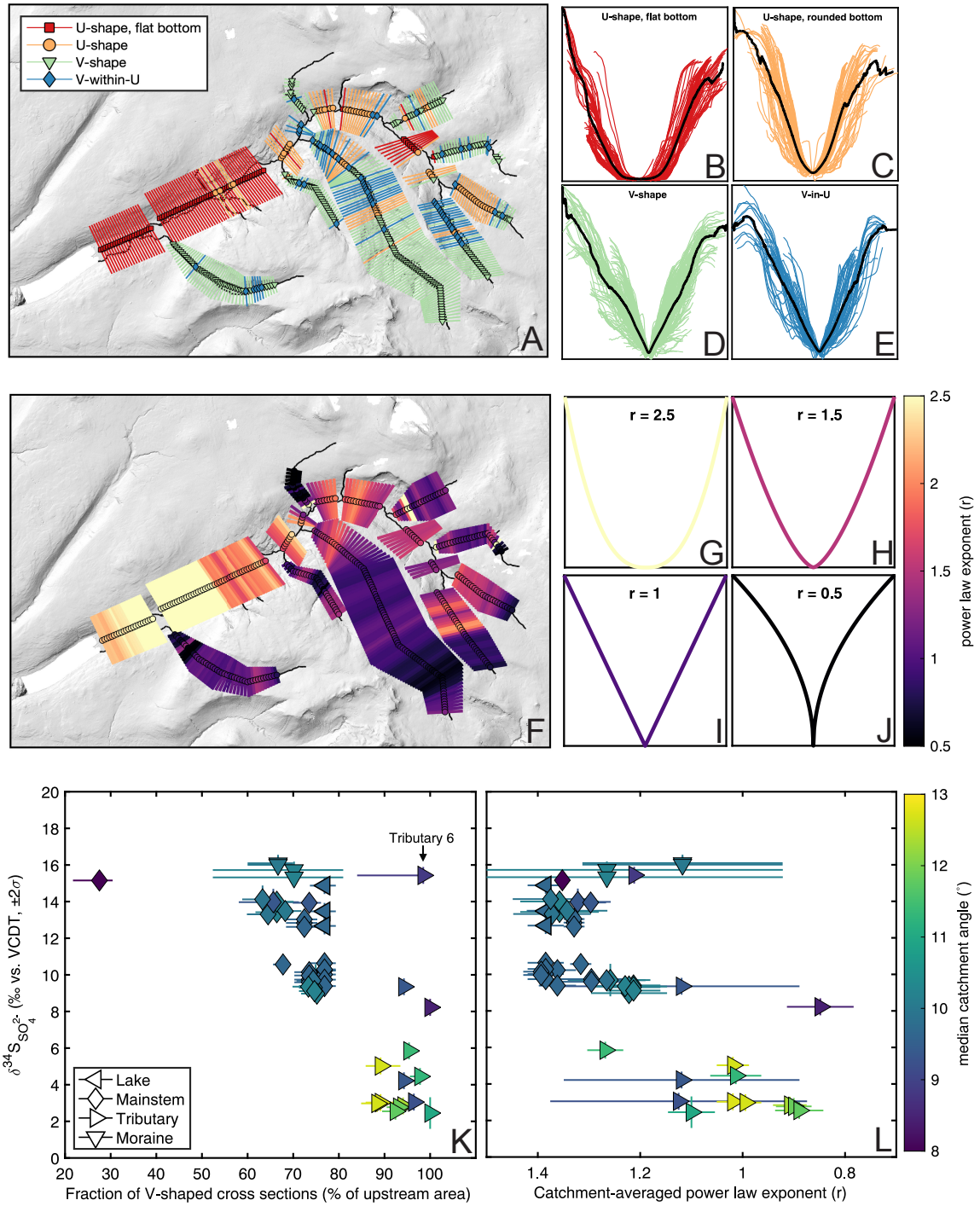
U-shape, flat bottom
U-shape
V-shape
V-within-U
A
U-shape, flat bottom
B
U-shape, rounded bottom
C
V-shape
D
V-in-U
E
F
r = 2.5
G
r = 1.5
H
r = 1
I
r = 0.5
J
power law exponent (r)
2.5
2
1.5
1
0.5
Tributary 6
Lake
Mainstem
Tributary
Moraine
K
L
$\delta^{34}S_{SO_4^{2-}}$ (‰ vs. VCDT, ±2σ)
Fraction of V-shaped cross sections (% of upstream area)
Catchment-averaged power law exponent (r)
median catchment angle (°)

Fig. III-8: Geomorphic analyses. (A) Each of 405 cross sections generated throughout the Efri Haukadalsá catchment was visually inspected and assigned into one of five groups: U-shaped with flat bottom, U-shaped, V-shaped, V-within-U shaped, and N/A. (B) Aligned and averaged cross sections identified as U-shaped with flat bottom (C) U-shaped with rounded bottom, (D) V-shaped, and (E) V-in-U shaped. Results in (A) through (E) are plotted for one of three rounds of manual classification, all of which yielded similar spatial distributions of cross section geometry and averaged elevation profiles. (F) Power law exponent fitted to each cross section, with examples for four different values of the shape parameter *r*: (G) 2.5, (H) 1.5, (I) 1, (J) 0.5 (Allen et al., 2018). (K) Values of $\delta^{34}S_{SO4}$ against the fraction of V-shaped cross sections in each catchment, color-coded by median catchment angle. Error bars indicate the minimum and maximum fraction of V-shaped cross sections in each catchment across the three rounds of manual identification and accounting for cross sections characterized as N/A. Overall, results indicated lower values of $\delta^{34}S_{SO4}$ in samples with higher fractions of V-shaped cross sections upstream of the sampling site. The sample from tributary 6 was notable for having a high $\delta^{34}S_{SO4}$ value despite its upstream region being dominated by V-shaped cross sections. (L) Values of $\delta^{34}S_{SO4}$ against the average power law exponent *r* upstream of each sampling site. Error bars indicate the range in power law exponent calculated for two different treatments of the elevation data. Again, lower values of $\delta^{34}S_{SO4}$ were associated with V-shaped upstream cross sections.

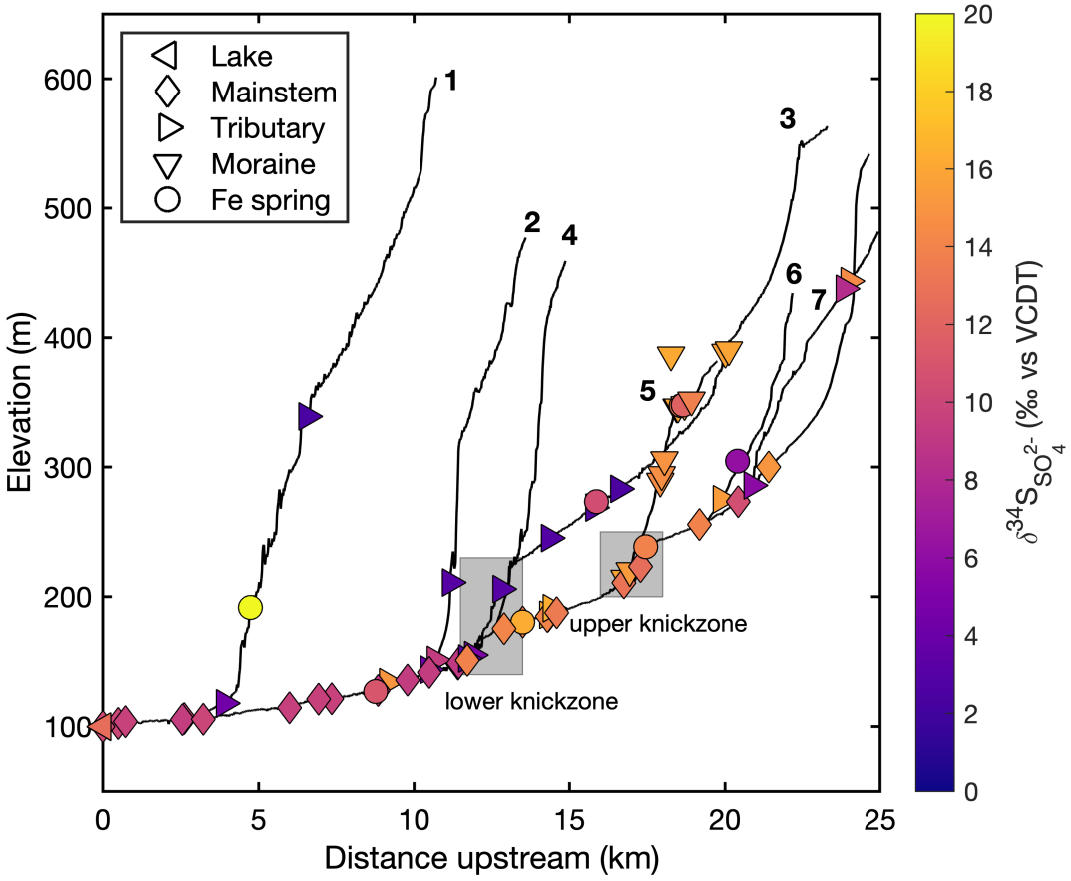

Fig. III-9: River channel long profile with water samples coded by sample type and $\delta^{34}S_{SO4}$ value. The lower knickzone occurred near the confluence with tributary 3, and the upper knickzone occurred near confluence with tributary 5. The given numbers indicate tributary numbers (Fig. III-2C).

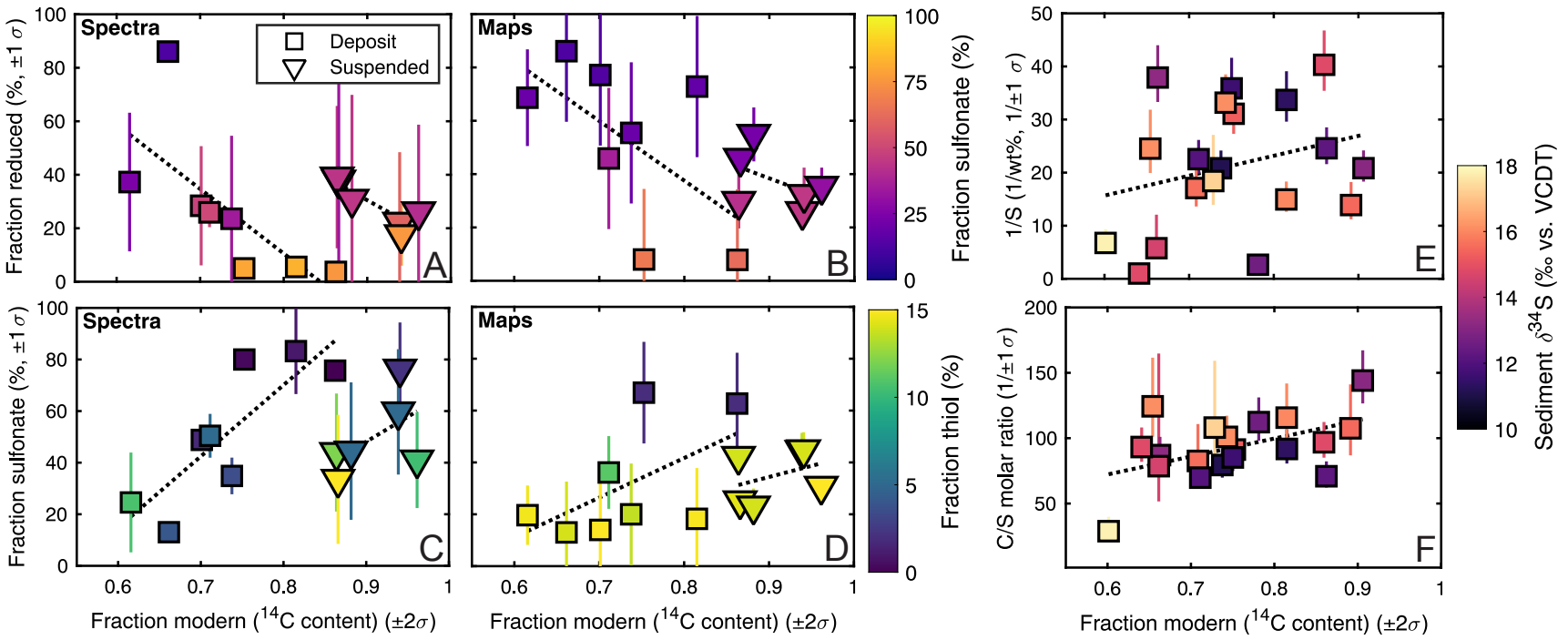

Fig. III-10: Relationships among fitted spectroscopic data, fraction modern (^{14}C content), 1/S and C/S ratios, and sediment δ^{34}S. (A) $F_{reduced}$ (the sum of fractional contributions from disulfide, thiol, and sulfoxide speciation) derived from X-ray absorption spectra and from (B) multiple-energy maps against fraction modern, shape-coded as deposit samples (squares) or suspended sediment (triangles) and color-coded by the fractional contribution of sulfonate. Within each sample type, lower fraction modern was associated with more reduced speciation and a lower contribution of sulfonate. (C) Fractional contribution of sulfonate against fraction modern, from X-ray absorption spectra and from (D) multiple energy maps, color-coded by the fractional contribution of thiols. Within each sample type, the lower fractional contribution from sulfonate with decreasing ^{14}C content was related to increasing fractional contribution of thiols. Note that changes in the relative contributions of moieties are not independent due to the unit-sum constraint of our fitting; decreases in the relative contribution of sulfonate must be balanced by increases in the fractional contribution of other moieties, even if all other moieties have the same absolute contributions. (E) 1/S and (F) C/S molar ratio against fraction modern, color-coded by δ^{34}S. Sediment ^{14}C content was only weakly related with 1/S or C/S ratio. In all panels the moraine sample from site LHSS-06 was out of plotting range and excluded from regression.

III.10: References

Allen, G.H., Pavelsky, T.M., Barefoot, E.A., Lamb, M.P., Butman, D., Tashie, A. and Gleason, C.J., 2018. Similarity of stream width distributions across headwater systems. *Nature Communications*, 9(1), pp.1-7. https://doi.org/10.1038/s41467-018-02991-w.

Andreae, M.O., Berresheim, H., Bingemer, H., Jacob, D.J., Lewis, B.L., Li, S.M. and Talbot, R.W., 1990. The atmospheric sulfur cycle over the Amazon Basin: 2. Wet season. *Journal of Geophysical Research: Atmospheres*, 95(D10), pp.16813-16824. https://doi.org/10.1029/JD095iD10p16813.

Autry, A.R. and Fitzgerald, J.W., 1990. Sulfonate S: A major form of forest soil organic sulfur. *Biology and Fertility of Soils*, 10(1), pp.50-56. https://doi.org/10.1007/BF00336124.

Bern, C.R., Chadwick, O.A., Kendall, C. and Pribil, M.J., 2015. Steep spatial gradients of volcanic and marine sulfur in Hawaiian rainfall and ecosystems. *Science of the Total Environment*, 514, pp.250-260. https://doi.org/10.1016/j.scitotenv.2015.02.001.

Blum, J.D. and Erel, Y., 1995. A silicate weathering mechanism linking increases in marine $^{87}Sr/^{86}$ Sr with global glaciation. *Nature*, 373(6513), pp.415-418. https://doi.org/10.1038/373415a0.

Bohic, S., Murphy, K., Paulus, W., Cloetens, P., Salome, M., Susini, J. and Double, K., 2008. Intracellular chemical imaging of the developmental phases of human neuromelanin using synchrotron X-ray microspectroscopy. *Analytical Chemistry*, 80(24), pp.9557-9566. https://doi.org/10.1021/ac801817k.

Boye, K., Noel, V., Tfaily, M.M., Bone, S.E., Williams, K.H., Bargar, J.R. and Fendorf, S., 2017. Thermodynamically controlled preservation of organic carbon in floodplains. *Nature Geoscience*, 10(6), pp.415-419. https://doi.org/10.1038/ngeo2940.

Burke, A., Present, T.M., Paris, G., Rae, E.C., Sandilands, B.H., Gaillardet, J., Peucker-Ehrenbrink, B., Fischer, W.W., McClelland, J.W., Spencer, R.G. and Voss, B.M., 2018. Sulfur isotopes in rivers: Insights into global weathering budgets, pyrite oxidation, and the modern sulfur cycle. *Earth and Planetary Science Letters*, 496, pp.168-177. https://doi.org/10.1016/j.epsl.2018.05.022.

Calmels, D., Gaillardet, J., Brenot, A. and France-Lanord, C., 2007. Sustained sulfide oxidation by physical erosion processes in the Mackenzie River basin: Climatic perspectives. *Geology*, 35(11), pp.1003-1006. https://doi.org/10.1130/G24132A.1.

Church, M. and Ryder, J.M., 1972. Paraglacial sedimentation: A consideration of fluvial processes conditioned by glaciation. *Geological Society of America Bulletin*, 83(10), pp.3059-3072. https://doi.org/10.1130/0016-7606(1972)83[3059:PSACOF]2.0.CO;2.

Gaillardet, J., Dupré, B., Louvat, P. and Allegre, C.J., 1999. Global silicate weathering and CO_2 consumption rates deduced from the chemistry of large rivers. *Chemical Geology*, 159(1-4), pp.3-30. https://doi.org/10.1016/S0009-2541(99)00031-5.

Galy, V., Peucker-Ehrenbrink, B. and Eglinton, T., 2015. Global carbon export from the terrestrial biosphere controlled by erosion. *Nature*, 521(7551), pp.204-207. https://doi.org/10.1038/nature14400.

Geirsdóttir, Á., Miller, G.H., Thordarson, T. and Ólafsdóttir, K.B., 2009. A 2000 year record of climate variations reconstructed from Haukadalsvatn, West Iceland. *Journal of Paleolimnology*, 41(1), pp.95-115. https://doi.org/10.1007/s10933-008-9253-z.

Gislason, S.R., Arnorsson, S. and Armannsson, H., 1996. Chemical weathering of basalt in Southwest Iceland: Effects of runoff, age of rocks and vegetative/glacial cover. *American Journal of Science*, 296(8), pp.837-907. https://doi.org/10.2475/ajs.296.8.837.

Gislason, S.R. and Torssander, P., 2006. Response of sulfate concentration and isotope composition in Icelandic rivers to the decline in global atmospheric SO_2 emissions into the North Atlantic region. *Environmental Science & Technology*, 40(3), pp.680-686. https://doi.org/10.1021/es051325o.

Gudmundsson, H.J., 1997. A review of the Holocene environmental history of Iceland. *Quaternary Science Reviews*, 16(1), pp.81-92. https://doi.org/10.1016/S0277-3791(96)00043-1.

Hemingway, J.D., Olson, H., Turchyn, A.V., Tipper, E.T., Bickle, M.J. and Johnston, D.T., 2020. Triple oxygen isotope insight into terrestrial pyrite oxidation. *Proceedings of the National Academy of Sciences*, 117(14), pp.7650-7657. https://doi.org/10.1073/pnas.1917518117.

Hjartarson, A. and Sæmundsson, K., 2014. Geological map of Iceland, bedrock. 1: 600,000. Iceland GeoSurvey, Reykjavík.

Hildebrand, L. and Torssander, P., 1998. Sulphur isotope ratios from the Katla volcanic centre—implications for mantle heterogeneity. *Proceedings of the Water–Rock Interaction*, 9, pp.451-454.

Jalilehvand, F., 2005. Sulfur speciation in intact plant leaves by XANES spectroscopy.

John, S.G. and Adkins, J.F., 2010. Analysis of dissolved iron isotopes in seawater. *Marine Chemistry*, 119(1-4), pp.65-76. https://doi.org/10.1016/j.marchem.2010.01.001.

Johnson, J.E., Gerpheide, A., Lamb, M.P. and Fischer, W.W., 2014. O_2 constraints from Paleoproterozoic detrital pyrite and uraninite. *Bulletin*, 126(5-6), pp.813-830. https://doi.org/10.1130/B30949.1.

Kemeny, P.C., Lopez, G.I., Dalleska, N.F., Torres, M., Burke, A., Bhatt, M.P., West, A.J., Hartmann, J. and Adkins, J.F., 2021. Sulfate sulfur isotopes and major ion chemistry reveal that pyrite oxidation counteracts CO_2 drawdown from silicate weathering in the Langtang-Trisuli-Narayani River system, Nepal Himalaya. *Geochimica et Cosmochimica Acta*, 294, pp.43-69. https://doi.org/10.1016/j.gca.2020.11.009.

Kertesz, M.A. and Mirleau, P., 2004. The role of soil microbes in plant sulphur nutrition. *Journal of Experimental Botany*, 55(404), pp.1939-1945. https://doi.org/10.1093/jxb/erh176.

Kump, L. and Garrels, R.M., 1986. Modeling atmospheric O_2 in the global sedimentary redox cycle. *American Journal of Science*, 286(5), pp.337-360. https://doi.org/10.2475/ajs.286.5.337.

Lajeunesse, P., 2014. Buried preglacial fluvial gorges and valleys preserved through Quaternary glaciations beneath the eastern Laurentide Ice Sheet. *Bulletin*, 126(3-4), pp.447-458. https://doi.org/10.1130/B30911.1.

MacGregor, K.R., Anderson, R.S., Anderson, S.P. and Waddington, E.D., 2000. Numerical simulations of glacial-valley longitudinal profile evolution. *Geology*, 28(11), pp.1031-1034. https://doi.org/10.1130/0091-7613(2000)28<1031:NSOGLP>2.0.CO;2.

Manceau, A. and Nagy, K.L., 2012. Quantitative analysis of sulfur functional groups in natural organic matter by XANES spectroscopy. *Geochimica et Cosmochimica Acta*, 99, pp.206-223. https://doi.org/10.1016/j.gca.2012.09.033.

Montgomery, D.R. and Korup, O., 2011. Preservation of inner gorges through repeated Alpine glaciations. *Nature Geoscience*, 4(1), pp.62-67. https://doi.org/10.1038/ngeo1030.

Moulton, K.L., West, J. and Berner, R.A., 2000. Solute flux and mineral mass balance approaches to the quantification of plant effects on silicate weathering. *American Journal of Science*, 300(7), pp.539-570. https://doi.org/10.2475/ajs.300.7.539.

Paris, G., Sessions, A.L., Subhas, A.V. and Adkins, J.F., 2013. MC-ICP-MS measurement of $\delta^{34}S$ and $\Delta^{33}S$ in small amounts of dissolved sulfate. *Chemical Geology*, 345, pp.50-61. https://doi.org/10.1016/j.chemgeo.2013.02.022.

Prietzel, J., Botzaki, A., Tyufekchieva, N., Brettholle, M., Thieme, J. and Klysubun, W., 2011. Sulfur speciation in soil by S K-edge XANES spectroscopy: Comparison of spectral deconvolution and linear combination fitting. *Environmental Science & Technology*, 45(7), pp.2878-2886. https://doi.org/10.1021/es102180a.

Robinson, Z.P., Fairchild, I.J. and Spiro, B., 2009. The sulphur isotope and hydrochemical characteristics of Skeiðarársandur, Iceland: Identification of solute sources and implications for weathering processes. *Hydrological Processes: An International Journal*, 23(15), pp.2212-2224. https://doi.org/10.1002/hyp.7368.

Sakai, H., Gunnlaugsson, E., Tomasson, J. and Rouse, J.E., 1980. Sulfur isotope systematics in Icelandic geothermal systems and influence of seawater circulation at Reykjanes. *Geochimica et Cosmochimica Acta*, 44(8), pp.1223-1231. https://doi.org/10.1016/0016-7037(80)90076-9.

Schwanghart, W. and Kuhn, N.J., 2010. TopoToolbox: A set of Matlab functions for topographic analysis. *Environmental Modelling & Software*, 25(6), pp.770-781. https://doi.org/10.1016/j.envsoft.2009.12.002.

Sigvaldason, G.E. and Óskarsson, N., 1976. Chlorine in basalts from Iceland. *Geochimica et Cosmochimica Acta*, 40(7), pp.777-789. https://doi.org/10.1016/0016-7037(76)90030-2.

Solomon, D., Lehmann, J., de Zarruk, K.K., Dathe, J., Kinyangi, J., Liang, B. and Machado, S., 2011. Speciation and long-and short-term molecular-level dynamics of soil organic sulfur studied by X-ray absorption near-edge structure spectroscopy. *Journal of Environmental Quality*, 40(3), pp.704-718. https://doi.org/10.2134/jeq2010.0061.

Stefánsson, A., Keller, N.S., Robin, J.G. and Ono, S., 2015. Multiple sulfur isotope systematics of Icelandic geothermal fluids and the source and reactions of sulfur in volcanic geothermal systems at divergent plate boundaries. *Geochimica et Cosmochimica Acta*, 165, pp.307-323. https://doi.org/10.1016/j.gca.2015.05.045.

Tcherkez, G. and Tea, I., 2013. $^{32}S/^{34}S$ isotope fractionation in plant sulphur metabolism. *New Phytologist*, 200(1), pp.44-53. https://doi.org/10.1111/nph.12314.

Thorpe, M.T., Hurowitz, J.A. and Dehouck, E., 2019. Sediment geochemistry and mineralogy from a glacial terrain river system in southwest Iceland. *Geochimica et Cosmochimica Acta*, 263, pp.140-166. https://doi.org/10.1016/j.gca.2019.08.003.

Torres, M.A., West, A.J. and Li, G., 2014. Sulphide oxidation and carbonate dissolution as a source of CO_2 over geological timescales. *Nature*, 507(7492), pp.346-349. https://doi.org/10.1038/nature13030.

Torres, M.A., West, A.J., Clark, K.E., Paris, G., Bouchez, J., Ponton, C., Feakins, S.J., Galy, V. and Adkins, J.F., 2016. The acid and alkalinity budgets of weathering in the Andes–Amazon system: Insights into the erosional control of global biogeochemical cycles. *Earth and Planetary Science Letters*, 450, pp.381-391. https://doi.org/10.1016/j.epsl.2016.06.012.

Torres, M.A., Limaye, A.B., Ganti, V., Lamb, M.P., West, A.J. and Fischer, W.W., 2017. Model predictions of long-lived storage of organic carbon in river deposits. *Earth Surface Dynamics*, 5(4), pp.711-730. https://doi.org/10.5194/esurf-5-711-2017.

Torres, M.A., Kemeny, P.C., Lamb, M.P., Cole, T.L. and Fischer, W.W., 2020. Long-term storage and age-biased export of fluvial organic carbon: Field evidence from west Iceland. *Geochemistry, Geophysics, Geosystems*, 21(4), p.e2019GC008632. https://doi.org/10.1029/2019GC008632.

Torssander, P., 1989. Sulfur isotope ratios of Icelandic rocks. *Contributions to Mineralogy and Petrology*, 102(1), pp.18-23. https://doi.org/10.1007/BF01160187.

Trust, B. A., & Fry, B. 1992. Stable sulphur isotopes in plants: A review. *Plant, Cell & Environment*, 15(9), 1105-1110. https://doi.org/10.1111/j.1365-3040.1992.tb01661.x.

Turchyn, A.V., Tipper, E.T., Galy, A., Lo, J.K. and Bickle, M.J., 2013. Isotope evidence for secondary sulfide precipitation along the Marsyandi River, Nepal, Himalayas. *Earth and Planetary Science Letters*, 374, pp.36-46. https://doi.org/10.1016/j.epsl.2013.04.033.

Vance, D., Teagle, D.A. and Foster, G.L., 2009. Variable Quaternary chemical weathering fluxes and imbalances in marine geochemical budgets. *Nature*, 458(7237), pp.493-496. https://doi.org/10.1038/nature07828.

Walker, J.C., Hays, P.B. and Kasting, J.F., 1981. A negative feedback mechanism for the long-term stabilization of Earth's surface temperature. *Journal of Geophysical Research: Oceans*, 86(C10), pp.9776-9782. https://doi.org/10.1029/JC086iC10p09776.

Webb, S.M., 2005. SIXpack: A graphical user interface for XAS analysis using IFEFFIT. *Physica scripta*, 2005(T115), p.1011.

Webb, S.M., 2011, September. The MicroAnalysis Toolkit: X-ray fluorescence image processing software. In AIP Conference Proceedings (Vol. 1365, No. 1, pp. 196-199). American Institute of Physics.

Xia, K., Weesner, F., Bleam, W.F., Helmke, P.A., Bloom, P.R. and Skyllberg, U.L., 1998. XANES studies of oxidation states of sulfur in aquatic and soil humic substances. *Soil Science Society of America Journal*, 62(5), pp.1240-1246. https://doi.org/10.2136/sssaj1998.03615995006200050014x.

Yi-Balan, A.S., Amundson, R., & Buss H.L., 2014. Decoupling of sulfur and nitrogen cycling due to biotic processes in a tropical rainforest. *Geochimica et Cosmochimica Acta*, 142, pp.411-428. https://doi.org/10.1016/j.gca.2014.05.049.

Zhu, M.X., Chen, L.J., Yang, G.P., Huang, X.L. and Zhao, Y.D., 2016. Composition of organic sulfur in riverine and marine sediments: Insights from sulfur stable isotopes and XANES spectroscopy. *Organic Geochemistry*, 99, pp.102-112. https://doi.org/10.1016/j.orggeochem.2016.07.002.

III.11: Supplementary text

III.11.1: Images of the Efri Haukadalsá catchment

Images of the Efri Haukadalsá catchment were collected by drone (Fig. III-S1), hand-held photography (Fig. III-S2), and satellite (Fig. III-S3).

III.11.2: Chromatography measurements of cation concentration

During collection, one split of each river water sample was acidified with concentrated high-purity HNO_3 to prevent adsorption of ions to container walls and precipitation of secondary phases. This acidified split was then measured by ion chromatography to quantify $[Ca^{2+}]$, $[Mg^{2+}]$, $[Na^{+}]$, and $[K^{+}]$. A subset of acidified samples was measured on the same run as both acidified and non-acidified calibration solutions, a subset was measured with only acidified solutions, and a final subset was measured with only non-acidified calibration solutions. For samples measured with both acidified and non-acidified solutions, the calibrated values were extremely similar when calibrated with acidified or unacidified solutions (Fig. III-S4A). The fractional difference between values calibrated using acidified or non-acidified calibration solutions was < 2% for Ca^{2+}, Na^{+}, and Mg^{2+} (Fig. III-S4B). The difference was larger for K^{+}, closer to ~5-10%, but the absolute change was less than ~1 μM due to the very low $[K^{+}]$ values of the samples (Fig. III-S4B). The proportional offset between the two sets of calibrated values was related to the sample dilution factor, suggesting that the cause of the variation was the acid content of each solution. Where available, we reported measurements of acidified samples calibrated with acidified calibration solutions.

There was no acidified split collected for several precipitation samples due to insufficient volume. To test if cations measurements could be made on the unacidified split, we measured the acidified and unacidified splits of other precipitation, snow, and ice samples in the same run as both acidified and unacidified calibration solutions. As found for river water samples, the calibrated values of $[Ca^{2+}]$, $[Mg^{2+}]$, $[Na^{+}]$, and $[K^{+}]$ in acidified samples were extremely similar when calibrated with acidified or unacidified calibration solutions (Fig. III-S4C). However, there were differences when comparing the acidified samples calibrated with acidified solutions to the unacidified samples calibrated with unacidified solutions (Fig. III-S4D). Because the deviation of calibrated values was to both sides of the 1:1 line, the discrepancy was not clearly attributed to either a blank associated with the added HNO_3, adsorption of ions to container walls, or precipitation of secondary phases. Overall, we do not report cation concentrations measured on unacidified samples.

III.11.3: Synchrotron filter blank and vegetation mapping

Suspended sediment from the Efri Haukadalsá was filtered onto combusted Glass Fiber Filters. Subsequently, multiple-energy mapping of an unwashed, blank filter at the SLAC National Accelerator Laboratory identified abundant sulfur (Torres et al., 2020). The flourescence response was strong at 2481.0 eV and 2482.5 eV, with no coherent response at the incident energies characteristic of reduced sulfur moities. X-ray absorption spectra of the blank filter were consistent with sulfate and a variable contribution from sulfonate. We note that, if this blank was present in our synchrotron measurements, it could only have existed in observations of supended sediment because X-ray absorption spectra of deposit and vegetation samples were collected directly on raw materials. As argued

previously in Torres et al. (2020), the sulfur blank on the filters used to sample suspended sediment was highly soluble and likely rinsed off during filtration; a blank filter rinsed lightly with water showed a substantially lower flourscence response than an unwashed filter. Moreover, due to attenuation of the incoming X-ray beam, the incident beam was unlikely to penetrate through the sample to the underlying fitler.

III.11.4: Seasonality of precipitation

Two meteorological stations near the Efri Haukadalsá catchment, the Ásgarður station and the Stykkishólm station, have historical data that partially constrained meteoric inputs into the catchment (Figs. III-2 and III-S6). In the historical data both stations typically recorded less precipitation during the summer months than during the winter months (Fig. III-S6A), and both the Ásgarður and Stykkishólm stations also showed summer declines in wind speed (Fig. III-S6B).

Data collected further from the Efri Haukadalsá catchment constrained seasonal changes in precipitation chemistry (Fig. III-S7). Two meteorological stations contributed data on precipitation chemistry as part of the European Monitoring and Evaluation Programme under the Convention on Long-Range Transboundary Air Pollution. A station at Íráfoss (code: IS0002R) has been operational since 1980, and a station at Stórhöfði (code: IS0091R) has been operational since 1995 (Fig. III-2). Íráfoss is inland, while the Stórhöfði station is on an island off the southern coast of Iceland. The amount of precipitation at Íráfoss exhibited a summer reduction, analogous to Ásgarður and Stykkishólmur, while the amount of precipitation at Stórhöfði did not (Figs. III-S7A and B). During the winter months Cl^-/SO_4^{2-}, Cl^-/Ca^{2+}, Cl^-/Na^+, and Cl^-/Mg^{2+} at both the Íráfoss

and Stórhöfði meteorological stations resembled marine ratios (Figs. III-S7C, D, E, and F). During the summer months, the Cl^-/SO_4^{2-} and Cl^-/Ca^{2+} of precipitation at Íráfoss declined substantially (Figs. III-S7C and D, orange curves), while the Cl^-/Na^+ and Cl^-/Mg^{2+} ratios stayed near seawater values.

Values of Cl^-/SO_4^{2-} for summer precipitation, winter precipitation, and annually-integrated precipitation were calculated from measurements of dissolved chemistry reported at Íráfoss (Figs. III-2, III-S7, and III-S8). However, our major ion determinations in summer precipitation samples collected near the Efri Haukadalsá catchment indicated a lower Cl^-/SO_4^{2-} ratio than calculated from the summer data at Íráfoss. We thus considered two possible end-members for annually-integrated precipitation, the first based on direct observations from Íráfoss and the second based on our observations in precipitation samples collected near the Efri Haukadalsá catchment. In either case, we used the mean $\delta^{34}S_{SO4}$ measured in our precipitation samples as the $^{34}S/^{32}S$ ratio of summer precipitation. Motivated by the observation that the major ion chemistry of winter precipitation from both Íráfoss and Stórhöfði resembled seawater (Fig. III-S7), we assumed the $\delta^{34}S_{SO4}$ of winter precipitation equaled the marine value of 21‰. The fractional contribution of summer precipitation to annually-integrated precipitation was then calculated using observations of precipitation intensity from the two meteorological stations close to the Efri Haukadalsá catchment: Ásgarður with 23.1% of annual precipitation in summer, and Stykkishólmur with 22.2% of annual precipitation in summer (Fig. III-2). A summer contribution of 22.6% was thus used to estimate the $\delta^{34}S_{SO4}$, and Cl^-/SO_4^{2-} in one case, of annually-integrated precipitation. Notably, our calculated value for the $\delta^{34}S_{SO4}$ of annually-integrated

precipitation was near the maximum value observed in samples from Langjökull (Gislason and Torssander, 2006).

We thus reached two possible end-members representing annually-integrated precipitation with the same $\delta^{34}S_{SO4}$ but different Cl^-/SO_4^{2-} ratios (Fig. III-S8). In the first end-member, the Cl^-/SO_4^{2-} ratio was derived from direct observations of annual precipitation chemistry at Íráfoss. In the second, the Cl^-/SO_4^{2-} ratio of annual precipitation was calculated from mixing fractions based on precipitation amounts at Ásgarður and Stykkishólm, our samples of summer precipitation, and the winter precipitation chemistry at Íráfoss. The Cl^-/SO_4^{2-} of annual precipitation calculated from the second approach was lower than directly observed at Íráfoss. However, in both cases the majority of river water samples were consistent with mixing between basalt and annually-integrated precipitation. Moreover, differences in the mixing lines due to the different precipitation end-members were somewhat subsumed within uncertainty in the Cl^-/SO_4^{2-} ratio of the basalt end-member. Because it is unlikely that our few observations of precipitation chemistry captured the integrated chemical composition of summer precipitation, our favored annually-integrated precipitation end-member was that derived using the annual Cl^-/SO_4^{2-} observations from Íráfoss.

Previously published observations from several rivers in SW Iceland showed a seasonal transition in Cl^-/SO_4^{2-} and $\delta^{34}S_{SO4}$ (Fig. III-S9; Gislason and Torssander, 2006). This shift may reflect a lowering of summertime precipitation Cl^-/SO_4^{2-} as seen in the precipitation data from Íráfoss. Furthermore, some rivers showed a corresponding decline in $\delta^{34}S_{SO4}$ with decreasing Cl^-/SO_4^{2-}, suggesting that the $\delta^{34}S_{SO4}$ of summer precipitation was lower than the $\delta^{34}S_{SO4}$ of winter precipitation (Fig. III-S9).

III.11.5: River inversion model with Monte Carlo error propagation

Measured $[Ca^{2+}]$, $[Mg^{2+}]$, $[Na^{+}]$, $[K^{+}]$, $[Cl^{-}]$, $[SO_4^{2-}]$, and $\delta^{34}S_{SO4}$ were inverted using a mixing model with Monte Carlo error propagation to calculate the fractional contributions from summer precipitation, winter precipitation, basalt weathering, formation of secondary clays, and carbonate weathering (Table III-S1; Gaillardet et al., 1999). The chemical composition of Icelandic basalts was based on values reported in Torssander (1989), Gislason et al. (1996), and Moulton et al. (2000), the chemistry of clays was after Thorpe et al. (2019), and the carbonate end-member was assumed to be stoichiometric calcite (Table III-S1). The chemistry of summer precipitation was based either on our precipitation samples from near the Efri Haukadalsá or on data from the Íráfoss meteorological station (Fig. III-S8), and the chemistry of winter precipitation was calculated using observations from the Íráfoss meteorological station.

Dissolved chemistry was normalized to the charge-equivalent sum of cations ($\Sigma^{+} = 2*Ca^{2+} + 2*Mg^{2+} + Na^{+} + K^{+}$) (Torres et al., 2016; Kemeny et al., 2021). On each iteration, the values of Ca^{2+}/Σ^{+}, Mg^{2+}/Σ^{+}, Na^{+}/Σ^{+}, K^{+}/Σ^{+}, Cl^{-}/Σ^{+}, SO_4^{2-}/Σ^{+}, and $\delta^{34}S_{SO4}$ were pulled from normal distributions with predefined means and standard deviations. One cation ratio for each end-member was calculated by mass balance to ensure internal consistency, and the entire set of compositions was regenerated if any end-member ratios were negative. Moreover, on each iteration the dissolved chemistry of river samples was altered by values pulled from a distribution with mean of zero and a standard deviation corresponding to analytical precision. Each simulation optimized a cost function for misfit between observations and model results, using proportional misfit for concentration ratios and absolute misfit for $\delta^{34}S_{SO4}$. The fractional contribution of the clay end-member was

constrained to be negative and contributions from all other end-members were constrained to be positive. Solutions were only accepted if each dissolved concentration was reconstructed within 25% and the value of $\delta^{34}S_{SO4}$ was reconstructed within 2‰. The river inversion model was run with and without the carbonate end-member and for two different summer precipitation end-members (Table III-S1).

Prior observations have demonstrated that secondary clay formation occurs throughout Icelandic catchments, with evidence from dissolved major ion concentrations, isotopic ratios, and the chemistry of soils (Gislason et al., 1996; Moulton et al., 2000; Stefánsson and Gislason, 2001; von Strandmann et al., 2006, 2012; Georg et al., 2007; Vigier et al., 2009; Pearce et al., 2010; Hindshaw et al., 2013; Opfergelt et al., 2017). Consistent with this prior work, our inversion model constrained the median consumption of cations by clay formation to be 3-6% of Σ^+ in samples from the Efri Haukadalsá and 15-18% of Σ^+ in samples from the Hvítá catchment (Fig. III-S10). Our results were thus consistent with Hindshaw et al. (2013), who interpreted Ca^{2+} isotope ratios as showing enhanced clay formation in currently glaciated catchments relative to catchments without glaciers. The fractional uptake of cations by clay and the inversion-constrained chemical composition of the clay end-member only changed minimally when also including a calcite end-member in the inversion, as suggested by some interpretations of Ca^{2+} and Sr^{2+} isotope data (Fig. III-S11; Jacobson et al., 2015; Andrews and Jacobson, 2017). Notably, these results were not meant to fully constrain the nature of clay formation or carbonate weathering in the Efri Haukadalsá catchment, but simply to demonstrate that our interpretation of measured $\delta^{34}S_{SO4}$ values was consistent with the broader understanding of active weathering processes in Iceland.

III.11.6: Extended geomorphic analysis

We conducted three analyses to quantitatively relate the topographic structure of the Efri Haukadalsá catchment with river chemistry. The first and third analyses are presented above (Fig. III-8), and results for the second analysis are below (Fig. III-S12). We compared $\delta^{34}S_{SO4}$ to the mean power law exponent *b* for cross sections upstream of each sample site and found that lower $\delta^{34}S_{SO4}$ values are associated with V-shaped profiles (Figs. III-S12A and B). The mean power law exponent upstream of each sample were similar for the two quantitative analyses (Fig. III-S12C).

III.11.7: Additional maps of dissolved chemistry

Our analysis identified spatial gradients in the $\delta^{34}S_{SO4}$ and $[SO_4^{2-}]$ values of river water samples in the Efri Haukadalsá catchment (Fig. III-7). Maps for $[Ca^{2+}]$, $[Mg^{2+}]$, $[Na^{+}]$, $[K^{+}]$, $[Cl^{-}]$ and the sum of cations $[\Sigma^{+}]$ are below (Fig. III-S13).

III.11.8: Chemostatis in the Efri Haukadalsá

River water samples in this study that were collected close in space were also often collected close in time, meaning that it is formally possible that our observations of spatial structure in dissolved chemistry reflected sampling bias. That is, if the Efri Haukadalsá had a uniform isotopic composition that changed on a timescale of hours to days, our sampling could theoretically have reflected whole-river changes in isotopic composition rather than strong morphologic control on $\delta^{34}S_{SO4}$. We rejected this possibility on the basis of two experiments: sampling many locations along the Efri Haukadalsá within a single day and sampling the same locations at multiple times.

On July 30th, 2019 we collected 21 river water samples along the lower and middle reaches of the Efri Haukadalsá (Fig. III-S14). The $\delta^{34}S_{SO4}$ of these samples ranged from 3.0‰ to 16.0‰ and reflected the same isotopic structure seen in our full sample suite. Samples from tributary 1 and tributary 3 had low $\delta^{34}S_{SO4}$ values, the river near the moraine had high $\delta^{34}S_{SO4}$ values, and the lower valley had intermediate $\delta^{34}S_{SO4}$ values. Moreover, locations sampled multiple times over a single field season or across field seasons retained their chemical characteristics. For example, river water samples LHWS19-04 and LHWS19-25 were collected from the same location in the Efri Haukadalsá on July 28th and July 30th of 2019, respectively. These samples had extremely similar [SO_4^{2-}] values of 12.2 μM and 12.9 μM, as well as indistinguishable $\delta^{34}S_{SO4}$ values of 12.8‰ and 12.6‰, respectively. Samples collected in 2016 and 2019 from either a tributary (LHWS16-11, LHWS19-03) or the Efri Haukadalsá mainstem (LHWS16-08d, LHWS19-9) were also similar despite the three years separating sample collection (Table III-S2). These data showed that the Efri Haukadalsá was not isotopically uniform at any instant, that chemical gradients were sustained through time, and that our observation of spatial structure in $\delta^{34}S_{SO4}$ was not a sampling artifact.

III.11.9: Temporal changes in Haukadalsvatn chemistry

We collected one sample of lake water from Haukadalsvatn in 2016 and another in 2019. The two samples had relatively similar [SO_4^{2-}] values, 14.6 μM and 17.0 μM, and similar $\delta^{34}S_{SO4}$ values of 14.9‰ and 12.7‰. However, the value of [Cl^-] in the two samples was quite different, with the 2016 sample having 340 μM and the 2019 sample having 186 μM, resulting in Cl^-/SO_4^{2-} values of 23.3 and 10.9, respectively. The 2016 sample was also

enriched by a factor of 1.4 to 1.7 in the values of [Ca^{2+}], [Mg^{2+}], [Na^{+}], and [K^{+}] relative to the 2019 sample. A 2016 sample collected near the lake outflow had chemical concentrations mostly intermediate between the two lake samples, although with higher [SO_4^{2-}]. Moreover, the 2016 and 2019 lake samples differed in [SO_4^{2-}] from a sample previously collected from Haukadalsvatn reported in Langdon et al. (2008).

The residence time of water in Haukadalsvatn is only approximately 2-3 months, as calculated using a discharge of 13.4 m^3/sec and depth estimates from the bathymetry map of Geirsdóttir et al. (2009). Such a short residence time indicated that observed chemical changes could reflect short-term changes in lacustrine dynamics. However, the observed chemical differences may also be attributable to sampling location; the 2016 sample was collected from the lake shore in extremely shallow water, while the more dilute 2019 sample was collected while standing in the lake approximately 10 meters from shore in >1 m water depth. The differences between the 2016 and 2019 samples could thus reflect either terrestrial runoff or inputs from shallow sediment to the perimeter of the lake.

III.11.10: Rayleigh model for sediment $\delta^{34}S$

We modeled the Cl^-/SO_4^{2-} and $\delta^{34}S_{SO4}$ values of river water samples as reflecting the mixing of basalt and annually-integrated precipitation (Eqs. III-S1 and III-S2) followed by closed-system fractionation (Eq. III-S3). Our model had two measured parameters, Cl^-/SO_4^{2-} and $\delta^{34}S_{SO4}$, and three unknowns: the basalt mixing fraction (f_{mix}), the fraction of SO_4^{2-} remaining ($f_{remaining}$), and the isotope effect of the SO_4^{2-}-consuming process ($^{34}\alpha$). As described, we estimated that no more than 10% of the initial SO_4^{2-} budget was likely reduced to S_{org}, and thus constrained the model to have 90% of initial SO_4^{2-} remaining

($f_{remaining}$=90%; we used the range 85-95% as error bars on the calculation). We then optimized a cost function $\mathbf{c}(f_{mix}, {}^{34}\alpha)$ for the mixing fraction and isotope effect that minimized proportional misfit from observations (Eq. III-S4; Figs. III-S15A and B) and solved for the $\delta^{34}S$ of sulfur that would be produced from the fractionating process (Figs. III-S15E and F). The calculation found isotope effects lower in magnitude than commonly expected for MSR (Figs. III-S15C and D). Moreover, the model predicted sediment $\delta^{34}S$ values lower than observed, leading us to conclude that observed S_{org} phases were not derived from microbial SO_4^{2-} reduction. Rather, we concluded that S_{org} likely formed from SO_4^{2-} assimilation and reduction within biomass.

$$ {}^{34}R_{mix} = {}^{34}R_{VCDT}\left(f_{mix}\left(\frac{\delta^{34}S_{basalt}}{10^3}+1\right)+(1-f_{mix})\left(\frac{\delta^{34}S_{precipitation}}{10^3}+1\right)\right) \quad \text{(III-S1)} $$

$$ \left(\frac{Cl^-}{SO_4^{2-}}\right)_{model} = \frac{\left(f_{mix}\left(\frac{Cl^-}{SO_4^{2-}}\right)_{basalt}+(1-f_{mix})\left(\frac{Cl^-}{SO_4^{2-}}\right)_{precipitation}\right)}{f_{remaining}} \quad \text{(III-S2)} $$

$$ \delta^{34}S_{model} = \left(\frac{{}^{34}R_{mix}*(f_{remaining})^{{}^{34}\alpha-1}}{{}^{34}R_{VCDT}}-1\right)10^3 \quad \text{(III-S3)} $$

$$ \mathbf{c}(f_{mix}, {}^{34}\alpha) = \sqrt{\left(\frac{\delta^{34}S_{river}-\delta^{34}S_{model}}{\delta^{34}S_{river}}\right)^2+\left(\frac{\left(\frac{Cl^-}{SO_4^{2-}}\right)_{river}-\left(\frac{Cl^-}{SO_4^{2-}}\right)_{model}}{\left(\frac{Cl^-}{SO_4^{2-}}\right)_{river}}\right)^2} \quad \text{(III-S4)} $$

III.12: Supplementary figures

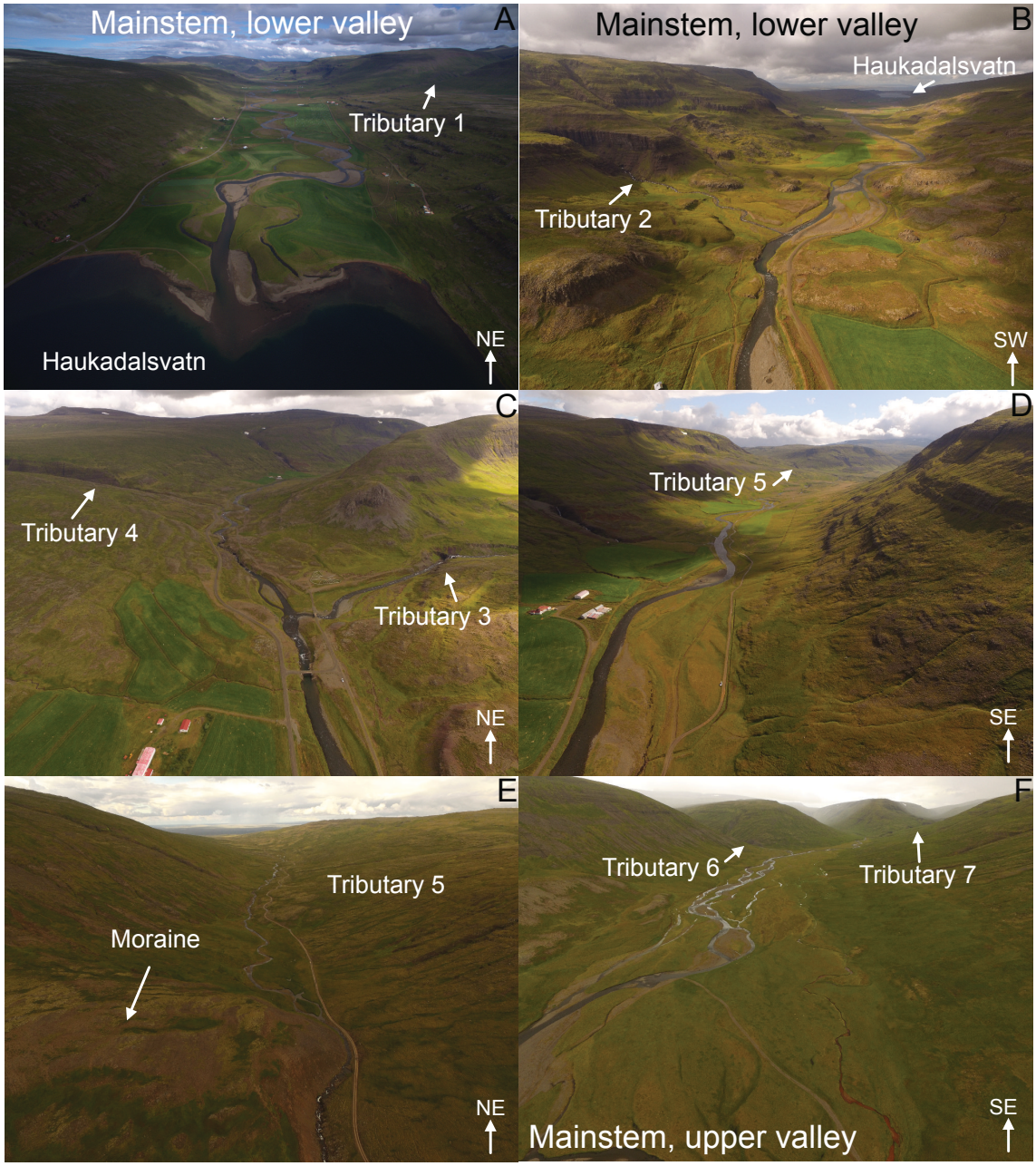

Fig. III-S1: Drone images of the Efri Haukadalsá catchment. (A) The lower valley of the catchment viewed from the mouth of Haukadalsvatn and (B) from slightly upstream of the confluence with tributary 2. (C) Confluence of tributary 3 with the Efri Haukadalsá, with tributary 4 also visible. (D) The Efri Haukadalsá between the two knickzones. (E) Tributary 5, which partially drains the moraine. (F) The upper valley of the catchment, with tributary 6 and tributary 7 visible. Arrows in bottom right of each panel indicate approximate image orientation.

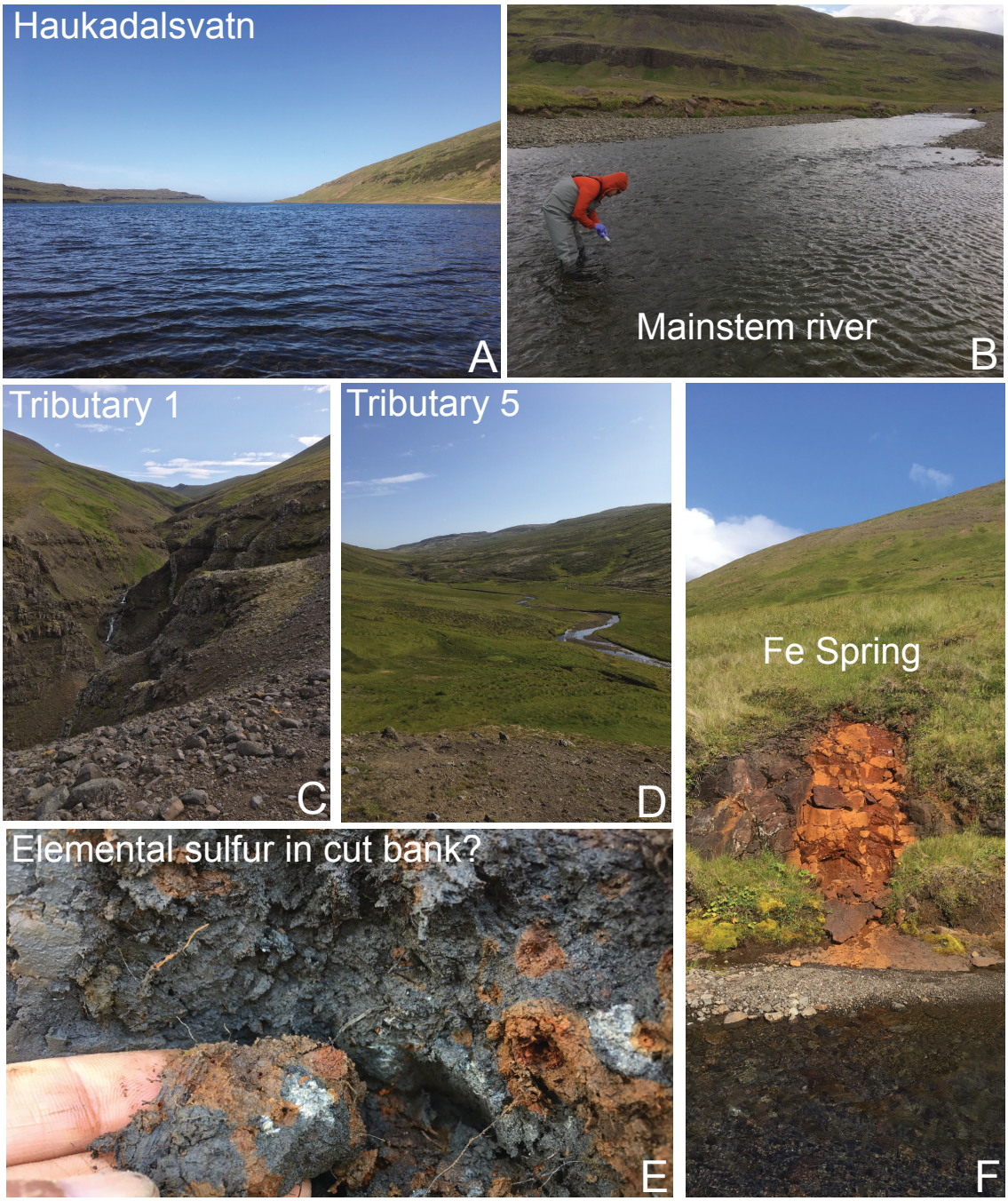

Fig. III-S2: Photographs of the Efri Haukadalsá catchment. (A) Lake Haukadalsvatn viewed from the junction with the Efri Haukadalsá. (B) Collecting a water sample from the mainstem river. The person in this image is ~ 2 m tall. (C) Tributary 1, several hundred meters upstream of the confluence with the mainstem. (D) Tributary 5, as seen from the moraine. (E) The smell of white material observed in a cutbank of the lower valley suggested sulfur, but this was not experimentally confirmed. (F) Example of a Fe spring, which are found throughout the Efri Haukadalsá catchment.

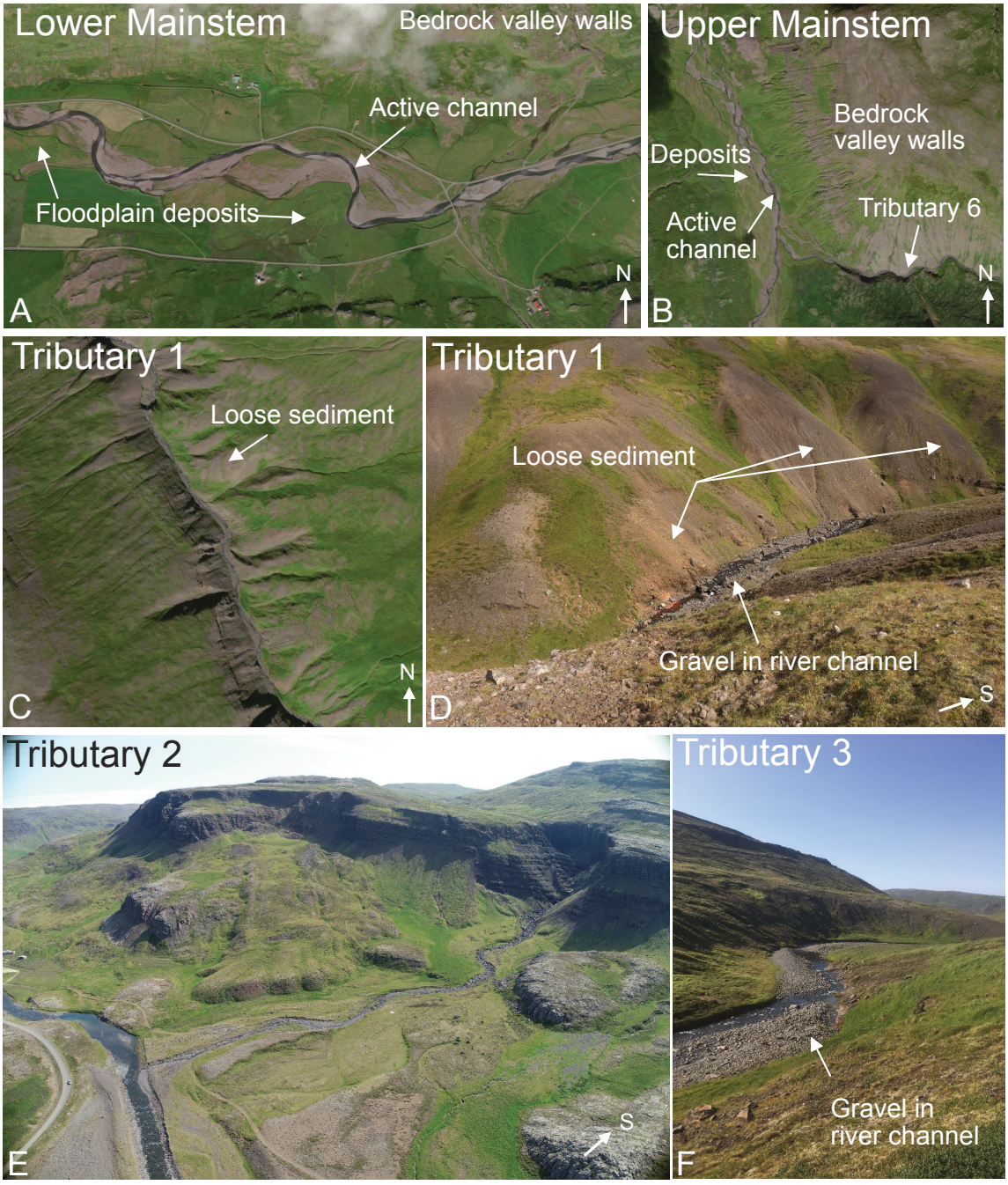

Fig. III-S3: Satellite and drone images of the Efri Haukadalsá catchment. (A, B, C) Satellite images from Google Earth and (D, E, F) drone and hand-held photographs of tributaries in the Efri Haukadalsá catchment. (A) The lower mainstem river with floodplain deposits and bedrock valley walls. In this reach the Efri Haukadalsá is a meandering, alluvial river with wide floodplain disconnected from bedrock sources. (B) The upper mainstem river. (C) Satellite and (D) hand-held photograph of tributary 1 with loose sediment and gravel in the river channel. (E) Drone photograph of tributary 2 and (F) hand-held photograph of tributary 3. Arrows in the bottom-right of each panel indicate approximate image orientation.

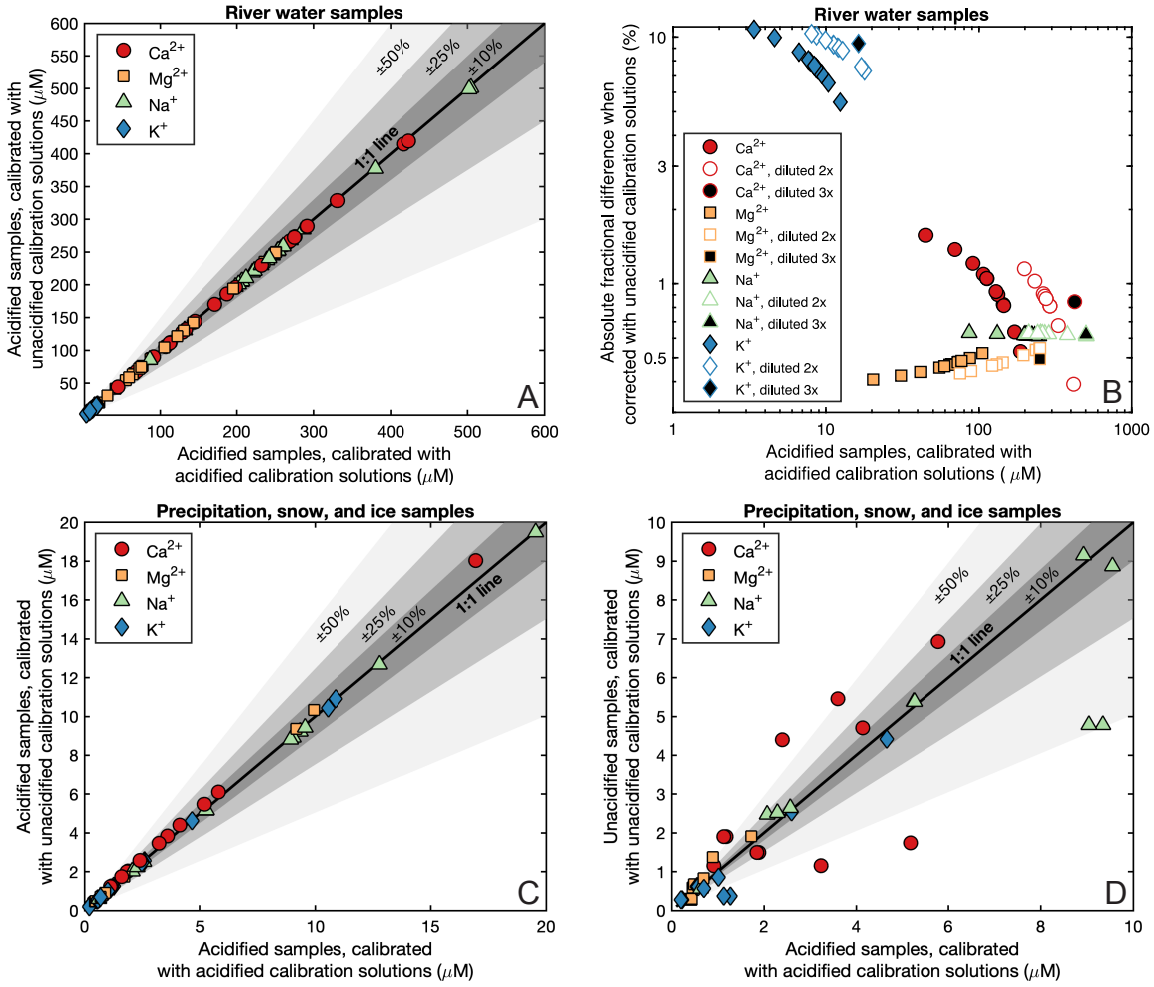

Fig. III-S4: Cation chromatography measurements. (A) [Ca^{2+}], [Mg^{2+}], [Na^{+}], and [K^{+}] determined on acidified river water samples calibrated with either acidified or unacidified calibration solutions. (B) The fractional difference of the two determinations was minimal for all cations other than K^{+}, where the absolute difference was minimal (~1 μM). (C) [Ca^{2+}], [Mg^{2+}], [Na^{+}], and [K^{+}] determined on acidified precipitation, snow, and ice samples calibrated with either acidified or unacidified calibration solutions. (D) The calibrated values of [Ca^{2+}], [Mg^{2+}], [Na^{+}], and [K^{+}] determined on unacidified precipitation, snow, and ice samples calibrated with unacidified solutions plotted against values determined on acidified precipitation, snow, and ice samples calibrated with acidified solutions. The lack of agreement between the acidified and unacidified samples precludes using unacidified splits of precipitation samples to quantify [Ca^{2+}], [Mg^{2+}], [Na^{+}], and [K^{+}] in cases where no acidified split was collected.

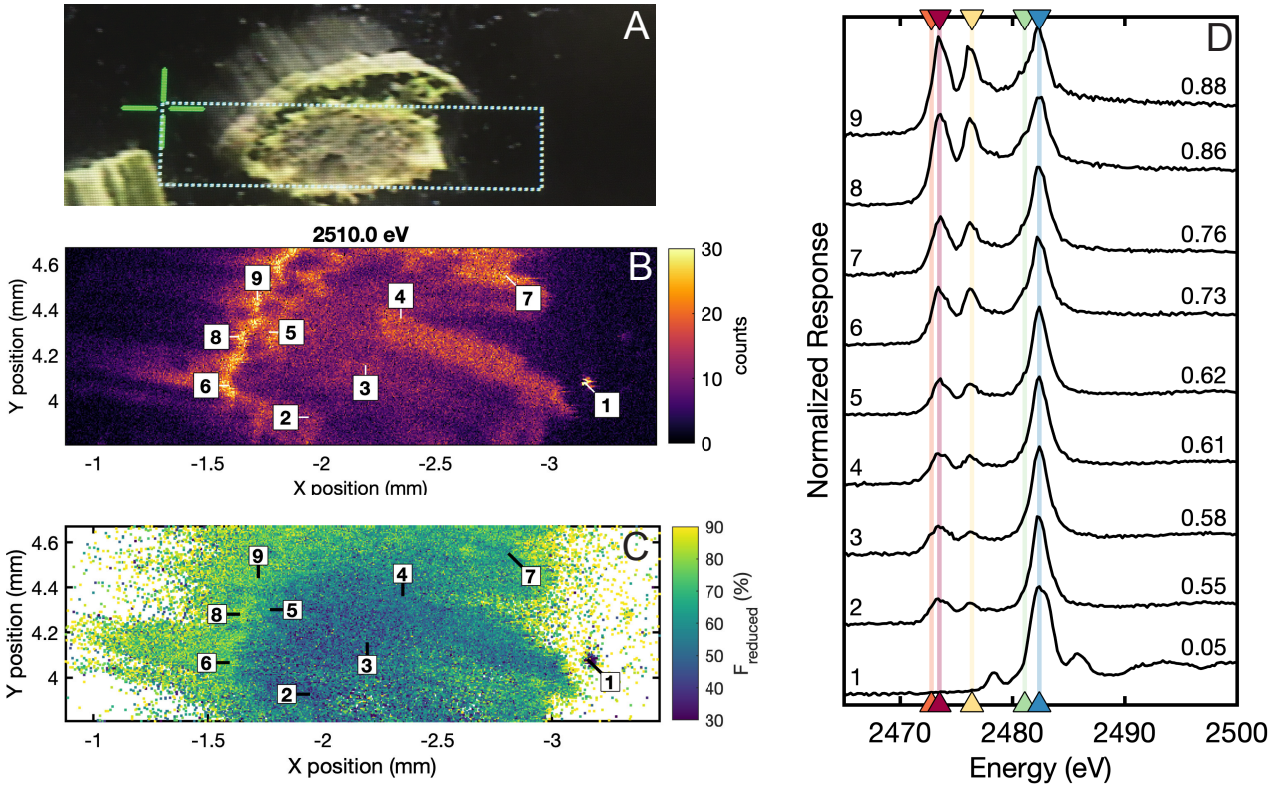

Fig. III-S5: Synchrotron analysis of vegetation cross section. (A) Photograph of LHVS19-01 cross section, with dotted box indicating the approximate region of synchrotron analysis. (B) Fluorescence response at an incident energy of 2510.0 eV. This incident energy is above the sulfur K-edge and the response qualitatively reflected the abundance of S at each pixel. Cells along the outer surface of the cross section were enriched in S relative to those inside. (C) Pixel-by-pixel fitting of multiple energy maps to reference spectra from the ID 21 database of the European Synchrotron Radiation Facility. Each pixel indicates the value of $F_{reduced}$, which is the sum of fractional contributions from disulfide, thiol, and sulfoxide relative to the sum of all fractional contributions. Sulfur along the outer surface of the sample was reduced relative to sulfur inside. (D) X-ray absorption spectra collected at the indicated points of (B) and (C) identified a variety of reduced and oxidized S moieties. The numbers on the right of each spectra are $F_{reduced}$ values. Lines indicate characteristic locations for fluorescence peaks corresponding to disulfide (orange), thiol (red), sulfoxide (yellow), sulfonate (green), and sulfate (blue).

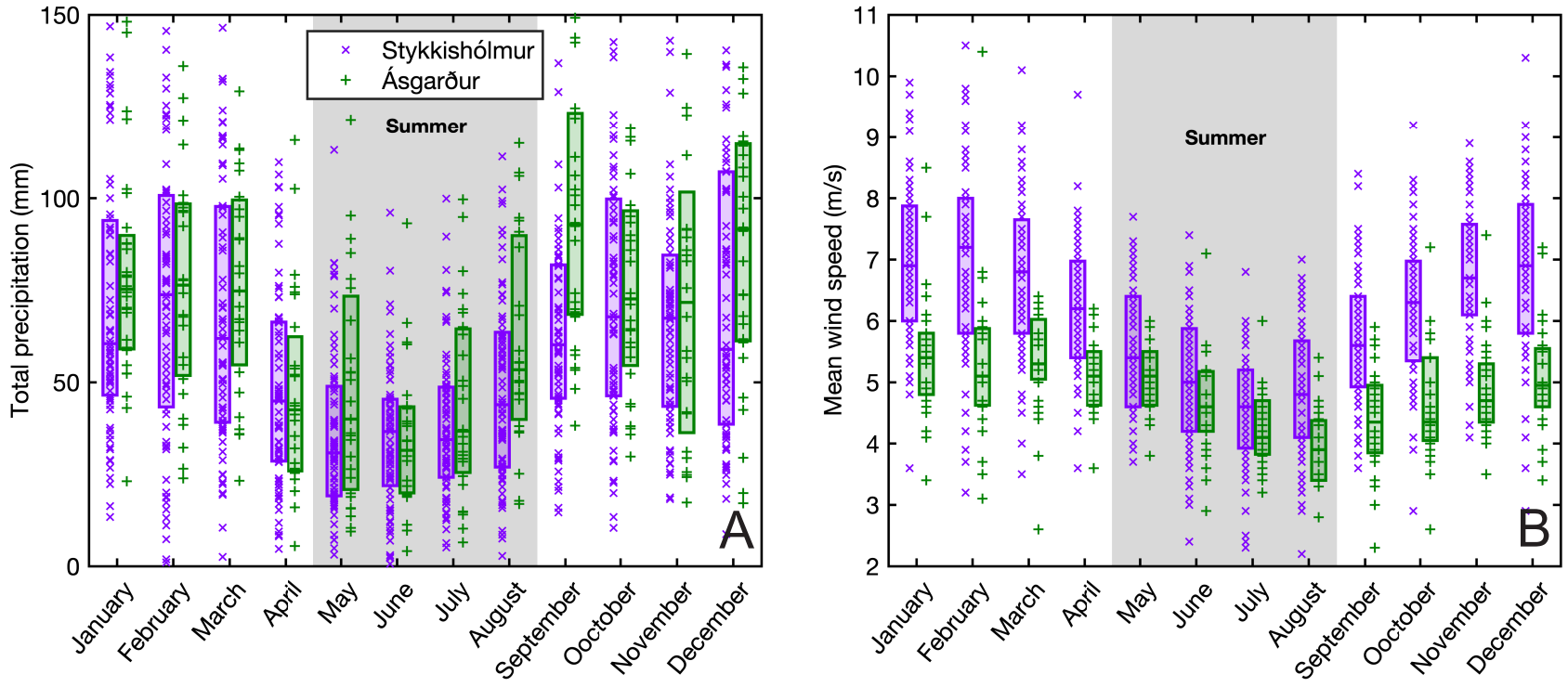

Fig. III-S6: Seasonality in precipitation and wind speed at the Ásgarður and Stykkishólmur meteorological stations. (A) Monthly amount of precipitation and (B) wind speed. Shaded boxes extend from the 25th to the 75th percentile of observed values for each month. At both stations precipitation and wind speed were lower during the summer season than during the rest of the year. The locations of the Ásgarður and Stykkishólmur meteorological stations are indicated in Fig. III-2B.

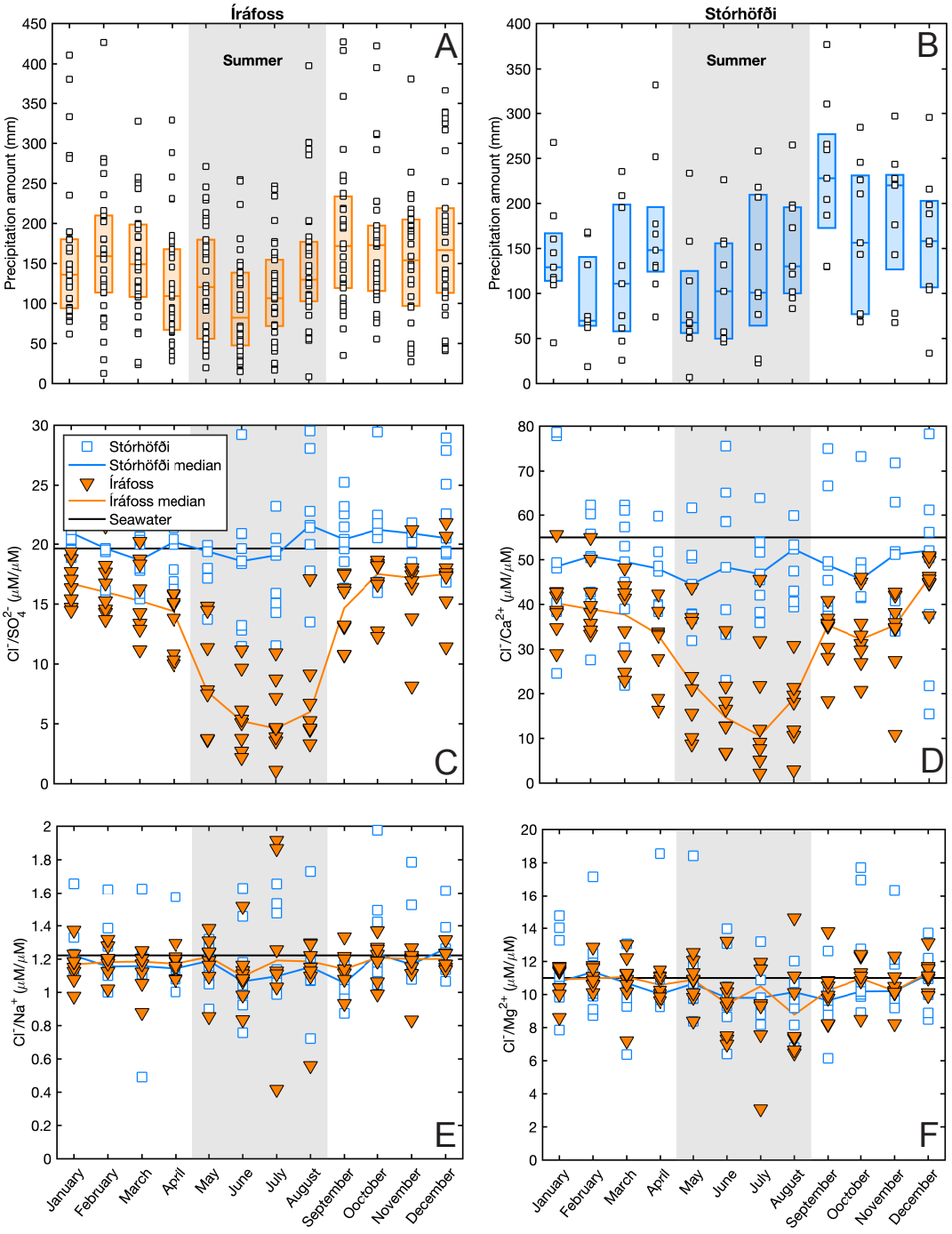

Fig. III-S7: Seasonal changes in the (A, B) amount of precipitation and (C, D, E, F) ion chemistry at Íráfoss from 2006-2016 and Stórhöfði from 2002-2015. (A) There was generally less precipitation at Íráfoss during summer months than winter months, while (B) precipitation at Stórhöfði did not show clear seasonal behavior. (C) Cl^-/SO_4^{2-} and (D) Cl^-/Ca^{2+} were lower at Íráfoss during the summer months, while at Stórhöfði both ratios were relatively constant near seawater values. (E) Cl^-/Na^+ and (F) Cl^-/Mg^{2+} were constant near seawater values throughout the year at both Íráfoss and Stórhöfði. The location of the Íráfoss station is indicated in Fig. III-2A.

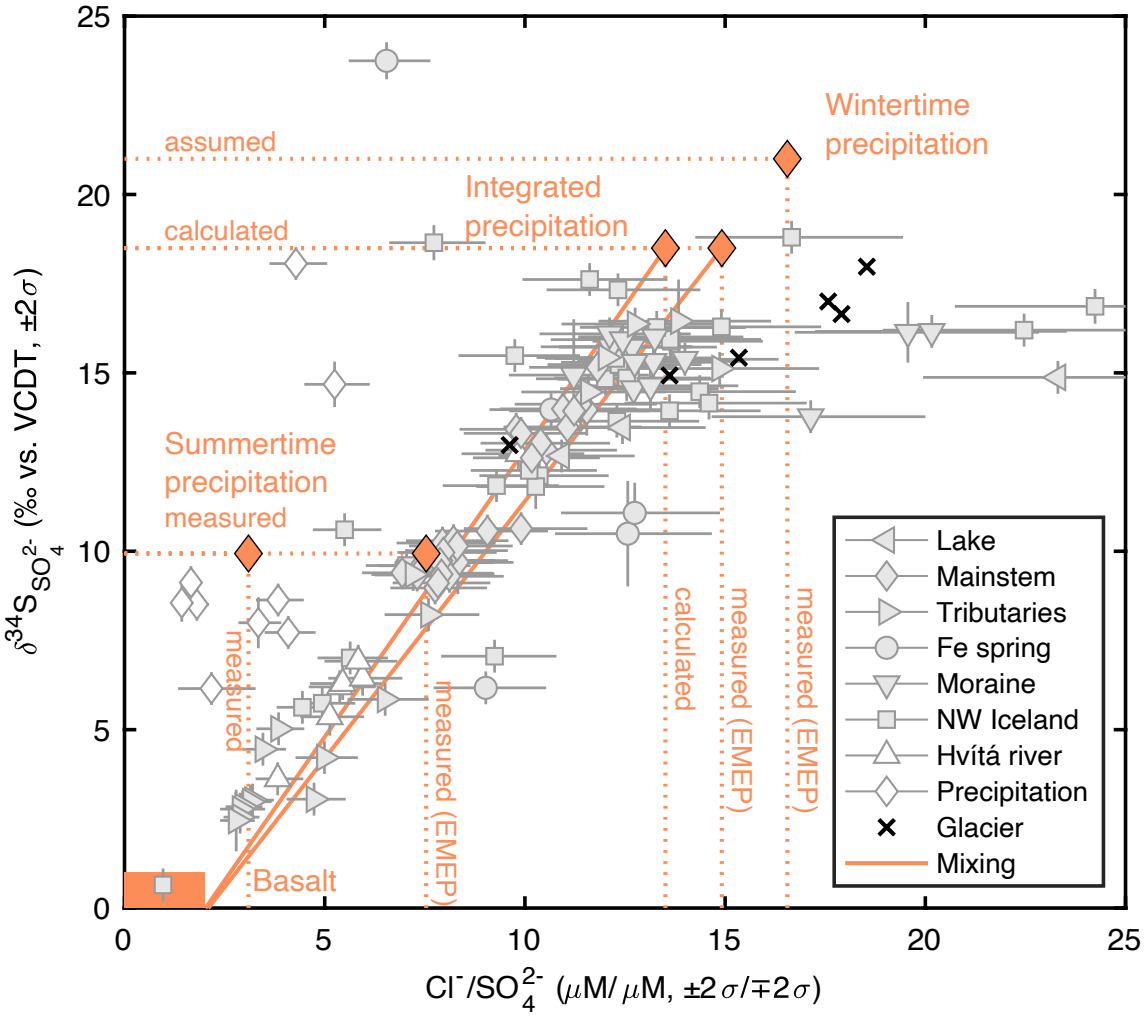

Fig. III-S8: Sulfur isotope mixing diagram. River $\delta^{34}S_{SO4}$ against Cl^-/SO_4^{2-} with precipitation and basalt end-members. Note that two possible chemical compositions are plotted for summer precipitation and annually-integrated precipitation. Clay and carbonate end-members are not plotted because they do not contain SO_4^{2-} (Table III-S1). EMEP refers to data from Íráfoss measured as part of European Monitoring and Evaluation Programme.

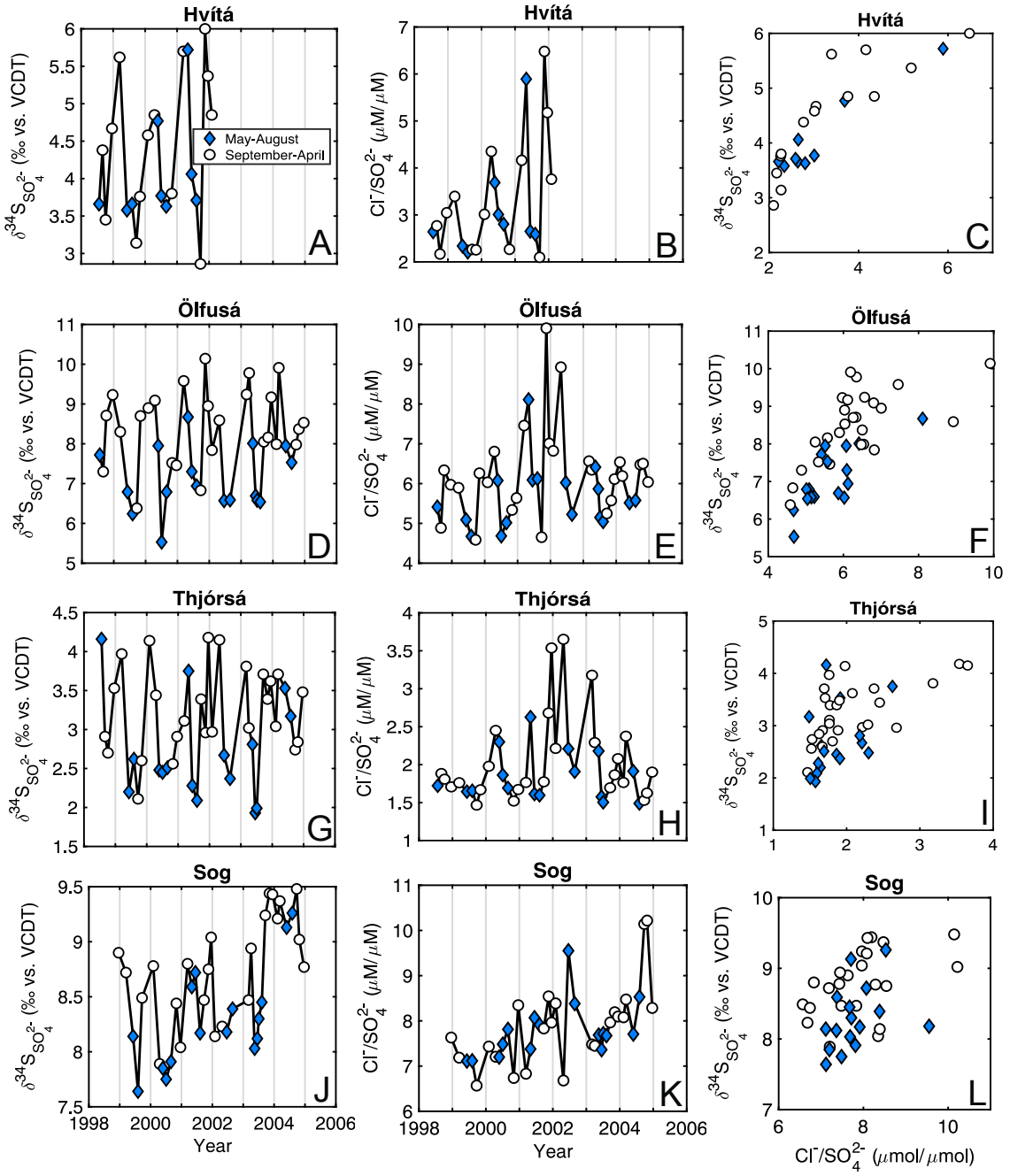

Fig. III-S9: Seasonal changes in $\delta^{34}S_{SO4}$ and Cl^-/SO_4^{2-} of four rivers in Iceland. (A, B, C) The Hvítá River, (D, E, F) the Ölfusá River, (G, H, I) the Thjórsá River, and (J, K, L) the Sog river. Overall, river $\delta^{34}S_{SO4}$ and Cl^-/SO_4^{2-} appear lower during the summer months (blue diamonds) than during the remainder of the year (white circles). These data were consistent with summer changes in precipitation to lower $\delta^{34}S_{SO4}$ and Cl^-/SO_4^{2-} values. All measurements are from Gislason and Torssander (2006), replotted here.

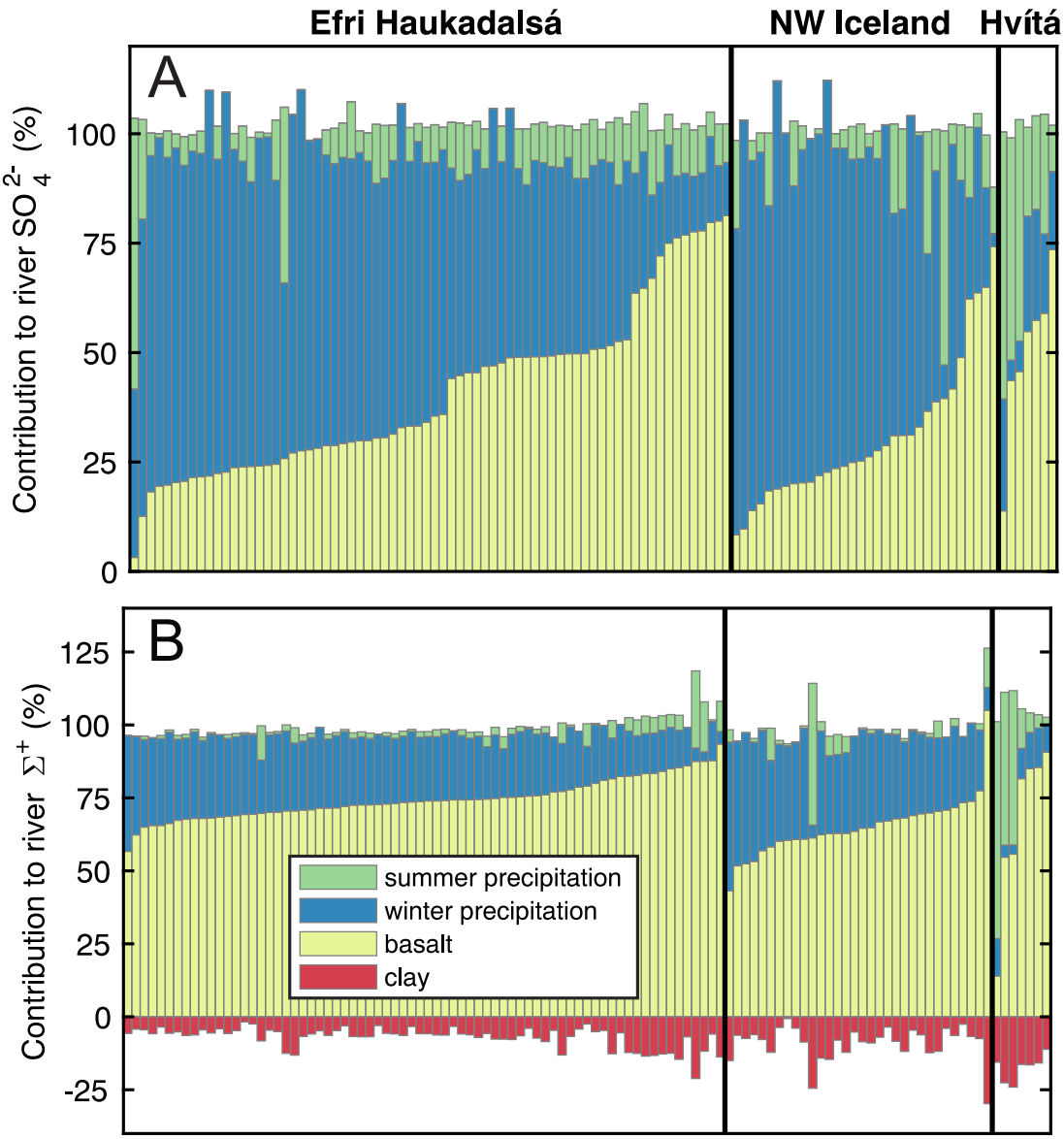

Fig. III-S10: Inversion results for the fractional contributions of summer precipitation, winter precipitation, basalt weathering, and clay formation to measured (A) [SO_4^{2-}] and (B) [Σ^+]. The clay end-member plots as a negative contribution to [Σ^+] because it removes cations from solution and does not contribute to [SO_4^{2-}] because it does not contain SO_4^{2-} (Table III-S1). Results are for an inversion where summer precipitation Cl^-/SO_4^{2-} reflects measurements in samples collected near the Efri Haukadalsá catchment.

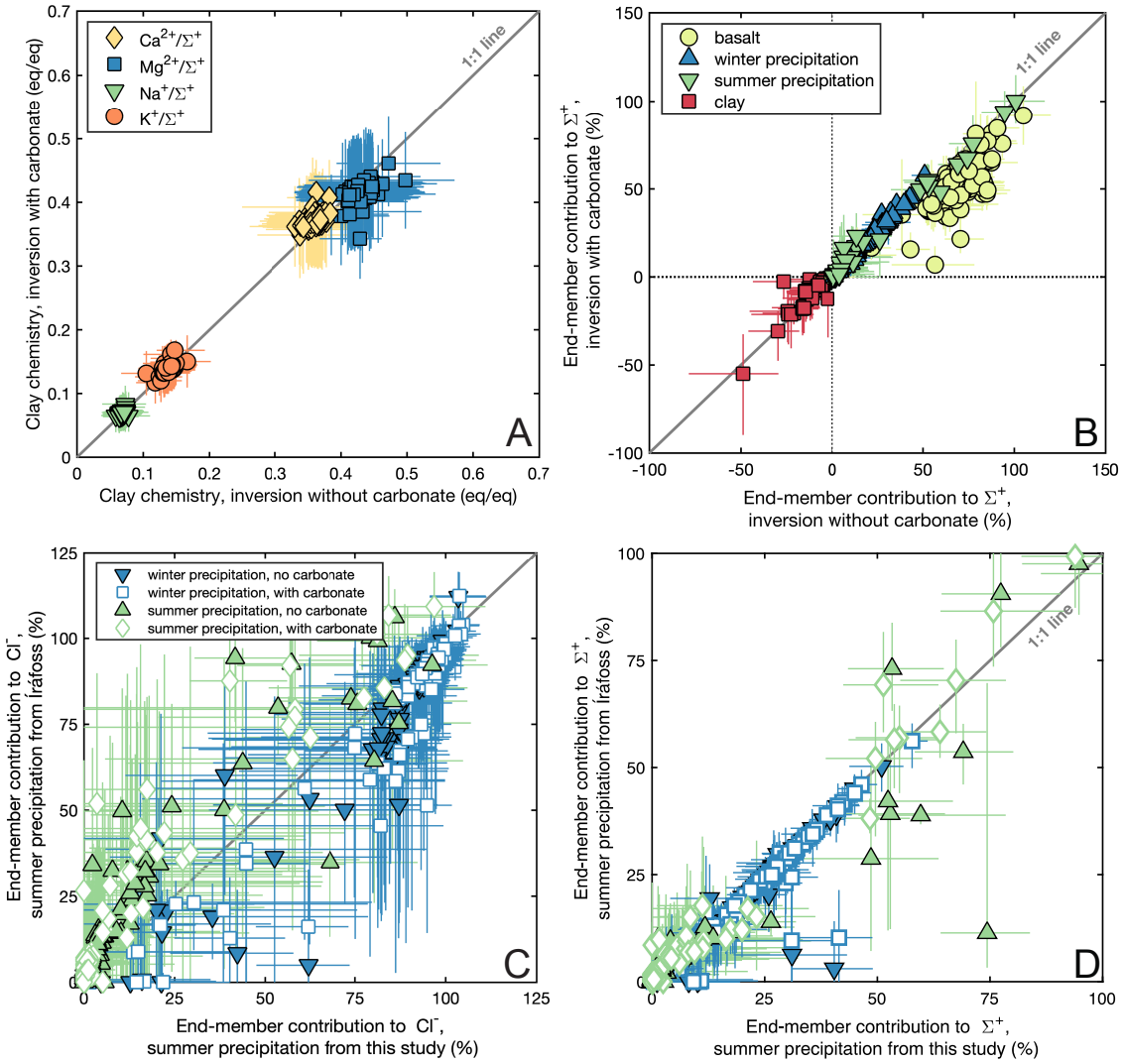

Fig. III-S11: Results of inversion models with Monte Carlo error propagation. (A) Comparison of Mg^{2+}/Σ^{+}, Ca^{2+}/Σ^{+}, Na^{+}/Σ^{+}, and K^{+}/Σ^{+} of the clay end-member in calculations with and without a carbonate end-member. The inversion-constrained chemistry of the clay end-member was similar in the two cases, although shifted to slightly higher Ca^{2+}/Σ^{+} and slightly lower Mg^{2+}/Σ^{+} when carbonate was included in the inversion. (B) Contribution of basalt, clay, summer precipitation, and winter precipitation to Σ^{+} in inversions with and without a carbonate end-member. The inversion results were again similar for the two cases. (C) The fractional contribution of summer (green symbols) and winter precipitation (blue symbols) to river $[Cl^{-}]$ or (D) $[\Sigma^{+}]$ in inversions with (open symbols) and without (closed symbols) a carbonate end-member when summer precipitation was either our observations in samples collected near the Efri Haukadalsá or observations from the Íráfoss meteorological station. The choice of precipitation end-member mostly had a minimal impact on results, but did substantially change the fractional contribution of summertime precipitation for several samples. Error bars in all panels range from the 25th to 75th percentile of accepted inversion results.

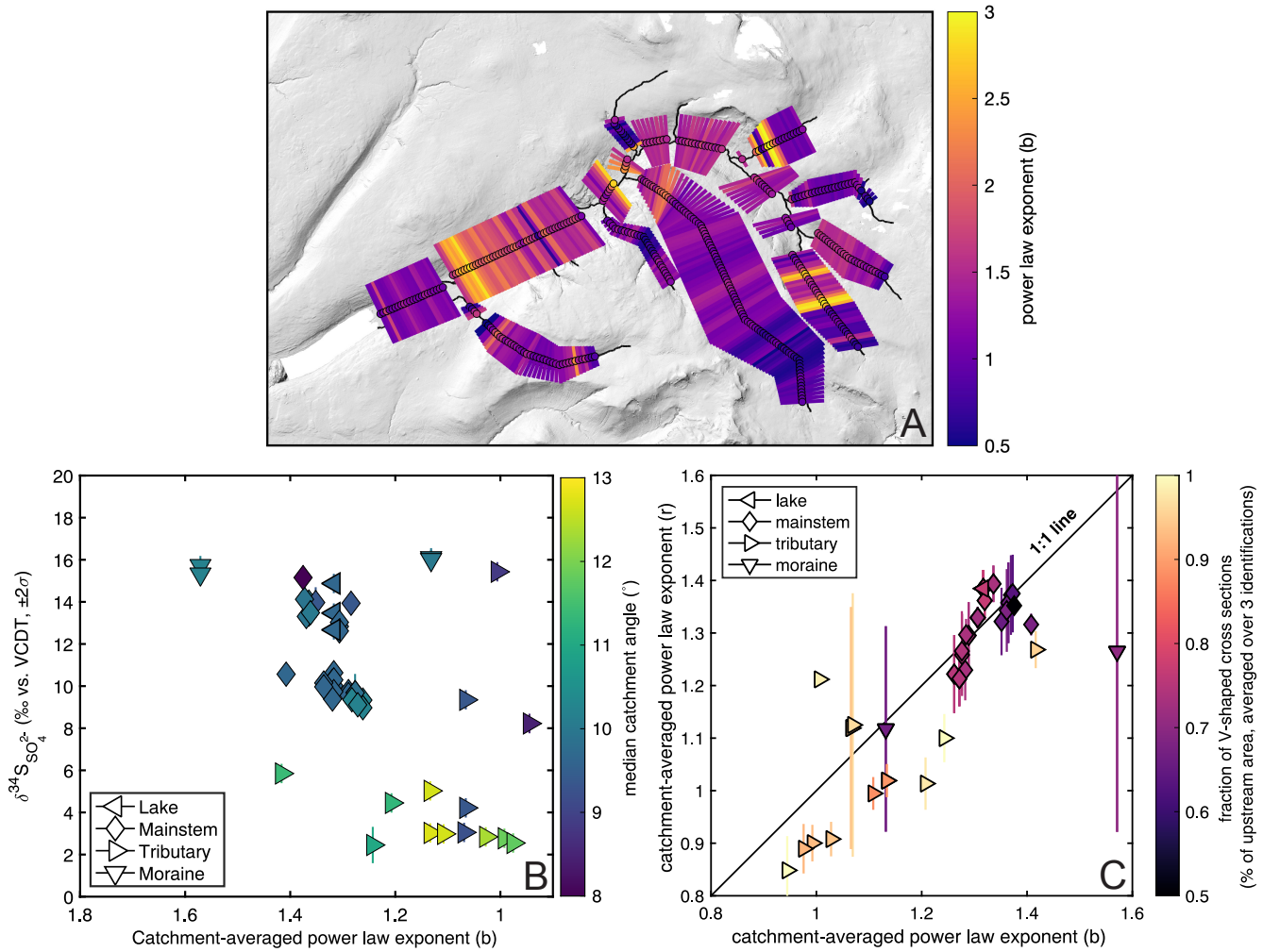

Fig. III-S12: Results of quantitative cross section fitting. To calculate the mean power law exponent (*b*), each cross section was split at a center point and the two sides were independently fit to power law functions. (A) Map of *b* for each profile. (B) Values of $\delta^{34}S_{SO4}$ against the mean *b* upstream of each sampling site. Lower values of $\delta^{34}S_{SO4}$ were associated with V-shaped cross sections. (C) Comparison of the power law exponent calculated as the mean of the two-sided fits (*b*) against the single power-law exponent fit (*r*) after Allen et al. (2018) coded by the fraction of upstream V-shaped cross section identified manually. The three approaches were largely in mutual agreement.

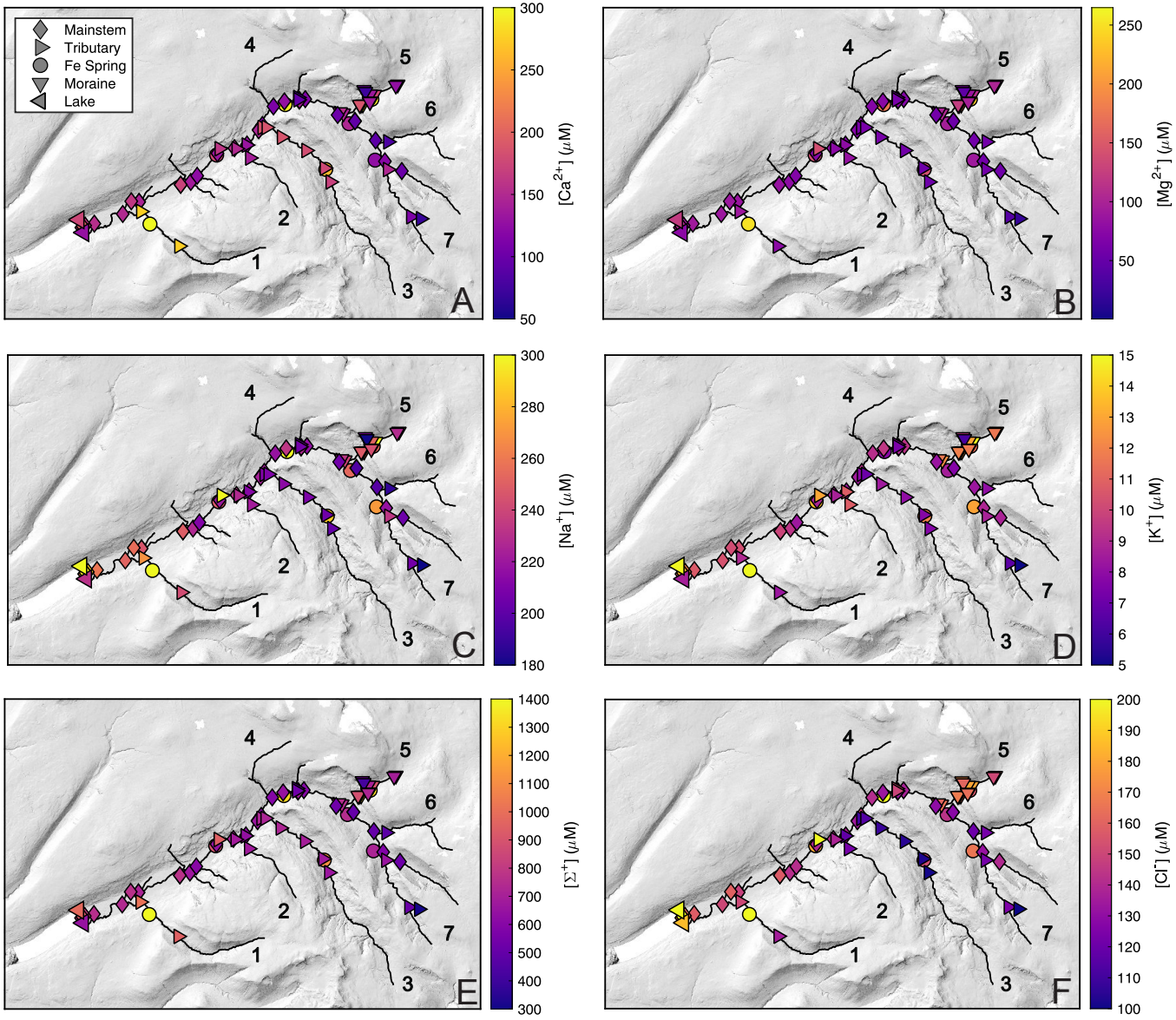

Fig. III-S13: Dissolved chemistry of river water samples collected throughout the Efri Haukadalsá. (A) $[Ca^{2+}]$, (B) $[Mg^{2+}]$, (C) $[Na^{+}]$, (D) $[K^{+}]$, (E) $[\Sigma^{+}]$, and (F) $[Cl^{-}]$.

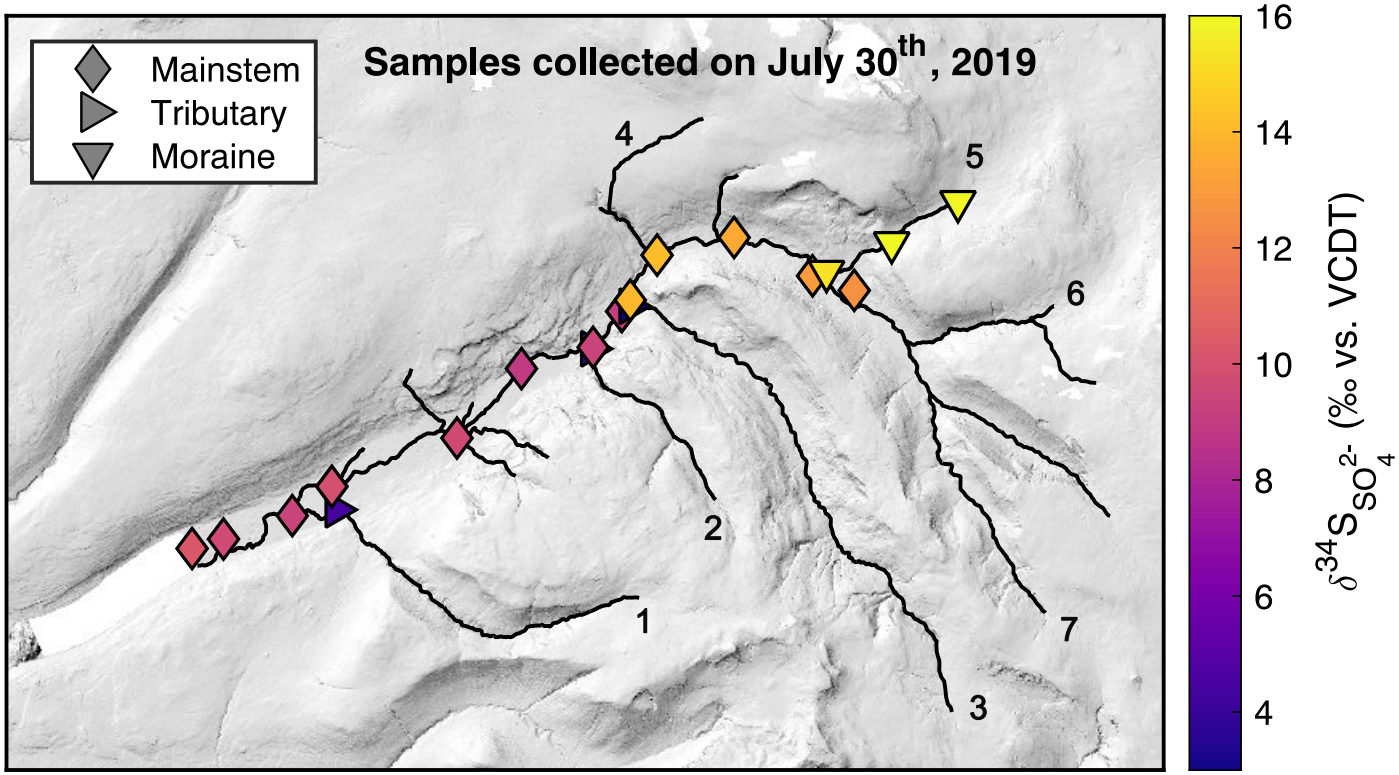

Fig. III-S14: Values of river water $\delta^{34}S_{SO4}$ in samples collected on a single day throughout the Efri Haukadalsá catchment. Consistent with our full sample suite, values of $\delta^{34}S_{SO4}$ were low in tributaries 1, 2, and 3, elevated in the upper valley and tributary 5, and intermediate in the lower valley. These results led us to conclude that the observed patterns in $[SO_4^{2-}]$ and $\delta^{34}S_{SO4}$ did not reflect whole-river changes giving the appearance of spatial organization due to sampling artifacts.

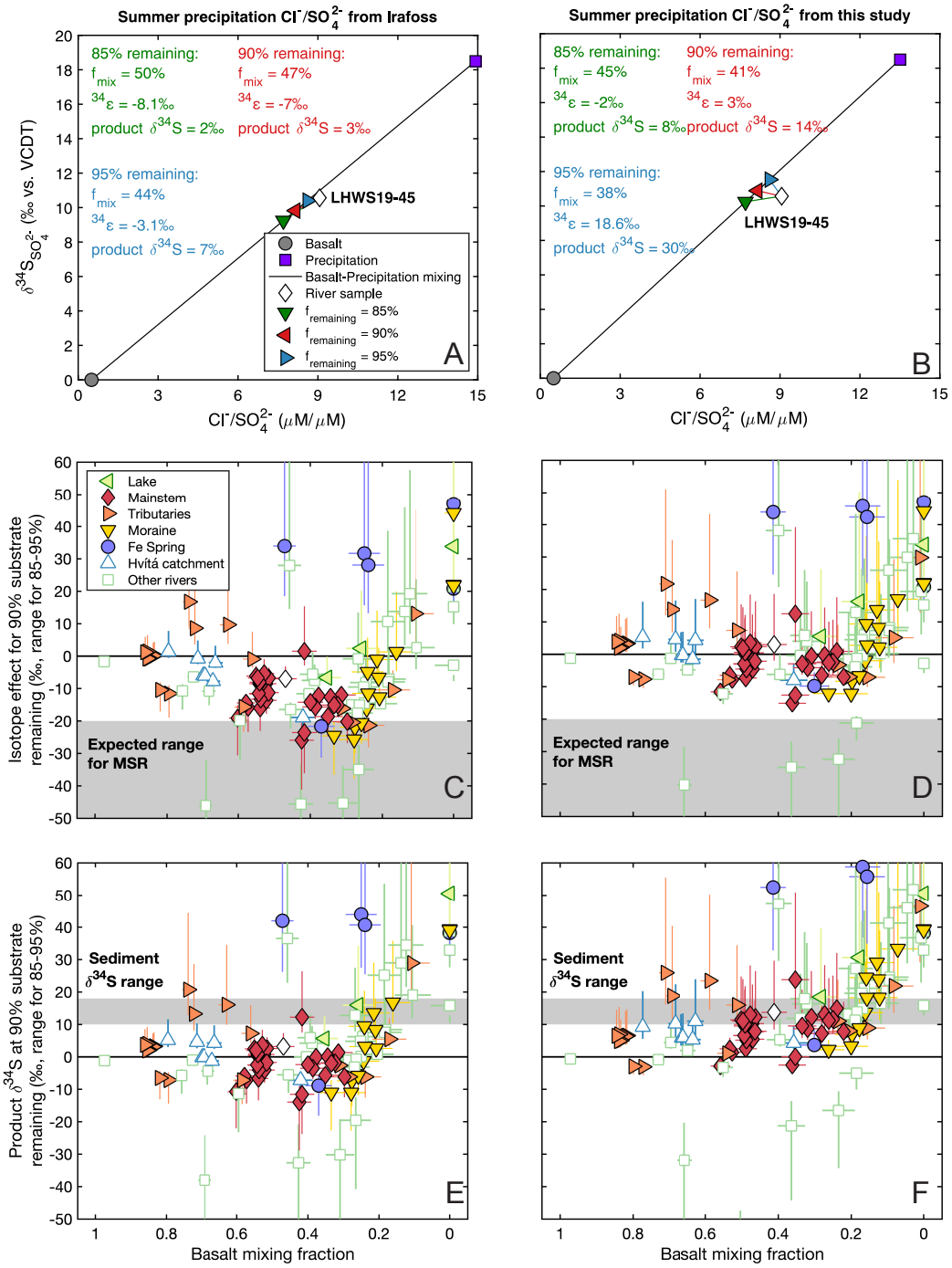

Fig. III-S15: Rayleigh calculations. (A, B) Example for sample LHWS19-45. (C, D) The isotope effect and (E, F) integrated product $\delta^{34}S$ required to explain deviations from mixing of basalt and annually-integrated precipitation when 90% of SO_4^{2-} remains in solution (range is given for 85-95%). While the isotope effects were potentially consistent with MSR, the required $\delta^{34}S$ of the product was lower than measured sediment $\delta^{34}S$. Panels (A, C, E) show results when the annually-integrated precipitation end-member has Cl^-/SO_4^{2-} derived using data at Íráfoss, and panels (B, D, F) show results when the annually-integrated precipitation end-member has Cl^-/SO_4^{2-} derived from our samples of summer precipitation collected near the Efri Haukadalsá catchment.

III.13: Supplementary tables

Table III-S1: End-member values and distributions for Monte Carlo inversion model. Values for integrated precipitation (final two rows of the table) are not used in the Monte Carlo inversion model but are provided here as the $\delta^{34}S_{SO4}$ and Cl^-/SO_4^{2-} ratios are used in the Rayleigh model calculations described below (III.11.10). The chemistry of basalt was calculated from measurements presented in Torssander (1989), Gislason et al. (1996), and Moulton et al. (2000), the chemistry of summertime and wintertime precipitation was calculated from precipitation samples collected near the Efri Haukadalsá and measurements reported as part of the European Monitoring and Evaluation Programme, and the chemistry of clays was calculated using measurements from Thorpe et al. (2019). The chemistry of the carbonate end-member was a stoichiometric calcite.

End-Member	Ca^{2+}/Σ^+	Mg^{2+}/Σ^+	Na^+/Σ^+	K^+/Σ^+	Cl^-/Σ^+	SO_4^{2-}/Σ^+	Cl^-/SO_4^{2-}	$\delta^{34}S_{SO4}$
Basalt	0.48 ± 0.06	0.39 ± 0.11	0.12 ± 0.07	0.01 ± 0.02	0.00 ± 0.00	0.00 - 0.25	0	-2.0 - 2.5
Summer prec. (Íráfoss)	0.09 ± 0.06	0.16 ± 0.03	0.69 ± 0.09	0.06 ± 0.06	0.91 ± 0.30	0.24 ± 0.12	7.5	9.9 ± 3.8
Summer prec. (Efri Haukadalsá)	0.34 ± 0.21	0.09 ± 0.04	0.47 ± 0.18	0.09 ± 0.04	0.49 ± 0.16	0.34 ± 0.20	3.1	9.9 ± 3.8
Winter prec.	0.05 ± 0.02	0.17 ± 0.02	0.76 ± 0.03	0.03 ± 0.01	0.88 ± 0.12	0.11 ± 0.02	16.6	21 ± 0.5
Clay	0.37 ± 0.10	0.42 ± 0.07	0.07 ± 0.04	0.14 ± 0.05	0.00 ± 0.00	0.00 ± 0.00	-	-
Carbonate	1.00 ± 0.00	0.00 ± 0.00	0.00 ± 0.00	0.00 ± 0.00	0.00 ± 0.00	0.00 ± 0.00	-	-
Integrated prec. (Íráfoss)	0.05 ± 0.05	0.17 ± 0.02	0.75 ± 0.07	0.03 ± 0.04	0.88 ± 0.55	0.12 ± 0.11	14.9	18.5
Integrated prec. (Efri Haukadalsá)	-	-	-	-	-	-	13.5	18.5

Table III-S2: Dissolved chemistry (mean ± 2σ) of samples collected from approximately the same locations within one field season (LHWS19-04 and LHWS19-25) or in two different field seasons (LHWS16-11 and LHWS19-03, LHWS16-08d and LHWS19-19). In the latter two examples, the chemistry of samples is extremely consistent despite the three years separating collection. These paired samples represent three different locations within the catchment of the Efri Haukadalsá.

Sample	$\delta^{34}S_{SO4}$	$[SO_4^{2-}]$	$[Cl^-]$	$[Ca^{2+}]$	$[Mg^{2+}]$	$[Na^+]$	$[K^+]$
LHWS19-04	12.8 ± 0.5	12.2 ± 0.9	128.4 ± 10.6	95.3 ± 12.8	55.8 ± 3.9	196.3 ± 7.3	7.7 ± 0.6
LHWS19-25	12.6 ± 0.5	12.9 ± 0.9	130.9 ± 10.8	97.8 ± 13.2	57.0 ± 4.0	202.8 ± 7.6	8.2 ± 0.6
LHWS16-11	16.4 ± 0.5	11.7 ± 0.9	149.5 ± 12.3	96.7 ± 13.0	64.1 ± 4.5	207.0 ± 7.7	7.4 ± 0.6
LHWS19-03	16.4 ± 1.2	11.1 ± 0.8	153.3 ± 12.6	83.3 ± 11.2	63.4 ± 4.5	206.1 ± 7.7	8.0 ± 0.6
LHWS16-08d	9.4 ± 0.5	19.4 ± 1.4	134.5 ± 11.1	146.2 ± 19.7	71.6 ± 5.1	223.9 ± 8.3	8.5 ± 0.7
LHWS19-19	9.1 ± 0.5	17.6 ± 1.3	137.5 ± 11.3	132.2 ± 17.8	70.3 ± 5.0	219.9 ± 8.2	8.8 ± 0.7

III.14: Supplementary references

Allen, G.H., Pavelsky, T.M., Barefoot, E.A., Lamb, M.P., Butman, D., Tashie, A. and Gleason, C.J., 2018. Similarity of stream width distributions across headwater systems. *Nature Communications*, 9(1), pp.1-7. https://doi.org/10.1038/s41467-018-02991-w.

Andrews, M.G. and Jacobson, A.D., 2017. The radiogenic and stable Sr isotope geochemistry of basalt weathering in Iceland: Role of hydrothermal calcite and implications for long-term climate regulation. *Geochimica et Cosmochimica Acta*, 215, pp.247-262. https://doi.org/10.1016/j.gca.2017.08.012.

Gaillardet, J., Dupré, B., Louvat, P. and Allegre, C.J., 1999. Global silicate weathering and CO_2 consumption rates deduced from the chemistry of large rivers. *Chemical Geology*, 159(1-4), pp.3-30. https://doi.org/10.1016/S0009-2541(99)00031-5.

Georg, R.B., Reynolds, B.C., West, A.J., Burton, K.W. and Halliday, A.N., 2007. Silicon isotope variations accompanying basalt weathering in Iceland. *Earth and Planetary Science Letters*, 261(3-4), pp.476-490. https://doi.org/10.1016/j.epsl.2007.07.004.

Geirsdóttir, Á., Miller, G.H., Thordarson, T. and Ólafsdóttir, K.B., 2009. A 2000 year record of climate variations reconstructed from Haukadalsvatn, West Iceland. *Journal of Paleolimnology*, 41(1), pp.95-115. https://doi.org/10.1007/s10933-008-9253-z.

Gislason, S.R., Arnorsson, S. and Armannsson, H., 1996. Chemical weathering of basalt in Southwest Iceland: Effects of runoff, age of rocks and vegetative/glacial cover. *American Journal of Science*, 296(8), pp.837-907. https://doi.org/10.2475/ajs.296.8.837.

Gislason, S.R. and Torssander, P., 2006. Response of sulfate concentration and isotope composition in Icelandic rivers to the decline in global atmospheric SO_2 emissions into the North Atlantic region. *Environmental Science & Technology*, 40(3), pp.680-686. https://doi.org/10.1021/es051325o.

Hindshaw, R.S., Bourdon, B., von Strandmann, P.A.P., Vigier, N. and Burton, K.W., 2013. The stable calcium isotopic composition of rivers draining basaltic catchments in Iceland. *Earth and Planetary Science Letters*, 374, pp.173-184. https://doi.org/10.1016/j.epsl.2013.05.038.

Jacobson, A.D., Andrews, M.G., Lehn, G.O. and Holmden, C., 2015. Silicate versus carbonate weathering in Iceland: New insights from Ca isotopes. *Earth and Planetary Science Letters*, 416, pp.132-142. https://doi.org/10.1016/j.epsl.2015.01.030.

Kemeny, P.C., Lopez, G.I., Dalleska, N.F., Torres, M., Burke, A., Bhatt, M.P., West, A.J., Hartmann, J. and Adkins, J.F., 2021. Sulfate sulfur isotopes and major ion chemistry reveal that pyrite oxidation counteracts CO_2 drawdown from silicate weathering in the Langtang-Trisuli-Narayani River system, Nepal Himalaya. *Geochimica et Cosmochimica Acta*, 294, pp.43-69. https://doi.org/10.1016/j.gca.2020.11.009.

Langdon, P.G., Holmes, N. and Caseldine, C.J., 2008. Environmental controls on modern chironomid faunas from NW Iceland and implications for reconstructing climate change. *Journal of Paleolimnology*, 40(1), pp.273-293. https://doi.org/10.1007/s10933-007-9157-3.

Moulton, K.L., West, J. and Berner, R.A., 2000. Solute flux and mineral mass balance approaches to the quantification of plant effects on silicate weathering. *American Journal of Science*, 300(7), pp.539-570. https://doi.org/10.2475/ajs.300.7.539.

Opfergelt, S., Williams, H.M., Cornelis, J.T., Guicharnaud, R.A., Georg, R.B., Siebert, C., Gislason, S.R., Halliday, A.N. and Burton, K.W., 2017. Iron and silicon isotope behaviour accompanying weathering in Icelandic soils, and the implications for iron export from peatlands. *Geochimica et Cosmochimica Acta*, 217, pp.273-291. https://doi.org/10.1016/j.gca.2017.08.033.

Pearce, C.R., Burton, K.W., von Strandmann, P.A.P., James, R.H. and Gíslason, S.R., 2010. Molybdenum isotope behaviour accompanying weathering and riverine transport in a basaltic terrain. *Earth and Planetary Science Letters*, 295(1-2), pp.104-114. https://doi.org/10.1016/j.epsl.2010.03.032.

Stefánsson, A. and Gíslason, S.R., 2001. Chemical weathering of basalts, Southwest Iceland: effect of rock crystallinity and secondary minerals on chemical fluxes to the ocean. *American Journal of Science*, 301(6), pp.513-556. https://doi.org/10.2475/ajs.301.6.513.

Thorpe, M.T., Hurowitz, J.A. and Dehouck, E., 2019. Sediment geochemistry and mineralogy from a glacial terrain river system in southwest Iceland. *Geochimica et Cosmochimica Acta*, 263, pp.140-166. https://doi.org/10.1016/j.gca.2019.08.003.

Torres, M.A., West, A.J., Clark, K.E., Paris, G., Bouchez, J., Ponton, C., Feakins, S.J., Galy, V. and Adkins, J.F., 2016. The acid and alkalinity budgets of weathering in the Andes–Amazon system: Insights into the erosional control of global biogeochemical cycles. *Earth and Planetary Science Letters*, 450, pp.381-391. https://doi.org/10.1016/j.epsl.2016.06.012.

Torres, M.A., Kemeny, P.C., Lamb, M.P., Cole, T.L. and Fischer, W.W., 2020. Long-term storage and age-biased export of fluvial organic carbon: Field evidence from west Iceland. *Geochemistry, Geophysics, Geosystems*, 21(4), p.e2019GC008632. https://doi.org/10.1029/2019GC008632.

Torssander, P., 1989. Sulfur isotope ratios of Icelandic rocks. *Contributions to Mineralogy and Petrology*, 102(1), pp.18-23. https://doi.org/10.1007/BF01160187.

Vigier, N., Gislason, S.R., Burton, K.W., Millot, R. and Mokadem, F., 2009. The relationship between riverine lithium isotope composition and silicate weathering rates in Iceland. *Earth and Planetary Science Letters*, 287(3-4), pp.434-441. https://doi.org/10.1016/j.epsl.2009.08.026.

von Strandmann, P.A.P., Burton, K.W., James, R.H., van Calsteren, P., Gíslason, S.R. and Mokadem, F., 2006. Riverine behaviour of uranium and lithium isotopes in an actively glaciated basaltic terrain. *Earth and Planetary Science Letters*, 251(1-2), pp.134-147. https://doi.org/10.1016/j.epsl.2006.09.001.

von Strandmann, P.A.P., Opfergelt, S., Lai, Y.J., Sigfússon, B., Gislason, S.R. and Burton, K.W., 2012. Lithium, magnesium and silicon isotope behaviour accompanying weathering in a basaltic soil and pore water profile in Iceland. *Earth and Planetary Science Letters*, 339, pp.11-23. https://doi.org/10.1016/j.epsl.2012.05.035.

Chapter IV

Sulfate Sulfur Isotopes and Major Ion Chemistry Reveal that Pyrite Oxidation Counteracts CO_2 Drawdown from Silicate Weathering in the Langtang-Trisuli-Narayani River System, Nepal Himalaya

Preston Cosslett Kemeny[1], Grecia I. Lopez[1], Nathan F. Dalleska[1], Mark A. Torres[2], Andrea Burke[3], Maya P. Bhatt[4], A. Josh West[5], Jens Hartmann[6], Jess F. Adkins[1]

[1] Division of Geological and Planetary Sciences, California Institute of Technology, Pasadena, CA, USA
[2] Department of Earth, Environmental, and Planetary Sciences, Rice University, Houston, TX, USA
[3] School of Earth and Environmental Sciences, University of St Andrews, St Andrews, UK
[4] Department of Physical and Environmental Sciences, Concord University, Athens, WV, USA
[5] Department of Earth Sciences, University of Southern California, Los Angeles, CA, USA
[6] Institute for Geology, Universität Hamburg, Bundesstrasse, Hamburg, Germany

Highlights:

- $\delta^{34}S_{SO4}$ and major ions are set by lithology principally and seasonality secondarily
- Sulfide and S_{org} oxidation source 62-101% of SO_4^{2-} in Langtang-Trisuli-Narayani
- The fraction of H_2SO_4-driven weathering varies seasonally with system hydrology
- Narayani catchment weathering does not reduce pCO_2 on timescales >5 kyr and <10 Myr

Keywords: Silicate weathering, Pyrite oxidation, Sulfur isotopes, Carbon dioxide, Himalaya

Kemeny, P.C., Lopez, G.I., Dalleska, N.F., Torres, M., Burke, A., Bhatt, M.P., West, A.J., Hartmann, J. and Adkins, J.F., 2021. Sulfate sulfur isotopes and major ion chemistry reveal that pyrite oxidation counteracts CO_2 drawdown from silicate weathering in the Langtang-Trisuli-Narayani River system, Nepal Himalaya. *Geochimica et Cosmochimica Acta*, 294, pp.43-69. https://doi.org/10.1016/j.gca.2020.11.009.

IV.1: Abstract

Drawdown of atmospheric carbon dioxide (CO_2) due to silicate weathering in the Himalaya has previously been implicated in Cenozoic cooling. However, over timescales shorter than that of the removal of marine sulfate (SO_4^{2-}), the oxidation of pyrite (FeS_2) in weathering systems can counteract the alkalinity flux of silicate weathering and modulate pCO_2. Here we present evidence from $^{34}S/^{32}S$ isotope ratios in dissolved SO_4^{2-} ($\delta^{34}S_{SO4}$), together with dissolved major ion concentrations, that reveals FeS_2 oxidation throughout the Langtang-Trisuli-Narayani River system of the Nepal Himalaya. River water samples were collected monthly to bimonthly throughout 2011 from 16 sites ranging from the Lirung Glacier catchment through the Narayani River floodplain. This sampling transect begins in the High Himalayan Crystalline (HHC) formation and passes through the Lesser Himalayan (LH) formation with upstream influences from the Tethyn Sedimentary Series (TSS). Average $\delta^{34}S_{SO4}$ in the Lirung Glacier outlet is 3.6‰, increases downstream to 6.3‰ near the confluence with the Bhote Kosi, and finally declines to -2.6‰ in the lower elevation sites. Using new measurements of major ion concentrations, inversion shows 62-101% of river SO_4^{2-} is derived from the oxidation of sulfide minerals and/or organic sulfur, with the former process likely dominant. The fraction of H_2SO_4-driven weathering is seasonally variable and lower during the monsoon season, attributable to seasonal changes in the relative influence of shallow and deep flow paths with distinct residence times. Inversion results indicate that the primary control on $\delta^{34}S_{SO4}$ is lithologically variable isotope composition, with the expressed $\delta^{34}S$ value for the LH and TSS formations (median values -7.0-0.0‰ in 80% of samples) lower than that in the HHC (median values 1.7-6.2‰ in 80% of samples). Overall, our analysis indicates that FeS_2 oxidation counteracts much of the alkalinity flux from silicate weathering throughout the Narayani River system such that weathering along the sampled transect exerts minimal impact on pCO_2 over timescales >5-10 kyr and <10 Myr. Moreover, reanalysis of prior datasets suggests that our findings are applicable more widely across several of the frontal Himalayan drainages.

IV.2: Introduction

Chemical weathering exerts a first-order influence on climate by regulating the flux of dissolved inorganic carbon (DIC) and alkalinity (ALK) delivered from the terrestrial surface into the ocean-atmosphere system (Walker et al., 1981; Gaillardet et al., 1999). Previously, silicate weathering of the Himalaya has been implicated in the long-term cooling of the Cenozoic (Raymo et al., 1988; Raymo and Ruddiman, 1992; Zachos et al., 2001). The associated "uplift-weathering" hypothesis has inspired extensive debate on the nature and controls of silicate weathering, both in the Himalaya and globally, with a particular emphasis on interpreting the Cenozoic rise in marine $^{87}Sr/^{86}Sr$ (Elderfield, 1986; Veizer, 1989; Edmond, 1992; Krishnaswami and Singh, 1998; Krishnaswami et al., 1999; Myrow et al., 2015). The controls on chemical weathering have been traditionally posed as a dichotomy between physical processes like uplift and erosion (Raymo and Ruddiman, 1992; Huh et al., 1998; Riebe et al., 2001; Millot et al., 2002) versus climate mechanisms related to temperature and the hydrologic cycle (Walker et al., 1981; White and Blum, 1995; Dessert et al., 2003). The debate has now shifted to reflect the continuum between chemical and physical controls as reflected in kinetically-limited weathering regimes and transport-limited or supply-limited weathering regimes (Stallard and Edmond, 1983; West et al., 2005; Maher and Chamberlain, 2014; Hilton and West, 2020). The Himalaya has continued to feature prominently in this discussion due to its varied lithology, topography, and potential role in Cenozoic cooling.

The role of the Himalaya in modulating Cenozoic atmospheric carbon dioxide (CO_2) levels remains an open question in part because the flux of silicate alkalinity from the major Himalayan rivers is relatively minor in the global context (France-Lanord and

Derry, 1997; Galy and France-Lanord, 1999). This seemingly modest flux raises basic questions about whether Himalayan silicate weathering could have driven Cenozoic pCO_2 decline. At the same time, without compensatory feedbacks, even modest increases in silicate weathering fluxes caused by Himalayan uplift could have quickly removed all CO_2 from the atmosphere (Berner and Caldeira, 1997; Kerrick and Caldeira, 1999). To counteract such an over-drawdown of pCO_2, prior work has invoked a coincident flux of negative alkalinity through pyrite (FeS_2) oxidation (Torres et al., 2014), synorogenic metamorphic decarbonation (Bickle, 1996; Becker et al., 2008; Evans et al., 2008), a decrease in the magnitude of silicate weathering elsewhere (François and Walker, 1992; Kump and Arthur, 1997; Li and Elderfield, 2013), a decrease in burial of organic carbon (C_{org}) (Raymo, 1994), an increase in oxidation of petrogenic C_{org} (Beck et al., 1995), an increase in the subduction of pelagic carbonate sediments (Caldeira, 1992), or an increase in the formation of authigenic aluminosilicate minerals (Raymo and Ruddiman, 1992). This article explores the feasibility of the first hypothesis, that of sulfide mineral oxidation (Torres et al., 2014), through measurements of the $^{34}S/^{32}S$ isotope ratio of dissolved sulfate (SO_4^{2-}) and the concentrations of dissolved major ions in river water from the Langtang-Trisuli-Narayani River system in the Nepal Himalaya.

Previous research on chemical weathering of the Himalaya has focused primarily on the alkalinity flux from weathering of silicate minerals. This focus follows from the canonical framework of chemical weathering as the titration of carbonic acid (H_2CO_3) on silicate minerals (approximated as $CaSiO_3$) to generate alkalinity (Eq. IV-1), which is subsequently consumed during formation and burial of marine carbonate mineral ($CaCO_3$) (Eq. IV-2; Urey, 1952). By removing one mole DIC from the ocean-atmosphere system for

each mole of Ca^{2+} transferred from $CaSiO_3$ to $CaCO_3$, the chemical weathering of silicates is often described as regulating atmospheric pCO_2 over geologic timescales (Eq. IV-3; Sundquist, 1991). Within this same framework, the ALK and DIC sourced from weathering of carbonate minerals (Eq. IV-4) are consumed during burial of marine carbonate rock. Weathering of carbonate has thus traditionally been thought to have no net impact on atmospheric pCO_2 over timescales longer than the 5-10 kyr timescale of marine carbonate compensation (Archer et al., 1997; 2000). Because the Nepal Himalaya is dominated by carbonate weathering (Blum et al., 1998; Galy and France-Lanord, 1999), prior studies argued that the dominant influence of Himalayan weathering on the geologic carbon cycle relates to organic carbon burial (France-Lanord and Derry, 1997; Galy et al., 2007) or metamorphic carbon fluxes (Bickle, 1996; Becker et al., 2008; Evans et al., 2008).

$$\frac{1}{2}CaSiO_3 + H^+ \rightarrow \frac{1}{2}Ca^{2+} + \frac{1}{2}SiO_2 + \frac{1}{2}H_2O \quad \text{(IV-1)}$$

$$\frac{1}{2}Ca^{2+} + \frac{1}{2}H_2CO_3 \rightarrow \frac{1}{2}CaCO_3 + H^+ \quad \text{(IV-2)}$$

$$CaSiO_3 + H_2CO_3 \rightarrow CaCO_3 + SiO_2 + H_2O \quad \text{(IV-3)}$$

$$\frac{1}{2}CaCO_3 + H^+ \rightarrow \frac{1}{2}Ca^{2+} + \frac{1}{2}H_2CO_3 \quad \text{(IV-4)}$$

The canonical weathering framework outlined above ignores sources of H^+ other than DIC, yet the oxidation of sulfide minerals can also provide H^+ that impacts the global carbon cycle (Eq. IV-5; Spence and Telmer, 2005; Lerman et al., 2007; Calmels et al., 2007). The oxidation of minerals such as FeS_2 generates sulfuric acid (H_2SO_4) that rapidly deprotonates to SO_4^{2-}, removing both ALK and dioxygen (O_2) from the ocean-atmosphere system. The oxidation of FeS_2 can also proceed through reduction of Fe^{3+} to Fe^{2+} (Eq. IV-

6; Balci et al., 2007) with greater consumption of ALK per mole of released SO_4^{2-}. However, aerobic re-oxidization of Fe^{2+} results in the net reaction being equivalent to that of direct O_2 reduction (Eq. IV-5). Alkalinity lost through FeS_2 oxidation is ultimately returned to the ocean-atmosphere system over the timescale for SO_4^{2-} to be removed from the ocean in marine sediments through reduction to FeS_2; the residence time of SO_4^{2-} in the modern ocean is approximately 10 Myr (Burke et al., 2018). The impacts of FeS_2 oxidation on pCO_2 are thus manifest during the period over which FeS_2-derived SO_4^{2-} accumulates in seawater. Although a role for sulfide oxidation was recognized early in major river systems (Rabinovich and Grinenko, 1979; Stallard and Edmond, 1983), including in the Himalaya (Galy and France-Lanord, 1999), FeS_2 oxidation as a globally-relevant sink of alkalinity has only recently been appreciated (Torres et al., 2014; Burke et al., 2018).

$$\frac{1}{2}FeS_2 + \frac{15}{8}O_2 + H_2O \rightarrow 2H^+ + SO_4^{2-} + \frac{1}{4}Fe_2O_3 \qquad \text{(IV-5)}$$

$$\frac{1}{2}FeS_2 + \frac{15}{2}Fe^{3+} + \frac{19}{4}H_2O \rightarrow \frac{19}{2}H^+ + SO_4^{2-} + \frac{1}{4}Fe_2O_3 + \frac{15}{2}Fe^{2+} \qquad \text{(IV-6)}$$

More broadly, any source of SO_4^{2-} entering the ocean-atmosphere system without charge compensation by conservative cations removes ALK. For example, the oxidation of organo-sulfate moieties to SO_4^{2-} and DIC consumes 2 moles ALK per mole SO_4^{2-}, the same stoichiometry as FeS_2 oxidation (Eq. IV-5). When considering the role of sulfur as a source of H^+ for weathering, what matters is thus the provision of SO_4^{2-} without the addition of conservative cations, rather than the oxidation of sulfide within any particular mineral phase. The relative importance of sulfide mineral oxidation versus the oxidation of modern or rock-bound organic sulfur (S_{org}) depends on factors such as the relative abundance of S-

bearing phases, the availability of oxidants, and the presence of relevant microbial communities. However, because most S in typical siliciclastic sedimentary rocks is as sulfide minerals and not S_{org}, it is reasonable to assume that the majority of non-evaporite SO_4^{2-} liberated from rocks during weathering derives from FeS_2 oxidation. Here we thus combine all sources of SO_4^{2-} without accompanying cation release under the umbrella term of "FeS_2 oxidation" and note that this includes SO_4^{2-} sourced to the river through oxidation of reduced carbon, as well as the oxidation of additional sulfide minerals where partner cations remain in the solid phase.

Although reactions releasing SO_4^{2-} without compensating cations have similar effects on ALK, they can have different implications for DIC and thus for pCO_2; sources of SO_4^{2-} associated with S-C bonds will typically increase ocean-atmosphere DIC upon oxidation, while sources of SO_4^{2-} from inorganic minerals are unlikely to directly impact DIC. By not resolving the DIC fluxes associated with oxidation and production of organic matter, our work thus provides only a partial view of the full influence of chemical weathering on atmospheric pCO_2 (Hilton and West, 2020). Furthermore, we do not consider the nitrogen or cation fluxes associated with biomass growth and oxidation, which may counteract or reinforce the ALK dynamics of SO_4^{2-} addition to river water. Over geologic timescales, the different sources of SO_4^{2-} may also have distinct implications for pO_2. Estimates of the full balance of organic and inorganic weathering are only available for a few settings globally (Horan et al., 2019; Hilton and West, 2020), and the Nepal Himalaya is a natural choice for future research quantifying such budgets, for example, by analysis of dissolved rhenium in river water to constrain the role of C_{org} oxidation (Hilton et al., 2014).

Here, we focus on quantifying the oxidation of mineral-bound sulfide and organic sulfur in the Himalaya as one of the main understudied levers on the global carbon cycle, with particular relevance for understanding Cenozoic pCO_2 decline. In their pioneering work, Galy and France-Lanord (1999) proposed that 70% of SO_4^{2-} in samples from the Narayani River system of the Nepal Himalaya derived from FeS_2 oxidation. Using measurements of DIC $^{13}C/^{12}C$ from the same study, Torres et al. (2014) proposed that sulfide oxidation in the Ganges-Brahmaputra fully counteracts the ALK flux of silicate weathering and potentially helped to sustain pCO_2 at moderate levels throughout the Cenozoic. Any increase in pCO_2 from sulfide oxidation could have offset drawdown from increases in silicate weathering, land surface reactivity, or Cenozoic C_{org} storage (France-Lanord and Derry, 1997), or accentuated increases in pCO_2 due to synorogenic decarbonation (Bickle, 1996; Becker et al., 2008). While the role of Himalayan FeS_2 oxidation has been proposed in the work of Galy and France-Lanord (1999) and Torres et al. (2014), it has yet to be understood in detail.

Analogous to silicate weathering, FeS_2 oxidation in the Himalaya has both physical and climatic controls. Foremost, lithology controls the abundance of available sulfide minerals and thus the ability of those lithologies to generate sulfuric acid. Moreover, FeS_2 cannot be transported more than a few km through O_2-rich environments without oxidation (Johnson et al., 2014). As a corollary, sulfide oxidation is thought to almost always be supply-limited, suggesting a strong erosional control on FeS_2 oxidation and thus a gradient across geomorphic setting (Calmels et al., 2007). Oxidation of FeS_2 may also be influenced by runoff and temperature (Brantley et al., 2013), convolving H_2SO_4 into the seasonal weathering cycle, for example, if seasonal variations in hydrology control the depth of

penetration of oxidizing fluids (Winnick et al., 2017). Here we present evidence for seasonal changes in the fraction of H_2SO_4-driven weathering, complementing prior evidence from throughout the Himalaya for seasonality in carbonate weathering (Tipper et al., 2006).

Sulfur isotope ratios of dissolved SO_4^{2-} ($\delta^{34}S_{SO4} = {}^{34}R_{sample}/{}^{34}R_{VCDT}-1$, commonly reported in ‰ relative to Vienna Canyon Diablo Troilite (VCDT) and where ^{34}R is the $^{34}S/^{32}S$ ratio of SO_4^{2-}) are a useful tool for studying FeS_2 oxidation. Previously, $\delta^{34}S_{SO4}$ was measured in the Marsyandi River of the Nepal Himalaya (Turchyn et al., 2013; Hemingway et al., 2020). Because the studied region of the Marsyandi River represents only a relatively small fraction of the total Narayani River catchment, the Nepal Himalaya remains largely uncharacterized for $\delta^{34}S_{SO4}$.

In this article, we report the dissolved major ion chemistry and $\delta^{34}S_{SO4}$ of seasonal river water samples from throughout the Langtang-Trisuli-Narayani River system in order to test the impacts of lithology and seasonality on FeS_2 oxidation. Using a Monte Carlo inversion model, we show that the Narayani catchment hosts FeS_2 oxidation. We find that $\delta^{34}S_{SO4}$ is principally set by lithology and identify seasonal changes in the fraction of H_2SO_4-driven weathering. Over timescales less than approximately 10 Myr, the ALK flux of sulfuric acid weathering may completely counteract the drawdown of pCO_2 due to silicate weathering in the Langtang-Trisuli-Narayani River system.

IV.3: Methods

IV.3.1: Field methods and sample context

IV.3.1.1: Sample collection

The samples analyzed in this study are river waters from the Langtang-Trisuli-Narayani River system in central Nepal (Fig. IV-1), previously presented in Bhatt et al. (2018). Briefly, samples were collected monthly or bimonthly throughout 2011 at 16 sites (LNS-1 through LNS-16) ranging in elevation from 169 m to 3989 m (Fig. IV-1B). During collection each sample was filtered through a 0.45 μm polycarbonate filter into a single 100 mL acid-washed polyethylene bottle (Bhatt et al., 2018). Samples were not acidified, but our testing did not reveal carbonate precipitation or sorption of ions to container walls (IV.12.1). These samples are an important resource for future studies on weathering in the Nepal Himalaya because they record conditions prior to the 2015 Gorkha earthquake and associated landsliding (Roback et al., 2018).

Prior to collection, sample bottles were washed with a mixture of KOH and Neodisher LaboClean A 8 (NaOH, Na_2CO_3, $Na_2SiO_3*5H_2O$, $C_3Cl_2N_3NaO_3$), cleaned with 2% HCl, rinsed with water and then several times with DI water, and dried in an oven. Overall, measurements of [Cl^-] in our samples are higher than prior measurements from the same river system (Fig. IV-S3; IV.12.1). Moreover, our data show coherent variations in [K^+] and [Cl^-], which are two components of the cleaning solution. However, we do not believe that these observations reflect contamination of the samples through the cleaning protocol. The samples enriched in [Cl^-] also tend to be elevated in other dissolved ions, showing coherent variability across ion systems that argues against Cl^- contamination. Likewise, the [Cl^-] and [K^+] variation is nearly independent of [Na^+], another major

component of the cleaning solution, and thus not suggestive of contamination from bottle washing as a major cause of chemical variability. The results and data analyses presented below include measurements of [K^+], [Na^+], and [Cl^-], while calculations without [K^+] and [Cl^-] are presented as supplementary materials (IV.12.4).

IV.3.1.2: Sampling map and geologic context

The sampling transect begins in the Langtang River's headwaters in the Lirung Glacier catchment, passes through the confluence with the Bhote Kosi to join the Trisuli River at Syabru Besi, and ends in the Narayani River after crossing confluences with the Budhi Gandaki, Marsyandi River, Seti River, and Kali Gandaki (Fig. IV-1B). Stations LNS-16 through LNS-7 are along the Langtang River. LNS-6 is on the Bhote Kosi upstream of the confluence with the Langtang River, and LNS-5 is directly downstream of the confluence (Fig. IV-1C). For much of the year, the chemistry of samples from LNS-5 resembles that of LNS-6, suggesting a dominant influence from the western side of the confluence. Stations LNS-1 through LNS-4 sit on the Trisuli and Narayani Rivers and are interspersed by major tributaries. The Budhi Gandaki enters the Narayani River between LNS-3 and LNS-2, and the Marsyandi River, Seti River, and Kali Gandaki enter between LNS-2 and LNS-1. The sites are thus broadly distinguishable into three subsets based on geographic distribution: stations LNS-1 to LNS-6 along the Bhote Kosi-Trisuli-Narayani, stations LNS-7 to LNS-10 along the lower Langtang River, and stations LNS-11 to LNS-16 in the upper Langtang River as far upstream as the Lirung Glacier outlet.

The sampling transect passes through the major lithotectonic units of the Nepal Himalaya, including the High Himalayan Crystalline (HHC), the Lesser Himalayan (LH),

the Siwaliks, and a portion of the floodplain (Fig. IV-1D). The HHC is a highly metamorphosed suite characterized by orthogneiss, paragneiss, migmatites, metapelite, and numerous leucogranite bodies (Galy and France-Lanord, 1999). The Main Central Thrust separates the HHC from the LH, and along this boundary are numerous hot springs (Bhattarai, 1980; Evans et al., 2001; 2004; 2008; Girault et al., 2014). The LH is composed of variably altered Precambrian metasediments including quartz-pelitic schist, massive dolomitic carbonates, and black shales (Pierson-Wickmann et al., 2000). The confluence of the Langtang River and the Bhote Kosi occurs at the boundary of the HHC with the LH, where hot springs are located at the town of Syabru Besi. Stations LNS-4 through LNS-2 are predominately within the LH formation, while LNS-1 sits below the Main Boundary Thrust on the floodplain built of detrital sediments.

The Tethyn Sedimentary Series (TSS) is exposed in the catchments of LNS-1 through LNS-6 and exerts a strong chemical influence on samples from these stations. The TSS is principally composed of the Phanerozoic marine shelf carbonates formed on the Indian margin prior to the collision with Eurasia, and includes black shales (Wolff-Boenisch et al., 2009). No direct observations of halite or gypsum are reported for the TSS in the Narayani catchment, although some work suggests their presence (Tshering and Bhandari, 1973 in Fort, 1996; IV.12.2). The TSS was previously found to contain FeS_2 (Bordet et al., 1971) and FeS_2 oxidation is reported in the Marsyandi River (Turchyn et al., 2013; Hemingway et al., 2020), which drains the TSS and is included in the headwaters of the catchment area captured by the most downstream sampling site in this study, LNS-1. The fraction of each catchment in our study occupied by TSS mostly decreases downstream from LNS-6, although the particular fraction depends on how much unmapped area is

assigned to TSS. Here we assume 90% of the unmapped region for catchments LNS-2 through LNS-6 are composed of TSS, with the other 10% occupied by HHC, and that unmapped catchment area for LNS-1 is in proportion to the mapped fractions. Notably, our observations do not depend on these fractions; rather, the critical dynamic is simply that the catchments for LNS-1 through LNS-6 contain large exposures of TSS and LH while the catchments for stations LNS-7 through LNS-16 contain much smaller exposures, if any.

IV.3.1.3: Anthropogenic impacts on river chemistry

All samples were collected within 100 km of Kathmandu and a subset of samples were collected closer to urban centers such as Betrawati. The possibility for anthropogenic SO_4^{2-} contamination warrants particular attention given prior findings that approximately 30% of SO_4^{2-} in rivers globally is derived from pollution (Berner, 1971). Although the $\delta^{34}S$ of such pollution was previously thought to be low (Ivanov et al., 1983), recent research shows that polluted rivers can have a wide range of $\delta^{34}S_{SO4}$ values (Burke et al., 2018). We account for the indirect input of anthropogenic SO_4^{2-}, such as through atmospheric transport of pollutants and subsequent deposition, by using observations of precipitation chemistry reflecting both natural and pollutant inputs. However, our analysis does not account for any direct inputs of SO_4^{2-} to the samples. If present, such pollution would lead us to overestimate the importance of FeS_2 oxidation. Although direct inputs are unlikely in the remote upstream sites above LNS-5, the potential for direct contamination increases downstream towards the urban centers of the floodplain; if present, anthropogenic inputs are expected to be largest at stations LNS-1 through LNS-4 (Fig. IV-1). Such a direct SO_4^{2-} source would likely result in a progressive downstream trend in $\delta^{34}S_{SO4}$. Counter to this

expectation, our data show that $\delta^{34}S_{SO4}$ changes sharply at a lithologic boundary, which argues against a dominant role for the direct input of anthropogenic SO_4^{2-}. Although there are ultimately few constraints from river pH, $[NH_4^+]$, or $[PO_4^{3-}]$ with which to evaluate direct inputs from anthropogenic activities (Collins and Jenkins, 1996), the major ion chemistry of samples leads us to suspect sources of ions from pollution are minor relative to sources from chemical weathering (Fig. IV-S6; IV.12.2).

IV.3.2: Experimental methods

IV.3.2.1: Ion chromatography

The concentration of major cations and anions was measured by ion chromatography in the Environmental Analysis Center at the California Institute of Technology. The concentration of Ca^{2+}, Mg^{2+}, K^+, and Na^+ was measured on a Dionex ICS-2000 equipped with a CG12A guard column (2 mm x 50 mm) and a CS12A separator column (2 mm x 250 mm) with an isocratic 20 mM methanesulfonic eluent. SO_4^{2-} and Cl^- concentrations were measured on a Dionex ISC-3000 equipped with an AG29 guard column (2 mm x 50 mm) and an AS29 separator column (2 mm x 250 mm) with an isocratic 4.5 mM / 2.5 mM Na_2CO_3 / $NaHCO_3$ eluent. All major ion concentrations were measured with suppressed conductivity detection. The precision of IC measurements was typically better than 4% for samples (2σ, relative standard deviation) and always better than 11.6% (the least-reproducible ion in the least-reproducible solution, including reference solutions measured both before and after addition of HNO_3^-) but varied by element and solution (Table IV-S1; IV.12.1). Bicarbonate (HCO_3^-) is calculated by charge balance for plotting purposes but is not included in our inversion model.

The concentration of major ions in these samples was previously measured in Hamburg and reported in Bhatt et al. (2018). During the course of this study we identified systematic differences between new measurements and the previously published values, with the discrepancy correlated to the month of sample collection (Figs. IV-S1, IV-S2, and IV-S3; IV.12.1). In this analysis we use the new measurements of [Ca^{2+}], [Mg^{2+}], [Na^{+}], [K^{+}], [Cl^{-}], and [SO_4^{2-}] generated at Caltech.

IV.3.2.2: MC-ICP-MS measurements of $\delta^{34}S_{SO4}$

River samples were evaporated to dryness overnight in acid-washed Savillex containers, dissolved in dilute hydrochloric acid, and passed through anion-exchange resin (AG 1-X8 analytical grade 100-200 mesh chloride form) to isolate SO_4^{2-}, similar to the chromatography protocols of Paris et al. (2013) and Burke et al. (2018). The isolated SO_4^{2-} was then matrix-matched to an in-house Na_2SO_4 solution previously calibrated to international reference materials and $\delta^{34}S$ was measured by Multi-Collector Inductively-Coupled-Plasma-Mass-Spectrometry (MC-ICP-MS) with sample-standard bracketing (Paris et al., 2013). Measurement cycles were analyzed both visually and statistically to determine outliers and a post-run correction was applied to remove instrument blank and procedural blank. The analytical method typically included two attempts to measure each eluate on a given run, and the observed differences between the two observations relative to their expected difference based on internal precision was quantified using Error-Normalized Deviation (END) (John and Adkins, 2010). After removal of samples with measurement artifacts such as rapid changes in mass biasing, the standard deviation of the internal END distribution over 10 runs ranged from 1.3 to 8.3.

The $\delta^{34}S_{SO4}$ of IAPSO seawater was measured as 20.99±0.25‰ (n=53, 2σ). The $\delta^{34}S_{SO4}$ of Switzer Falls, a local river used as an internal reference material (Burke et al., 2018), was measured as 4.25±0.39‰ (n=53, 2σ). All 121 river water samples were measured at least twice, and 48 samples were fully processed twice with a mean $\delta^{34}S$ difference of 0.20‰ between the two determinations. The reported error on each sample is taken to be the larger of either the standard deviation of blank-corrected $^{34}S/^{32}S$ ratios, or the reproducibility of references across all analytical sessions (taken to be 2σ = 0.40‰).

IV.3.3: Principal component analysis

Variation in the concentration of Ca^{2+} is responsible for much of the absolute variance among dissolved ions. To identify trends related to the location of sampling and season of collection, we subtract the mean and divide by the standard deviation (Z-score) of the major ion chemistry and $\delta^{34}S_{SO4}$ measurements prior to performing principal component analysis (PCA) (Glover et al., 2011). Some prior work normalized dissolved ion concentrations by Na^{+} prior to analysis, following an a-priori assumption of systematic changes due to seasonal dilution (Négrel et al., 1993). Here we do not further normalize the Z-scored data, meaning that any trends related to seasonal decreases in solute concentrations will be reflected in the results of the PCA. We plot factor loadings, which are the correlation coefficient of the Z-scored data with its projection into the basis of principal components (Négrel et al., 1993). We also plot normalized sample factor scores, which are a projection of the Z-scored data into the basis of principal components scaled by singular values and then normalized to the ratio of the maximum factor score to the maximum Euclidean distance of the plotted factor loadings.

IV.3.4: Monte Carlo inversion model

IV.3.4.1: Using solute chemistry to reconstruct weathering

At circumneutral pH, HCO_3^- dominates the anion budgets of many rivers and is the major reservoir of riverine DIC. As a result, the *in-situ* ALK/DIC ratio of many rivers is close to one. However, the parameter that ultimately impacts the long-term carbon cycle is the ΔALK/ΔDIC ratio of the overall weathering system sourcing ions to the river, which is different from the *in-situ* value of ALK/DIC measured in a river at any given point in space and time. Two reasons for this discrepancy are that rivers undergo gas exchange with the atmosphere (Striegl et al., 2012; Raymond et al., 2013), as well as exchange of CO_2 with the environment through aquatic respiration and photosynthesis (Quay et al., 1995). Due to this non-conservative behavior, *in-situ* [HCO_3^-] reflects the integrated history of biological and physical processes within the river, in addition to chemical weathering. These processes may be important for understanding how in-river processes contribute to the global balance of photosynthesis and respiration but do not reflect the weathering processes that regulate pCO_2 on geologic timescales. Simply measuring [HCO_3^-] fails to account for the upstream fluxes that have continuously modified the *in-situ* values of ALK and DIC, and thus cannot be used to calculate the ΔALK/ΔDIC ratio of the overall weathering system.

Unlike [HCO_3^-], dissolved major ions are largely conservative in most river systems and can be used to reconstruct the ΔALK/ΔDIC ratio of weathering. To do so for samples from the Langtang-Trisuli-Narayani River system, the contribution of distinct lithologies to the river dissolved load was calculated using a Monte-Carlo inversion model (Négrel et al., 1993; Gaillardet et al., 1999; Torres et al., 2016; Burke et al., 2018; Hemingway et al.,

2020). This inversion is analogous to prior studies of river chemistry both globally (Gaillardet et al., 1999) and in the Himalaya specifically (Bickle et al., 2015), but differs from the forward-modeling common in some prior work in the region (Galy and France-Lanord, 1999; Tipper et al., 2006). We discuss the results of our full inversion model below and include as supplementary material a subset of analogous results for a forward model (Fig. IV-S18; IV.12.4) that uses seawater ratios for precipitation (Sarmiento and Gruber, 2006). We derive two parameters from inversion results previously introduced in Torres et al. (2016), R and Z, which reflect the relative amount of silicate and carbonate weathering and the relative importance of CO_2 and H_2SO_4 as sources of H^+ for weathering reactions, respectively. Because the $\Delta ALK/\Delta DIC$ of the weathering system is a simple function of the values of R and Z, our analysis focuses on their relative values as well as spatial and seasonal changes in the two parameters.

IV.3.4.2: Inversion end-members

The inversion uses two carbonate end-members, two silicate end-members, and precipitation (Table IV-1). Motivating observations for our selections are given in IV.12.2, including comparison of our carbonate and silicate end-members with those used in prior work and our decision to exclude evaporite minerals and hot springs from our primary inversion; results including evaporites (Claypool et al., 1980; Valdiya, 1980; Sarin and Krishnaswami, 1984; Singh and Singh, 2010) and hot springs (Evans et al., 2004) are given in Figs. IV-S15 and IV-S16. Guided by observations of downstream changes in Mg^{2+}/Σ^+ (where $\Sigma^+ = Ca^{2+} + Mg^{2+} + Na^+ + K^+$ in units of charge equivalents) we separate carbonate contributions into those from calcite and dolomite. We do not include Na^+ or K^+ in the

carbonate end-members; this decision is enabled by the normalization to Σ^+ rather than Na^+, which leaves the end-members free to be stoichiometric. Coherently changing K^+/Na^+ ratios motivates the use of two silicate end-members. The first end-member is called 'silicate' and is assigned a high Na^+/Σ^+ and low K^+/Σ^+, while the second end-member is called 'biotite' and is assigned Na^+/Σ^+ and K^+/Σ^+ opposite to the silicate end-member (Table IV-1). The silicate end-member represents generic silicate weathering (e.g., feldspars, muscovite), while the biotite end-member represents a K^+-rich phase which may be preferentially weathered during the monsoon season to increase K^+/Na^+.

Most studies in the Himalaya have appealed to the existence of an end-member with a Cl^-/Na^+ ratio near 1. Galy and France-Lanord (1999) accounted for the Cl^- in excess of rainwater inputs using a NaCl end-member, and subsequent work has often used a Cl-rich hot spring (Evans et al., 2004; Tipper et al., 2006) or seawater (Bhatt et al., 2018). The lack of evaporite minerals or high-Cl^-/Σ^+ hot springs along most of our sampling transect (Fig. IV-S4) suggests that precipitation sources nearly 100% of Cl^- in our samples. As a result, the precipitation end-member is the only source of Cl^- in our primary inversion model. Changing this assumption impacts results for the fraction of carbonate weathering but exerts only minimal influence on the calculated fraction of H_2SO_4-driven weathering (IV.12.4). The chemical ratios of the precipitation end-member are determined from observation (Fig. IV-S5; Handa, 1968; Sequeira and Kelkar, 1978; Galy and France-Lanord, 1999; Bhatt et al., 2000; Shrestha et al., 2002; Hren et al., 2007; Andermann et al., 2011; Balestrini et al., 2014; Tripathee et al., 2014; Panthi et al., 2015).

Torres et al. (2016) and Burke et al. (2018) represent two different approaches to account for FeS_2 oxidation in river chemistry. In Torres et al. (2016), FeS_2 oxidation is

included directly in the inversion by allowing silicate and carbonate end-members to have non-zero SO_4^{2-}/Σ^+ and well-defined $\delta^{34}S$ values. In Burke et al. (2018), FeS_2 oxidation is calculated post-inversion through SO_4^{2-} mass balance. Our analysis combines the SO_4^{2-}/Σ^+ approach of Torres et al. (2016) with the post-inversion calculation for the $\delta^{34}S$ of FeS_2 ($\delta^{34}S_{FeS2}$) allowed in the approach of Burke et al. (2018). Following Torres et al. (2016), we take the SO_4^{2-}/Σ^+ ratio of the non-precipitation end-members to reflect H_2SO_4-driven weathering. Using the measured sample $\delta^{34}S_{SO4}$ and precipitation $\delta^{34}S_{SO4}$, we then calculate by mass balance the $\delta^{34}S$ of the SO_4^{2-} sourced from the calcite, dolomite, silicate, and biotite end-members, which we take as the value of $\delta^{34}S_{FeS2}$. Each river sample thus constrains a distribution of possible $\delta^{34}S_{FeS2}$ values. Note that these inversion-constrained values of $\delta^{34}S_{FeS2}$ reflect the net $\delta^{34}S$ of SO_4^{2-} delivered without conservative cations; that is, values of $\delta^{34}S_{FeS2}$ formally reflect SO_4^{2-} sourced from both sulfide mineral oxidation and S_{org} oxidation, as opposed to the $\delta^{34}S$ of FeS_2 mineral specifically.

IV.3.4.3: Inversion methodology

On a given iteration, the Ca^{2+}/Σ^+, Na^+/Σ^+, K^+/Σ^+, and Cl^-/Σ^+ of each end-member were pulled randomly from normal distributions with end-member-specific means and standard deviations (Table IV-1). The ratio SO_4^{2-}/Σ^+ was pulled from a normal distribution for the precipitation end-member, where observations inform the expected range of values. Because there is little empirical evidence for the fraction of H_2SO_4-driven weathering associated with each lithology, the SO_4^{2-}/Σ^+ for each non-precipitation end-member was pulled from a uniform distribution between 0 and 1. All distributions were truncated with a lower bound of zero, and those with a numerator constituent to Σ^+ were truncated with

an upper bound of 1. The ratios of Mg^{2+}/Σ^{+} for each end-member were calculated to ensure mass balance based on the other cation ratios (although indicated in Table IV-1, the Mg^{2+}/Σ^{+} distributions were not drawn directly). If a calculated Mg^{2+}/Σ^{+} was negative, the entire process was repeated up to 500 times or until a set of physically realizable, mass balanced end-members was generated. On a given iteration the river data for $[Ca^{2+}]$, $[Mg^{2+}]$, $[Na^{+}]$, $[K^{+}]$, $[Cl^{-}]$, and $[SO_4^{2-}]$ were altered by values pulled randomly from a normal distribution with mean of zero and standard deviation corresponding to analytical precision (IV.12.1).

The resulting set of river observations and end-member chemistry was solved using the MATLAB function *fmincon*; the optimization cost function was the sum of squared proportional offsets between observations and model estimate, constrained to deliver positive solutions, and used as an initial condition the solution from standard least-squares inversion. Simulation results were not accepted if any variable was more than 15% discrepant from observations, meaning that in all accepted inversion instances the sum of fractional contributions from end-members was between 85% and 115% of each observation. Up to one hundred thousand simulations were attempted; the first one thousand successful simulations for each sample were kept. All samples were successfully inverted one thousand times except the July and August samples at LNS-4 (0 successes) and the August sample at LNS-7 (233 successes). In most calculations we use the median of accepted simulation results and take the 5th and 95th percentiles of accepted simulation results as the inversion error. We note that the full 5th to 95th percentile range should be considered possible because the results of river inversions can be sensitive to the introduction of additional elemental or isotope systems (Torres et al., 2016). All inversion

calculations were conducted in MATLAB through the High Performance Computing Center at Caltech.

IV.3.4.4: Influence of secondary carbonate precipitation

Two assumptions of the Monte Carlo inversion are that the net solute release from each end-member is described by the range of chemical ratios we sample, and that these weathering products mix conservatively. However, evidence from dissolved chemistry (Jacobson et al., 2002), bedload chemistry (Bickle et al., 2015), and Ca^{2+} isotope ratios (Tipper et al., 2008) all indicate that there is secondary calcite precipitation in Himalayan rivers. Some evidence positively correlates the fraction of Ca^{2+} lost from solution with the strength of silicate weathering (Bickle et al., 2015), so that the impacts of secondary calcite formation are expected to be largest during the non-monsoon season (Tipper et al., 2006). Bickle et al. (2015) estimate the magnitude of Ca^{2+} remaining after secondary carbonate precipitation to be 5-40% in the TSS and 40-100% in the HHC.

Secondary carbonate precipitation biases the interpretation of which end-members are weathering but not which acids are responsible for weathering. The first impact of secondary calcite precipitation is to decrease observed Ca^{2+}/Σ^{+}, causing inversions to underestimate the true fraction of carbonate weathering (Fig. IV-S8). Assuming 50% of Ca^{2+} was removed as secondary carbonate precipitation in our HHC-dominated samples (Bickle et al., 2015), we calculate that the effect of secondary carbonate precipitation would be to lower absolute Ca^{2+}/Σ^{+} by ~10% (Fig. IV-S8). Second, secondary carbonate precipitation will increase SO_4^{2-}/Σ^{+} so that it does not reflect the fraction of gross weathering driven through sulfide oxidation. We again estimate the absolute magnitude of

this effect to be ~10% (Fig. IV-S8). Given that the importance of secondary carbonate precipitation likely varies throughout the catchment, our calculations are only approximations. However, because the formation of $CaCO_3$ produces H^+, observed Σ^+ still remains a valid metric of net H^+ consumption during weathering. That is, even in the presence of secondary carbonate precipitation, the ratio SO_4^{2-}/Σ^+ reflects net sulfuric acid weathering. In detail, the shift in the relative fraction of carbonate and silicate weathering also biases the inversion-constrained ranges of end-member SO_4^{2-}/Σ^+ (Fig. IV-S8). Because our analysis is primarily concerned with variation in SO_4^{2-}/Σ^+, $\delta^{34}S_{SO4}$, and the seasonality of FeS_2 oxidation, our findings are largely insulated against impacts from secondary carbonate precipitation. We thus do not correct the data for this process.

IV.3.5: Construction of a synthetic hydrograph

Three gauging stations along the sampling transect (Fig. IV-1, Q1-Q3) record similar annual hydrographs with elevated flow during the monsoon season and reduced flow during the non-monsoon (Fig. IV-S7; IV.12.3). Discharge at Q1 and Q3 during 2011 were similar to historical data (Figs. IV-S7A and E). Discharge data at Q2 during 2011 were mostly similar to prior data, but with an anomalously large pulse during the monsoon (Fig. IV-S7C). To compare weathering dynamics against seasonal discharge, we constructed a synthetic hydrograph for the entire sampling transect during 2011 by combining data from the three different gauging stations. In other words, all samples are assumed to have the same relative changes in discharge with time such that the collection date can be used as a proxy for discharge. First, we normalized by the maximum flow of each year to calculate the daily fraction of maximum annual discharge. Then, these

fractional terms from the three stations were summed, normalized, and averaged by month to reach a single metric for the average monthly fraction of maximum annual discharge (Fig. IV-S7), and it is this derived parameter against which we compare changes in chemical weathering. We also considered a synthetic hydrograph constructed from historically averaged discharge, as opposed to only the discharge data of 2011, and found similar results (Fig. IV-S7).

IV.4: Results

IV.4.1: Major ion chemistry

Ternary diagrams and timeseries of major ion concentrations and elemental ratios reveal both spatial and seasonal patterns (Figs. IV-2 and IV-3). The ion Ca^{2+} is the dominant cation throughout the Langtang-Trisuli-Narayani River system and accounts for 46-79% of the sum of Ca^{2+}, Mg^{2+}, Na^{+}, and K^{+}, in units of charge equivalents, except for one sample at 25% (Fig. IV-2A). The cation Mg^{2+} is of secondary importance and accounts for 8-32% of Σ^{+}. With the exception that both Na^{+} and K^{+} have a single outlier sample at 37%, Na^{+} accounts for 5-22% of Σ^{+} and K^{+} accounts for 2-22% of Σ^{+}. Overall, the major ion chemistry of the samples is consistent with prior observations from this region (IV.12.1; Harris et al., 1998; Galy and France-Lanord, 1999; Bhatt et al., 2009). As found previously, samples from the Bhote Kosi and Trisuli Rivers are slightly enriched in Na^{+} and K^{+} relative to Ca^{2+} and Mg^{2+} when compared to samples from the greater Narayani River system (Evans et al., 2004).

In the high-elevation sites, values of $(Na^{+}+K^{+})/\Sigma^{+}$ and Ca^{2+}/Σ^{+} fall along a line of constant Mg^{2+}/Σ^{+} near 10% (Fig. IV-2A). Conversely, differences among the lower-elevation stations LNS-1 to LNS-6 are predominantly between Ca^{2+}/Σ^{+} and Mg^{2+}/Σ^{+} with muted differences in $(Na^{+}+K^{+})/\Sigma^{+}$ around 10-20%. These observations are consistent with the high elevation sites weathering the Na^{+}-rich and K^{+}-rich HHC gneiss and schist, while lower elevation sites within the LH are dominated by calcite and dolomite weathering. While the aggregate changes in $(Na^{+}+K^{+})/\Sigma^{+}$ are related to the site of sample collection, Na^{+}/Σ^{+} and K^{+}/Σ^{+} also exhibit strong trends related to the month of sample collection (Fig.

IV-2B). At a given value of $(Ca^{2+}+Mg^{2+})/\Sigma^{+}$, monsoon samples are shifted to higher K^{+}/Σ^{+} and lower Na^{+}/Σ^{+} relative to samples from the non-monsoon.

The ratios Ca^{2+}/Na^{+} and Ca^{2+}/Mg^{2+} are elevated at most stations during the monsoon season (Figs. IV-3A and B). At LNS-4, however, both ratios are highly variable. Because $[K^{+}]$ does not coherently decline during the monsoon season and $[Na^{+}]$ does decline during the monsoon, K^{+}/Na^{+} is highest during the monsoon season at all stations. Likewise, monsoon K^{+}/Σ^{+} is elevated at all stations (Fig. IV-3D). Thus, while Ca^{2+}/Na^{+} is highest during the monsoon, the increase of $[K^{+}]$ relative to $[Na^{+}]$ and decline in absolute $[Ca^{2+}]$ and $[Mg^{2+}]$ results in muted seasonal change in Ca^{2+}/Σ^{+}, although with Ca^{2+}/Σ^{+} still generally higher during the monsoon season (Fig. IV-3C). Like $[K^{+}]$, $[Cl^{-}]$ is not always lower during the monsoon; the ratio Cl^{-}/Na^{+} is highest during the monsoon, and Cl^{-}/Σ^{+} is weakly elevated during the monsoon at most sites (Fig. IV-3E). While Ca^{2+}/Σ^{+} is elevated during the monsoon relative to the non-monsoon, some of this increase is associated with the weak increase in Cl^{-}/Σ^{+}. That is, because Cl^{-}/Σ^{+} increases during the monsoon, the relative supply of Ca^{2+} from precipitation also increases during the monsoon and partly decreases the Ca^{2+} attributed to lithologic weathering. Coupled with the monsoon increase in the K^{+}/Na^{+} ratio, these observations qualitatively suggest that we only weakly recover the monsoon increase in carbonate weathering fraction previously found in some datasets from Nepal (Tipper et al., 2006) and the Ganga-Brahmaputra basin (Sarin et al., 1989).

The dissolved anion budget in all of our samples is dominated by HCO_3^{-}, which comprises 49-84% of Σ^{+} (the sum of conservative cations is equal to the sum of anions here because HCO_3^{-} is solved by charge balance) (Fig. IV-2C). The anion SO_4^{2-} typically represents 5-30% of the budget but rises as high as 49% in a subset of samples from the

headwaters at the Lirung Glacier. The anion Cl^- is typically 1-13% of the anion budget but reaches 20-39% for the July and August sampling of LNS-4 and the August sampling of LNS-7 (Fig. IV-2D). Notably, these three samples are those where the inversion model either found only few solutions or was unable to find any solutions. The ratio of SO_4^{2-}/Σ^+ decreases at almost all stations during the monsoon season, with the lowest ratios found in July and August (Fig. IV-3F). These raw data suggest seasonality in the fraction of weathering driven by FeS_2 oxidation.

IV.4.2: Spatial and seasonal variability of $\delta^{34}S_{SO4}$

Values of $\delta^{34}S_{SO4}$ range from -4.5‰ to 9.0‰ (Fig. IV-4A). Averaged annually, $\delta^{34}S_{SO4}$ is 3.9‰ at station LNS-16 and increases to 6.0-6.8‰ moving downstream along the Langtang River through LNS-9, LNS-8, and LNS-7. Conversely, LNS-6 on the Bhote Koshi has an average $\delta^{34}S_{SO4}$ of -2.0‰. Station LNS-5, which is after the confluence of these two river systems, has an intermediate $\delta^{34}S_{SO4}$ value of 0.0‰. The value of $\delta^{34}S_{SO4}$ increases within the Trisuli River to reach 0.8-2.3‰ at stations LNS-4 and LNS-3, declines to -3.7‰ at LNS-2, and finally increases to -1.5‰ at LNS-1 (Fig. IV-4A). Overall, the range of measured $\delta^{34}S_{SO4}$ is largely consistent with prior values from the Himalaya including from the Alakananda-Bhagirathi rivers (Chakrapani and Veizer, 2006) and the Indus River Basin (Karim and Veizer, 2000).

The most notable trend in $\delta^{34}S_{SO4}$ is that samples from stations LNS-1 through LNS-6 (the downstream and Bhote Kosi stations) tend to be ^{34}S-depleted relative to samples from stations LNS-7 through LNS-16 (the upstream stations) (Fig. IV-4B). Annual variability in $\delta^{34}S_{SO4}$ at a given site is muted relative to this larger spatial pattern. Stations

LNS-4 and LNS-5 have the largest seasonal $\delta^{34}S_{SO4}$ variability; this is consistent with their position directly downstream of the confluence of the Bhote Koshi and Langtang Rivers, as the relative contribution of SO_4^{2-} from each upstream river likely varies seasonally. Additionally, variability in LNS-4 may be partially attributable to pollution from the urban center of Betrawati (IV.12.2).

Values of $\delta^{34}S_{SO4}$ are negatively correlated with $[SO_4^{2-}]$ when viewed across the whole dataset (Fig. IV-4C). At sites LNS-3 through LNS-6, $\delta^{34}S_{SO4}$ decreases seasonally with increasing $[SO_4^{2-}]$. For example, the May and September samples of LNS-5 with low $[SO_4^{2-}]$ have higher $\delta^{34}S_{SO4}$ values than samples with higher $[SO_4^{2-}]$. The non-linear decrease in $\delta^{34}S_{SO4}$ with increasing $[SO_4^{2-}]$, at the scale of either individual stations of the entire data suite, ostensibly resembles a mixing curve with multiple ‰ of scatter in $\delta^{34}S_{SO4}$ at a given value of $[SO_4^{2-}]$. However, $\delta^{34}S_{SO4}$ values are not clearly related to changes in Cl^-/SO_4^{2-} (Fig. IV-4D) or other major ion ratios (Fig. IV-S9). For example, while samples from LNS-5 have a wide range of $\delta^{34}S_{SO4}$ values inversely related with $[SO_4^{2-}]$, they have only a narrow range of Cl^-/SO_4^{2-} ratios (Fig. IV-4D). Likewise, the set of $\delta^{34}S_{SO4}$ measurements from LNS-1 through LNS-6, although systematically lower than the set from LNS-7 through LNS-16, is not distinct in Cl^-/SO_4^{2-} (Fig. IV-4D). Values of $\delta^{34}S_{SO4}$ at stations LNS-1, LNS-2, and LNS-7 through LNS-10 are invariant, with seasonal shifts towards higher $[SO_4^{2-}]$ during the non-monsoon season (Fig. IV-4C) and have little relationship with Cl^-/SO_4^{2-} (Fig. IV-4D). The major ion chemistry of our samples thus precludes two-component mixing as an explanation for the trend of $\delta^{34}S_{SO4}$ with $[SO_4^{2-}]$; as described below, the observations require multiple lithologic end-members with variable $\delta^{34}S$.

IV.4.3: Principal component analysis

The PCA of Z-scored [Ca^{2+}], [Mg^{2+}], [Na^{+}], [K^{+}], [Cl^{-}], [SO_4^{2-}], and $\delta^{34}S_{SO4}$ identifies that 3 components explain 95.1% of normalized variance. The first component (PC-1) explains 66.3% of variance and relates changes among all dissolved ion concentrations with opposite changes in $\delta^{34}S_{SO4}$ (Fig. IV-5A). PC-1 predominantly distinguishes samples by the site of collection, not by the season of collection (Fig. IV-5B), and thus indicates that lithology is the first-order control on dissolved ion chemistry (as found in other settings; e.g., Bluth and Kump, 1994). PC-1 also shows seasonal influences; at a given site, factor scores of PC-1 are generally higher in samples collected during the monsoon period and lower in samples collected in the non-monsoon (Fig. IV-5B). The second principal component (PC-2) explains 21.0% of the normalized variance and also shows both spatial and seasonal trends (Fig. IV-5C). These results indicate that seasonality exerts a secondary control on major ion chemistry along the Langtang-Trisuli-Narayani River system (Bhatt et al., 2018). Using cluster analysis, Pant et al. (2018) likewise showed that in river waters from the Narayani basin, lithology exerts the dominant control on dissolved chemistry and seasonality exerts a secondary influence.

PC-2 also inversely relates $\delta^{34}S_{SO4}$ with [SO_4^{2-}]. Unlike PC-1, PC-2 does not strongly relate changes in $\delta^{34}S_{SO4}$ with changes in [Ca^{2+}], [Mg^{2+}], or [Na^{+}], which are the major products of chemical weathering. This result indicates a mode of variability between [SO_4^{2-}] and $\delta^{34}S_{SO4}$ largely independent from shifts in weathering lithology. One qualitative explanation for this observation is a shift in the $\delta^{34}S$ and weatherability of an end-member providing SO_4^{2-} to solution. An alternative explanation is microbial sulfate reduction in

either the river sediments or tributaries, which would remove SO_4^{2-} and increase $\delta^{34}S_{SO4}$ (Turchyn et al., 2013).

The strongest relation in PC-2 is a positive correlation between $[K^+]$ and $[Cl^-]$. Monsoon samples from the Lirung Glacier outlet show systematically higher factor scores for PC-2 than samples from the non-monsoon (Fig. IV-5C). Given that these samples are relatively distant from direct anthropogenic influences, the covariation of $[K^+]$ and $[Cl^-]$ may reflect a true weathering dynamic.

IV.5: Discussion

IV.5.1: Mixing relations require source of ^{34}S-depleted SO_4^{2-}

The high Ca^{2+}/Σ^+ and low Na^+/Σ^+ ratios of samples from throughout the Langtang-Trisuli-Narayani River system indicate that the majority of positive charge in solution derives from either the carbonate mineral or precipitation end-members (Fig. IV-6A). The contribution of rainwater to the dissolved ion budgets is ultimately limited by the relative abundance of Cl^- (Fig. IV-6B). Given that the majority of cation charge must be derived from weathering of calcite and dolomite, river water samples have higher SO_4^{2-}/Σ^+ than can be explained without an additional source of SO_4^{2-} (Fig. IV-6C). Furthermore, the $\delta^{34}S_{SO4}$ of the samples is lower than the $\delta^{34}S$ values of calcite, dolomite, or precipitation (Fig. IV-6D). The elevated SO_4^{2-}/Σ^+ and low $\delta^{34}S_{SO4}$ of samples thus require an additional source of ^{34}S-depleted SO_4^{2-}. As previously suggested for the Langtang River (Bhatt et al., 2000; 2018) and shown in the Marsyandi catchment (Turchyn et al., 2013; Hemingway et al., 2020), a likely source of this sulfur is the oxidation of FeS_2. The oxidation of FeS_2 to H_2SO_4 and subsequent weathering of minerals could increase river SO_4^{2-}/Σ^+ and, depending on the value of $\delta^{34}S_{FeS2}$, decrease $\delta^{34}S_{SO4}$ to observed values (Figs. IV-6C and D, red boxes).

IV.5.2: Sources of dissolved ions

Our inversion model finds that the contribution of each end-member to river chemistry varies by element, site, and season (Figs. IV-7 and IV-S10). Calcite sources the majority of Ca^{2+} in solution, while Mg^{2+} is sourced from both dolomite and the two silicate end-members. The importance of dolomite weathering increases at the expense of calcite moving downstream (Figs. IV-7C and D). This shift reflects an increasing influence of LH

lithologies, which include massive dolomites, as the river leaves the predominantly silicate mineralogy of the HHC formation (Fig. IV-1). This observation again demonstrates the first-order control of site location on dissolved chemistry (Bluth and Kump, 1994), consistent with the results of the principal component analysis (Fig. IV-5).

The silicate end-member and biotite end-member dominate contributions to the budgets of Na^+ and K^+ (Figs. IV-7A, B, and IV-S10). Seasonally, results indicate a strong monsoon increase in weathering of the biotite end-member relative to weathering of the silicate end-member. One explanation for seasonal changes in biotite contribution is changing glacial weathering. Researchers have previously demonstrated that glacial weathering is typically enriched in K^+ and Ca^{2+} (Anderson et al., 1997; 2000). Following mechanical abrasion and the build-up of strain in biotite, K^+ release can occur through leaching or vermiculitization of the damaged mineral lattice. These processes may be exacerbated through either seasonal melting or higher subglacial discharge, explaining the higher biotite contribution during the monsoon. Because the monsoon increase in biotite weathering is reflected across all sample locations, an explanation from glacial weathering would require a meaningful contribution of meltwater to the lower Trisuli River. The monsoon increase in K^+/Σ^+ might alternatively reflect seasonal landslides and the exposure of freshly abraded surfaces (Emberson et al., 2017). Another explanation for the increase in K^+/Na^+ (Fig. IV-2B) could be a change in clay formation; a simultaneous release from clays of K^+ and Cl^- would explain both the shift towards biotite weathering and the strong covariation of K^+ with Cl^- (Fig. IV-3). Finally, leucogranites in the Langtang valley have variable K^+/Na^+ ratios, and leucogranites generally show inverse abundances of K^+ and Na^+ (Inger and Harris, 1993). The seasonal shift from the silicate end-member to the biotite

end-member in our model results may thus represent a seasonal transition from weathering of HHC gneiss to a high-K^+/Na^+ leucogranite.

IV.5.3: Inversion-constrained fraction of FeS_2-derived SO_4^{2-} and $\delta^{34}S_{FeS2}$

The median fraction of FeS_2-derived SO_4^{2-} ranges from 62% to 101% (Fig. IV-8A). These findings are consistent with the prior estimate that 70% of $[SO_4^{2-}]$ in this river system derives from FeS_2 oxidation (Galy and France-Lanord, 1999). If this FeS_2-derived SO_4^{2-} had a single characteristic $\delta^{34}S$ across all of our samples, mass balance would result in a clear relationship between the measured $\delta^{34}S_{SO4}$ and the fraction of total SO_4^{2-} attributed to FeS_2 oxidation (Fig. IV-8B). That is, an increase in the fraction of SO_4^{2-} attributed to FeS_2 oxidation should pull measured $\delta^{34}S_{SO4}$ values towards the $\delta^{34}S$ of the FeS_2 end-member. In contrast, our inversion results do not recover a clear relationship between $\delta^{34}S_{SO4}$ and the fraction of FeS_2-derived SO_4^{2-} at the scale of either individual sampling sites or the entire sample set (Fig. IV-8B). For example, while station LNS-1 exhibits a range of chemical compositions indicating that 64-93% of SO_4^{2-} is derived from FeS_2 oxidation, varying throughout the year, measured $\delta^{34}S_{SO4}$ remains nearly constant throughout the year at -1.5±0.6‰ (1σ). This result emerges directly from our raw observations of only a weak relationship between $\delta^{34}S_{SO4}$ and Cl^-/SO_4^{2-} (Fig. IV-4B).

We conclude that our results must be explained by variable $\delta^{34}S$ of FeS_2-derived SO_4^{2-}. Using the model-constrained fraction of FeS_2-derived SO_4^{2-}, measured $\delta^{34}S_{SO4}$, and a range of values of the $\delta^{34}S_{SO4}$ of precipitation, we use mass balance to calculate the $\delta^{34}S$ of FeS_2 required by each sample. The uncertainty associated with each determination of $\delta^{34}S_{FeS2}$ reflects the possible range in the fraction of SO_4^{2-} derived from FeS_2 oxidation and

uncertainty in the $^{34}S/^{32}S$ ratios of the precipitation end-member (Table IV-1). Calculated $\delta^{34}S_{FeS2}$ values fall broadly into two groups (Figs. IV-8C and D). At station LNS-7 through LNS-16, 80% of the data are explained with median $\delta^{34}S_{FeS2}$ values of 1.7-6.2‰. In contrast, 80% of the data from LNS-1 through LNS-6 are explained with median $\delta^{34}S_{FeS2}$ values of -7.0-0.0‰.

The two groups of samples with distinct $\delta^{34}S_{FeS2}$ values reflect the larger lithological context of the Nepal Himalaya. The catchments of stations LNS-7 through LNS-16 (with 80% of median calculated $\delta^{34}S_{FeS2}$ values between 1.7‰ and 6.2‰) are entirely underlain by HHC, with no exposure of LH or TSS lithologies (Fig. IV-8D). The FeS_2-derived SO_4^{2-} in the Langtang River is thus likely sourced principally from igneous or metamorphic sulfides in the metapelites and leucogranites of the HHC formation. FeS_2 has been observed as an accessory phase in Langtang rocks (Inger and Harris, 1992; 1993). The isotope composition of igneous sulfide minerals has previously been estimated to range from -10 to +10‰ (Thode, 1991; Karim and Veizer, 2000). Overall, the median $\delta^{34}S_{FeS2}$ values of these HHC sites are ^{34}S-enriched relative to bulk Earth and are similar to the average global river $\delta^{34}S_{SO4}$ of approximately 4.5‰ (Macnamara and Thode, 1950; Burke et al., 2018).

Conversely, the catchments of stations LNS-1 through LNS-6 (with 80% of median calculated $\delta^{34}S_{FeS2}$ values between -7.0‰ and 0.0‰) contain substantial outcroppings of the TSS and LH formations (Fig. IV-8D). As described above, the inversion-constrained values of $\delta^{34}S_{FeS2}$ reflect the net $\delta^{34}S$ of SO_4^{2-} sourced from both sulfide mineral oxidation and S_{org} oxidation. Because organic matter in the TSS can influence $\delta^{34}S_{FeS2}$, the shift in $\delta^{34}S_{FeS2}$ relative to LNS-7 through LNS-16 may reflect either a change in the $\delta^{34}S$ of

weathering sulfide minerals or possibly the oxidation of ^{34}S-depleted S_{org} that was not present in HHC bedrock. Given that organic matter tends to have a molar C_{org}: S_{org} ratio of approximately 100:1, sourcing any consequential fraction of dissolved [SO_4^{2-}] from oxidation of organic matter entails a large flux of carbon. Attributing 100% of [HCO_3^-] to organic matter oxidation at stations LNS-1 through LNS-6 would explain only 4-25% of [SO_4^{2-}], strongly suggesting that most river SO_4^{2-} is not derived from S_{org} oxidation. Furthermore, major ion concentrations and prior measurements of DIC $\delta^{13}C$ (Galy and France-Lanord, 1999) both indicate that carbonate weathering is a significant source of HCO_3^-. However, because CO_2 can be lost from river systems through degassing (Raymond et al., 2013), the relative abundance of DIC and SO_4^{2-} would not be expected to strictly match the C_{org}:S_{org} ratio of organic matter. Moreover, gas exchange can offset DIC $^{13}C/^{12}C$ from the primary carbon isotope ratio in organic matter. While a contribution from S_{org} oxidation to river SO_4^{2-} in the Langtang-Trisuli-Narayani River system is thus still possible, it is more parsimonious to attribute the downstream shift in $\delta^{34}S_{FeS2}$ to a change in the $\delta^{34}S$ of weathering sulfide minerals. Sedimentary pyrites tend to have low $\delta^{34}S$ values due to their formation by the fractionating process of microbial sulfate reduction (Thode et al., 1951; Sim et al., 2011), and could feasibly be ^{34}S-depleted relative to the sulfide minerals of the HHC. Previous work in the Marsyandi river has shown that SO_4^{2-} derived from FeS_2 oxidation in the TSS reaches $\delta^{34}S$ values as low as approximately -25‰, consistent with but lower than our minimum estimates of $\delta^{34}S_{FeS2}$ in downstream stations (Turchyn et al., 2013; Hemingway et al., 2020).

Our findings are similar to prior observations from the Indus River Basin where a decline in $\delta^{34}S_{SO4}$ from headwater to lowland samples was likewise attributed to a transition

from weathering igneous and metamorphic sulfide minerals to the weathering of sedimentary sulfide (Karim and Veizer, 2000). Similarly, our results are in agreement with the finding that weathering of magmatic sulfides may impact dissolved chemistry in the Marsyandi River downstream of the TSS (Turchyn et al., 2013). However, our measurements emphasize the possibility that, as previously considered and rejected in Turchyn et al. (2013), a second FeS_2 end-member with relatively high $^{34}S/^{32}S$ ratio, or alternatively a range of end-members with variable $^{34}S/^{32}S$ ratios, may contribute to the observed rise in $\delta^{34}S_{SO4}$ within the TSS section of the Marsyandi River.

IV.5.4: Carbon cycle implications of weathering in the Langtang-Trisuli-Narayani River system

Weathering of carbonate and silicate minerals by H_2CO_3 or H_2SO_4 has distinct impacts on the fluxes of ALK and DIC. After formalizing a framework introduced in Torres et al. (2016) we apply this methodology to show that weathering in the Langtang-Trisuli-Narayani River system is not a source or sink of CO_2 over timescales greater than marine carbonate compensation (5-10 kyr) (Archer et al., 1997; 2000) and shorter than the marine SO_4^{2-} residence time (approximately 10 Myr).

IV.5.4.1: Impacts of sulfuric acid weathering on ΔALK and ΔDIC

The chemical weathering of carbonate and silicate minerals can be described as titration reactions (Eqs. IV-1 and IV-4) where the source of H^+ can be either H_2CO_3 or H_2SO_4 (Eq. IV-5). Because the chemical reactions are written with each chemical species in the dominant form it would take at the CO_2 equivalence point, the ΔALK and ΔDIC of

each equation are the stoichiometric factors on H^+ and H_2CO_3, respectively (Zeebe and Wolf-Gladrow, 2001). Taking β and α to represent the production of ALK through silicate (Eq. IV-1) and carbonate weathering (Eq. IV-4), respectively, and γ the consumption of ALK through FeS_2 oxidation by reduction of O_2 (Eq. IV-5), a generic weathering reaction is constructed from their weighted sum (Eq. IV-7). This net reaction shows that ΔALK= α + β - γ and ΔDIC = α/2. Note that, unlike Torres et al. (2016), here we do not require the explicit coupling of H^+ production and H^+ consumption. Because α and β reflect the flux of ALK and not Ca^{2+} specifically, these formulations of ΔALK and ΔDIC are general across mineral stoichiometries.

$$(\alpha+\beta-\gamma)H^+ + \frac{\alpha}{2}CaCO_3 + \frac{\beta}{2}CaSiO_3 + \frac{\gamma}{4}FeS_2 + \frac{15\gamma}{16}O_2 + \frac{\gamma-\beta}{2}H_2O \rightarrow$$
$$\frac{\alpha+\beta}{2}Ca^{2+} + \frac{\alpha}{2}H_2CO_3 + \frac{\beta}{2}SiO_2 + \frac{\gamma}{2}SO_4^{2-} + \frac{\gamma}{8}Fe_2O_3 \qquad \text{(IV-7)}$$

The parameter R is defined as the ratio of carbonate weathering to total weathering (Eq. IV-8) and is equal to $\frac{\alpha}{\alpha+\beta}$. The parameter Z is defined as the fraction of weathering done with H_2SO_4 (Eq. IV-9) and is equal to $\frac{\gamma}{\alpha+\beta}$. The fraction of silicate weathering to total weathering is 1-R, and the fraction of CO_2-driven weathering is 1-Z. Following inversion, R and Z can be defined explicitly as the sum of ionic contributions from each of the four lithologic end-members in our inversion (Eqs. IV-8 and IV-9). Brackets in Eqs. IV-8 and IV-9 indicate the concentration of the indicated element that can be attributed to the subscripted end-member, and factors convert concentrations to units of charge equivalents. The numerator of R is thus the sum of Ca^{2+} and Mg^{2+} contributions from calcite and from

dolomite, and the numerator of Z is the sum of SO_4^{2-} contributions from each of the four non-precipitation end-members shown as the sum over the ith end-member. Lastly, the denominator of both R and Z is the sum of Ca^{2+}, Mg^{2+}, Na^+, and K^+ contributions from each of the 4 weathering end-members, also shown as a sum over the ith end-member. The net ΔALK/ΔDIC due to a weathering system can then be calculated as a simple function of R and Z (Eq. IV-10).

$$R = \frac{\alpha}{\alpha+\beta} = \frac{\left(2*[Ca^{2+}]_{calcite} + 2*[Ca^{2+}]_{dolomite} + 2*[Mg^{2+}]_{dolomite}\right)}{\Sigma_{i=1}^{4}(2*[Ca^{2+}]_i + 2*[Mg^{2+}]_i + [Na^+]_i + [K^+]_i)} \quad \text{(IV-8)}$$

$$Z = \frac{\gamma}{\alpha+\beta} = \frac{\Sigma_{i=1}^{4}(2*[SO_4^{2-}]_i)}{\Sigma_{i=1}^{4}(2*[Ca^{2+}]_i + 2*[Mg^{2+}]_i + [Na^+]_i + [K^+]_i)} \quad \text{(IV-9)}$$

$$\frac{\Delta ALK}{\Delta DIC} = \frac{(\alpha+\beta-\gamma)}{\alpha/2} = 2\left(\frac{\frac{\alpha+\beta-\gamma}{\alpha+\beta}}{\frac{\alpha}{\alpha+\beta}}\right) = 2\left(\frac{1-\frac{\gamma}{\alpha+\beta}}{\frac{\alpha}{\alpha+\beta}}\right) = 2\frac{(1-Z)}{R} \quad \text{(IV-10)}$$

When viewed instantaneously, any flux with ΔALK/ΔDIC>1 will sequester CO_2 into the ocean while fluxes with ΔALK/ΔDIC<1 will source CO_2 to the atmosphere. The boundary for this instantaneous CO_2 flux is Z=1-R/2 (Eq. IV-10). The influence of chemical fluxes over longer timescales depends on the removal rate of individual ions from the global ocean-atmosphere system. Because the reduction of SO_4^{2-} in marine sediments consumes H^+ and counteracts the ALK flux of terrestrial FeS_2 oxidation, FeS_2 oxidation during weathering influences climate on timescales shorter than the ~10 Myr marine residence time of SO_4^{2-}. During a transient period of time in which sulfide oxidation increases pCO_2, marine SO_4^{2-} concentrations increase in tandem (Torres et al., 2014; Rennie et al., 2018). Carbonate mineral burial ultimately removes most of the alkalinity supplied to the global ocean from rivers, so a second relevant timescale is that of carbonate

compensation. Because carbonate mineral burial removes ALK and DIC in a 2:1 ratio, fluxes with $\Delta ALK/\Delta DIC<2$ represent sources of CO_2 to the atmosphere on timescales longer than carbonate compensation but shorter than the marine SO_4^{2-} residence time. The boundary for this long time-scale CO_2 flux is Z=1-R, which implies that fluxes with $1<\Delta ALK/\Delta DIC<2$ are short-term sinks of atmospheric CO_2 but long-term sources (Torres et al., 2016).

IV.5.4.2: R and Z in the Langtang-Trisuli-Narayani River system

Except for one low value of R and two samples without successful inversion results, the median fraction of cations sourced from carbonate end-members in our samples ranges between 60% and 86% (Fig. IV-9). These values are consistent with previous studies of the Langtang-Trisuli-Narayani River system (West et al., 2002; Tipper et al., 2006; Galy and France-Lanord, 1999). The median fraction of weathering acid sourced from FeS_2 oxidation ranges from 10% to 55%, similar to values calculated for the Andean middle mountains and floodplain of southern Peru (Torres et al., 2016). Values of R and Z in the Langtang-Trisuli-Narayani River system exhibit both seasonal and spatial trends, but overall the data scatter around the line Z = 1-R (Figs. IV-9A, B, IV-S11, and IV-S12). As discussed above, the line Z=1-R corresponds to $\Delta ALK/\Delta DIC=2$ (Eq. IV-10) and defines the line across which chemical weathering has no implications for the carbon cycle on timescales greater than 5-10 kyr and less than approximately 10 Myr. Our data thus straddle the line between long-term sources and sinks of pCO_2; we conclude that, within uncertainty, FeS_2 oxidation in the Narayani River catchment may completely compensate for the canonical pCO_2 drawdown of silicate weathering. However, the spatial and seasonal

changes in R and Z do shift whether the instantaneous flux is a source or sink of CO_2. Understanding the origin of this chemical variability is critical for characterizing how the global carbon cycle has responded to Himalayan weathering throughout the Cenozoic.

IV.5.4.2.1: Spatial changes in R and Z

The inversion results indicate minimal spatial variation in the fraction of carbonate weathering (R) (Fig. IV-9C). This lack of downstream variation is unexpected given the change in lithology from the silicate-dominated HHC to the dolomite-rich LH (Figs. IV-1 and IV-S13). The lack of clear trend may reflect the supersaturation of Himalayan waters with respect to calcite, such that any downstream change in the magnitude of carbonate weathering is obscured by secondary carbonate precipitation (Bickle et al., 2015). An alternative explanation is that enhanced carbonate weathering associated with the transition to a dolomite-rich lithology is compensated by enhanced weathering of silicates as the river moves into a warmer and wetter environment (West et al., 2002).

In contrast, the fraction of acid sourced through FeS_2 oxidation (Z) decreases downstream (Fig. IV-9D). The mean Z value of the Lirung Glacier sites is 35%, decreasing to a mean value of 28% at LNS-7 and LNS-8 in the downstream Langtang, and reaching a mean value of 23% in the lowermost 4 sampling sites. The downstream decrease in the fraction of sulfuric acid weathering reflects the transition from a mountainous, highly erosive regime to a flatter environment with limited access to primary FeS_2 from bedrock erosion. The highest values of Z are found in glacial catchments, consistent with prior observations from glacial rivers (Anderson et al., 2000; Emberson et al., 2017) and inversion of global data (Torres et al., 2017). This effect can be explained because glaciers

generate enhanced mineral surface area and disproportionately express weathering reactions with rapid kinetics, such as sulfide oxidation and carbonate dissolution (Gabet et al., 2008; Tranter and Wadham, 2014; Torres et al., 2017). The net effect of the consistently elevated Z values for some of our sampling sites in the headwaters, e.g., in the upper Langtang valley, together with little difference in R, is that these locations lie within the R-Z space characterized by long-term CO_2 release, even though the Narayani system as a whole falls in the region where sources and sinks are approximately balanced.

IV.5.4.2.2: Seasonal changes in R

Prior studies have identified an increase in the fraction of carbonate weathering during the monsoon season in several sites throughout the Narayani River system, including the Lirung Glacier outlet within the upper Langtang Valley (Bhatt et al., 2000; Tipper et al., 2006), four sites in the Marsyandi basin with detailed time series data (Tipper et al., 2006), a series of small TSS-draining tributaries in the Marsyandi catchment with paired April/May and September samplings (Bickle et al., 2005; Tipper et al., 2006), the Trisuli River sampled at Betrawati (equivalent to our site LNS-4; Galy and Frace-Lanord, 1999), and the greater Ganges rivers (Sarin et al., 1989). One explanation for the observed seasonal increase in the fraction of carbonate weathering is a hydrological transition in which, during the monsoon season, flow paths with shorter residence times become relatively more important than during the non-monsoon season (Tipper et al., 2006).

Due to the rapid dissolution kinetics of carbonate mineral relative to the slow dissolution kinetics of silicate minerals, a parcel of water given longer time for water-rock interaction may accumulate a larger fraction of silicate-derived cations (Tipper et al.,

2006). As a result, water sourced from deeper flow paths with a longer residence time can be expected to have a larger fraction of silicate-derived cations. As the monsoon seasons begins and the water table rises, the source of water in the river channel may become dominated by flow paths with shorter residence times, potentially at shallower depths, and may thus express a higher fraction of carbonate-derived cations. In turn, the fraction of carbonate weathering may decline as the monsoon season wanes and deeper flow-paths with longer residences times increase their fractional contribution to water in the river channel (Tipper et al., 2006). This hydrological explanation for seasonal changes in the carbonate weathering ratio relies on changes in the ratio of water sourced from shallow flow paths to total discharge; this ratio may increase or decrease even if the absolute quantity of water sourced from both shallow and deeper flow paths increases due to intense monsoon precipitation, an elevated groundwater table, and an increase in hydraulic head.

Unlike prior work, our analysis does not recover clear seasonal changes in R (Figs. IV-9C and E); this finding is seen when model results are plotted for individual months against sampling location (Fig. IV-9C top, colored symbols), clustered into those belonging to either the monsoon season (June – September) or the non-monsoon season (January through May and October through November) (Fig. IV-9C bottom, black and white symbols), or as a timeseries (Fig. IV-9E). Although we do not have discharge measurements at all stations, we consider the values of R for different relative discharges using a synthetic hydrograph (Fig. IV-S7). Opposite to expectations from prior findings, regressions of R against the synthetic discharge curve do not show consistently positive relationships (Fig. IV-10). Thus, when considering all of the major ion concentration

measurements (Figs. IV-9C and E), we do not recover the monsoon increase in R reported in previous work (Fig. IV-S14; Sarin et al., 1989; Tipper et al., 2006).

Application of our inversion calculation to previously published datasets shows that the lack of seasonality in R is not simply a result of the modeling approach we use (Fig. IV-S14): our inversion model recovers monsoon increases in R for samples of the Trisuli River at Betrawati reported in Galy and France-Lanord (1999) (Fig. IV-S14A) and in the Lirung Glacier outflow data of Bhatt et al. (2000) (Fig. IV-S14D). Conversely, we find only minimal seasonal changes in R for the time-series data of Tipper et al. (2006) from tributaries of the Marsyandi River (Fig. IV-S14G). However, the evidence for seasonal changes in carbonate weathering reported in Tipper et al. (2006) is primarily based on observations of $Si(OH)_4/Ca^{2+}$ ratios and $^{87}Sr/^{86}Sr$ ratios, yet neither [Si] nor $^{87}Sr/^{86}Sr$ ratios are included in our inversion model (Figs. IV-S14G and H). A second potential reason for this disagreement is that the Marsyandi catchment contains hot springs that may source Cl^- to the river, which are also not included in our primary inversion (Figs. IV-S4 and IV-S16), and thus the contribution of precipitation to the dissolved load may be overstated in our treatment of data from Tipper et al. (2006).

If observations of $[K^+]$ and $[Cl^-]$ are removed from the inversion, we do recover a clear seasonal increase in the fraction of carbonate weathering, broadly similar to that seen in prior work (Fig. IV-S17; IV.12.4). The key difference between our results and those reported previously is thus our observation of elevated K^+/Σ^+ during the monsoon season (Fig. IV-3D), which sustains the silicate weathering contribution to the solute load. This relative invariance of $[K^+]$ during the monsoon season (i.e., lack of dilution as seen for other solutes including $[Ca^{2+}]$) has been not documented in prior studies from the Nepal

Himalaya. One explanation for our observation that K^+ behavior differs from that found in previous work could be that the processes responsible for sourcing K^+ have strengthened with time, for example if preferential leaching from glacially-ground minerals has become more efficient as glaciers have retreated. Such a change in weathering dynamics might explain why samples collected in the 1990s and early 2000s did not capture the effect that we see in samples from 2011, with potentially important implications for how changes in glacial dynamics over decadal timescales affect solute chemistry. Alternatively, we recognize that our observations of elevated [K^+] may be an experimental artifact of bottle washing or sample collection. Inclusion of hot springs in the inversion results in a monsoon decrease in carbonate weathering fraction, opposite to prior findings (Fig. IV-S16), while inclusion of an evaporite end-member does not meaningfully change our results (Fig. IV-S15). Likewise, the results of our primary inversion model are similar to those of a simple forward model (Fig. IV-S18). In all cases, further study is warranted on the seasonally changing solute chemistry in rivers fed by Himalayan glaciers.

IV.5.4.2.3: Seasonal changes in Z

Seasonal shifts in Z are more pronounced than those in R in our data, with the Z value of a given location lower during the monsoon season than during the non-monsoon (Figs. IV-9D and F). This monsoon decline in the proportion of solutes from H_2SO_4-driven weathering is seen in 13 out of 16 stations and has an absolute magnitude of 1-13%, corresponding to a 3-40% relative change in the fraction of weathering driven by H_2SO_4 (Fig. IV-9D). This seasonal change in Z is larger in the TSS-influenced sites than in the

HHC-influenced sites. One consequence of the observed seasonality is that the fraction of H_2SO_4-driven weathering declines with higher fractional discharge (Fig. IV-10).

Our results agree with those reported for the Trisuli River by Galy and France-Lanord (1999), who report a seasonal decline in the ratio of SO_4^{2-} from sulfide oxidation and evaporite dissolution relative to the sum of total SO_4^{2-} and HCO_3^-. Application of our inversion model to their data recovers a monsoon-season decrease in Z (Fig. IV-S14B). A monsoon decrease in Z is also recovered in data from the Lirung Glacier outlet reported by Bhatt et al. (2000) (Fig. IV-S14E) and in the Chame and Nar Khola timeseries data from Tipper et al. (2006) (Fig. IV-S14H).

Explanations for seasonal changes in Z depend on the subsurface structure of chemical weathering fronts, which are themselves determined by the long-term interaction of tectonics and weathering. Without additional observations of the FeS_2 and $CaCO_3$ weathering profiles in our sampling catchments, at this time we can only hypothesize as to the relevant mechanisms driving the observed seasonal solute dynamics. Below, we briefly evaluate the consistency of our observations with different erosional scenarios (Fig. IV-11).

When the residence time of a mineral in the weathering zone is short relative to the time required for weathering, insufficient time for complete dissolution prevents the development of a complete subsurface dissolution front (i.e., the zone where mineral abundances decline to zero; Brantley and Lebedeva, 2011). This regime, termed “kinetic limitation,” contrasts with “supply limitation” wherein sufficient time is available for weathering such that the mineral abundances decline to zero below the weathering zone surface. Holding all other factors equal, minerals will transition from supply limitation to

kinetic limitation as the erosion rate increases owing to a faster transit through the weathering zone (West, 2012). The exact crossover point between kinetic limitation and supply limitation varies among different minerals depending upon their reactivity and abundance in the weathering zone; a reasonable expectation is that reactive minerals will remain supply limited over a larger range of erosion rates than will less reactive minerals (Gu et al., 2020). Under supply limitation, the position of a subsurface dissolution front may still shoal with increasing erosion.

When the residence time of FeS_2 in the weathering zone is relatively long, there may be sufficient time for the development of a deep FeS_2 dissolution front (Fig. IV-11, purple FeS_2 front). In this case, shallow flow paths would have minimal access to FeS_2 while deeper flow paths could accumulate SO_4^{2-} through FeS_2 oxidation. During the higher discharge of the monsoon season, an increase in the fraction of river channel water derived from shallower flow paths above a deep FeS_2 weathering front would lead to a seasonal reduction in the Z value recorded by the river chemistry. That is, enhanced discharge would result in a lower observed fraction of weathering driven by H_2SO_4, consistent with our observations (Figs. IV-9 and IV-10). Although a deep FeS_2 weathering front is difficult to reconcile with the high erosion rates of the Himalaya, much of the weathering in rapidly-eroding mountain belts takes place in bedrock, as opposed to soil profiles, and with influences from groundwater (Andermann et al., 2012; West, 2012).

When erosion rates are very high, FeS_2 may remain supply limited while only being depleted in a thin near-surface zone (Fig. IV-11, blue FeS_2 front). Under this condition, where all flow paths would have access to FeS_2, seasonal transitions in the source of water entering the river channel are unlikely to explain the observed seasonality in Z. In this case,

an alternative explanation for observed seasonality comes from considering the changing supply of CO_2 and O_2 to the weathering system. During periods of high precipitation, an enhanced flux of CO_2 and O_2 are supplied to the subsurface for potential consumption in weathering reactions. If the waters hosting such weathering reactions are rapidly exported into the channel, this seasonal supply of acids and oxidants could influence the observed values of R and Z. When a seasonal flux of oxidant does not reach the FeS_2 weathering front, the seasonal reduction in Z could be caused by an increase in H_2CO_3-driven weathering (Winnick et al., 2017). Alternatively, if the FeS_2 front is shallow, seasonal increases in the supply ratio of CO_2/O_2 could induce depletions in Z; such an increase could be due to the oxidation of organic carbon formed during the non-monsoon season. In these cases, the observed changes in Z would result from altering the chemistry of water in shallow flow paths rapidly exported to the river channel, as opposed to changing the relative contributions of water from different hydrologic regions.

IV.5.4.4: Extension to geologic timescales

The tectonic and erosional dynamics of the weathering system impact how seasonal changes might be representative of climate changes over longer timescales. When extrapolated beyond seasonal timescales, our observations of seasonal change in Z ostensibly could indicate a negative feedback between discharge and FeS_2 oxidation (Fig. IV-10). Climate models show that global warming is associated with a strengthened hydrologic cycle and location-specific changes in runoff (Otto-Bliesner, 1995). Thus, if the patterns we observe are representative of responses over long time-scales, then higher temperatures forced by higher pCO_2 could result in greater discharge, lower fractions of

FeS_2 oxidation, and a more effective silicate weathering cycle. Preliminary evidence for such a feedback can be found in the Cenozoic increase of dissolved marine [SO_4^{2-}] during the corresponding decline in pCO_2 inferred from $CaCO_3$ $\delta^{18}O$ (Zachos et al., 2001; Horita et al., 2002; Torres et al. 2014). However, the feedback between discharge and H_2SO_4-driven weathering relies on the supply of O_2 and CO_2 relative to the position of the water table and relative to the FeS_2 and $CaCO_3$ weathering fronts (Fig. IV-11). Although presumably stable on the decadal timescales of concentration-discharge observations, this weathering dynamic is likely to shift due to long-term changes in tectonics and climate (Godsey et al., 2009, 2019; Ibarra et al., 2016). For example, if we assume that erosion rates balance uplift rates over tectonic timescales, the long-term control of Himalayan sulfide oxidation is likely to be tectonic shortening rather than river discharge. Indeed, the interplay between seasonal weathering dynamics and discharge likely changed throughout the uplift of the Himalaya and the initiation and development of the seasonal monsoon.

IV.5.5: Inversion of published river observations from the Nepal Himalaya

Prior datasets of dissolved river chemistry from throughout the Nepal Himalaya were inverted using the same model applied to our samples from the Langtang-Trisuli-Narayani River system (Fig. IV-12; Table IV-1). The inverted data come from the Langtang River (Bhatt et al., 2009), the Marsyandi catchment (Bickle et al., 2005; Tipper et al., 2006, Wolff-Boenisch et al., 2009; Turchyn et al., 2013), the Yamuna catchment (Dalai et al., 2002), the greater Narayani basin (Galy and France-Lanord, 1999; Pant et al., 2018), rivers of the western Himalayan (English et al., 2000; Quade et al., 2003), and the Ganges floodplain rivers (Sarin et al., 1989; Bickle et al., 2018) (Fig. IV-12A). Analogous

to our samples from the Langtang-Trisuli-Narayani River system, the larger dataset reveals that carbonate weathering sources the majority of cations to solution, and there is strong evidence of extensive weathering driven by H_2SO_4 (Figs. IV-12B, C, D, and E).

Overall, analysis of R and Z in the previously published data reveals a transition from weathering as CO_2-neutral in the mountainous fronts of the Himalaya (Figs. IV-12B, C, and D) to weathering as a sink of CO_2 in the floodplain (Fig. IV-12E). Samples from prior study of the Langtang-Trisuli-Narayani River system are similar to those reported here and show that FeS_2 oxidation largely offsets CO_2 drawdown due to silicate weathering throughout the Narayani catchment. In a few cases, similar to the Langtang headwaters in our study, mountainous sites are characterized by long-term CO_2 release. Conversely, samples from the Ganges floodplain (Sarin et al., 1989; Galy and France-Lanord, 1999; Bickle et al., 2018) show lower fractions of carbonate weathering and sulfuric acid weathering, consistent with previous work showing that silicate weathering occurs predominantly in the lowland hills and Himalayan floodplain (Galy and France-Lanord, 1999; West et al., 2002; Lupker et al., 2012; Bickle et al., 2018; Bhatt et al., 2018).

IV.6: Conclusions

Here we report the major ion concentrations and $\delta^{34}S_{SO4}$ of water samples collected monthly or bimonthly during 2011 from 16 sites along the Langtang-Trisuli-Narayani River system in the Nepal Himalaya. We evaluate the role of lithology and seasonality in the supply and $^{34}S/^{32}S$ isotope ratio of river SO_4^{2-} and account for the alkalinity flux from FeS_2 oxidation when evaluating the effect of Himalayan weathering on atmospheric pCO_2 over geologic time. Monte Carlo inversion modeling finds that, except for two samples, FeS_2 oxidation sources between 62% and 101% of dissolved SO_4^{2-} in our samples. We find that $\delta^{34}S_{SO4}$ principally reflects lithological $\delta^{34}S$ and is relatively constant at a given location throughout the sampled year. We recover spatial gradients in the magnitude of FeS_2 oxidation linked with weathering regime, as well as seasonal changes attributable to shifts in the relative importance of shallow and deep flow paths. Our results indicate that sulfide oxidation in the Narayani catchment may fully counteract the CO_2 drawdown associated with silicate weathering on timescales longer than carbonate compensation (5-10 kyr) but shorter than the marine residence time of SO_4^{2-} (approximately10 Myr).

IV.7: Data availability

The measurements of $\delta^{34}S_{SO4}$ and dissolved major ion concentrations described in this article are available as supplementary materials.

IV.8: Acknowledgments

P.C.K. is supported by the Fannie and John Hertz Foundation Cohan-Jacobs and Stein Families Fellowship. This research was conducted with government support under and awarded by DoD, Air Force Office of Scientific Research, National Defense Science and Engineering Graduate (NDSEG) Fellowship, 32 CFR 168a. This research was supported by the US National Science Foundation (grants 1349858 and 1834492). N.F.D. is grateful to the Linde Center for support. The Caltech Environmental Analysis Center is supported by the Linde Center and the Beckman Institute at Caltech. This research was also supported by the German Research Foundation DFG through the Cluster of Excellence 'CliSAP' (EXC177), Universität Hamburg. The authors acknowledge the Department of Hydrology and Meteorology (DHM), Government of Nepal, for discharge measurements. Initial computing costs were covered by startup research funds provided by Caltech to F. Tissot. T. Jappinen and P. Bartsch helped with logistics and analysis. The authors are grateful to W. Fischer for helpful conversations and to A. Phillips and P. Mateo for advice on the design of figures. We thank associate editor Novak and three anonymous reviewers for providing insightful comments.

IV.9: Figures

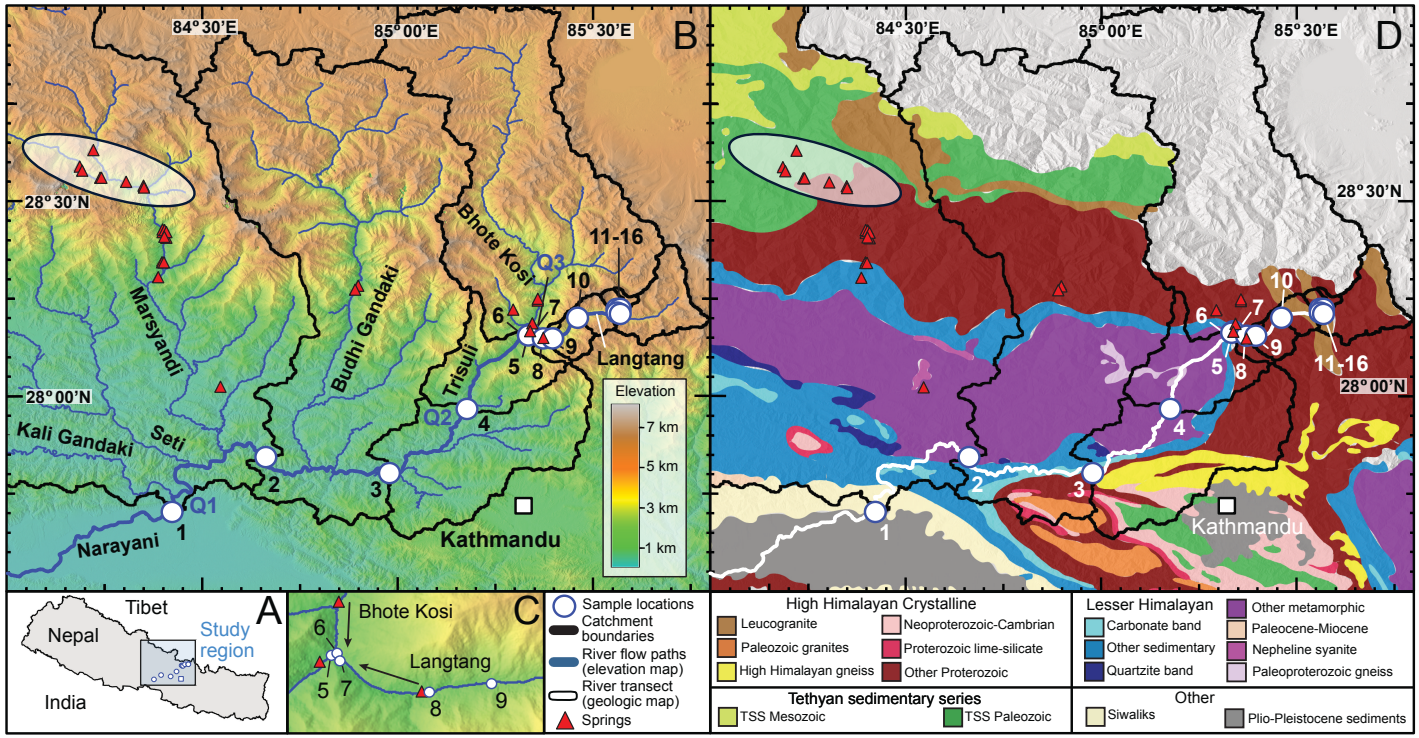

Fig. IV-1: Sampling locations and geologic map of the Langtang-Trisuli-Narayani River system. (A) The study region in central Nepal. (B) Elevation map with sample locations (white circles), labeled river network (blue), catchment boundaries (black), and geothermal springs (red triangles). Q1-Q3 indicate the locations of gauging stations. Shaded oval indicates approximate location of samples described in Turchyn et al. (2013) and Hemingway et al. (2020). Elevation color bar applies to (B) and (C) panels. (C) Elevation map at the confluence of the Langtang and Bhote Kosi rivers showing the relative positions of LNS-5 through LNS-9. (D) Geologic map of Nepal (Roback et al. (2018) after Dhital (2015)). Sample sites span the High Himalayan Crystalline and Lesser Himalayan sequences; although incompletely mapped, the Tethyn Sedimentary Series likely extends east into Tibet to be drained through the Bhote Kosi. Elevation data are from the Shuttle Radar Topography Mission, and locations of geothermal springs are from Evans et al. (2008) and Becker et al. (2008).

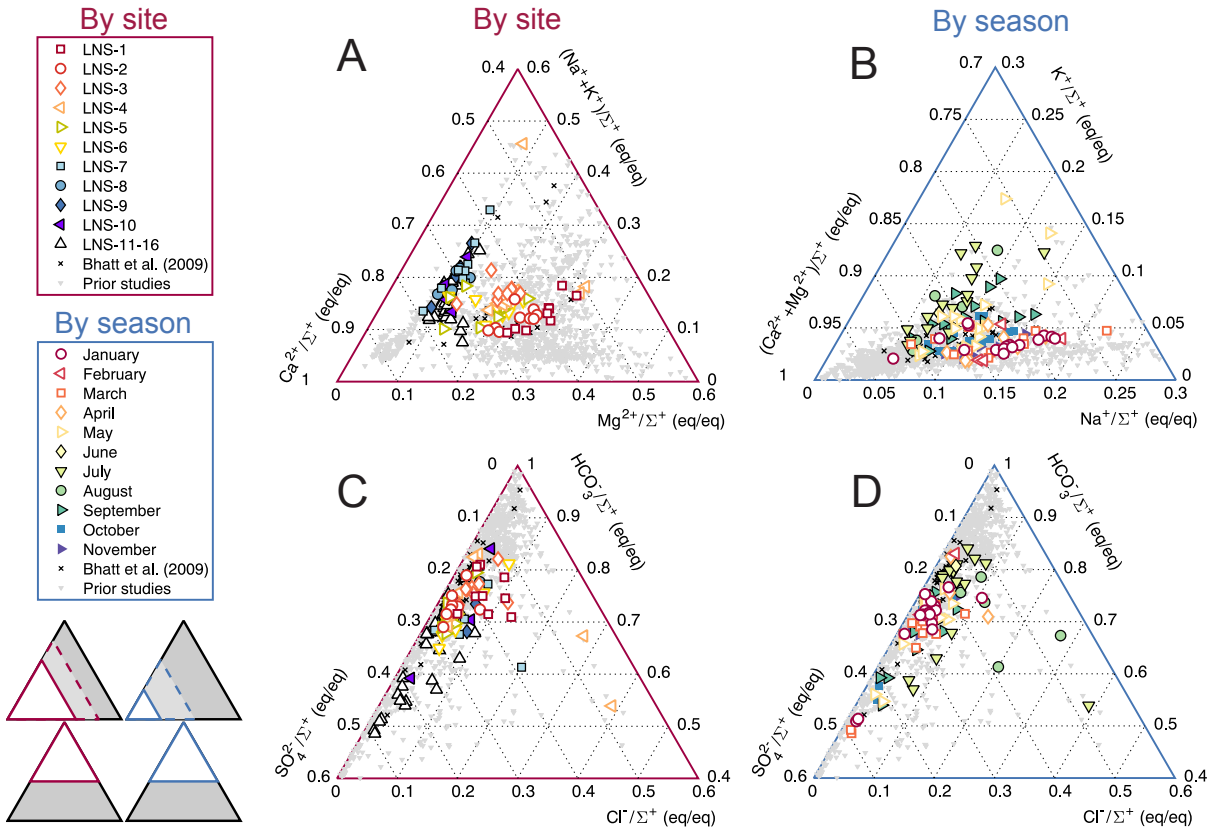

Fig. IV-2: Ternary diagrams for river water samples from the Langtang-Trisuli-Narayani River system show spatial and temporal patterns. Panels are color coded by either station number (A, C) or month of collection (B, D), and are subsets of the full parameter space as indicated in the schematics (lower-left: filled white triangles are plotted areas, dashed triangles contain the full dataset, and grey triangles represent the full space). (A) The dominant cation in solution is Ca^{2+}. The cation Mg^{2+} is second in relative abundance, and $Na^{+}+K^{+}$ represents a limited fraction of the charge budget. Spatial transitions between $(Na^{+}+K^{+})/\Sigma^{+}$ and Mg^{2+}/Σ^{+} indicate the differing abundance of silicate and carbonate minerals in the HHC and LH. (B) The ratios Na^{+}/Σ^{+} and K^{+}/Σ^{+} shift seasonally in relative importance, with higher K^{+}/Na^{+} ratio during the monsoon and lower ratio during the non-monsoon season. (C) The major anion in solution is HCO_3^{-}, except near the Lirung Glacier catchment where SO_4^{2-} occasionally has subequal contribution. (D) Monsoon season samples are occasionally enriched in Cl^{-}/Σ^{+} relative to samples from the non-monsoon season. Plotted values reflect raw measurements without correction for inputs from precipitation. All samples from this study are plotted in (C) and (D). One sample with $(Na^{+}+K^{+})/\Sigma^{+}$ ~60% is out of the plotting range in (A), and three samples are out of the plotting range in (B). Data from prior studies (grey triangles) are river water samples reported in Sarin et al. (1989), Galy and France-Lanord (1999), English et al. (2000), Bhatt et al. (2000), Dalai et al. (2002), Quade et al. (2003), Evans et al. (2004), Bickle et al. (2005, 2018), Tipper et al. (2006), Wolff-Boenisch et al. (2009), Turchyn et al. (2013), and Pant et al. (2018).

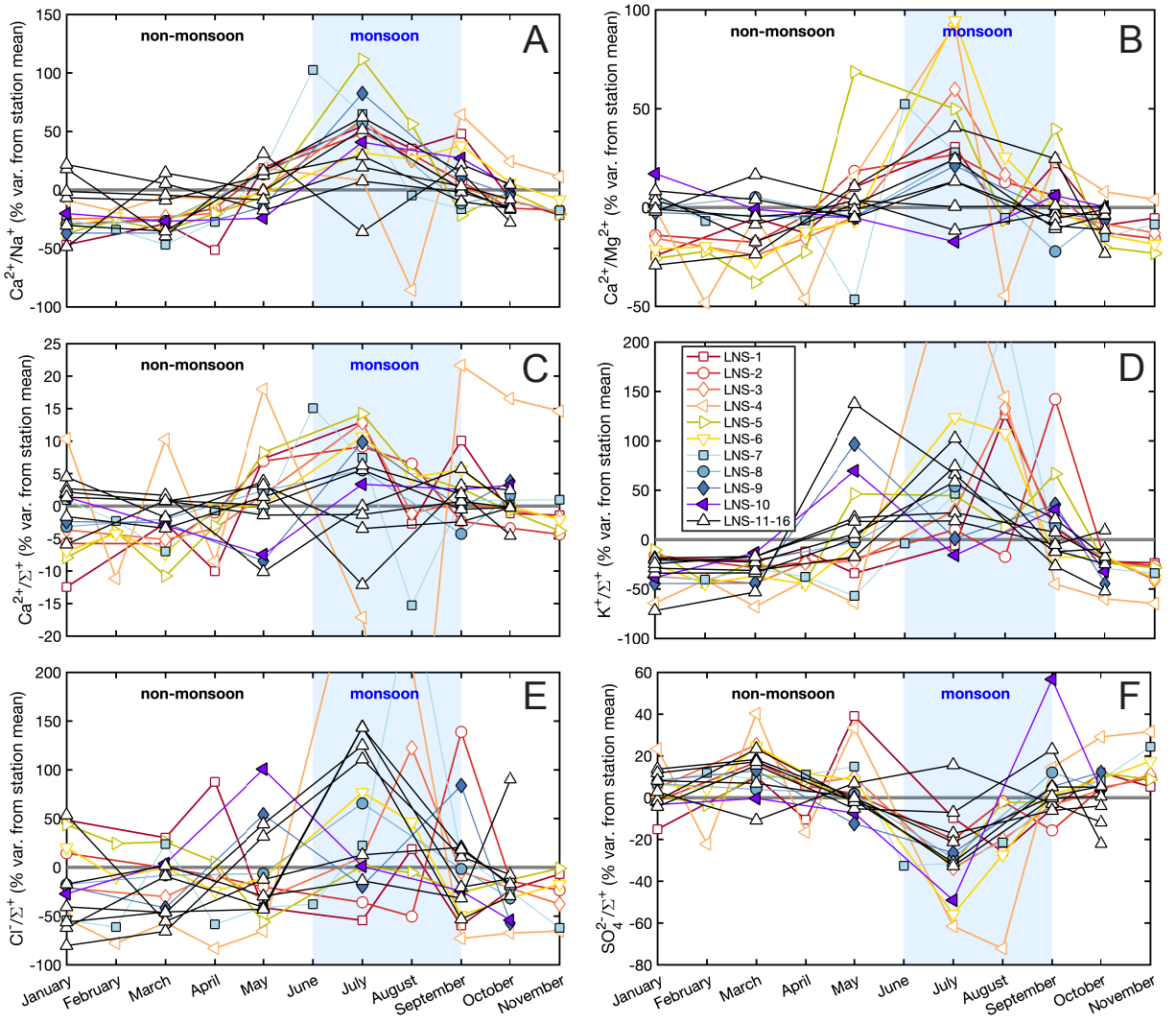

Fig. IV-3: Timeseries of dissolved ratios reported as the % variations from annual station means. (A) The cation ratio Ca^{2+}/Na^{+} increases during the monsoon season relative to the non-monsoon. (B) The ratio Ca^{2+}/Mg^{2+} also increases during the monsoon, consistent with a shift in either the relative fraction of silicate and carbonate weathering or a shift from dolomite to calcite weathering. (C) The ratio Ca^{2+}/Σ^{+} tends to increase weakly during the monsoon. (D) The ratio K^{+}/Σ^{+} increases strongly during the monsoon. (E) The ratio Cl^{-}/Σ^{+} shows a weak increase during the monsoon, which partially offsets the observed monsoon rise in Ca^{2+}/Σ^{+} due to the high Ca^{2+}/Cl^{-} of precipitation (Table IV-1). (F) The ratio SO_4^{2-}/Σ^{+} declines during the monsoon, suggesting a seasonal reduction in the fraction of weathering driven by sulfide oxidation. Note that each panel has a variable y-axis range, and that blue shading indicates the monsoon season.

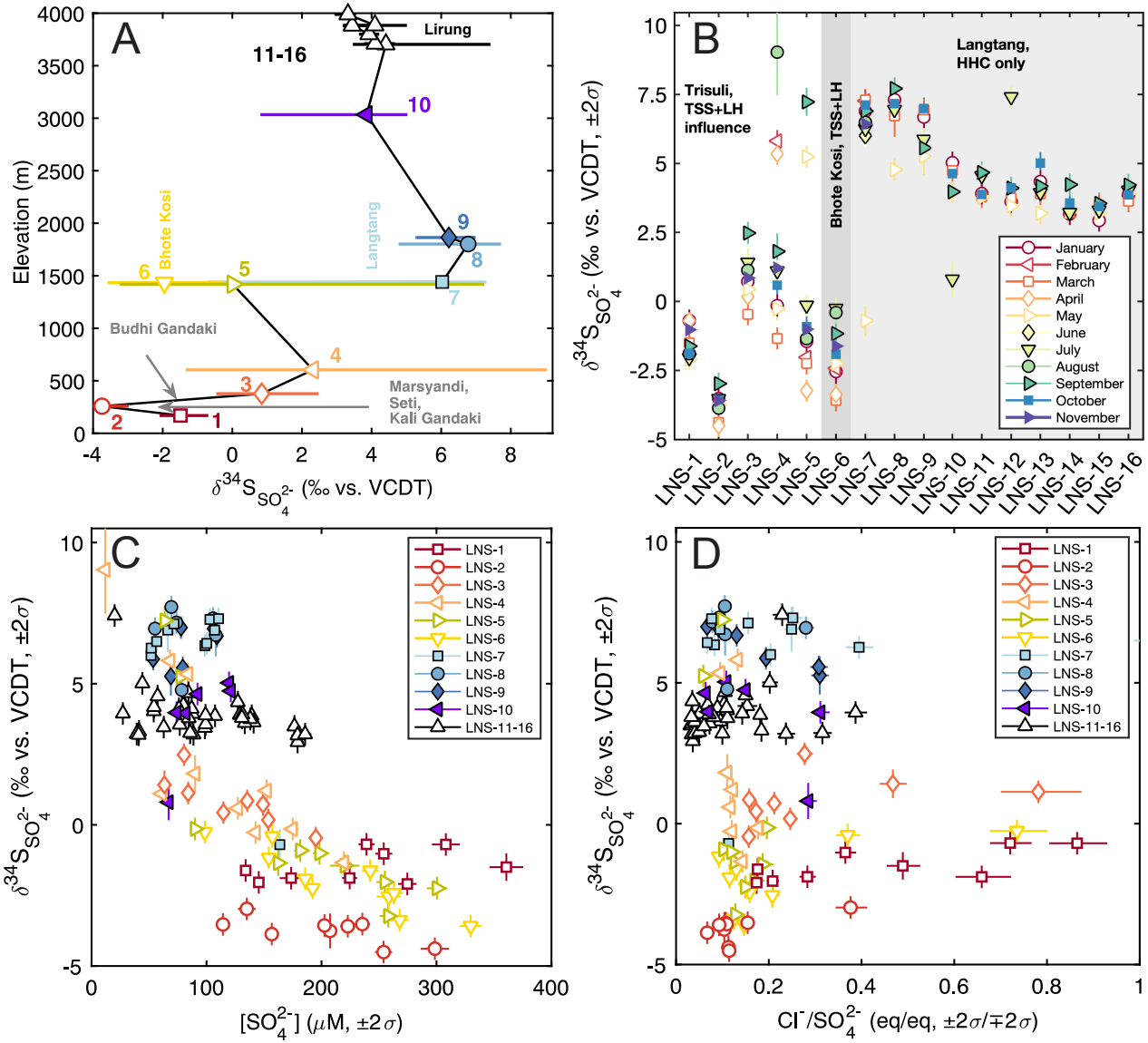

Fig. IV-4: River water $\delta^{34}S_{SO4}$, $[SO_4^{2-}]$, and Cl^-/SO_4^{2-} coded by either (A, C, D) station number or (B) month of collection. (A) Mean station $\delta^{34}S_{SO4}$ and annual range. Grey lines indicate confluences with major Narayani River tributaries. The catchments of stations LNS-7 through LNS-16 contain only HHC, while those of LNS-1 through LNS-6 contain TSS and LH as well. (B) Values of $\delta^{34}S_{SO4}$ are typically higher at sites LNS-7 through LNS-16 than at sites LNS-1 through LNS-6. Values of $\delta^{34}S_{SO4}$ are relatively constant throughout the year at a given station. (C) Values of $\delta^{34}S_{SO4}$ against $[SO_4^{2-}]$. Across the sample suite, $\delta^{34}S_{SO4}$ decreases downstream with increasing $[SO_4^{2-}]$, although this relationship only seems to hold specifically for stations LNS-3 through LNS-6. (D) Values of $\delta^{34}S_{SO4}$ against Cl^-/SO_4^{2-}. The lack of clear relationship argues against two-end member mixing as an explanation for the relation between $\delta^{34}S_{SO4}$ and $[SO_4^{2-}]$.

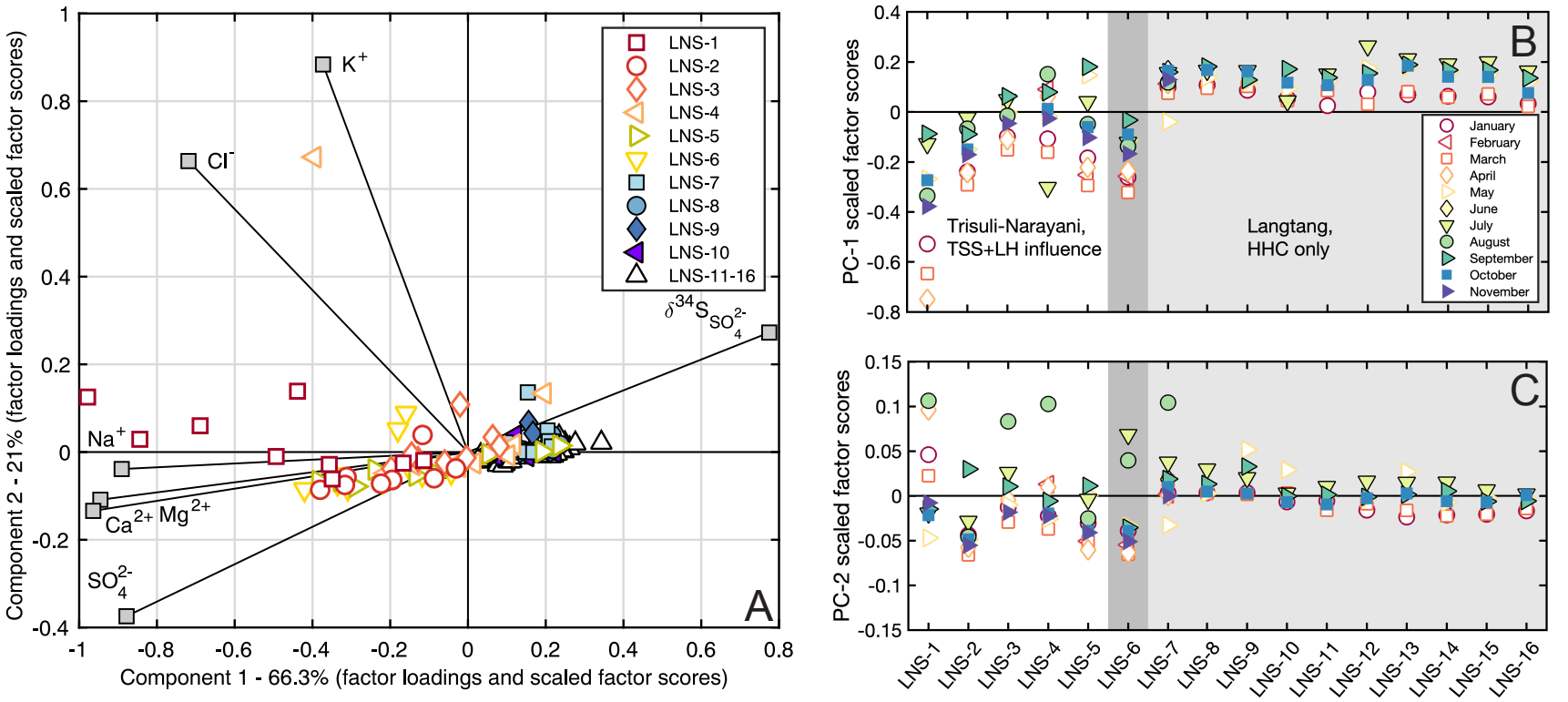

Fig. IV-5: Principal component analysis. (A) Biplot of principal component 1 (PC-1) and principal component 2 (PC-2). Labeled vectors indicate factor loadings, and symbols show the normalized factor scores of samples (Glover et al., 2011). Principal component 1 inversely relates $\delta^{34}S_{SO4}$ with the concentration of all cations and anions. Principal component 2 inversely relates $[SO_4^{2-}]$ and $\delta^{34}S_{SO4}$, and positively relates K^+ and Cl^-. (B) Sample factor scores of the first component, which captures the primary axis of variability in our chemical observations, principally vary by sampling site with a secondary seasonal influence. (C) Sample factor scores of the second component reflect seasonal variability, with larger seasonal changes in the Trisuli and Narayani Rivers than in the Langtang River.

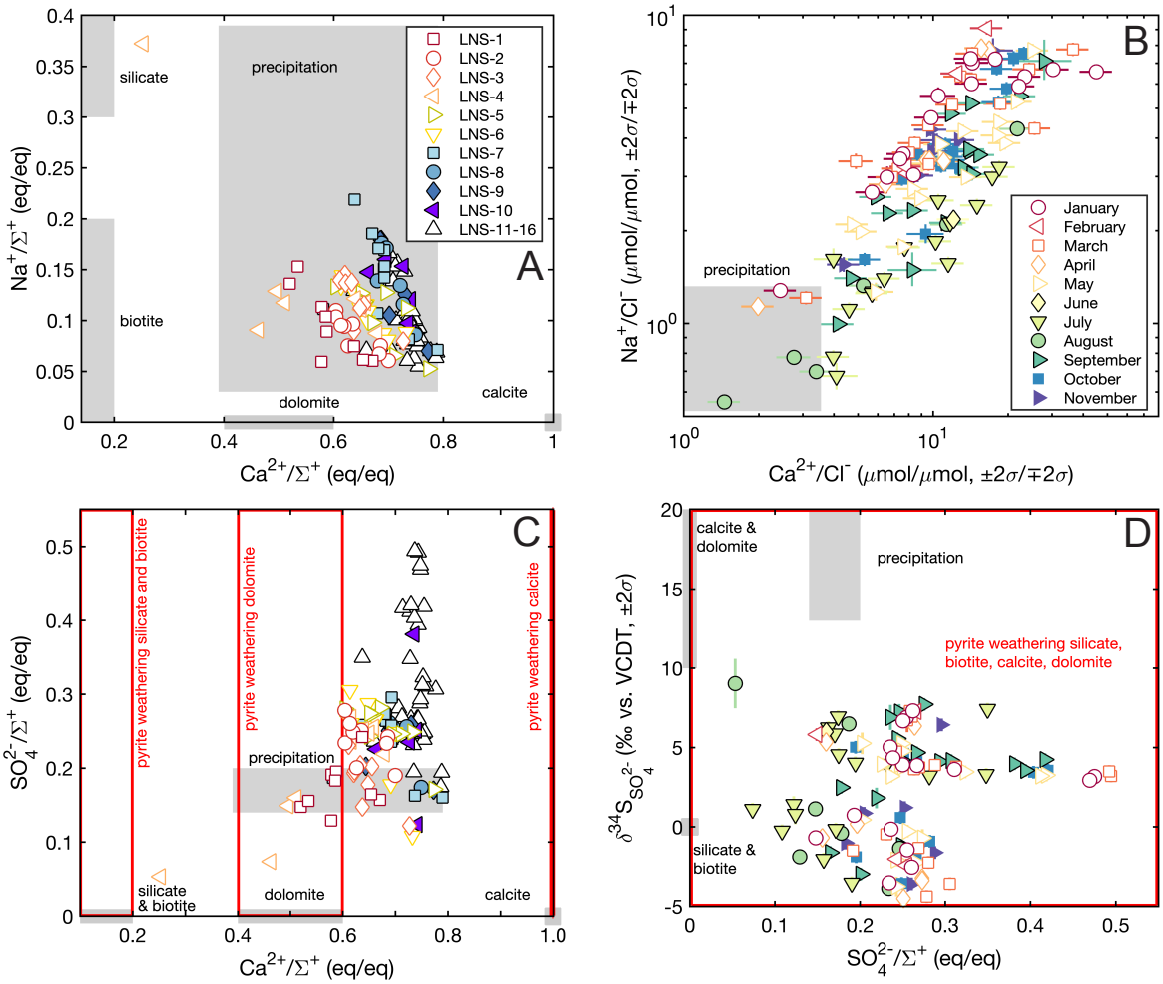

Fig. IV-6: Mixing diagrams color coded by (A, C) site location, or (B, D) month of collection. (A) The cross plot of Na^+/Σ^+ against Ca^{2+}/Σ^+ indicates that most cation charge is derived from either the carbonate mineral end-members or the precipitation end-member, with a relatively small fraction derived from silicate weathering. (B) The cross plot of Na^+/Cl^- against Ca^{2+}/Cl^- indicates mixing between a high-Cl^- end-member such as precipitation with the low-Cl^- of silicate and carbonate end-members. The two samples not successfully inverted have low Na^+/Cl^- or Ca^{2+}/Cl^- and are out of plotting range. (C) River water samples show SO_4^{2-}/Σ^+ in excess of precipitation. The missing SO_4^{2-} can be provided through FeS_2 oxidation and subsequent weathering of carbonate and silicate minerals (red boxes), which sources both SO_4^{2-} and cations to solution. (D) Values of $\delta^{34}S_{SO4}$ are lower than the rainwater or the carbonate end-members. The low $\delta^{34}S_{SO4}$ values could be attained through FeS_2 oxidation (red box). For (A)-(D) grey boxes are centered around the mean of end-members distributions and extend 1σ. The red boxes define the mean and 1σ of end-members subject to H_2SO_4 weathering, although the $\delta^{34}S$ of those end-members is not prescribed during inversion. Although not used in the inversion, for illustrative purposes the $\delta^{34}S$ of the calcite and dolomite end-members are plotted as the range of Phanerozoic evaporites and the $\delta^{34}S$ of the silicate and biotite end-members are plotted as the value of terrestrial sulfur.

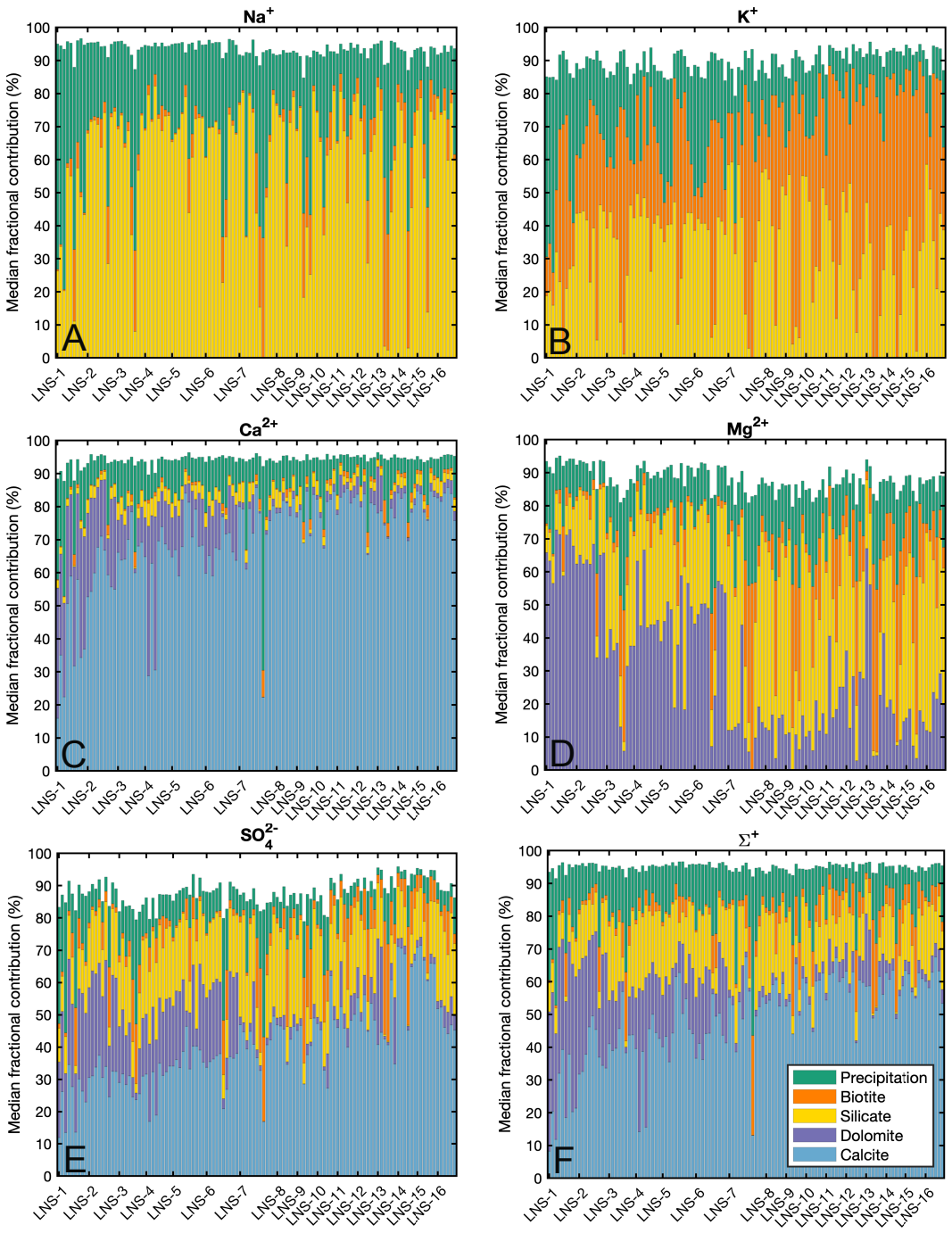

Fig. IV-7: Median fractional contributions of end-members to (A) [Na^+], (B) [K^+], (C), [Ca^{2+}], (D) [Mg^{2+}], (E) [SO_4^2], and (F) [Σ^+]. Each bar represents a single water sample, organized by collection site, and multiple bars at the same site reflect samples collected in different months. Major trends include a downstream increase in the fraction of Mg^{2+} and SO_4^{2-} sourced from dolomite, as well as seasonal changes in the relative contribution of the silicate and biotite end-members to the budgets of Na^+ and K^+. Although the sum of median contributions is not constrained to equal 100%, in any individual simulation the sum of fractional contributions to each budget must fall between 85% and 115% of observations. Cumulative distribution curves of model results are presented in Fig. IV-S10.

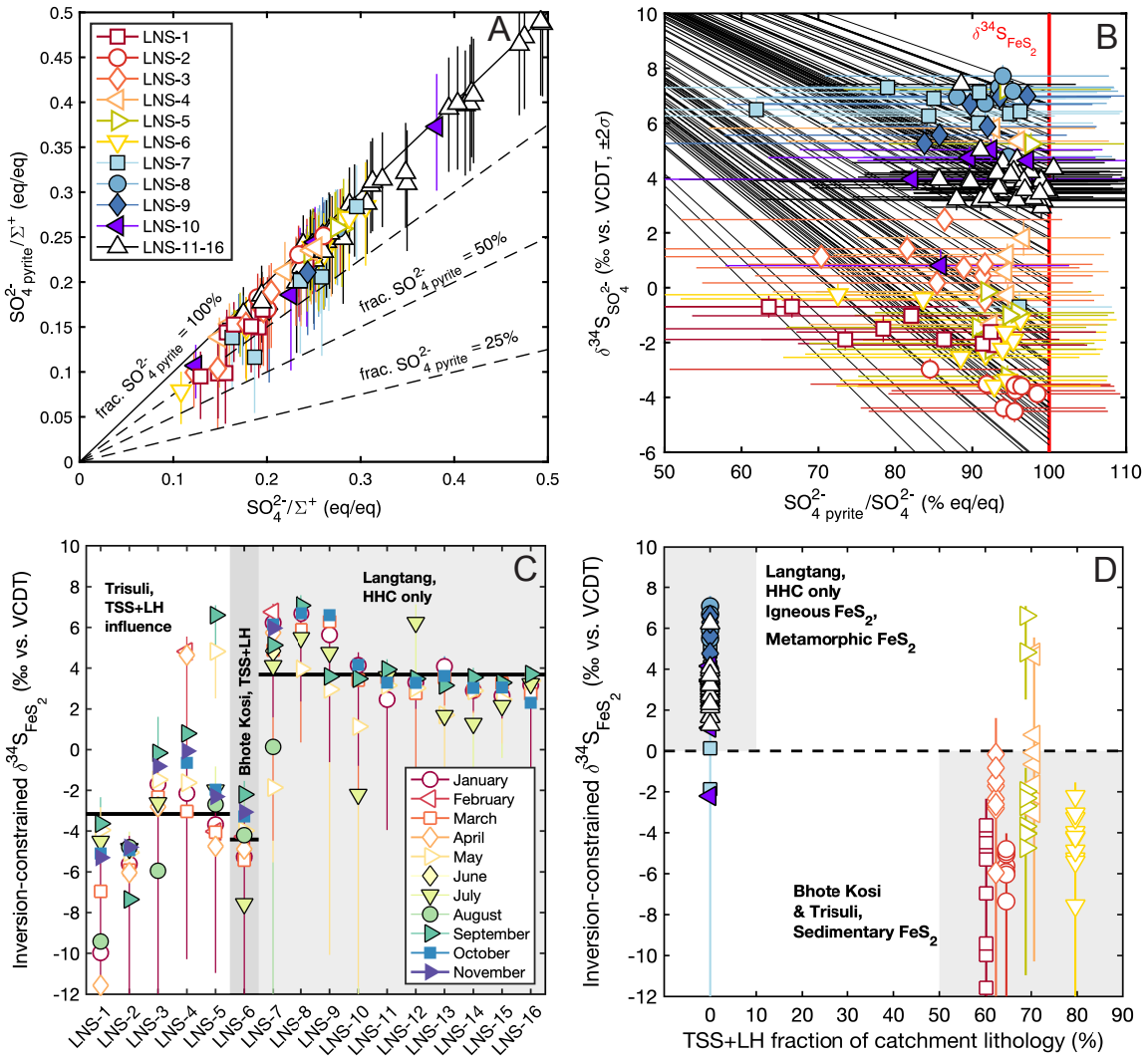

Fig. IV-8: Sulfur inversion results. (A) FeS_2-derived SO_4^{2-}/Σ^+ against observed SO_4^{2-}/Σ^+. The Monte Carlo inversion finds that, except for two samples, a median value of 62%-101% of dissolved SO_4^{2-} is derived from the oxidation of FeS_2. (B) Measured $\delta^{34}S_{SO4}$ and the fraction of FeS_2-derived SO_4^{2-}. Any relationship between $\delta^{34}S_{SO4}$ and the fraction of FeS_2-derived SO_4^{2-} is weak. The inversion-constrained $\delta^{34}S_{FeS2}$ value is calculated through mass balance and is conceptually similar to the $\delta^{34}S$ value at 100% FeS_2-derived SO_4^{2-} on a mixing line passing through both the sample and the precipitation end-member (black lines). (C) Inversion-constrained $\delta^{34}S_{FeS2}$ against site location shows two distributions. The inversion model recovers a ^{34}S-enriched population in samples draining the HHC formation and an ^{34}S-depleted population for samples with influence from the TSS and LH formations. (D) Inversion-constrained $\delta^{34}S_{FeS2}$ against the catchment fraction of TSS and LH. A $\delta^{34}S_{FeS2}$ of 0‰ largely separates the two sets of samples. Error bars for model output range from the 5th to 95th percentile of accepted simulation results.

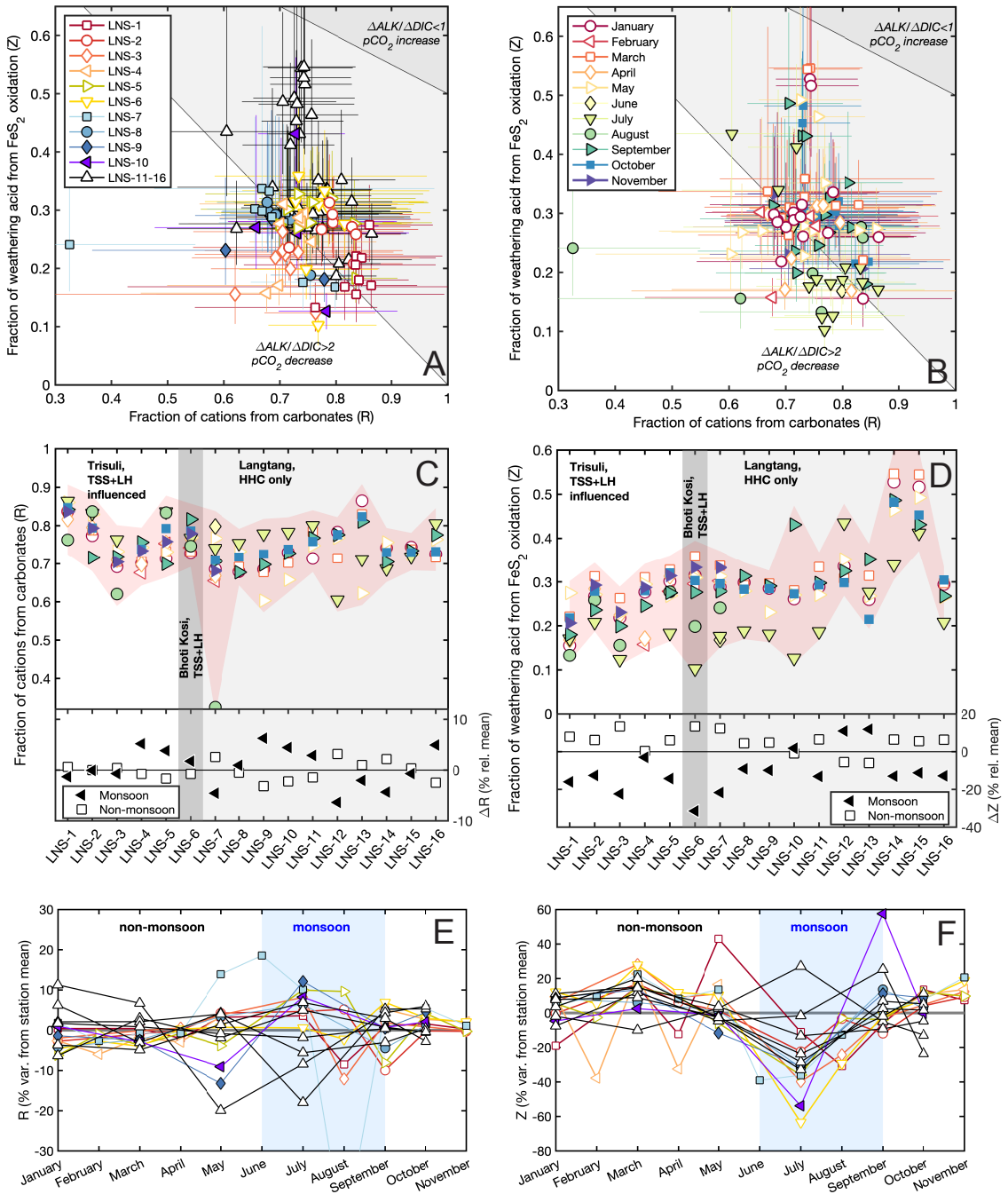
A
B
C
D
E
F
LNS-1
LNS-2
LNS-3
LNS-4
LNS-5
LNS-6
LNS-7
LNS-8
LNS-9
LNS-10
LNS-11-16
January
February
March
April
May
June
July
August
September
October
November
ΔALK/ΔDIC<1
pCO2 increase
ΔALK/ΔDIC>2
pCO2 decrease
Fraction of weathering acid from FeS2 oxidation (Z)
Fraction of cations from carbonates (R)
Trisuli,
TSS+LH
influenced
Langtang,
HHC only
Bhoti Kosi,
TSS+LH
Monsoon
Non-monsoon
ΔR (% rel. mean)
ΔZ (% rel. mean)
non-monsoon
monsoon
R (% var. from station mean)
Z (% var. from station mean)

Fig. IV-9: Character and seasonality of chemical weathering. (A, B) Fraction of weathering acid sourced from FeS_2 oxidation (Z) against the fraction of carbonate weathering (R), coded by (A) sample site or (B) month of collection. Most data cluster around Z=1-R, the boundary between short-term and long-term CO_2 release. (C) R arranged by site location and coded by season. Inversion results do not show clear spatial or seasonal changes. (D) Z arranged by site location and coded by season. Inversion results show a downstream decline in sulfuric acid weathering, and samples from the monsoon season generally have lower Z values than those from the non-monsoon season. In (C) and (D) samples are also aggregated as belonging to either the monsoon season (June through September, black triangles) or non-monsoon season (other months, white squares) and are plotted relative to the mean of the median R or Z values at each location. (E) Timeseries of variations in R relative to the annual station mean. R does not strongly covary with season. (F) Timeseries of variations in Z relative to the annual station mean. The value of Z is reduced during the monsoon at most sampling sites. In (E) and (F), blue shading indicates the monsoon season. Error bars for model output range from the 5th to 95th percentile of accepted simulation results.

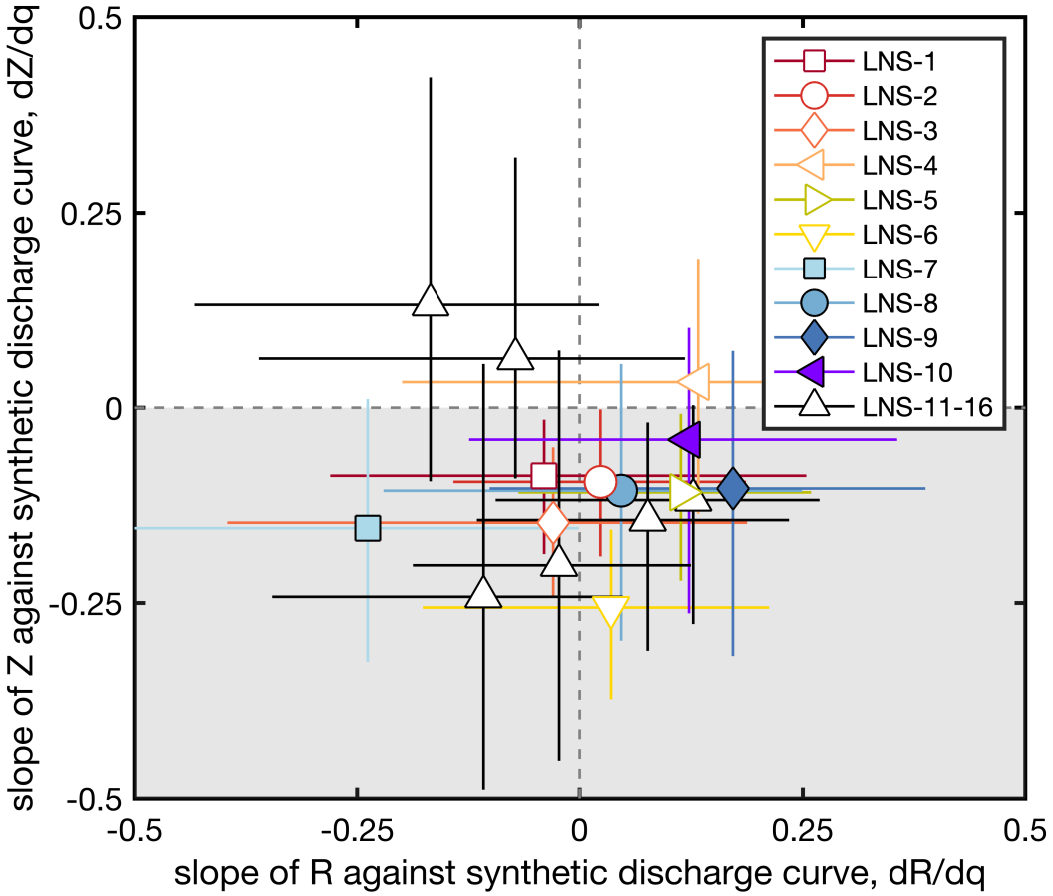

Fig. IV-10: Regression of R against the monthly fraction of maximum annual discharge shows positive and negative slopes, while regression of Z shows mostly negative slopes. Grey shading indicates the region with dZ/dq < 0. Error bars on dR/dq and dZ/dQ reflect the 5th to 95th percentile of Monte Carlo modeling for the regression slope of R or Z against a synthetic discharge curve (Fig. IV-S7).

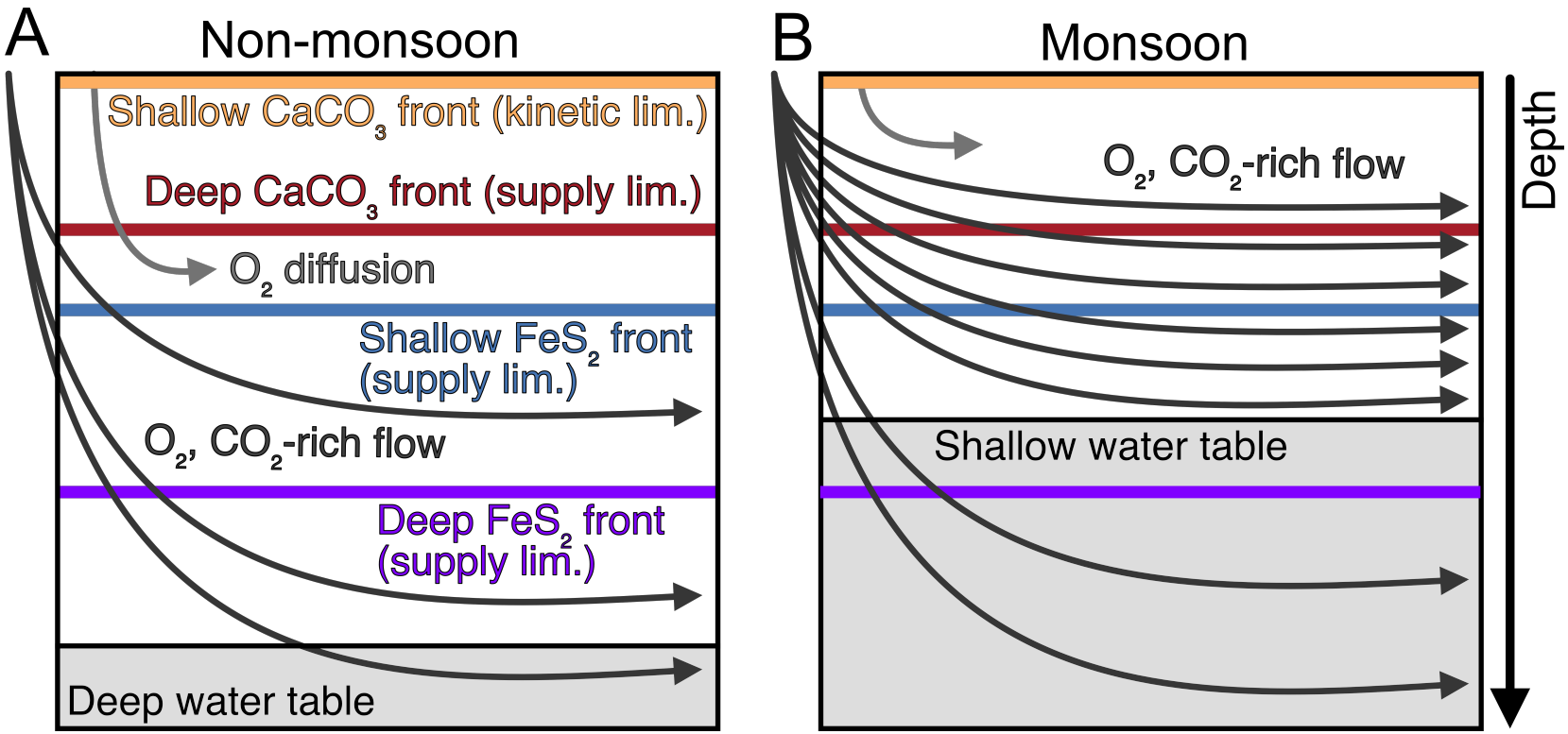

Fig. IV-11: Schematic of seasonal weathering cycle with two possible positions for the $CaCO_3$ weathering front (orange, red) and FeS_2 weathering front (blue, purple). During all seasons O_2 and CO_2 reach the subsurface from both diffusive exchange with the atmosphere and advection of waters (Brantley et al., 2013). (A) Deep flow paths with long residence times accumulate SO_4^{2-} from FeS_2 oxidation and source water to the river channel during the non-monsoon. (B) During the monsoon, the ratio of water in the river channel sourced from shallow flow paths with shorter residence times may increase even as the absolute discharge through both shallow and deep flow paths increases. If the FeS_2 weathering front is deep (purple, lower erosion rates), a seasonal change in the contributions of flow paths with distinct residence times could cause lower Z values in river samples. If the FeS_2 weathering front is shallower (blue, higher erosion rates), a transition in the hydrology of the system may not explain the observed seasonality of Z, which could instead reflect seasonal changes in the chemistry of water in flow paths with short residence times.

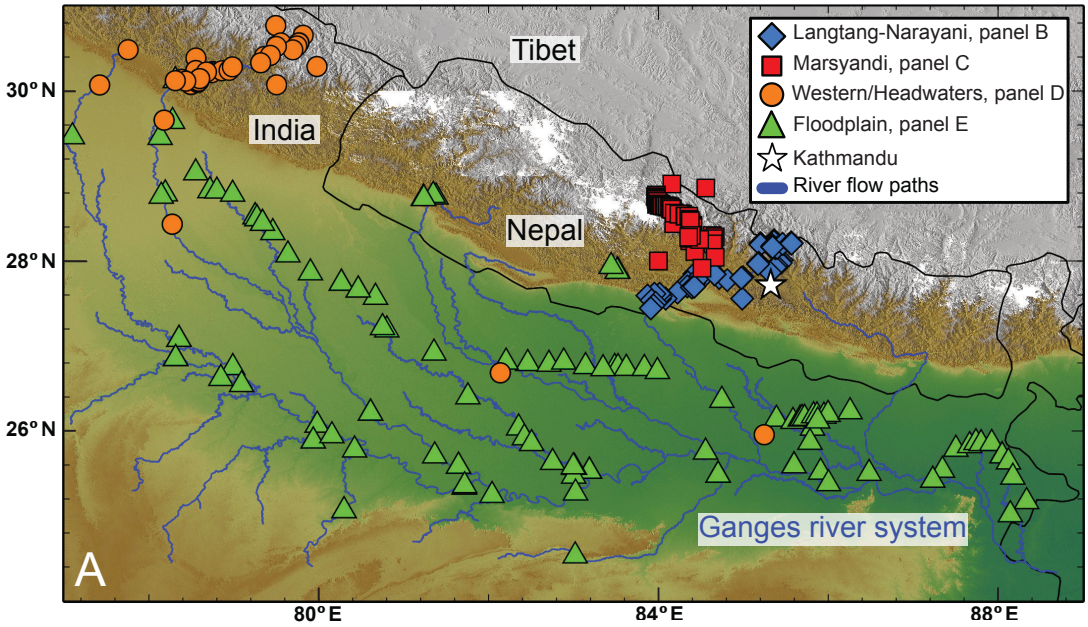
Tibet
India
Nepal
Ganges river system
Langtang-Narayani, panel B
Marsyandi, panel C
Western/Headwaters, panel D
Floodplain, panel E
Kathmandu
River flow paths
30° N
28° N
26° N
80° E
84° E
88° E
A

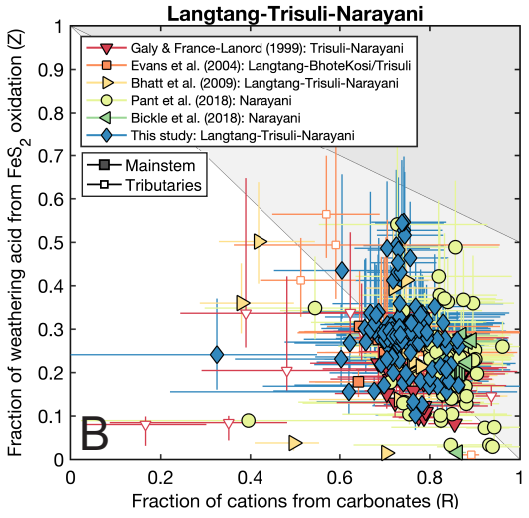
Langtang-Trisuli-Narayani
Galy & France-Lanorc (1999): Trisuli-Narayani
Evans et al. (2004): Langtang-BhoteKosi/Trisuli
Bhatt et al. (2009): Langtang-Trisuli-Narayani
Pant et al. (2018): Narayani
Bickle et al. (2018): Narayani
This study: Langtang-Trisuli-Narayani
Mainstem
Tributaries
Fraction of weathering acid from FeS2 oxidation (Z)
Fraction of cations from carbonates (R)
B

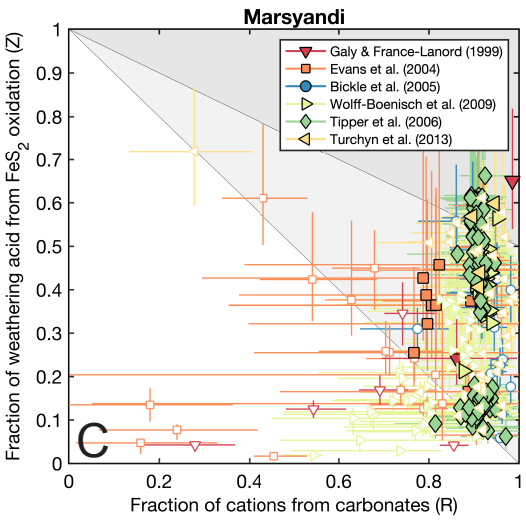
Marsyandi
Galy & France-Lanord (1999)
Evans et al. (2004)
Bickle et al. (2005)
Wolff-Boenisch et al. (2009)
Tipper et al. (2006)
Turchyn et al. (2013)
Fraction of weathering acid from FeS2 oxidation (Z)
Fraction of cations from carbonates (R)
C

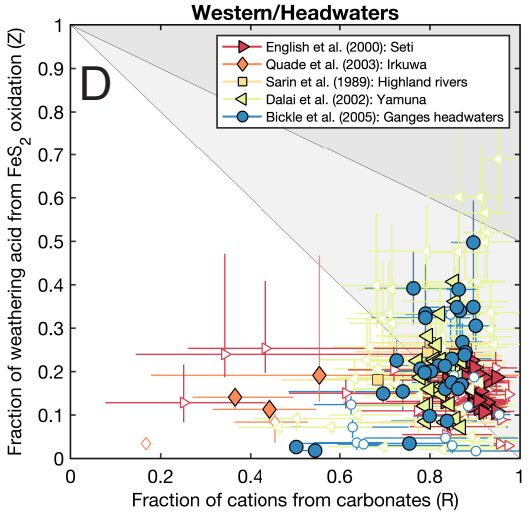
Western/Headwaters
English et al. (2000): Seti
Quade et al. (2003): Irkuwa
Sarin et al. (1989): Highland rivers
Dalai et al. (2002): Yamuna
Bickle et al. (2005): Ganges headwaters
Fraction of weathering acid from FeS2 oxidation (Z)
Fraction of cations from carbonates (R)
D

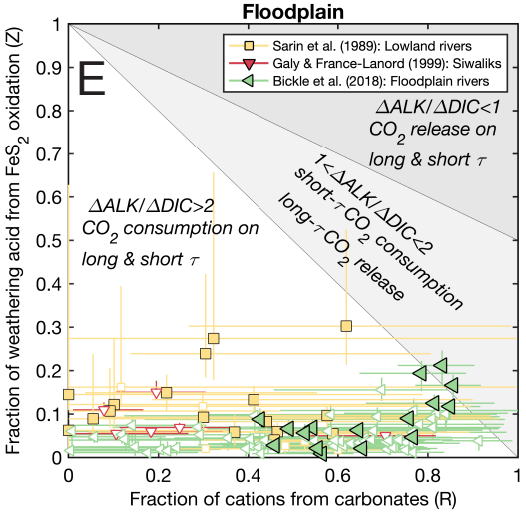
Floodplain
Sarin et al. (1989): Lowland rivers
Galy & France-Lanord (1999): Siwaliks
Bickle et al. (2018): Floodplain rivers
ΔALK/ΔDIC<1
CO2 release on
long & short τ
1<ΔALK/ΔDIC<2
short-τ CO2 consumption
long-τ CO2 release
ΔALK/ΔDIC>2
CO2 consumption on
long & short τ
Fraction of weathering acid from FeS2 oxidation (Z)
Fraction of cations from carbonates (R)
E

Fig. IV-12: Pyrite oxidation and carbonate weathering across the Ganges catchment. (A) Sample locations from prior publications reporting the dissolved chemistry of Himalayan rivers. Water chemistry is inverted and presented in subsequent panels even if detailed location data are unavailable. Latitude and longitude for samples from Sarin et al. (1989) and Galy and France-Lanord (1999) were estimated using Google Earth. The two Western/Headwater samples that appear in the floodplain are Highland Rivers from Sarin et al. (1989). Elevation data are from the Shuttle Radar Topography Mission. (B)-(E) Fraction of weathering acid sourced from FeS_2 oxidation (Z) against the fraction of carbonate weathering (R) grouped by location and coded by publication. Data are shown for both mainstem (closed symbols) and tributary samples (open symbols), as identified in original publications. Shading indicates regions of $\Delta ALK/\Delta DIC < 1$, $1 < \Delta ALK/\Delta DIC < 2$, and $\Delta ALK/\Delta DIC > 2$, with different implications for pCO_2 drawdown over short and long timescales (τ). (B) Langtang-Trisuli-Narayani River system samples tend to cluster around the line $Z = 1-R$, indicating that sulfide oxidation offsets much of the CO_2 drawdown associated with silicate weathering. (C) Marsyandi samples have high Z and high R values consistent with long-term CO_2 supply to the atmosphere. Samples draining the TSS are particularly high in Z. (D) Samples from the western headwaters of the Ganges and the Seti River are chemically similar to those from the Trisuli-Narayani catchment. (E) Samples from the floodplain have low Z and low R values, indicative of silicate weathering driven predominantly with H_2CO_3 (Lupker et al., 2012; Bickle et al., 2018). Error bars for model output range from the 5th to 95th percentile of accepted simulation results.

IV.10: Tables

Table IV-1: End-member means and uncertainty. Precipitation is assigned a $\delta^{34}S_{SO4}$ value of 17±4‰.

End-Member	Ca^{2+}/Σ^{+}	Mg^{2+}/Σ^{+}	Na^{+}/Σ^{+}	K^{+}/Σ^{+}	Cl^{-}/Σ^{+}	SO_4^{2-}/Σ^{+}
Precipitation	0.59 ± 0.20	0.13 ± 0.04	0.21 ± 0.18	0.07 ± 0.04	0.25 ± 0.23	0.17 ± 0.03
Silicate	0.15 ± 0.05	0.35 ± 0.10	0.40 ± 0.10	0.10 ± 0.10	0.00 ± 0.00	0.00 - 1.00
Biotite	0.15 ± 0.05	0.35 ± 0.10	0.10 ± 0.10	0.40 ± 0.10	0.00 ± 0.00	0.00 - 1.00
Calcite	1.00 ± 0.00	0.00 ± 0.00	0.00 ± 0.00	0.00 ± 0.00	0.00 ± 0.00	0.00 - 1.00
Dolomite	0.50 ± 0.10	0.50 ± 0.10	0.00 ± 0.00	0.00 ± 0.00	0.00 ± 0.00	0.00 - 1.00

IV.11: References

Andermann, C., Bonnet, S. and Gloaguen, R., 2011. Evaluation of precipitation data sets along the Himalayan front. *Geochemistry, Geophysics, Geosystems*, 12(7). https://doi.org/10.1029/2011GC003513.

Andermann, C., Longuevergne, L., Bonnet, S., Crave, A., Davy, P. and Gloaguen, R., 2012. Impact of transient groundwater storage on the discharge of Himalayan rivers. *Nature Geoscience*, 5(2), pp.127-132. https://doi.org/10.1038/ngeo1356.

Anderson, S.P., Drever, J.I. and Humphrey, N.F., 1997. Chemical weathering in glacial environments. *Geology*, 25(5), pp.399-402. https://doi.org/10.1130/0091-7613(1997)025<0399:CWIGE>2.3.CO;2.

Anderson, S.P., Drever, J.I., Frost, C.D. and Holden, P., 2000. Chemical weathering in the foreland of a retreating glacier. *Geochimica et Cosmochimica Acta*, 64(7), pp.1173-1189. https://doi.org/10.1016/S0016-7037(99)00358-0.

Archer, D., Kheshgi, H. and Maier-Reimer, E., 1997. Multiple timescales for neutralization of fossil fuel CO_2. *Geophysical Research Letters*, 24(4), pp.405-408. https://doi.org/10.1029/97GL00168.

Archer, D., Winguth, A., Lea, D. and Mahowald, N., 2000. What caused the glacial/interglacial atmospheric pCO_2 cycles? *Reviews of Geophysics*, 38(2), pp.159-189. https://doi.org/10.1029/1999RG000066.

Balci, N., Shanks III, W.C., Mayer, B. and Mandernack, K.W., 2007. Oxygen and sulfur isotope systematics of sulfate produced by bacterial and abiotic oxidation of pyrite. *Geochimica et Cosmochimica Acta*, 71(15), pp.3796-3811. https://doi.org/10.1016/j.gca.2007.04.017.

Balestrini, R., Polesello, S. and Sacchi, E., 2014. Chemistry and isotopic composition of precipitation and surface waters in Khumbu valley (Nepal Himalaya): N dynamics of high elevation basins. *Science of the Total Environment*, 485, pp.681-692. https://doi.org/10.1016/j.scitotenv.2014.03.096.

Beck, R.A., Burbank, D.W., Sercombe, W.J., Riley, G.W., Barndt, J.K., Berry, J.R., Afzal, J., Khan, A.M., Jurgen, H., Metje, J. and Cheema, A., 1995. Stratigraphic evidence for an early collision between northwest India and Asia. *Nature*, 373(6509), pp.55-58. https://doi.org/10.1038/373055a0.

Becker, J.A., Bickle, M.J., Galy, A. and Holland, T.J., 2008. Himalayan metamorphic CO_2 fluxes: Quantitative constraints from hydrothermal springs. *Earth and Planetary Science Letters*, 265(3-4), pp.616-629. https://doi.org/10.1016/j.epsl.2007.10.046.

Berner, R.A., 1971. Worldwide sulfur pollution of rivers. *Journal of Geophysical Research*, 76(27), pp.6597-6600. https://doi.org/10.1029/JC076i027p06597.

Berner, R.A. and Caldeira, K., 1997. The need for mass balance and feedback in the geochemical carbon cycle. *Geology*, 25(10), pp.955-956. https://doi.org/10.1130/0091-7613(1997)025<0955:TNFMBA>2.3.CO;2.

Bhatt, M.P., Masuzawa, T., Yamamoto, M., Sakai, A. and Fujita, K., 2000. Seasonal changes in dissolved chemical composition and flux of meltwater draining from Lirung Glacier in the Nepal Himalayas. *IAHS Publication*, pp.277-288.

Bhatt, M.P., Masuzawa, T., Yamamoto, M. and Gardner, K.H., 2009. Spatial variations in chemical compositions along Langtang–Narayani river system in central Nepal. *Environmental Geology*, 57(3), pp.557-569. https://doi.org/10.1007/s00254-008-1325-x.

Bhatt, M.P., Hartmann, J. and Acevedo, M.F., 2018. Seasonal variations of biogeochemical matter export along the Langtang-Narayani river system in central Himalaya. *Geochimica et Cosmochimica Acta*, 238, pp.208-234. https://doi.org/10.1016/j.gca.2018.06.033.

Bhattarai, D.R., 1980. Some geothermal springs of Nepal. *Tectonophysics*, 62(1-2), pp.7-11. https://doi.org/10.1016/0040-1951(80)90071-2.

Bickle, M.J., 1996. Metamorphic decarbonation, silicate weathering and the long-term carbon cycle. *Terra Nova*, 8(3), pp.270-276. https://doi.org/10.1111/j.1365-3121.1996.tb00756.x.

Bickle, M.J., Chapman, H.J., Bunbury, J., Harris, N.B., Fairchild, I.J., Ahmad, T. and Pomiès, C., 2005. Relative contributions of silicate and carbonate rocks to riverine Sr fluxes in the headwaters of the Ganges. *Geochimica et Cosmochimica Acta*, 69(9), pp.2221-2240. https://doi.org/10.1016/j.gca.2004.11.019.

Bickle, M.J., Tipper, E.D., Galy, A., Chapman, H. and Harris, N., 2015. On discrimination between carbonate and silicate inputs to Himalayan rivers. *American Journal of Science*, 315(2), pp.120-166. https://doi.org/10.2475/02.2015.02.

Bickle, M.J., Chapman, H.J., Tipper, E., Galy, A., Christina, L. and Ahmad, T., 2018. Chemical weathering outputs from the flood plain of the Ganga. *Geochimica et Cosmochimica Acta*, 225, pp.146-175. https://doi.org/10.1016/j.gca.2018.01.003.

Blum, J.D., Gazis, C.A., Jacobson, A.D. and Page Chamberlain, C., 1998. Carbonate versus silicate weathering in the Raikhot watershed within the High Himalayan Crystalline Series. *Geology*, 26(5), pp.411-414. https://doi.org/10.1130/0091-7613(1998)026<0411:CVSWIT>2.3.CO;2.

Bluth, G.J. and Kump, L.R., 1994. Lithologic and climatologic controls of river chemistry. *Geochimica et Cosmochimica Acta*, 58(10), pp.2341-2359. https://doi.org/10.1016/0016-7037(94)90015-9.

Bordet, P., Colchen, M., Krummenacher, D., Le Fort, P., Mouterde, R. and Remy, M., 1971. Recherches géologiques dans l'Himalaya du Népal, région de la Thakkhola. Centre National de la Recherche Scientifique, Paris, p. 279.

Brantley, S.L. and Lebedeva, M., 2011. Learning to read the chemistry of regolith to understand the critical zone. *Annual Review of Earth and Planetary Sciences*, 39, pp.387-416. https://doi.org/10.1146/annurev-earth-040809-152321.

Brantley, S.L., Holleran, M.E., Jin, L. and Bazilevskaya, E., 2013. Probing deep weathering in the Shale Hills Critical Zone Observatory, Pennsylvania (USA): the hypothesis of nested chemical reaction fronts in the subsurface. *Earth Surface Processes and Landforms*, 38(11), pp.1280-1298. https://doi.org/10.1002/esp.3415.

Burke, A., Present, T.M., Paris, G., Rae, E.C., Sandilands, B.H., Gaillardet, J., Peucker-Ehrenbrink, B., Fischer, W.W., McClelland, J.W., Spencer, R.G. and Voss, B.M., 2018. Sulfur isotopes in rivers: Insights into global weathering budgets, pyrite oxidation, and the modern sulfur cycle. *Earth and Planetary Science Letters*, 496, pp.168-177. https://doi.org/10.1016/j.epsl.2018.05.022.

Caldeira, K., 1992. Enhanced Cenozoic chemical weathering and the subduction of pelagic carbonate. *Nature*, 357(6379), pp.578-581. https://doi.org/10.1038/357578a0.

Calmels, D., Gaillardet, J., Brenot, A. and France-Lanord, C., 2007. Sustained sulfide oxidation by physical erosion processes in the Mackenzie River basin: Climatic perspectives. *Geology*, 35(11), pp.1003-1006. https://doi.org/10.1130/G24132A.1.

Chakrapani, G.J. and Veizer, J., 2006. Source of dissolved sulphate in the Alakananda–Bhagirathi rivers in the Himalayas. *Current Science*, 90(4), pp.500-503.

Claypool, G.E., Holser, W.T., Kaplan, I.R., Sakai, H. and Zak, I., 1980. The age curves of sulfur and oxygen isotopes in marine sulfate and their mutual interpretation. *Chemical Geology*, 28, pp.199-260. https://doi.org/10.1016/0009-2541(80)90047-9.

Collins, R. and Jenkins, A., 1996. The impact of agricultural land use on stream chemistry in the middle hills of the Himalayas, Nepal. *Journal of Hydrology*, 185(1-4), pp.71-86. https://doi.org/10.1016/0022-1694(95)03008-5.

Dalai, T.K., Krishnaswami, S. and Sarin, M.M., 2002. Major ion chemistry in the headwaters of the Yamuna river system: Chemical weathering, its temperature dependence and CO_2 consumption in the Himalaya. *Geochimica et Cosmochimica Acta*, 66(19), pp.3397-3416. https://doi.org/10.1016/S0016-7037(02)00937-7.

Dessert, C., Dupré, B., Gaillardet, J., François, L.M. and Allegre, C.J., 2003. Basalt weathering laws and the impact of basalt weathering on the global carbon cycle. *Chemical Geology*, 202(3-4), pp.257-273. https://doi.org/10.1016/j.chemgeo.2002.10.001.

Dhital, M.R., 2015. Geology of the Nepal Himalaya: Regional perspective of the classic collided orogen. Springer, Switzerland, p 498. https://doi.org/10.1007/978-3-319-02496-7.

Edmond, J.M., 1992. Himalayan tectonics, weathering processes, and the strontium isotope record in marine limestones. *Science*, 258(5088), pp.1594-1597. https://doi.org/10.1126/science.258.5088.1594.

Elderfield, H., 1986. Strontium isotope stratigraphy. *Palaeogeography, Palaeoclimatology, Palaeoecology*, 57(1), pp.71-90. https://doi.org/10.1016/0031-0182(86)90007-6.

Emberson, R., Galy, A. and Hovius, N., 2017. Combined effect of carbonate and biotite dissolution in landslides biases silicate weathering proxies. *Geochimica et Cosmochimica Acta*, 213, pp.418-434. https://doi.org/10.1016/j.gca.2017.07.014.

English, N.B., Quade, J., DeCelles, P.G. and Garzione, C.N., 2000. Geologic control of Sr and major element chemistry in Himalayan Rivers, Nepal. *Geochimica et Cosmochimica Acta*, 64(15), pp.2549-2566. https://doi.org/10.1016/S0016-7037(00)00379-3.

Evans, M.J., Derry, L.A., Anderson, S.P. and France-Lanord, C., 2001. Hydrothermal source of radiogenic Sr to Himalayan rivers. *Geology*, 29(9), pp.803-806. https://doi.org/10.1130/0091-7613(2001)029<0803:HSORST>2.0.CO;2.

Evans, M.J., Derry, L.A. and France-Lanord, C., 2004. Geothermal fluxes of alkalinity in the Narayani river system of central Nepal. *Geochemistry, Geophysics, Geosystems*, 5(8). https://doi.org/10.1029/2004GC000719.

Evans, M.J., Derry, L.A. and France-Lanord, C., 2008. Degassing of metamorphic carbon dioxide from the Nepal Himalaya. *Geochemistry, Geophysics, Geosystems*, 9(4). https://doi.org/10.1029/2007GC001796.

Fort, M., 1996. Late Cenozoic environmental changes and uplift on the northern side of the central Himalaya: A reappraisal from field data. *Palaeogeography, Palaeoclimatology, Palaeoecology*, 120(1-2), pp.123-145. https://doi.org/10.1016/0031-0182(94)00038-7.

France-Lanord, C. and Derry, L.A., 1997. Organic carbon burial forcing of the carbon cycle from Himalayan erosion. *Nature*, 390(6655), pp.65-67. https://doi.org/10.1038/36324.

François, L.M. and Walker, J.C., 1992. Modelling the Phanerozoic carbon cycle and climate: constraints from the $^{87}Sr/^{86}Sr$ isotopic ratio of seawater. *American Journal of Science*, 292(2), pp.81-135. https://doi.org/10.2475/ajs.292.2.81.

Gabet, E.J., Burbank, D.W., Pratt-Sitaula, B., Putkonen, J. and Bookhagen, B., 2008. Modern erosion rates in the High Himalayas of Nepal. *Earth and Planetary Science Letters*, 267(3-4), pp.482-494. https://doi.org/10.1016/j.epsl.2007.11.059.

Gaillardet, J., Dupré, B., Louvat, P. and Allegre, C.J., 1999. Global silicate weathering and CO_2 consumption rates deduced from the chemistry of large rivers. *Chemical Geology*, 159(1-4), pp.3-30. https://doi.org/10.1016/S0009-2541(99)00031-5.

Galy, A. and France-Lanord, C., 1999. Weathering processes in the Ganges–Brahmaputra basin and the riverine alkalinity budget. *Chemical Geology*, 159(1-4), pp.31-60. https://doi.org/10.1016/S0009-2541(99)00033-9.

Galy, V., France-Lanord, C., Beyssac, O., Faure, P., Kudrass, H. and Palhol, F., 2007. Efficient organic carbon burial in the Bengal fan sustained by the Himalayan erosional system. *Nature*, 450(7168), pp.407-410. https://doi.org/10.1038/nature06273.

Girault, F., Bollinger, L., Bhattarai, M., Koirala, B.P., France-Lanord, C., Rajaure, S., Gaillardet, J., Fort, M., Sapkota, S.N. and Perrier, F., 2014. Large-scale organization of carbon dioxide discharge in the Nepal Himalayas. *Geophysical Research Letters*, 41(18), pp.6358-6366. https://doi.org/10.1002/2014GL060873.

Glover, D.M., Jenkins, W.J. and Doney, S.C., 2011. Modeling methods for marine science. Cambridge University Press.

Godsey, S.E., Kirchner, J.W. and Clow, D.W., 2009. Concentration–discharge relationships reflect chemostatic characteristics of US catchments. *Hydrological Processes: An International Journal*, 23(13), pp.1844-1864. https://doi.org/10.1002/hyp.7315.

Godsey, S.E., Hartmann, J. and Kirchner, J.W., 2019. Catchment chemostasis revisited: Water quality responds differently to variations in weather and climate. *Hydrological Processes*, 33(24), pp.3056-3069. https://doi.org/10.1002/hyp.13554.

Gu, X., Rempe, D.M., Dietrich, W.E., West, A.J., Lin, T.C., Jin, L. and Brantley, S.L., 2020. Chemical reactions, porosity, and microfracturing in shale during weathering: The effect of erosion rate. *Geochimica et Cosmochimica Acta*, 269, pp.63-100. https://doi.org/10.1016/j.gca.2019.09.044.

Handa B.K. 1968. The chemical composition of rain water in some parts of North India. *Indian Journal of Meteorology & Geophysics,* 19, 175-180.

Harris, N., Bickle, M., Chapman, H., Fairchild, I. and Bunbury, J., 1998. The significance of Himalayan rivers for silicate weathering rates: Evidence from the Bhote Kosi tributary. *Chemical Geology*, 144(3-4), pp.205-220. https://doi.org/10.1016/S0009-2541(97)00132-0.

Hemingway, J.D., Olson, H., Turchyn, A.V., Tipper, E.T., Bickle, M.J. and Johnston, D.T., 2020. Triple oxygen isotope insight into terrestrial pyrite oxidation. *Proceedings of the National Academy of Sciences*, 117(14), pp.7650-7657. https://doi.org/10.1073/pnas.1917518117.

Hilton, R.G., Gaillardet, J., Calmels, D. and Birck, J.L., 2014. Geological respiration of a mountain belt revealed by the trace element rhenium. *Earth and Planetary Science Letters*, 403, pp.27-36. https://doi.org/10.1016/j.epsl.2014.06.021.

Hilton, R.G. and West, A.J., 2020. Mountains, erosion and the carbon cycle. *Nature Reviews Earth & Environment*, 1(6), pp.284-299. https://doi.org/10.1038/s43017-020-0058-6.

Horan, K., Hilton, R.G., Dellinger, M., Tipper, E., Galy, V., Calmels, D., Selby, D., Gaillardet, J., Ottley, C.J., Parsons, D.R. and Burton, K.W., 2019. Carbon dioxide emissions by rock organic carbon oxidation and the net geochemical carbon budget of the Mackenzie River Basin. *American Journal of Science*, 319(6), pp.473-499. https://doi.org/10.2475/06.2019.02.

Horita, J., Zimmermann, H. and Holland, H.D., 2002. Chemical evolution of seawater during the Phanerozoic: Implications from the record of marine evaporites. *Geochimica et Cosmochimica Acta*, 66(21), pp.3733-3756. https://doi.org/10.1016/S0016-7037(01)00884-5.

Hren, M.T., Chamberlain, C.P., Hilley, G.E., Blisniuk, P.M. and Bookhagen, B., 2007. Major ion chemistry of the Yarlung Tsangpo–Brahmaputra river: chemical weathering, erosion, and CO_2 consumption in the southern Tibetan plateau and eastern syntaxis of the Himalaya. *Geochimica et Cosmochimica Acta*, 71(12), pp.2907-2935. https://doi.org/10.1016/j.gca.2007.03.021.

Huh, Y., Tsoi, M.Y., Zaitsev, A. and Edmond, J.M., 1998. The fluvial geochemistry of the rivers of Eastern Siberia: I. Tributaries of the Lena River draining the sedimentary platform of the Siberian Craton. *Geochimica et Cosmochimica Acta*, 62(10), pp.1657-1676. https://doi.org/10.1016/S0016-7037(98)00107-0.

Ibarra, D.E., Caves, J.K., Moon, S., Thomas, D.L., Hartmann, J., Chamberlain, C.P. and Maher, K., 2016. Differential weathering of basaltic and granitic catchments from concentration–discharge relationships. *Geochimica et Cosmochimica Acta*, 190, pp.265-293. https://doi.org/10.1016/j.gca.2016.07.006.

Inger, S., and Harris, N.B.W., 1992. Tectonothermal evolution of the High Himalayan crystalline sequence, Langtang Valley, northern Nepal. *Journal of Metamorphic Geology*, 10(3), pp.439-452. https://doi.org/10.1111/j.1525-1314.1992.tb00095.x.

Inger, S., and Harris, N., 1993. Geochemical constraints on leucogranite magmatism in the Langtang Valley, Nepal Himalaya. *Journal of Petrology*, 34(2), pp.345-368. https://doi.org/10.1093/petrology/34.2.345.

Ivanov, M.V., Grinenko, V.A. and Rabinovich, A.P., 1983. The sulphur cycle in continental reservoirs. *The Global Biogeochemical Sulphur Cycle*–Scope, 39, pp.297-356.

Jacobson, A.D., Blum, J.D. and Walter, L.M., 2002. Reconciling the elemental and Sr isotope composition of Himalayan weathering fluxes: Insights from the carbonate geochemistry of stream waters. *Geochimica et Cosmochimica Acta*, 66(19), pp.3417-3429. https://doi.org/10.1016/S0016-7037(02)00951-1.

John, S.G. and Adkins, J.F., 2010. Analysis of dissolved iron isotopes in seawater. *Marine Chemistry*, 119(1-4), pp.65-76. https://doi.org/10.1016/j.marchem.2010.01.001.

Johnson, J.E., Gerpheide, A., Lamb, M.P. and Fischer, W.W., 2014. O_2 constraints from Paleoproterozoic detrital pyrite and uraninite. *Bulletin*, 126(5-6), pp.813-830. https://doi.org/10.1130/B30949.1.

Karim, A. and Veizer, J., 2000. Weathering processes in the Indus River Basin: Implications from riverine carbon, sulfur, oxygen, and strontium isotopes. *Chemical Geology*, 170(1-4), pp.153-177. https://doi.org/10.1016/S0009-2541(99)00246-6.

Kerrick, D.M. and Caldeira, K., 1999. Was the Himalayan orogen a climatically significant coupled source and sink for atmospheric CO_2 during the Cenozoic? *Earth and Planetary Science Letters*, 173(3), pp.195-203. https://doi.org/10.1016/S0012-821X(99)00229-0.

Krishnaswami, S. and Singh, S.K., 1998. Silicate and carbonate weathering in the drainage basins of the Ganga-Ghaghara-Indus head waters: Contributions to major ion and Sr isotope geochemistry. *Proceedings of the Indian Academy of Sciences-Earth and Planetary Sciences*, 107(4), pp.283-291.

Krishnaswami S., Singh S. K., and Dalai T. K. 1999. Silicate weathering in the Himalaya: Role in contributing to major ions and radiogenic Sr to the Bay of Bengal. In *Ocean Science, Trends and Future Directions* (pp. 23–51), ed. B. L. K. Somayajulu. India.

Kump, L.R. and Arthur, M.A., 1997. Global chemical erosion during the Cenozoic: Weatherability balances the budgets. In *Tectonic uplift and climate change* (pp. 399-426). Springer, Boston, MA. https://doi.org/10.1007/978-1-4615-5935-1_18.

Lerman, A., Wu, L. and Mackenzie, F.T., 2007. CO_2 and H_2SO_4 consumption in weathering and material transport to the ocean, and their role in the global carbon balance. *Marine Chemistry*, 106(1-2), pp.326-350. https://doi.org/10.1016/j.marchem.2006.04.004.

Li, G. and Elderfield, H., 2013. Evolution of carbon cycle over the past 100 million years. *Geochimica et Cosmochimica Acta*, 103, pp.11-25. https://doi.org/10.1016/j.gca.2012.10.014.

Lupker, M., France-Lanord, C., Galy, V., Lavé, J., Gaillardet, J., Gajurel, A.P., Guilmette, C., Rahman, M., Singh, S.K. and Sinha, R., 2012. Predominant floodplain over mountain weathering of Himalayan sediments (Ganga basin). *Geochimica et Cosmochimica Acta*, 84, pp.410-432. https://doi.org/10.1016/j.gca.2012.02.001.

MacNamara, J. and Thode, H.G., 1950. Comparison of the isotopic constitution of terrestrial and meteoritic sulfur. *Physical Review*, 78(3), p.307. https://doi.org/10.1103/PhysRev.78.307.

Maher, K. and Chamberlain, C.P., 2014. Hydrologic regulation of chemical weathering and the geologic carbon cycle. *Science*, 343(6178), pp.1502-1504. https://doi.org/10.1126/science.1250770.

Millot, R., Gaillardet, J., Dupré, B. and Allègre, C.J., 2002. The global control of silicate weathering rates and the coupling with physical erosion: New insights from rivers of the Canadian Shield. *Earth and Planetary Science Letters*, 196(1-2), pp.83-98. https://doi.org/10.1016/S0012-821X(01)00599-4.

Myrow, P.M., Hughes, N.C., Derry, L.A., McKenzie, N.R., Jiang, G., Webb, A.A.G., Banerjee, D.M., Paulsen, T.S. and Singh, B.P., 2015. Neogene marine isotopic evolution and the erosion of Lesser Himalayan strata: Implications for Cenozoic tectonic history. *Earth and Planetary Science Letters*, 417, pp.142-150. https://doi.org/10.1016/j.epsl.2015.02.016.

Négrel, P., Allègre, C.J., Dupré, B. and Lewin, E., 1993. Erosion sources determined by inversion of major and trace element ratios and strontium isotopic ratios in river water: The Congo Basin case. *Earth and Planetary Science Letters*, 120(1-2), pp.59-76. https://doi.org/10.1016/0012-821X(93)90023-3.

Otto-Bliesner, B.L., 1995. Continental drift, runoff, and weathering feedbacks: Implications from climate model experiments. *Journal of Geophysical Research: Atmospheres*, 100(D6), pp.11537-11548. https://doi.org/10.1029/95JD00591.

Pant, R.R., Zhang, F., Rehman, F.U., Wang, G., Ye, M., Zeng, C. and Tang, H., 2018. Spatiotemporal variations of hydrogeochemistry and its controlling factors in the Gandaki River Basin, Central Himalaya Nepal. *Science of the Total Environment*, 622, pp.770-782. https://doi.org/10.1016/j.scitotenv.2017.12.063.

Panthi, J., Dahal, P., Shrestha, M.L., Aryal, S., Krakauer, N.Y., Pradhanang, S.M., Lakhankar, T., Jha, A.K., Sharma, M. and Karki, R., 2015. Spatial and temporal variability of rainfall in the Gandaki River Basin of Nepal Himalaya. *Climate*, 3(1), pp.210-226. https://doi.org/10.3390/cli3010210.

Paris, G., Sessions, A.L., Subhas, A.V. and Adkins, J.F., 2013. MC-ICP-MS measurement of $\delta^{34}S$ and $\Delta^{33}S$ in small amounts of dissolved sulfate. *Chemical Geology*, 345, pp.50-61. https://doi.org/10.1016/j.chemgeo.2013.02.022.

Pierson-Wickmann, A.C., Reisberg, L. and France-Lanord, C., 2000. The Os isotopic composition of Himalayan river bedloads and bedrocks: Importance of black shales. *Earth and Planetary Science Letters*, 176(2), pp.203-218. https://doi.org/10.1016/S0012-821X(00)00003-0.

Quade, J., English, N. and DeCelles, P.G., 2003. Silicate versus carbonate weathering in the Himalaya: A comparison of the Arun and Seti River watersheds. *Chemical Geology*, 202(3-4), pp.275-296. https://doi.org/10.1016/j.chemgeo.2002.05.002.

Quay, P.D., Wilbur, D.0., Richey, J.E., Devol, A.H., Benner, R. and Forsberg, B.R., 1995. The ^{18}O:^{16}O of dissolved oxygen in rivers and lakes in the Amazon Basin: determining the ratio of respiration to photosynthesis rates in freshwaters. *Limnology and Oceanography*, 40(4), pp.718-729. https://doi.org/10.4319/lo.1995.40.4.0718.

Rabinovich, A.L. and Grinenko, V.A., 1979. Sulfate sulfur isotope ratios for USSR river water. *Geochemistry International*, 16(2), pp.68-79.

Raymo, M.E., Ruddiman, W.F. and Froelich, P.N., 1988. Influence of late Cenozoic mountain building on ocean geochemical cycles. *Geology*, 16(7), pp.649-653. https://doi.org/10.1130/0091-7613(1988)016<0649:IOLCMB>2.3.CO;2.

Raymo, M.E. and Ruddiman, W.F., 1992. Tectonic forcing of late Cenozoic climate. *Nature*, 359(6391), pp.117-122. https://doi.org/10.1038/359117a0.

Raymo, M.1., 1994. The Himalayas, organic carbon burial, and climate in the Miocene. *Paleoceanography*, 9(3), pp.399-404. https://doi.org/10.1029/94PA00289.

Raymond, P.A., Hartmann, J., Lauerwald, R., Sobek, S., McDonald, C., Hoover, M., Butman, D., Striegl, R., Mayorga, E., Humborg, C. and Kortelainen, P., 2013. Global carbon dioxide emissions from inland waters. *Nature*, 503(7476), pp.355-359. https://doi.org/10.1038/nature12760.

Rennie, V.C., Paris, G., Sessions, A.L., Abramovich, S., Turchyn, A.V. and Adkins, J.F., 2018. Cenozoic record of $\delta^{34}S$ in foraminiferal calcite implies an early Eocene shift to deep-ocean sulfide burial. *Nature Geoscience*, 11(10), pp.761-765. https://doi.org/10.1038/s41561-018-0200-y.

Riebe, C.S., Kirchner, J.W., Granger, D.E. and Finkel, R.C., 2001. Strong tectonic and weak climatic control of long-term chemical weathering rates. *Geology*, 29(6), pp.511-514. https://doi.org/10.1130/0091-7613(2001)029<0511:STAWCC>2.0.CO;2.

Roback, K., Clark, M.K., West, A.J., Zekkos, D., Li, G., Gallen, S.F., Chamlagain, D. and Godt, J.W., 2018. The size, distribution, and mobility of landslides caused by the 2015 Mw7. 8 Gorkha earthquake, Nepal. *Geomorphology*, 301, pp.121-138. https://doi.org/10.1016/j.geomorph.2017.01.030.

Sarin, M.M. and Krishnaswami, S., 1984. Major ion chemistry of the Ganga–Brahmaputra river systems, India. *Nature*, 312(5994), pp.538-541. https://doi.org/10.1038/312538a0.

Sarin, M.M., Krishnaswami, S., Dilli, K., Somayajulu, B.L.K. and Moore, W.S., 1989. Major ion chemistry of the Ganga-Brahmaputra river system: Weathering processes and fluxes to the Bay of Bengal. *Geochimica et Cosmochimica Acta*, 53(5), pp.997-1009. https://doi.org/10.1016/0016-7037(89)90205-6.

Sarmiento J. L., & Gruber, N., 2006. Ocean Biogeochemical Dynamics. Princeton University Press.

Sequeira, R. and Kelkar, D., 1978. Geochemical implications of summer monsoonal rainwater composition over India. *Journal of Applied Meteorology* (1962-1982), pp.1390-1396. https://www.jstor.org/stable/26178852.

Shrestha, A.B., Wake, C.P., Dibb, J.E. and Whitlow, S.I., 2002. Aerosol and precipitation chemistry at a remote Himalayan site in Nepal. *Aerosol Science and Technology*, 36(4), pp.441-456. https://doi.org/10.1080/027868202753571269.

Sim, M.S., Bosak, T. and Ono, S., 2011. Large sulfur isotope fractionation does not require disproportionation. *Science*, 333(6038), pp.74-77. https://doi.org/10.1126/science.1205103.

Singh, S.P. and Singh, B.P., 2010. Geothermal evolution of the evaporite-bearing sequences of the Lesser Himalaya, India. *International Journal of Earth Sciences*, 99(1), pp.101-108. https://doi.org/10.1007/s00531-008-0361-9.

Spence, J. and Telmer, K., 2005. The role of sulfur in chemical weathering and atmospheric CO_2 fluxes: Evidence from major ions, $\delta^{13}C_{DIC}$, and $\delta^{34}S_{SO4}$ in rivers of the Canadian Cordillera. *Geochimica et Cosmochimica Acta*, 69(23), pp.5441-5458. https://doi.org/10.1016/j.gca.2005.07.011.

Stallard, R.F. and Edmond, J.M., 1983. Geochemistry of the Amazon: 2. The influence of geology and weathering environment on the dissolved load. *Journal of Geophysical Research: Oceans*, 88(C14), pp.9671-9688. https://doi.org/10.1029/JC088iC14p09671.

Striegl, R.G., Dornblaser, M.M., McDonald, C.P., Rover, J.R. and Stets, E.G., 2012. Carbon dioxide and methane emissions from the Yukon River system. *Global Biogeochemical Cycles,* 26(4). https://doi.org/10.1029/2012GB004306.

Sundquist, E.T., 1991. Steady-and non-steady-state carbonate-silicate controls on atmospheric CO_2. *Quaternary Science Reviews*, 10(2-3), pp.283-296. https://doi.org/10.1016/0277-3791(91)90026-Q.

Tipper, E.T., Bickle, M.J., Galy, A., West, A.J., Pomiès, C. and Chapman, H.J., 2006. The short term climatic sensitivity of carbonate and silicate weathering fluxes: Insight from seasonal variations in river chemistry. *Geochimica et Cosmochimica Acta*, 70(11), pp.2737-2754. https://doi.org/10.1016/j.gca.2006.03.005.

Tipper, E.T., Galy, A. and Bickle, M.J., 2008. Calcium and magnesium isotope systematics in rivers draining the Himalaya-Tibetan-Plateau region: Lithological or fractionation control? *Geochimica et Cosmochimica Acta*, 72(4), pp.1057-1075. https://doi.org/10.1016/j.gca.2007.11.029.

Thode, H.G., Kleerekoper, H. and McElcheran, D., 1951. Isotope fractionation in the bacterial reduction of sulphate. *Research*, 4(12), p.581.

Thode, H.G., 1991. Sulphur isotopes in nature and the environment: An overview. *Stable Isotopes: Natural and Anthropogenic Sulphur in the Environment*, SCOPE 43, edited by Krouse, H.R. and Grinenko, V.A., John Wiley & Sons, pp.1-26.

Torres, M.A., West, A.J. and Li, G., 2014. Sulphide oxidation and carbonate dissolution as a source of CO_2 over geological timescales. *Nature*, 507(7492), pp.346-349. https://doi.org/10.1038/nature13030.

Torres, M.A., West, A.J., Clark, K.E., Paris, G., Bouchez, J., Ponton, C., Feakins, S.J., Galy, V. and Adkins, J.F., 2016. The acid and alkalinity budgets of weathering in the Andes–Amazon system: Insights into the erosional control of global biogeochemical cycles. *Earth and Planetary Science Letters*, 450, pp.381-391. https://doi.org/10.1016/j.epsl.2016.06.012.

Torres, M.A., Moosdorf, N., Hartmann, J., Adkins, J.F. and West, A.J., 2017. Glacial weathering, sulfide oxidation, and global carbon cycle feedbacks. *Proceedings of the National Academy of Sciences*, 114(33), pp.8716-8721. https://doi.org/10.1073/pnas.1702953114.

Tranter, M. and Wadham, J.L., 2014. 7.5 - Geochemical Weathering in Glacial and Proglacial Environments in *Treatise on Geochemistry (Second Edition)*, eds. Holland, H.D., Turekian, K.K. Elsevier, pp.157-173. ISBN 9780080983004. https://doi.org/10.1016/B978-0-08-095975-7.00505-2.

Tripathee, L., Kang, S., Huang, J., Sharma, C.M., Sillanpää, M., Guo, J. and Paudyal, R., 2014. Concentrations of trace elements in wet deposition over the central Himalayas, Nepal. *Atmospheric Environment*, 95, pp.231-238. https://doi.org/10.1016/j.atmosenv.2014.06.043.

Tshering, L.D. and Bhandari, A.N., 1973. Geological report on the Salt Occurrences of Mustang area. Ministry of Industry & Commerce, Nepal Geological Survey.

Turchyn, A.V., Tipper, E.T., Galy, A., Lo, J.K. and Bickle, M.J., 2013. Isotope evidence for secondary sulfide precipitation along the Marsyandi River, Nepal, Himalayas. *Earth and Planetary Science Letters*, 374, pp.36-46. https://doi.org/10.1016/j.epsl.2013.04.033.

Urey, H.C., 1952. On the early chemical history of the earth and the origin of life. P*roceedings of the National Academy of Sciences of the United States of America*, 38(4), p.351. https://doi.org/10.1073/pnas.38.4.351.

Valdiya, K.S., 1980. Geology of Kumaun Lesser Himalaya (Dehradun: Wadia Institute of Himalayan Geology). Interim Report, 291.

Veizer, J., 1989. Strontium isotopes in seawater through time. *Annual Review of Earth and Planetary Sciences*, 17(1), pp.141-167. https://doi.org/10.1146/annurev.ea.17.050189.001041.

Walker, J.C., Hays, P.B. and Kasting, J.F., 1981. A negative feedback mechanism for the long-term stabilization of Earth's surface temperature. *Journal of Geophysical Research: Oceans*, 86(C10), pp.9776-9782. https://doi.org/10.1029/JC086iC10p09776.

West, A.J., Bickle, M.J., Collins, R. and Brasington, J., 2002. Small-catchment perspective on Himalayan weathering fluxes. *Geology*, 30(4), pp.355-358. https://doi.org/10.1130/0091-7613(2002)030<0355:SCPOHW>2.0.CO;2.

West, A.J., Galy, A. and Bickle, M., 2005. Tectonic and climatic controls on silicate weathering. *Earth and Planetary Science Letters*, 235(1-2), pp.211-228. https://doi.org/10.1016/j.epsl.2005.03.020.

West, A.J., 2012. Thickness of the chemical weathering zone and implications for erosional and climatic drivers of weathering and for carbon-cycle feedbacks. *Geology*, 40(9), pp.811-814. https://doi.org/10.1130/G33041.1.

White, A.F. and Blum, A.E., 1995. Effects of climate on chemical weathering in watersheds. *Geochimica et Cosmochimica Acta*, 59(9), pp.1729-1747. https://doi.org/10.1016/0016-7037(95)00078-E.

Winnick, M.J., Carroll, R.W., Williams, K.H., Maxwell, R.M., Dong, W. and Maher, K., 2017. Snowmelt controls on concentration-discharge relationships and the balance of oxidative and acid-base weathering fluxes in an alpine catchment, East River, Colorado. *Water Resources Research*, 53(3), pp.2507-2523. https://doi.org/10.1002/2016WR019724.

Wolff-Boenisch, D., Gabet, E.J., Burbank, D.W., Langner, H. and Putkonen, J., 2009. Spatial variations in chemical weathering and CO_2 consumption in Nepalese High Himalayan catchments during the monsoon season. *Geochimica et Cosmochimica Acta*, 73(11), pp.3148-3170. https://doi.org/10.1016/j.gca.2009.03.012.

Zachos, J., Pagani, M., Sloan, L., Thomas, E. and Billups, K., 2001. Trends, rhythms, and aberrations in global climate 65 Ma to present. *Science*, 292(5517), pp.686-693. https://doi.org/10.1126/science.1059412.

Zeebe, R.E. and Wolf-Gladrow, D., 2001. CO_2 in seawater: equilibrium, kinetics, isotopes (No. 65). Gulf Professional Publishing.

IV.12: Supplementary text

IV.12.1: Ion chromatography

Initial MC-ICP-MS measurements of $\delta^{34}S_{SO4}$ revealed lower S abundances than expected based on the [SO_4^{2-}] values reported in Bhatt et al. (2018). Subsequent ion chromatography (IC) measurements at Caltech of [Ca^{2+}], [Mg^{2+}], [Na^{+}], [K^{+}], [Cl^{-}], and [SO_4^{2-}] revealed systematic differences from the published values, with trends related to the month of sample collection (Fig. IV-S1). Two potential causes of the discrepancy are analytical uncertainty and changes in sample chemistry due to storage artifacts.

IV.12.1.1: Analytical uncertainty

To ascertain if the discrepancy in measured ion concentrations is attributable to experimental uncertainty, we quantified precision through replicate analysis of external reference materials and river water samples. For reference materials, we used *Environment and Climate Change Canada* certified materials MAURI-09 (lot 0316) and CRANBERRY-05 (lot 0815). A subset of references and samples were also measured after addition of variable quantities of HNO_3^-; we report precision both for all determinations of major ion chemistry (Table IV-S1, row tops) and for determinations on only solutions without added HNO_3^- (Table IV-S1, bottom rows). When calculated as the mean of the relative standard deviation of measurements on the two reference materials, we find the following precisions across all determinations of major ion concentration (2σ): [Ca^{2+}]: 8.4%, [Mg^{2+}]: 5.7%, [Na^{+}]: 1.6%, [K^{+}]: 3.1%, [Cl^{-}]: 2.8%, [SO_4^{2-}]: 2.7%. When quantified as the relative standard deviation of replicate sample measurements, we find the following measurement precisions across all determinations of major ion concentration (2σ): [Ca^{2+}]:

3.6%, [Mg^{2+}]: 3.7%, [Na^{+}]: 1.1%, [K^{+}]: 1.4%, [Cl^{-}]: 2.8%, [SO_4^{2-}]: 2.5% (Table IV-S1). Overall, we conservatively quantify the 2σ precision of any given ion measurement to be <12%, which represents the least-reproducible ion (Ca^{2+}) in the least-reproducible solution, when also including measurements with added HNO_3^{-} (Table IV-S1). When measurements are only considered on references and samples without added HNO_3^{-}, we conservatively quantify the 2σ precision of any given ion measurement to be <7%. Given the large differences between Caltech measurement and those of Bhatt et al. (2018) (Fig. IV-S1), low analytical precision is unable to explain the discrepancy.

For MAURI-09, the fractional offset between the mean measured value and the mean certified values were: [Ca^{2+}]: 9.8%; [Mg^{2+}]: 4.8%; [Na^{+}]: 2.2%; [K^{+}]: 5.2%; [Cl^{-}]: 2.1%; [SO_4^{2-}]: 2.0%. For CRANBERRY-05 the fractional offset between the mean measured value and the mean certified values were: [Ca^{2+}]: 4.6%; [Mg^{2+}]: 3.5%; [K^{+}]: 3.7%; [SO_4^{2-}]: 3.0%, with [Na^{+}] and [Cl^{-}] outside of the calibration range. Despite the relatively high difference for the measured and reported concentration of [Ca^{2+}] in MAURI-09, we accept our [Ca^{2+}] determinations because (i) the measured [Ca^{2+}] is close to being within the stated 2σ uncertainty window of the certified value, (ii) the same calibration standards generated a reasonable match with the reported [Ca^{2+}] of CRANBERRY-05, (iii) our [Ca^{2+}] measurements match expected values for a different set of standards prepared by a different analyst and made from a separate Ca^{2+} stock solution, and (iv) the consistency of our measurements with all other reported ion systems argues against mistakes during sample handling or data processing.

IV.12.1.2: Artifacts of sample storage

The samples measured in this study were collected in 2011 in a variety of bottles. Except for the fact that samples from a given month tend to have been collected in the same type of container, the trendlines in Fig. IV-S1 are not associated with the type of sample bottle. After collection, only a minimal number of primary liquids were transferred into secondary containers. The samples were stored refrigerated without acidification in Germany until their shipment to California in early 2018, where they were again stored refrigerated and unacidified.

During storage ions could have either adsorbed to the sides of the sample bottles, precipitated as solids (Jacobson et al., 2002), or been concentrated through evaporation. In the first two cases, we expect the Caltech measurements of ion concentration to be lower than those reported in Bhatt et al. (2018). However, for certain ions and time periods, the Caltech measurement is significantly higher than that of Bhatt et al. (2018). Moreover, no solids are visually identifiable in the sample containers, and precipitation of a carbonate phase would be unlikely to explain the discrepancy of ions such as $[Cl^-]$ and $[K^+]$. To test if the discrepancy is attributable to artifacts of sample storage, two subsets of ten samples each were acidified with nitric acid, one set to ~0.1% and the second set to ~0.2%. Measurements of $[Ca^{2+}]$, $[Mg^{2+}]$, $[Na^+]$, and $[K^+]$ before and after acidification were very similar for both sets of samples, typically within 5% (Fig. IV-S2). There is a general tendency for measured $[Ca^{2+}]$ and $[Mg^{2+}]$ to be approximately 2.5% to 3.5% lower in acidified samples than in unacidified samples, which is opposite to the shift expected if cations were attached to the walls of the sample bottles or precipitated as an acid-soluble phase. Notably, measurement of $[Ca^{2+}]$ in acidified MAURI-09 and calibrated with

acidified standards was significantly more consistent with the reported value than measurement of [Ca^{2+}] in unacidified MAURI-09 calibrated with unacidified standards. Given the similarity of cation measurements in samples before and after acidification, we do not believe that either ion attachment to the walls of sample containers or precipitation of solids can explain the discrepancy between the Caltech measurements and those of Bhatt et al. (2018).

Evaporation of samples during storage is expected to increase the concentration of each major ion in solution by the same proportion. Contrary to this expectation, the sign and magnitude of discrepancy between the Caltech measurements and those of Bhatt et al. (2018) differ across ion systems within the same samples. For example, the two sets of measurements of [Mg^{2+}] in samples from April are much more consistent than the two sets of measurements of [Na^{+}] in the same sample bottles (Fig. IV-S1). This indicates that evaporation of samples during storage is unable to explain the discrepancy between the Caltech measurements and those of Bhatt et al. (2018).

IV.12.1.3: Comparison with prior measurements

The 2011 sampling campaign is one of several in the Lirung Glacier catchment and the Trisuli River at Betrawati. Samples from the Lirung Glacier catchment were previously analyzed in Bhatt et al. (2000) and Bhatt et al. (2009), and the major ion composition of waters from the Trisuli River at Betrawati were previously reported in Galy and France-Lanord (1999) and Bhatt et al. (2009). For the Lirung samples, the Caltech measurements of [Cl^{-}] and Cl^{-}/Σ^{+} are higher than previous observations (Figs. IV-S3A and B). Although the fractional difference in [Cl^{-}] is large, the change translates to only a few percent of Cl^{-}

/Σ^+. For the Trisuli River at Betrawati, the major ion composition of our samples is largely similar to that reported in Galy and France-Lanord (1999).

IV.12.1.4: Re-evaluation of the Bhatt et al. (2018) measurements

A subset of the chromatographic measurements underlying the reported values in Bhatt et al. (2018) were recovered and reprocessed. In particular, the original measurements of [Na^+], [SO_4^{2-}], and [Ca^{2+}] for several samples from January, March, and November were re-evaluated and compared with the new Caltech measurements. For [Na^+], the updated analysis brought samples from January, March, and November into much stronger agreement, although several samples from March still remain >10% discrepant. For [SO_4^{2-}] in November samples, the updated values brought most of the measured concentrations within 10% agreement. For [SO_4^{2-}] in January samples, the updated values increased the difference in measured concentrations beyond 10%. No reprocessing of the original [Ca^{2+}] data was required.

IV.12.1.5: Summary of major ion discrepancy

If the difference in the Caltech and Bhatt et al. (2018) measurements were due to random errors, the Caltech measurements would scatter around a 1:1 line with those reported in Bhatt et al. (2018). Rather, the data show clear trends correlated with the month of sample collection (Fig. IV-S1). If the discrepancy were due to a constant accuracy offset, the measurements of a given ion at Caltech should be systematically lower or higher than those published previously. However, in some months the Caltech measurements show higher ion concentrations, while in other months the measurements of Bhatt et al. (2018)

are higher. Acidification testing rules out storage artifacts, and the changing magnitude of discrepancy across ion systems argues against evaporation during sample storage. To promote comparison between our $\delta^{34}S_{SO4}$ measurements and ionic weathering products, we remeasured the major ion chemistry in all samples used for sulfur isotope analysis. In the main text of this article, we report the major ion chemistry measured at Caltech.

IV.12.2: Inversion end-members

IV.12.2.1: Carbonate end-members

In forward models, the contribution of carbonate lithologies to river dissolved load is often found by differencing after attributing portions of the river dissolved load to cyclic salts and silicate lithologies (Galy and France-Lanord 1999; Quade et al., 2003). In contrast, inversion modeling requires defining parameter ranges for the composition of carbonate end-members. Here we use stoichiometric calcite and dolomite as two carbonate end-members with $Na^+/\Sigma^+ = K^+/\Sigma^+ = 0$. This choice is enabled by our normalization to Σ^+, rather than Na^+, which allows the carbonate end-members to not provide Na^+ to river water. In prior work, Gaillardet et al. (1999) used a Ca^{2+}/Na^+ of 50 and Mg^{2+}/Na^+ of 10, while Burke et al. (2018) followed the Congo study of Négrel et al. (1993) to use a carbonate Ca^{2+}/Na^+ of 60±30 and Mg^{2+}/Na^+ of 30±15.

IV.12.2.2: Silicate end-members

Coherently changing K^+/Na^+ ratios (Fig. IV-3B) motivates the use of two silicate end-members, which we call ‘silicate’ and ‘biotite’. We take the silicate and biotite end-members to have Ca^{2+}/Σ^+ of 0.15±0.05 and Mg^{2+}/Σ^+ of 0.35±0.10, informed by XRF

measurements of HHC bedrock (France-Lanord and Derry, 1997). The Na^+/Σ^+ and K^+/Σ^+ ratios of the two end-members are 0.1±0.1 and 0.4±0.1 (Table IV-1).

Quade et al. (2003) report a silicate end-member $Ca^{2+}/Na^+ = 0.41\pm0.18$ based on a subset of Himalayan rivers thought to be draining only silicate minerals, similar to the value of 0.45 derived from suspended sediments in the Marsyandi (Wolf-Boenisch et al., 2009). However, both values are higher than the range of 0.18-0.30 reported in Galy and France-Lanord (1999) for Himalayan silicates and are higher than the value 0.35±0.15 used to invert global river observations (Gaillardet et al., 1999). Conversely, these values are all lower than the Ca^{2+}/Na^+ of 0.7±0.3 reported in Krishnaswami and Singh (1998). The Ca^{2+}/Na^+ ratio of silicates may also change across lithostratigraphic units; according to Dalai et al. (2002), Krishnaswami et al. (1999) indicate a Ca^{2+}/Na^+ ratio of 0.46±0.28 for granite and gneiss in the LH, but 0.32±0.29 for the HHC.

Quade et al. (2003) report a silicate Mg^{2+}/Na^+ ratio of 0.24±0.1, which is quoted as a likely maximum due to detection limitations, and which is almost identical to the value of 0.24±0.12 inferred from the global compilation of Gaillardet et al. (1999). Conversely, Dalai et al. (2002) reports Mg^{2+}/Na^+ from the Yamuna River system of 0.65±0.45 for the LH and 0.31±0.28 for the HHC. Spanning this entire range, values of Mg^{2+}/Na^+ in suspended sediments from the Marsyandi River range from 0.11-1.30 (Wolff-Boenisch et al., 2009).

IV.12.2.3: Evaporite end-member

Sarin and Krishnaswami (1984) raised the prospect that evaporites may exist in the central Nepal Himalaya based on the observation of gypsum associated with the Kumaun

Himalya (Valdiya, 1980). Subsequently, the presence of western evaporites was confirmed through direct observations of gypsum and halite near the Main Boundary Trust in North India (Singh and Singh, 2010). While general thinking holds that evaporites are unlikely to be a major influence in the Narayani River catchment, they may still be important locally. For example, Fort (1996) cites a study by Tshering and Bhandari (1973) ostensibly showing the existence of evaporitic layers in the Thakkhola-Mustang Valley. Citing Bordet et al. (1971), Tipper et al. (2006) writes that no evaporites have been identified in TSS sediment near the Marsyandi headwaters. Turchyn et al. (2013) provided support for this claim by not recovering a clear correlation between $[Cl^-]$ and $\delta^{34}S_{SO4}$. If present, evaporite $\delta^{34}S$ is expected to reflect the range of Phanerozoic evaporites and thus fall between 10‰ and 30‰ (Claypool et al., 1980). Given the lack of direct observation of evaporites along the Langtang-Trisuli-Narayani River system, we do not include an evaporite end-member in our primary inversion (see IV.12.4 for results from an inversion including an evaporite end-member).

IV.12.2.4: Geothermal spring end-member

The dissolved chemistry of Himalayan geothermal springs varies over multiple orders of magnitude and exhibits large spatial gradients (Fig. IV-S4; Evans et al., 2001, 2004; Becker et al., 2008). In part, the chemical variability is attributable to mixing between a geothermal end-member and river waters influenced by weathering. Ion ratios in spring waters often resemble seawater, although this observation could reflect the excess of sampling from the Marsyandi River relative to springs from elsewhere in the Narayani River system. In the space of Ca^{2+}/Σ^+ against Na^+/Σ^+, the data appear consistent with

mixing between an end-member resembling seawater and another end-member resembling river water (Fig. IV-S4A). However, this trend breaks down when considering Na^+/Cl^- and K^+/Cl^- (Fig. IV-S4E).

Previously, Bickle et al. (2005) estimated the chemistry of a spring end-member by selecting 11 springs from Evans et al. (2001) with $Na^+/Cl^- < 1.2$. This choice was influenced by initial work in the Marsyandi River that found springs tend to be highly enriched in Cl^-, suggestive of an influence from deep evaporites (Evans et al., 2001). Although subsequent work showed that the dominant anion in Himalayan geothermal springs is HCO_3^-, with Cl^- thought to derive from metamorphism, a potential role for evaporite weathering at depth in the Marsyandi is still supported by a single hot spring $\delta^{34}S_{SO4}$ measurement of +12.4‰ (Turchyn et al., 2013). While the criteria of Bickle et al. (2005) thus may be appropriate for the Marsyandi, it does not necessary reflect the chemistry of geothermal springs in the Langtang-Trisuli-Narayani River system.

Springs are found in the general vicinity of LNS-5, LNS-6, and LNS-7 on the Langtang River upstream of the junction at Syabru Besi and along the Bhote Kosi (Evans et al., 2004, 2008; Becker et al., 2008). These springs have Cl^-/Na^+ ratios between 0.3% and 9.8%. In contrast, springs near the Marsyandi have Cl^-/Na^+ ratios close to or slightly exceeding 100%, which represent an exception to the general observation that HCO_3^- dominates the anion budgets of Himalayan hot springs (Evans et al., 2004). Overall, the data show that geothermal springs along the Langtang-Trisuli have significantly lower Na^+/Cl^- ratios than seawater and springs from the Marsyandi River (Fig. IV-S4C). In all samples from this study, correcting for 100% of $[Cl^-]$, even using the highest Cl^-/Na^+ ratio of the relevant springs, would remove >100% of $[Na^+]$. Attributing 10% of the river Cl^-

budget to springs would, on average, source 43% of dissolved [Na^+]. Although this magnitude of input is potentially acceptable, the remaining 90% of Cl^- in solution would still require an alternative explanation. Given the large chemical difference between springs and river samples, we do not anticipate significant inputs from springs and do not include a spring end-member in our primary analysis (see IV.12.4 for results from an inversion model including springs).

If springs do contribute Cl^- to our samples, we expect only a moderate influence on river $\delta^{34}S_{SO4}$. The SO_4^{2-}/Cl^- of the relevant springs ranges from 0.4 to 26, and a contribution of 10% of river [Cl^-] would entail median contributions of 0.5% to 33% of river [SO_4^{2-}]. Taking a spring $\delta^{34}S_{SO4}$ value of 12.5‰ (Turchyn et al., 2013), the median shift in $\delta^{34}S_{SO4}$ due to this spring contribution would be less than ~4.5‰. The ^{34}S-enriched signal of this input would cause an increase in $\delta^{34}S_{SO4}$ near Syabru Besi, while our data clearly show a decrease in $\delta^{34}S_{SO4}$ at the same junction (Fig. IV-4).

IV.12.2.5: Precipitation end-member

In our primary inversion 100% of river [Cl^-] is assumed to derive from precipitation. While the amount, distribution, and major ion composition of precipitation in the Himalaya varies widely, when compared with seawater the dissolved chemistry tends to be enriched in cations relative to Cl^- (Fig. IV-S5; Handa, 1968; Galy and France-Lanord, 1999; Bhatt et al., 2000; Andermann et al., 2011; Balestrini et al., 2014; Panthi et al., 2015). This addition of cations to precipitation occurs through incorporation of terrestrial dust (Sequeira and Kelkar, 1978). The uncertainty of our precipitation end-member captures the range of observed compositions, including some level of seasonal variability due to

changes in atmospheric circulation (Shrestha et al., 2002). Overall, the inversion-constrained precipitation end-member generally agrees with observations, although reaches slightly higher values of Mg^{2+}/Σ^{+} and Cl^{-}/Σ^{+} than are observed (Fig. IV-S5).

Except for three samples, attributing 100% of river [Cl^{-}] to precipitation entails sourcing 3% to 54% of the sum of cations in solution. Although the latter portion of this range may seem high, this magnitude of meteoric input is consistent with prior research. For example, Galy and France-Lanord (1999) report that >65% of total dissolved solids in small high-latitude silicate catchments derive from precipitation, Harris et al. (1998) cite Sarin et al. (1989) in writing that 29±7% of Na^{+} is derived through atmospheric deposition in highland rivers, and recent work attributed >50% of Na^{+} in streams from the Eastern Himalaya to precipitation, evaporites, and hot springs (Hren et al., 2007). The most direct comparison comes from West et al. (2002), who calculated that 17% to 61% of the cation flux in small Himalayan catchments is due to atmospheric deposition. That analysis included a re-evaluation of data from the Lirung catchment originally reported in Bhatt et al. (2000), which differed from most other catchments in the West et al. (2002) analysis by showing only 2.3% of [Ca^{2+}] derived from atmospheric deposition (Bhatt et al., 2000; West et al., 2002). For their analysis, West et al. (2002) corrected for Cl^{-} inputs using snow samples from Yala glacier. However, these samples varied in their Ca^{2+}/Cl^{-} ratios between 0.1 and 2.4. In part, this large range in Ca^{2+}/Cl^{-} reflects that the samples were collected at differing depths and in differing seasons, and thus reflect a heterogeneous material averaged over different durations of time (Bhatt et al., 2000). Using rainwater measurements (Table IV-1) as opposed to snow, a forward model finds that 2-13% of the Ca^{2+} and 7-29% of the Na^{+} in the Bhatt et al. (2000) Lirung data is attributable to

atmospheric inputs. Similarly, our full inversion model finds 1-9% of the Ca^{2+} and 5-28% of Na^{+} in that data is attributable to atmospheric inputs. These updated calculations bring the magnitude of atmospheric deposition in line with expectations from the other catchments in West et al. (2002).

IV.12.2.6: Anthropogenic impacts on river chemistry

All sample sites in this study are located within 100 km of Kathmandu, and LNS-4 and LNS-3 are only approximately 30 km away from the city. Because prior research has identified ubiquitous SO_4^{2-} pollution in rivers globally (Berner, 1971), even in relatively isolated systems, either global anthropogenic inputs or local urban pollution could influence our observations. At the local scale, Collins and Jenkins (1996) identified significant impacts from agricultural activity on the dissolved chemistry of rivers within the Middle Mountains approximately 10 km north of Kathmandu; soil tillage was found to increase weathering rate and the overall ion budget of rivers, but with disproportionate increases in $[NO_3^-]$ and $[SO_4^{2-}]$ due to fertilizer application.

Anthropogenic pollution was previously proposed to be ^{34}S-depleted, but recent research reveals a lack of correlation between river pollution and $\delta^{34}S_{SO4}$ (Burke et al., 2018); our analysis of pollution is thus based on measurements of ion concentrations. The concentration of dissolved ions indicate that pollution has only a minimal impact on our samples (Fig. IV-S6A). The ratios SO_4^{2-}/Σ^+ and SO_4^{2-}/Cl^- generally decrease with elevation, opposite to the trend expected if pollution from SO_4^{2-}-bearing fertilizers were entering the river at sites near Kathmandu. However, changes in SO_4^{2-}/Σ^+ are also influenced by downstream changes in lithology. As a result, these observations can only

be considered evidence that pollution, if present, is of secondary importance to downstream changes in chemical weathering.

A second approach to identifying pollution is to consider the ratio of Cl^- to Na^+. Only 7 of our samples have Na^+/Cl^- less than 1.1, which was previously used as a threshold value for pollution (Burke et al., 2018). These 7 samples are distributed across sampling sites and were all collected in July, August, and September. Because these samples are unrelated with proximity to Kathmandu, they do not clearly indicate anthropogenic inputs.

Conversely, river pH measurements do provide tentative evidence of anthropogenic inputs (Fig. IV-S6B). Of the 76 samples with pH measurements, 10 values are lower than 6.5 and 1 sample has a pH lower than 5.5. The samples with low pH values are found in stations LNS-3 through LNS-7, all relatively close to Kathmandu (Fig. IV-1). These acidic samples span the seasonal cycle but are concentrated during the pre-monsoon season. The lack of low pH values in other stations and seasons may be attributed to sampling bias because sites upstream of LNS-7 each have only a single pH measurement, all from October, and all of which are circumneutral. The low pH values thus potentially indicate either a seasonal pollutant dominant in the pre-monsoon season, or alternatively a constant input of pollution diluted by higher discharge during the monsoon season, and which may or may not be localized to the region near Kathmandu. Because low values of SO_4^{2-}/Σ^+ argue against the addition of SO_4^{2-}-bearing fertilizer, the low-pH samples may indicate the formation of HNO_3 following oxidation of anthropogenic NH_4^+. It is notable that some of the highest measured [NH_4^+] values are found in the Langtang headwaters (Fig. IV-S6C), with several lower values closer to Kathmandu, and which likely also reflects the grazing activities of livestock near the Langtang headwaters. We are unable to interpret original

$[NO_3^-]$ (Fig. IV-S6D) determinations or measure $[NO_3^-]$ in the sample bottles now due to artifacts of sample storage (IV.12.1).

IV.12.3: Extended data figures

IV.12.3.1: Discharge curves

A fractional discharge curve was calculated based on observations at Q1, Q2, and Q3 (Figs. IV-1 and IV-S7).

IV.12.3.2: Impacts of secondary carbonate precipitation

A river dominated by $CaCO_3$ weathering with limited FeS_2 oxidation would be expected to have high Ca^{2+}/Σ^+ and low SO_4^{2-}/Σ^+ ratios (Fig. IV-S8, red square). Precipitation of $CaCO_3$ would decrease Ca^{2+}/Σ^+ and bias the interpretation to lower fractions of carbonate weathering (Fig. IV-S8, blue diamond). It would also increase SO_4^{2-}/Σ^+, making observed SO_4^{2-}/Σ^+ lower than the gross H_2SO_4-driven weathering fraction. Furthermore, the shift in Ca^{2+}/Σ^+ would alter the inversion-constrained range of end-member SO_4^{2-}/Σ^+. However, because the formation of $CaCO_3$ consumes Ca^{2+} and sources H^+, observed SO_4^{2-}/Σ^+ remains an accurate reflection of the net weathering driven by H_2SO_4. The magnitude of these effects depends on the relative abundance of Ca^{2+}, SO_4^{2-}, and the other major ions. Using the median values of our samples and assuming 50% of Ca^{2+} was removed as $CaCO_3$ (Bickle et al., 2015) the absolute shifts in Ca^{2+}/Σ^+ and SO_4^{2-}/Σ^+ are estimated to be ~10%.

IV.12.3.3: Sulfur isotope mixing diagrams

Sulfur isotope mixing diagrams of $\delta^{34}S_{SO4}$ against $1/SO_4^{2-}$, Cl^-/SO_4^{2-}, Ca^{2+}/SO_4^{2-}, Mg^{2+}/SO_4^{2-}, Na^+/SO_4^{2-}, and K^+/SO_4^{2-} argue against two end-member mixing as an explanation for observed $\delta^{34}S_{SO4}$ variability (Fig. IV-S9).

IV.12.3.4: Cumulative distributions of model results

Cumulative distribution functions for end-member contributions to river SO_4^{2-}, Ca^{2+}, Mg^{2+}, Na^+, and K^+ constrain the range of fractional lithologic inputs (Fig. IV-S10).

IV.12.3.5: Month-specific and location-specific RZ regressions

Plots of Z against R by month (Fig. IV-S11) or site (Fig. IV-S12) of sample collection show both positive and negative slopes.

IV.12.3.6: Inversion-constrained $\delta^{34}S_{FeS2}$ and R, Z against catchment lithology

Inversion-constrained $\delta^{34}S_{FeS2}$, R, and Z vary with the fractional exposure of TSS and LH within the catchment of each sample (Fig. IV-S13).

IV.12.3.7: Seasonality of R and Z in prior datasets

Inversion of prior data from the Narayani River catchment shows some evidence of seasonality in chemical weathering dynamics (Fig. IV-S14).

IV.12.4: Sensitivity analysis

IV.12.4.1: Model results including an evaporite end-member

Model results when including an evaporite end-member show similar trends as our primary inversion model (Fig. IV-S15). In this inversion the evaporite end member has Ca^{2+}/Σ^{+} = 0.45±0.18, Mg^{2+}/Σ^{+} = 0.09±0.06, Na^{+}/Σ^{+} = 0.45±0.16, K^{+}/Σ^{+}=0±0, SO_4^{2-}/Σ^{+} = 0.34±0.23, Cl^{-}/Σ^{+} = 0.44±0.18. However, as in Torres et al. (2017), we force set the chemical composition of the evaporite end-member to reflect a stoichiometry of $CaSO_4$ and HCl. As a result, the values of SO_4^{2-}/Σ^{+} and Cl^{-}/Σ^{+} are not pulled from the indicated distributions, but rather are set to equal the sum of Ca^{2+}/Σ^{+} and Mg^{2+}/Σ^{+} or Na^{+}/Σ^{+}, respectively. Rather than assigning values of $Cl_{Critical}$, the inversion apportions the Cl^{-} budget between precipitation and the evaporite end-member.

IV.12.4.2: Model results including a hot spring end-member

In this simulation (Fig. IV-S16), the hot spring end member has Ca^{2+}/Σ^{+} = 0.17±0.12, Mg^{2+}/Σ^{+} = 0.09±0.11, Na^{+}/Σ^{+} = 0.69±0.25, K^{+}/Σ^{+}=0.06±0.03, SO_4^{2-}/Σ^{+} = 0.06±0.02, Cl^{-}/Σ^{+} = 0.02±0.04. Rather than assigning values of $Cl_{Critical}$, the inversion apportions the Cl^{-} budget between precipitation and the spring end-member. Because the spring has very high Na^{+}/Cl^{-}, a small apportionment of the Cl^{-} budget to springs explains a significant fraction of the Na^{+} budget. As a result, inclusion of a hot spring increases the fraction of carbonate weathering (R).

IV.12.4.3: Model results without [K^+] or [Cl^-] in the inversion

Pre-collection acid washing is a potential source of Na^+, K^+, and Cl^- contamination. While [Na^+] exhibits a monsoon decline seen in prior data, [K^+] and [Cl^-] do not decline coherently with increases in discharge. We argue in the main text that this observation is a robust feature of the data related to dynamics of glacial weathering (Anderson et al., 1997, 2000) or landslides (Emberson et al., 2017), but it is also possibly indicative of a procedural blank. When only [Ca^{2+}], [Mg^{2+}], [Na^+], and [SO_4^{2-}] are inverted without [K^+] or [Cl^-], we recover monsoon increases in the fraction of carbonate weathering consistent with prior studies (Fig. IV-S17, Tipper et al., 2006).

IV.12.4.4: Forward model of carbonate and silicate contributions

Prior research has used a forward-model to calculate the fractional contributions of carbonate and silicate rocks (Galy and France-Lanord, 1999). The outline of this calculation is to (1) remove [Cl^-] from observations, (2) attribute a fraction of the remaining [Ca^{2+}] and [Mg^{2+}] to silicate weathering and the residual to carbonate weathering, and (3) calculate the flux of carbonate and silicate alkalinity. Below we show that the results of this calculation are extremely similar to those of our full inversion model (Fig. IV-S18).

(1) Assume all Cl^- derives from seawater (Eq. IV-S1), either through dissolution of evaporites or direct input through precipitation. For this correction we use the seawater chemistry of Sarmiento and Gruber (2006). In Eq. IV-S1, the variable Z stands for any dissolved ion concentration, and concentrations corrected for Cl^- are indicated with a superscripted *.

$$[Z_i]^*_{riv} = [Z_i]_{riv} - [Cl^-]_{riv}\left(\frac{[Z_i]_{seawater}}{[Cl^-]_{seawater}}\right) \quad \text{(IV-S1)}$$

(2) Assume all remaining Na^+ and K^+ derive from silicate weathering (Eqs. IV-S2 and IV-S3). For Ca^{2+} and Mg^{2+}, scale by the Ca^{2+}/Na^+ ($X^{slct}_{Ca^{2+}/Na^+}$) and Mg^{2+}/K^+ ratios ($X^{slct}_{Mg^{2+}/K^+}$) of silicate rocks (Eqs. IV-S4 to IV-S7). We take $X^{slct}_{Ca^{2+}/Na^+}$=0.2±0.1 and $X^{slct}_{Mg^{2+}/K^+}$=0.5±0.2 (Galy and France-Lanord, 1999).

$$[Na]_{silicate} = [Na]^* \quad \text{(IV-S2)}$$

$$[K]_{silicate} = [K]^* \quad \text{(IV-S3)}$$

$$[Ca]_{sililcate} = [Na]^* * X^{slct}_{Ca^{2+}/Na^+} \quad \text{(IV-S4)}$$

$$[Mg]_{silicate} = [K]^* * X^{slct}_{Mg^{2+}/K^+} \quad \text{(IV-S5)}$$

$$[Ca]_{carbonate} = [Ca]^* - [Ca]_{silicate} \quad \text{(IV-S6)}$$

$$[Mg]_{carbonate} = [Mg]^* - [Mg]_{silicate} \quad \text{(IV-S7)}$$

(3) Calculate R as the fraction of Cl-corrected cations derived from carbonate weathering (Eq. IV-S8). Calculate Z by assuming that 100% of $[SO_4^{2-}]^*$ is sourced from FeS_2 oxidation (Eq. IV-S9).

$$R = \frac{2[Ca^{2+}]_{carbonate}+2[Mg^{2+}]_{carbonate}}{2[Ca^{2+}]^*+2[Mg^{2+}]^*+[Na^+]^*+[K^+]^*} \quad \text{(IV-S8)}$$

$$Z = \frac{2[SO_4^{2-}]^*}{2[Ca^{2+}]^*+2[Mg^{2+}]^*+[Na^+]^*+[K^+]^*} \quad \text{(IV-S9)}$$

IV.13: Supplementary figures

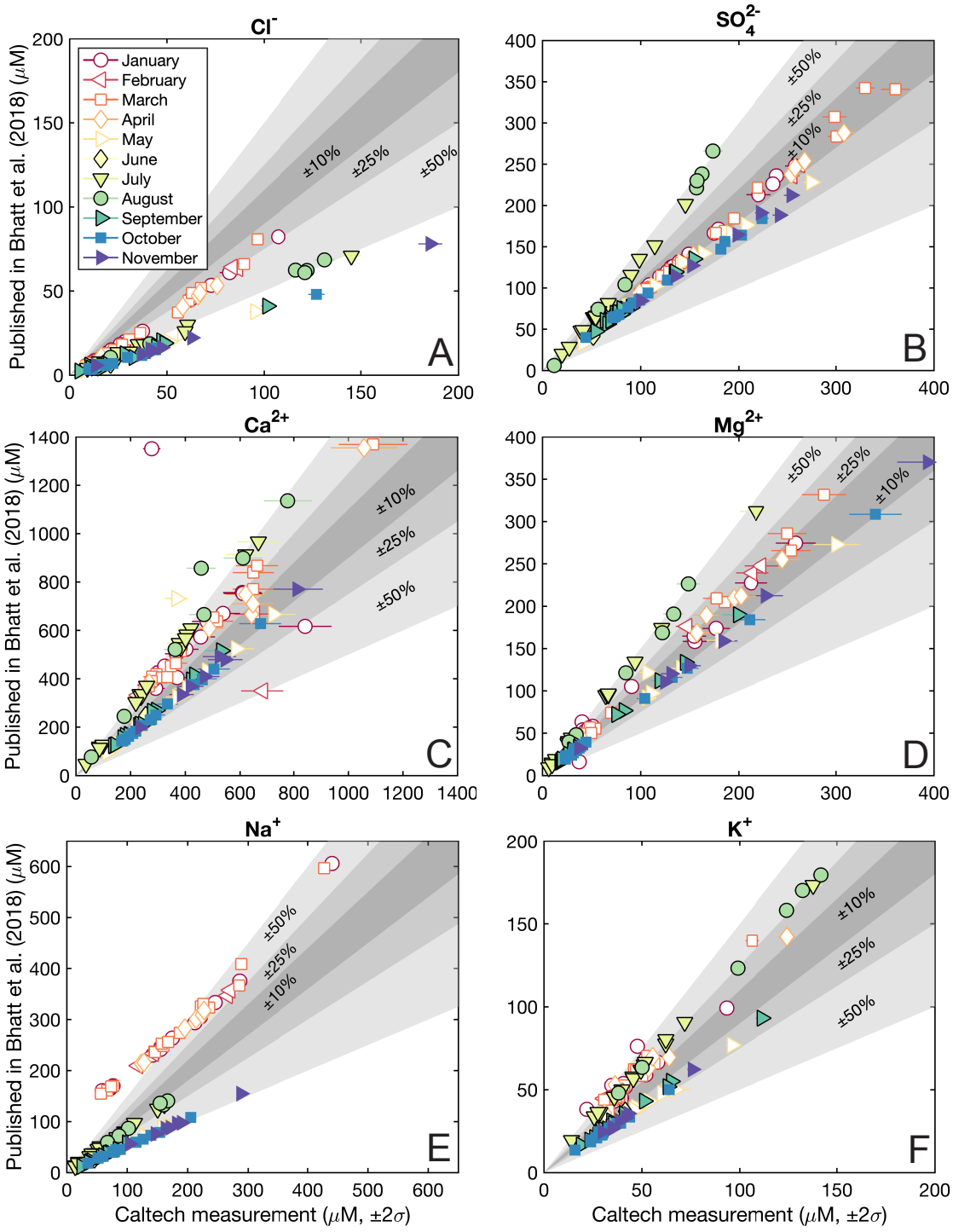

Fig. IV-S1: Comparison of major ion chemistry in samples measured at Caltech and previously published in Bhatt et al. (2018). (A) [Cl^-], (B) [SO_4^{2-}], (C) [Ca^{2+}], (D) [Mg^{2+}], (E) [Na^+], and (F) [K^+]. Shaded regions show ±10%, ±25%, and ±50% from mutual agreement. Systematic offsets group by month of sample collection.

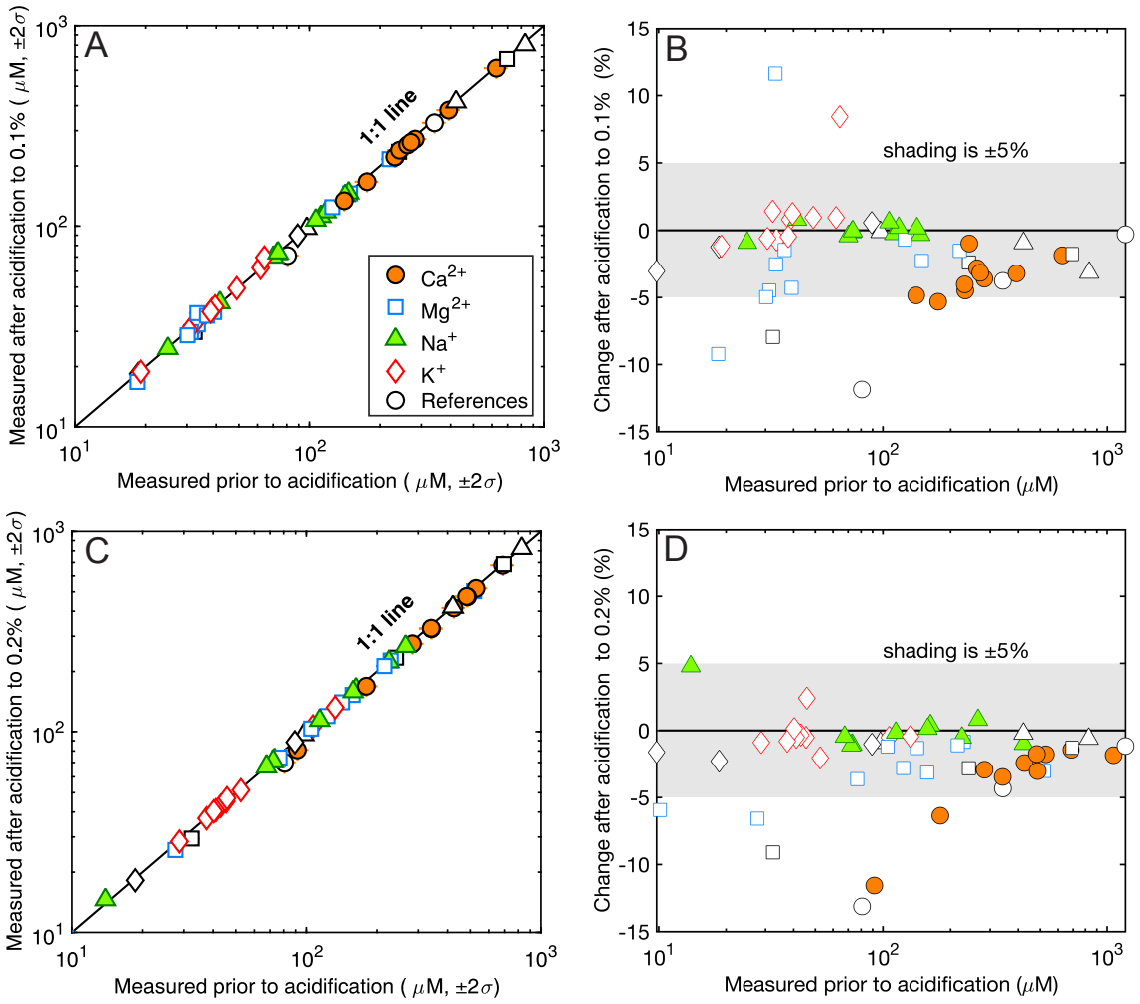

Fig. IV-S2: $[Ca^{2+}]$, $[Mg^{2+}]$, $[Na^{+}]$, and $[K^{+}]$ in river samples before and after acidification to approximately (A, B) 0.1% and (C, D) 0.2% with high-purity HNO_3. (B, D) Proportional change following acidification is mostly within 5%.

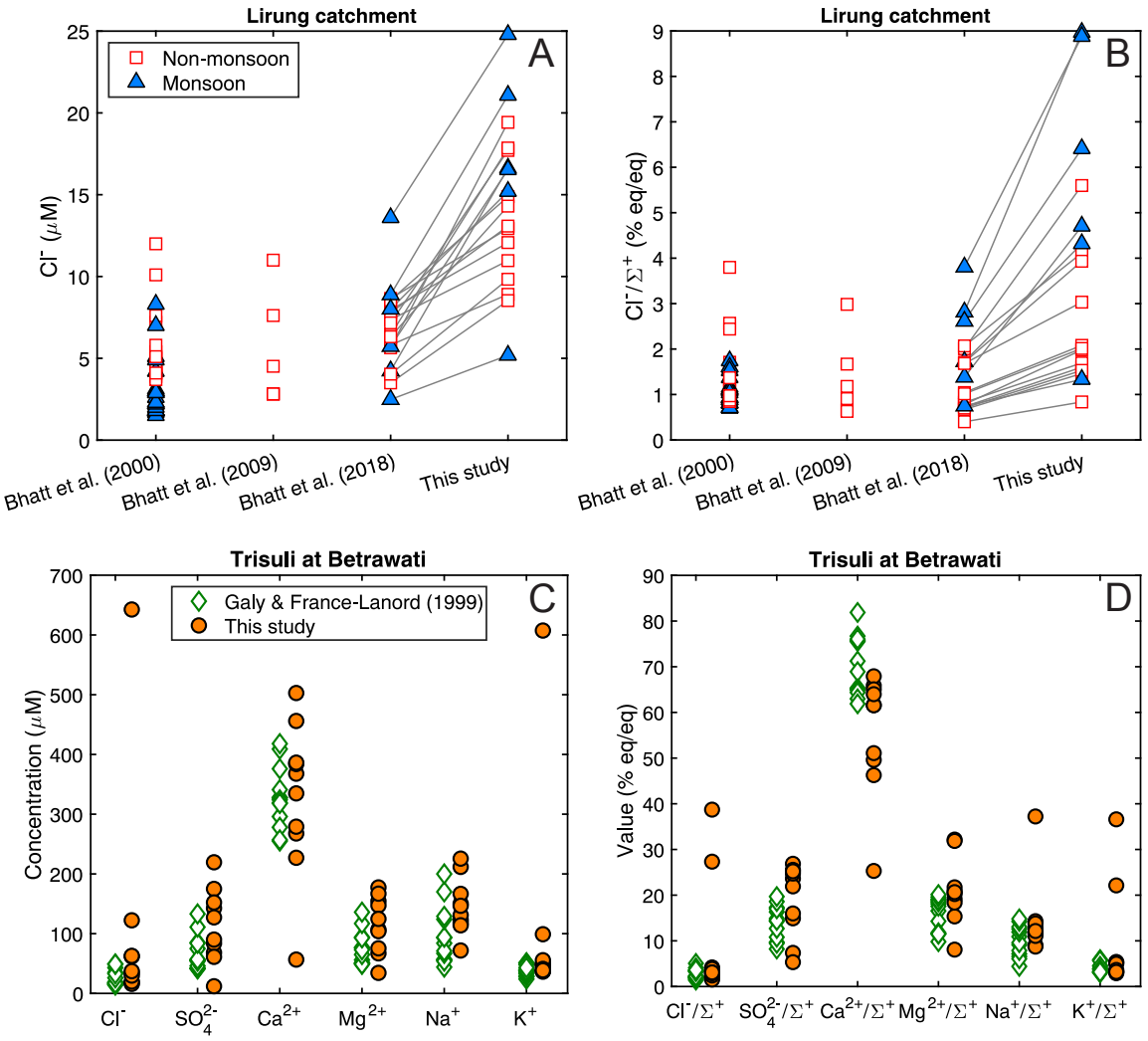

Fig. IV-S3: $[Cl^-]$ and Cl^-/Σ^+ in samples from the Lirung Glacier catchment. (A) $[Cl^-]$ and (B) Cl^-/Σ^+ for samples reported in Bhatt et al. (2000, 2009, 2018) and in this study. Samples from Bhatt et al. (2009, 2018) and this study are those from LNS-13, LNS-14, and LNS-15. Grey lines link the measurement of Bhatt et al. (2018) to the measurement of the same sample in this study. With some exceptions, these two measurements are on liquid taken from the same original sample bottle. (C) $[Cl^-]$, $[SO_4^{2-}]$, $[Ca^{2+}]$, $[Mg^{2+}]$, $[Na^+]$, and $[K^+]$ and (D) ratios relative to the sum of cations ($[Ca^{2+}] + [Mg^{2+}] + [Na^+] + [K^+]$ in units of charge equivalents) for samples from LNS-4 and from the Trisuli River sampled at Betrawati (Galy and France-Lanord, 1999). Measurements are comparable to those previously reported at Betrawati, but with several outliers to higher Cl^-/Σ^+, higher K^+/Σ^+, and lower Ca^{2+}/Σ^+.

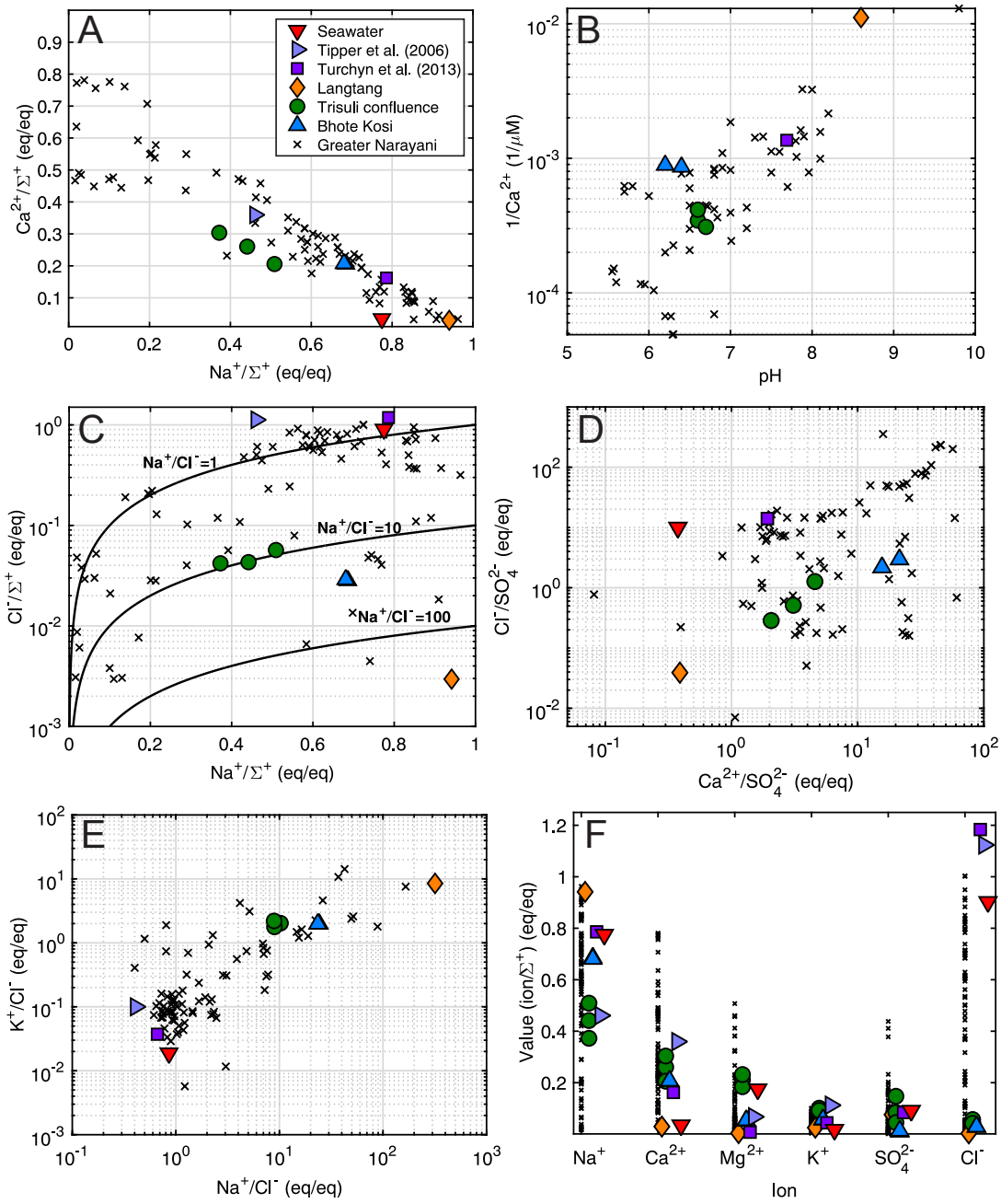

Fig. IV-S4: Dissolved chemistry of springs in the Narayani River system. (A) Ca^{2+}/Σ^{+} against Na^{+}/Σ^{+} suggests mixing between a seawater-like end-member and a low-Na^{+}/Σ^{+} end-member similar to Himalayan river water. (B) The Ca^{2+} dynamic is complicated by an apparent relationship with pH, likely resulting from calcite dissolution at low pH and calcite precipitation at high pH. (C) Cl^{-}/Σ^{+} against Na^{+}/Σ^{+} shows that most data plot near a Na^{+}/Cl^{-} of 1, consistent with seawater, but this observation may simply reflect the abundance of data from the Marsyandi River. Springs near the Langtang-Trisuli Rivers have lower Na^{+}/Cl^{-} ratios. (D) Cl^{-}/SO_4^{2-} against Ca^{2+}/SO_4^{2-} is suggestive of mixing, but at lower Cl^{-} than implied by a seawater end-member. (E) K^{+}/Cl^{-} and Na^{+}/Cl^{-} again show evidence for mixing, but in the opposite sense as Ca^{2+}/Σ^{+} against Na^{+}/Σ^{+} (compare relative position of seawater and the Langtang spring). (F) Summary of data on spring chemistry.

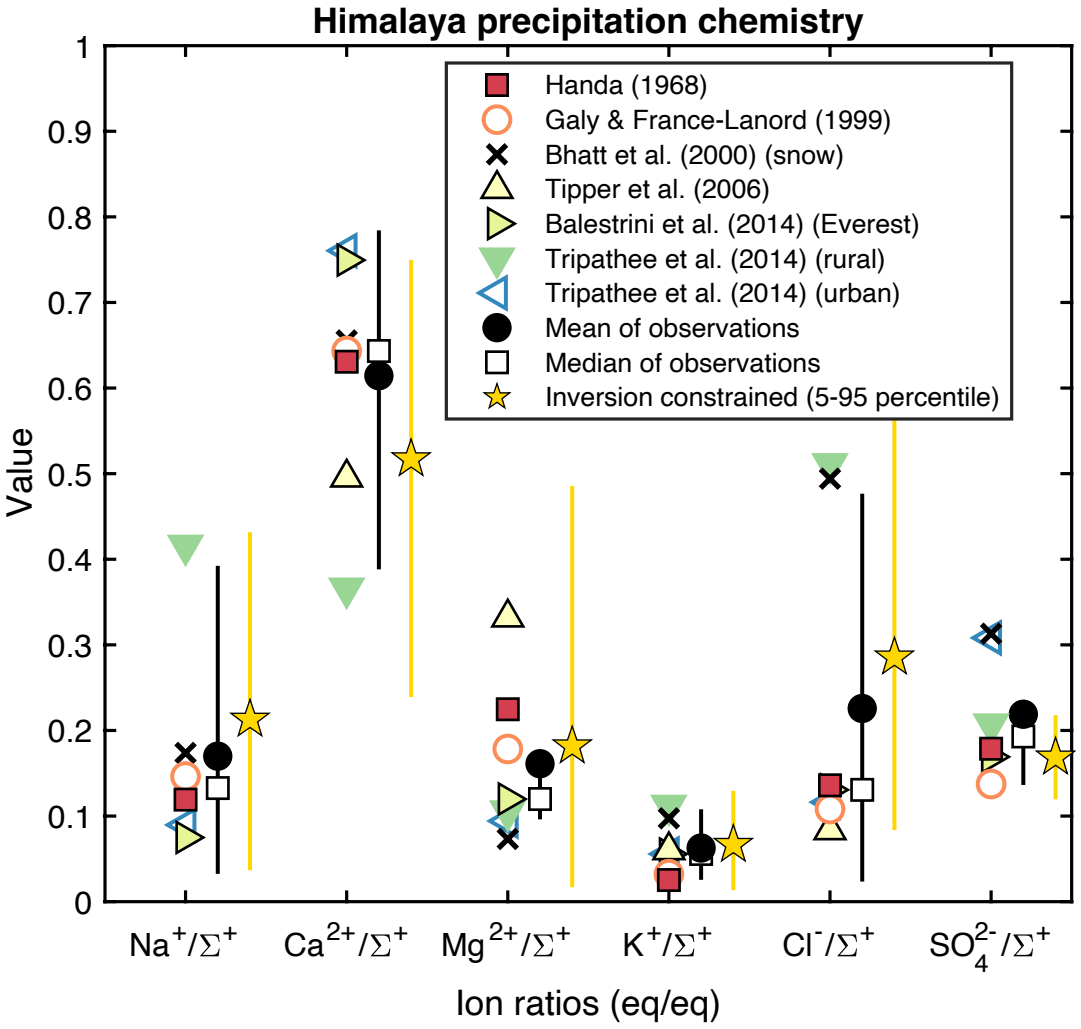

Fig. IV-S5: Major ions chemistry normalized to the sum of cations ($[Ca^{2+}]$ + $[Mg^{2+}]$ + $[Na^{+}]$ + $[K^{+}]$ in units of charge equivalents) in Himalayan precipitation. Precipitation tends to be enriched in Ca^{2+} and depleted in Cl^{-} relative to seawater. The mean (black circles) and median (white squares) of observations are shown, as is the inversion-constrained range of precipitation chemistry (yellow star and line). Data are from Handa (1968), Galy and France-Lanord (1999), Bhatt et al. (2000), Tipper et al. (2006), Balestrini et al. (2014), and Tripathee et al. (2014).

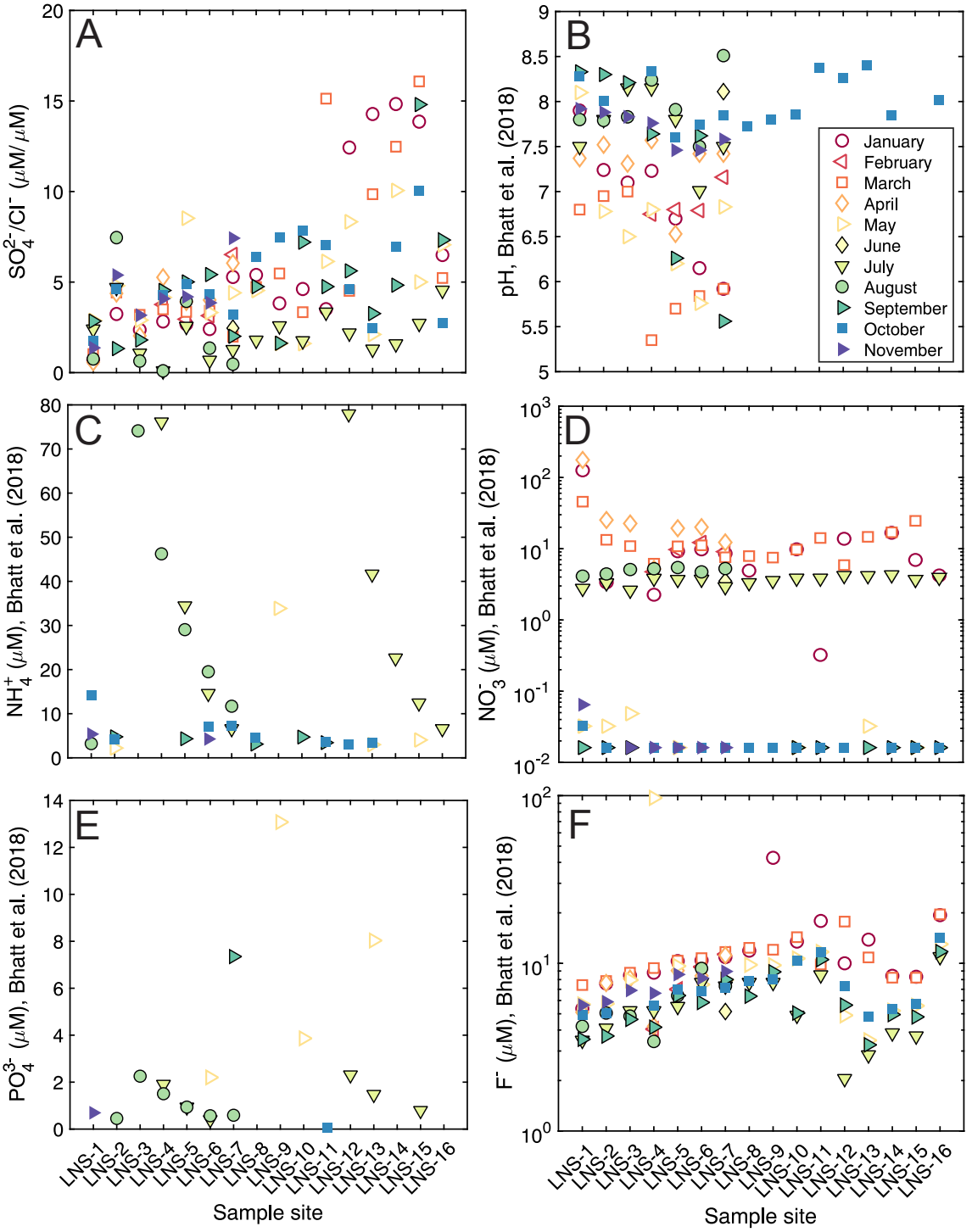

Fig. IV-S6: Chemical indicators of anthropogenic pollution. (A) SO_4^{2-}/Cl^- measurements (Caltech dataset) decline moving downstream. (B) pH of water samples, as reported in Bhatt et al. (2018). The lowest pH values tend to occur during the pre-monsoon season but may p artly reflect a sampling bias. (C) NH_4^+, (D) NO_3^-, (E) PO_4^{3-}, (F) F^- measurements (data from Bhatt et al. (2018)), are not clearly related with proximity to Kathmandu. Seasonal signals in (C)-(F) may reflect measurement artifacts (IV.12.1).

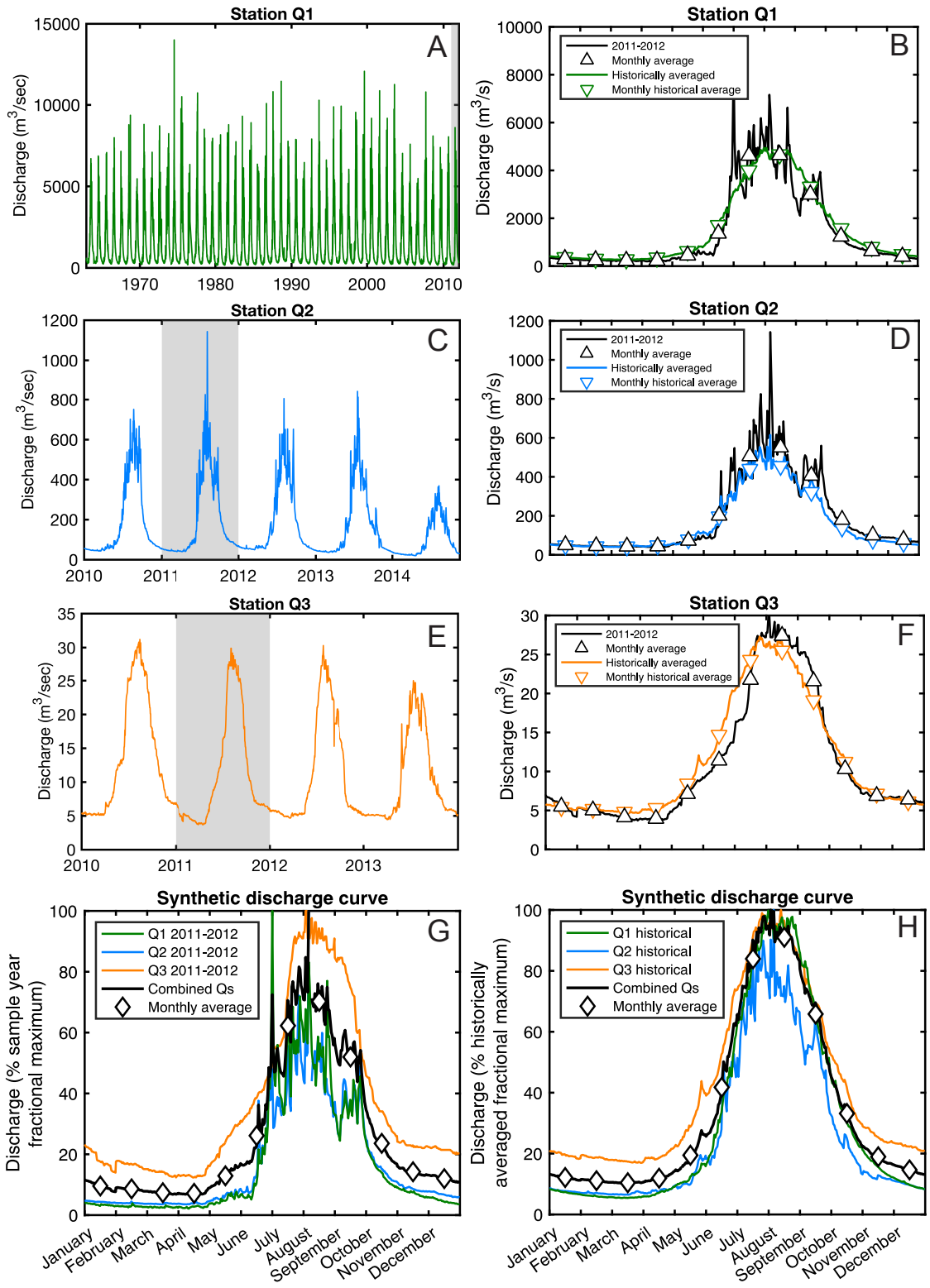

Fig. IV-S7: Derivation of the fractional discharge curve used for sample regression. (A, C, E) Data from the three gauging stations: Q1, Q2, and Q3 (Fig. IV-1). (B, D, F) 2011 data, historical average, and monthly averages. (G) The derived fractional discharge curves for 2011 data or (H) for all historical data.

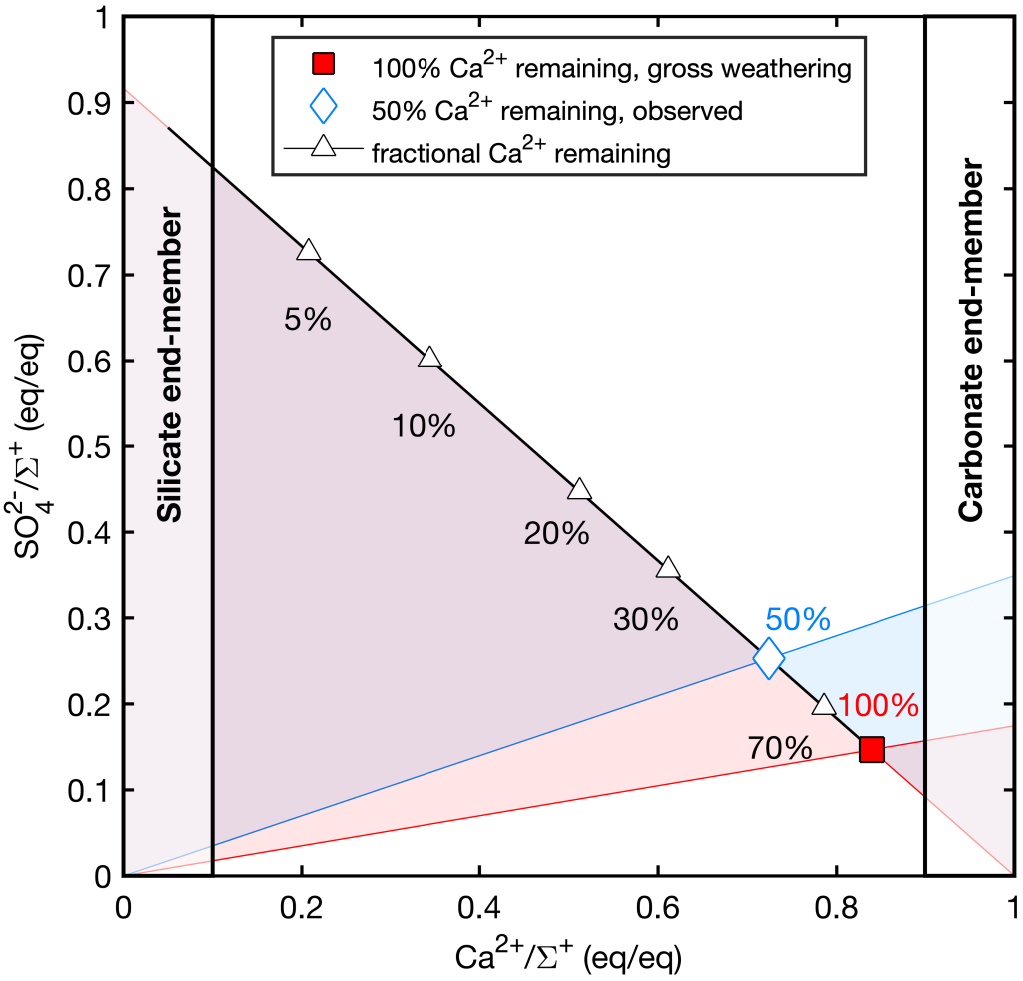

Fig. IV-S8: Impact of secondary carbonate precipitation on dissolved chemistry. Labeled percentages are the fraction of $[Ca^{2+}]$ remaining in solution. This calculation uses approximations to the median observations from this study ($[Na^+]_{median}+[K^+]_{median}+[Mg^{2+}]_{median} \sim 240$ eq., $[SO_4^{2-}]_{median} \sim 220$ eq.), and assumes 50% of Ca^{2+} was removed as $CaCO_3$ prior to our observation ($[Ca^{2+}]_{median} \sim 630$ eq.).

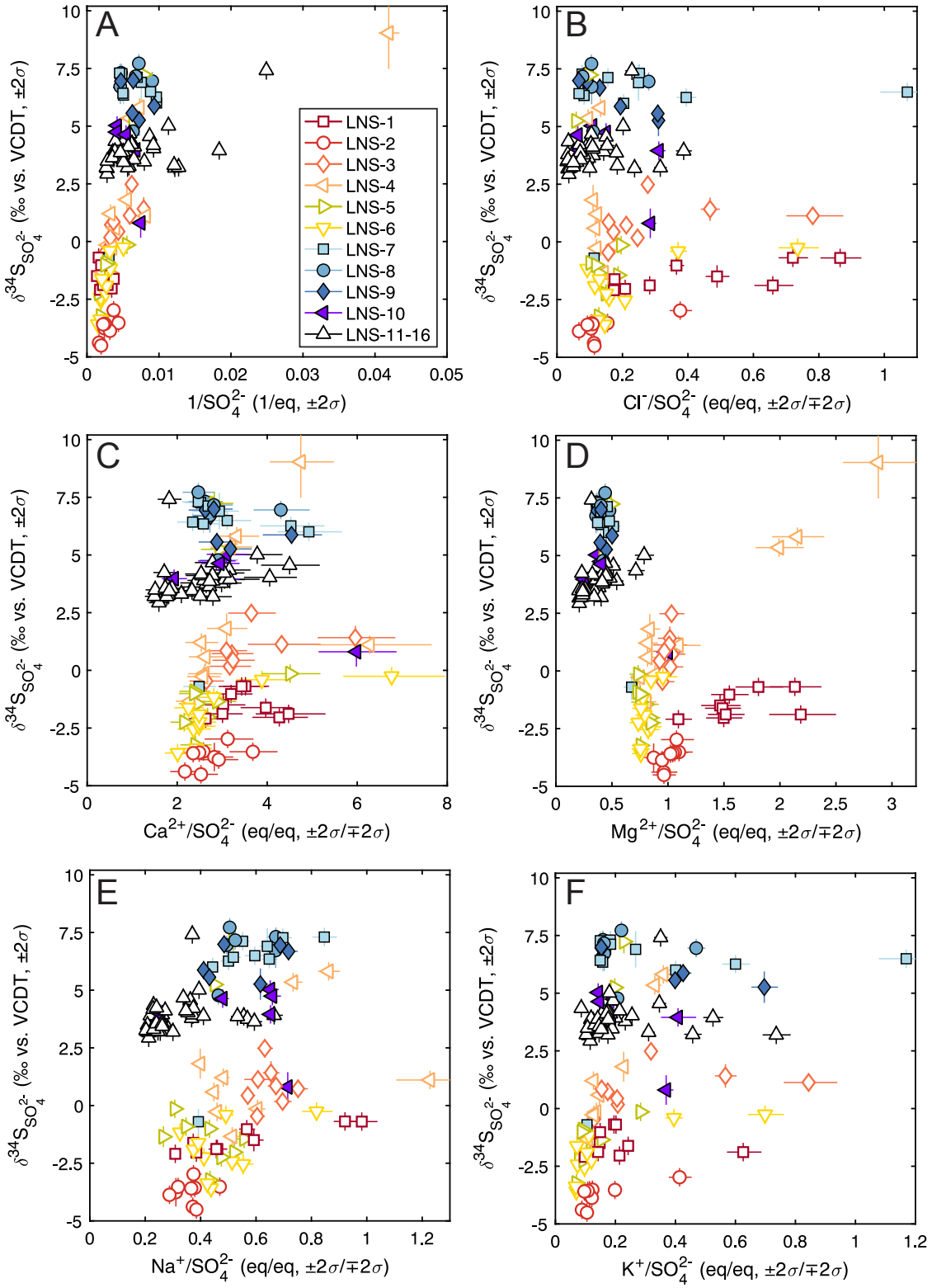

Fig. IV-S9: Sulfur isotope mixing diagrams. Measured $\delta^{34}S_{SO4}$ against (A) $1/SO_4^{2-}$, (B) Cl^-/SO_4^{2-}, (C) Ca^{2+}/SO_4^{2-}, (D) Mg^{2+}/SO_4^{2-}, (E) Na^+/SO_4^{2-}, and (F) K^+/SO_4^{2-}. The lack of coherent relationships argues against simple two end-member mixing as an explanation for observed $\delta^{34}S_{SO4}$ variability.

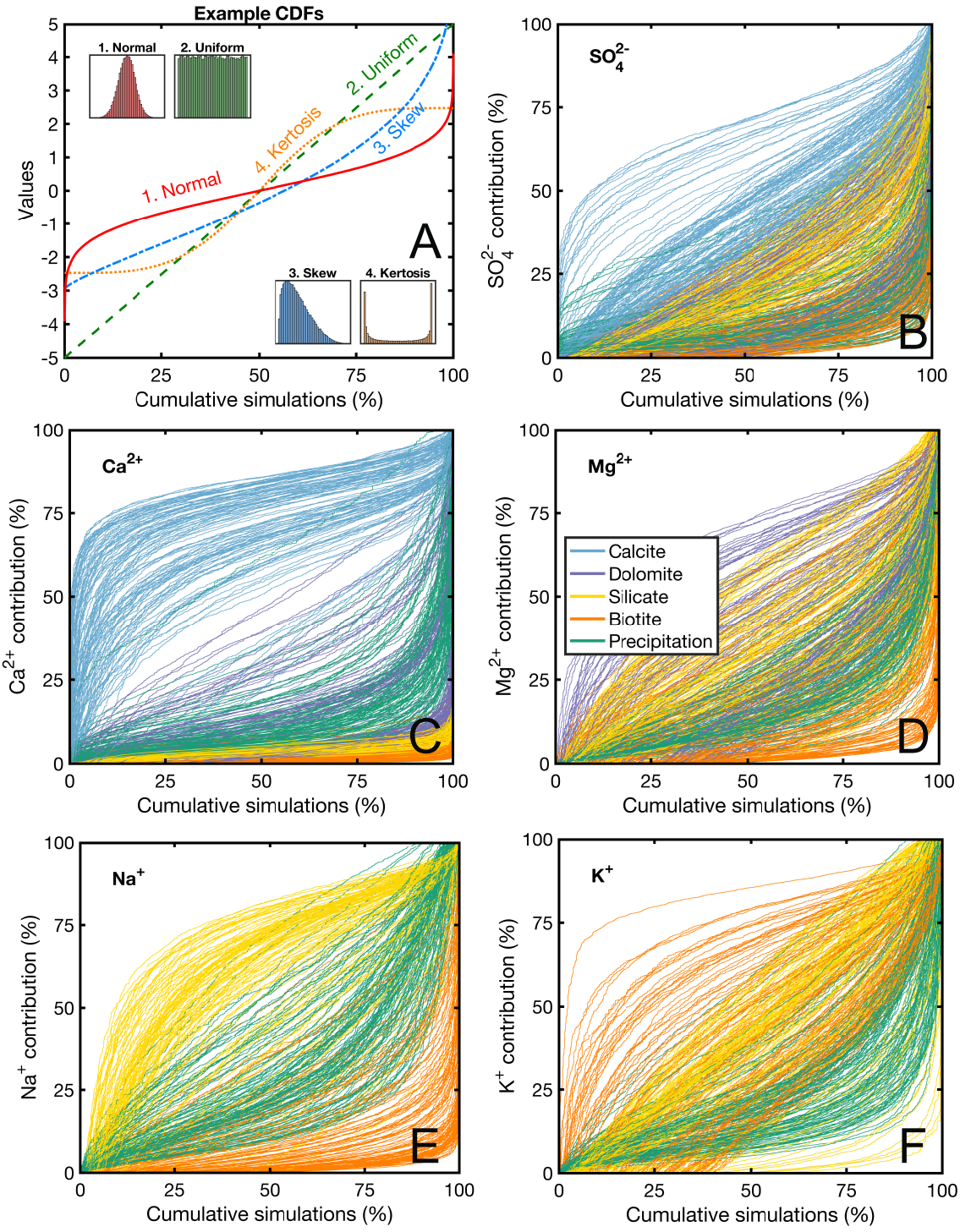

Fig. IV-S10: Cumulative distributions of inversion-constrained end-member contributions. (A) Example cumulative distribution functions for common distributions (inset panels). Cumulative distribution functions for the fractional contributions of (B) SO_4^{2-} (C) Ca^{2+}, (D) Mg^{2+}, (E) Na^+, and (F) K^+ for the primary inversion model described in the main text.

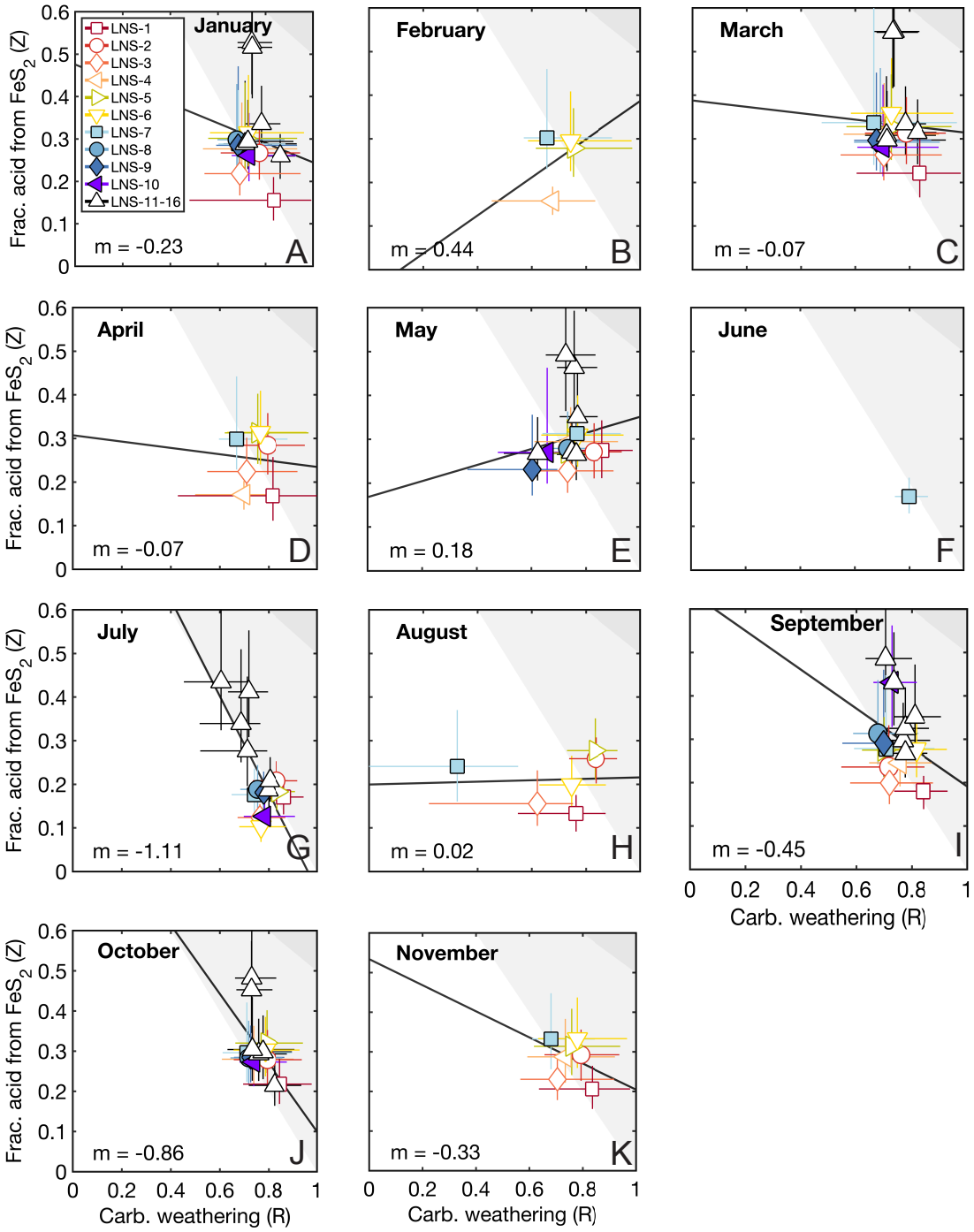

Fig. IV-S11: Regressions by month of the fraction of weathering done by sulfuric acid (Z) against the fraction of carbonate weathering (R) yields both positive and negative slopes.

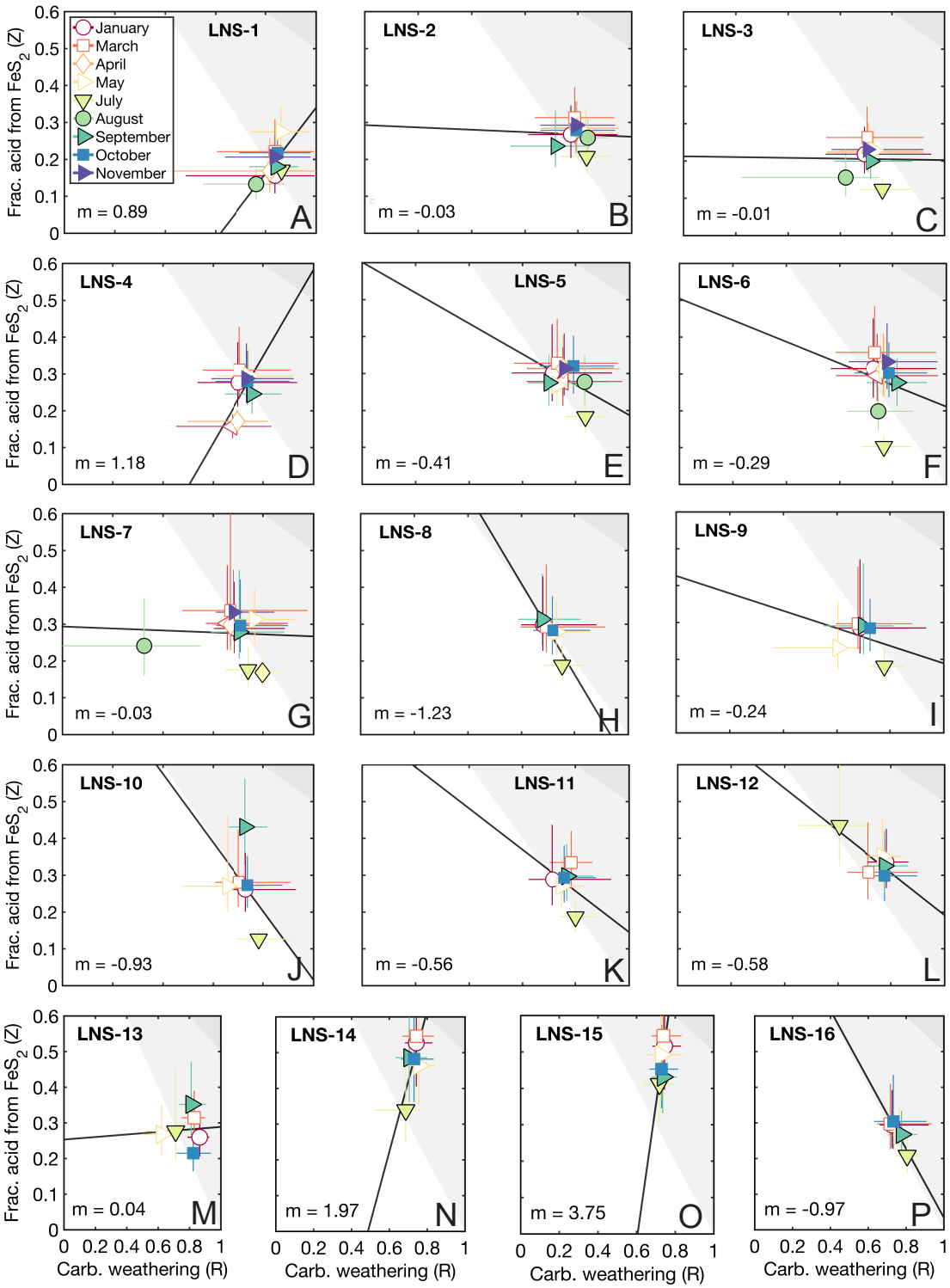

Fig. IV-S12: Regressions by site of the fraction of weathering done by sulfuric acid (Z) against the fraction of carbonate weathering (R) yields both positive and negative slopes.

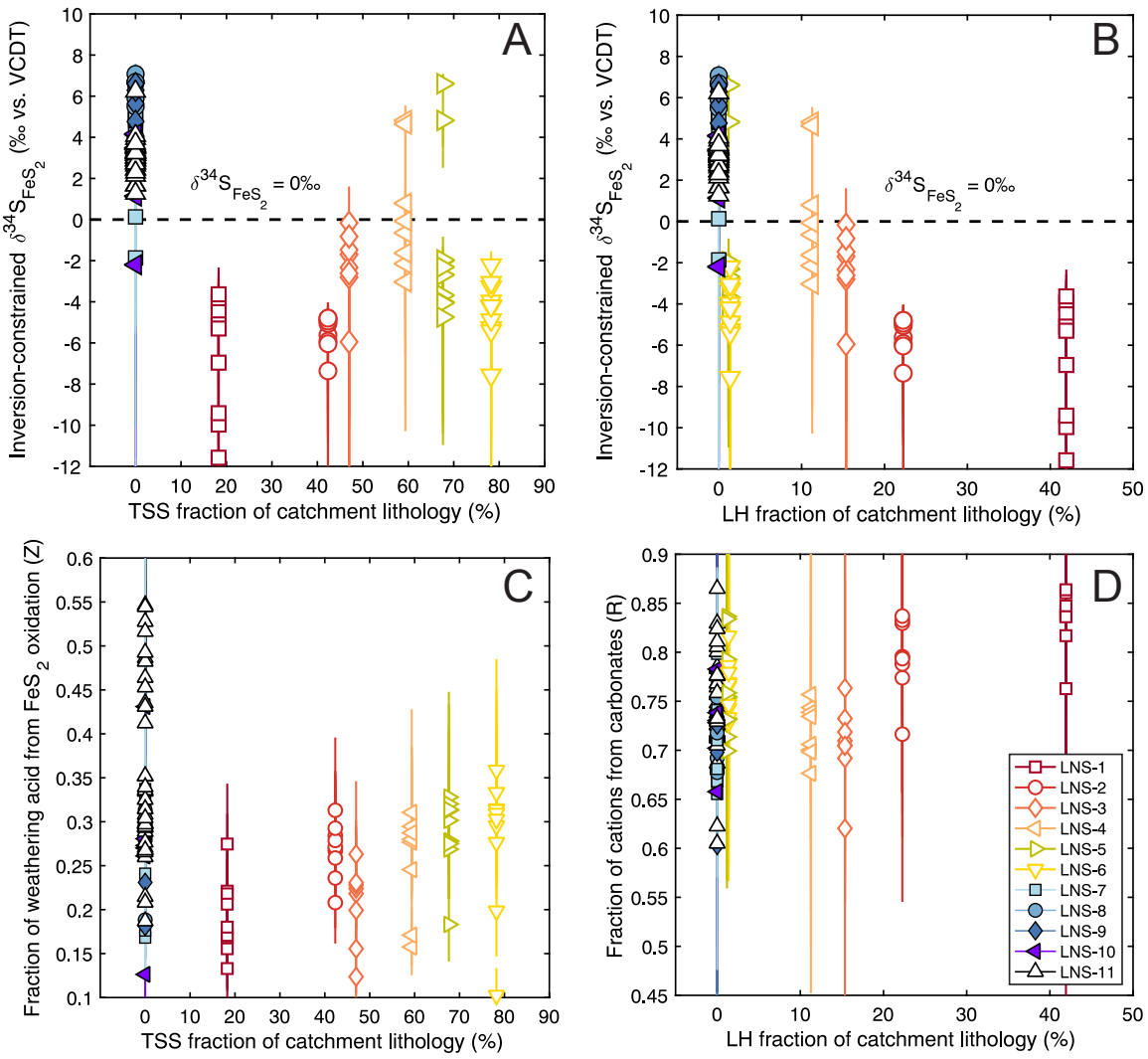

Fig. IV-S13: Inversion-constrained $\delta^{34}S_{FeS2}$ against the fractional exposure of the (A) Tethyn Sedimentary Series (TSS) and (B) Lesser Himalayan (LH) formations within each sample catchment. (C) Fraction of weathering acid sourced from FeS_2 oxidation (Z) against the fractional exposure of TSS in each catchment. (D) Fraction of cations sourced from carbonate weathering (R) against the fractional exposure of LH in each catchment. For all panels, error bars range from the 5th to 95th percentiles of accepted simulation results.

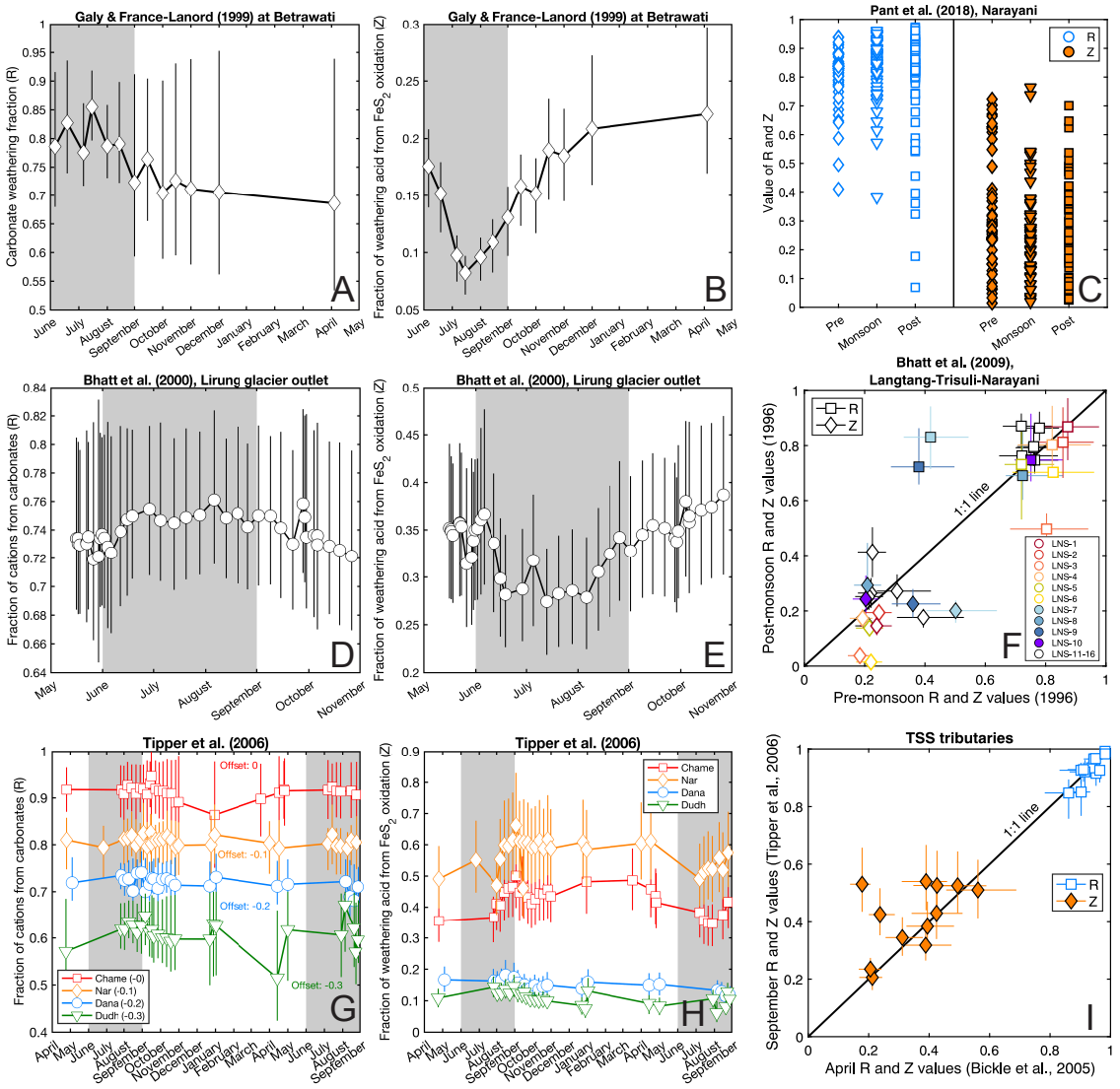

Fig. IV-S14: Seasonality of R and Z in prior data from the Narayani River catchment. (A) R and (B) Z in the Trisuli River at Betrawati (Galy and France-Lanord, 1999). R is higher and Z lower during the monsoon than during the non-monsoon season. (C) R and Z are similar during the pre-monsoon, monsoon, and post-monsoon season in Narayani samples (Pant et al., 2018). (D) R and (E) Z in meltwater from the Lirung Glacier (Bhatt et al., 2000). Seasonal change in R is present, although muted relative to the Trisuli River, and is clear in Z. (F) R and Z of pre-monsoon and post-monsoon samples from the same 16 sites in this study (Fig. IV-1), collected in 1996 (Bhatt et al., 2009). Neither R nor Z is systematically higher in either season. (G) R and (H) Z values at four sites in the Marsyandi (Tipper et al., 2006). The Chame and Nar show lower monsoon values of Z, while seasonality in R is not recovered clearly. This result contrasts with that reached when considering $Si(OH)_4/Ca^{2+}$ and $^{87}Sr/^{86}Sr$ ratios. (I) R and Z in Marsyandi samples collected in April/May (Bickle et al., 2005) and September (Tipper et al., 2006) from tributaries draining the TSS. Neither R nor Z is systematically enriched in either month. In all panels grey shading indicates monsoon season.

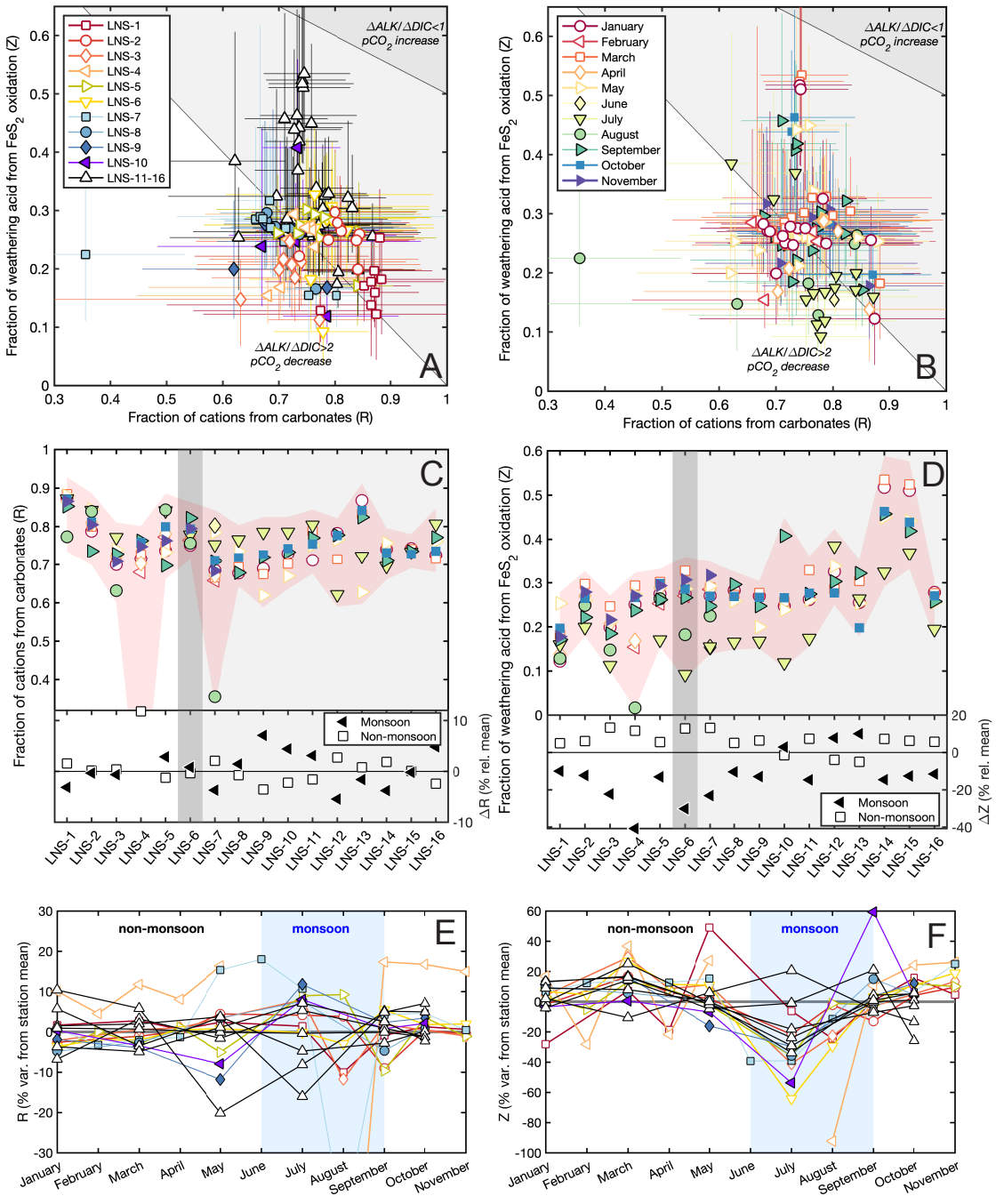

Fig. IV-S15: Fraction of weathering acid from FeS_2 oxidation (Z) against the fraction of cations from carbonate weathering (R) when the inversion includes an evaporite, color-coded by either (A) site of sample collection or (B) month of sample collection. (C, D) R and Z against sample location. (E, F) Timeseries of R and Z.

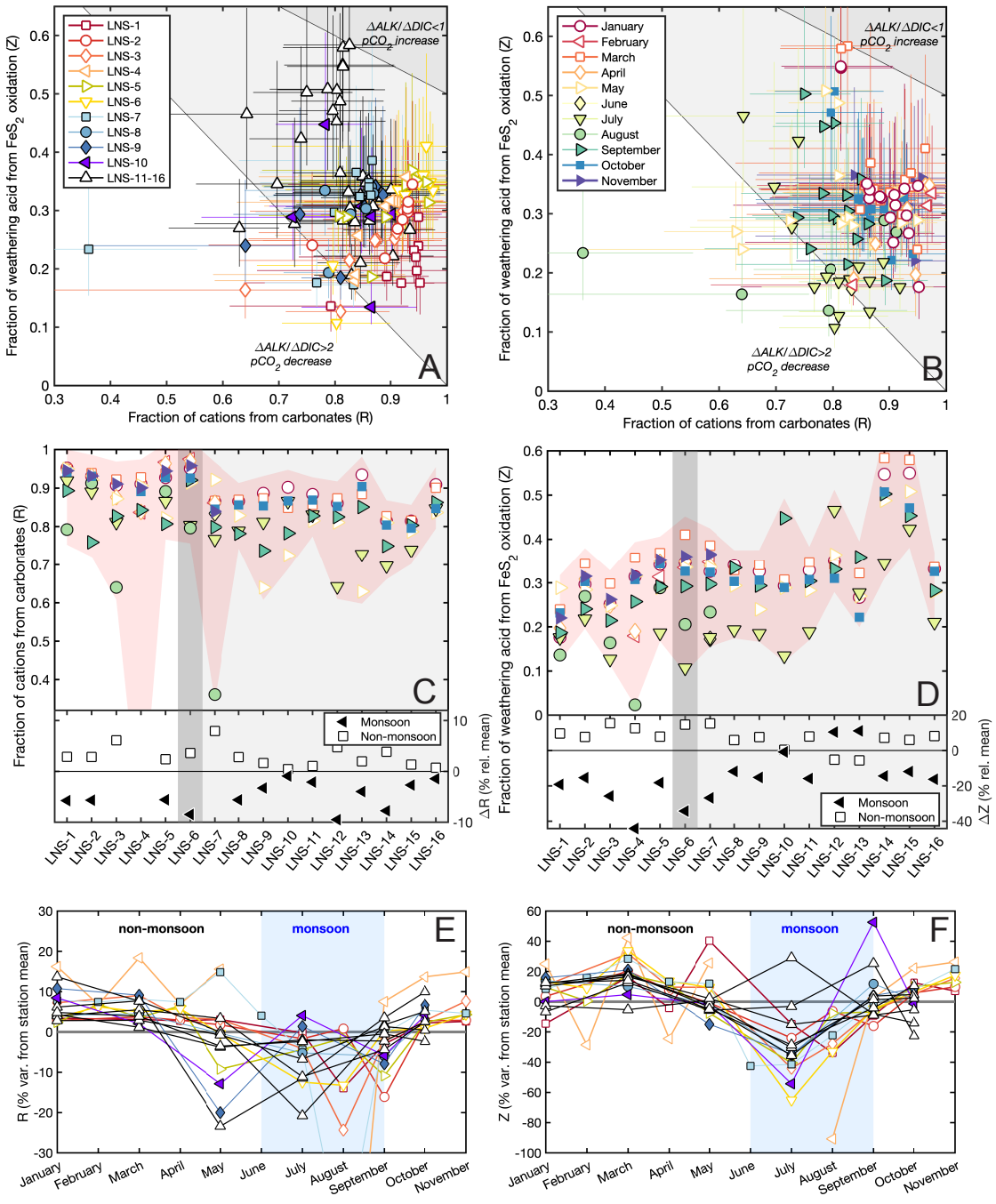

Fig. IV-S16: Fraction of weathering acid from FeS_2 oxidation (Z) against the fraction of cations from carbonate weathering (R) when the inversion includes a hot spring, color-coded by either (A) site of sample collection or (B) month of sample collection. (C, D) R and Z against sample location. (E, F) Timeseries of R and Z.

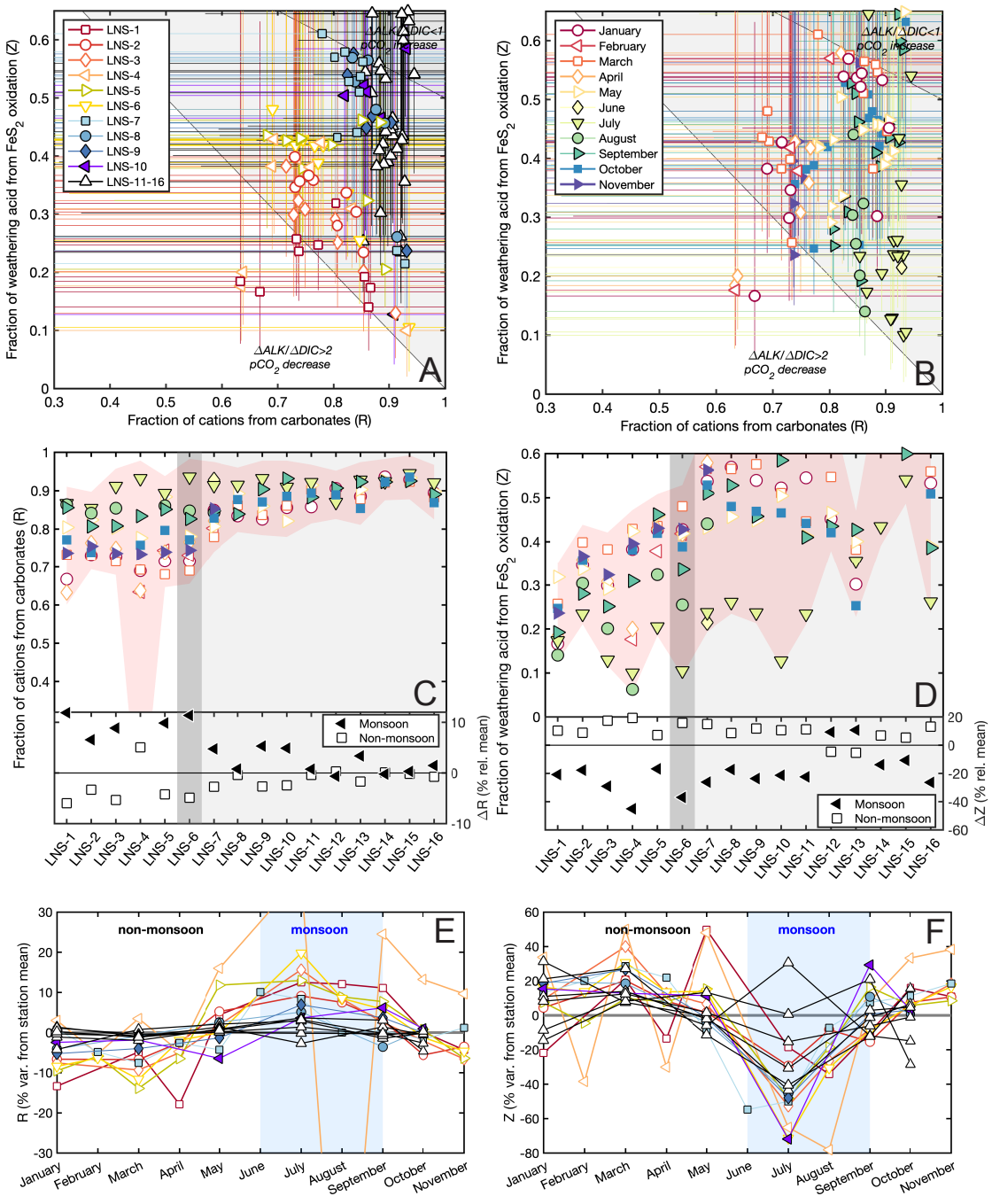

Fig. IV-S17: Fraction of weathering acid from FeS_2 oxidation (Z) against the fraction of cations from carbonate weathering (R) when the inversion does not include K^+ or Cl^-, color-coded by either (A) site of sample collection or (B) month of sample collection. Note the extreme range of successful simulation results. (C, D) R and Z against sample location. (E, F) Timeseries of R and Z. These results show a monsoon increase in R consistent with prior studies (Tipper et al., 2006).

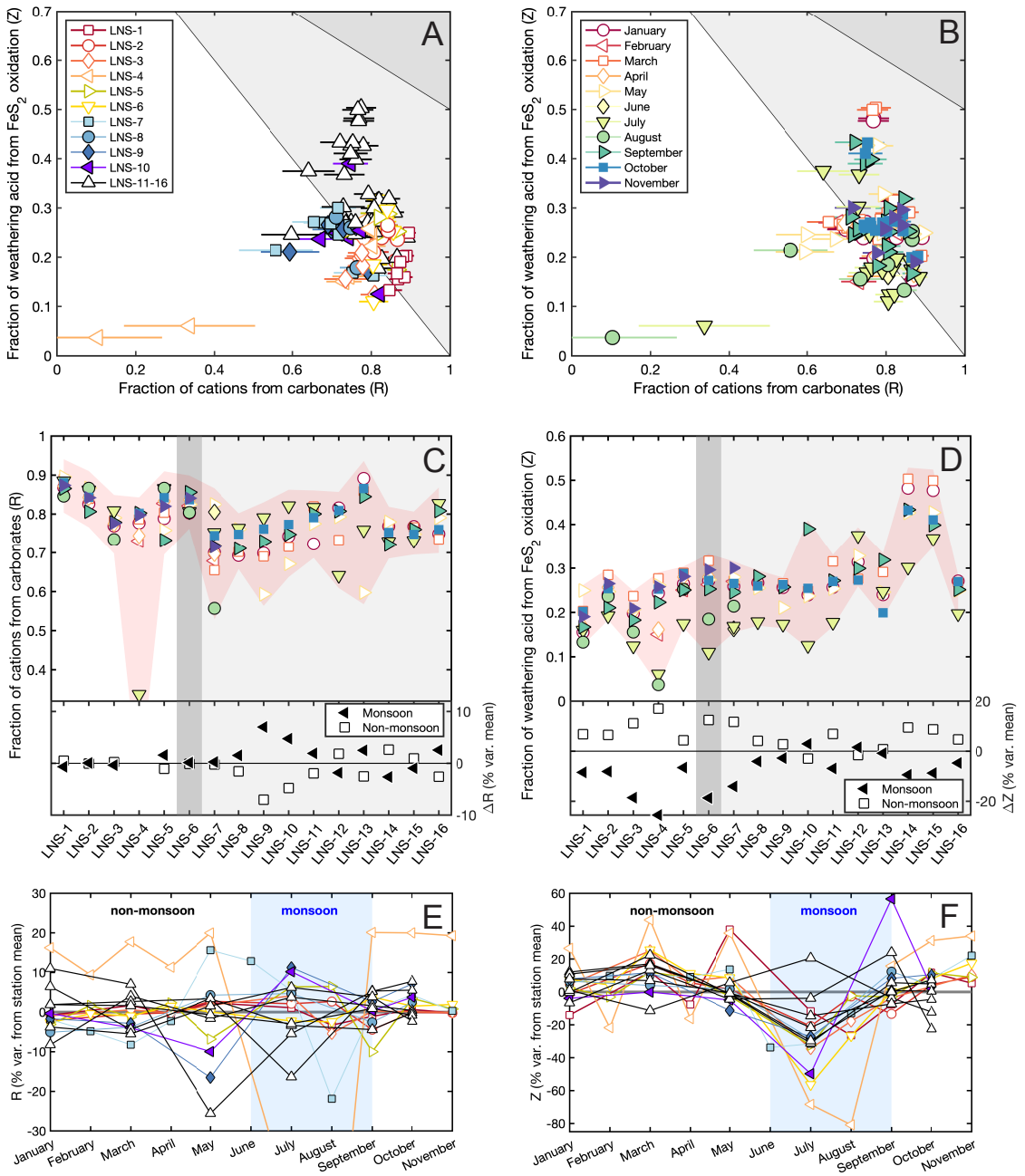

Fig. IV-S18: Fraction of weathering acid from FeS_2 oxidation (Z) against the fraction of cations from carbonate weathering (R) calculated using a forward model, color-coded by either (A) site of sample collection or (B) month of sample collection. (C) R against sample location and (D) Z against sampling location. (E, F) Timeseries of R and Z. Results are very similar to those reached using the full inversion model discussed in the text (Fig. IV-9).

IV.14: Supplementary tables

Table IV-S1: Precision of Caltech IC measurements (2σ, relative standard deviation). For MAURI-09 and CRANBERRY-05 the value n in parentheses refers to the number of unique determinations, while for samples the value n in parentheses refers to the number of samples measured twice or more. Precision is given in the top section of the table for all determinations of major ion concentrations, including references and samples with added HNO_3, and in the bottom section for determinations of major ion chemistry in only un-acidified standard and references.

	Ion	MAURI-09 2σ, RSD	CRANBERRY-05 2σ, RSD	SAMPLES, mean 2σ RSD
Solutions with or without addition of HNO_3^-	Ca^{2+}	11.6% (n=16)	5.2% (n=7)	3.6% (n=42)
	Mg^{2}	7.9% (n=16)	3.5% (n=7)	3.7% (n=41)
	Na^{+}	1.6% (n=16)	-	1.1% (n=41)
	K^{+}	3.4% (n=16)	2.8% (n=7)	1.4% (n=42)
	Cl^{-}	2.8% (n=73)	-	2.8% (n=44)
	SO_4^{2-}	2.7% (n=73)	2.8% (n=15)	2.5% (n=54)
Solutions without addition of HNO_3^-	Ca^{2+}	6.8% (n=14)	2.4% (n=5)	2.2% (n=26)
	Mg^{2}	4.8% (n=14)	2.1% (n=5)	2.3% (n=25)
	Na^{+}	1.6% (n=14)	-	1.2% (n=25)
	K^{+}	2.7% (n=14)	2.3% (n=5)	1.0% (n=26)

IV.15: Supplementary references

Andermann, C., Bonnet, S. and Gloaguen, R., 2011. Evaluation of precipitation data sets along the Himalayan front. *Geochemistry, Geophysics, Geosystems*, 12(7). https://doi.org/10.1029/2011GC003513.

Anderson, S.P., Drever, J.I. and Humphrey, N.F., 1997. Chemical weathering in glacial environments. *Geology*, 25(5), pp.399-402. https://doi.org/10.1130/0091-7613(1997)025<0399:CWIGE>2.3.CO;2.

Anderson, S.P., Drever, J.I., Frost, C.D. and Holden, P., 2000. Chemical weathering in the foreland of a retreating glacier. *Geochimica et Cosmochimica Acta*, 64(7), pp.1173-1189. https://doi.org/10.1016/S0016-7037(99)00358-0.

Balestrini, R., Polesello, S. and Sacchi, E., 2014. Chemistry and isotopic composition of precipitation and surface waters in Khumbu valley (Nepal Himalaya): N dynamics of high elevation basins. *Science of the Total Environment*, 485, pp.681-692. https://doi.org/10.1016/j.scitotenv.2014.03.096.

Becker, J.A., Bickle, M.J., Galy, A. and Holland, T.J., 2008. Himalayan metamorphic CO_2 fluxes: Quantitative constraints from hydrothermal springs. *Earth and Planetary Science Letters*, 265(3-4), pp.616-629. https://doi.org/10.1016/j.epsl.2007.10.046.

Berner, R.A., 1971. Worldwide sulfur pollution of rivers. *Journal of Geophysical Research*, 76(27), pp.6597-6600. https://doi.org/10.1029/JC076i027p06597.

Bhatt, M.P., Masuzawa, T., Yamamoto, M., Sakai, A. and Fujita, K., 2000. Seasonal changes in dissolved chemical composition and flux of meltwater draining from Lirung Glacier in the Nepal Himalayas. *IAHS Publication*, pp.277-288.

Bhatt, M.P., Masuzawa, T., Yamamoto, M. and Gardner, K.H., 2009. Spatial variations in chemical compositions along Langtang–Narayani river system in central Nepal. *Environmental Geology*, 57(3), pp.557-569. https://doi.org/10.1007/s00254-008-1325-x.

Bhatt, M.P., Hartmann, J. and Acevedo, M.F., 2018. Seasonal variations of biogeochemical matter export along the Langtang-Narayani river system in central Himalaya. *Geochimica et Cosmochimica Acta*, 238, pp.208-234. https://doi.org/10.1016/j.gca.2018.06.033.

Bickle, M.J., Chapman, H.J., Bunbury, J., Harris, N.B., Fairchild, I.J., Ahmad, T. and Pomiès, C., 2005. Relative contributions of silicate and carbonate rocks to riverine Sr fluxes in the headwaters of the Ganges. *Geochimica et Cosmochimica Acta*, 69(9), pp.2221-2240. https://doi.org/10.1016/j.gca.2004.11.019.

Bickle, M.J., Tipper, E.D., Galy, A., Chapman, H. and Harris, N., 2015. On discrimination between carbonate and silicate inputs to Himalayan rivers. *American Journal of Science*, 315(2), pp.120-166. https://doi.org/10.2475/02.2015.02.

Bordet, P., Colchen, M., Krummenacher, D., Le Fort, P., Mouterde, R. and Remy, M., 1971. Recherches géologiques dans l'Himalaya du Népal, région de la Thakkhola. Centre National de la Recherche Scientifique, Paris, p. 279.

Burke, A., Present, T.M., Paris, G., Rae, E.C., Sandilands, B.H., Gaillardet, J., Peucker-Ehrenbrink, B., Fischer, W.W., McClelland, J.W., Spencer, R.G. and Voss, B.M., 2018. Sulfur isotopes in rivers: Insights into global weathering budgets, pyrite oxidation, and the modern sulfur cycle. *Earth and Planetary Science Letters*, 496, pp.168-177. https://doi.org/10.1016/j.epsl.2018.05.022.

Claypool, G.E., Holser, W.T., Kaplan, I.R., Sakai, H. and Zak, I., 1980. The age curves of sulfur and oxygen isotopes in marine sulfate and their mutual interpretation. *Chemical Geology*, 28, pp.199-260. https://doi.org/10.1016/0009-2541(80)90047-9.

Collins, R. and Jenkins, A., 1996. The impact of agricultural land use on stream chemistry in the middle hills of the Himalayas, Nepal. *Journal of Hydrology*, 185(1-4), pp.71-86. https://doi.org/10.1016/0022-1694(95)03008-5.

Dalai, T.K., Krishnaswami, S. and Sarin, M.M., 2002. Major ion chemistry in the headwaters of the Yamuna river system: Chemical weathering, its temperature dependence and CO_2 consumption in the Himalaya. *Geochimica et Cosmochimica Acta*, 66(19), pp.3397-3416. https://doi.org/10.1016/S0016-7037(02)00937-7.

Emberson, R., Galy, A. and Hovius, N., 2017. Combined effect of carbonate and biotite dissolution in landslides biases silicate weathering proxies. *Geochimica et Cosmochimica Acta*, 213, pp.418-434. https://doi.org/10.1016/j.gca.2017.07.014.

Evans, M.J., Derry, L.A., Anderson, S.P. and France-Lanord, C., 2001. Hydrothermal source of radiogenic Sr to Himalayan rivers. *Geology*, 29(9), pp.803-806. https://doi.org/10.1130/0091-7613(2001)029<0803:HSORST>2.0.CO;2.

Evans, M.J., Derry, L.A. and France-Lanord, C., 2004. Geothermal fluxes of alkalinity in the Narayani river system of central Nepal. *Geochemistry, Geophysics, Geosystems*, 5(8). https://doi.org/10.1029/2004GC000719.

Evans, M.J., Derry, L.A. and France-Lanord, C., 2008. Degassing of metamorphic carbon dioxide from the Nepal Himalaya. *Geochemistry, Geophysics, Geosystems*, 9(4). https://doi.org/10.1029/2007GC001796.

Fort, M., 1996. Late Cenozoic environmental changes and uplift on the northern side of the central Himalaya: A reappraisal from field data. *Palaeogeography, Palaeoclimatology, Palaeoecology*, 120(1-2), pp.123-145. https://doi.org/10.1016/0031-0182(94)00038-7.

France-Lanord, C. and Derry, L.A., 1997. Organic carbon burial forcing of the carbon cycle from Himalayan erosion. *Nature*, 390(6655), pp.65-67. https://doi.org/10.1038/36324.

Gaillardet, J., Dupré, B., Louvat, P. and Allegre, C.J., 1999. Global silicate weathering and CO_2 consumption rates deduced from the chemistry of large rivers. *Chemical Geology*, 159(1-4), pp.3-30. https://doi.org/10.1016/S0009-2541(99)00031-5.

Galy, A. and France-Lanord, C., 1999. Weathering processes in the Ganges–Brahmaputra basin and the riverine alkalinity budget. *Chemical Geology*, 159(1-4), pp.31-60. https://doi.org/10.1016/S0009-2541(99)00033-9.

Handa B.K. 1968. The chemical composition of rain water in some parts of North India. *Indian Journal of Meteorology & Geophysics,* 19, 175-180.

Harris, N., Bickle, M., Chapman, H., Fairchild, I. and Bunbury, J., 1998. The significance of Himalayan rivers for silicate weathering rates: Evidence from the Bhote Kosi tributary. *Chemical Geology*, 144(3-4), pp.205-220. https://doi.org/10.1016/S0009-2541(97)00132-0.

Hren, M.T., Chamberlain, C.P., Hilley, G.E., Blisniuk, P.M. and Bookhagen, B., 2007. Major ion chemistry of the Yarlung Tsangpo–Brahmaputra river: Chemical weathering, erosion, and CO_2 consumption in the southern Tibetan plateau and eastern syntaxis of the Himalaya. *Geochimica et Cosmochimica Acta*, 71(12), pp.2907-2935. https://doi.org/10.1016/j.gca.2007.03.021.

Jacobson, A.D., Blum, J.D. and Walter, L.M., 2002. Reconciling the elemental and Sr isotope composition of Himalayan weathering fluxes: Insights from the carbonate geochemistry of stream waters. *Geochimica et Cosmochimica Acta*, 66(19), pp.3417-3429. https://doi.org/10.1016/S0016-7037(02)00951-1.

Krishnaswami, S. and Singh, S.K., 1998. Silicate and carbonate weathering in the drainage basins of the Ganga-Ghaghara-Indus head waters: Contributions to major ion and Sr isotope geochemistry. *Proceedings of the Indian Academy of Sciences-Earth and Planetary Sciences*, 107(4), pp.283-291.

Krishnaswami S., Singh S. K., and Dalai T. K. 1999. Silicate weathering in the Himalaya: Role in contributing to major ions and radiogenic Sr to the Bay of Bengal. In *Ocean Science, Trends and Future Directions* (pp. 23–51), ed. B. L. K. Somayajulu. India.

Négrel, P., Allègre, C.J., Dupré, B. and Lewin, E., 1993. Erosion sources determined by inversion of major and trace element ratios and strontium isotopic ratios in river water: The Congo Basin case. *Earth and Planetary Science Letters*, 120(1-2), pp.59-76. https://doi.org/10.1016/0012-821X(93)90023-3.

Pant, R.R., Zhang, F., Rehman, F.U., Wang, G., Ye, M., Zeng, C. and Tang, H., 2018. Spatiotemporal variations of hydrogeochemistry and its controlling factors in the Gandaki River Basin, Central Himalaya Nepal. *Science of the Total Environment*, 622, pp.770-782. https://doi.org/10.1016/j.scitotenv.2017.12.063.

Panthi, J., Dahal, P., Shrestha, M.L., Aryal, S., Krakauer, N.Y., Pradhanang, S.M., Lakhankar, T., Jha, A.K., Sharma, M. and Karki, R., 2015. Spatial and temporal variability of rainfall in the Gandaki River Basin of Nepal Himalaya. *Climate*, 3(1), pp.210-226. https://doi.org/10.3390/cli3010210.

Quade, J., English, N. and DeCelles, P.G., 2003. Silicate versus carbonate weathering in the Himalaya: A comparison of the Arun and Seti River watersheds. *Chemical Geology*, 202(3-4), pp.275-296. https://doi.org/10.1016/j.chemgeo.2002.05.002.

Sarin, M.M. and Krishnaswami, S., 1984. Major ion chemistry of the Ganga–Brahmaputra river systems, India. *Nature*, 312(5994), pp.538-541. https://doi.org/10.1038/312538a0.

Sarin, M.M., Krishnaswami, S., Dilli, K., Somayajulu, B.L.K. and Moore, W.S., 1989. Major ion chemistry of the Ganga-Brahmaputra river system: Weathering processes and fluxes to the Bay of Bengal. *Geochimica et Cosmochimica Acta*, 53(5), pp.997-1009. https://doi.org/10.1016/0016-7037(89)90205-6.

Sarmiento J. L., & Gruber, N., 2006. Ocean Biogeochemical Dynamics. Princeton University Press.

Sequeira, R. and Kelkar, D., 1978. Geochemical implications of summer monsoonal rainwater composition over India. *Journal of Applied Meteorology* (1962-1982), pp.1390-1396. https://www.jstor.org/stable/26178852.

Shrestha, A.B., Wake, C.P., Dibb, J.E. and Whitlow, S.I., 2002. Aerosol and precipitation chemistry at a remote Himalayan site in Nepal. *Aerosol Science and Technology*, 36(4), pp.441-456. https://doi.org/10.1080/027868202753571269.

Singh, S.P. and Singh, B.P., 2010. Geothermal evolution of the evaporite-bearing sequences of the Lesser Himalaya, India. *International Journal of Earth Sciences*, 99(1), pp.101-108. https://doi.org/10.1007/s00531-008-0361-9.

Tipper, E.T., Bickle, M.J., Galy, A., West, A.J., Pomiès, C. and Chapman, H.J., 2006. The short term climatic sensitivity of carbonate and silicate weathering fluxes: Insight from seasonal variations in river chemistry. *Geochimica et Cosmochimica Acta*, 70(11), pp.2737-2754. https://doi.org/10.1016/j.gca.2006.03.005.

Torres, M.A., Moosdorf, N., Hartmann, J., Adkins, J.F. and West, A.J., 2017. Glacial weathering, sulfide oxidation, and global carbon cycle feedbacks. *Proceedings of the National Academy of Sciences*, 114(33), pp.8716-8721. https://doi.org/10.1073/pnas.1702953114.

Tripathee, L., Kang, S., Huang, J., Sharma, C.M., Sillanpää, M., Guo, J. and Paudyal, R., 2014. Concentrations of trace elements in wet deposition over the central Himalayas, Nepal. *Atmospheric Environment*, 95, pp.231-238. https://doi.org/10.1016/j.atmosenv.2014.06.043.

Tshering, L.D. and Bhandari, A.N., 1973. Geological report on the Salt Occurrences of Mustang area. Ministry of Industry & Commerce, Nepal Geological Survey.

Turchyn, A.V., Tipper, E.T., Galy, A., Lo, J.K. and Bickle, M.J., 2013. Isotope evidence for secondary sulfide precipitation along the Marsyandi River, Nepal, Himalayas. *Earth and Planetary Science Letters*, 374, pp.36-46. https://doi.org/10.1016/j.epsl.2013.04.033.

Valdiya, K.S., 1980. Geology of Kumaun Lesser Himalaya (Dehradun: Wadia Institute of Himalayan Geology). Interim Report, 291.

West, A.J., Bickle, M.J., Collins, R. and Brasington, J., 2002. Small-catchment perspective on Himalayan weathering fluxes. *Geology*, 30(4), pp.355-358. https://doi.org/10.1130/0091-7613(2002)030<0355:SCPOHW>2.0.CO;2.

Wolff-Boenisch, D., Gabet, E.J., Burbank, D.W., Langner, H. and Putkonen, J., 2009. Spatial variations in chemical weathering and CO_2 consumption in Nepalese High Himalayan catchments during the monsoon season. *Geochimica et Cosmochimica Acta*, 73(11), pp.3148-3170. https://doi.org/10.1016/j.gca.2009.03.012.

Chapter V

Permafrost Degradation and Sulfide Oxidation in the Koyukuk River, AK

Preston Cosslett Kemeny[1], Gen Li[1], Madison Douglas[1], Jess F. Adkins[1], Austin Chadwick[1], Nathan F. Dalleska[1], Michael P. Lamb [1], Will Larsen[2], John Magyar[1], Anastasia Piliouras[3], Nick E. Rollins[4], Joel Rowland[3], Jonathan P. Schwenk[3], Mark A. Torres[2], Samuel M. Webb[5], A. Josh West[4], Woodward W. Fischer [1]

[1] Division of Geological and Planetary Sciences, California Institute of Technology, Pasadena, California, USA
[2] Department of Earth, Environmental, and Planetary Sciences, Rice University, Houston, Texas, USA
[3] Earth and Environmental Sciences Division, Los Alamos National Laboratory, Los Alamos, New Mexico, USA
[4] Department of Earth Sciences, University of Southern California, Los Angeles, California, USA
[5] Stanford Synchrotron Radiation Lightsource, SLAC National Accelerator Laboratory, Menlo Park, California, USA

Keywords: Climate change, permafrost degradation, sulfate isotopes, river inversion, Alaska

V.1: Abstract

Permafrost degradation due to anthropogenic climate change is altering biogeochemical processes throughout Arctic landscapes. In turn, these changes can feedback on atmospheric carbon dioxide (CO_2) over a range of temporal and spatial scales by altering the fluxes of dissolved inorganic carbon (DIC) and alkalinity (ALK) associated with organic matter oxidation, sulfide oxidation, and silicate or carbonate weathering. However, understanding the modern balance of these reactions remains a major knowledge gap both for predicting the response of permafrost landscapes to further warming and for interpreting evidence of changing fluvial solute fluxes. Here we report new observations of chemical weathering dynamics from the Koyukuk River in central Alaska, a relatively unstudied tributary of the Yukon River within discontinuous permafrost, based on water and sediment samples collected near the town of Huslia in summer 2018. Sulfate (SO_4^{2-}) sulfur ($^{34}S/^{32}S$) and oxygen ($^{18}O/^{16}O$) isotope ratios in mainstem river water samples indicated that approximately 2/3 of SO_4^{2-} derived from sulfide oxidation and the remainder from evaporite dissolution. The relative $^{34}S/^{32}S$ ratios, major ion abundances, DIC $^{13}C/^{12}C$ ratios, and sulfur x-ray absorption spectra of slough, pore fluid, and mainstem river water and sediment samples indicated minor amounts of assimilatory and dissimilatory sulfur reduction within the floodplain. The MEANDIR inversion model was used to quantify the relative importance of weathering processes and showed that weathering fluxes of ALK and DIC are comparable in both mainstem and slough water samples. Furthermore, comparison with historical observations indicated increases in the absolute and relative concentration of SO_4^{2-} in the Koyukuk River through time. This increase was interpreted as enhanced sulfide oxidation and may reflect changes in hydrology due to permafrost melting. Overall, this research implicates sulfide oxidation as a major component of permafrost degradation and suggests that the sulfur cycle responds to permafrost thaw through a positive feedback on warming.

V.2: Introduction

Anthropogenic climate change is driving permafrost degradation throughout Arctic landscapes (Osterkamp and Romanovsky, 1999; Jorgenson et al., 2001, 2013; Oelke et al., 2004; Schuur et al., 2008; O'Donnell et al., 2012; Biskaborn et al., 2019). Melting of frozen sediment is manifest as warming and deepening in the depth of annual thaw, called the active layer, with associated changes in the hydrology of Arctic rivers and in the supply of oxidants and acids for chemical weathering reactions (Woo, 1986; Walvoord and Striegl, 2007; Bense et al., 2009; Frey and McClelland, 2009; Walvoord et al., 2012; Walvoord and Kurylyk, 2016). Previously, the impact of permafrost degradation on climate has mostly been viewed from the perspective of organic carbon (C_{org}) oxidation, which is often considered a climate tipping point due to the large reservoir of high-latitude frozen organic matter (Striegl et al., 2005; Schuur et al., 2015). However, the impact of melting permafrost on atmospheric carbon dioxide (CO_2) depends on both the flux of both dissolved inorganic carbon (DIC) and alkalinity (ALK) (Tank et al., 2012, 2016; Toohey et al., 2016; Zolkos et al., 2018). While increases in silicate weathering secondary to permafrost degradation may offset the CO_2 flux associated with C_{org} oxidation, sulfide oxidation could act as a positive feedback on climate change (Spence and Telmer, 2005; Lerman et al., 2007).

Previously, Toohey et al. (2016) suggested an enhanced role for sulfide oxidation during permafrost degradation based on observations of increasing sulfate (SO_4^{2-}) fluxes in the Yukon River. Similarly, Zolkos et al. (2018) identified sulfide oxidation in the Mackenzie River catchment and suggested a climate feedback between warming and sulfide oxidation. These studies indicate that the sulfur cycle may have a substantial role

in the response of permafrost systems to melting and motivate additional study on sulfide oxidation within permafrost landscapes.

This work reports new geochemical observations in water and sediment samples from the Koyukuk River in central Alaska, which is a tributary to the Yukon River underlain by discontinuous permafrost (Brabets et al., 2000). We report the concentration of calcium (Ca^{2+}), magnesium (Mg^{2+}), sodium (Na^{+}), potassium (K^{+}), chloride (Cl^{-}) and sulfate (SO_4^{2-}), as well as the sulfate $^{34}S/^{32}S$ ratio ($\delta^{34}S_{SO4}$), sulfate $^{18}O/^{16}O$ ratio ($\delta^{18}O_{SO4}$), water $^{18}O/^{16}O$ ratio ($\delta^{18}O_{H2O}$), water D/H ratio (δD_{H2O}), DIC $^{13}C/^{12}C$ ratio ($\delta^{13}C_{DIC}$), dissolved organic carbon (DOC) $^{13}C/^{12}C$ ratio ($\delta^{13}C_{DOC}$), DOC ^{14}C activity ($F_{mod\text{-}DOC}$), sediment $^{34}S/^{32}S$ ($\delta^{34}S_{sediment}$) ratio, and sulfur K-edge x-ray absorption spectra. These observations indicate that the catchment of the Koyukuk River hosts sulfide oxidation, modulated by inputs from evaporite dissolution, with assimilatory sulfate reduction occurring in the floodplain. Furthermore, we invert river observations to quantitatively constrain the relative importance of weathering process and calculate the relative fluxes of DIC and ALK. Finally, we compare our new measurements against historical observations from the Koyukuk catchment and from the greater Yukon River Basin to evaluate how the relative importance of weathering processes has changed over the preceding decades and may continue to change under a warming climate. These analyses collectively show that sulfide oxidation is an important component of permafrost degradation and may feedback positively on anthropogenic warming.

V.3: Methods

V.3.1: Field methods

V.3.1.1: Field sites

Water and sediment samples were collected from the Koyukuk River and its floodplain in June-July 2018, with sampling focused near the town of Huslia, and four additional water samples were collected from the Koyukuk's headwaters in August 2019 (Fig. V-1; Fig. V-S1 for drone imagery). Water sampling was focused along the active channel of the Koyukuk River, with additional samples collected from sloughs and pore fluids, while sediment collection focused on sampling both permafrost and non-permafrost deposits. Observations of microbial community composition and particulate organic carbon in the sediment samples were previously reported in Douglas et al. (2021) and Douglas et al. (2022), respectively.

The Koyukuk River meanders through discontinuous permafrost with a mean depth of 12.4 m and an average width of 250 m near Huslia. Fluvial geomorphologic features litter the landscape, which is characterized by scroll bars, oxbow lakes, sloughs, and km-scale meanders in the active channel (Fig. V-1D; Fig. V-S1). Thermokarst lakes and undercut banks provide evidence of permafrost, which was confirmed through identification of frozen sediment and ice lenses within sediment cores. The mean width of the Koyukuk has remained constant since at least 1978 (Rowland et al., 2019), and the system remained unglaciated throughout the Last Glacial Maximum. The Koyukuk's headwaters in the Brooks Range drain a wide variety of sedimentary, igneous, and metamorphic lithologies, including Upper Cretaceous shale, sandstone, and conglomerate, Jurassic-to-Permian mafic volcanic rock, Lower Paleozoic metasediments and carbonates,

and several other Paleozoic and Precambrian units. The river passes through a large section of Lower Cretaceous shales, sandstones, and conglomerates as it descends from the mountains, and the bedrock surrounding Huslia is mapped as Lower Cretaceous intermediate volcanics. Huslia sits on a Pleistocene-aged dune field and an exposure of cross-bedded sediment was clearly visible from town. However, for the most part, the Koyukuk is currently reworking its own floodplain and no bedrock exposures were seen or sampled during the 2018 campaign.

V.3.1.2: Sample collection

Water samples were classified as belonging to one of six groups: river water from the Koyukuk headwater (n=4), river water from the Koyukuk mainstem (n=75), river water from sloughs (n=10), lake water (n=6), meteoric precipitation (n=4), and pore fluids (n=19). The headwater samples, 31 of the mainstem samples, 6 of the slough samples, and the lake samples were surface waters collected into 50 mL plastic syringes that were sampled either from shore or onboard small boats. The four precipitation samples were collected ~1.5 km from the mainstem river. When possible, temperature, conductivity, and pH was measured by multiprobe. The samples were filtered through 0.22 μm 25 mm nylon syringe filters into MQ-washed 60 mL polypropylene bottles for anion analysis, acid-washed 60 mL polypropylene bottles for cation analysis, and two 12 mL Labco exetainer vials for DIC and water isotope analysis. For 8 samples collected near an upstream confluence (Figs. V-S1J, K), the anion and cations splits were collected into exetainer vials instead of polypropylene bottles. Sample containers were rinsed with filtrate prior to collection and cation splits were acidified with 2 drops 16 N high-purity HNO_3^-.

In addition to the syringe-filtered samples, 44 mainstem and 4 slough samples were collected while filtering water for suspended sediment analyses. These samples were passed through either a 0.2 μm 142 mm nitrocellulose mixed ester (MCE) filter or a 0.2 μm 142 mm polyethersulfone (PES) filter. Glass fiber filters were not used for this work because they can have a sizable but soluble sulfate blank and it can be difficult to extract sediment off the filters for grain size analysis (Torres et al., 2020; Douglas et al., 2022). MCE filters were used for 31 mainstem and 1 slough sample and PES filters were used for 13 mainstem and 3 slough samples. MQ blanks collected for filtering with nylon, MCE, and PES all had negligible SO_4^{2-} concentrations and suggest no sulfur leaching from the PES filters. Furthermore, no systematic chemical distinctions were observed for mainstem samples processed using the different filtration methods. Additionally, filtrate from three mainstem, one slough, and one lake sample was collected into five 1L amber bottles for measurement of the ^{14}C activity of dissolved organic carbon (DOC), which were acidified with 20 drops of high-purity HCl. Two of these mainstem samples were passed through PES filters and the other three samples through MCE filters.

Pore fluid samples were collected using rhizons. 14 pore fluid samples were collected from a single site along a transect roughly orthogonal to the river, 3 samples were collected from core 1, and another 2 samples were collected from a third location (Fig. V-1D; Fig. V-S5). Different types of samples were collected based on the available volume of pore fluid and cation splits were again acidified with 16 N HNO_3^-.

Sediment samples were collected from the region surrounding Huslia (Fig. V-1D). Unfrozen cut banks and point bars were sampled by hand, cores were augered in unfrozen material, and in permafrost we used a Snow, Ice, and Permafrost Research Establishment

(SPIRE) corer. Sediment samples were stored in Whirlpak bags and kept frozen until processing. Douglas et al. (2022) reported full stratigraphic sections, measurements of grain size, and the $\delta^{13}C$ and ^{14}C activity of C_{org} in these samples.

Lastly, to collect suspended sediment ~8L of river water was collected using a Van Dorn sampler, stored in 10L dairy bags, and then passed through either PES or MCE filters. This sediment was harvested from the filters by sonicating in MQ, gently scraping with a spatula, and drying the sediment. We do not report sulfur observations on suspended sediment harvested from PES filters.

V.3.2: Laboratory methods

V.3.2.1: Ion chromatography measurements

Major ion concentrations were measured by ion chromatography in the Resnick Water and Environment Laboratory at the California Institute of Technology. Concentrations of Ca^{2+}, Mg^{2+}, Na^{+}, and K^{+} were measured on a Dionex ICS-2000 with guard column (CG12A 2x50 mm), separator column (CS12A 2x250mm), suppressed conductivity, and a 20 mM isocratic methanesulfonic eluent. Concentrations of Cl^{-} and SO_4^{2-} were measured on a Dionex ISC-3000 with guard column (AG29 2x50 mm), separator column (AS29 2x250 mm), suppressed conductivity, and an isocratic 4.5 mM Na_2CO_3 / 2.5 mM $NaHCO_3$ eluent. Measurement precision was quantified through replicate analysis of the MAURI-09, SUPER-05, and CRANBERRY-05 reference materials from Environment and Climate Change Canada, the in-house river water consistency standard Switzer Falls (Burke et al., 2018), and unknown samples. Full information on the precision of major ion measurements, determined from both consistency

standards and replicate sample measurements, is given in Table V-S1. Overall, the 1σ precision of SO_4^{2-} (3.9%), Mg^{2+} (3.2%), Na^+ (2.4%), and K^+ (4.4%), when quantified as the least reproducible value across materials, were consistent with expectations. Although the relative standard deviation of Cl^- measurements in SUPER-05 (2.1%) and MAURI-09 (7.3%) were also reasonable, the precision of Cl^- in replicate sample measurements was worse (14.4%). This lower precision likely reflects that the concentration of Cl^- in 90% of our samples is <10 μM, which also means that the absolute error is lower than other ions despite the higher RSD. The 1σ RSD for Ca^{2+} was 3.3% in CRANBERRY-05 (n=2), 12.1% in MAURI-09 (n=3), and had a mean value of 1.1% across 15 sets of sample replicates with 2-3 measurements each. An anomalously poor Ca^{2+} precision was previously observed for MAURI-09 (Kemeny et al., 2021b) and does not appear to represent the precision of our Ca^{2+} measurements. The precision of each major ion measurement was taken as the larger of replicate sample measurements or the least reproducible consistency standard for that element, excluding the Ca^{2+} measurements of MAURI-09. The concentration of HCO_3^- was calculated by charge balance. Our analysis references both the sum of dissolved cations ($\Sigma^+ = Ca^{2+} + Mg^{2+} + Na^+ + K^+$, in charge equivalents) and the sum of dissolved cations and SO_4^{2-} ($\Sigma^{\pm} = \Sigma^+ + SO_4^{2-}$, in charge equivalents).

V.3.2.2: MC-ICP-MS measurements of $\delta^{34}S_{SO4}$

The $\delta^{34}S_{SO4}$ values ($^{34}R_{sample}/^{34}R_{standard}$ -1, where ^{34}R is the $^{34}S/^{32}S$ ratio of SO_4^{2-} and $\delta^{34}S$ is reported in ‰) of 67 river water, pore fluid, and precipitation samples was measured by multicollector inductively coupled plasma mass spectrometry (MC-ICP-MS) at the California Institute of Technology (Paris et al., 2013; 2014, Burke et al., 2018). Briefly,

sample aliquots containing approximately 7.5 to 470 nmol SO_4^{2-} were evaporated within Savillex PFA vials, SO_4^{2-} was chromatographically isolated using AG 1-X8 anion exchange resin, column effluent was matrix matched to an in-house Na_2SO_4 standard, and $^{34}S/^{32}S$ was measured as sets of 50 cycles with sample-standard bracketing. Anomalous $^{34}S/^{32}S$ measurements were identified statistically (>3σ) and removed from the analysis, as were individual cycles associated with large changes in signal strength and entire sets of cycles following substantial fluctuations in mass biasing. The standard deviation of error-normalized deviations ranged from 2.2 to 8.8 across six analytical sessions (John and Adkins, 2010). We report $\delta^{34}S$ values derived from the means of $^{34}S/^{32}S$ ratios corrected for both instrument blank and procedural blank, the latter of which averaged 0.44 nmol of SO_4^{2-}. Consistency standards included seawater, which was measured as having a $\delta^{34}S_{SO4}$ value of 21.09 ± 0.31‰ (n=34, 2σ), and an in-house reference material Switzer Falls, which was measured as having a $\delta^{34}S_{SO4}$ value of 4.23 ± 0.21‰ (n=38, 2σ) (Burke et al., 2018). Among 15 samples independently processed twice, the mean of twice the difference in $\delta^{34}S$ between the two external replicates was 0.27‰. Overall, 17 samples were measured more than twice, 39 samples were measured twice, and 11 samples were measured only once. The precision of SO_4^{2-} $\delta^{34}S$ is reported for each sample as the larger of either the standard deviation of blank-corrected $^{34}S/^{32}S$ determinations or the reproducibility of seawater (2σ=0.31‰).

V.3.2.3: IRMS measurement of $\delta^{18}O_{SO4}$

The $\delta^{18}O_{SO4}$ values of 14 water samples were measured at the Environmental Isotope Laboratory in the Department of Geosciences at the University of Arizona. Briefly,

unacidified water samples were passed through a 0.45 μm filter to remove particulates, a few drops 1N HCl was added to prevent subsequent precipitation of $BaCO_3$, the solution was put on a hot plate, 0.5M $BaCl_2$ was added to induce precipitation of $BaSO_4$, the solution was passed through a second 0.45 μm filter, the filter was dried, and $BaSO_4$ was recovered by scratching the powder off the filter without digging into the underlying material. The recovered powder was combusted in a ThermoQuest Finnigan TC/EA at 1375°C in the presence of excess carbon and the $^{18}O/^{16}O$ ratio of produced CO was measured on a Thermo Electron Delta V mass spectrometer. Values of $\delta^{18}O_{SO4}$ were corrected to the VSMOW scale using the in-house QG barium sulfate standard, which was calibrated against NSB-127, and are reported with a precision of 0.8‰ (2σ). The 14 $\delta^{18}O_{SO4}$ measurements span multiple sample types including the mainstem river, sloughs, headwater samples, and pore fluids. However, due to low collected volumes (~50 mL), most samples did not contain sufficient SO_4^{2-} for recovery of $BaSO_4$; our $\delta^{18}O_{SO4}$ measurements are thus biased to samples with the highest SO_4^{2-} concentrations and may not capture $\delta^{18}O_{SO4}$ variations in samples with low SO_4^{2-} concentrations.

V.3.2.4: Laser spectroscopy measurements of DIC and $\delta^{13}C$

The DIC concentration and $\delta^{13}C_{DIC}$ values of 82 water samples were measured using a Picarro cavity ring-down laser spectrometer at the University of Southern California in August 2018. Values of $\delta^{13}C_{DIC}$ were calibrated to the VPDB scale using OPT Calcite ($\delta^{13}C$ = 2.47‰, 12.002 wt% C) in the first analytical session and using AR-15 ($\delta^{13}C$ = -9.65 ± 0.03‰, 8.23 ± 0.1 wt% C) in three subsequent sessions, while the concentration of DIC was calibrated using OPT Calcite in all four analytical sessions. Both OPT-Calcite

and AR-15 are in-house standards that were previously calibrated to the VPDB scale at UC Davis. When not being used as an accuracy standard, OPT Calcite was measured as having a $\delta^{13}C$ value of 2.41 ± 0.35‰ (n=11, 2σ). AR-15, never used as an abundance standard, was measured as having 8.16 ± 0.54 wt% C (n=20, 2σ). Uncertainty in $\delta^{13}C_{DIC}$ was taken as the reproducibility of OPT-calcite $\delta^{13}C$ (0.31‰, 2σ) and uncertainty in DIC concentration was reached through scaling measured DIC concentration by the relative standard deviation of repeated AR-15 measurements (6.67%, 2σ).

In water samples at circumneutral pH, such as our mainstem samples from the Koyukuk River, the concentration of DIC is expected to approximately match the concentration of HCO_3^-. Consistent with this expectation, in our mainstem and slough samples the mean absolute difference between DIC and the concentration of HCO_3^- derived through charge balance was only 4.1%. The difference exceeded 10% for a pore-fluid sample (15.4% in AKW-27#1) and two lake samples (28.5% in AKW-22 and 215% in AKW-20); the two lake samples are also notable for having the two highest values of measured $\delta^{13}C_{DIC}$ and low pH values (6.7 in AKW-22 and 5.6 in AKW-20).

V.3.2.5: Accelerator mass spectrometry measurements of $\delta^{13}C_{DOC}$ and $F_{mod\text{-}DOC}$

The $^{13}C/^{12}C$ and $^{14}C/^{12}C$ ratios of dissolved organic carbon (DOC) were measured at the Accelerator Mass Spectrometry Lab at the University of Arizona. Organic carbon was extracted at the AMS facility approximately 1 month after collection. The samples were later combusted and CO_2 was cryogenically purified before conversion to graphite. We report the $^{13}C/^{12}C$ measurements as $\delta^{13}C_{DOC}$ and the $^{14}C/^{12}C$ measurements as fraction modern ($F_{mod\text{-}DOC}$).

V.3.2.6: Laser spectroscopy measurements of water $\delta^{18}O$ and δD

Water sample $\delta^{18}O$ and δD were measured using a Picarro cavity ring-down laser spectrometer at Rice University in July 2018. Instrument drift was corrected using an in-house standard analyzed periodically throughout the run and a memory correction was performed following Van Geldern and Barth (2012). Measurements were calibrated using the international reference standards VSMOW2 and SLAP2, and reference materials included CIT17 ($\delta^{18}O$ = -9.8 ± 0.2‰ (2σ); δD = -73.8 ± 1.2‰ (2σ)) and IA-R064 ($\delta^{18}O$= -12.3 ± 0.3‰ (2σ); δD = -98.3 ± 2.3‰ (2σ)). CIT17 was measured as having a $\delta^{18}O$ value of -9.7 ± 0.4‰ (n=6, 2σ) and a δD value of -74.6 ± 2.2‰ (n=6, 2σ), and IA-R064 was measured as having $\delta^{18}O$ of -12.4 ± 0.2‰ (n=5, 2σ) and δD of -97.6 ± 1.2‰ (n=5, 2σ). The precision of unknown samples was taken as the larger of the internal precision among repeated injections and the least reproducible $\delta^{18}O$ and δD measurements of CIT17 and IA-R064 ($\delta^{18}O$ precision of 0.4‰ (2σ) and δD precision of 2.2‰ (2σ)). The $\delta^{18}O$ and δD values of the headwater samples (KY19-AKW-65 through KY19-AKW-68) were not meausred because they were collected opportunistically in 2019 while water isotope ratios were measured immediately after the 2018 field season.

V.3.2.7: EA-IRMS measurements of sediment $\delta^{34}S$

The $\delta^{34}S$ of 17 sediment samples from 9 unique sites was measured at the California Institute of Technology across three analytical sessions during August 2020. Collected sediment samples were oven-dried, homogenized with agate mortar and pestle, and split with cone-and-quarter or riffle splitter (Douglas et al., 2022). The sediment was then weighed and burned in the presence of V_2O_5 within a Thermo Flash Elemental

Analyzer and the gas was directed through a Conflo-IV interface into a Thermo Delta V mass spectrometer. Samples were corrected for capsule blank and calibrated to the VCDT scale using IAEA-S1 and IAEA-S2. No samples were measured only once, 11 samples were measured twice, 5 samples were measured three times, and the sample KY18-Bank1-Peat was measured 6 times. The precision of sediment $\delta^{34}S$ was taken as the larger of either repeat $\delta^{34}S$ determinations or the precision of sample KY18-Bank1-Peat, which was measured to have a $\delta^{34}S$ value of 1.6 ± 0.5‰ (n=6, 2σ). The sulfur abundance of sediments ranged from 0.023 wt% to 0.176 wt%. The precision of sulfur abundance was taken as the larger of either repeat determinations or the 17% relative standard deviation of repeated KY18-Bank1-Peat measurements (0.176 ± 0.03 wt%, n = 6, 2σ). Sedimentary sulfur abundance and $\delta^{34}S$ values were compared with prior observations of carbon abundance, $\delta^{13}C$, and ^{14}C activity (Fig. V-S4; Douglas et al., 2022).

V.3.2.8: SLAC X-ray absorption near-edge structure measurements

X-ray Absorption Near-Edge Structure (XANES) spectroscopy provided μm-scale information on the redox state and electronic structure of sulfur in samples of floodplain and suspended sediment. XANES measurements across the sulfur K-edge were conducted on beamline 14-3 of the Stanford Synchrotron Radiation Lightsource at the SLAC National Accelerator Laboratory during four analytical sessions between February 2019 and March 2020. The x-ray beam was calibrated to define the first pre-edge feature of sodium-thiosulfate at 2472.02 eV. Samples were prepared by inverting sediment vials onto sulfur-free tape, which was then covered with mylar film, secured to sample trays, and placed inside a helium-purged chamber. In general, our workflow was to map a region of each

sample at an incident energy at or above the sulfur K-edge at relatively coarse resolution to identify areas of high sulfur abundance and then either collect spectra at those positions or further characterize interesting regions through high-resolution mapping at multiple incident energies characteristic of the resonances of specific sulfur moieties. In turn, a principal component analysis of the resulting maps could be used to identify areas of spectral diversity that were then targeted for collection of complete spectra. XANES spectra were collected either singularly, in duplicate, or in triplicate, and the iF/i1 signals of replicate spectra were averaged and baseline corrected in SIXPACK (Webb, 2005). Spectra from 94 positions were collected, but 10 of the 41 spectra on suspended sediment and 9 of the 53 spectra on floodplain sediment were removed from the analysis because they exhibited substantial baseline noise indicative of low sulfur abundances. The remaining 75 spectra were fit to five transmission reference spectra from the European Synchrotron Radiation Facility ID21 sulfur XANES spectra database: oxidized glutathione (disulfide), cysteine (thiol), methionine sulfoxide (sulfoxide), taurine (sulfonate), and anhydrite (sulfate) (Bohic et al., 2008). The fitting was performed in MATLAB as an optimization to minimize proportional misfit, with fractional contributions constrained to be positive and without constraint on their sum, and with equal weighting for all points between 2470 eV and 2490 eV where the relative fluorescence response was >0.1 (Prietzel et al., 2011; Manceau and Nagy, 2012). The normalized fractional contributions of the disulfide, thiol, and sulfoxide reference spectra were then summed to reach the statistic F_{red}, previously reported in Torres et al. (2020) and Kemeny et al. (2021b), which approximately reflects the fractional importance of reduced sulfur phases in each spectra. Spectra collected on floodplain sediment are likely representative of the sample as they

were homogenized prior to analysis. Conversely, spectra collected on suspended sediment may be partially biased because the sediment was not homogenized after harvesting from MCE filters.

V.3.3: Numerical methods

V.3.3.1: Binary Monte Carlo mixing model for calculating sulfide $\delta^{34}S$

A two end-member Monte Carlo mass balance model was used to calculate the $\delta^{34}S$ of sulfate formed through sulfide oxidation within the Koyukuk River catchment. This calculation followed Relph et al. (2021) and was based on five parameters: sample $\delta^{34}S_{SO4}$, sample $\delta^{18}O_{SO4}$, evaporite $\delta^{34}S$, evaporite $\delta^{18}O$, and the $\delta^{18}O$ of sulfate produced through sulfide oxidation. Parameter ranges are given in Table V-1. Note that this calculation does not account for SO_4^{2-} input from precipitation, which are estimated to be very small based on the low ratios of Cl^-/SO_4^{2-} in river water samples (Fig. V-2B). The calculated ranges for sulfide $\delta^{34}S$ were then used in a larger river inversion model to constrain inputs from sulfide oxidation and evaporite weathering in samples without measured values of $\delta^{18}O_{SO4}$.

V.3.3.2: Monte Carlo inversion model

The MEANDIR inversion model was used to conduct two Monte Carlo calculations that partitioned river dissolved load among end-member contributions (Kemeny and Torres, 2021; Kang et al., 2022). In the first scenario, observations of dissolved Ca^{2+}, Mg^{2+}, Na^+, K^+, Cl^-, SO_4^{2-}, and $\delta^{34}S_{SO4}$ were inverted for contributions from carbonate weathering, silicate weathering, meteoric precipitation, evaporite dissolution, sulfide oxidation, and organic carbon oxidation (Table V-2). In the second inversion, carbon degassing with a

fractionation between -15‰ and -5‰ was also included (Table V-2). The composition of the carbonate end-member in both scenarios ranged between calcite and dolomite, the elemental ratios and uncertainty of the precipitation end-member reflected the four rain samples, sulfide oxidation provided only SO_4^{2-} to river water, organic carbon oxidation sourced only DIC, and degassing removed only DIC (Table V-2). Based on low ratios of Cl^-/SO_4^{2-} and Cl^-/Σ^+ but moderate values of $\delta^{18}O_{SO4\text{-}H2O}$ in mainstem samples, the evaporite end-member was assumed to source only Ca^{2+} and SO_4^{2-} with the $\delta^{18}O_{SO4}$ and $\delta^{34}S_{SO4}$ values of Phanerozoic evaporites (Claypool et al., 1980).

The lithologic heterogeneity of the Koyukuk catchment, coupled with the lack of bedrock exposures near Huslia, precluded defining a defensible prior for the chemical composition of the silicate end-member. Rather, contributions from silicate weathering were quantified by employing four end-members that each provided exclusively either Ca^{2+}, Mg^{2+}, Na^+, or K^+. A composite silicate end-member was then constructed after the inversion using the contributions from each of the four single-cation end-members. This approach allowed MEANDIR to define a silicate end-member for each sample that best accommodated the contributions from the other end-members rather than using prior knowledge to define the silicate end-member. In essence, this approach applied the same technique used for quantifying sulfide oxidation to silicate weathering because the silicate end-member had unknown chemistry (Kemeny and Torres, 2021; Cole et al., in review).

The inversions employed a Monte Carlo sampling strategy to account for uncertainty in the chemical composition of water samples and end-members, normalized observations to the charge-equivalent sum of Ca^{2+}, Mg^{2+}, Na^+, K^+, SO_4^{2-}, and DIC, converted $\delta^{34}S_{SO4}$ and $\delta^{13}C_{DIC}$ values to $^{34}S/^{32}S$ and $^{13}C/^{12}C$ ratios for the calculations, used

a cost function of proportional misfit with equal weighting on all variables, treated meteoric precipitation as a common end-member, constrained end-member fractional contributions between 0% and 100%, and only considered simulations successful if they recreated between 95% and 105% of all major ion observations and were within 2‰ of $\delta^{34}S_{SO4}$ and $\delta^{13}C_{DIC}$ (Gaillardet et al., 1999; Kemeny and Torres, 2021). All but two mainstem, slough, and headwater samples collected from the Koyukuk were successfully inverted 200 times. The sample KY18-DP06-S1 was inverted 125 times and the sample KY18-AKW-22 was never successful inverted. Calculations for the fraction of weathering alkalinity generated through carbonate weathering, the fraction of weathering alkalinity offset through sulfide oxidation, and the amount of organic carbon oxidation relative to weathering alkalinity, called R, Z, and C, respectively, included Ca^{2+}, Mg^{2+}, Na^{+}, and K^{+} (Torres et al., 2016; Kemeny and Torres, 2021). The inversion calculations were conducted through the Resnick High Performance Computing Center at the California Institute of Technology.

V.3.4: Compilation of prior observations from the United States Geological Survey

Water quality observations from the Koyukuk River and the Yukon River were compiled for comparison with our collected samples and to evaluate temporal changes in dissolved river chemistry. The United States Geological Survey (USGS) has conducted multiple survey and fixed-station studies on the Yukon River and its tributaries over the last seventy years. First, our dataset includes 733 samples compiled from USGS sites within the catchment of the Koyukuk River, 148 of which include measurements of Ca^{2+}, Mg^{2+}, Na^{+}, K^{+}, SO_4^{2-}, and Cl^{-} concentrations. 61 of these samples were collected between 1955 and 1978 from the mainstem Koyukuk River at the town of Hughes (site number

15564900), which is located one meander bend above Huslia, and 23 of the Hughes samples include measurements of major ion concentrations. Second, data was compiled from five USGS sites with historical observations and which were sampled multiple times annually between 2000 and 2005 (Fig. V-1A; Schuster 2003; 2005a; 2005b; 2006; 2007). The compilation includes USGS water quality records for the Yukon River at Pilot Station (site number 15565447; samples collected from 1954-1956 and from 1975-2022; n=1250 total observations), the Yukon River at Stevens Village (site number 15453500; 1970-1978, 2000-2005; n=215), the Yukon River at Eagle (site number 15356000; 1950-1979, 2000-2005; n=311), the Tenana River at Nenana (site number 15515500; 1954-2021; n=626), and the Porcupine River near Fort Yukon (site number 15389000; 1966–1978, 2001-2005; n=216). Lastly, the compilation includes data from surveys characterizing different stretches of the Yukon River. These data include the 2002-2003 survey of Dornblaser and Halm (2006) and the 2004 survey of Halm and Dornblaser (2007), the 2006-2008 survey of Schuster et al. (2010) and the 2009-2014 survey of Herman-Mercer (2016), and the 2014-2018 survey data of Foks et al. (2020). Survey data from within the Koyukuk River catchment was isolated and, when not specifically presenting data from either Hughes or one of the five time-series sites, we distinguish only whether samples were collected from within the Koyukuk catchment or from the broader Yukon River Basin.

V.4: Results

The cation budget of river water and pore fluid samples was dominated by Ca^{2+} with a substantial secondary role for Mg^{2+}. Ca^{2+} represented 49% to 80% of positive charge in solution, Mg^{2+} accounted for 18% to 50%, Na^{+} comprised 1% to 11%, and K^{+} took up the remaining 0% to 4% (Fig. V-2A). The highest Mg^{2+}/Σ^{+} ratios occurred in headwater and mainstem samples, while pore fluid and slough samples had larger Ca^{2+}/Σ^{+} ratios and both higher and lower values of $(Na^{+}+K^{+})/\Sigma^{+}$. These relatively low ratios of $(Na^{+}+K^{+})/\Sigma^{+}$ overall suggest either substantial carbonate weathering (Brabets et al., 2000; Tank et al., 2012), or that the weathering silicate lithologies are dominantly mafic rather than felsic. For anions, SO_4^{2-}/Σ^{+} ranged from 6% to 98% and HCO_3^{-}/Σ^{+} ranged from 2% to 93% (Fig. V-2B). Headwater and mainstem samples had the highest relative sulfur abundances, while pore fluid and slough samples showed higher ratios of HCO_3^{-}/SO_4^{2-}. The ratio Cl^{-}/Σ^{+} was <2% in all river water and pore fluid samples, and Cl^{-}, Na^{+}, and K^{+} abundances were elevated in precipitation samples. Overall, the major ion chemistry data showed that headwater and mainstem water samples had higher $SO_4^{2-}/\Sigma^{\pm}$ and lower $Ca^{2+}/\Sigma^{\pm}$ than pore fluids and slough samples (Fig. V-2C). The 0.43 decrease in $SO_4^{2-}/\Sigma^{\pm}$ from mainstem to slough and pore fluids was mostly compensated by a 0.42 increase in $Ca^{2+}/\Sigma^{\pm}$, as evidenced by the relative invariance of $Mg^{2+}/\Sigma^{\pm}$ (Fig. V-2D). Values of $(Mg^{2+}+Na^{+}+K^{+})/\Sigma^{\pm}$ varied between 16% and 34%.

Values of $\delta^{34}S_{SO4}$ ranged from -6.8‰ to 6.2‰. Mainstem samples ranged in $\delta^{34}S_{SO4}$ from -0.9‰ to -0.4‰, with a mean value of -0.6 ± 0.2‰ (n = 36, 2σ). The headwater sample from Middle Fork was isotopically identical to the mainstem Koyukuk, with a $\delta^{34}S_{SO4}$ value of -0.6‰, while the other headwater samples ranged in $\delta^{34}S_{SO4}$ from -6.8‰

at Marion Creek to -4.0‰ at South Fork. The catchment area of the Middle Fork sample is comparable to that of the South Fork sample and substantially larger than those of the Marion Creek or Slate Creek samples (Fig. V-1C). Precipitation $\delta^{34}S_{SO4}$ values ranged from 4.7‰ to 6.2‰, consistent with their higher Cl^-/SO_4^{2-} ratios and the expectation that a fraction of SO_4^{2-} in precipitation is sourced from seawater with $\delta^{34}S_{SO4}$. Slough $\delta^{34}S_{SO4}$ values were slightly elevated from the mainstem, ranging from -0.6‰ to 2.4‰. Notably, the slough sample collected ~50 m upstream of its confluence with the mainstem appears identical to the mainstem and likely is mainstem water. Pore fluid $\delta^{34}S_{SO4}$ was more variable, ranging from -6.0‰ to 3.6‰ (Fig. V-S5), but only three samples had $\delta^{34}S_{SO4}$ values elevated above the average mainstem value. The data overall indicate substantial sulfur isotopic variability with most variation occurring between different sample types rather than within sample groupings.

The $\delta^{18}O_{SO4}$ value of three mainstem samples were -5.7‰, -4.9‰, and -3.8‰, nearly indistinguishable given the 2σ measurement uncertainty of 0.8‰. The $\delta^{18}O_{SO4}$ values of four pore fluid samples ranged from -4.2‰ to -3.2‰, while $\delta^{18}O_{SO4}$ values in three slough samples ranged from -3.8‰ to -0.5‰. The Middle Fork headwater sample, which matched the Koyukuk mainstem for $\delta^{34}S_{SO4}$, had a $\delta^{18}O_{SO4}$ value of -6.0‰. The other three headwater samples, which had lower $\delta^{34}S_{SO4}$ values, had $\delta^{18}O_{SO4}$ values ranging from -1.4‰ to 1.2‰.

Values of $\delta^{18}O_{H2O}$ in the samples collected near Huslia ranged from -20.4‰ to -17.5‰. Slough samples had higher values of $\delta^{18}O_{H2O}$ than mainstem samples and partially offset their higher values of $\delta^{18}O_{SO4}$. Overall, $\delta^{18}O_{SO4\text{-}H2O}$ values ranged from 14.5‰ to

17.1‰. Values of δD_{H2O} ranged from -157.7‰ to -141‰ and were consistent with both $\delta^{18}O_{H2O}$ measurements and prior observations (Fig. V-S2).

Values of $\delta^{13}C_{DIC}$ ranged from -16.7‰ to -2.7‰ and DIC concentrations ranged from 699 μM in a lake sample to nearly 6 mM in a pore fluid sample. Samples from the mainstem Koyukuk were tightly clustered around a mean $\delta^{13}C_{DIC}$ value of -7.7 ± 0.4‰ (2σ, n=64), similar to 2 prior observations from the Koyukuk and slightly elevated from the -8.5‰ value of atmospheric $\delta^{13}C_{CO2}$ in 2018 (Keeling et al., 2017). Slough samples had lower values of $\delta^{13}C_{DIC}$ than the mainstem, suggesting a greater role for the oxidation of organic carbon, and DIC concentrations were higher in sloughs than in the mainstem except for four samples from the Huslia river (Fig. V-1). The lowest $\delta^{13}C_{DIC}$ value occurred in the only analyzed pore fluid, which also had the highest concentration of DIC. The highest and second lowest $\delta^{13}C_{DIC}$ were both from lakes with low pH values; one at pH 4.6 with a $\delta^{13}C_{DIC}$ value of -16.2‰, and the other at pH 5.6 with a $\delta^{13}C_{DIC}$ of -2.7‰.

Values of $\delta^{13}C_{DOC}$ ranged from -28.8‰ to -26.5‰ and values of $F_{mod\text{-}DOC}$ ranged from 0.9432 to 1.0191. These $\delta^{13}C_{DOC}$ values were very similar to prior measurements of $\delta^{13}C$ in sedimentary organic carbon, which ranged from -30.5‰ to -25.5‰ (Douglas et al., 2021), and constrained the value of $\delta^{13}C_{DIC}$ produced through C_{org} respiration near -27.5‰. $F_{mod\text{-}DOC}$ values were higher than in sedimentary organic carbon but consistent with prior observations showing that DOC in permafrost rivers is often dominated by the oxidation of young organic matter (Benner et al., 2004; Neff et al., 2006 Striegl et al., 2007).

Sediment $\delta^{34S}S$ values ranged from -4.2‰ to 7.5‰ and sediment S contents ranged from 0.02 wt% to 0.18 wt%. Neither sediment $\delta^{34}S$ nor S abundance were clearly related to whether a sample was from a permafrost or non-permafrost deposit. Most sediment

samples had $\delta^{34}S$ values between 0‰ and -2‰, comparable to the $\delta^{34}S_{SO4}$ of the mainstem river. Samples from core 9 had relatively elevated $\delta^{34}S$ values of 2.4‰, 5.6‰, and 7.5‰, where the two higher values occurred in peat samples. This site is stratigraphically the oldest analyzed deposit and, due to its physical distance from the active channel, it may have a larger fraction of sulfur sourced from high-$\delta^{34}S_{SO4}$ precipitation than the other sites. Conversely, two other high $\delta^{34}S$ values from bank 9 (orange square) and bank 1 (red star), as well as the lowest $\delta^{34}S$ value from core 3 (light green diamond), are also peat samples and may indicate that biological processes can express sulfur fractionation in either direction. In core 1, which was the only sediment sample with associated pore fluid, the value of $\delta^{34}S_{SO4}$ was 4.2‰ higher than the corresponding sediment $\delta^{34}S$ value.

Synchrotron spectra indicated thiol, disulfide, sulfoxide, sulfonate, and sulfate moieties within floodplain and suspended sediment. The presence of these phases was consistent with production and cycling of organic sulfur within the Koyukuk floodplain.

The primary river inversion model constrained inputs from precipitation, silicate weathering, evaporite dissolution, carbonate weathering, sulfide oxidation, and organic carbon oxidation (Table V-2). Cl^- was only sourced from precipitation, SO_4^{2-} was derived from sulfide oxidation and evaporite dissolution, Na^+ and K^+ were sourced from silicate weathering, DIC was derived from C_{org} oxidation and carbonate weathering, Mg^{2+} was sourced from silicate and carbonate weathering, and Ca^{2+} was derived from carbonate weathering, silicate weathering, and evaporite dissolution (Figs. V-S6 and V-S7). Slough samples had lower contributions from sulfide oxidation and higher contributions from C_{org} oxidation than mainstem samples. The inversion-constrained chemistry of the carbonate end-member spanned from calcite to dolomite while the silicate end-member had elevated

$Mg^{2+}/\Sigma^{\pm}$ with $Ca^{2+}/\Sigma^{\pm} \leq 0.3$ and $Na^{+}/\Sigma^{\pm} \leq 0.3$ (Fig. V-S8). Results from the inversion with carbon degassing were similar to the inversion results without degassing (Figs. V-S7 and V-S9).

V.5: Discussion

V.5.1: Sulfide oxidation and evaporite dissolution in the Koyukuk River catchment

Values of $\delta^{34}S_{SO4}$ and $\delta^{18}O_{SO4}$ track the relative importance of evaporite dissolution and sulfide oxidation as sources of fluvial SO_4^{2-} (Calmels et al., 2007). In the former case, $\delta^{18}O_{SO4}$ reflects the isotopic composition of evaporites, which ranges from 10‰ to 20‰ across the Phanerozoic (Claypool et al., 1980). In the latter case oxygen in sulfate derives from a combination of atmospheric O_2 and ambient H_2O, where the fraction of O_2-derived oxygen in SO_4^{2-} tends to be ≤15% (Balci et al., 2007). For the modern $\delta^{18}O_{O2}$ value of 23.5‰ and with $\delta^{18}O_{H2O}$ varying between about -20‰ and 0‰, sulfide oxidation coupled to either O_2 or Fe^{3+} reduction results in lower $\delta^{18}O_{SO4}$ values than are produced during evaporite dissolution. The dependence of $\delta^{18}O_{SO4}$ on $\delta^{18}O_{H2O}$ can be partially removed by considering their difference, referenced as $\delta^{18}O_{SO4\text{-}H2O}$, which has been observed to range from several ‰ to nearly 25‰ across river systems (Calmels et al., 2007; Turchyn et al., 2013). However, the interpretation of $\delta^{18}O_{SO4\text{-}H2O}$ values also depends on the fractionation between SO_4^{2-} and H_2O ($\varepsilon_{SO4\text{-}H2O}$) and between SO_4^{2-} and O_2 ($\varepsilon_{SO4\text{-}O2}$). Estimates of $\varepsilon_{SO4\text{-}H2O}$ range between 0‰ and 4‰ (Lloyd, 1968; Taylor et al., 1984; van Everdingen and Krouse, 1985; Balci et al., 2007), consistent with observations of $\delta^{18}O_{SO4\text{-}H2O}$ equal to only a few ‰ in natural systems, and the value of $\varepsilon_{SO4\text{-}O2}$ is estimated between about -11.4‰ and -8.7‰ (Lloyd, 1968; Taylor et al., 1984; Balci et al., 2007).

For the mean measured $\delta^{18}O_{H2O}$ value of -20.3‰ and assuming that $\varepsilon_{SO4\text{-}H2O}$ = 3‰ and $\varepsilon_{SO4\text{-}O2}$ = -10‰ (Balci et al., 2007), the incorporation of 0% to 15% atmospheric O_2 would generate $\delta^{18}O_{SO4\text{-}H2O}$ values between 3‰ and 7.6‰. Sample $\delta^{18}O_{SO4\text{-}H2O}$ values range from 15‰ to 17‰ and thus exceed these reference values by approximately 10‰,

implying that SO_4^{2-} does not derive entirely from sulfide oxidation (Fig. V-3). Rather, these $\delta^{18}O_{SO4\text{-}H2O}$ values indicate either the dissolution of a gypsum-bearing evaporite lithology or the catchment-scale expression of biological processes such as SO_4^{2-} reduction.

The more likely explanation for our observed $\delta^{18}O_{SO4\text{-}H2O}$ values is that gypsum dissolution sourced SO_4^{2-} with high $\delta^{18}O_{SO4}$ values into the Koyukuk River system. Using moderate values for the isotopic composition of Phanerozoic evaporites and fitting through the mainstem data, our $\delta^{18}O_{SO4\text{-}H2O}$ observations are consistent with evaporite dissolution sourcing 30% to 40% of river SO_4^{2-} (Fig. V-3). In this case, the low Cl^-/Σ^+ ratios of the headwater and mainstem samples require the inferred evaporite to contain very little halite.

The second possible interpretation of the data is motivated by observations from the Marsyandi catchment of the Nepal Himalaya showing that microbial sulfate reduction can increase $\delta^{34}S_{SO4}$ and $\delta^{18}O_{SO4}$ by preferentially consuming SO_4^{2-} isotopologues bearing ^{32}S and ^{16}O (Turchyn et al., 2013). By increasing the $\delta^{34}S_{SO4}$ and $\delta^{18}O_{SO4}$ values of residual SO_4^{2-}, MSR can result in SO_4^{2-} isotopic compositions suggestive of evaporite dissolution even when SO_4^{2-} is derived from sulfide oxidation. Furthermore, the oxidation of reduced sulfur back to sulfate can incorporate environmental oxygen and alter $\delta^{18}O_{SO4}$ values without impacting $\delta^{34}S_{SO4}$. MSR and sulfate cycling can also occur in tandem, as evidenced by $\Delta'^{17}O_{SO4}$ measurements from the Marsyandi catchment interpreted as indicating both MSR and incorporation of tropospheric O_2 (Hemingway et al., 2020). While it is theoretically plausible that the same sulfur cycling processes could decrease $\delta^{18}O_{SO4}$ values, specifically in cases where SO_4^{2-} is sourced through evaporite dissolution, we are unaware of any such observations. Moreover, while microbial processes have been shown to increase fluvial $\delta^{34}S_{SO4}$ and $\delta^{18}O_{SO4}$ values in certain catchments (Turchyn et al., 2013;

Hemingway et al., 2020; Joo et al., 2022), there is also evidence that $\delta^{34}S_{SO4}$ (Kemeny et al., 2021b) and $\delta^{18}O_{SO4}$ (Burt et al., 2021) can behave conservatively within river systems.

Because the magnitude of the kinetic oxygen isotope effect for sulfate reduction is about 25% that of the sulfur isotope effect (Mizutani and Rafter, 1969; Mandernack et al., 2003; Aharon and Fu, 2000; Turchyn et al., 2013), a 10‰ increase in $\delta^{18}O_{SO4}$ relative to the initial value formed through sulfide oxidation would require a 40‰ increase in $\delta^{34}S_{SO4}$. Given that mainstem $\delta^{34}S_{SO4}$ values were ~0‰, this scenario would require that bedrock sulfide $\delta^{34}S$ is about -40‰. There are two primary reasons that this scenario is unlikely. Foremost, the isotope effect required to increase river water $\delta^{34}S_{SO4}$ by 40‰ is likely too large to be expressed at the catchment scale. Because rivers are open systems rather than batch reactors, with continuous supply of fresh reactants that mix with reaction products, isotopic distillation is unlikely and the largest attainable isotopic difference between initial and final materials is set by the isotope effect (Hayes, 2004). That is, the difference in $\delta^{34}S$ between bedrock sulfide and $\delta^{34}S_{SO4}$ can only equal ε_{MSR}*f, where ε is the relevant isotope effect and f is the fractional utilization of SO_4^{2-}. For the highest observed sulfate reduction isotope effects, ~80‰ (Sim et al., 2011), nearly 50% of fluvial SO_4^{2-} would need to be reduced to generate a 10‰ increase in $\delta^{18}O_{SO4}$. Moreover, these extremely large isotope effects are generally expressed only in quiescent environments at low sulfate reduction rates, which are not the conditions of an actively meandering river system such as the Koyukuk. At more moderate isotope effects, such as the commonly used choice of 35‰, about 100% of fluvial SO_4^{2-} would need to be reduced. Identifying a physical mechanism for expressing isotopic distillation, rather than steady-state dynamics, would be required to produce a 10‰ increase in $\delta^{18}O_{SO4}$ without requiring large fractions of SO_4^{2-} consumption.

The second and related requirement of catchment-scale sulfate reduction is storing or exporting product sulfide with low $\delta^{34}S$ values. However, our observations of $\delta^{34}S_{sediment}$ are comparable to the mainstem river and have only modest sulfur abundances (≤0.18 wt%; Fig. V-4). It is very unlikely that sulfide with low $\delta^{34}S$ values is exported from the system as reduced inorganic phases (Johnson et al., 2014), although it is possible but speculative that product H_2S has degassed into the atmosphere. The observations admit a relatively small amount of SO_4^{2-} reduction, as discussed below, but not at the scale of consumption or the magnitude of fractionation required to increase mainstem $\delta^{34}S_{SO4}$ values by 40‰. Overall, our observations of $\delta^{34}S_{sediment}$ and the required magnitude of SO_4^{2-} reduction indicate that biological processes are not responsible for the increase in $\delta^{18}O_{SO4}$ or $\delta^{34}S_{SO4}$ and that elevated $\delta^{18}O_{SO4\text{-}H2O}$ values instead reflect dissolution of high-$\delta^{18}O_{SO4}$ evaporites with low Cl^-/SO_4^{2-} ratios.

Input of evaporite SO_4^{2-} must be accounted for when using river chemistry to quantify the amount of sulfide oxidation and the impact of chemical weathering on climate. However, only a subset of collected samples had sufficient SO_4^{2-} for measurement of $\delta^{18}O_{SO4}$. To constrain the contribution of evaporites in other samples, we used the set of samples with $\delta^{18}O_{SO4}$ measurements to constrain the $\delta^{34}S$ of the sulfide oxidation end-member (Kemeny et al., 2021a; Relph et al., 2021) and then used $\delta^{34}S_{SO4}$ measurements in the other samples to distinguish SO_4^{2-} derived from sulfide oxidation and evaporite dissolution. The range of sulfide $\delta^{34}S$ values was calculated using a Monte Carlo binary mixing model (Table V-1) that accounted for possible $\delta^{18}O_{O2}$, $\varepsilon_{SO4\text{-}H2O}$ and $\varepsilon_{SO4\text{-}O2}$ values (Relph et al., 2021). Our mixing model constrained the $\delta^{34}S_{SO4}$ produced through sulfide oxidation between -18.6‰ and -3.3‰ in 90% of simulations for mainstem samples. In

headwater samples, which had lower $\delta^{34}S_{SO4}$ and higher $\delta^{18}O_{SO4}$ values, sulfide $\delta^{34}S$ was constrained between -39.4‰ and -12.8‰ in 90% of simulations. For the Monte Carlo inversion conducted with MEANDIR, we assumed that SO_4^{2-} derived from sulfide oxidation had $\delta^{34}S_{SO4}$ values between -25‰ and -5‰ (Table V-2). These ranges reflect the net composition of all weathering sulfide and need not reflect the mean $^{34}S/^{32}S$ ratio of any particular sulfide-bearing lithological unit.

V.5.2: Sulfur cycling in the Koyukuk River catchment

Values of $\delta^{34}S_{SO4}$ in mainstem samples were consistent with mixing between the Middle Fork headwater sample and precipitation (Fig. V-5A). However, the $\delta^{34}S_{SO4}$ values of slough samples were higher than expected based on Cl^-/SO_4^{2-} ratios and the $\delta^{34}S_{SO4}$ values of pore fluid were lower than expected based on Cl^-/SO_4^{2-} ratios (Fig. V-5A). We attributed these observations to a combination of mixing and biological processing. Mixing between the mainstem river and precipitation would generate large changes in Cl^-/SO_4^{2-} but only minor changes in $\delta^{34}S_{SO4}$. For example, sourcing 2% of SO_4^{2-} from precipitation would modify Cl^-/SO_4^{2-} by nearly an order of magnitude from the mainstem ratio while the shift in $\delta^{34}S_{SO4}$ would be within analytical uncertainty. Conversely, partial consumption of SO_4^{2-} through a fractionating process could modify $\delta^{34}S_{SO4}$ values while only minimally impacting the Cl^-/SO_4^{2-} ratio relative to the large range of our observations. The products of such sulfate reduction would likely be depleted in ^{34}S relative to river water, potentially consistent with our observation that $\delta^{34}S_{sediment}$ values were comparable to mainstem $\delta^{34}S_{SO4}$ values (Fig. V-4).

The relatively minor sulfur isotopic offset between slough and mainstem samples suggests assimilatory SO_4^{2-} reduction, which has only a minor isotopic fractionation, rather than the highly fractionating process of dissimilatory microbial SO_4^{2-} reduction (Trust and Fry, 1992; Sim et al., 2011). Assimilatory SO_4^{2-} reduction in plants has a fractionation of approximately 1.5‰, albeit with substantial variability, and with additional isotopic variation among individual metabolites (Trust and Fry, 1992; Tcherkez and Tea, 2013). In addition to the minor isotopic distinction, modest amounts of assimilatory SO_4^{2-} reduction in the sloughs are supported by observations of organic sulfur phases within both floodplain sediment and suspended sediment (Fig. V-6). Conversely, modest amount of dissimilatory SO_4^{2-} reduction are suggested by the observation that slough samples with elevated $\delta^{34}S_{SO4}$ values also have lower $\delta^{13}C_{DIC}$ values and reduced SO_4^{2-}/DIC ratios (Fig. V-7). For either assimilatory or dissimilatory SO_4^{2-} reduction, SO_4^{2-} removal would generate only minor changes in Cl^-/SO_4^{2-} relative to the three orders of magnitude that we observed for this ratio. The intermediate Cl^-/SO_4^{2-} and $\delta^{34}S_{SO4}$ values of the slough samples were thus interpreted to result both from minor mixing of the mainstem river with precipitation and some combination of both assimilatory and dissimilatory biological SO_4^{2-} reduction.

Opposite the slough samples, pore fluid $\delta^{34}S_{SO4}$ values tended to be lower than expected from Cl^-/SO_4^{2-} ratios. These low values likely also result from biological sulfate reduction in the floodplain but reflect the product sulfur rather than the reactant SO_4^{2-}. That is, low pore fluid $\delta^{34}S_{SO4}$ values were interpreted to reflect that the measured pore fluid SO_4^{2-} was the oxidized product of either sulfide formed through dissimilatory SO_4^{2-} reduction or organic sulfur produced during assimilatory SO_4^{2-} reduction.

Mixing and sulfate reduction, while consistent with observations of $\delta^{34}S_{SO4}$ and Cl^-/SO_4^{2-}, are insufficient to explain relationships between $\delta^{34}S_{SO4}$ and $(Ca^{2+}+Mg^{2+})/SO_4^{2-}$ (Fig. V-5B). Samples from both sloughs and pore fluids have Ca^{2+}/SO_4^{2-} and Mg^{2+}/SO_4^{2-} ratios exceeding both mainstem and precipitation samples and, because the degree of SO_4^{2-} reduction required to reach these values is unreasonable, strongly suggest another source of alkaline cations. This source is unlikely to be evaporite dissolution, which has $(Ca^{2+}+Mg^{2+})/SO_4^{2-} = 1$. Rather, the observations were interpreted as reflecting the input of carbonate and silicate weathering products, the former of which is also constrained by the relationship of $\delta^{13}C_{DIC}$ to $(Ca^{2+}+Mg^{2+})/DIC$ (Fig. V-7).

V.5.3: Koyukuk River weathering and the global carbon cycle

The MEANDIR model quantified the relative amount of carbonate weathering, silicate weathering, sulfide oxidation, and organic carbon oxidation in mainstem samples, slough samples, and a single pore fluid sample (Fig. V-8). The inversion found higher median carbonate weathering fractions and lower median sulfide oxidation fractions in slough samples than in mainstem samples, consistent with the former having higher $Ca^{2+}/\Sigma^{\pm}$ and lower $SO_4^{2-}/\Sigma^{\pm}$ ratios (Figs. V-2C and V-8A). When only considering R and Z, the higher R and lower Z values of slough samples resulted in higher $\Delta ALK/\Delta DIC$ ratios than in mainstem samples. Following the framework of Torres et al. (2016), the mainstem samples represented weathering regimes associated with short-term pCO_2 decrease but pCO_2 increase over timescales longer than that of marine carbonate compensation. However, slough samples also had higher C values than mainstem samples, consistent with their lower SO_4^{2-}/DIC ratios and $\delta^{13}C_{DIC}$ values (Fig. V-8B; Kemeny and Torres, 2021).

Notably, incorporating C into the calculation of ΔALK/ΔDIC implicitly categorizes C_{org} oxidation as a new flux of DIC to the ocean-atmosphere system and does not account for the component of C_{org} oxidation returning DIC that was only recently fixed from atmospheric CO_2. When accounting for R, Z, and C, the ALK effect of sulfide oxidation in the mainstem samples and DIC effect of organic carbon oxidation in the slough samples resulted in both sample types having net ΔALK/ΔDIC weathering ratios near 1. Similar results, although shifted to slightly lower ΔALK/ΔDIC ratios, were found in the inversion scenario accounting for CO_2 degassing (Fig. V-S9).

There is important timescale-dependent complexity in the interpretation of our result that the ΔALK/ΔDIC ratio of weathering in the Koyukuk River is approximately 1. Foremost, we reiterate that this value arises only when C_{org} oxidation is considered a net source of DIC to the ocean-atmosphere system. Within the modern carbon cycle, atmospheric CO_2 is insensitive to equal changes in ALK and DIC. As face value, an ΔALK/ΔDIC weathering ratio of 1 thus suggests that lithologic and oxidative weathering in the Koyukuk River balance to result in weathering that does not modify atmospheric pCO_2. In detail, however, this result requires that the age of the C_{org} being oxidized exceeds the timescale associated with change in the marine inventory of DIC. Moreover, the inversion-constrained ΔALK/ΔDIC ratio applies only to the weathering system and lacks context from the broader global carbon cycle, which also responds to the longer-term dynamics regulating the input and output of SO_4^{2-} and C_{org} to and from the floodplain and marine sediment. For example, if the sulfur cycle were in steady-state such that sedimentary SO_4^{2-} reduction balanced terrestrial sulfide oxidation, then sulfide oxidation in the Koyukuk River would not be impacting pCO_2 in a net sense. Overall, given that

much of the DOC in the Koyukuk River appears modern, the inversion-constrained values of C may only be relevant over timescales shorter than the centennial storage time of organic matter with the floodplain. Although this timescale is relevant for considering human adaptation to warming, it is much shorter than the timescales commonly associated with the geologic carbon cycle. Furthermore, on these shorter timescales, the dynamics regulating CO_2 fluxes relate more to degassing across the river-atmosphere boundary than to changes in marine ALK and DIC.

V.5.4: Temporal trends in the Koyukuk River and Yukon River

V.5.4.1: The Koyukuk River

Comparison of our 2018 observations with prior measurements suggests increases through time in the concentration of SO_4^{2-}, Ca^{2+}, and Mg^{2+} within the Koyukuk River (Fig. V-9; Fig. V-S10). One explanation for these trends is that the degradation of permafrost is exposing previously frozen sulfide for oxidative weathering; if correct, these dynamics suggest that sulfide oxidation may be a positive feedback on modern climate change (Toohey et al., 2016; Zolkos et al., 2018). However, an alternative interpretation is that local mining activities have increased since the 1950s, driving exposure of lithologic sulfides. In either case, the observed increases in sulfide oxidation and SO_4^{2-}/Σ^+ suggest an anthropogenic influence on the carbon fluxes of the Koyukuk River catchment.

V.5.4.2: The Yukon River

Observations of discharge and major ion chemistry in the Yukon River at Pilot, Stevens Village, and Eagle, as well as the Tanana River at Nenana and the Porcupine River

near Fort Yukon (Fig. V-1A), show both seasonal and long-term trends (Fig. V-10; Figs. V-S11 to V-S16; Keller et al., 2007, 2010). The seasonal pattern appears to span three phases. First, during the winter months of February, March, and April, frozen sediment presents a mostly impermeable barrier to groundwater flow and the system is characterized by low discharge, low SO_4^{2-}/Σ^+ ratios, and moderate Ca^{2+}/Σ^+ and Mg^{2+}/Σ^+ ratios (Fig. V-11A). Discharge rises rapidly with the spring in May and June, resulting in lower Ca^{2+}, Mg^{2+}, and SO_4^{2-} concentrations but higher ratios of Ca^{2+}/Σ^+ and SO_4^{2-}/Σ^+. As previously suggested, these springtime waters are likely constrained to surface flow paths with short residence times that favor chemical reactions with rapid kinetics such as carbonate weathering, sulfide oxidation, and gypsum dissolution (Fig. V-11B). Although we cannot currently distinguish between the sources of Ca^{2+} and SO_4^{2-} to the Yukon at Pilot during June, future measurements of $\delta^{34}S_{SO4}$ and $\delta^{18}O_{SO4}$ could shed light into which chemical weathering reactions are sourcing SO_4^{2-}. During the late-summer summer months of August and September, discharge is reduced to a sustained intermediate value (Fig. V-10A). The concentrations of Ca^{2+}, Mg^{2+}, and SO_4^{2-} are higher than in May and June, with Mg^{2+}/Σ^+ exceeding Ca^{2+}/Σ^+ and SO_4^{2-}/Σ^+ attaining higher values. Despite the higher discharge, SO_4^{2-} concentrations during this late-summer phase are comparable to, or even elevated from, SO_4^{2-} concentrations in the winter months. We interpreted these observations to reflect the propagation of the seasonal thaw front into sediment over the course of the summer and associated exposure of phases like sulfide, dolomite, and Mg silicate to weathering acids and oxidants (Fig. V-11C). This three-phase cycle, including observations of late-summer SO_4^{2-} concentrations comparable to wintertime measurements

and a mid-summer shift from high Ca^{2+}/Σ^{+} to high Mg^{2+}/Σ^{+} ratios, was seen at multiple timeseries site (Figs. V-1; V-S12 to V-S16).

The long-term trends in discharge, Ca^{2+}/Σ^{+}, Mg^{2+}/Σ^{+}, and SO_4^{2-}/Σ^{+} are not as well-constrained. Although the trends are clear in observations from Pilot Station, trends at Nenana and Eagle are nebulous and observations from Stevens Village and near Fort Yukon only cover five years. Regardless, we speculate that the long-term trends at Pilot Station potentially reflect decreases in the impermeable permafrost barriers that inhibit subsurface flow (Fig. V-11D, E; Toohey et al., 2016; Walvoord and Kurylyk, 2016). As these barriers degrade due to anthropogenic climate change, wintertime discharge increases (Walvoord and Striegl, 2007). Moreover, as was seen in the late-summer component of the seasonal cycle and in the time-series data from the Koyukuk, the direction of the long-term trend in the Yukon River at Pilot Station is towards increased Mg^{2+}/Σ^{+} and SO_4^{2-}/Σ^{+} ratios.

V.6: Conclusions

Permafrost landscapes include large reservoirs of organic carbon, sulfide, and silicate and carbonate minerals susceptible to rapid oxidation and weathering under a warming climate. While prior work has focused on quantifying oxidation of thawing organic matter, changes in the production and consumption of dissolved inorganic carbon and alkalinity through lithologic weathering and sulfide oxidation may also contribute to the carbon-climate feedbacks associated with melting landscapes. Here we report geochemical observations of water and sediment samples collected from the Koyukuk River and its floodplain, which is underlain by discontinuous permafrost, in central Alaska. The data indicated that evaporite dissolution sourced approximately 2/3 of SO_4^{2-} in headwaters and mainstem samples and that assimilatory and dissimilatory biological sulfate reduction within the floodplain modestly altered $\delta^{34}S_{SO4}$ values. A river inversion model revealed subequal weathering fluxes of alkalinity and dissolved inorganic carbon, with timescale-dependent implications. Comparison with prior data suggests that the absolute and relative importance of sulfide oxidation is increasing through time, attributed to either permafrost degradation or anthropogenic activities.

V.7: Acknowledgments

PCK is supported by the Cohan-Jacobs and Stein Families Fellowship from the Fannie and John Hertz Foundation. This research was conducted with government support under and awarded by DoD, Air Force Office of Scientific Research, National Defense Science and Engineering Graduate (NDSEG) Fellowship, 32 CFR 168a (PCK and MD). Use of the Stanford Synchrotron Radiation Lightsource, SLAC National Accelerator Laboratory, is supported under Contract No. DE-AC02-76SF00515 by the U.S. Department of Energy, Office of Science, Office of Basic Energy Sciences, and we acknowledge the Polar Geospatial Center for providing a digital elevation model through NSF-OPP awards 1043681, 1559691, and 1542736. We gratefully thank the Huslia Tribal Council for permitting field access, S. Huffman, A. Attla, and V. Umphenour for assistance in the field, A. Sessions, F. Wu, and A. Phillips for assistance with EA-IRMS measurements, E. Eitel, S. Bone, N. Edwards, C. Roach, and J. Richardson for assistance with synchrotron measurements, G. Lopez for assistance with MC-ICP-MS measurements, X. Zhang and D. Dettman for measuring sulfate oxygen isotope ratios, and the AMS facility at the University of Arizona for measuring dissolved organic carbon isotope ratios.

V.8: Figures

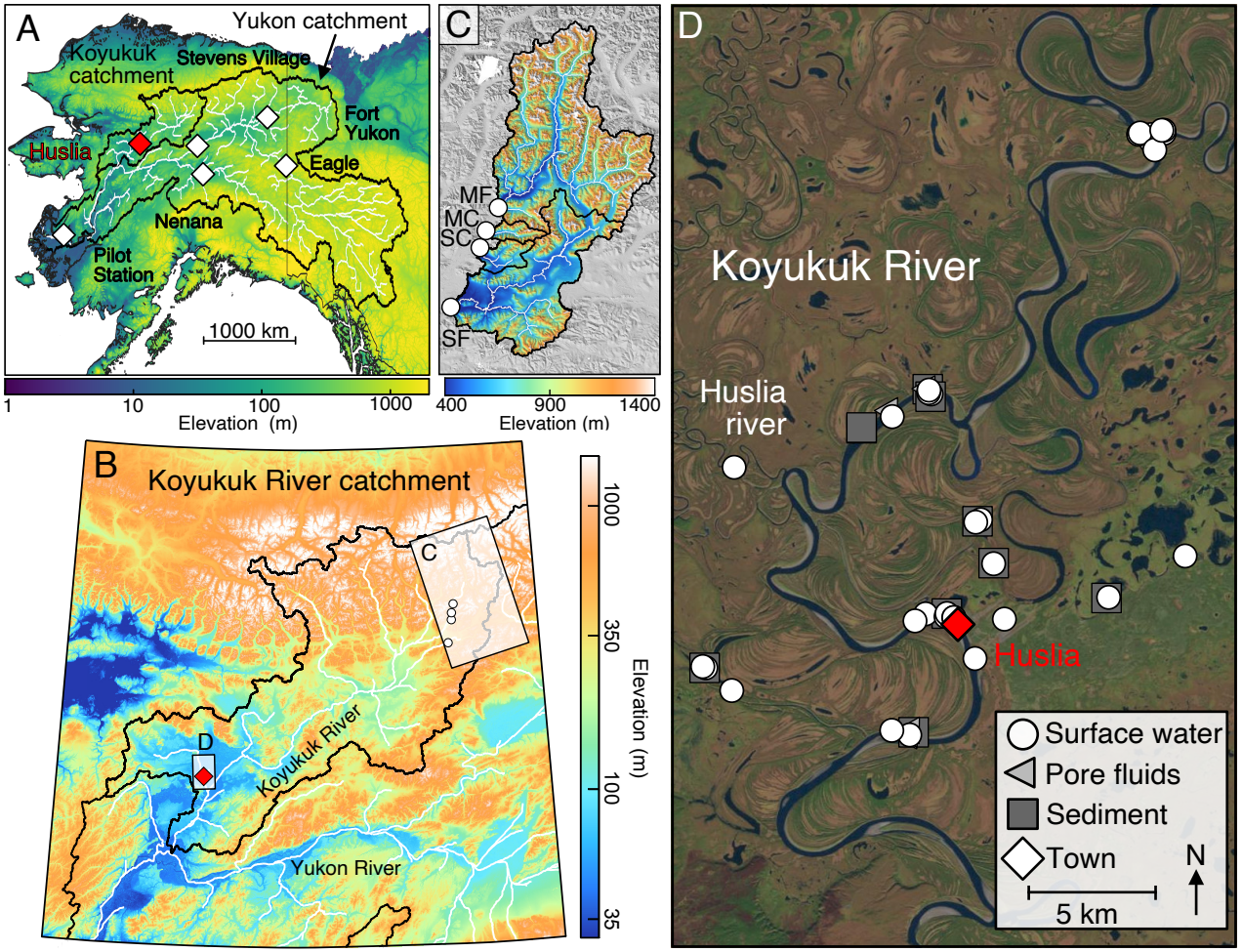

Fig. V-1: Site context and sampling map. (A) The Koyukuk River is a tributary to the Yukon River within central Alaska. The town of Huslia (red diamond) is indicated, as are five USGS monitoring sites (Pilot Station, Nenana, Stevens Village, Eagle, and near Fort Yukon; white diamonds), and river catchment boundaries (black lines). (B) Samples of water and sediment were collected in 2018 from the area surrounding Huslia. Additionally, four water samples were collected from the Koyukuk headwaters in 2019. (C) The four headwater samples (circles) and their catchments: Middle Fork (MF), Marion Creek (MC), Slate Creek (SC), and South Fork (SF). (D) Water sample, pore fluid (triangles), and sediment sample (squares) locations near Hulsia. Sediment samples, described thoroughly in Douglas et al. (2022), include both permafrost and non-permafrost deposits. Elevation data are (A) ASTER GDEM V2 (EPSG: 4087), (B) USGS NED Digital Surface Model (EPSG: 3338), and (C) Arctic DEM from the Polar Geospatial Center (EPSG: 3413). Panel (D) is a Global Land Survey image (EPSG: 32605).

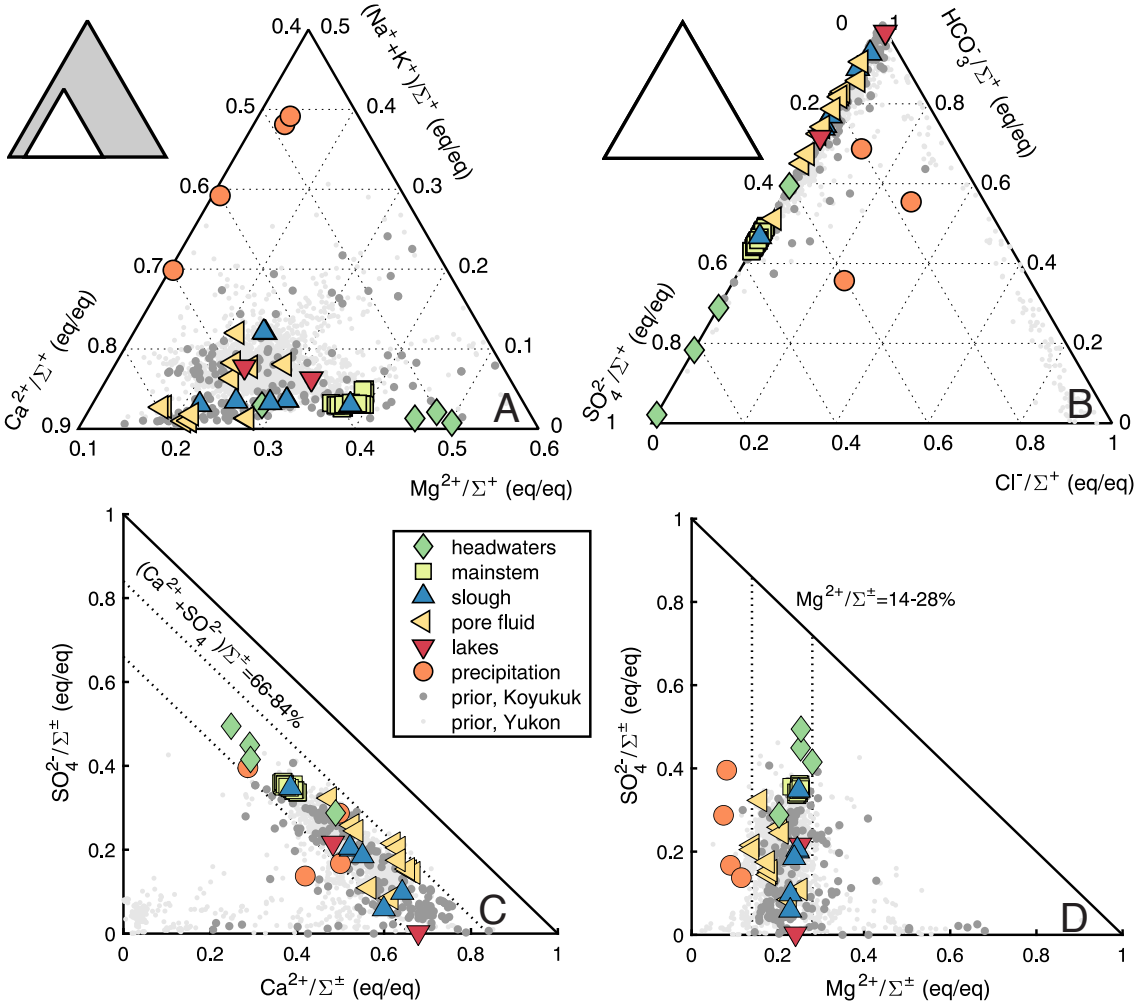

Fig. V-2: Major ion chemistry. (A) Cation ternary diagram of Ca^{2+}-Mg^{2+}-Na^{+}+K^{+}. The plotted triangle is a subset of the full space, as indicated in the top-left schematic (grey triangle is the full domain and white triangle is the plotted space). The cation Ca^{2+} dominates positive charge in the Koyukuk River samples, Mg^{2+} has a substantial secondary role, and Na^{+} and K^{+} are scarce. These relative cation abundances agree with prior observations from throughout the Koyukuk catchment (dark grey circles) and the Yukon River Basin (light grey circles), although with slightly lower $(Na^{+}+K^{+})/\Sigma^{+}$ values than the latter. (B) Anion ternary diagram of SO_4^{2-}-Cl^{-}-HCO_3^{-} for the full domain. Water samples span between dominance of SO_4^{2-} and HCO_3^{-}, while the only samples with appreciable Cl^{-}/Σ^{+} are precipitation. River water samples plotting near $Cl^{-}/\Sigma^{+}\sim1$ are from near the Alaskan coast and not the Koyukuk River catchment. (C) Headwater and mainstem samples have elevated $SO_4^{2-}/\Sigma^{\pm}$ and reduced $Ca^{2+}/\Sigma^{\pm}$ ratios relative to pore fluid and slough samples. (D) The ratio of $Mg^{2+}/\Sigma^{\pm}$ is relatively constant across sample types and, due to the low ratios of $Na^{+}/\Sigma^{\pm}$ and $K^{+}/\Sigma^{\pm}$, implies that changes in $Ca^{2+}/\Sigma^{\pm}$ largely compensate changes in $SO_4^{2-}/\Sigma^{\pm}$.

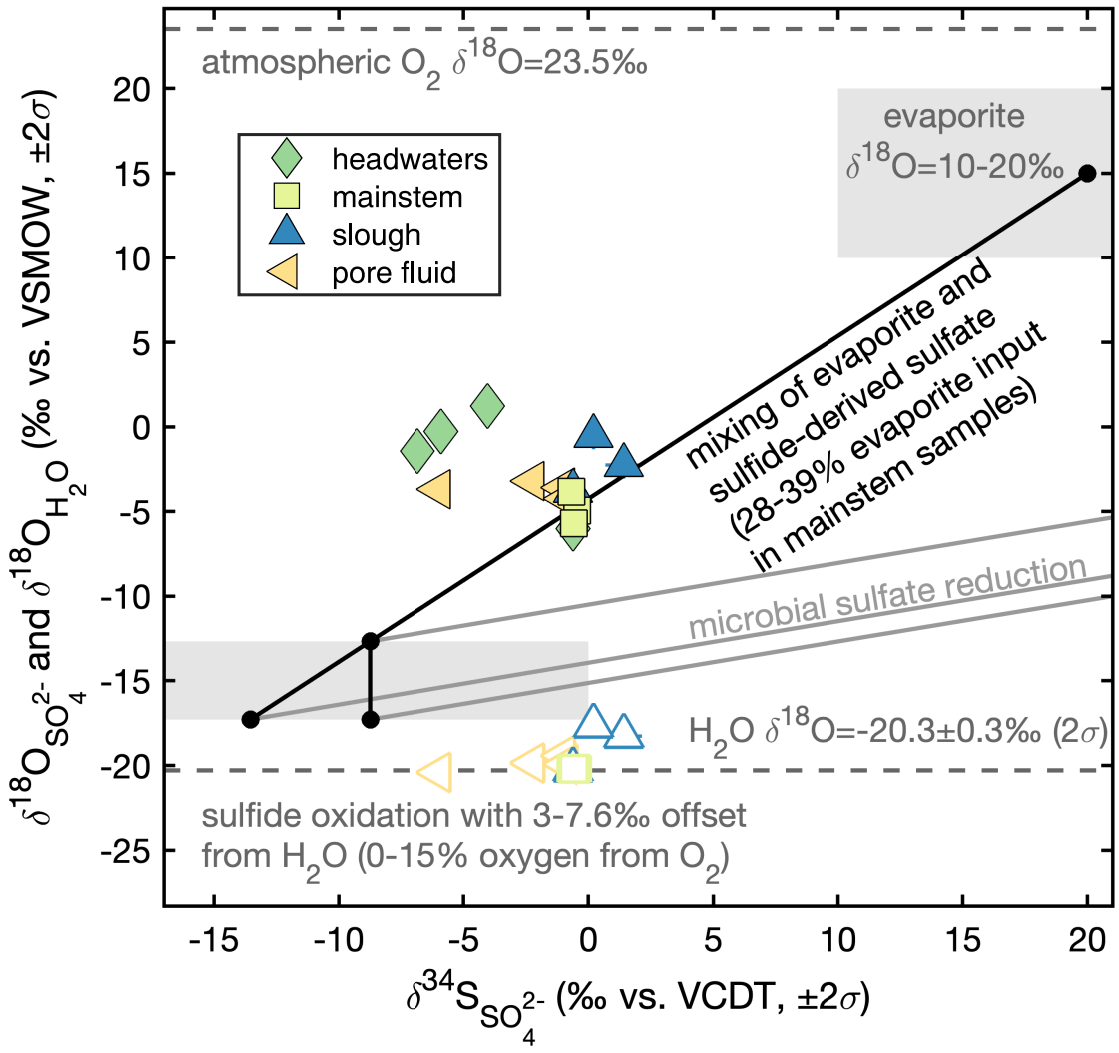

Fig. V-3: Sulfur and oxygen isotope ratios in SO_4^{2-} and H_2O. Sample $\delta^{18}O_{SO4}$ (closed symbols) and $\delta^{18}O_{H2O}$ (open symbols) against $\delta^{34}S_{SO4}$ with reference lines for mean mainstem $\delta^{18}O_{H2O}$ and atmospheric $\delta^{18}O_{O2}$. Shaded regions indicate the expected ranges for Phanerozoic evaporites (Claypool et al., 1980) and for sulfide oxidation incorporating ≤15% atmospheric O_2 when $\varepsilon_{SO4\text{-}H2O}$ = 3‰ and $\varepsilon_{SO4\text{-}O2}$ = -10‰ (Balci et al., 2007). All analyzed samples have $\delta^{18}O_{SO4\text{-}H2O}$ values substantially above expectations for sulfide oxidation alone and indicate either gypsum dissolution or fractionation through sulfate reduction. We favor the former explanation, and a Monte Carlo binary mixing model constrained the range of sulfide $\delta^{34}S$ values for each sample (Table V-1). Extremely high river water SO_4^{2-}/Cl^- ratios (Fig. V-2B) indicated that SO_4^{2-} inputs from precipitation are negligible and, for simplicity, precipitation was excluded from this figure and the binary mixing model, but is included in the full Monte Carlo inversion model (Table V-2).

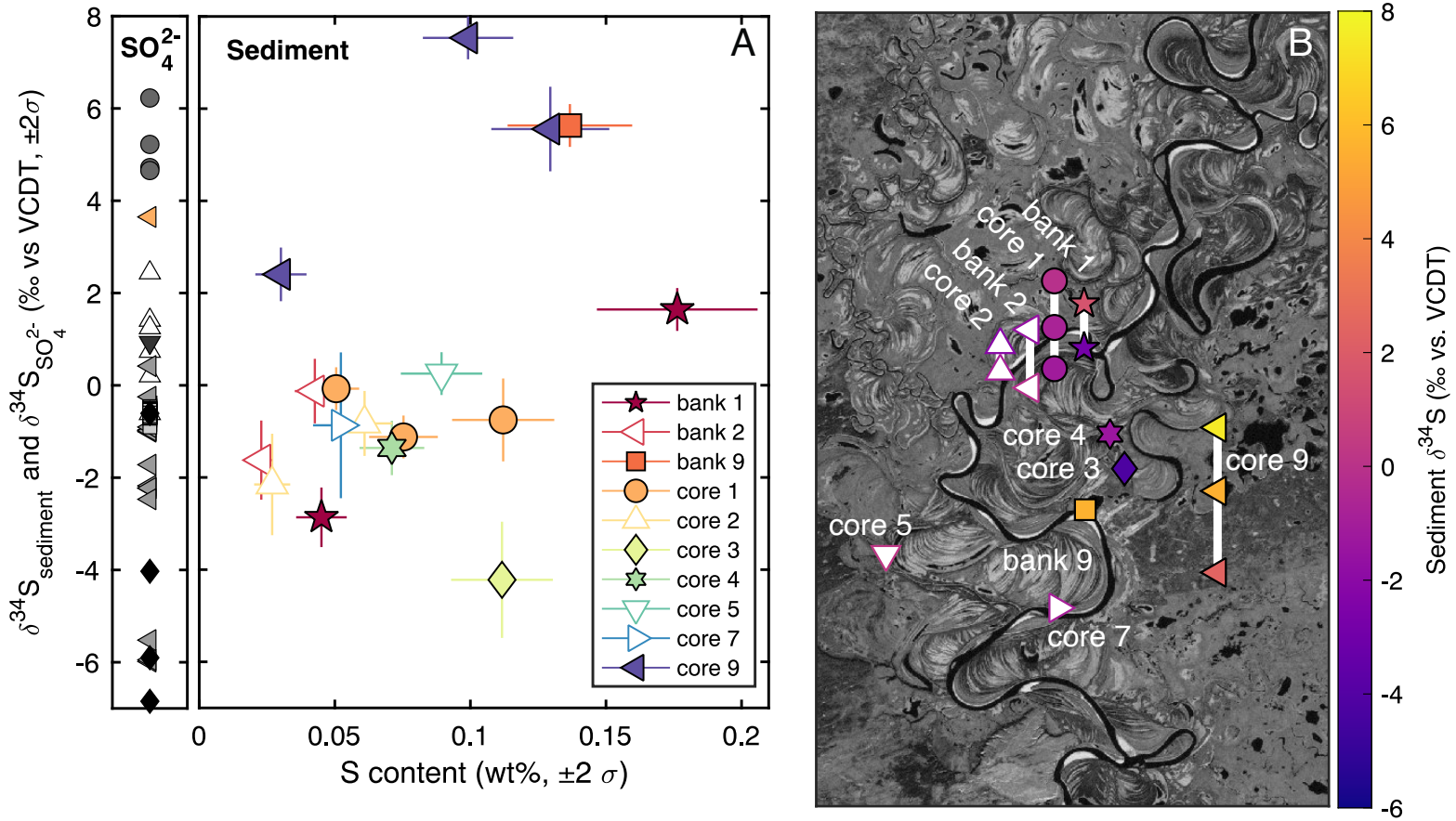

Fig. V-4: Sedimentary sulfur isotope ratios. (A) Values of $\delta^{34}S_{sediment}$ (cross plot) were comparable to river $\delta^{34}S_{SO4}$ (left stack) and are not correlated with S content or whether samples are from permafrost (closed symbols) or non-permafrost (open symbols) deposits. These moderate $\delta^{34}S_{sediment}$ values are consistent with modest amounts of sulfate reduction capable of minor modifications to $\delta^{34}S_{SO4}$ in sloughs and pore fluids but are inconsistent with massive catchment-scale sulfate reduction. (B) Sediment $\delta^{34}S$ values in geographic context (Landsat 5, 9/24/10). Samples collected from depth profiles are vertically offset proportional to collection depth and sites that would otherwise overlap are horizontally offset (see Fig. V-1D for exact sample locations). Core 9 is stratigraphically the oldest sampled deposit and has many of the highest $\delta^{34}S_{sediment}$ values.

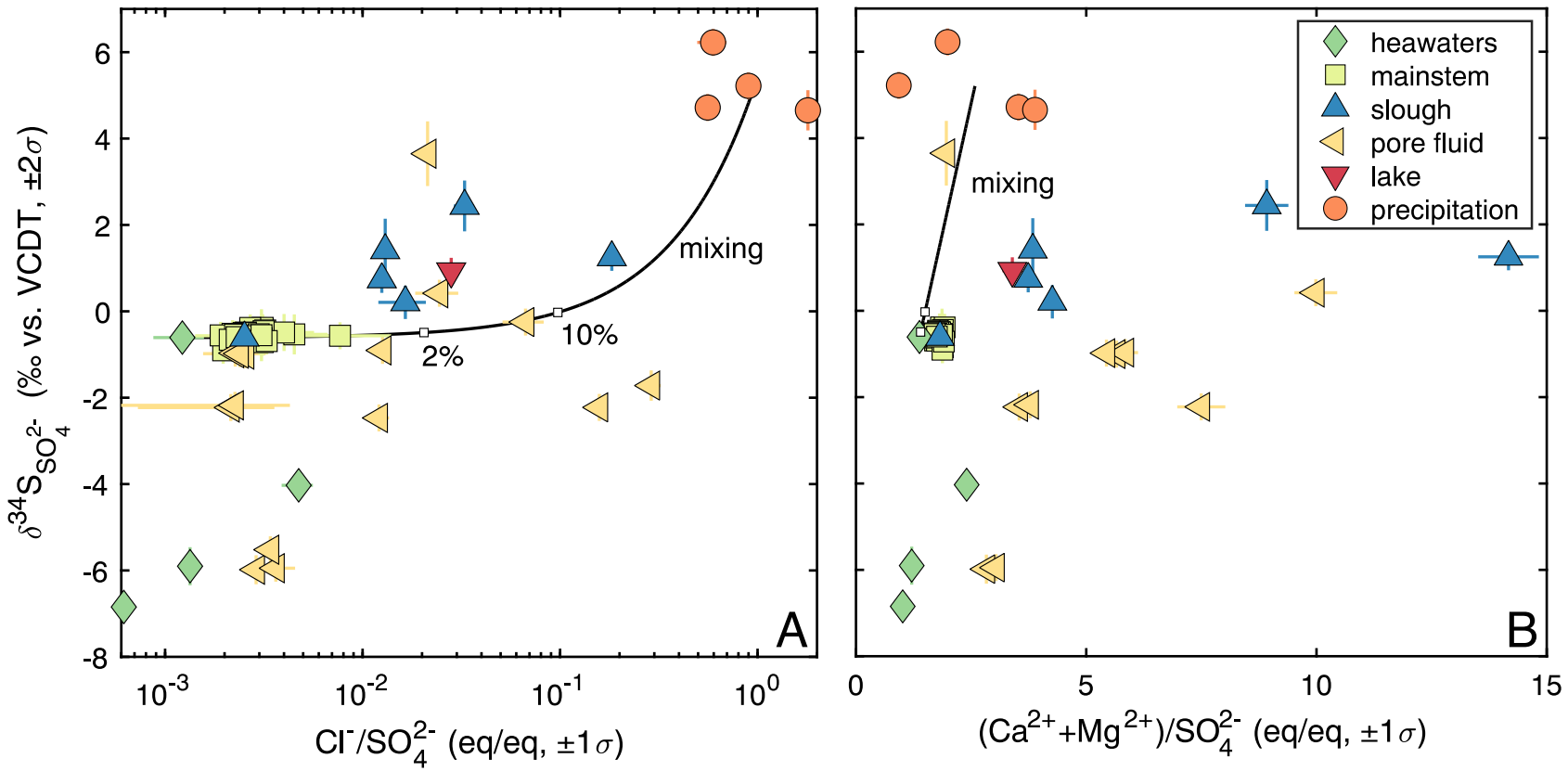

Fig. V-5: Sulfate sulfur isotope mixing diagrams. $\delta^{34}S_{SO4}$ against (A) Cl^-/SO_4^{2-} and (B) Ca^{2+}/SO_4^{2-}. The observations are consistent with a combination of mixing between the Middle Fork headwater sample and precipitation, a modest amount of sulfate reduction that increases slough $\delta^{34}S_{SO4}$ values and reduces pore fluid $\delta^{34}S_{SO4}$ values relative to the mixing curve, and the addition of Ca^{2+} and Mg^{2+} through floodplain weathering. Additional sulfur isotope mixing diagrams are consistent with the same dynamics (Fig. V-S3).

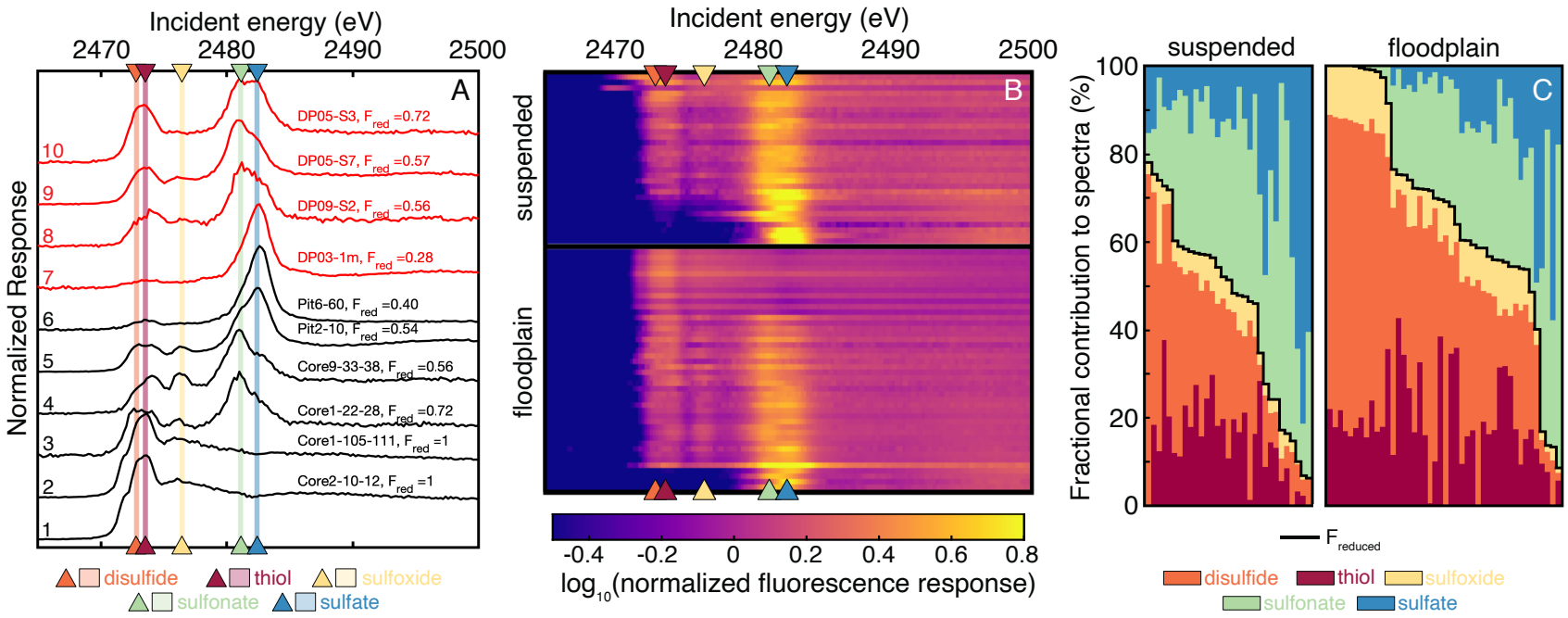

Fig. V-6: XANES results on floodplain and suspended sediment. (A) Ten example spectra showing a range of sulfur moieties in both suspended sediment (red) and floodplain sediment (black). Vertical colored bars indicate characteristic spectral features of disulfide, thiol, sulfoxide, sulfonate, and sulfate moieties. F_{red} is the normalized sum of fractional contributions from disulfide, thiol, and sulfoxide moieties. (B) Waterfall plot of all spectra, where color is the intensity of the fluorescence response. (C) Fractional contributions of sulfur moieties to measured spectra. Samples of both floodplain and suspended sediment contained a diversity of redox phases. In (B) and (C) spectra are arranged within sample types in order of F_{red} value.

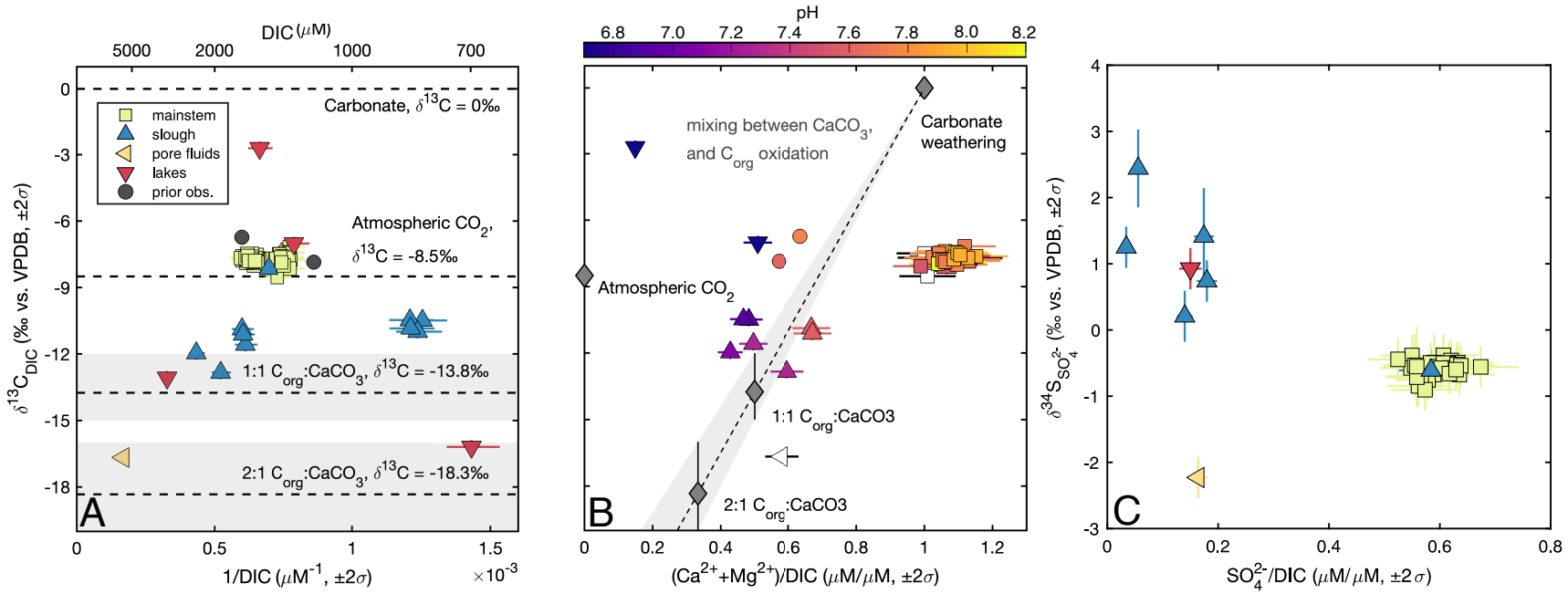

Fig. V-7: DIC concentrations and $^{13}C/^{12}C$ isotope ratios. (A) $\delta^{13}C_{DIC}$ against 1/DIC. Reference lines are given for the $\delta^{13}C_{DIC}$ that would be produced from 1:1 and 2:1 combinations of organic carbon oxidation and $CaCO_3$ weathering, where $\delta^{13}C_{sediment}$ and $\delta^{13}C_{DOC}$ constrained the former and the latter was assumed to equal 0‰. Mainstem samples from the Koyukuk cluster near -7.7‰, as do two prior observations, which is slightly elevated from the -8.5‰ value of $\delta^{13}C_{CO2}$ in 2018 (Keeling et al., 2017). Values of $\delta^{13}C$ in mainstem samples are higher than in the sloughs and suggest a greater role for carbonate weathering and sulfide oxidation. The sloughs tended to have higher DIC concentrations than the mainstem, consistent with relatively more C_{org} oxidation, while lake samples exhibited a wide range of both DIC abundances and $\delta^{13}C_{DIC}$ values. (B) $\delta^{13}C_{DIC}$ against $(Ca^{2+}+Mg^{2+})/DIC$. The mainstem samples plot off the mixing line between carbonate weathering and C_{org} oxidation. This observation implies either inputs of Ca^{2+} and Mg^{2+} from evaporite dissolution or silicate weathering or that a process, such as CO_2 degassing, has increased $(Ca^{2+}+Mg^{2+})/DIC$. The mainstem samples also tend to have higher pH values than the slough samples. The slough data mostly fall near the mixing line. (C) Mainstem samples have lower $\delta^{34}S_{SO4}$ and higher SO_4^{2-}/DIC than sloughs, consistent with weathering of carbonate and sulfide oxidation. Sloughs samples had lower SO_4^{2-}/DIC ratios and higher $\delta^{34}S_{SO4}$ values, consistent with more C_{org} oxidation than in the mainstem samples and SO_4^{2-} reduction.

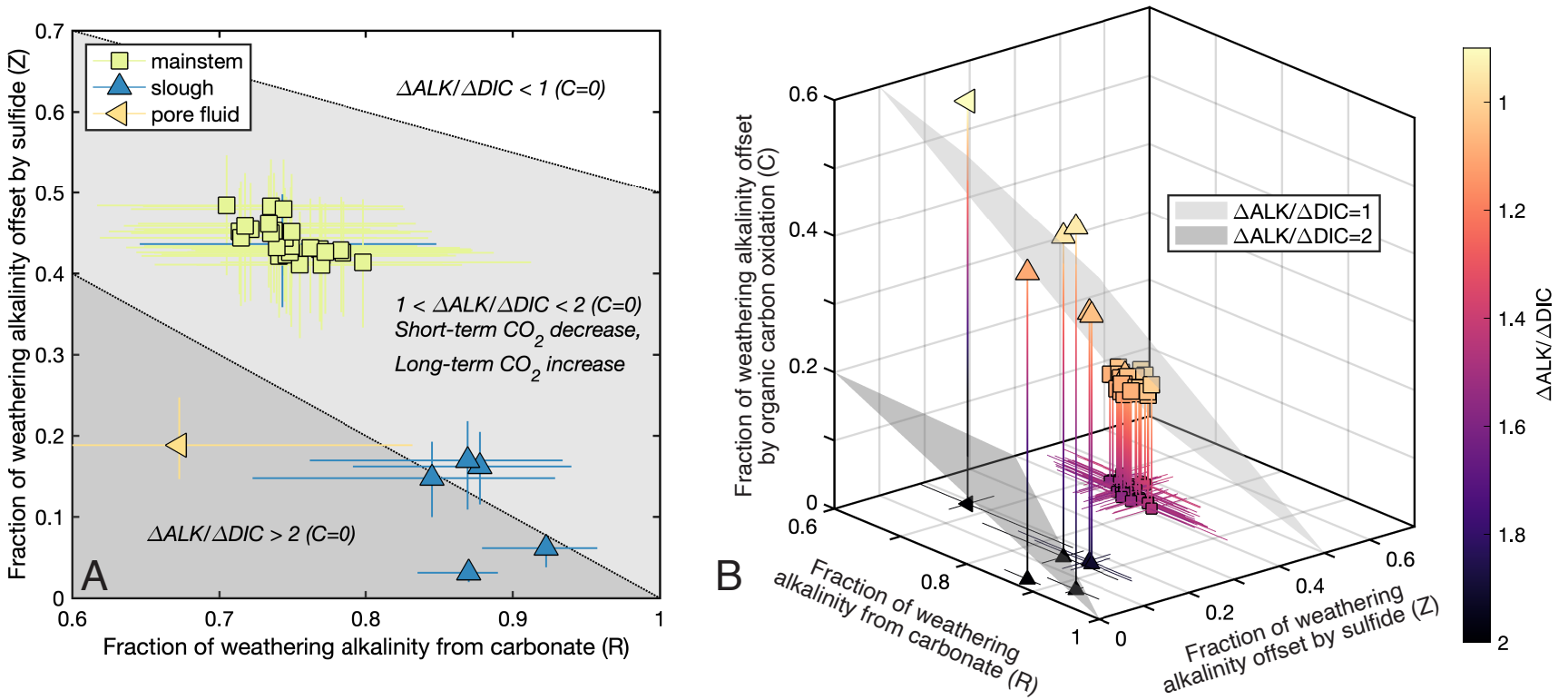

Fig. V-8: Carbon cycle impacts of weathering in the Koyukuk. (A) Fraction of weathering alkalinity offset by sulfide oxidation (Z) against the fraction of alkalinity from carbonate weathering (R) with reference lines for ΔALK/ΔDIC = 1 and ΔALK/ΔDIC = 2 when C = 0. Slough samples have higher R and lower Z values than mainstem samples. (B) The fraction of weathering alkalinity offset by organic carbon oxidation (C) against R and Z. Although mainstem samples have lower ΔALK/ΔDIC ratios when not considering organic carbon oxidation, they have higher ΔALK/ΔDIC ratios than the slough samples after accounting for non-zero C values. Overall, inversion results show that ΔALK/ΔDIC is relatively close to the 1:1 plane for samples from both the mainstem and the sloughs, corresponding to weathering that does not impact pCO_2 on instantaneous timescales. Inversion results are relatively similar when including degassing in the inversion (Figs. V-S7, S8, and S9).

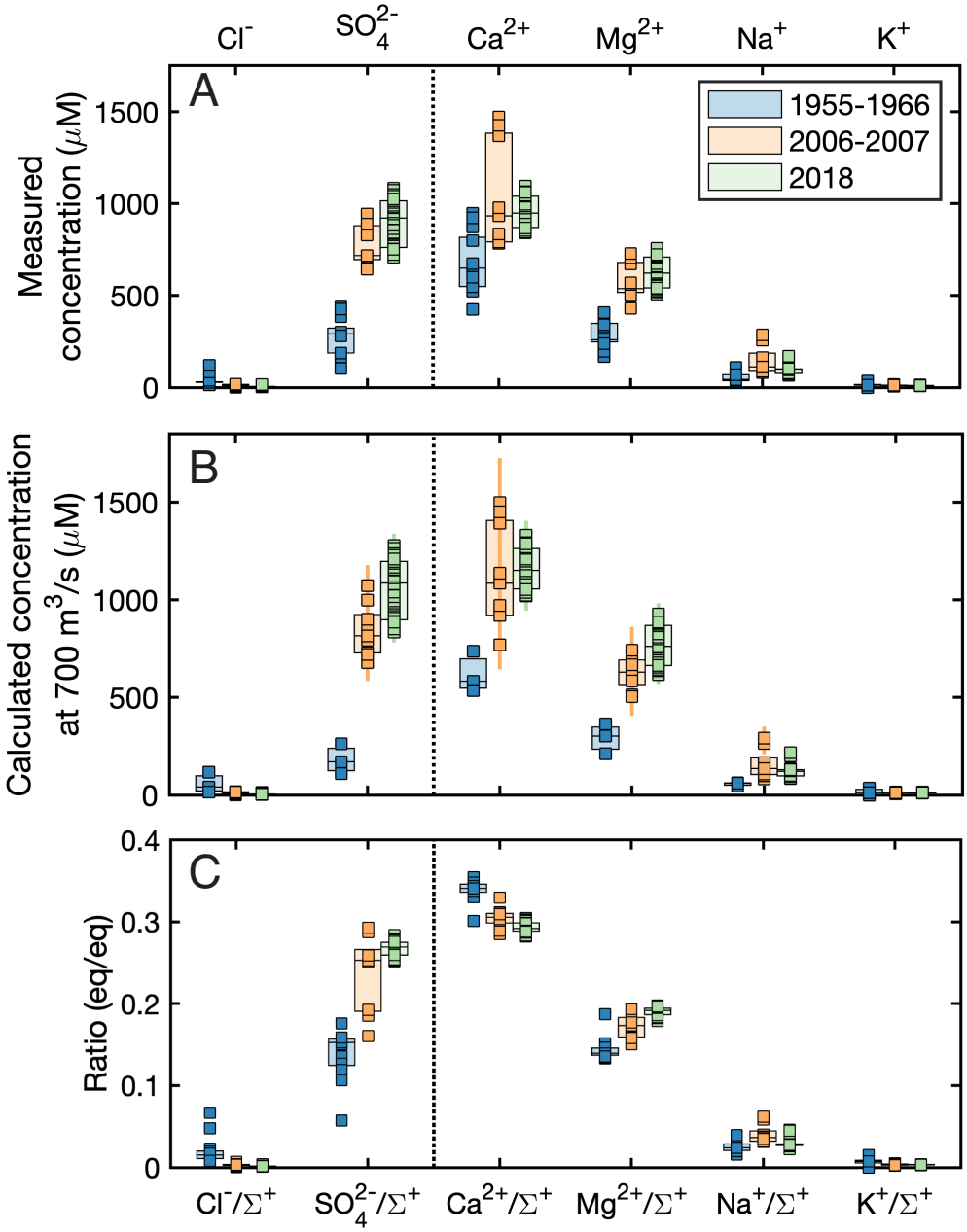

Fig. V-9: Temporal changes in the major ion chemistry of the Koyukuk River. Observations are USGS data from Hughes (blue), two USGS sites on the Koyukuk between Huslia and Hughes (red), and the 2018 Koyukuk River data collected near Huslia (green). All plotted data was collected in June, July, or August. (A) Measured concentrations and (B) concentrations scaled to 700 m^3/s. For the 2006-2007 data, which do not have discharge measurements, scaling to 700 m^3/s was done using the average monthly discharge at Hughes. For either raw or scaled observations, data from 2006-2007 and 2018 have higher SO_4^{2-} concentrations than observations from 1955-1996, and the data suggest roughly similar increases in Ca^{2+} and Mg^{2+} concentrations. (C) Elemental ratios show increases in SO_4^{2-}/Σ^+ and Mg^{2+}/Σ^+ through time, as well as decreases in Ca^{2+}/Σ^+. Similar trends are observed for the Yukon River at Pilot Station (Fig. V-10; Toohey et al., 2016) and are consistent with permafrost degradation driving enhanced sulfide oxidation and weathering.

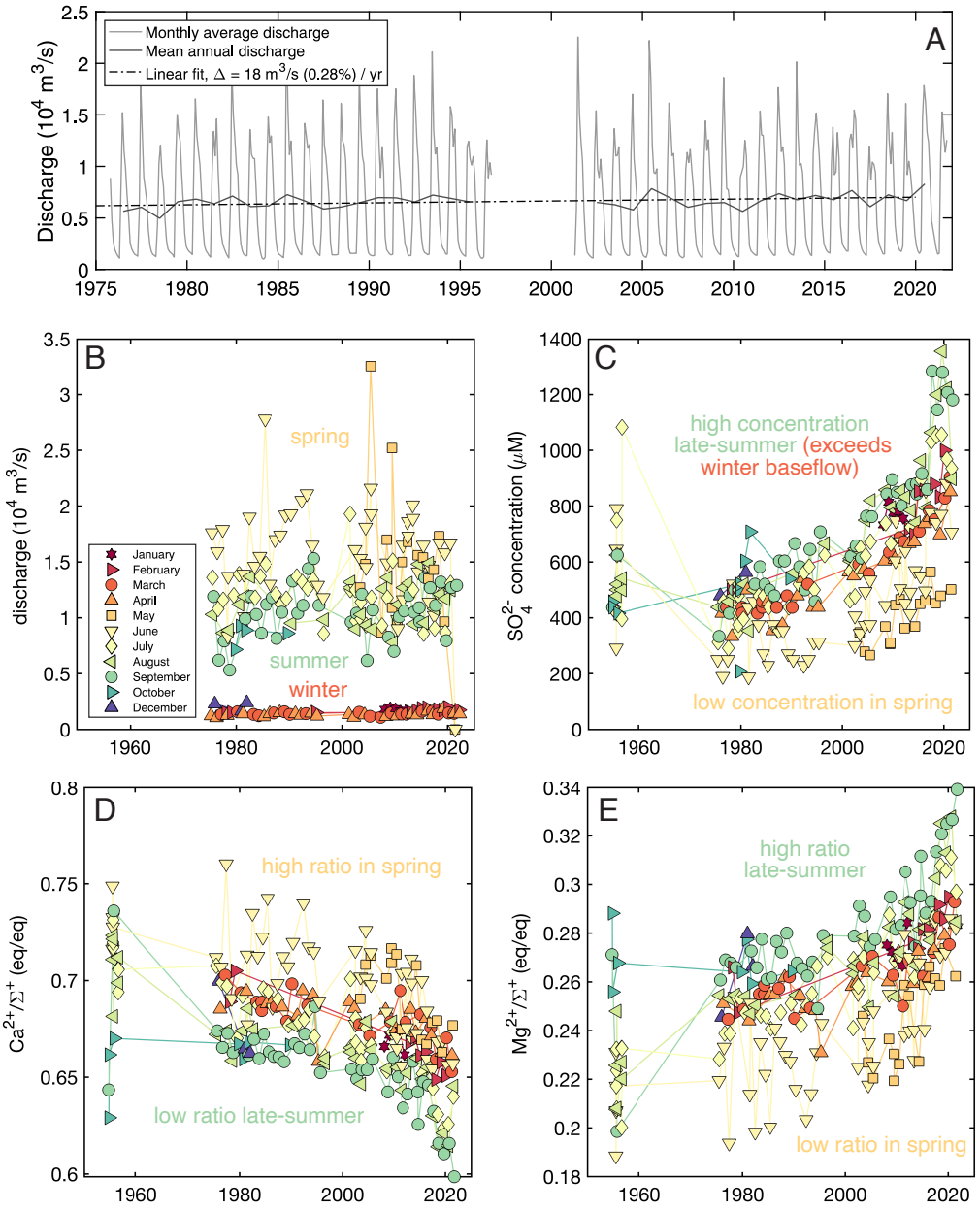

Fig. V-10: Discharge and major ion chemistry of the Yukon River at Pilot Station show seasonal and long-term signals. (A) Monthly discharge and (B) discharge during sample collection. Discharge was highest in June and then elevated for July through October before dropping to base flow, which has increased through time. (C) SO_4^{2-}, (D) Ca^{2+}/Σ^+, (E) and Mg^{2+}/Σ^+. Ca^{2+}/Σ^+ is highest during the period of elevated discharge in June and lowest during the late-summer. Mg^{2+}/Σ^+ exhibits the opposite behavior and is highest during late summer. SO_4^{2-}/Σ^+ is lowest during the winter, increases during the Spring flood, and then stays elevated for the duration of the summer months. The concentration of SO_4^{2-} is lower in June than in the winter months, but is highest in September, which suggests a source of sulfur accessed during the late summer. The dissolved chemistry data also shows long-term trends towards higher SO_4^{2-}/Σ^+, higher Mg^{2+}/Σ^+, and lower Ca^{2+}/Σ^+, which may reflect permafrost degradation altering the composition of river base flow.

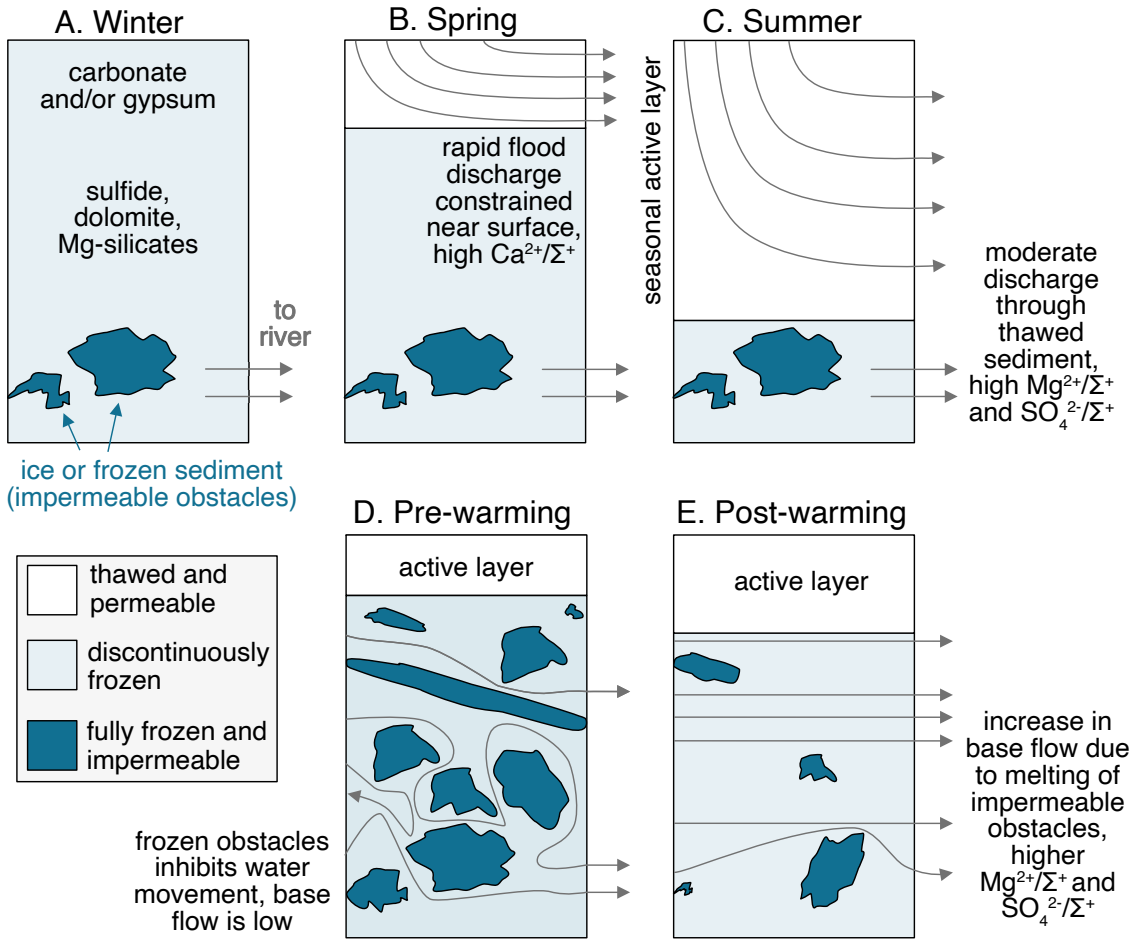

Fig. V-11: Schematic of proposed seasonal and long-term changes in discharge and major ion concentrations. (A) Base flow in permafrost landscapes is low during the winter months due to a mostly impermeable barrier of frozen sediment (Woo et al., 1986). (B) Spring flooding in May and June is focused near the thawed shallow surface. The spring flow paths have short residence times and result in lower absolute Ca^{2+}, Mg^{2+}, and SO_4^{2-} concentrations than during the winter but higher Ca^{2+}/Σ^+ and SO_4^{2-}/Σ^+ ratios. These trends suggest either gypsum dissolution, sulfide oxidation coupled with carbonate weathering, or weathering of a Ca-rich silicate lithology. (C) Flow in the late summer passes through the full thickness of the active layer. These flow paths have longer residences times and access to minerals that have already been removed from shallower layers of the profile (Keller et al., 2007; 2010), resulting in SO_4^{2-} concentrations comparable to the low-discharge winter and Mg^{2+}/Σ^+ ratios exceeding Ca^{2+}/Σ^+ ratios. (D) Prior to warming, river base flow was impeded by impermeable permafrost. (E) Base flow is now increasing under a warming climate due to the removal of the permafrost barrier and has elevated ratios of Mg^{2+}/Σ^+ and SO_4^{2-}/Σ^+. Schematic informed by Douglas et al. (2013).

V.9: Tables

Table V-1: Parameters for Monte Carlo binary mixing model. For headwater samples lacking measurements of $\delta^{18}O_{H2O}$ we used the mean and standard deviation of $\delta^{18}O_{H2O}$ in mainstem Koyukuk samples. Several parameter values are after Relph et al. (2021).

Uniform distributions		
Model parameter	Minimum	Maximum
Evaporite $\delta^{34}S$	10‰	30‰
Evaporite $\delta^{18}O$	10‰	20‰
$\delta^{18}O$ of atmospheric O_2	23.5‰	70‰
Fraction O_2-derived oxygen in SO_4^{2-}	0%	17%
$\varepsilon_{SO4\text{-}O2}$	-12.1‰	-8.1‰
$\varepsilon_{SO4\text{-}H2O}$	0‰	4‰
Normal distributions		
Model parameter	Mean	Standard deviation (1σ)
Sample $\delta^{34}S_{SO4}$	Measured	Measured
Sample $\delta^{18}O_{SO4}$	Measured	Measured
Sample $\delta^{18}O_{H2O}$	Measured	Measured

Table V-2: End-member distributions for Monte Carlo inversion model. Values are normalized to the sum of Ca^{2+}, Mg^{2+}, Na^{+}, K^{+}, SO_4^{2-}, and DIC, blank entries indicate a value of zero, and individual numbers indicate constants. All distributions are uniform. The silicate end-member represents four different end-members, each of which only sources one of either Ca^{2+}, Mg^{2+}, Na^{+}, or K^{+}, which were aggregated into a composite silicate end-member after the inversion. The degassing end-member was only included in the second scenario, where it was treated as a secondary phase that made a negative contribution to river DIC and formed with carbon isotope fractionation. The minimum and maximum contributions refer to bounds on the fractional contribution of each end-member to the normalization variable. For example, carbonate weathering was constrained to source between 0% and 100% of the normalization value, while degassing was constrained to remove no more than 20% of the normalization value. One chemical ratio for each end-member was calculated from the other ratios to ensure consistency; when an end-member had only one non-zero ratio, such as SO_4^{2-} for FeS_2 oxidation or DIC for C_{org} oxidation and CO_2 degassing, that ratio was always calculated to equal 1. See Kemeny and Torres (2021) for additional explanation and discussion of inversion parameters.

	Carbonate	**Silicate**	**Evaporite**	**Precipitation**	**FeS_2 oxidation**	**C_{org} oxidation**	**Degassing**
Ca^{2+}	calculated	calculated	calculated	calculated			
Mg^{2+}	0.00 – 0.33	calculated		0.07 – 0.11			
Na^{+}		calculated		0.12 – 0.27			
K^{+}		calculated		0.03 – 0.06			
Cl^{-}				0.10 – 0.33			
SO_4^{2-}			0.5	0.13 – 0.37	calculated (1)		
$\delta^{34}S$			10‰ – 30‰	4.5‰ – 6‰	-25‰ – -5‰		
DIC	0.33					calculated (1)	calculated (1)
$\delta^{13}C$	0‰					-30‰ – -24‰	
degassing $^{13}\varepsilon$							-15‰ – -5‰
Min. contribution	0	0	0	0	0	0	-0.20
Max. contribution	1	1	1	1	1	1	0

V.10: References

Aharon, P. and Fu, B., 2000. Microbial sulfate reduction rates and sulfur and oxygen isotope fractionations at oil and gas seeps in deepwater Gulf of Mexico. *Geochimica et Cosmochimica Acta*, 64(2), pp.233-246. https://doi.org/10.1016/S0016-7037(99)00292-6.

Balci, N., Shanks III, W.C., Mayer, B. and Mandernack, K.W., 2007. Oxygen and sulfur isotope systematics of sulfate produced by bacterial and abiotic oxidation of pyrite. *Geochimica et Cosmochimica Acta*, 71(15), pp.3796-3811. https://doi.org/10.1016/j.gca.2007.04.017.

Benner, R., Benitez-Nelson, B., Kaiser, K. and Amon, R.M., 2004. Export of young terrigenous dissolved organic carbon from rivers to the Arctic Ocean. *Geophysical Research Letters*, 31(5). https://doi.org/10.1029/2003GL019251.

Bense, V.F., Ferguson, G. and Kooi, H., 2009. Evolution of shallow groundwater flow systems in areas of degrading permafrost. *Geophysical Research Letters*, 36(22). https://doi.org/10.1029/2009GL039225.

Biskaborn, B.K., Smith, S.L., Noetzli, J., Matthes, H., Vieira, G., Streletskiy, D.A., Schoeneich, P., Romanovsky, V.E., Lewkowicz, A.G., Abramov, A. and Allard, M., 2019. Permafrost is warming at a global scale. *Nature Communications*, 10(1), pp.1-11. https://doi.org/10.1038/s41467-018-08240-4.

Bohic, S., Murphy, K., Paulus, W., Cloetens, P., Salome, M., Susini, J. and Double, K., 2008. Intracellular chemical imaging of the developmental phases of human neuromelanin using synchrotron X-ray microspectroscopy. *Analytical Chemistry*, 80(24), pp.9557-9566. https://doi.org/10.1021/ac801817k.

Brabets, T.P., Wang, B. and Meade, R.H., 2000. Environmental and hydrologic overview of the Yukon River Basin, Alaska and Canada. Water-Resources Investigations Report, 99, p.4204.

Burke, A., Present, T.M., Paris, G., Rae, E.C., Sandilands, B.H., Gaillardet, J., Peucker-Ehrenbrink, B., Fischer, W.W., McClelland, J.W., Spencer, R.G. and Voss, B.M., 2018. Sulfur isotopes in rivers: Insights into global weathering budgets, pyrite oxidation, and the modern sulfur cycle. *Earth and Planetary Science Letters*, 496, pp.168-177. https://doi.org/10.1016/j.epsl.2018.05.022.

Burt, E.I., Bill, M., Conrad, M.E., Quispe, A.J.C., Christensen, J.N., Hilton, R.G., Dellinger, M. and West, A.J., 2021. Conservative transport of dissolved sulfate across the Rio Madre de Dios floodplain in Peru. *Geology*, 49(9), pp.1064-1068. https://doi.org/10.1130/G48997.1.

Calmels, D., Gaillardet, J., Brenot, A. and France-Lanord, C., 2007. Sustained sulfide oxidation by physical erosion processes in the Mackenzie River basin: Climatic perspectives. *Geology*, 35(11), pp.1003-1006. https://doi.org/10.1130/G24132A.1.

Claypool, G.E., Holser, W.T., Kaplan, I.R., Sakai, H. and Zak, I., 1980. The age curves of sulfur and oxygen isotopes in marine sulfate and their mutual interpretation. *Chemical Geology*, 28, pp.199-260. https://doi.org/10.1016/0009-2541(80)90047-9.

Dornblaser, M.M. and Halm, D.R. eds., 2006. Water and sediment quality of the Yukon River and its tributaries, from Eagle to St. Marys, Alaska, 2002-2003. U.S. Geological Survey Open-File Report 2006-1228.

Douglas, M.M., Lingappa, U.F., Lamb, M.P., Rowland, J.C., West, A.J., Li, G., Kemeny, P.C., Chadwick, A.J., Piliouras, A., Schwenk, J. and Fischer, W.W., 2021. Impact of river channel lateral migration on microbial communities across a discontinuous permafrost floodplain. *Applied and Environmental Microbiology*, 87(20), pp.e01339-21. https://doi.org/10.1128/AEM.01339-21.

Douglas, M.M., Li, G.K., Fischer, W.W., Rowland, J.C., Kemeny, P.C., West, A.J., Schwenk, J., Piliouras, A.P., Chadwick, A.J. and Lamb, M.P., 2022. Organic carbon burial by river meandering partially offsets bank erosion carbon fluxes in a discontinuous permafrost floodplain. *Earth Surface Dynamics*, 10(3), pp.421-435. https://doi.org/10.5194/esurf-10-421-2022.

Douglas, T.A., Blum, J.D., Guo, L., Keller, K. and Gleason, J.D., 2013. Hydrogeochemistry of seasonal flow regimes in the Chena River, a subarctic watershed draining discontinuous permafrost in interior Alaska (USA). *Chemical Geology*, 335, pp.48-62. https://doi.org/10.1016/j.chemgeo.2012.10.045.

Foks, S.S., Dornblaser, M.M., Bogard, M.J., Butman, D., Campbell, D.A., Johnston, S.E., Koch, J.C., Li, Z., Spencer, R.G.M., Textor, S.R., Whiddon, E.T., Wickland, K.P., and Striegl, R.G, 2020, Water quality and gas fluxes of Interior Alaska (2014-2018): U.S. Geological Survey data release, https://doi.org/10.5066/P9C6BDBQ.

Frey, K.E. and McClelland, J.W., 2009. Impacts of permafrost degradation on arctic river biogeochemistry. *Hydrological Processes: An International Journal*, 23(1), pp.169-182. https://doi.org/10.1002/hyp.7196.

Gaillardet, J., Dupré, B., Louvat, P. and Allegre, C.J., 1999. Global silicate weathering and CO_2 consumption rates deduced from the chemistry of large rivers. *Chemical Geology*, 159(1-4), pp.3-30. https://doi.org/10.1016/S0009-2541(99)00031-5.

Halm, Douglas R., and Mark M. Dornblaser. Water and sediment quality in the Yukon River and its tributaries between Atlin, British Columbia, Canada, and Eagle, Alaska, USA, 2004. No. 2007-1197. Geological Survey (US), 2007. https://doi.org/10.3133/ofr20071197

Hayes, J.M., 2004. An introduction to isotopic calculations. Woods Hole Oceanographic Institution, Woods Hole, MA, 2543.

Hemingway, J.D., Olson, H., Turchyn, A.V., Tipper, E.T., Bickle, M.J. and Johnston, D.T., 2020. Triple oxygen isotope insight into terrestrial pyrite oxidation. *Proceedings of the National Academy of Sciences*, 117(14), pp.7650-7657. https://doi.org/10.1073/pnas.1917518117.

Herman-Mercer, N.M., 2016, Water-Quality Data from the Yukon River Basin in Alaska and Canada: U.S. Geological Survey data release, http://dx.doi.org/10.5066/F77D2S7B.

John, S.G. and Adkins, J.F., 2010. Analysis of dissolved iron isotopes in seawater. *Marine Chemistry*, 119(1-4), pp.65-76. https://doi.org/10.1016/j.marchem.2010.01.001.

Johnson, J.E., Gerpheide, A., Lamb, M.P. and Fischer, W.W., 2014. O_2 constraints from Paleoproterozoic detrital pyrite and uraninite. *Bulletin*, 126(5-6), pp.813-830. https://doi.org/10.1130/B30949.1.

Joo, Y.J., Sim, M.S., Elwood Madden, M.E. and Soreghan, G.S., 2022. Significance of the Terrestrial Sink in the Biogeochemical Sulfur Cycle. *Geophysical Research Letters*, 49(4), p.e2021GL097009. https://doi.org/10.1029/2021GL097009.

Jorgenson, M.T., Racine, C.H., Walters, J.C. and Osterkamp, T.E., 2001. Permafrost degradation and ecological changes associated with a warming climate in central Alaska. *Climatic Change*, 48(4), pp.551-579. https://doi.org/10.1023/A:1005667424292.

Jorgenson, M.T., Harden, J., Kanevskiy, M., O'Donnell, J., Wickland, K., Ewing, S., Manies, K., Zhuang, Q., Shur, Y., Striegl, R. and Koch, J., 2013. Reorganization of vegetation, hydrology and soil carbon after permafrost degradation across heterogeneous boreal landscapes. *Environmental Research Letters*, 8(3), p.035017. https://doi.org/10.1088/1748-9326/8/3/035017.

Kang, M., Skierszkan, E., Brennan, S., Fernandez, D.P., Yang, Z., Girard, I., Gammon, P., de Laplante, G. and Bataille, C.P., 2022. Controls of lithium isotope spatial variability across the Yukon River: Implications for weathering processes in a warming subarctic basin. *Geochimica et Cosmochimica Acta*, 323, pp.1-19. https://doi.org/10.1016/j.gca.2022.02.016.

Keeling, R.F., Graven, H.D., Welp, L.R., Resplandy, L., Bi, J., Piper, S.C., Sun, Y., Bollenbacher, A. and Meijer, H.A., 2017. Atmospheric evidence for a global secular increase in carbon isotopic discrimination of land photosynthesis. *Proceedings of the National Academy of Sciences*, 114(39), pp.10361-10366. https://doi.org/10.1073/pnas.1619240114.

Keller, K., Blum, J.D. and Kling, G.W., 2007. Geochemistry of soils and streams on surfaces of varying ages in arctic Alaska. *Arctic, Antarctic, and Alpine Research*, 39(1), pp.84-98. doi.org/10.1657/1523-0430(2007)39[84:GOSASO]2.0.CO;2.

Keller, K., Blum, J.D. and Kling, G.W., 2010. Stream geochemistry as an indicator of increasing permafrost thaw depth in an arctic watershed. *Chemical Geology*, 273(1-2), pp.76-81. https://doi.org/10.1016/j.chemgeo.2010.02.013.

Kemeny, P.C., Lopez, G.I., Dalleska, N.F., Torres, M., Burke, A., Bhatt, M.P., West, A.J., Hartmann, J. and Adkins, J.F., 2021a. Sulfate sulfur isotopes and major ion chemistry reveal that pyrite oxidation counteracts CO_2 drawdown from silicate weathering in the Langtang-Trisuli-Narayani River system, Nepal Himalaya. *Geochimica et Cosmochimica Acta*, 294, pp.43-69. https://doi.org/10.1016/j.gca.2020.11.009.

Kemeny, P.C., Torres, M.A., Lamb, M.P., Webb, S.M., Dalleska, N., Cole, T., Hou, Y., Marske, J., Adkins, J.F. and Fischer, W.W., 2021b. Organic sulfur fluxes and geomorphic control of sulfur isotope ratios in rivers. *Earth and Planetary Science Letters*, 562, p.116838. https://doi.org/10.1016/j.epsl.2021.116838.

Lerman, A., Wu, L. and Mackenzie, F.T., 2007. CO_2 and H_2SO_4 consumption in weathering and material transport to the ocean, and their role in the global carbon balance. *Marine Chemistry*, 106(1-2), pp.326-350. https://doi.org/10.1016/j.marchem.2006.04.004.

Lloyd, R.M., 1968. Oxygen isotope behavior in the sulfate-water system. *Journal of Geophysical Research*, 73(18), pp.6099-6110. https://doi.org/10.1029/JB073i018p06099.

Manceau, A. and Nagy, K.L., 2012. Quantitative analysis of sulfur functional groups in natural organic matter by XANES spectroscopy. *Geochimica et Cosmochimica Acta*, 99, pp.206-223. https://doi.org/10.1016/j.gca.2012.09.033.

Mandernack, K.W., Krouse, H.R. and Skei, J.M., 2003. A stable sulfur and oxygen isotopic investigation of sulfur cycling in an anoxic marine basin, Framvaren Fjord, Norway. *Chemical Geology*, 195(1-4), pp.181-200. https://doi.org/10.1016/S0009-2541(02)00394-7.

Mizutani, Y. and Rafter, T.A., 1969. Oxygen isotopic composition of sulphates. Part 5. Isotopic composition of sulphate in rain water, Gracefield, New Zealand. Inst. of Nuclear Sciences, Lower Hutt, NZ.

Neff, J.C., Finlay, J.C., Zimov, S.A., Davydov, S.P., Carrasco, J.J., Schuur, E.A.G. and Davydova, A.I., 2006. Seasonal changes in the age and structure of dissolved organic carbon in Siberian rivers and streams. *Geophysical Research Letters*, 33(23). https://doi.org/10.1029/2006GL028222.

O'Donnell, J.A., Jorgenson, M.T., Harden, J.W., McGuire, A.D., Kanevskiy, M.Z. and Wickland, K.P., 2012. The effects of permafrost thaw on soil hydrologic, thermal, and carbon dynamics in an Alaskan peatland. *Ecosystems*, 15(2), pp.213-229. https://doi.org/10.1007/s10021-011-9504-0.

Oelke, C., Zhang, T. and Serreze, M.C., 2004. Modeling evidence for recent warming of the Arctic soil thermal regime. *Geophysical Research Letters*, 31(7). https://doi.org/10.1029/2003GL019300.

Osterkamp, T.E. and Romanovsky, V.E., 1999. Evidence for warming and thawing of discontinuous permafrost in Alaska. *Permafrost and Periglacial Processes*, 10(1), pp.17-37.https://doi.org/10.1002/(SICI)1099-1530(199901/03)10:1<17::AID-PPP303>3.0.CO;2-4.

Paris, G., Sessions, A.L., Subhas, A.V. and Adkins, J.F., 2013. MC-ICP-MS measurement of $\delta^{34}S$ and $\Delta^{33}S$ in small amounts of dissolved sulfate. *Chemical Geology*, 345, pp.50-61. https://doi.org/10.1016/j.chemgeo.2013.02.022.

Paris, G., Adkins, J.F., Sessions, A.L., Webb, S.M. and Fischer, W.W., 2014. Neoarchean carbonate–associated sulfate records positive $\Delta^{33}S$ anomalies. *Science*, 346(6210), pp.739-741. https://doi.org/10.1126/science.1258211.

Prietzel, J., Botzaki, A., Tyufekchieva, N., Brettholle, M., Thieme, J. and Klysubun, W., 2011. Sulfur speciation in soil by S K-edge XANES spectroscopy: Comparison of spectral deconvolution and linear combination fitting. *Environmental Science & Technology*, 45(7), pp.2878-2886. https://doi.org/10.1021/es102180a.

Rowland, J., Stauffer, S. and Schwenk, J., 2019. Pan-arctic river bank erosion and accretion, and planform metrics measured over intervals ranging from 1973 to 2016. Environmental System Science Data Infrastructure for a Virtual Ecosystem; Incorporating the Hydrological Controls on Carbon Cycling in Floodplain Ecosystems into Earth System Models (ESMs). https://doi.org/10.15485/1571527.

Schuster, P.F., 2003. Water and sediment quality in the Yukon River basin, Alaska, during water year 2001: U.S. Geological Survey Open-File Report 03-427, 120 p. https://pubs.usgs.gov/of/2003/ofr03427/.

Schuster, P.F., 2005a. Water and sediment quality in the Yukon River basin, Alaska, during water year 2002: U.S. Geological Survey Open-File Report 2005-1199, 82 p. https://pubs.usgs.gov/of/2005/1199/.

Schuster, P.F., 2005b. Water and sediment quality in the Yukon River basin, Alaska, during water year 2003: U.S. Geological Survey Open-File Report 2005-1397, 74 p. https://pubs.usgs.gov/of/2005/1397/.

Schuster, P.F., 2006. Water and sediment quality in the Yukon River basin, Alaska, during water year 2004: U.S. Geological Survey Open-File Report 2006-1258, 67 p. https://pubs.usgs.gov/of/2006/1258/.

Schuster, P.F., 2007. Water and sediment quality in the Yukon River basin, Alaska, during water year 2005: U.S. Geological Survey Open-File Report 2007-1037, 65 p. https://pubs.usgs.gov/of/2007/1037/.

Schuster, P. F., Maracle, K. T. B. and Herman-Mercer, N., 2010. Water quality in the Yukon River Basin, Alaska, water years 2006-2008. U. S. Geological Survey Open-File Report 2010-1241 , 220 p. https://pubs.usgs.gov/of/2010/1241/.

Schuur, E.A., Bockheim, J., Canadell, J.G., Euskirchen, E., Field, C.B., Goryachkin, S.V., Hagemann, S., Kuhry, P., Lafleur, P.M., Lee, H. and Mazhitova, G., 2008. Vulnerability of permafrost carbon to climate change: Implications for the global carbon cycle. *BioScience*, 58(8), pp.701-714. https://doi.org/10.1641/B580807.

Schuur, E.A., McGuire, A.D., Schädel, C., Grosse, G., Harden, J.W., Hayes, D.J., Hugelius, G., Koven, C.D., Kuhry, P., Lawrence, D.M. and Natali, S.M., 2015. Climate change and the permafrost carbon feedback. *Nature*, 520(7546), pp.171-179. https://doi.org/10.1038/nature14338.

Sim, M.S., Bosak, T. and Ono, S., 2011. Large sulfur isotope fractionation does not require disproportionation. *Science*, 333(6038), pp.74-77. https://doi.org/10.1126/science.1205103.

Spence, J. and Telmer, K., 2005. The role of sulfur in chemical weathering and atmospheric CO_2 fluxes: evidence from major ions, $\delta^{13}C_{DIC}$, and $\delta^{34}S_{SO4}$ in rivers of the Canadian Cordillera. *Geochimica et Cosmochimica Acta*, 69(23), pp.5441-5458. https://doi.org/10.1016/j.gca.2005.07.011.

Striegl, R.G., Aiken, G.R., Dornblaser, M.M., Raymond, P.A. and Wickland, K.P., 2005. A decrease in discharge-normalized DOC export by the Yukon River during summer through autumn. *Geophysical Research Letters*, 32(21). https://doi.org/10.1029/2005GL024413.

Striegl, R.G., Dornblaser, M.M., Aiken, G.R., Wickland, K.P. and Raymond, P.A., 2007. Carbon export and cycling by the Yukon, Tanana, and Porcupine rivers, Alaska, 2001–2005. *Water Resources Research*, 43(2). https://doi.org/10.1029/2006WR005201.

Tank, S.E., Raymond, P.A., Striegl, R.G., McClelland, J.W., Holmes, R.M., Fiske, G.J. and Peterson, B.J., 2012. A land-to-ocean perspective on the magnitude, source and implication of DIC flux from major Arctic rivers to the Arctic Ocean. *Global Biogeochemical Cycles*, 26(4). https://doi.org/10.1029/2011GB004192.

Tank, S.E., Striegl, R.G., McClelland, J.W. and Kokelj, S.V., 2016. Multi-decadal increases in dissolved organic carbon and alkalinity flux from the Mackenzie drainage basin to the Arctic Ocean. *Environmental Research Letters*, 11(5), p.054015. https://doi.org/10.1088/1748-9326/11/5/054015.

Taylor, B.E., Wheeler, M.C. and Nordstrom, D.K., 1984. Stable isotope geochemistry of acid mine drainage: Experimental oxidation of pyrite. *Geochimica et Cosmochimica Acta*, 48(12), pp.2669-2678. https://doi.org/10.1016/0016-7037(84)90315-6.

Tcherkez, G. and Tea, I., 2013. $^{32}S/^{34}S$ isotope fractionation in plant sulphur metabolism. *New Phytologist*, pp. 44-53. https://doi.org/10.1111/nph.12314.

Toohey, R.C., Herman-Mercer, N.M., Schuster, P.F., Mutter, E.A. and Koch, J.C., 2016. Multidecadal increases in the Yukon River Basin of chemical fluxes as indicators of changing flowpaths, groundwater, and permafrost. *Geophysical Research Letters*, 43(23), pp.12-120. https://doi.org/10.1002/2016GL070817.

Torres, M.A., West, A.J., Clark, K.E., Paris, G., Bouchez, J., Ponton, C., Feakins, S.J., Galy, V. and Adkins, J.F., 2016. The acid and alkalinity budgets of weathering in the Andes–Amazon system: Insights into the erosional control of global biogeochemical cycles. *Earth and Planetary Science Letters*, 450, pp.381-391. https://doi.org/10.1016/j.epsl.2016.06.012.

Torres, M.A., Kemeny, P.C., Lamb, M.P., Cole, T.L. and Fischer, W.W., 2020. Long-term storage and age-biased export of fluvial organic carbon: Field evidence from west Iceland. *Geochemistry, Geophysics, Geosystems*, 21(4), p.e2019GC008632. https://doi.org/10.1029/2019GC008632.

Trust, B.A. and Fry, B., 1992. Stable sulphur isotopes in plants: a review. *Plant, Cell & Environment*, 15(9), pp.1105-1110. https://doi.org/10.1111/j.1365-3040.1992.tb01661.x.

Turchyn, A.V., Tipper, E.T., Galy, A., Lo, J.K. and Bickle, M.J., 2013. Isotope evidence for secondary sulfide precipitation along the Marsyandi River, Nepal, Himalayas. *Earth and Planetary Science Letters*, 374, pp.36-46. https://doi.org/10.1016/j.epsl.2013.04.033.

van Everdingen, R.O. and Krouse, H.R., 1985. Isotope composition of sulphates generated by bacterial and abiological oxidation. *Nature*, 315(6018), pp.395-396. https://doi.org/10.1038/315395a0.

van Geldern, R. and Barth, J.A., 2012. Optimization of instrument setup and post-run corrections for oxygen and hydrogen stable isotope measurements of water by isotope ratio infrared spectroscopy (IRIS). *Limnology and Oceanography: Methods*, 10(12), pp.1024-1036. https://doi.org/10.4319/lom.2012.10.1024.

Walvoord, M.A. and Striegl, R.G., 2007. Increased groundwater to stream discharge from permafrost thawing in the Yukon River basin: Potential impacts on lateral export of carbon and nitrogen. *Geophysical Research Letters*, 34(12). https://doi.org/10.1029/2007GL030216.

Walvoord, M.A., Voss, C.I. and Wellman, T.P., 2012. Influence of permafrost distribution on groundwater flow in the context of climate-driven permafrost thaw: Example from Yukon Flats Basin, Alaska, United States. *Water Resources Research*, 48(7). https://doi.org/10.1029/2011WR011595.

Walvoord, M.A. and Kurylyk, B.L., 2016. Hydrologic impacts of thawing permafrost—A review. *Vadose Zone Journal*, 15(6). https://doi.org/10.2136/vzj2016.01.0010.

Webb, S.M., 2005. SIXpack: A graphical user interface for XAS analysis using IFEFFIT. *Physica scripta*, 2005(T115), p.1011.

Woo, M.K., 1986. Permafrost hydrology in Noth America. *Atmosphere-Ocean*, 24(3), pp.201-234. https://doi.org/10.1080/07055900.1986.9649248.

Zolkos, S., Tank, S.E. and Kokelj, S.V., 2018. Mineral weathering and the permafrost carbon-climate feedback. *Geophysical Research Letters*, 45(18), pp.9623-9632. https://doi.org/10.1029/2018GL078748.

V.11: Supplementary figures

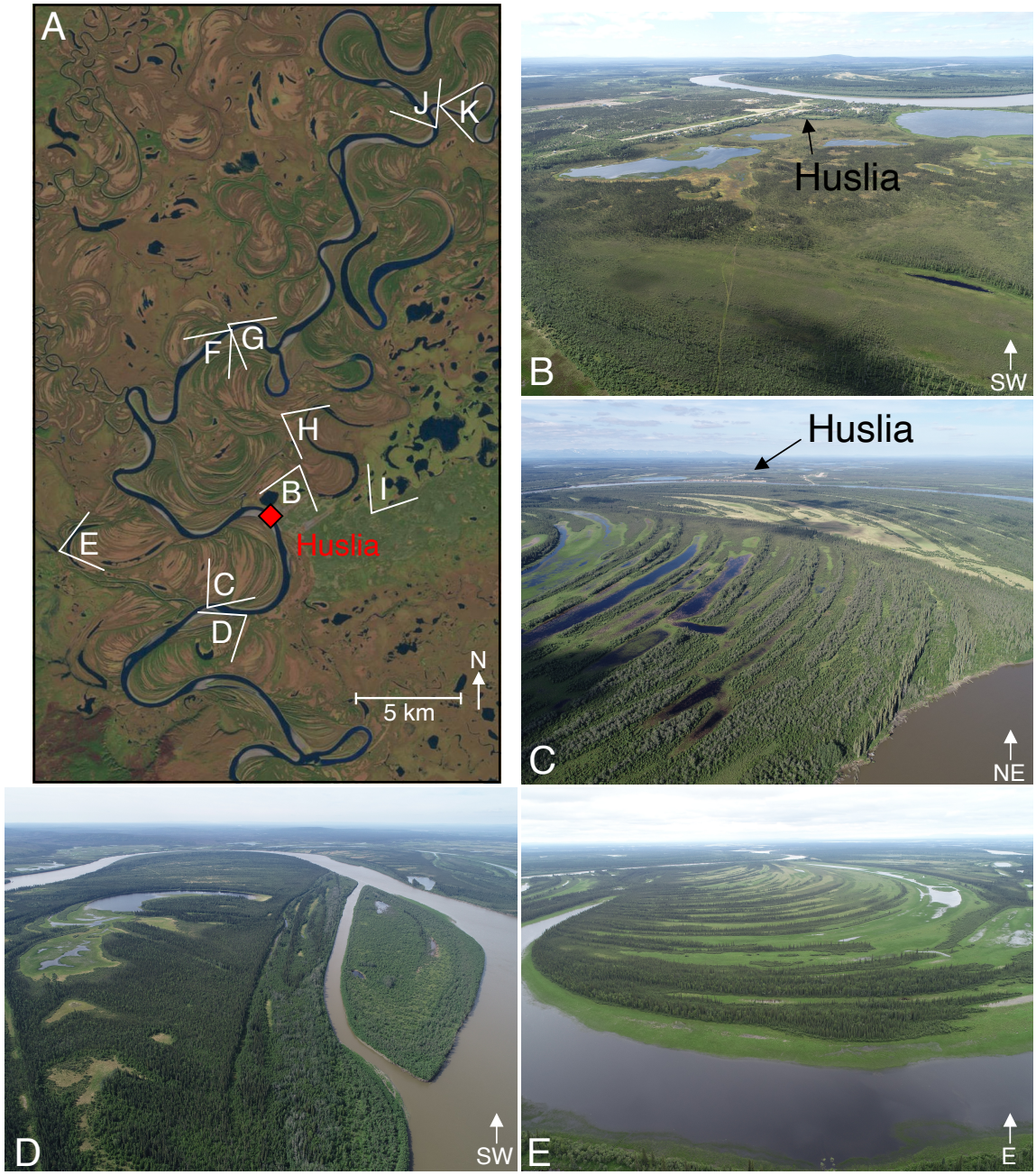

Fig. V-S1: Overview of field site. (A) Map of primary field site with indicated locations and approximate image orientation of 10 drone photographs. (B) The town of Huslia. (C) The river bend near Huslia, with scroll bar complex. (D) The most downstream sampled stretch of the Koyukuk River. (E) Looking towards Huslia from the tip of an abandoned meander, with visible scroll bars.

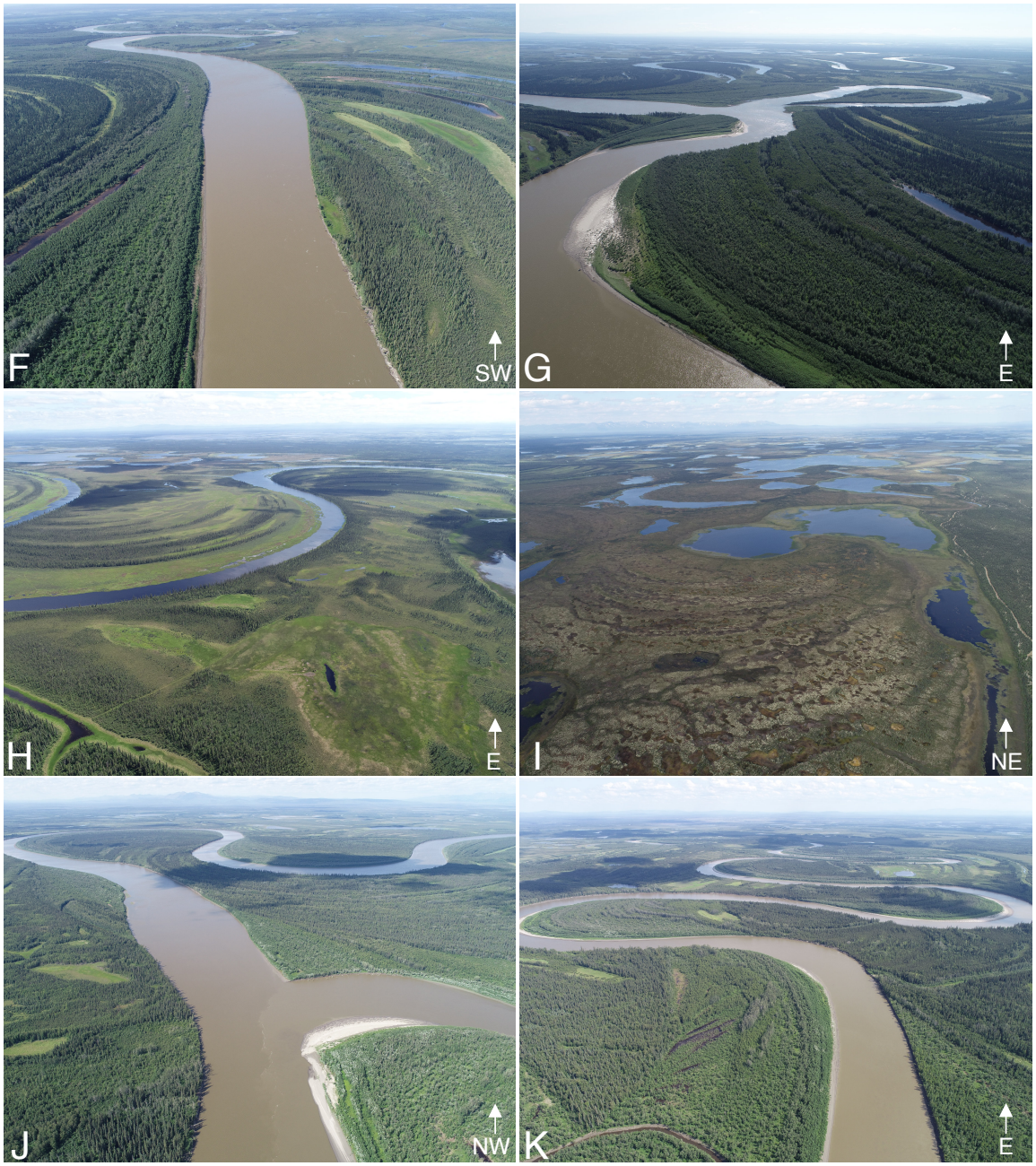

Fig. V-S1 (*continued*): (F) Linear stretch of the Koyukuk River where multiple suspended sediment depth profiles were collected. (G) Active river cutoff, with oxbow lake in the background. (H) Former meanders. (I) Multiple lakes east of Huslia, likely thermokarst. (J) Northern fork of the sampled confluence. (K) Southern fork of the sampled confluence.

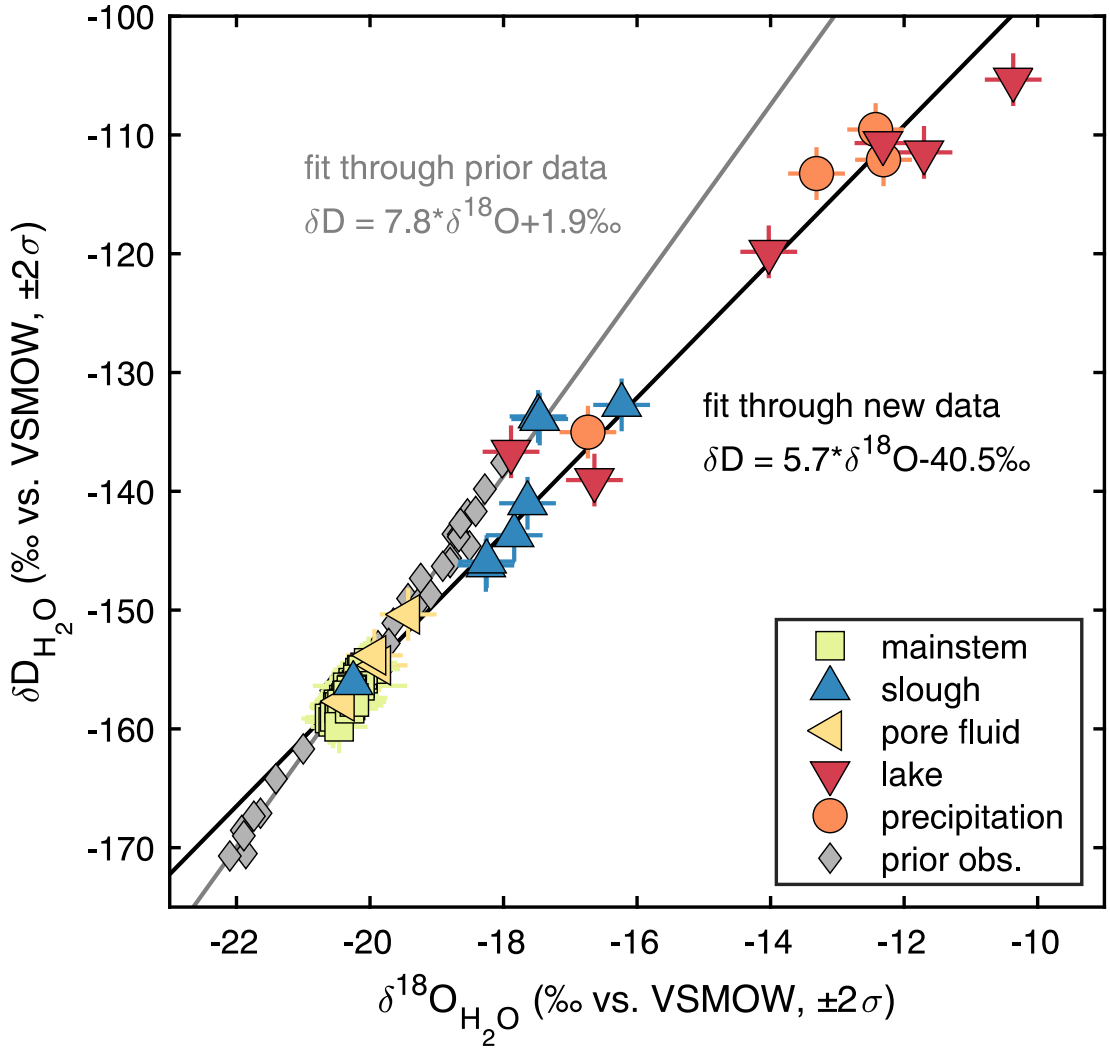

Fig. V-S2: Measurements of $\delta^{18}O_{H2O}$ and δD_{H2O} in samples from the Koyukuk River catchment and prior observations. The mainstem river and pore fluid samples agree with the trend defined by prior data while precipitation, slough, and lake sample deviate due to local hydrologic processes.

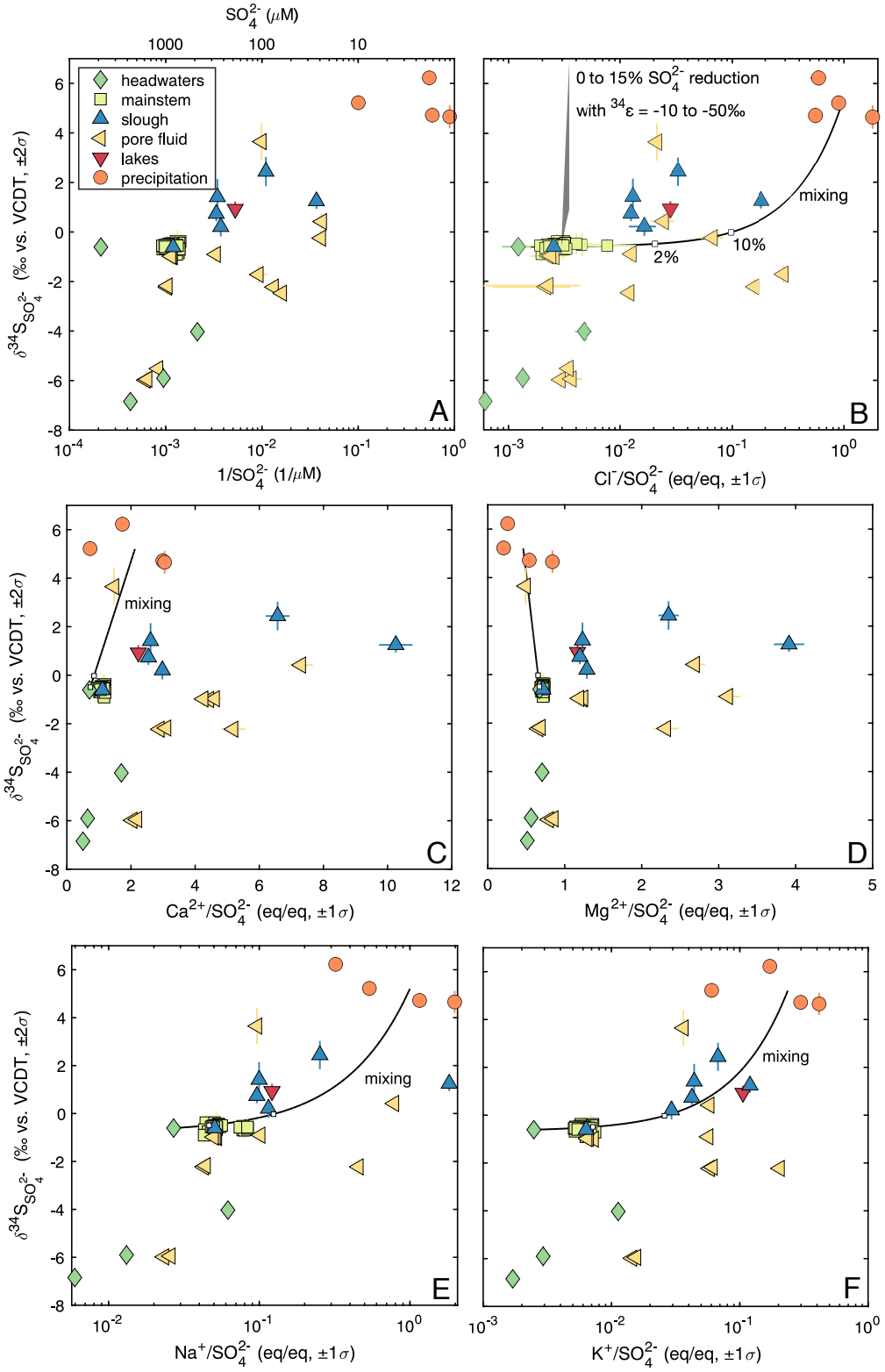

Fig. V-S3: Sulfur isotope mixing diagrams. $\delta^{34}S_{SO4}$ against (A) $1/SO_4^{2-}$, (B) Cl^-/SO_4^{2-}, (C) Ca^{2+}/SO_4^{2-}, (D) Mg^{2+}/SO_4^{2-}, (E) Na^+/SO_4^{2-}, and (F) K^+/SO_4^{2-}. River water major ion chemistry is consistent with a combination of mixing, modest sulfate reduction, and the addition of Ca^{2+} and Mg^{2+} through carbonate and silicate weathering in the floodplain.

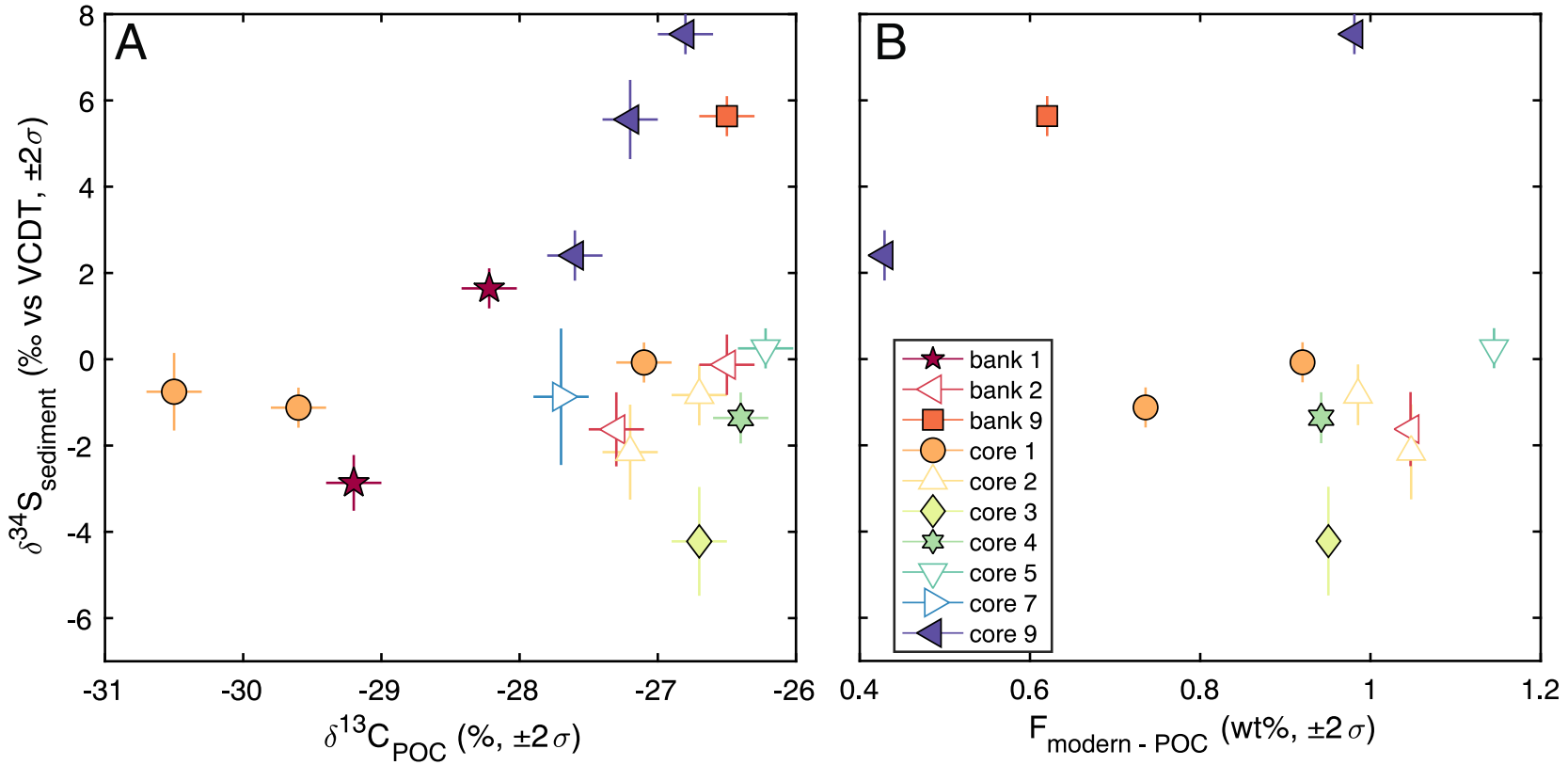

Fig. V-S4: Sedimentary sulfur and carbon isotope ratios. Sediment $\delta^{34}S$ against (A) the $\delta^{13}C$ of particulate organic carbon (POC) and (B) POC fraction modern (Douglas et al., 2022). There are no obvious relationships between $\delta^{34}S_{sediment}$ and either $\delta^{13}C_{POC}$ or $F_{mod\text{-}POC}$, or with whether samples are from permafrost (closed symbols) or non-permafrost (open symbols) deposits. The mean value of $\delta^{13}C_{POC}$ was used to calculate the value of $\delta^{13}C_{DIC}$ formed through the reaction of carbonate with respired organic matter (Fig.V-6).

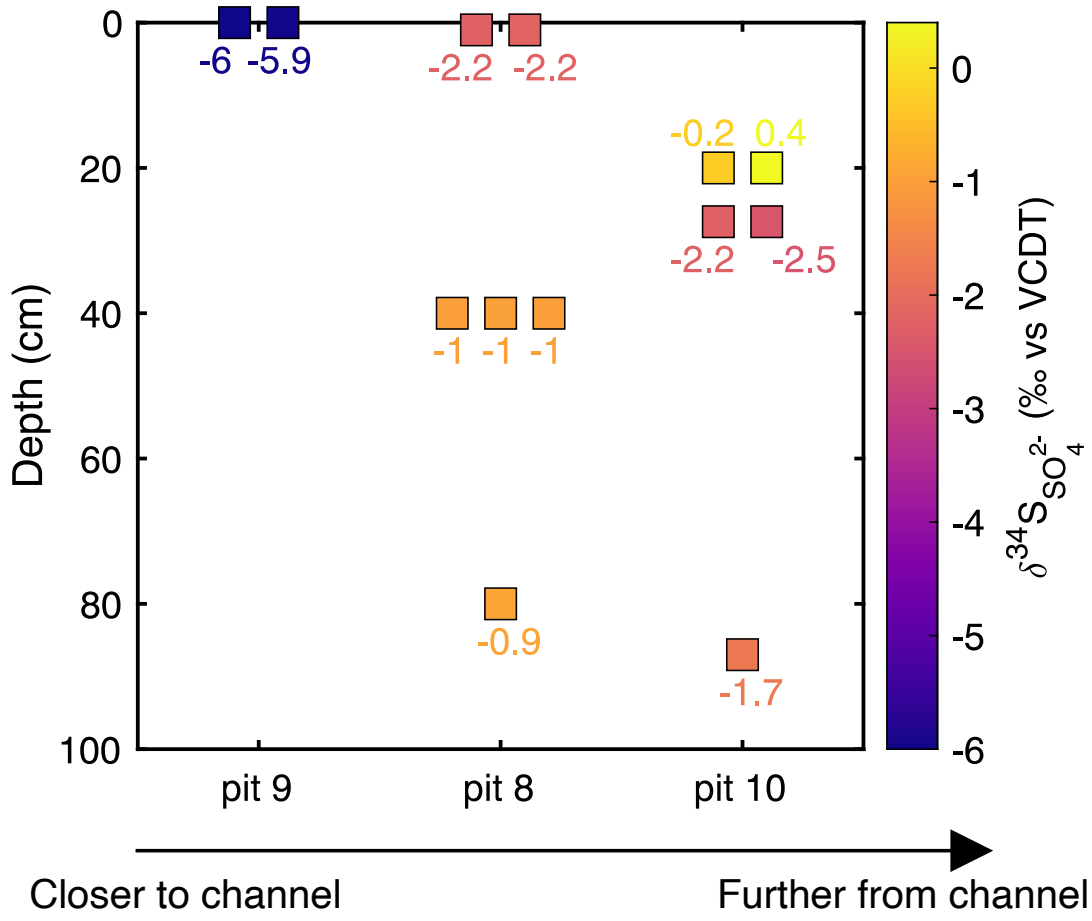

Fig. V-S5: Pore fluid $\delta^{34}S_{SO4}$ values. Samples were collected from multiple depths and time points at three neighboring sites: next to the active channel (pit 8), at an intermediate distance (pit 9), and furthest away (pit 10). Multiple points at the same depth within each core reflect multiple samples collected either in rapid succession (pit 8 and pit 9 samples) or several days apart (pit 10 samples), and the numbers next to symbols are the measured values of $\delta^{34}S_{SO4}$. The lowest $\delta^{34}S_{SO4}$ values are closet to the channel and the highest values are from the site furthest from the channel. Pore fluid $\delta^{34}S_{SO4}$ values increase with depth in pit 8 and decrease with depth in pit 10.

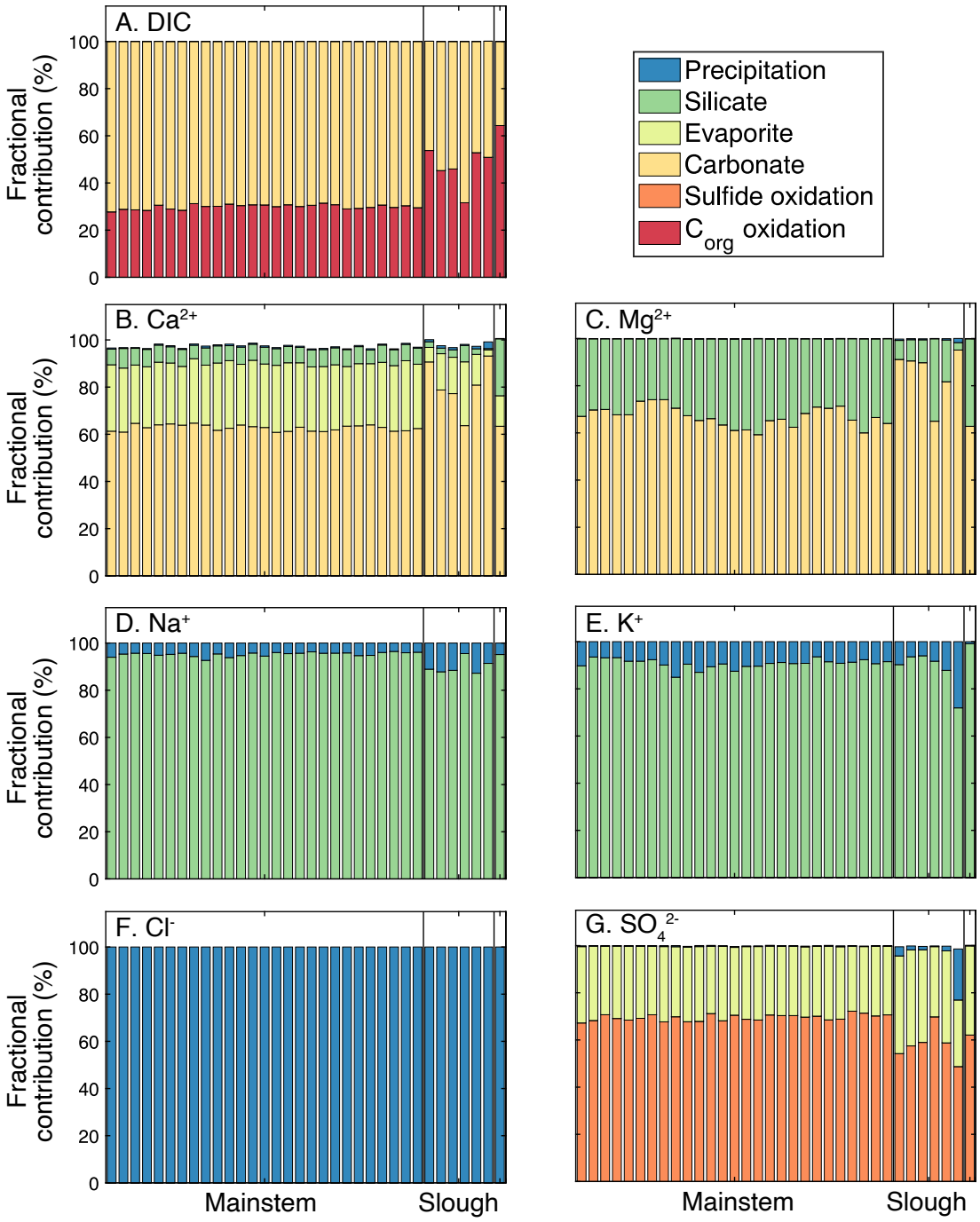

Fig. V-S6: Median end-member contributions in scenario without degassing. Fractional contributions of the precipitation, silicate, evaporite, carbonate, sulfide oxidation, and C_{org} oxidation end-members to (A) DIC, (B) Ca^{2+}, (C) Mg^{2+}, (D) Na^{+}, (E) K^{+}, (F) Cl^{-}, and (G) SO_4^{2-}. While most elements are sourced from two end-members, three end-members contribute to river Ca^{2+} and all Cl^{-} derives from precipitation.

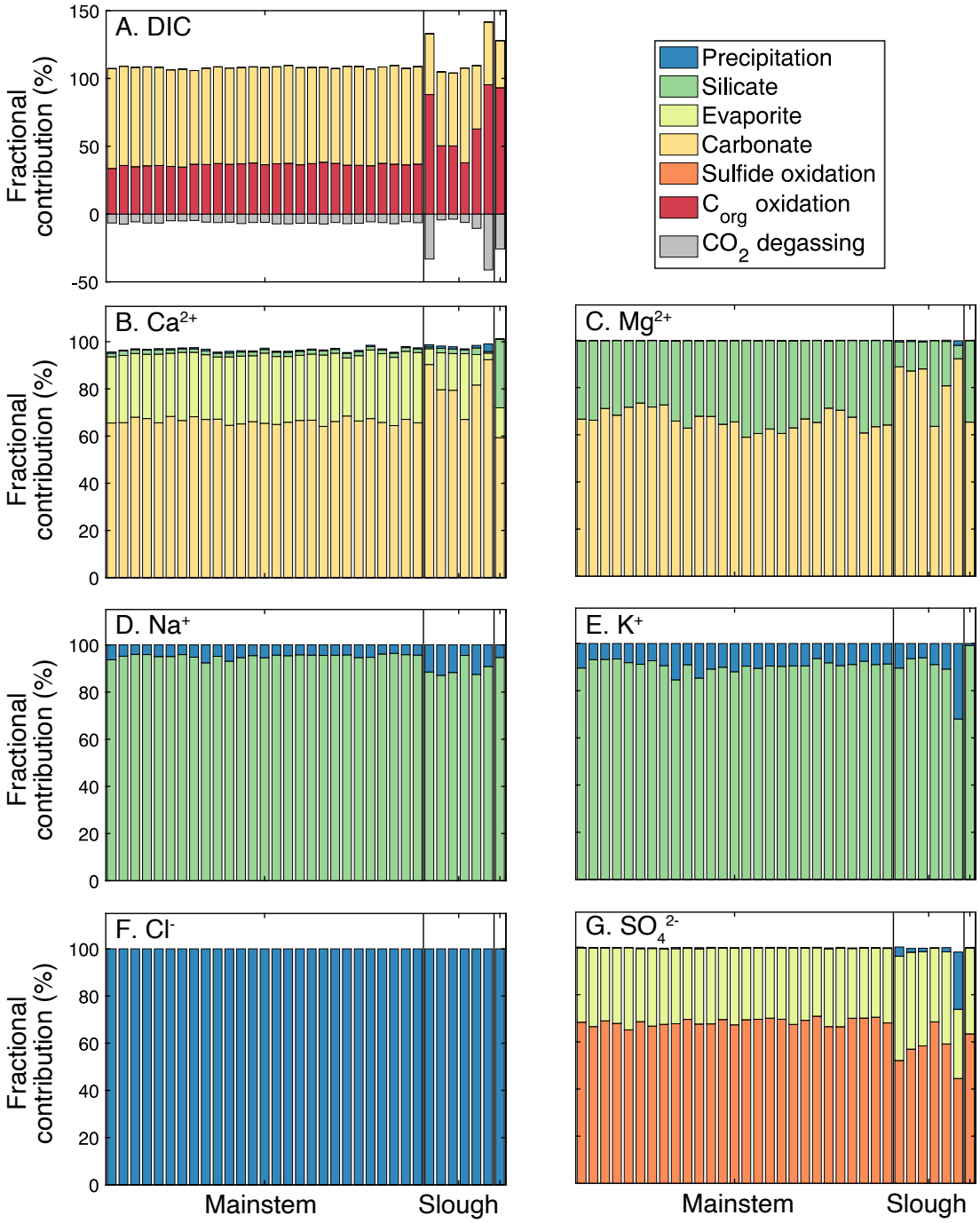

Fig. V-S7: Median end-member contributions in scenario with degassing. Fractional contributions of the precipitation, silicate, evaporite, carbonate, sulfide oxidation, C_{org} oxidation, and CO_2 degassing end-members to (A) DIC, (B) Ca^{2+}, (C) Mg^{2+}, (D) Na^{+}, (E) K^{+}, (F) Cl^{-}, and (G) SO_4^{2-}. While most elements are sourced from two end-members, three end-members contribute to river Ca^{2+} and DIC and all Cl^{-} derives from precipitation. Note that the fractional contribution of CO_2 degassing to DIC is negative and the sum of DIC sourced from carbonate weathering and C_{org} oxidation can thus exceed 100% of measured values.

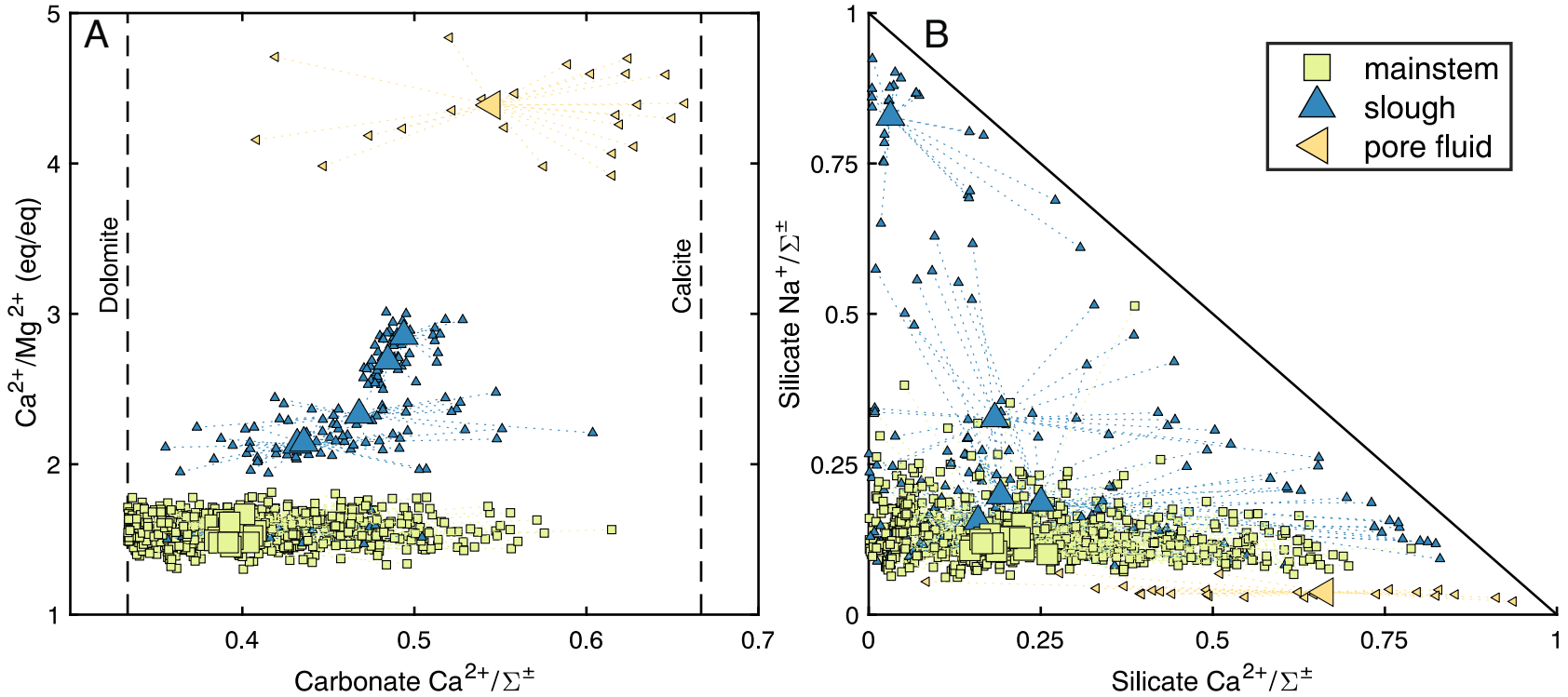

Fig. V-S8: Inversion-constrained end-member chemistry. Larger symbols reflect median sample results, which are connected by dotted lines to smaller symbols reflecting up to 25 individual simulations results for each sample. (A) Measured Ca^{2+}/Mg^{2+} against carbonate $Ca^{2+}/\Sigma^{\pm}$. MEANDIR constrained the carbonate end-member to have lower $Ca^{2+}/\Sigma^{\pm}$ in mainstem samples than in slough samples or pore fluids, consistent with the lower Ca^{2+}/Mg^{2+} ratio measured in mainstem samples. The reduced $Ca^{2+}/\Sigma^{\pm}$ values in mainstem samples likely indicates weathering of dolomite, and it is notable that very few results were found where the carbonate end-member resembled calcite. The inversion constrained the $Ca^{2+}/\Sigma^{\pm}$ of carbonate weathering in the slough samples at intermediate values; this indicates that the slough samples have insufficient dissolved Ca^{2+} and Mg^{2+}, relative to the carbonate contribution required by their DIC abundance and $\delta^{13}C_{DIC}$ observations, for the carbonate end-member to be either pure calcite or dolomite. (B) Inversion-constrained silicate $Na^{+}/\Sigma^{\pm}$ against silicate $Ca^{2+}/\Sigma^{\pm}$. The silicate end-member was unconstrained during inversion and attained primarily mafic compositions, with lower $Na^{+}/\Sigma^{\pm}$ ratios in mainstem samples than in the slough samples. Silicate $Na^{+}/\Sigma^{\pm}$ and $K^{+}/\Sigma^{\pm}$ were well correlated across all samples but showed distinct slopes (not shown).

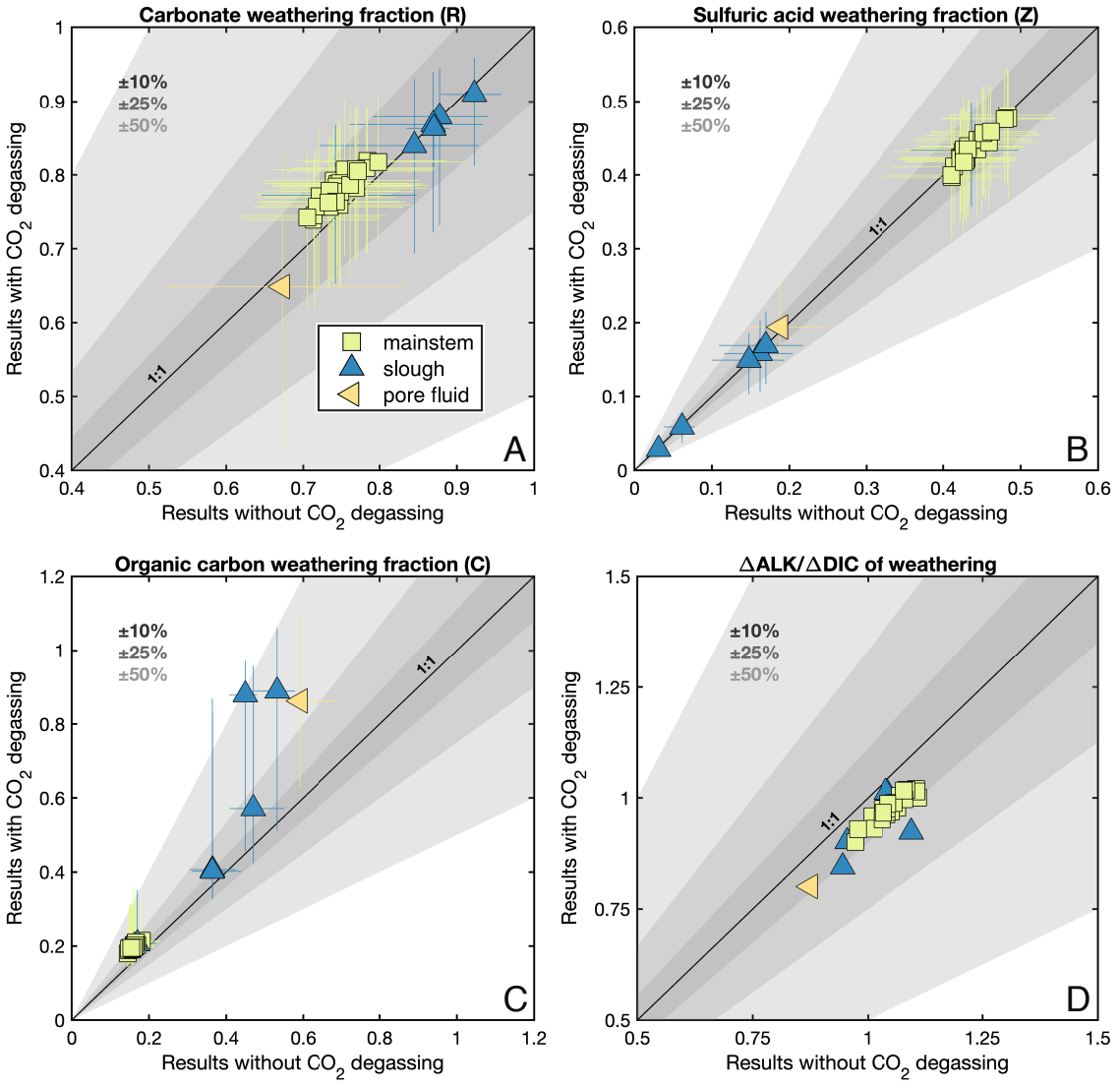

Fig. V-S9: Sensitivity of inversion results to inclusion of degassing. Results with degassing are plotted against inversion results without degassing for (A) the fraction of weathering alkalinity sourced from carbonate (R), (B) the fraction of weathering alkalinity offset through sulfide oxidation (Z), (C) the fraction of organic carbon oxidation relative to weathering alkalinity (C), and (D) the median ΔALK/ΔDIC of chemical weathering calculated from R, Z, and C. All panels include 1:1 lines, dark grey shading indicates ±10%, medium shading indicates ±25%, and light grey shading indicates ±50%. Including degassing in the inversion increased the R value of mainstem samples and increased the C value of both mainstem and slough samples. Results with degassing had lower ΔALK/ΔDIC weathering ratios in all samples, although typically differed from results without degassing by <10%. Given the overall uncertainty in inversion results, accounting for up to 20% loss of the normalization variable through degassing (Table V-2) does not meaningfully alter our results.

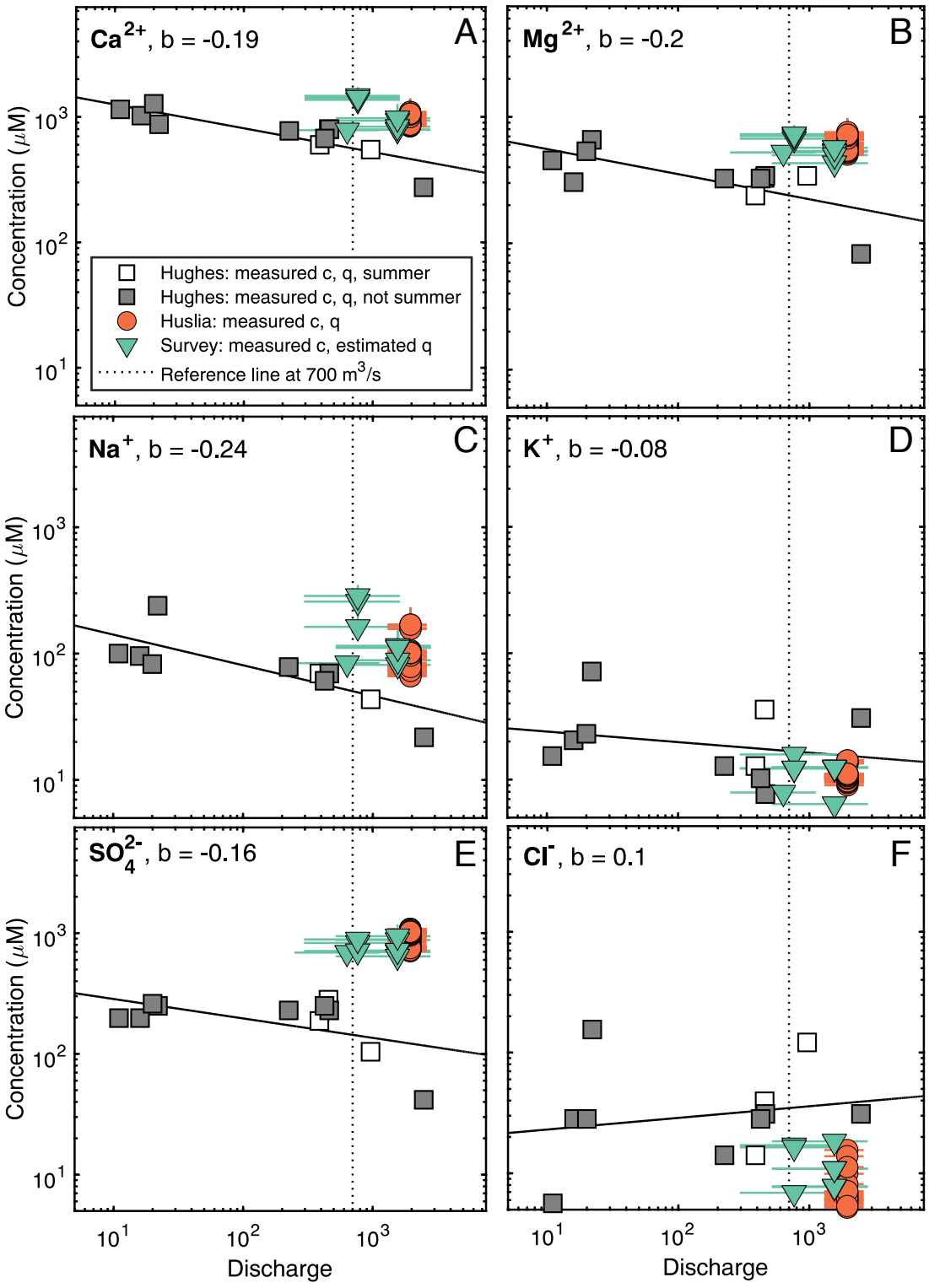

Fig. V-S10: Concentration and discharge for (A) Ca^{2+}, (B) Mg^{2+}, (C) Na^{+}, (D) K^{+}, (E) SO_4^{2-} and (F) Cl^{-}. Observations are plotted for Hughes summer months (white squares), Hughes non-summer months (grey squares), 2018 samples collected near Huslia (orange circles), and survey data (green triangles). Discharge for survey data was approximated as Hughes monthly averages. Concentrations were translated to 700 m^3/s using the indicated b values.

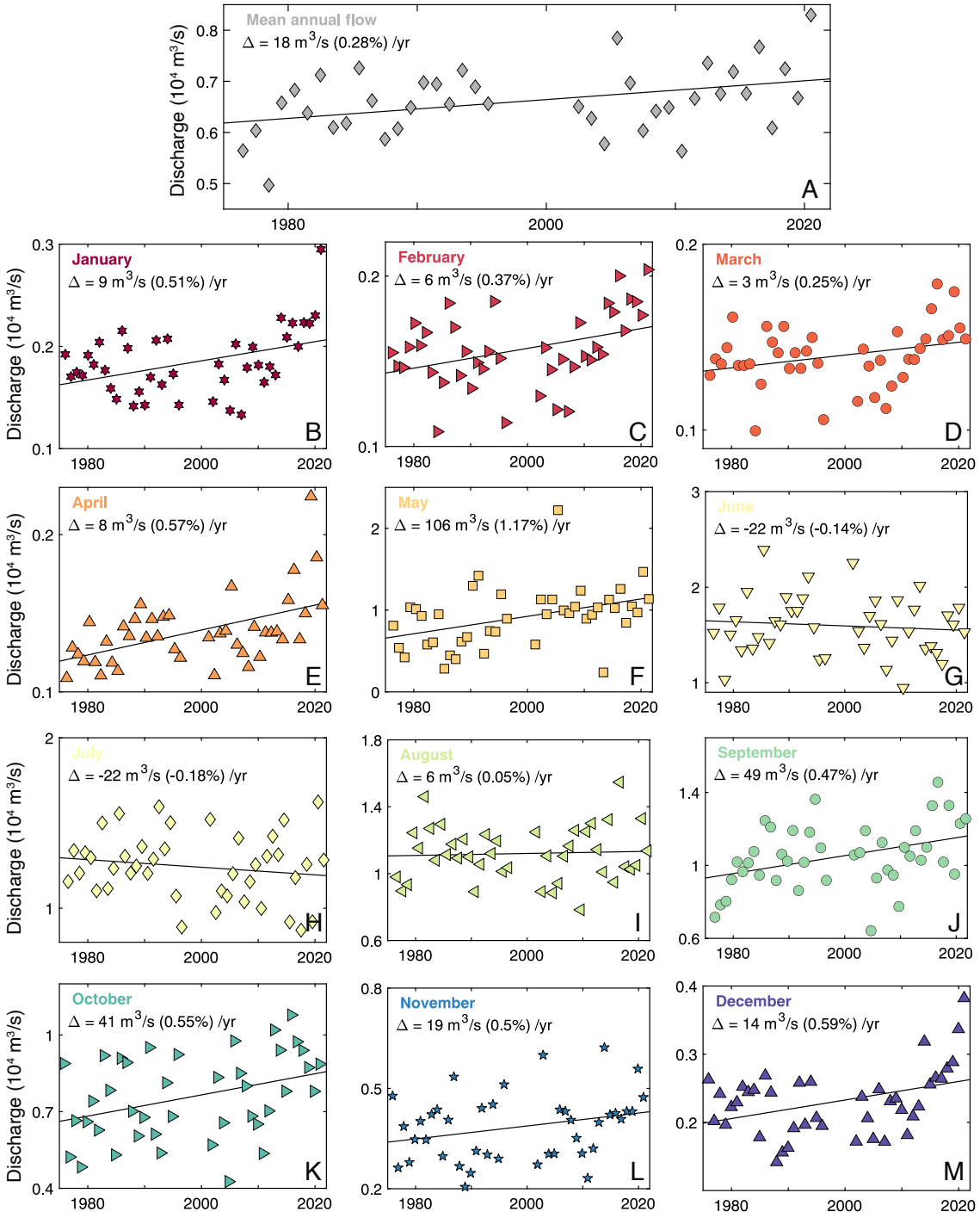

Fig. V-S11: Monthly discharge for timeseries data from the Yukon River at Pilot Station (USGS site number 15565447). Data are divided into (A) mean annual flow and observations from (B) January, (C) February, (D) March, (E) April, (F) May, (G) June, (H) July, (I) August, (J) September, (K) October, (L) November, and (M) December. Most months, except June and July, show discharge either stable or increasing.

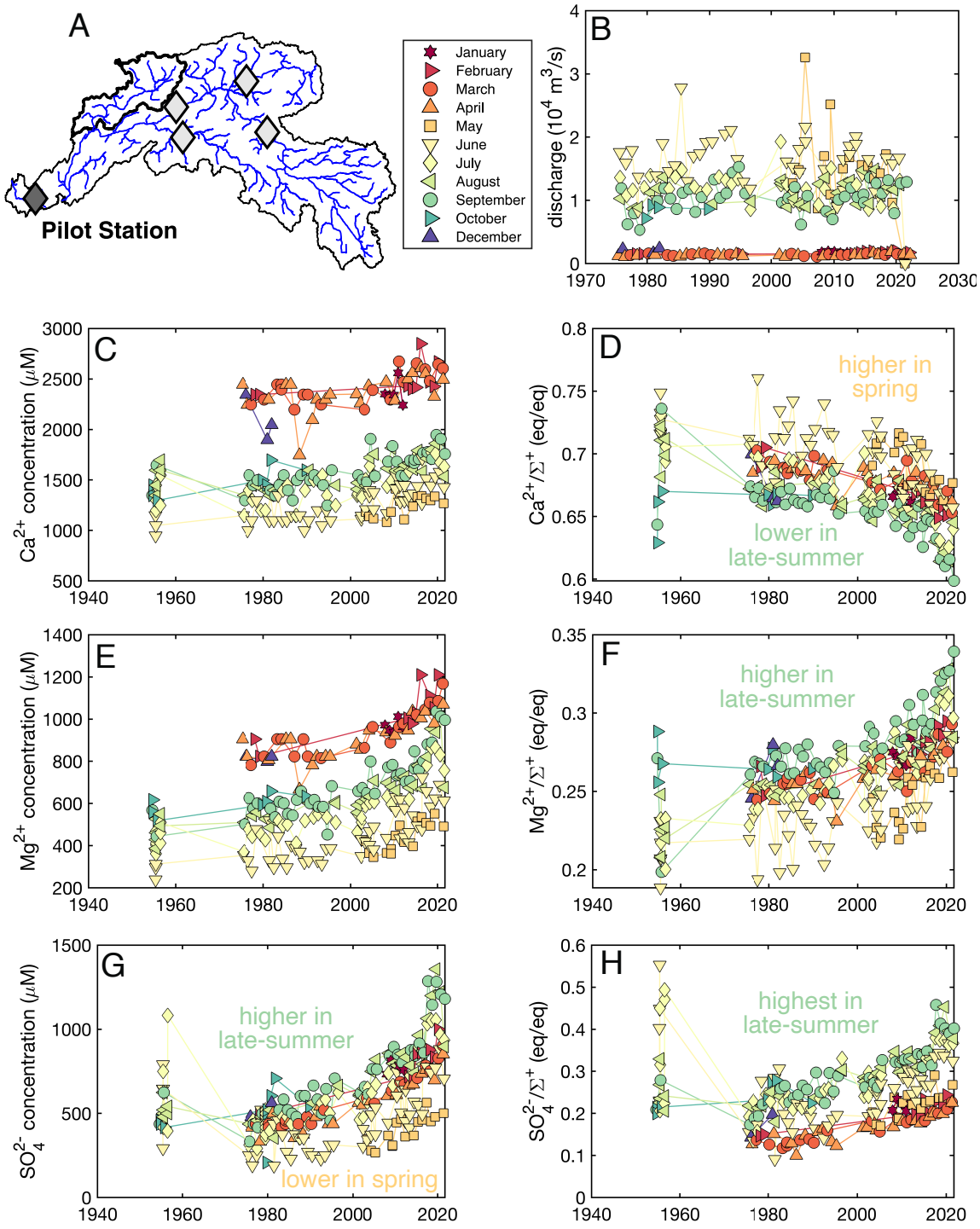

Fig. V-S12: Timeseries data from the Yukon River at Pilot Station (USGS site number 15565447). (A) Site location, (B) discharge, (C, E, G) concentration of Ca^{2+}, Mg^{2+}, and SO_4^{2-}, and (D, F, H) Ca^{2+}/Σ^+, Mg^{2+}/Σ^+, and SO_4^{2-}/Σ^+ ratios.

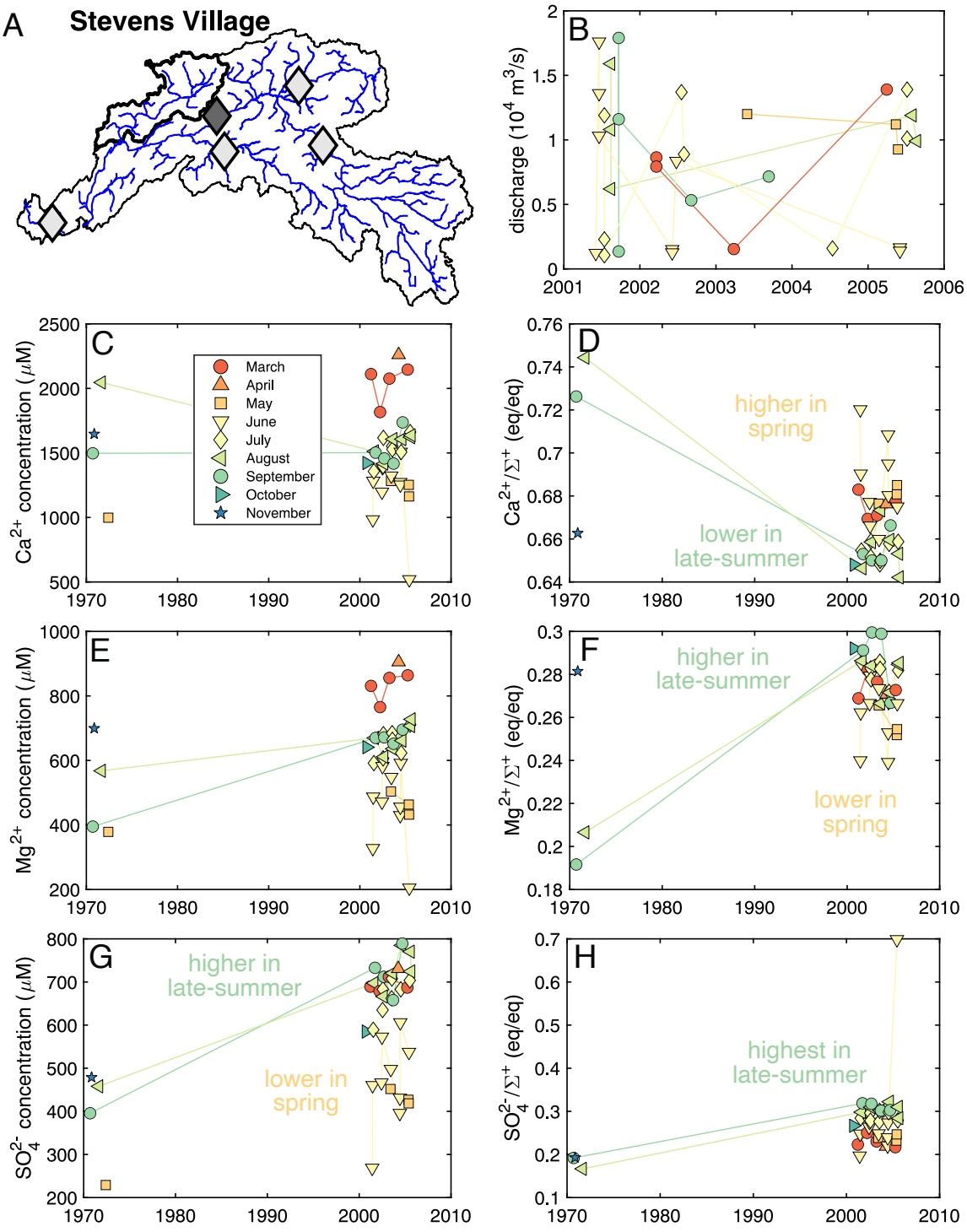

Fig. V-S13: Timeseries data from the Yukon River at Stevens Village (USGS site number 15453500). (A) Site location, (B) discharge, (C, E, G) concentration of Ca^{2+}, Mg^{2+}, and SO_4^{2-}, and (D, F, H) Ca^{2+}/Σ^+, Mg^{2+}/Σ^+, and SO_4^{2-}/Σ^+ ratios.

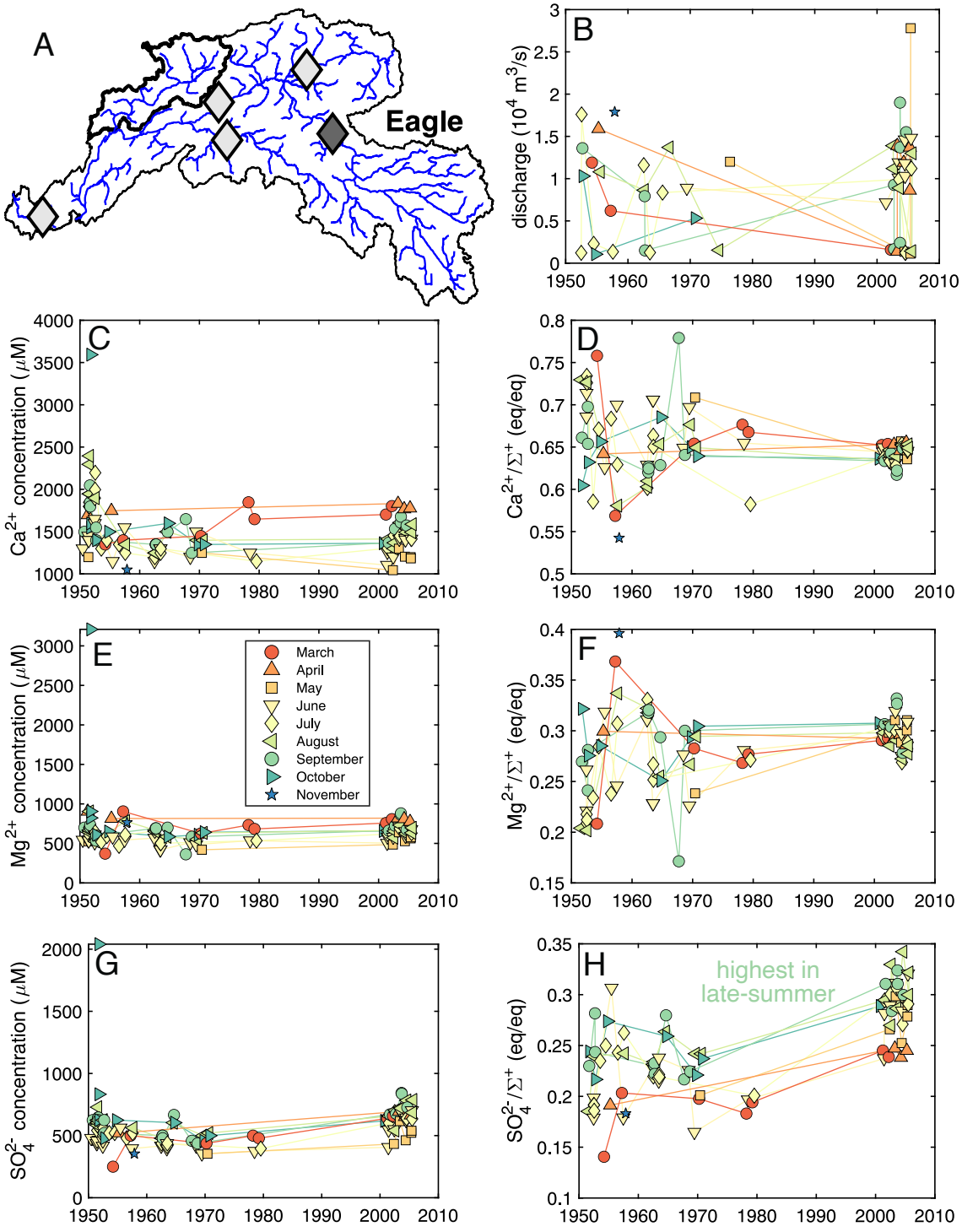

Fig. V-S14: Timeseries data from the Yukon River at Eagle (USGS site number 15356000). (A) Site location, (B) discharge, (C, E, G) concentration of Ca^{2+}, Mg^{2+}, and SO_4^{2-}, and (D, F, H) Ca^{2+}/Σ^+, Mg^{2+}/Σ^+, and SO_4^{2-}/Σ^+ ratios.

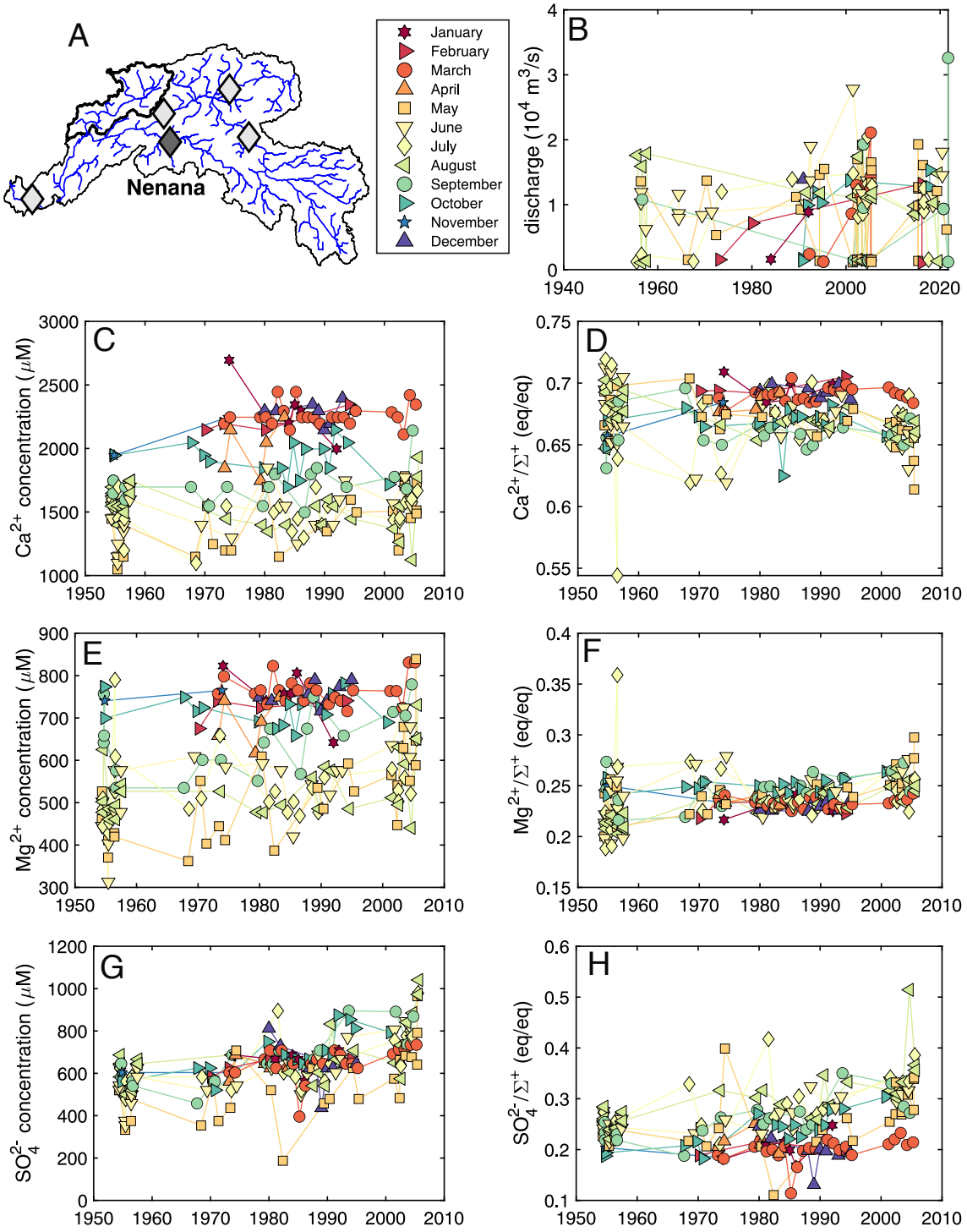

Fig. V-S15: Timeseries data from the Tanana River at Nenana (USGS site number 15515500). (A) Site location, (B) discharge, (C, E, G) concentration of Ca^{2+}, Mg^{2+}, and SO_4^{2-}, and (D, F, H) Ca^{2+}/Σ^+, Mg^{2+}/Σ^+, and SO_4^{2-}/Σ^+ ratios.

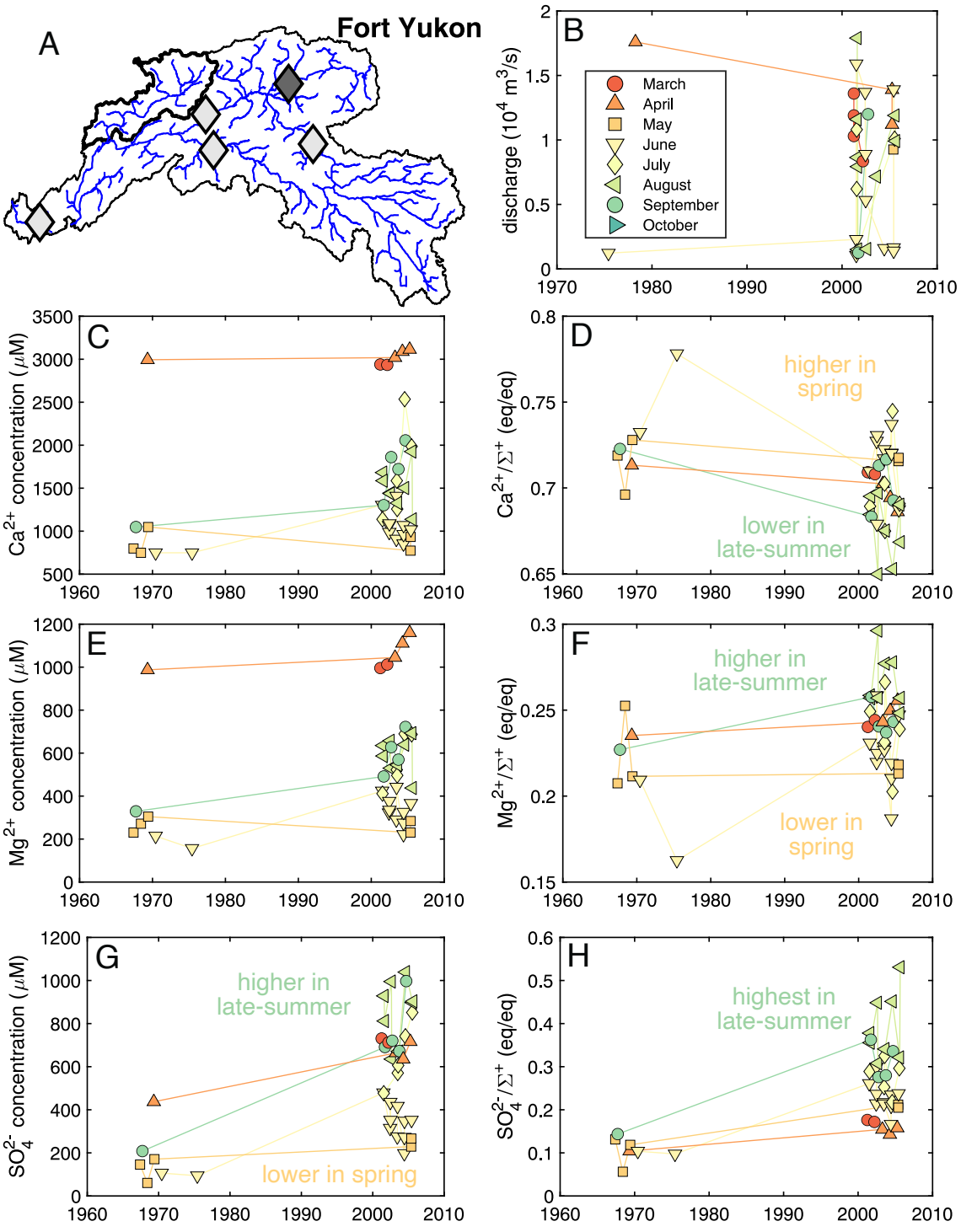

Fig. V-S16: Timeseries data from the Porcupine River near Fort Yukon (USGS site number 15389000). (A) Site location, (B) discharge, (C, E, G) concentration of Ca^{2+}, Mg^{2+}, and SO_4^{2-}, and (D, F, H) Ca^{2+}/Σ^+, Mg^{2+}/Σ^+, and SO_4^{2-}/Σ^+ ratios.

V.12: Supplementary tables

Table V-S1: Measured major ion concentrations in reference materials and precision of replicate sample measurements. For reference materials, measured values are given as μ±1σ in units of μM, the number of analyses is indicated in parentheses, and relative standard deviation (RSD) is 1σ. Switzer Falls, an in-house consistency standard, was repeatedly measured but does not have expected values. Reference materials without indicated values, such as Cl^- in CRANBERRY-05 and Mg^{2+} in Switzer Falls, reflect that values were outside the calibration range of standards. Sample values are the mean, median, 1σ standard deviation, and number of analyses for the distribution of RSDs among replicate measurements.

ANIONS						
	SO_4^{2-}			**Cl^-**		
References	*Expected*	*Measured*	*RSD*	*Expected*	*Measured*	*RSD*
SUPER-05	36.2	37.1 ± 1.4 (11)	3.9%	39.5	42.5 ± 0.9 (14)	2.1%
CRANBERRY-05	92.5	96.2 ± 3.4 (10)	3.5%			
MAURI-09	39.5	38.6 ± 1.2 (14)	3.1%	41.5	43.7 ± 3.2 (17)	7.3%
Switzer Falls		318.1 ± 3.7 (9)	1.2%			
Samples	*Mean / median of replicate RSDs*			*Mean / median of replicate RSDs*		
	1.9 / 1.1 ± 2.0% (45)			14.4 / 7.4 ± 18.4% (64)		
CATIONS						
	Ca^{2+}			**Mg^{2+}**		
References	*Expected*	*Measured*	*RSD*	*Expected*	*Measured*	*RSD*
SUPER-05	339.3	347.4 (1)		116.4	120.6 (1)	
CRANBERRY-05	324.4	352 ± 11.7 (2)	3.3%	232.0	241.8 ± 0.7 (2)	0.3%
MAURI-09	73.4	79.6 ± 9.6 (3)	12.1%	30.9	31.3 ± 1.0 (4)	3.2%
Switzer Falls						
Samples	*Mean / median of replicate RSDs*			*Mean / median of replicate RSDs*		
	1.1 / 0.7 ± 1.1% (15)			1.8 / 1.6 ± 1.6% (17)		
	Na^+			**K^+**		
References	*Expected*	*Measured*	*RSD*	*Expected*	*Measured*	*RSD*
SUPER-05	62.2	63.3 (1)		12.9	12.5 (1)	
CRANBERRY-05				17.9	18.6 ± 0.0 (2)	0.1%
MAURI-09	95.7	97.3 ± 2.3 (4)	2.4%	10.4	10.1 ± 0.4 (6)	4.4%
Switzer Falls					89.2 ± 0.2 (2)	0.3%
Samples	*Mean / median of replicate RSDs*			*Mean / median of replicate RSDs*		
	2.2 / 1.8 ± 2.2% (24)			3.5 / 3.0 ± 2.6% (13)		

Chapter VI

Global River Chemistry Constrains Crustal Sulfide $\delta^{34}S$ and $\Delta ALK/\Delta DIC$ of Inorganic Weathering

Preston Cosslett Kemeny[1], Andrea Burke[2], Mark A. Torres[3], Jess F. Adkins[1*], Woodward W. Fischer[1*]

[1] Division of Geological and Planetary Sciences, California Institute of Technology, Pasadena, CA, USA
[2] School of Earth and Environmental Sciences, University of St Andrews, St Andrews, UK
[3] Department of Earth, Environmental, and Planetary Sciences, Rice University, Houston, TX, USA

[*] These authors contributed equally

Keywords: River inversion, crustal sulfide, chemical weathering, carbon dioxide

VI.1: Abstract

The oxidation of crustal sulfide to river sulfate (SO_4^{2-}) and its removal in marine sediment contribute to the global cycles of sulfur, oxygen, carbon, and alkalinity. However, large uncertainties currently exist regarding the net impact of sulfide oxidation on climate and the relative output of oxidized and reduced sulfur from the ocean-atmosphere system. Here we constrain the sulfur isotopic composition of crustal sulfide by applying a novel inversion model to measurements of major ion chemistry and SO_4^{2-} $^{34}S/^{32}S$ ratios ($\delta^{34}S$) in a set of global river water samples. After accounting for inputs from evaporite dissolution and meteoric precipitation, we find that sulfide oxidation and anthropogenic pollution source between 2.6 and 3.6 Tmol SO_4^{2-}/yr with $\delta^{34}S$ value between -6.2‰ and 1.0‰. Crustal sulfide $\delta^{34}S$ is constrained between -11.0‰ and 0.6‰ (median: -3.5‰) in simulations accounting for 0.5 to 1.3 Tmol/yr of anthropogenic SO_4^{2-} and between -26.6‰ and 0.0‰ (median: -7.6‰) in simulations accounting for 1.3 to 2.4 Tmol/yr of anthropogenic SO_4^{2-}. These values indicate that crustal sulfide $\delta^{34}S$ is likely heavier than expected on the basis of a standard 1-input 2-output mass balance model. By modeling the relationship between the sulfur isotopic composition of weathering sulfide and that of sulfide formed in marine sediment, we conclude that approximately 35% to 65% of river SO_4^{2-} is output from seawater as sulfide. Furthermore, our calculations constrain the net ratio of alkalinity to dissolved inorganic carbon associated with global chemical weathering between 2.0 and 2.3, with several large river systems exhibiting weathering ratios between 1.8 and 2.2. These results demonstrate that inorganic chemical denudation, viewed at the global scale, results in drawdown of atmospheric carbon dioxide. We conclude by identifying several future steps to improve the inversions that underlie these results.

VI.2: Introduction

Chemical weathering modulates the abundance of atmospheric carbon dioxide (CO_2) by transferring alkalinity (ALK) and dissolved inorganic carbon (DIC) from the lithosphere to the ocean-atmosphere system. Previously, researchers have quantified the influence of chemical denudation on climate by apportioning observations of river dissolved load among contributions from end-members such as silicate and carbonate weathering, meteoric precipitation, evaporite dissolution, sulfide oxidation, organic carbon oxidation, and anthropogenic pollution (Négrel et al., 1993; Gaillardet et al., 1999; Burke et al., 2018). Such inversion calculations underlie the recognition that a substantial fraction of global river sulfate (SO_4^{2-}) derives from oxidation of sulfide in sedimentary and igneous lithologies, complicating the canonical hypothesis that silicate weathering regulates atmospheric CO_2 concentration over geologic time (Walker et al., 1981; Calmels et al., 2007; Torres et al., 2016; Burke et al., 2018, Hilton and West, 2020; Kemeny et al., 2021).

Burke et al. (2018) found that approximately 65% of global river SO_4^{2-} does not derive from meteoric inputs or evaporite dissolution; this "excess SO_4^{2-}" was instead interpreted to reflect approximately equal contributions from anthropogenic inputs and crustal sulfide oxidation. Here we apply a new inversion model to extend the analysis of Burke et al. (2018) and calculate the $\delta^{34}S$ of this excess SO_4^{2-} (Kemeny and Torres, 2021). In turn, we account for anthropogenic inputs to excess SO_4^{2-} to calculate the $\delta^{34}S$ of crustal sulfide and interpret that value in the context of the global sulfur cycle. Lastly, we show that the net $\Delta ALK/\Delta DIC$ ratio of inorganic chemical weathering is >2 and that the inorganic component of global chemical denudation results in pCO_2 decline.

VI.3: The $\delta^{34}S$ of global excess SO_4^{2-} is between -6.2‰ and 1.0‰

Inversion of the Burke et al. (2018) dataset finds that, for 90% of individual river water samples and when treating precipitation as an independent end-member, the median amount of excess SO_4^{2-} ranges from 32% to 99% of dissolved SO_4^{2-} and the median excess SO_4^{2-} $\delta^{34}S$ value ranges from -13.9‰ to 12.4‰ (Fig. VI-1; VI.10). In river water samples with high fractions of excess SO_4^{2-}, by mass balance the $\delta^{34}S$ of excess SO_4^{2-} must closely resemble the $\delta^{34}S$ of river SO_4^{2-}. As a result, in many samples the $\delta^{34}S$ of excess SO_4^{2-} is only slightly lower than measured SO_4^{2-} $\delta^{34}S$ (Fig. VI-S3). We find that globally integrated excess SO_4^{2-} accounts for 2.6 to 3.6 Tmol SO_4^{2-}/yr, consistent with the 3.1 Tmol SO_4^{2-}/yr value in Burke et al. (2018). The flux-weighted $\delta^{34}S$ of global excess SO_4^{2-} ranges from -6.2‰ to 1.0‰ in 90% of simulations, with a median value of -1.7‰ (Fig. VI-1). This value is indistinguishable from the bulk Earth value of 0‰ and is 6.1‰ lighter than the $\delta^{34}S$ of flux-weighted global river SO_4^{2-} (MacNamara and Thode, 1950; Burke et al., 2018).

The global excess SO_4^{2-} flux is dominated by contributions from a relatively small number of rivers (Fig. VI-S4). Only 25 rivers contribute >1% of the global excess SO_4^{2-} flux and only the Amazon, Mississippi, and Yangtze Rivers contribute >9%. While the flux-weighted $\delta^{34}S$ of global excess SO_4^{2-} is dominated by only a few samples, our findings are unlikely to be overtly biased by these particular systems because the $\delta^{34}S$ of excess SO_4^{2-} in those samples is similar to most other rivers in the compilation.

To explore the sensitivity of inversion output we also consider results when using Cl^- critical values to constrain inputs from the precipitation end-member. Cl^- critical values define the maximum amount of Cl^- in a river water sample that can be attributed to meteoric inputs and are calculated as the concentration of Cl^- in meteoric precipitation scaled by the

ratio of precipitation to discharge within a catchment (Gaillardet et al., 1999). The Burke et al. (2018) dataset contains 33 samples with Cl^- critical values and measurements of major ion chemistry. Results when applying Cl^- critical values differ substantially from results when treating precipitation as an independent end-member for both the full dataset and when inverting only the subset of samples with Cl^- critical values. For an inversion using Cl^- critical values, excess SO_4^{2-} accounts for 2.2 to 3.2 Tmol SO_4^{2-}/yr globally and the global flux-weighted excess SO_4^{2-} $\delta^{34}S$ ranges from -12.2‰ to -1.3‰ across 90% of simulations (Fig. VI-1). These results show less excess SO_4^{2-} and with lighter SO_4^{2-} $\delta^{34}S$ values than are calculated when precipitation is treated as an independent end-member.

The reason for the differing results is that inversion output using Cl^- critical values often has lower fractional Cl^- contributions from the precipitation end-member and higher fractional Cl^- contributions from the evaporite end-member than results where precipitation is treated as an independent end-member (Fig. VI-S10A). This difference reflects that the inversion can find successful results for nearly any fractional contribution of precipitation to river Cl^- but is statistically more likely to find results where the precipitation end-member provides more Cl^- than described by Cl^- critical values. The difference in model behavior is critical because the higher flux of Cl^- from evaporite dissolution also entails a larger contribution of the evaporite end-member to river SO_4^{2-} (Fig. VI-S10B). Because the SO_4^{2-}/Cl^- ratio of the evaporite end-member exceeds the same ratio in precipitation, the higher evaporite Cl^- flux causes a reduction in the amount of SO_4^{2-} sourced from the excess SO_4^{2-} end-member (Fig. VI-S10B). In turn, the enhanced input of high-$\delta^{34}S$ evaporite SO_4^{2-} results in lower excess SO_4^{2-} $\delta^{34}S$ values in many samples (Fig. VI-S10C) and in globally integrated excess SO_4^{2-} $\delta^{34}S$ (Figs. VI-S11 and VI-S12).

These results demonstrate that the attribution of river Cl^-, as well as the relative SO_4^{2-}/Cl^- ratios of the precipitation and evaporite end-members, are crucial and under-constrained components of calculating the $\delta^{34}S$ of sample and global excess SO_4^{2-}. In general, a chemical tracer distinguishing meteoric precipitation from evaporite inputs would be a large asset to inversion calculations. Future estimates for the amount and $\delta^{34}S$ of excess SO_4^{2-} could improve determinations of Cl^- critical values by considering the annual hydrological cycle at each river water sampling site or by performing a catchment-by-catchment tailoring of the chemical and isotopic composition of the evaporite and precipitation end-members to local conditions. In the interest of including as much data as possible in the inversion, for the remainder of the analysis we consider a broad range of possible excess SO_4^{2-} $\delta^{34}S$ values following the results that treat precipitation as an independent end-member.

VI.4: Accounting for anthropogenic inputs

The 2.6 to 3.6 Tmol excess SO_4^{2-}/yr primarily reflects inputs from sulfide oxidation and anthropogenic sources. Estimates for the magnitude of anthropogenic SO_4^{2-} pollution in rivers vary from about 30% (Berner, 1971; Meybeck, 2003) to about 50% (Husar and Husar, 1985; Ivanov, 1981; Ivanov et al., 1983; Brimblecombe et al., 1989) of all river SO_4^{2-}, corresponding to absolute anthropogenic inputs of approximately 1.3 to 2.4 Tmol/yr. However, these estimates are typically based on comparisons of the SO_4^{2-}/Cl^- ratio in river systems from different regions of the world and often do not account for how difference in catchment lithology, erosional intensity, or hydrology might alter the ratio independent of anthropogenic pollution. Burke et al. (2018) suggested Na^+/Cl^- as a different metric of anthropogenic inputs that, taken at face value, suggests the contribution of anthropogenic SO_4^{2-} may be closer to 0.5 Tmol/yr (VI.14.1.3). In this work we thus consider two ranges for the magnitude of anthropogenic inputs, a low-pollution case with 0.5 to 1.3 Tmol/yr and a high-pollution case with 1.3 to 2.4 Tmol/yr, and present results for both ranges. Furthermore, we impose the condition that at least 0.5 Tmol/yr of excess SO_4^{2-} derive from oxidation of crustal sulfide (Lerman et al., 2007). For these conditions we calculate that between 1.6 and 2.9 Tmol SO_4^{2-}/yr are derived from the oxidation of crustal sulfide in the low-pollution scenario and between 0.7 and 2.0 Tmol SO_4^{2-}/yr are derived from the oxidation of crustal sulfide in the high-pollution scenario.

Constraining the isotopic composition of crustal sulfide also requires constraining the $^{34}S/^{32}S$ ratio of anthropogenic SO_4^{2-}. We take four approaches to evaluating the $\delta^{34}S$ of pollution. First, we consider the SO_4^{2-} $\delta^{34}S$ value of rivers that are generally thought to be polluted, such as the Mississippi, the Yangtze, and the Indus Rivers. In these three systems

SO_4^{2-} $\delta^{34}S$ values range from -0.7‰ to 5.4‰, suggesting that the $\delta^{34}S$ of anthropogenic SO_4^{2-} may be only slightly elevated from 0‰. Second, we consider rivers with dissolved Na^+/Cl^- ratios less than 1.1, which was suggested as a threshold for substantial anthropogenic inputs (Fig. VI-S5; Burke et al., 2018). Values of SO_4^{2-} $\delta^{34}S$ in such low Na^+/Cl^- systems range from -2.2‰ to 7.6‰ with excess SO_4^{2-} $\delta^{34}S$ values from -7.1‰ to 4.6‰, consistent with anthropogenic SO_4^{2-} having a range of $\delta^{34}S$ values near bulk Earth. Third, we consider the $\delta^{34}S$ of atmospheric deposition; the $\delta^{34}S$ of anthropogenic sulfur in a Greenland ice core averaged 3±1.5‰ (Patris et al., 2002) while values of SO_4^{2-} $\delta^{34}S$ in meteoric precipitation range from approximately 0‰ to 5‰ (Hesslein et al, 1988; Likens et al., 2002; Patris et al., 2002; Gíslason and Torrsander, 2006; Zhu et al., 2016; Yan et al., 2020). Lastly, measurements $\delta^{34}S$ in sources of anthropogenic contamination, such as ore and coal, exhibit wide ranges but tend to center around values slightly elevated from 0‰ (Nielsen et al., 1991; Killingsworth and Bao, 2015). Motivated by these observations, we model anthropogenic SO_4^{2-} as having $\delta^{34}S$ values between 0‰ and 5‰.

Accounting for anthropogenic inputs constrains the $\delta^{34}S$ of crustal sulfide between -11.0‰ and 0.6‰ (median: -3.5‰) for the low-pollution scenario and between -26.6‰ and 0.0‰ (median: -7.6‰) for the high-pollution scenario (Fig. VI-2A). The lower values of crustal sulfide $\delta^{34}S$ within these ranges occur at higher anthropogenic SO_4^{2-} $\delta^{34}S$ values or larger fractions of anthropogenic SO_4^{2-} relative to excess SO_4^{2-} (Fig. VI-S6).

VI.5: Crustal sulfide $\delta^{34}S$ constrains the global sulfur cycle

The calculated distributions of crustal sulfide $\delta^{34}S$ are compared with predictions for the isotopic composition of sulfide in marine sediment reached using both a standard 1-input 2-output mass balance model of the global sulfur cycle (Rees, 1970) and two additional mass balance models accounting for shallow and deep marine sulfide, evaporite, and mantle reservoirs (VI.14.2). In all cases we assume that the amount and $^{34}S/^{32}S$ ratio of seawater SO_4^{2-} is in steady-state such that inputs of river SO_4^{2-} are balanced by outputs through formation of evaporite minerals and burial of sulfide in marine sediment; in these models the fractional output of sedimentary sulfide (f_{pyr}) is calculated using river SO_4^{2-} $\delta^{34}S$, seawater SO_4^{2-} $\delta^{34}S$, and fractionations for the formation of evaporite and sedimentary sulfide ($^{34}\Delta$) (Fig. VI-2B). We take sedimentary sulfide to also include organic sulfur, meaning that $^{34}\Delta$ reflects the difference between SO_4^{2-} and non-SO_4^{2-} outputs and may not reflect the fractionation associated with microbial sulfate reduction specifically.

The common 1-input 2-output mass balance model of the global sulfur cycle (Eqs. VI-1 and VI-2; VI.10) predicts that 47% of river SO_4^{2-} is removed as marine sulfide with a $\delta^{34}S$ value of -14‰ when common values are assumed for the fractionations associated with marine sulfide formation (-35‰), the formation of evaporite minerals (0‰), and the $\delta^{34}S$ of river SO_4^{2-} (4.4‰) (Fig. VI-2B grey triangle). For the larger fractionation of -50‰, f_{pyr} decreases to 33% and the calculated $\delta^{34}S$ of sedimentary sulfide decreases to -29‰ (Fig. VI-2 grey square). A key observation of this work is that the median excess SO_4^{2-} and crustal sulfide $\delta^{34}S$ values, as well as most of the distribution of crustal $\delta^{34}S$ values, are ^{34}S-enriched relative to this -14‰ to -29‰ isotopic range. As described above, however, we stress that this result is not necessarily replicated when the inversion uses Cl^- critical

values rather than treating meteoric precipitation as an independent end-member (Figs. VI-S10, VI-S11, VI-S12, and VI-S13). Below we discuss several possible explanations for the difference in $\delta^{34}S$ between crustal sulfide and the values expected for marine sulfide.

As a first explanation, the difference in $\delta^{34}S$ between weathering crustal sulfide and our predicted values for marine sedimentary sulfide may reflect non-steady-state behavior in the global sulfur cycle. If weathering sulfide has a $\delta^{34}S$ value substantially heavier than the sulfide output in marine sediment, then at constant seawater SO_4^{2-} concentrations our observations imply that the $^{34}S/^{32}S$ ratio of seawater SO_4^{2-} is currently increasing. Such a finding is consistent with long-term change in seawater SO_4^{2-} $\delta^{34}S$ (Claypool et al., 1980), but inconsistent with evidence from carbonate-associated sulfate for a decline in seawater SO_4^{2-} $\delta^{34}S$ over the last few Myr (Rennie et al., 2018). These considerations are complicated substantially when also considering that seawater SO_4^{2-} concentrations may be variable, with pore-fluid evidence indicating a Cenozoic increase in marine SO_4^{2-} concentrations (Lowenstein et al., 2001). Evidence for increasing seawater SO_4^{2-} concentrations with a decline in SO_4^{2-} $\delta^{34}S$ could be explained through either enhanced crustal sulfide oxidation with a $\delta^{34}S$ value near bulk-Earth or through a reduction in the formation of isotopically light sulfide within marine sediment.

Second, we can consider the implications of our results if the global sulfur cycle is in isotopic steady-state. Under this scenario, the results of our inversion model suggest that the fractionation associated with formation of marine sulfide may have a smaller magnitude than previously assumed. Using the 1-input 2-output model, the steady-state fraction of river SO_4^{2-} output from the ocean as sulfide is constrained between 52% and 81% (median: 68%) with an expressed fractionation between -32‰ and -20‰ (median: -25‰) in the case

of 0.5-1.3 Tmol/yr anthropogenic SO_4^{2-}, and between 35% and 79% (median: 58%) with an expressed fractionation of -48‰ to -21‰ (median: -29‰) in the case of 1.3-2.4 Tmol/yr anthropogenic SO_4^{2-}.

The standard 1-input 2-output mass balance model does not consider that inputs of mantle sulfur to the crustal sulfide reservoir could increase the $\delta^{34}S$ of weathering sulfide towards the bulk-Earth value of 0‰. If such mantle inputs are substantial, the $\delta^{34}S$ of crustal sulfide could remain elevated relative to low-$\delta^{34}S$ sulfide output in marine sediment. However, to ensure steady state in the isotopic composition of the mantle, the input of 0‰ sulfur to the crustal reservoir would require replacement by 0‰ sulfur derived from marine sediment and subducted SO_4^{2-}. Moreover, recent evidence of local influences on sulfide $\delta^{34}S$ have stressed the importance of distinguishing between deep-water sulfide and shallow-water sulfide (Pasquier et al., 2017, 2021). Using a steady-state mass balance model that accounts for mantle inputs, the evaporite reservoir, and two marine sulfide reservoirs, we identify a trade-off where larger steady-state $\delta^{34}S$ differences between crustal sulfide and total marine sulfide are associated with increases in the fraction of crustal sulfide derived from the mantle, lower values of f_{pyr}, and enhanced subduction of SO_4^{2-} into the mantle (Figs. VI-2C, D, VI-S15, and VI-S16). Using prior estimates from $\delta^{7}Li$ to constrain the fraction of mantle inputs to the surface weathering environment, our steady-state model with two sulfide reservoirs constrains f_{pyr} between about 35% and 65% (Figs. VI-S15 and VI-S16; Dellinger et al., 2014).

VI.6: The timescale-dependent interpretation of f_{pyr}

The results of our inversion, as interpreted through multiple steady-state mass balance models, constrain f_{pyr} between about 35% and 65%. This wide set of values occupies an interesting intermediate range between published estimates; Halevy et al. (2012) used a macrostratigraphic database to place f_{pyr} between 80% and 100% while Tostevin et al. (2014) used measurements of $^{33}S/^{32}S$ ratios in seawater SO_4^{2-} to constrain f_{pyr} between 10% and 45%. Because Halevy et al. (2012) reached their estimate for f_{pyr} by quantifying the abundance of evaporites preserved through geologic time, their elevated f_{pyr} value should be viewed as reflecting the behavior of the global sulfur cycle over hundreds of millions of years. If the same exercise were conducted several hundred million years from now, the time-averaged rate of evaporite preservation will likely have declined further and the long-term f_{pyr} value will have increased. This approach is fundamentally different from approaches that consider modern river SO_4^{2-} $\delta^{34}S$ in relation to one or multiple fractionation factors, which instead reflect the value of f_{pyr} over timescales corresponding to the average age of the rocks being weathered. The f_{pyr} value of this study and Tostevin et al. (2014) are relevant over that shorter timescale of fluvial denudation.

The reason that we find higher f_{pyr} values than Tostevin et al. (2014) over the timescale of rock weathering is not fully resolved. Tostevin et al. (2014) used a relatively low $\delta^{34}S$ value for sedimentary sulfide (-40‰) and found that weathering of igneous sulfide contributed substantially to the moderate $\delta^{34}S$ values of fluvial SO_4^{2-}. By limiting the fractional contribution of mantle-derived sulfide to 40%, our mass balance calculations require higher values for total marine sulfide $\delta^{34}S$ and f_{pyr} but did not account for any constraints from $^{33}S/^{32}S$ ratios (Fig. VI-2). Moreover, simply adjusting the Tostevin et al.

(2014) model to use an elevated $\delta^{34}S$ value for sedimentary sulfide and lower contributions from evaporite and igneous end-members did not necessarily result in higher f_{pyr} predictions because the calculation depended strongly on the $\Delta^{33}S$ of sedimentary sulfide. Direct measurements of $\Delta^{33}S$ in global river water samples would help to reconcile the different values of f_{pyr} diagnosed through minor sulfur isotopes and our inversion of major sulfur isotope ratios and dissolved ion chemistry.

VI.7: Sulfide oxidation and the global carbon cycle

Our inversion identifies large ranges in the fraction of carbonate mineral weathering (R) and fraction of weathering acid sourced from sulfide oxidation (Z) among individual river water samples (Figs. VI-3 and VI-S9). The median R values in 90% of the weathering systems range from 0.39 to 1.00, the median Z values range from 0.01 to 0.49, and the median ΔALK/ΔDIC ratios range from 1.2 to 4.3. Many of the world's largest rivers, such as the Amazon, Brahmaputra, Lena, Mississippi, Orinoco, and the Yangtze, have ΔALK/ΔDIC ratios between 1.8 and 2.2. These rivers plot near the line Z = 1-R, corresponding to the condition ΔALK/ΔDIC = 2, indicating that the alkalinity removed during sulfide oxidation approximately counteracts the alkalinity gained during silicate weathering. Weathering upstream of the sampling sites in these systems thus does not exert a substantial influence on atmospheric pCO_2 over timescales longer than the 5-10 kyr timescale of carbonate compensation and shorter than the 10 Myr residence time of seawater SO_4^{2-} (Torres et al., 2016). In future work the R and Z values reached through our global inversion should be compared with values reached through in-depth studies of individual catchments accounting for the chemistry of local lithologies and precipitation.

Globally integrated, inorganic chemical denudation has a median R value of 0.81, with 90% of distribution values between 0.76 and 0.85, and a median Z value of 0.13, with 90% of the distribution values between 0.11 and 0.15. These weathering fractions correspond to a median ΔALK/ΔDIC ratio of 2.2, with 90% of distribution values between 2.0 and 2.3. Accounting for 2 Tmol/yr of anthropogenic SO_4^{2-} lowers the median Z value to 0.05 and increases global median ΔALK/ΔDIC to 2.4 (Fig. VI-3). Because the ΔALK/ΔDIC ratio of global weathering is elevated above 2, alkalinity gained through

silicate weathering exceeds alkalinity lost during sulfide oxidation. We conclude that inorganic chemical denudation results in net pCO_2 decline, despite the recognition that some catchments host sufficient sulfide oxidation to locally drive pCO_2 increase (Torres et al., 2016). We also note that these calculations reflect the dynamics of the weathering systems and are not resolved to marine processes. That is, they inherently assume silicate-derived Na^+, K^+, and Mg^{2+}, as well as sulfide-derived SO_4^{2-}, accumulate in seawater for the duration over which pCO_2 is affected (Kemeny and Torres, 2021).

VI.8: Conclusions

We apply an inversion model to the global river data of Burke et al. (2018). In results that treated precipitation as an independent end-member, rather than using Cl^- critical values, the calculation constrains the $\delta^{34}S$ of global excess SO_4^{2-} between -6.2‰ and 1.0‰. The combined uncertainties in end-member chemical compositions, inversion-constrained mixing fractions, and the isotopic composition and magnitude of anthropogenic SO_4^{2-} inputs lead to a range of allowable values for the $^{34}S/^{32}S$ ratio of SO_4^{2-} derived from crustal sulfide oxidation. The $\delta^{34}S$ of crustal sulfide is constrained between -11.0‰ and 0.6‰ when accounting for 0.5 to 1.3 Tmol/yr anthropogenic SO_4^{2-} and between -26.6‰ and 0.0‰ when accounting for 1.3 to 2.4 Tmol/yr anthropogenic SO_4^{2-}. In results where anthropogenic SO_4^{2-} represents a substantial fraction of total excess SO_4^{2-} and has an elevated $\delta^{34}S$ value, the calculated $\delta^{34}S$ of weathering sulfide is consistent with expectations for a fractionation of -35‰ between seawater and marine sulfide. However, most of the crustal sulfide $\delta^{34}S$ distribution is higher than expected from a standard steady-state mass balance model of the global sulfur cycle. These observations suggest that either the modern sulfur cycle is not in isotopic steady-state, that the value of f_{pyr} and the $^{34}S/^{32}S$ isotope ratio of marine sulfide are heavier than expected, or that the crustal sulfide reservoir is elevated in $^{34}S/^{32}S$ relative to sulfide in marine sediment with the difference accommodated by incorporation of mantle sulfur. For the latter two cases, our results constrain f_{pyr} between about 35% and 65% over timescales similar to the average age of the rocks being weathered. Furthermore, we calculate that the global weathering ratio of alkalinity to dissolved inorganic carbon is between 2.0 and 2.3, with several large weathering systems exhibiting ratios between 1.8 and 2.2. These results demonstrate that

global chemical weathering, even in the presence of substantial sulfide oxidation within individual river catchments, results in net pCO_2 drawdown.

Future research could refine the estimated values for crustal sulfide $\delta^{34}S$ and f_{pyr} by improving the inversion underlying their calculation. Foremost, each of the river systems that contribute substantially to global excess SO_4^{2-} should be independently inverted with end-members specific to the local weathering environment. This effort will entail constraining the local chemistry of precipitation and silicate rocks, the presence and character of evaporites, and the seasonal and annually integrated chemistry of local anthropogenic pollution. Moreover, the inversions should utilize samples collected throughout the catchments and across different seasons. Although the major ion chemistry and SO_4^{2-} $\delta^{34}S$ data required for such analyses is unavailable for most catchments, we suspect that existing measurements from the Amazon, Mississippi, Ganges, and Mackenzie Rivers may underlie defensible estimates for those systems. Second, annually integrated ratios of precipitation to discharge should be established for each catchment to reach robust estimates of Cl^- critical values. Third, improving estimates of marine sulfide $\delta^{34}S$ and f_{pyr} will require stronger constraints on the input of mantle sulfur into the weathering system, which might be reached through measurement of radiogenic isotope systems. Lastly, the process of clay formation can strongly alter the dissolved chemistry of rivers away from a linear mixture of lithologic end-members. Measurement of Si and Li concentrations and isotope ratios in river water and suspended sediment may help to constrain the effects of clay formation on estimates of R and Z. Overall, improved estimates of global weathering dynamics will likely require combining results reached through catchment-level analyses.

VI.9: Acknowledgments

P.C.K. is supported by The Fannie and John Hertz Foundation Cohan-Jacobs and Stein Families Fellowship. The data underlying these calculations are from Burke et al. (2018) and are inverted using the model of Kemeny and Torres (2021). The computations were conducted in the Resnick High Performance Computing Center, a facility supported by the Resnick Sustainability Institute at the California Institute of Technology.

VI.10: Methods

The dataset of Burke et al. (2018) contains 67 river water samples with values of SO_4^{2-} $\delta^{34}S$ and concentrations of Ca^{2+}, Mg^{2+}, Na^{+}, Cl^{-}, and SO_4^{2-}. These samples represent approximately 47% of the world's freshwater discharge and 40% of global river SO_4^{2-}. The abundance and $^{34}S/^{32}S$ ratio of excess SO_4^{2-} in these samples is quantified using Mixing Elements ANd Dissolved Isotopes in Rivers (MEANDIR) (Kemeny and Torres, 2021). Our inversion includes end-members representing silicate weathering, carbonate weathering, evaporite dissolution, meteoric precipitation, and excess SO_4^{2-}, where the excess SO_4^{2-} end-member represents inputs from anthropogenic pollution and crustal sulfide oxidation (Table VI-1). Note that here we use "excess SO_4^{2-}" to refer to the concept described as "other SO_4^{2-}" in Kemeny and Torres (2021), which is calculated differently from the "excess SO_4^{2-}" of Burke et al. (2018). The evaporite end-member is constrained to reflect a stoichiometric combination of gypsum, epsomite, and halite. Lerman et al. (2007) estimated that the ratio of halite to gypsum in evaporites is near 2, and the prior of the evaporite end-member in the main analysis spans halite to gypsum and epsomite ratios of approximately 0.5 to 5 (Table VI-1). Results for different possible evaporite SO_4^{2-}/Cl^{-} ratios and $\delta^{34}S$ ranges are given in Fig. VI-S7.

The inversion uses a Monte Carlo technique to propagate uncertainty in end-member chemistry and uses a proportional cost function to solve for the fractional contributions of end-members. The model only accepts results that recreate between 95% and 105% of each river observation. The inverted data and end-members are normalized to the charge-equivalent sum of Ca^{2+}, Mg^{2+}, Na^{+}, and SO_4^{2-}, and most river water samples are successfully inverted 2,000 times. Following inversion, the $\delta^{34}S$ of excess SO_4^{2-} in

each sample is calculated by performing a second Monte Carlo simulation on successful results that accounts for the given ranges in end-member $^{34}S/^{32}S$ ratios. The results from each sample are then aggregated into a flux-weighted estimate for the $\delta^{34}S$ of global excess SO_4^{2-}. Finally, a third Monte Carlo calculation accounts for anthropogenic inputs by removing from global excess SO_4^{2-} either 0.5 to 1.3 Tmol SO_4^{2-}/yr or 1.3 to 2.4 Tmol SO_4^{2-}/yr with $\delta^{34}S$ value ranging from 0‰ to 5‰. Results for different anthropogenic SO_4^{2-} $\delta^{34}S$ ranges are given in Fig. VI-S8. We also calculate the ΔALK/ΔDIC of chemical weathering in individual river catchments and the flux-weighted global ΔALK/ΔDIC value.

Our results are considered in the context of a common 1-input 2-output mass balance model of the global sulfur cycle (Eqs. VI-1 and VI-2; Fig. VI-2B) and two other steady-state models (VI.14.2). In the first model the rate of change in the product of seawater SO_4^{2-} abundance (S_{ocn}) and its $\delta^{34}S$ value ($\delta^{34}S_{ocn}$) is equal to the difference between an input flux from rivers (subscript riv) and output fluxes from formation of sulfide (subscript pyr) and formation of evaporite minerals (subscript evap), where each term is the product of SO_4^{2-} flux (J) and $\delta^{34}S$ value. By assuming steady-state for seawater SO_4^{2-}, the fraction of river SO_4^{2-} leaving as marine sulfide simplifies to a function of river SO_4^{2-} $\delta^{34}S$, seawater SO_4^{2-} $\delta^{34}S$, and the fractionation associated with sulfide formation ($\delta^{34}S_{pyr}$ - $\delta^{34}S_{ocn}$) (Eq. VI-2). For this model we consider results under the assumption that the $\delta^{34}S$ of SO_4^{2-} derived from crustal sulfide reflects the isotopic composition of sulfide formed in marine sediment. Our calculations use a river SO_4^{2-} $\delta^{34}S$ value of 4.4‰ and seawater SO_4^{2-} $\delta^{34}S$ value of 21‰.

$$\frac{d}{dt}(S_{ocn}\delta^{34}S_{ocn}) = J_{riv}\delta^{34}S_{riv} - J_{pyr}\delta^{34}S_{pyr} - J_{evap}\delta^{34}S_{evap} \quad \text{(VI-1)}$$

$$f_{pyr} = \frac{\delta^{34}S_{riv} - \delta^{34}S_{ocn}}{\delta^{34}S_{pyr} - \delta^{34}S_{ocn}} \quad \text{(VI-2)}$$

VI.11: Figures

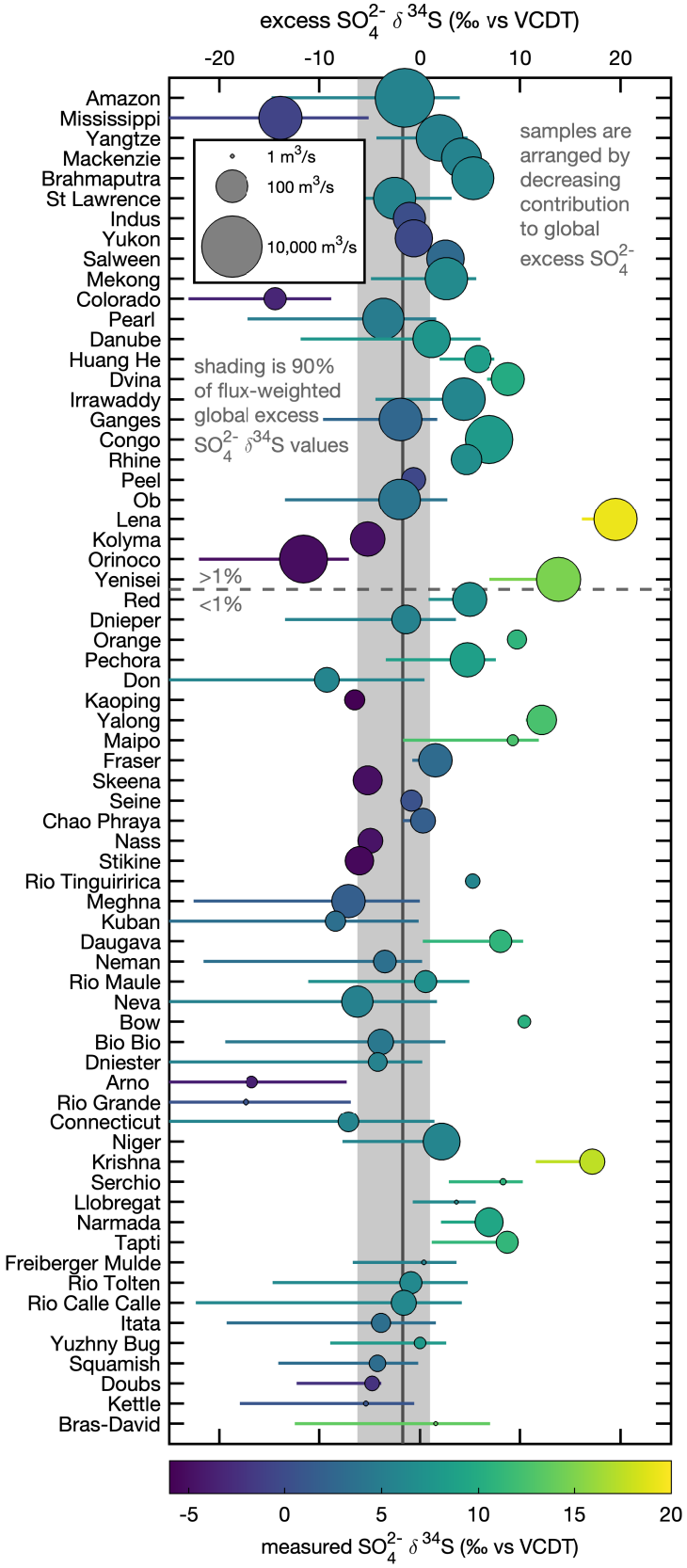

Fig. VI-1: Inversion-constrained $\delta^{34}S$ of excess SO_4^{2-}, arranged top-to-bottom by contribution to global excess SO_4^{2-}, color-coded by measured river SO_4^{2-} $\delta^{34}S$ and size-coded by discharge. Median excess SO_4^{2-} $\delta^{34}S$ values in individual samples range from -17.3‰ to 19.5‰. The horizontal dotted line separates rivers with a median contribution of at least 1% to global excess SO_4^{2-}. The distribution of flux-weighted global excess SO_4^{2-} $\delta^{34}S$ values is between -6.2‰ to 1.0‰ (5th to 95th percentile of results, grey shading). Error bars on individual samples extend from the 25th to 75th percentile of inversion-constrained results.

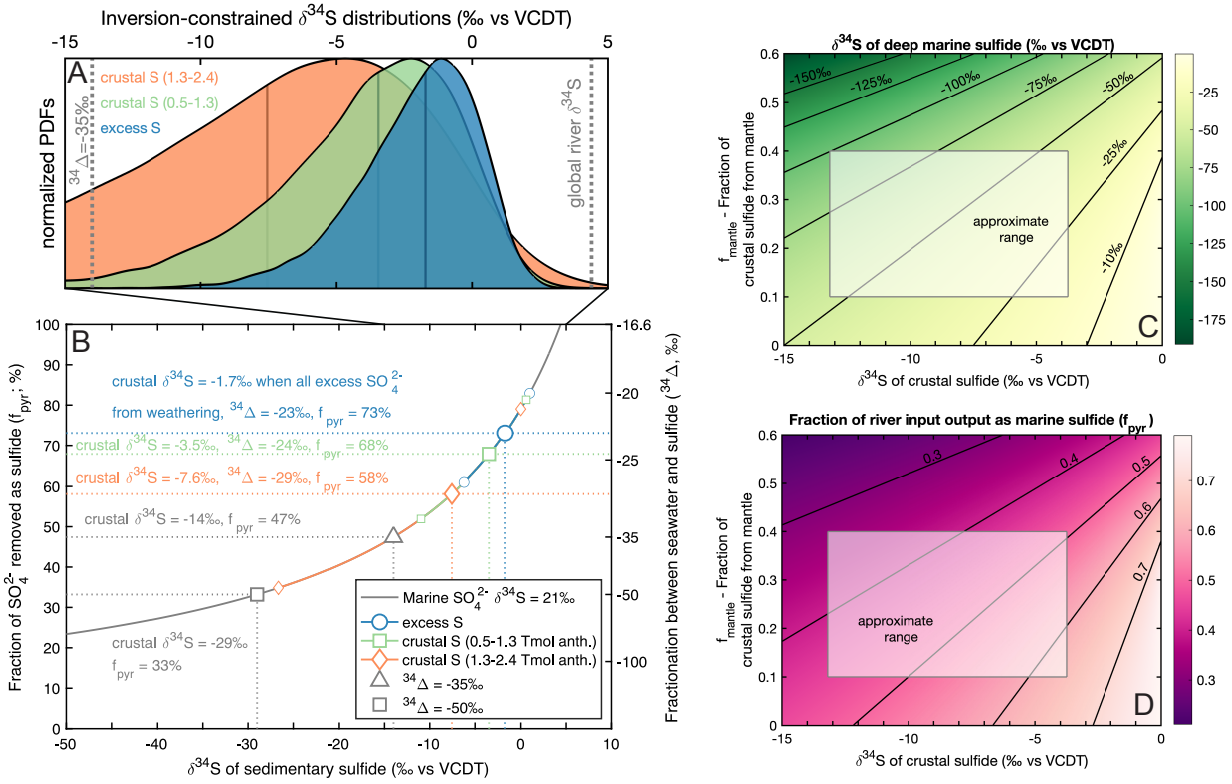

Fig. VI-2: Implications of results for the global sulfur cycle. (A) Normalized probability density functions for the $\delta^{34}S$ of global excess SO_4^{2-} (blue), crustal sulfide in the low-pollution scenario (0.5 to 1.3 Tmol/yr anthropogenic SO_4^{2-}; green), and crustal sulfide in the high-pollution scenario (1.3 to 2.4 Tmol/yr anthropogenic SO_4^{2-}; orange). Accounting for pollution decreases the median and increases the width of the crustal $\delta^{34}S$ distributions. (B) Results of a 1-input 2-output model of the sulfur cycle. When all excess SO_4^{2-} is assumed to derive from oxidation of crustal sulfide, fractionation during marine sulfide formation ($^{34}\Delta$) is constrained between -27‰ and -20‰ with f_{pyr} between 61% and 83% (blue). In the low-pollution scenario the $\delta^{34}S$ value of weathering sulfide is constrained between -11.0‰ and 0.6‰ with $^{34}\Delta$ between -32‰ and -20‰ and f_{pyr} between 52% and 81% (green). In the high-pollution scenario the $\delta^{34}S$ value of weathering sulfide is constrained between -26.6‰ and 0.0‰ with $^{34}\Delta$ between -48‰ and -21‰ and f_{pyr} between 35% and 79% (orange). Results are also shown for $^{34}\Delta$=35‰ (grey triangle) and $^{34}\Delta$=50‰ (grey square). These calculations assume that the $\delta^{34}S$ of sulfide output in marine sediment is equal to the $\delta^{34}S$ of crustal sulfide. (C, D) Results from a steady-state mass balance model resolving seawater, deep and shallow sulfide, mantle, and evaporites. (C) The $\delta^{34}S$ of deep marine sulfide and (D) the fractional output of river SO_4^{2-} as marine sulfide against the $\delta^{34}S$ of crustal sulfide and the fraction of weathering sulfide derived from mantle inputs (f_{mantle}). These results constrain f_{pyr} between approximately 35% and 65%, consistent with results from the 1-input 2-output mass balance model in (B). Results in (C) and (D) assume 30% of marine sulfide is output in the deep, highly fractionated reservoir and 70% is output in shelf sediment with a $\delta^{34}S$ of 0‰ (VI.14.2.2).

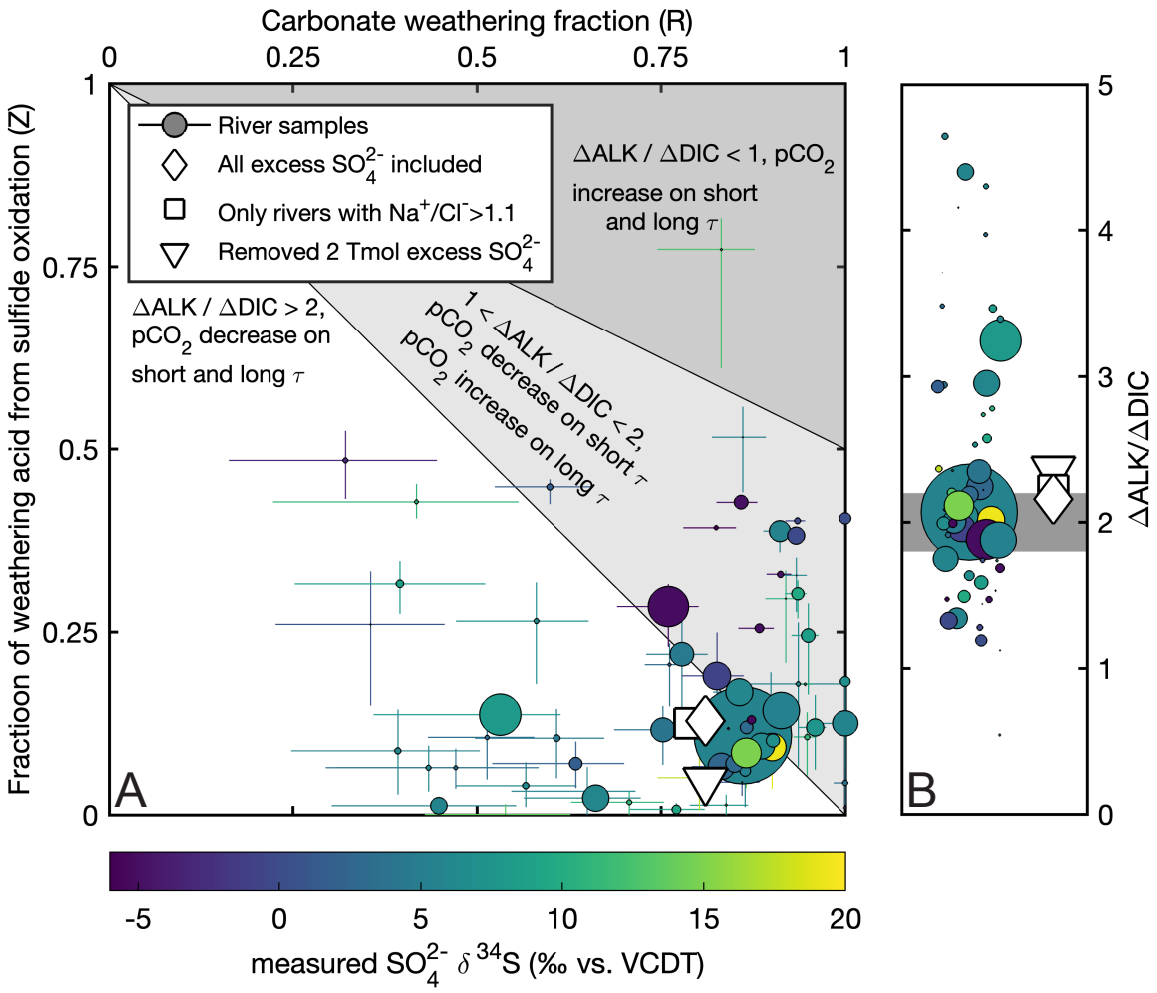

Fig. VI-3: Inversion results for the fraction of weathering acid sourced from sulfide oxidation (Z) and the carbonate weathering fraction (R) constrain the impact of chemical weathering on atmospheric carbon dioxide. (A) R and Z of individual river samples, color-coded by measured SO_4^{2-} $\delta^{34}S$ and size-coded by discharge. Many large river systems cluster around the line Z=1-R, corresponding to ΔALK/ΔDIC = 2. Flux-weighted global values are shown for all river data (diamond), without polluted rivers as identified on the basis of Na^+/Cl^- (square), and after accounting for 2 Tmol of anthropogenic SO_4^{2-} inputs (triangle). Overall, the fraction of the global chemical weathering budget that can be diagnosed from dissolved major ion chemistry indicates CO_2 drawdown. (B) The ΔALK/ΔDIC of each river water sample, shown with horizontal jitter to avoid overlap, and the flux-weighted global values. Several major river systems have ΔALK/ΔDIC ratios between 1.8 and 2.2 (grey shading), suggesting that weathering in these systems may exert only modest impacts on atmospheric pCO_2.

VI.12: Tables

Table VI-1: Inversion end-members. End-member chemistry is given relative to the sum of Ca^{2+}, Mg^{2+}, Na^{+}, and SO_4^{2-} in units of charge equivalents. Each end-member has one chemical ratio calculated using values pulled from the other distributions in order to ensure internal consistency ('calculated'), while the evaporite end-member is also subject to additional mineralogical constraints. The chemistry and $\delta^{34}S$ of the evaporite end-member are varied in a sensitivity analysis to determine the influence of the initial distribution on the distribution of crustal sulfide $\delta^{34}S$ values. (Fig. VI-S7).

Inversion end-members						
Notes	**Ratio**	**Precipitation**	**Carbonate**	**Silicate**	**Evaporite**	**Excess SO_4^{2-}**
Ratios relative to sum of Ca^{2+}, Mg^{2+}, Na^{+}, and SO_4^{2-} in eq/eq.	Ca^{2+}	0.005–0.061	calculated	0.050–0.400	0.222–0.422	0
	Mg^{2+}	0.133–0.185	0.000–0.500	0.050–0.400	0.000-0.022	0
	Na^{+}	calculated	0.000–0.000	calculated	calculated	0
	Cl^{-}	0.680–0.980	0.000–0.000	0.000–0.000	calculated	0
	SO_4^{2-}	0.061–0.113	0.000–0.000	0.000–0.000	calculated	1
	$\delta^{34}S$	15–20‰	–	–	10–30‰	–

VI.13: References

Berner, R.A., 1971. Worldwide sulfur pollution of rivers. *Journal of Geophysical Research*, 76(27), pp.6597-6600. https://doi.org/10.1029/JC076i027p06597.

Brimblecombe, P., Hammer, C., Rodhe, H., Ryaboshapko, A. and Boutron, C., 1989. Human Influence on the Sulphur Cycle. *Evolution of the Global Biogeochemical Sulphur Cycle*, SCOPE 39, edited by Brimblecombe, P. and Lein, A., John Wiley & Sons, pp. 77 - 121.

Burke, A., Present, T.M., Paris, G., Rae, E.C., Sandilands, B.H., Gaillardet, J., Peucker-Ehrenbrink, B., Fischer, W.W., McClelland, J.W., Spencer, R.G. and Voss, B.M., 2018. Sulfur isotopes in rivers: Insights into global weathering budgets, pyrite oxidation, and the modern sulfur cycle. *Earth and Planetary Science Letters*, 496, pp.168-177. https://doi.org/10.1016/j.epsl.2018.05.022.

Calmels, D., Gaillardet, J., Brenot, A. and France-Lanord, C., 2007. Sustained sulfide oxidation by physical erosion processes in the Mackenzie River basin: Climatic perspectives. *Geology*, 35(11), pp.1003-1006. https://doi.org/10.1130/G24132A.1.

Claypool, G.E., Holser, W.T., Kaplan, I.R., Sakai, H. and Zak, I., 1980. The age curves of sulfur and oxygen isotopes in marine sulfate and their mutual interpretation. *Chemical Geology*, 28, pp.199-260. https://doi.org/10.1016/0009-2541(80)90047-9.

Dellinger, M., Gaillardet, J., Bouchez, J., Calmels, D., Galy, V., Hilton, R.G., Louvat, P. and France-Lanord, C., 2014. Lithium isotopes in large rivers reveal the cannibalistic nature of modern continental weathering and erosion. *Earth and Planetary Science Letters*, 401, pp.359-372. https://doi.org/10.1016/j.epsl.2014.05.061.

Gaillardet, J., Dupré, B., Louvat, P. and Allegre, C.J., 1999. Global silicate weathering and CO_2 consumption rates deduced from the chemistry of large rivers. *Chemical Geology*, 159(1-4), pp.3-30. https://doi.org/10.1016/S0009-2541(99)00031-5.

Gislason, S.R. and Torssander, P., 2006. Response of sulfate concentration and isotope composition in Icelandic rivers to the decline in global atmospheric SO_2 emissions into the North Atlantic region. *Environmental Science & Technology*, 40(3), pp.680-686. https://doi.org/10.1021/es051325o.

Halevy, I., Peters, S.E. and Fischer, W.W., 2012. Sulfate burial constraints on the Phanerozoic sulfur cycle. *Science*, 337(6092), pp.331-334. https://doi.org/10.1126/science.1220224.

Hesslein, R.H., Capel, M.J. and Fox, D.E., 1988. Sulfur isotopes in sulfate in the inputs and outputs of a Canadian Shield watershed. *Biogeochemistry*, 5(3), pp.263-273. https://doi.org/10.1007/BF02180067.

Hilton, R.G. and West, A.J., 2020. Mountains, erosion and the carbon cycle. *Nature Reviews Earth & Environment*, 1(6), pp.284-299. https://doi.org/10.1038/s43017-020-0058-6.

Husar, R.B. and Husar, J.D., 1985. Regional river sulfur runoff. *Journal of Geophysical Research: Oceans*, 90(C1), pp.1115-1125. https://doi.org/10.1029/JC090iC01p01115.

Ivanov, M., 1981. The Global Biogeochemical Sulphur Cycle. *Some Perspectives of the Major Biogeochemical Cycles*, SCOPE 17, edited by Likens, G., John Wiley & Sons, pp. 61-78.

Ivanov, M., Grinenko, V. and Rabinovich, A., 1983. Sulphur Flux from Continents to Oceans. *The Global Biogeochemical Sulphur Cycle*, SCOPE 19, edited by Ivanov, M. and Freney, J.R., John Wiley & Sons, pp. 331-356.

Lerman, A., Wu, L. and Mackenzie, F.T., 2007. CO_2 and H_2SO_4 consumption in weathering and material transport to the ocean, and their role in the global carbon balance. *Marine Chemistry*, 106(1-2), pp.326-350. https://doi.org/10.1016/j.marchem.2006.04.004.

Kemeny, P.C., Lopez, G.I., Dalleska, N.F., Torres, M., Burke, A., Bhatt, M.P., West, A.J., Hartmann, J. and Adkins, J.F., 2021. Sulfate sulfur isotopes and major ion chemistry reveal that pyrite oxidation counteracts CO_2 drawdown from silicate weathering in the Langtang-Trisuli-Narayani River system, Nepal Himalaya. *Geochimica et Cosmochimica Acta*, 294, pp.43-69. https://doi.org/10.1016/j.gca.2020.11.009.

Killingsworth, B.A. and Bao, H., 2015. Significant human impact on the flux and $\delta^{34}S$ of sulfate from the Largest River in North America. *Environmental Science & Technology*, 49(8), pp.4851-4860. https://doi.org/10.1021/es504498s.

Likens, G.E., Driscoll, C.T., Buso, D.C., Mitchell, M.J., Lovett, G.M., Bailey, S.W., Siccama, T.G., Reiners, W.A. and Alewell, C., 2002. The biogeochemistry of sulfur at Hubbard Brook. *Biogeochemistry*, 60(3), pp.235-316. https://doi.org/10.1023/A:1020972100496.

MacNamara, J. and Thode, H.G., 1950. Comparison of the isotopic constitution of terrestrial and meteoritic sulfur. *Physical Review*, 78(3), p.307. https://doi.org/10.1103/PhysRev.78.307.

Meybeck, M., 2003. Global occurrence of major elements in rivers. Treatise on geochemistry, 5, p.605.

Négrel, P., Allègre, C.J., Dupré, B. and Lewin, E., 1993. Erosion sources determined by inversion of major and trace element ratios and strontium isotopic ratios in river water: the Congo Basin case. *Earth and Planetary Science Letters*, 120(1-2), pp.59-76. https://doi.org/10.1016/0012-821X(93)90023-3.

Nielsen, H., Pilot, J., Grinenko, L.N., Grinenko, V.A, Lein, A., Smith, J.W., and Pankina, R.G., 1991. Lithospheric Sources of Sulphur. *Stable Isotopes: Natural and Anthropogenic Sulphur in the Environment*, SCOPE 43, edited by Krouse, H.R. and Grinenko, V.A., John Wiley & Sons, pp. 65-132.

Patris, N., Delmas, R., Legrand, M., De Angelis, M., Ferron, F.A., Stiévenard, M. and Jouzel, J., 2002. First sulfur isotope measurements in central Greenland ice cores along the preindustrial and industrial periods. *Journal of Geophysical Research: Atmospheres*, 107(D11), pp.ACH-6. https://doi.org/10.1029/2001JD000672.

Rees, C.E., 1970. The sulphur isotope balance of the ocean: An improved model. *Earth and Planetary Science Letters*, 7(4), pp.366-370. https://doi.org/10.1016/0012-821X(69)90051-X.

Rennie, V.C., Paris, G., Sessions, A.L., Abramovich, S., Turchyn, A.V. and Adkins, J.F., 2018. Cenozoic record of $\delta^{34}S$ in foraminiferal calcite implies an early Eocene shift to deep-ocean sulfide burial. *Nature Geoscience*, 11(10), pp.761-765. https://doi.org/10.1038/s41561-018-0200-y.

Torres, M.A., West, A.J., Clark, K.E., Paris, G., Bouchez, J., Ponton, C., Feakins, S.J., Galy, V. and Adkins, J.F., 2016. The acid and alkalinity budgets of weathering in the Andes–Amazon system: Insights into the erosional control of global biogeochemical cycles. *Earth and Planetary Science Letters*, 450, pp.381-391. https://doi.org/10.1016/j.epsl.2016.06.012.

Tostevin, R., Turchyn, A.V., Farquhar, J., Johnston, D.T., Eldridge, D.L., Bishop, J.K. and McIlvin, M., 2014. Multiple sulfur isotope constraints on the modern sulfur cycle. *Earth and Planetary Science Letters*, 396, pp.14-21. https://doi.org/10.1016/j.epsl.2014.03.057.

Veizer, J. and Jansen, S.L., 1979. Basement and sedimentary recycling and continental evolution. *The Journal of Geology*, 87(4), pp.341-370. https://doi.org/10.1086/628425.

Veizer, J. and Jansen, S.L., 1985. Basement and sedimentary recycling-2: time dimension to global tectonics. *The Journal of Geology*, 93(6), pp.625-643. https://doi.org/10.1086/628992.

Walker, J.C., Hays, P.B. and Kasting, J.F., 1981. A negative feedback mechanism for the long-term stabilization of Earth's surface temperature. *Journal of Geophysical Research: Oceans*, 86(C10), pp.9776-9782. https://doi.org/10.1029/JC086iC10p09776.

Yan, Z., Han, X., Lang, Y., Guo, Q. and Li, S., 2020. The abatement of acid rain in Guizhou province, southwestern China: Implication from sulfur and oxygen isotopes. *Environmental Pollution*, 267, p.115444. https://doi.org/10.1016/j.envpol.2020.115444.

Zhu, G., Guo, Q., Chen, T., Lang, Y., Peters, M., Tian, L., Zhang, H. and Wang, C., 2016. Chemical and sulfur isotopic composition of precipitation in Beijing, China. *Environmental Science and Pollution Research*, 23(6), pp.5507-5515. https://doi.org/10.1007/s11356-015-5746-2.

VI.14: Supplementary text

VI.14.1: Extended analysis

VI.14.1.1: Mixing relationships require excess SO_4^{2-}

The dissolved ion chemistry of river water samples provides a qualitative sense for relative contributions from the carbonate, silicate, precipitation, evaporite, and excess SO_4^{2-} end-members (Fig. VI-S1; Table VI-1). The ratios of $Ca^{2+}/(\Sigma^{+}+SO_4^{2-})$ and $Na^{+}/(\Sigma^{+}+SO_4^{2-})$ form a coherent array that separates samples with large contributions from carbonate from those dominated by silicate and evaporite inputs (Fig. VI-S1A). Moreover, the ratio $Cl^{-}/(\Sigma^{+}+SO_4^{2-})$ helps to constrain the contribution of evaporites at lower values of $Ca^{2+}/(\Sigma^{+}+SO_4^{2-})$ (Fig. VI-S1B). In samples with major cation chemistry consistent with carbonate or silicate weathering, $SO_4^{2-}/(\Sigma^{+}+SO_4^{2-})$ often exceeds expectations (Fig. VI-S1C) while values of river SO_4^{2-} $\delta^{34}S$ are mostly lighter than could be reached through conservative mixing of Phanerozoic evaporites and precipitation (Fig. VI-S1D; Claypool et al., 1980). As previously found in Burke et al. (2018), sample dissolved ion chemistry provides strong evidence for a source of SO_4^{2-} in excess of precipitation and evaporites, and with a low value of $\delta^{34}S$. The two most likely sources of isotopically light SO_4^{2-} are the oxidation of crustal sulfide and anthropogenic inputs.

VI.14.1.2: Attribution of river dissolved load

Fractional contributions from the silicate, carbonate, precipitation, evaporite, and excess SO_4^{2-} end-members are quantified using MEANDIR (Kemeny and Torres, 2021). Inversion results show that the dominant source of Ca^{2+} is weathering of the carbonate end-member, while the dominant sources of Na^{+} are the precipitation, evaporite, and silicate

end-members (Fig. VI-S2). The inversion finds that the excess SO_4^{2-} end-member contributes more than 50% of dissolved SO_4^{2-} in 81% of samples (Figs. VI-S2 and VI-S3). The average median fractional contribution of the excess SO_4^{2-} end-member to dissolved SO_4^{2-} is 69% but ranges between 28% and 92% in 90% of samples (Fig. VI-S3A). At high values for the fraction of excess SO_4^{2-}, by mass balance the $\delta^{34}S$ of excess SO_4^{2-} is calculated to be similar to the $\delta^{34}S$ of river SO_4^{2-} (Fig. VI-S3B). For samples with river SO_4^{2-} near the isotopic composition of the evaporite and precipitation inputs, the $\delta^{34}S$ of excess SO_4^{2-} is likewise calculated to be similar to the $\delta^{34}S$ of river SO_4^{2-} (Fig. VI-S3B).

Several samples from large rivers have particularly high values of excess SO_4^{2-} $\delta^{34}S$, including the Lena (19.5‰), the Yenisei (13.9‰), and the Congo (6.9‰). These elevated values reflect that the $\delta^{34}S$ of SO_4^{2-} in these rivers is also high. For example, the Lena River has a SO_4^{2-} $\delta^{34}S$ value of 19.3‰, comparable to that of the evaporite and precipitation inputs (Table VI-1). If anthropogenic SO_4^{2-} dominates excess SO_4^{2-} in these samples, the elevated $\delta^{34}S$ values may reflect that pollution derives predominantly from oxidized forms of sulfur. Conversely, the elevated $\delta^{34}S$ values are difficult to explain if excess SO_4^{2-} in those samples is thought to reflect crustal sulfide oxidation. That is, very high values of sulfide $\delta^{34}S$ (>10‰) are rarely observed at the scale of entire catchments. A more likely interpretation of these results is that our inversion fails to capture local variations in the $\delta^{34}S$ of evaporites and precipitation. The global evaporite end-member in the inversion has $\delta^{34}S$ values ranging from 10‰ to 30‰, such that the median inversion result reflects an evaporite with a $\delta^{34}S$ of about 20‰ (Table VI-1). If gypsum-bearing evaporites in the catchment of the Lena River are elevated in $\delta^{34}S$ relative to this global evaporite end-member, an inversion tuned to local conditions would calculate a lower value

for the $\delta^{34}S$ of excess SO_4^{2-}. Information of the ages of sedimentary rocks in each catchment could be used to further narrow the range in the isotopic composition of evaporites and better constrain the $\delta^{34}S$ of excess SO_4^{2-}.

VI.14.1.3: Accounting for anthropogenic SO_4^{2-}

Several river samples in this analysis are thought to derive from rivers with substantial anthropogenic inputs. In the analysis of Burke et al. (2018) river water samples with Na^+/Cl^- ratios < 1.1 were identified as being polluted. As described above, the SO_4^{2-} $\delta^{34}S$ value of rivers with $Na^+/Cl^- < 1.1$ can thus provide approximate constraints on the isotopic composition of anthropogenic inputs (Fig. VI-S5). Considering rivers with $Na^+/Cl^- < 1.1$ can also provide an estimate for the amount of anthropogenic SO_4^{2-} in rivers. The 8 river samples in this analysis with $Na^+/Cl^- < 1.1$ are responsible for 0.18 Tmol/yr of excess SO_4^{2-}; if representative of rivers globally, up to 0.43 Tmol/yr of excess SO_4^{2-} could be derived from such low-Na^+/Cl^- weathering systems. Assuming all excess SO_4^{2-} in samples with $Na^+/Cl^- < 1.1$ derives from anthropogenic contamination, these samples suggest a maximum anthropogenic contribution of approximately 0.5 Tmol SO_4^{2-}/yr, motivating the lower end of the 0.5 - 1.3 Tmol/y range of anthropogenic SO_4^{2-} that we use in the low-pollution scenario. The value of 0.5 Tmol SO_4^{2-}/yr represents only 9% of total river SO_4^{2-} and is substantially less than estimates that between 30% and 50% of river SO_4^{2-} is derived from anthropogenic sources (Berner, 1971; Husar and Husar, 1985; Ivanov, 1981; Ivanov et al., 1983; Brimblecombe et al., 1989; Meybeck, 2003).

It is notable that the Na^+/Cl^- ratio also has substantial downsides. For example, weathering halite produces river water with $Na^+/Cl^- < 1.1$ even in the absence of

anthropogenic inputs. Moreover, substantial inputs of anthropogenic Cl^- are possible in a system with $Na^+/Cl^- > 1.1$ if there is also input from Na^+-bearing lithologies. As a result, pollutant SO_4^{2-} may have only an indirect relationship with Na^+/Cl^-. Because our study lacks a robust method to identify anthropogenic inputs in individual river water samples, we subtract an estimate of anthropogenic SO_4^{2-} inputs from the estimate of global excess SO_4^{2-}. Future quantification of anthropogenic SO_4^{2-} is likely best done on a site-by-site basis using parameters such as PO_4^{3-}, NO_3^-, NH_4^+, and trace metals. If an end-member representing anthropogenic contamination could be chemically constrained, either at a local or global scale, anthropogenic inputs could be simply represented as an additional inversion end-member in MEANDIR.

When the $\delta^{34}S$ of anthropogenic SO_4^{2-} and excess SO_4^{2-} are equal, by mass balance the $\delta^{34}S$ of crustal sulfide is calculated to equal the $\delta^{34}S$ of excess SO_4^{2-}. Using the 1-input 2-output mass balance model of the global sulfur cycle, this situation constrains f_{pyr} to relatively high values. Conversely, the $\delta^{34}S$ of crustal sulfide became distinct from that of excess SO_4^{2-} when the $\delta^{34}S$ of anthropogenic SO_4^{2-} differs from the $\delta^{34}S$ of excess SO_4^{2-}. Because most of the anthropogenic SO_4^{2-} $\delta^{34}S$ range is elevated from the inversion-constrained range of excess SO_4^{2-} $\delta^{34}S$, accounting for anthropogenic inputs tends to decrease the calculated $\delta^{34}S$ value of crustal sulfide relative to the $\delta^{34}S$ value of excess SO_4^{2-} (Figs. VI-S6 and VI-S8).

VI.14.1.4: Sensitivity of results to the composition of the evaporite end-member

The $\delta^{34}S$ of the evaporite end-member in our primary inversion ranges between 10‰ and 30‰ with a $SO_4^{2-}/(\Sigma^+ + SO_4^{2-})$ between 0.222 to 0.444 (Table VI-1). The isotopic

range of this end-member reflects the full Phanerozoic variability in the isotopic composition of seawater SO_4^{2-} (Claypool et al., 1980). However, if the rocks weathered by rivers do not reflect a uniform distribution across time, which they likely do not, then the expressed isotopic composition of the evaporite end-member could instead span a different range. Moreover, because the evaporite is chemically constrained to reflect a combination of gypsum, epsomite, and halite, the chemical range in our main simulation reflects a wide range of possible SO_4^{2-}/Cl^- ratios (Kemeny and Torres, 2021). However, it is possible that global evaporites are on the halite-rich side of this range or could alternatively be predominantly SO_4^{2-}-bearing. To evaluate the sensitivity of inversion results to the selection of evaporite chemistry we consider results when the $\delta^{34}S$ of evaporites is low (10‰ to 20‰), wide-ranging (10‰ to 30‰), or high (20‰ to 30‰). Furthermore, we evaluate results when the initial distribution of evaporite $SO_4^{2-}/(\Sigma^+ + SO_4^{2-})$ is low (0.222 to 0.375), wide-ranging (0.222 to 0.444), or high (0.375 to 0.444) (Table VI-1; Fig. VI-S7). Higher values of evaporite SO_4^{2-} $\delta^{34}S$ or higher ratios of $SO_4^{2-}/(\Sigma^+ + SO_4^{2-})$ result in lower median values for the $\delta^{34}S$ of excess SO_4^{2-} and the $\delta^{34}S$ of crustal sulfide. These shifts are often of a sufficient magnitude to substantially change the median crustal sulfide $\delta^{34}S$ value and impact the inferred range of possible f_{pyr} values.

VI.14.1.5: Sample R and Z values

The carbonate weathering fraction (R), fraction of weathering acid sourced from sulfide oxidation (Z), and $\Delta ALK/\Delta DIC$ weathering ratios vary across individual rivers (Fig. VI-S9). Future work could improve upon these calculations by tailoring the chemical and isotopic composition of end-members for each individual catchment.

VI.14.2: Using steady-state mass balance models to account for mantle inputs and relate inversion-constrained crustal sulfide $\delta^{34}S$ with marine sulfide $\delta^{34}S$ values

VI.14.2.1: Mass balance model with one sulfide reservoir

The analysis in the main text uses the $^{34}S/^{32}S$ ratios of river SO_4^{2-}, filtered through an inversion model, to constrain the $\delta^{34}S$ of crustal sulfide. We then equate the inversion-constrained distribution of crustal sulfide $\delta^{34}S$ values to the $\delta^{34}S$ of sulfide in marine sediment and, using a 1-input 2-output mass balance model, calculate the fraction of river SO_4^{2-} output as marine sulfide (f_{pyr}) (Fig. VI-2B). This calculation assumes that the $\delta^{34}S$ of crustal sulfide faithfully records the isotopic composition of marine sulfide without any addition of mantle sulfur or any fractionation during subduction or emplacement. However, if instead part of the crustal $\delta^{34}S$ signal derives from mantle sulfur, then the inversion-constrained isotopic composition of crustal sulfide is not a straightforward archive of marine sulfide $\delta^{34}S$. In this section we consider how changes in the isotopic composition of marine sediment due to the addition of mantle sulfur may alter the calculated sulfur isotope ratio of marine sulfide and, in turn, the calculated value of f_{pyr}. Moreover, over geologic time any input of mantle sulfur to crustal sulfide deposits must be balanced by the input of sulfur to the mantle through subduction of low-$\delta^{34}S$ marine sulfide and high-$\delta^{34}S$ SO_4^{2-} within pore fluids. Lastly, at steady-state the marine output of oxidized SO_4^{2-} must also balance the weathering flux from crustal evaporites. To constrain mantle inputs to the crustal sulfide reservoir while maintaining steady-state among all sulfur-bearing reservoirs, here we consider an additional mass balance model of the global sulfur cycle (Fig. VI-S14). The results of this model indicate that the value of f_{pyr} generally declines when accounting for inputs from mantle sulfur but that substantial shifts in f_{pyr} require large fractions of crustal sulfide to be sourced from the mantle.

Our mass balance model includes reservoirs for the mantle, crustal evaporites, crustal sulfide, seawater, marine sulfide, and SO_4^{2-} output from seawater (Fig. VI-S14A). Crustal gypsum and sulfide weather into rivers (f_{wxr} and 1-f_{wxr}) and a corresponding flux is output from seawater in the form of marine sulfide (f_{pyr}) and SO_4^{2-} (1-f_{pyr}). To ensure steady-state of the weathering gypsum reservoir, a SO_4^{2-} flux equal to that of gypsum weathering is returned to the crustal reservoir, with any remaining SO_4^{2-} output from seawater entering the mantle (f_{wxr}-f_{pyr}). A fraction of marine sulfide is also subducted into the mantle ($f_{pyr}f_{sub}$) and the remainder is input to the crustal sulfide reservoir (f_{pyr}*(1-f_{sub})).

We solve this mass balance model by defining values for the $\delta^{34}S$ of seawater SO_4^{2-} (21‰), river water SO_4^{2-} (4.4‰), mantle sulfur (0‰), and crustal sulfide (variable), as well as either the isotopic offset between seawater and marine sulfide ($^{34}\Delta$) or the fraction of crustal sulfide derived from mantle inputs (f_{mantle}). Depending on the chosen parameters, five equations are rearranged to solve for five unknown variables (f_{pyr}, f_{wxr}, f_{sub}, the $\delta^{34}S$ of marine sulfide, and either $^{34}\Delta$ or f_{mantle}; Eqs. VI-3 to VI-7). The equations describe the isotopic composition of river water (Eq. VI-3, where f_{wxr} is the fraction of river SO_4^{2-} derived from weathering of crustal sulfide), the output of SO_4^{2-} from seawater (Eq. VI-4, where f_{pyr} is the fraction of river SO_4^{2-} that leaves seawater as marine sulfide), the isotopic composition of marine sulfide (Eq. VI-5), the mass balance of the mantle (Eq. VI-6, with f_{sub} reflecting the subduction of marine sulfide), and the fraction of crustal sulfide derived from the mantle (Eq. VI-7). The model inherently assumes ongoing oxidation of the mantle because SO_4^{2-} input to the mantle is output as sulfide.

$$\delta^{34}S_{river} = f_{wxr}\delta^{34}S_{crustal\ sulfide} + (1 - f_{wxr})\delta^{34}S_{ocean} \quad \text{(VI-3)}$$

$$\delta^{34}S_{river} = f_{pyr}\left(\delta^{34}S_{ocean} + {}^{34}\Delta\right) + \left(1 - f_{pyr}\right)\delta^{34}S_{ocean} \quad \text{(VI-4)}$$

$$\delta^{34}S_{\text{marine sulfide}} = \delta^{34}S_{\text{ocean}} + {}^{34}\Delta \quad \text{(VI-5)}$$

$$\delta^{34}S_{\text{mantle}} = \frac{f_{pyr}f_{sub}\delta^{34}S_{\text{marine sulfide}} + (f_{wxr} - f_{pyr})\delta^{34}S_{\text{ocean}}}{f_{wxr} - f_{pyr} + f_{pyr}f_{sub}} \quad \text{(VI-6)}$$

$$f_{\text{mantle}} = 1 - \frac{f_{pyr}\,(1 - f_{sub})}{f_{wxr}} \quad \text{(VI-7)}$$

Model results are calculated crustal sulfide $\delta^{34}S$ values between -15‰ and 0‰ and f_{mantle} values between 0% and 60% (Figs. VI-S14D, E, F, and G). When no crustal sulfide is derived from the mantle (f_{mantle}=0), as in the 1-input 2-output model (Eqs. VI-1 and VI-2), the $\delta^{34}S$ of the crustal sulfide reservoir is equal to the $\delta^{34}S$ of the marine sulfide reservoir (Fig. VI-S14D). In the case that crustal sulfide has a similar $^{34}S/^{32}S$ ratio as the mantle, the addition of mantle sulfur exerts only a minor influence on the calculated $\delta^{34}S$ of marine sulfide. Conversely, at values of crustal sulfide $\delta^{34}S$ distinct from 0‰ and $f_{mantle} > 0$, the addition of mantle sulfur decouples the $\delta^{34}S$ of marine sulfide from that of crustal sulfide and results in lower values of marine sulfide $\delta^{34}S$ (Fig. VI-S14D) and f_{pyr} (Fig. VI-S14E). The lower value of marine sulfide $\delta^{34}S$ implies a larger magnitude of fractionation as well as changes in the fraction of marine sulfide subducted into the mantle (Fig. VI-S14F) and pore fluid SO_4^{2-} subducted into the mantle (Fig. VI-S14G).

Measurements of $\delta^{7}Li$ from the Amazon River, Ganges-Brahmaputra Rivers, and Mackenzie River suggest that 60-85% of global riverine particulate matter is sourced from sedimentary lithologies rather than igneous lithologies (Dellinger et al., 2014). The highly cannibalistic nature of fluvial sediment is also indicated by measurements of Nd isotope ratios in shales (Veizer and Jansen, 1979; 1985). Moreover, a majority of land area is comprised of sedimentary lithologies (Lerman et al., 2007) and river catchments hosting sedimentary lithologies tend to have higher SO_4^{2-} fluxes than catchments hosting igneous

lithologies. Based on these observations we estimate that between 10% and 40% of all weathering sulfide could reasonably be derived from mantle inputs, or that $0.10 \leq f_{mantle} \leq 0.40$. Within this range the value of f_{pyr} is constrained between about 35% and 65% while the expressed fractionation between seawater and marine sulfide is constrained between about -44‰ and -25‰. However, the upper range of f_{mantle} values would, for the lower range of crustal sulfide $\delta^{34}S$ values, require nearly that 5% to 10% of the total river SO_4^{2-} flux be subducted into the mantle within pore fluids (Fig. VI-S14G). Additional constraints on this system could come from quantifying fluxes of sulfur into the mantle or the fraction of crustal sulfide derived from mantle inputs. For example, the latter value could potentially be estimated using the relative frequency of crustal sulfide with $\delta^{34}S$ values near 0‰ and with $\delta^{34}S$ values substantially below 0‰.

VI.14.2.2: Mass balance model with shallow and deep sulfide reservoirs

Recent evidence has emphasized the role of local controls on the $\delta^{34}S$ of marine sulfide (Pasquier et al., 2017, 2021). In general, sulfide formed in coastal shelf sediment seems to have higher $^{34}S/^{32}S$ ratios than sulfide formed in pelagic open-ocean settings due to differences in sedimentation rate, organic matter quality and quantity, and iron availability. To partially account for these complexities we expand the mass balance model to include two types of marine sulfide, one representing shallow shelf sulfide and the other representing deeper pelagic settings. We assume that all coastal sulfide enters the surface weathering environment while sulfide in deep marine sediment is split between the mantle and the surface (Figs. VI-S15A and VI-S16A). Solving the resulting system of equations requires defining a new variable for the relative output of shallow and deep sulfide (f_{deep})

and separating the fractionation between marine SO_4^{2-} and sulfide into a shallow-water term ($^{34}\Delta_{shallow}$) and a deep-water term ($^{34}\Delta_{deep}$). We first evaluate model results over a range of crustal sulfide $\delta^{34}S$ and f_{mantle} values at constant f_{deep} and $^{34}\Delta_{shallow}$ (Fig. VI-S15), and then evaluate model results over a range of f_{deep} and $^{34}\Delta_{shallow}$ values at constant crustal sulfide $\delta^{34}S$ and f_{mantle} (Fig. VI-S16). A subset of results from the first formulation of the two-sulfide reservoir model are presented in Figs. VI-2C and D.

In the first formulation f_{deep} = 30%, meaning that 70% of marine sulfide is exported into the shallow shelf reservoir. Note that lower values of f_{deep} are associated with lower values of f_{pyr}, meaning that a relatively low f_{deep} value is conservative when estimating global sulfur cycle parameters (Fig. VI-S16). We set $^{34}\Delta_{shallow}$ = -21‰ such that sulfide in the shelf reservoir has a $\delta^{34}S$ value of 0‰. The results of this calculation are broadly similar to the results of the model with only a single reservoir of marine sulfide, although generally shifted to lower values of total sulfide $\delta^{34}S$, lower values of f_{pyr}, and higher values of f_{sub} (Figs. VI-S14 and VI-S15). For $0.1 < f_{mantle} < 0.4$, the deep sulfide reservoir has $\delta^{34}S$ values between approximately -10‰ and -100‰, consistent with observations of isotopically depleted sulfur in some marine settings. The model finds f_{pyr} is generally between 35% and 65%, consistent with results of the first model with only one sulfide reservoir.

Our second model runs consider the sensitivity of results to changes in f_{deep} and $^{34}\Delta_{shallow}$ when f_{mantle} = 0.3 and crustal sulfide $\delta^{34}S$ = -5‰ (Fig. VI-S16). Overall, changes in f_{deep} and $^{34}\Delta_{shallow}$ produce only muted changes in the total $\delta^{34}S$ of marine sulfide and in the value of f_{pyr}. However, the $\delta^{34}S$ value of deep marine sulfide reservoir is very sensitive to $^{34}\Delta_{shallow}$ at low values of f_{deep} (Fig. VI-S16C).

VI.15: Supplementary figures

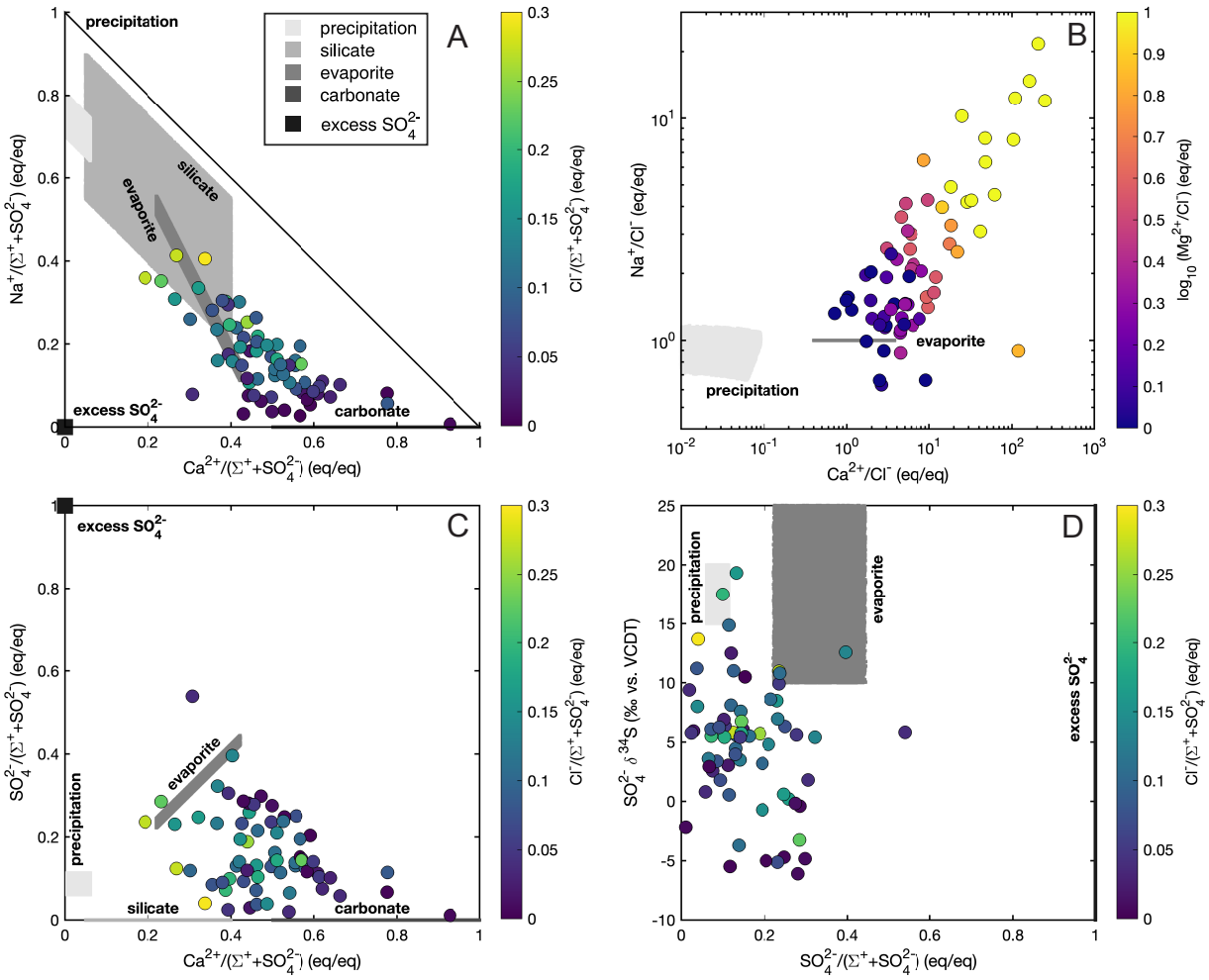

Fig. VI-S1: Dissolved ion chemistry for river water samples from Burke et al. (2018). (A) $Na^+/(\Sigma^+ + SO_4^{2-})$ and $Ca^{2+}/(\Sigma^+ + SO_4^{2-})$ indicate that much of the dissolved load is sourced from the carbonate and either silicate or evaporite end-members. Samples with lower $Ca^{2+}/(\Sigma^+ + SO_4^{2-})$ and higher $Cl^-/(\Sigma^+ + SO_4^{2-})$ are expected to have larger contributions from the evaporite end-member. (B) The contribution of evaporites and precipitation is limited by the ratio of Cl^- to other elements. (C) $SO_4^{2-}/(\Sigma^+ + SO_4^{2-})$ is elevated in many samples, indicative of sulfide oxidation and anthropogenic inputs. (D) River SO_4^{2-} $\delta^{34}S$ is substantially lower than expected from mixing of the precipitation and evaporite end-members, indicating a source of river SO_4^{2-} with relatively depleted $\delta^{34}S$ value. In all panels, end-member shading shows instances of end-member chemistry pulled from distributions (Table VI-1).

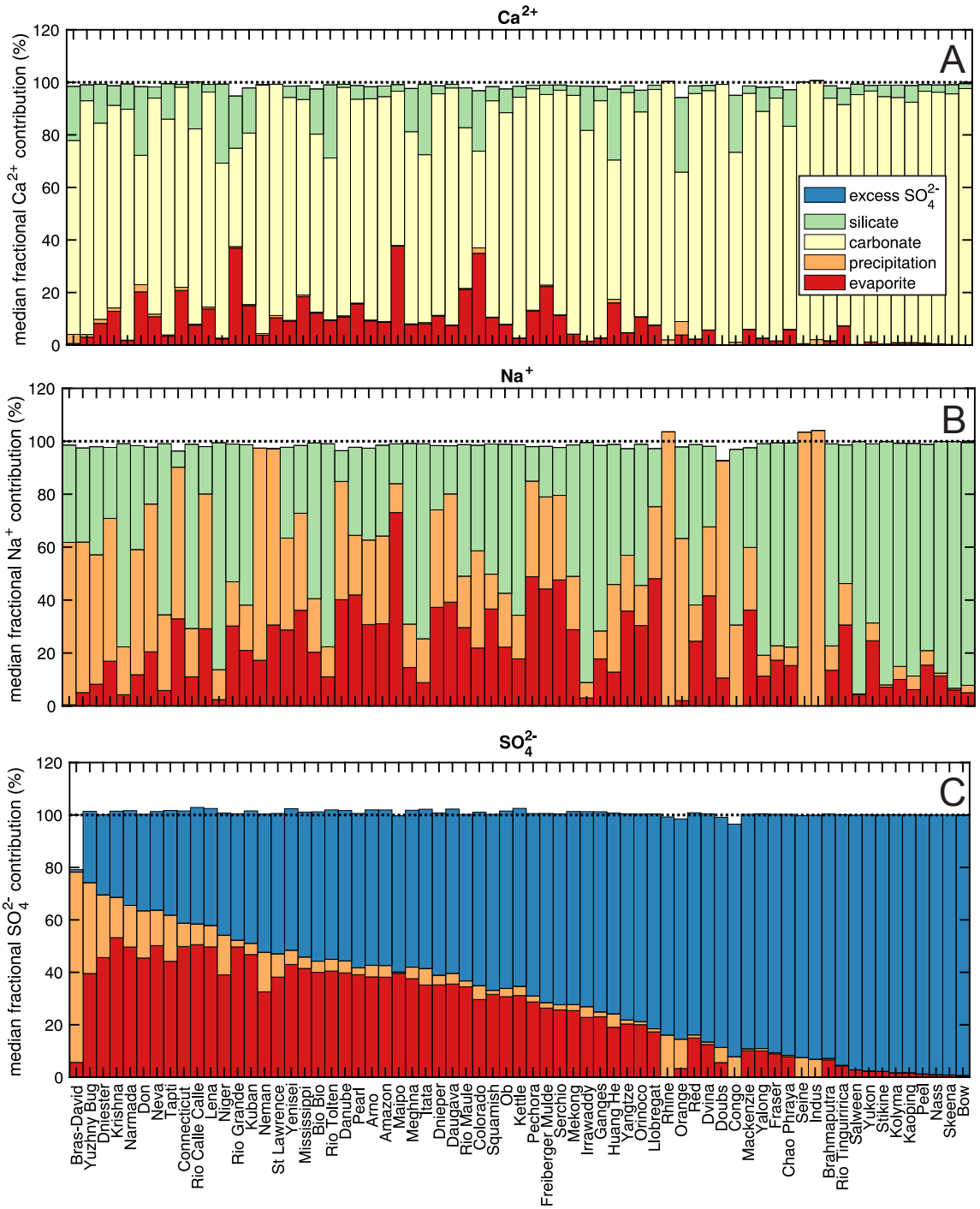

Fig. VI-S2: Inversion results showing the median fractional contributions of the silicate, carbonate, precipitation, evaporite, and excess SO_4^{2-} end-members to the budgets of (A) Ca^{2+}, (B) Na^{+}, and (C) SO_4^{2-}. While each inversion simulation reconstructed each dissolved variable between 95% and 105% of the observed value, the sum of median fractional contributions from each end-member is not constrained to fall within that range. (A) Most Ca^{2+} is sourced from the carbonate end-member. (B) Most Na^{+} is derived from the silicate, evaporite, and precipitation end-members. (C) The median fraction of SO_4^{2-} sourced from the excess SO_4^{2-} end-member ranges from approximately 1% to nearly 99%.

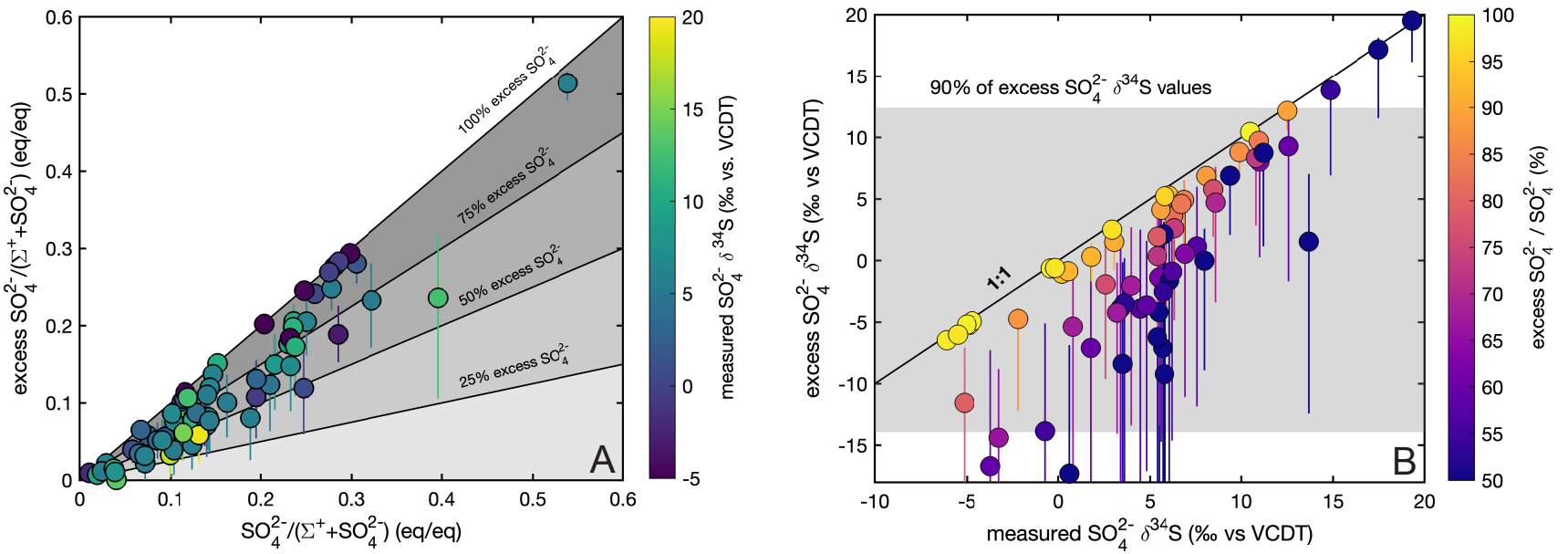

Fig. VI-S3: Sulfur inversion results. (A) Inversion-constrained excess SO_4^{2-} and river SO_4^{2-} normalized to the sum of cations and SO_4^{2-}. Greater than 50% of dissolved SO_4^{2-} in 81% of samples is derived from the excess SO_4^{2-} end-member. Shading indicates increasing fractions of excess SO_4^{2-}. (B) Inversion-constrained excess SO_4^{2-} δ^{34}S against the δ^{34}S of river SO_4^{2-}, color-coded by the excess SO_4^{2-} fraction. When the excess SO_4^{2-} fraction is high, or when measured δ^{34}S is similar to the δ^{34}S of SO_4^{2-} sourced from the evaporite and precipitation end-members, by mass balance the δ^{34}S of excess SO_4^{2-} must closely resemble the δ^{34}S of river SO_4^{2-}. Grey shading ranges from the 5th to 95th percentiles of excess SO_4^{2-} δ^{34}S values among individual samples.

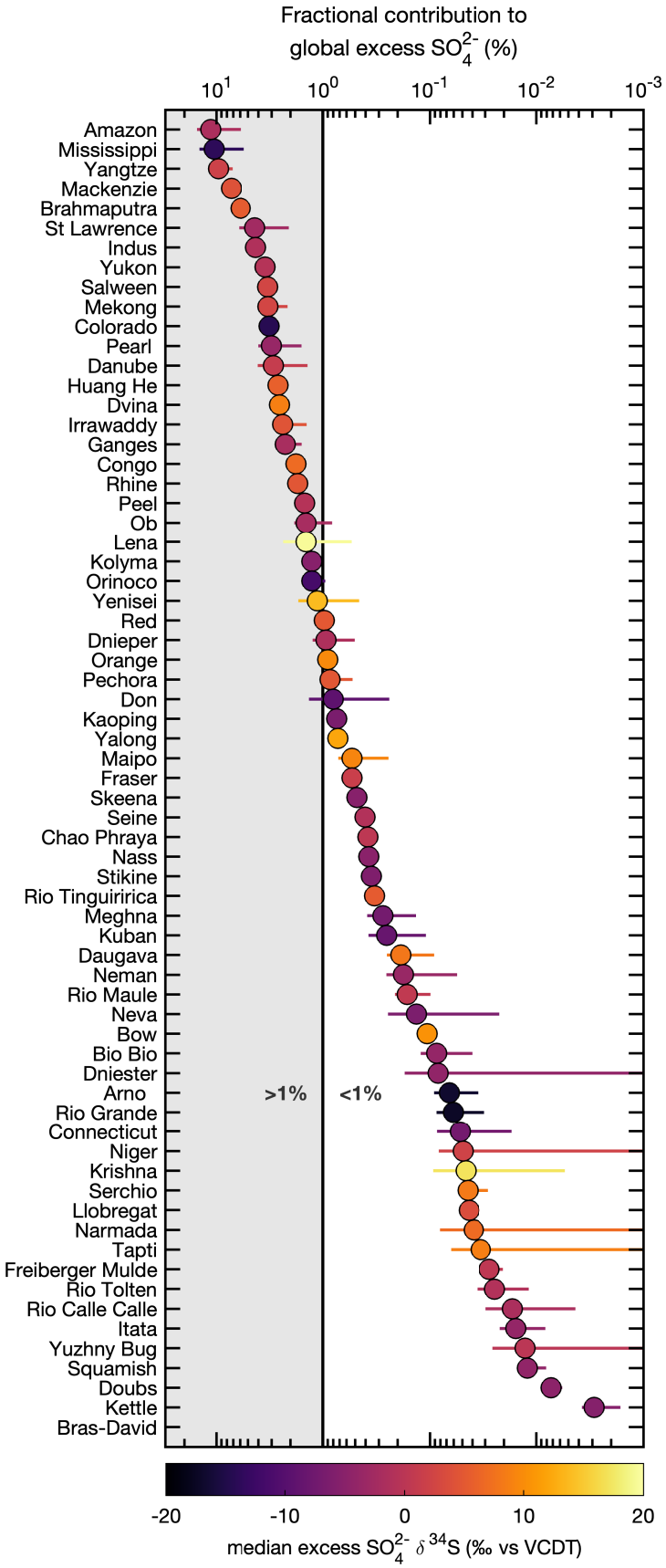

Fig. VI-S4: Fractional contribution of each river to global excess SO_4^{2-} color-coded by the median $\delta^{34}S$ of excess SO_4^{2-}. Plotted points are the medians of accepted inversion results and error bars extend from 25th to 75th percentiles of accepted results. Grey shading identifies samples that source >1% of global excess SO_4^{2-}.

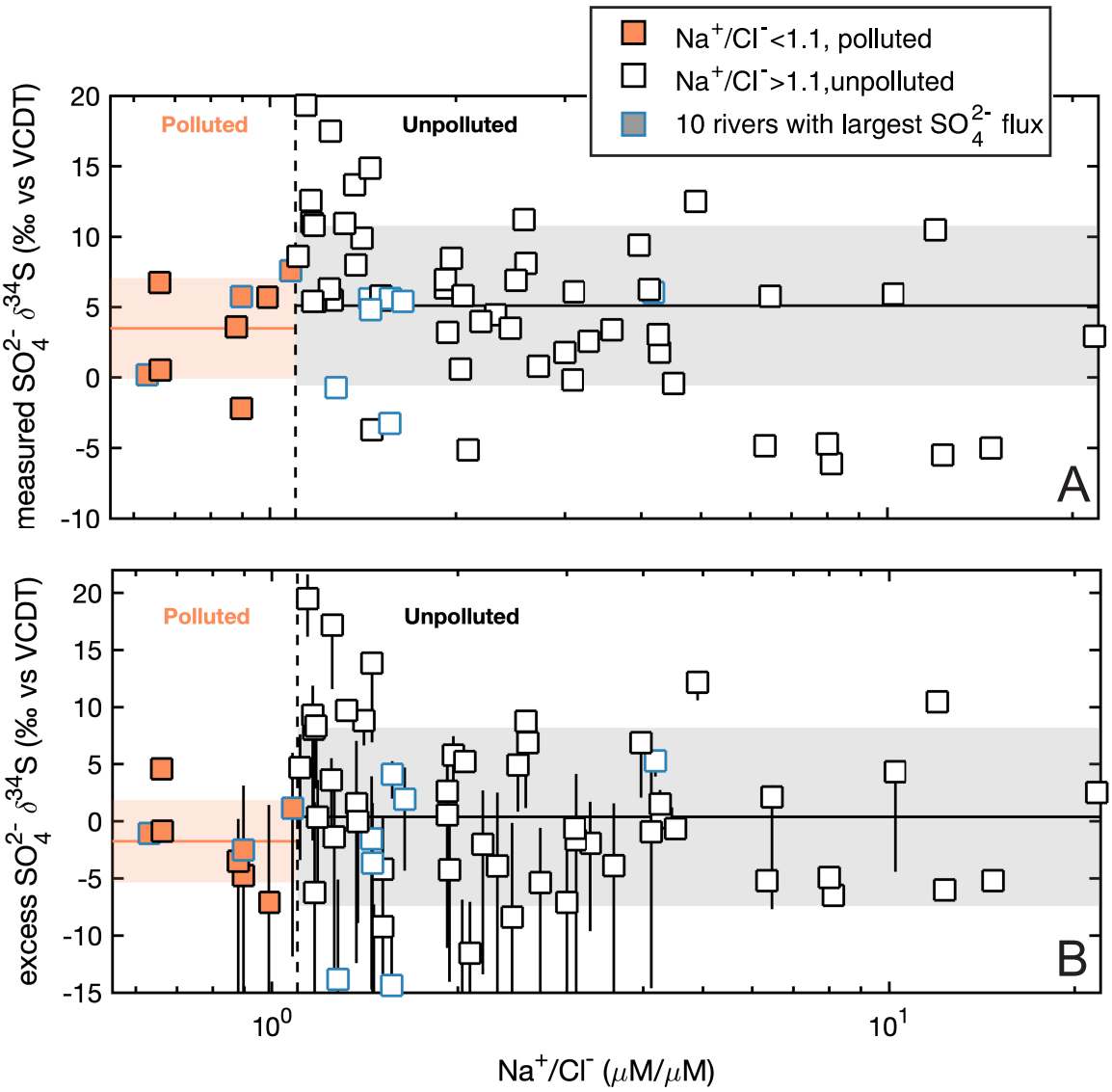

Fig. VI-S5: Rivers with low Na^+/Cl^- ratios constrain the $\delta^{34}S$ of anthropogenic inputs. (A) Observed SO_4^{2-} $\delta^{34}S$ and (B) excess SO_4^{2-} $\delta^{34}S$ against Na^+/Cl^-. The distribution of SO_4^{2-} $\delta^{34}S$ values in samples with $Na^+/Cl^- < 1.1$ is not substantially different from the distribution in rivers with Na^+/Cl^- ratios > 1.1. Solid horizontal lines indicate means and shading extends ±1σ.

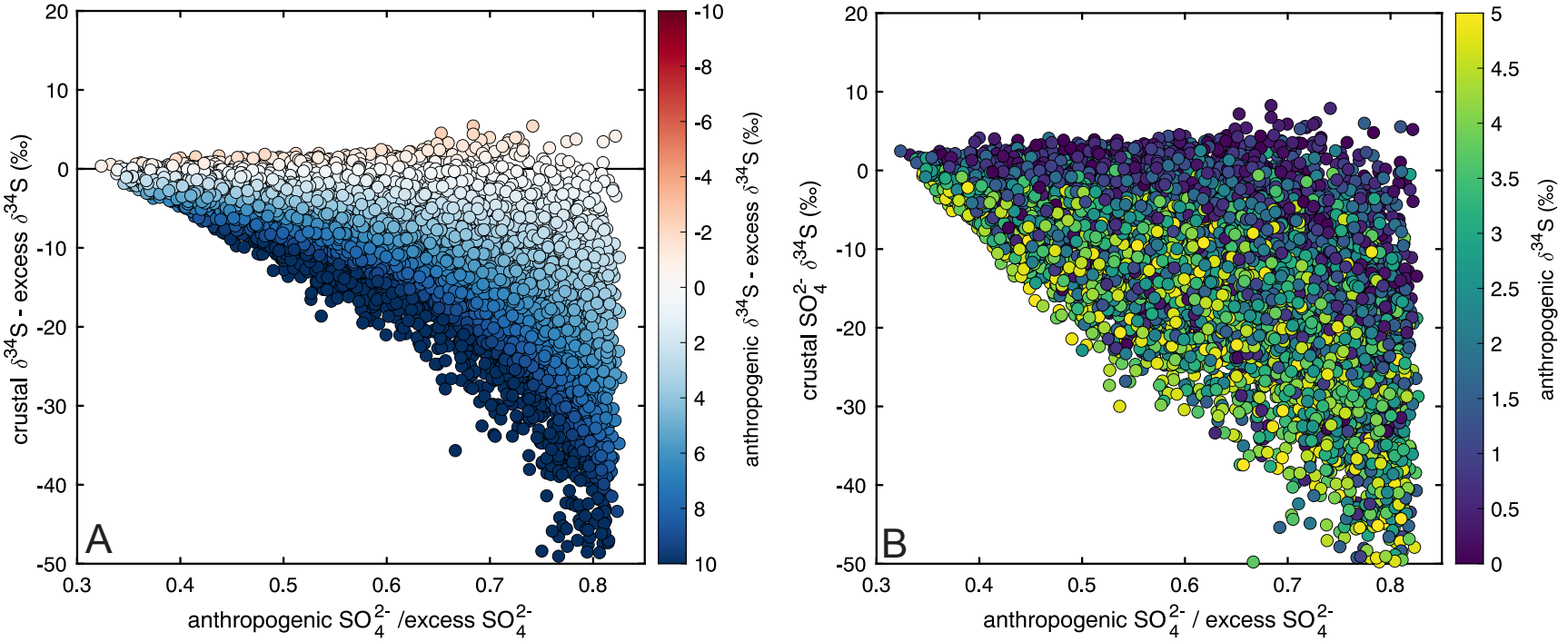

Fig. VI-S6: Impacts of anthropogenic SO_4^{2-} on the calculated $\delta^{34}S$ of crustal sulfide. (A) The difference in $\delta^{34}S$ between crustal sulfide and excess SO_4^{2-} increases with larger fractional contributions of anthropogenic SO_4^{2-} or larger isotopic offsets between anthropogenic and excess SO_4^{2-}. (B) The inversion-constrained $\delta^{34}S$ of weathering crustal sulfide departs from the $\delta^{34}S$ of excess SO_4^{2-} $\delta^{34}S$ at elevated contributions of anthropogenic SO_4^{2-} and generally becomes increasingly negative with higher $^{34}S/^{32}S$ ratios in anthropogenic SO_4^{2-}.

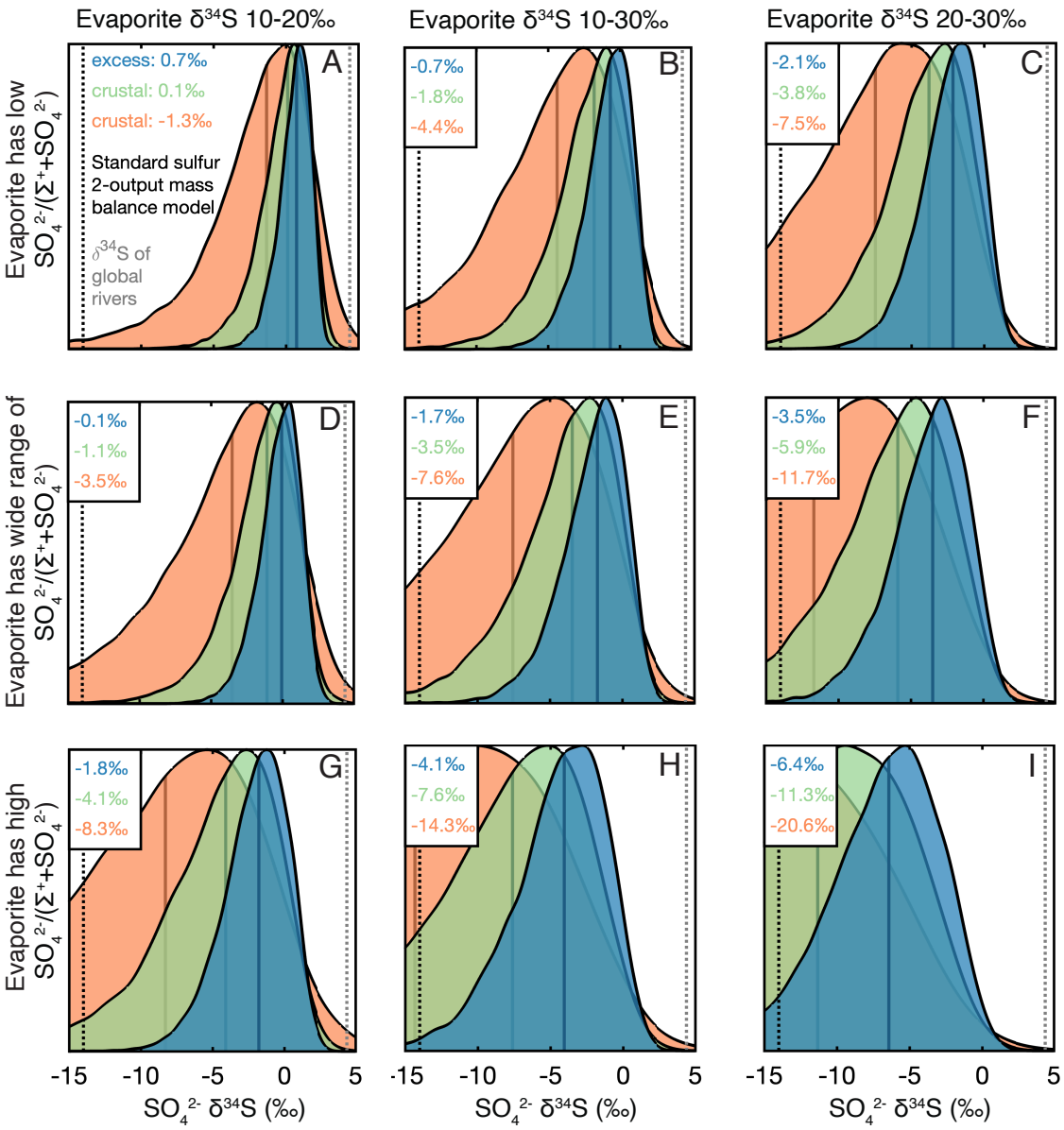

Fig. VI-S7: Sensitivity of results to the chemical composition of the evaporite end-member. For different distributions of evaporite $SO_4^{2-}/(\Sigma^+ + SO_4^{2-})$ and SO_4^{2-} $\delta^{34}S$, panels show results for global excess SO_4^{2-} $\delta^{34}S$ (blue) and crustal $\delta^{34}S$ at 0.5 to 1.3 Tmol/yr anthropogenic SO_4^{2-} (low-pollution scenario; green) or 1.3 to 2.4 Tmol/yr anthropogenic SO_4^{2-} (high-pollution scenario; orange). Results are shown for (A, B, C) low, (D, E, F) wide, and (G, H, I) high ratios of $SO_4^{2-}/(\Sigma^+ + SO_4^{2-})$, as well as for evaporite $\delta^{34}S$ ranges from (A, D, G) 10-20‰, (B, E, H) 10-30‰, and (C, F, I) 20-30‰. Darker vertical lines and inset text indicate the median value of each distribution. The $\delta^{34}S$ of global excess SO_4^{2-} and crustal sulfide decline at higher relative abundances of evaporite SO_4^{2-} or higher evaporite $\delta^{34}S$ values. Model results in the main text are for an inversion with a wide range in evaporite $SO_4^{2-}/(\Sigma^+ + SO_4^{2-})$ and $\delta^{34}S$ values ranging from 10-30‰ (E).

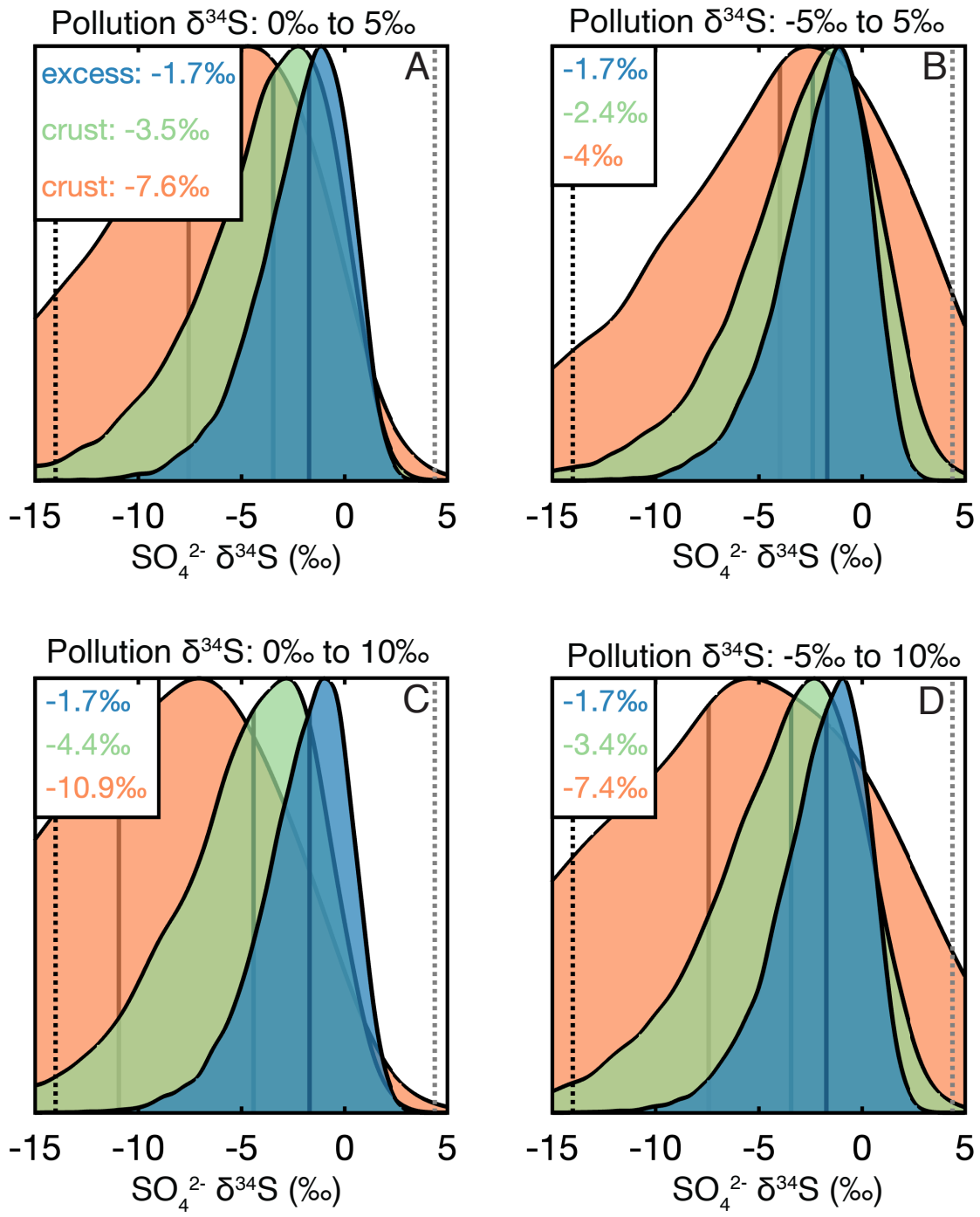

Fig. VI-S8: Sensitivity of results to the isotopic composition of anthropogenic SO_4^{2-}. Panels show global excess SO_4^{2-} $\delta^{34}S$ (blue) and crustal $\delta^{34}S$ for 0.5 to 1.3 Tmol/yr anthropogenic SO_4^{2-} (low-pollution scenario; green) or 1.3 to 2.4 Tmol/yr anthropogenic SO_4^{2-} (high-pollution scenario; orange). Results are shown for anthropogenic SO_4^{2-} $\delta^{34}S$ values ranging from (A) 0‰ to 5‰, (B) -5‰ to 5‰, (C) 0‰ to 10‰, and (D) -5‰ to 10‰. Darker vertical lines and inset text indicate the median value of each distribution. Model results in the main text are for an inversion with pollution $\delta^{34}S$ constrained between 0‰ and 5‰ (A).

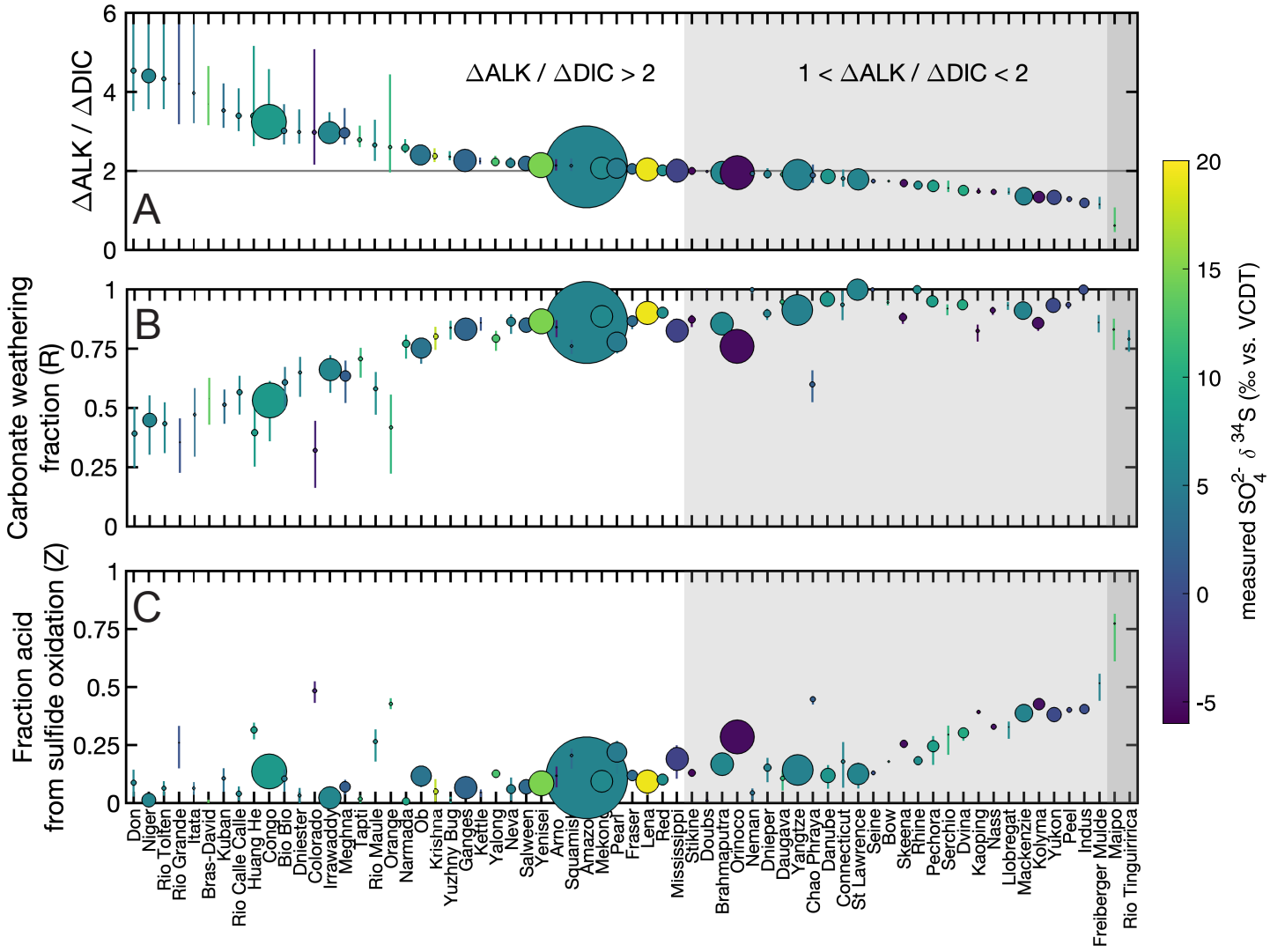

Fig. VI-S9: Weathering parameters for individual river water samples. (A) ΔALK/ΔDIC of weathering in the catchment upstream of each river water sampling site. (B) Carbonate weathering fraction (R) for each river. (C) Fraction of weathering acid sourced from sulfide oxidation (Z) for each river. In all panels plotted points are the medians of accepted inversion results and error bars extend from the 25th to 75th percentiles of accepted results.

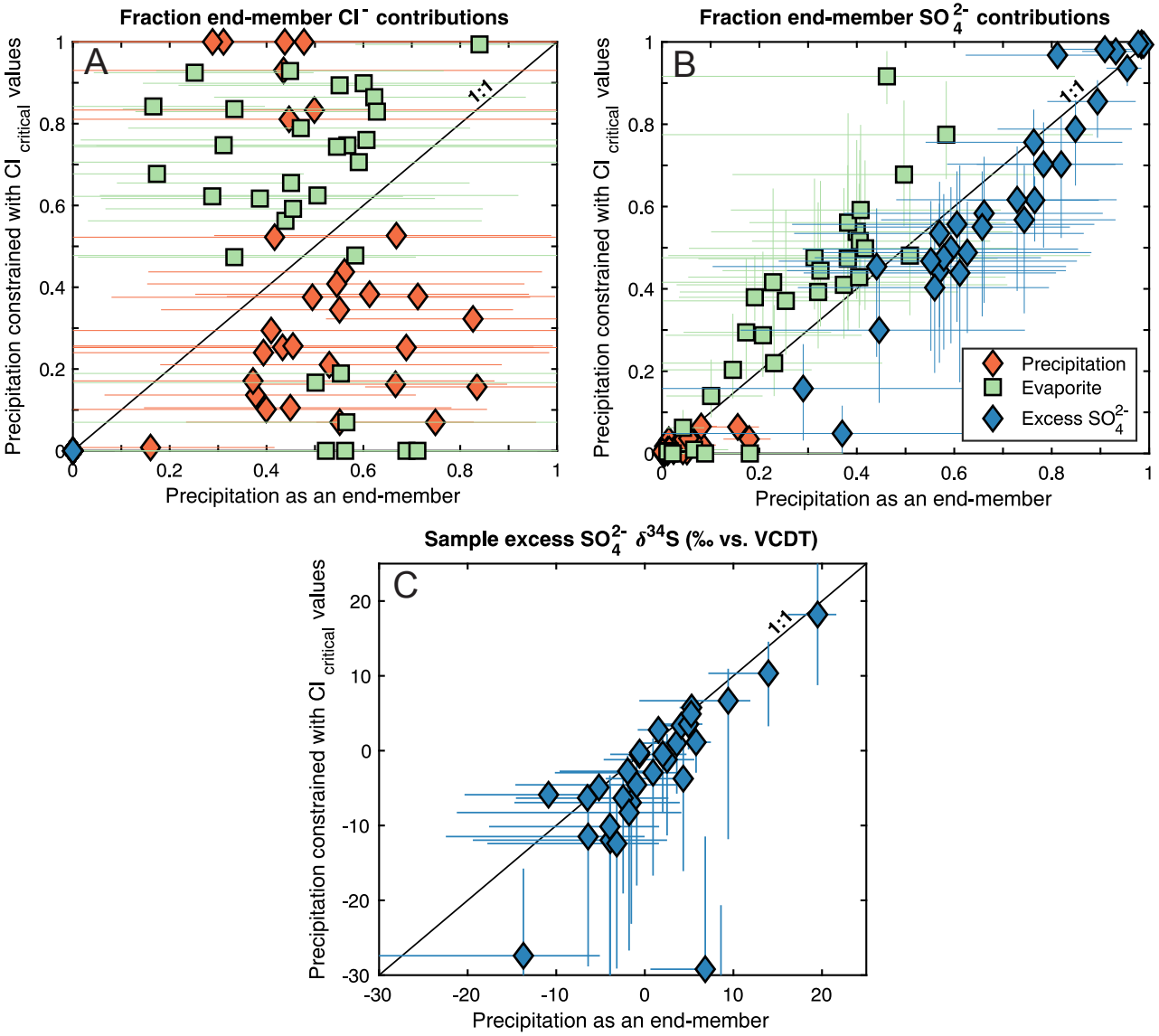

Fig. VI-S10: Comparison of (A) fractional Cl^- contribution, (B) fractional SO_4^{2-} contributions and (C) excess SO_4^{2-} $\delta^{34}S$ for inversion results where precipitation is either treated as an end-member (x-axis) or constrained using Cl^- critical values (y-axis). (A) The inversion finds a smaller fraction of Cl^- is derived from precipitation when using Cl^- critical values and more is derived from the evaporite end-member. (B) The inversion finds a larger fraction of river SO_4^{2-} is derived from the excess SO_4^{2-} end-member when treating precipitation as an end-member and a larger fraction derives from the evaporite end-member when constraining precipitation inputs with Cl^- critical values. (C) The relatively higher amount of SO_4^{2-} sourced from the excess SO_4^{2-} end-member when treating precipitation as an end-member results in higher inversion-constrained values of excess SO_4^{2-} $\delta^{34}S$.

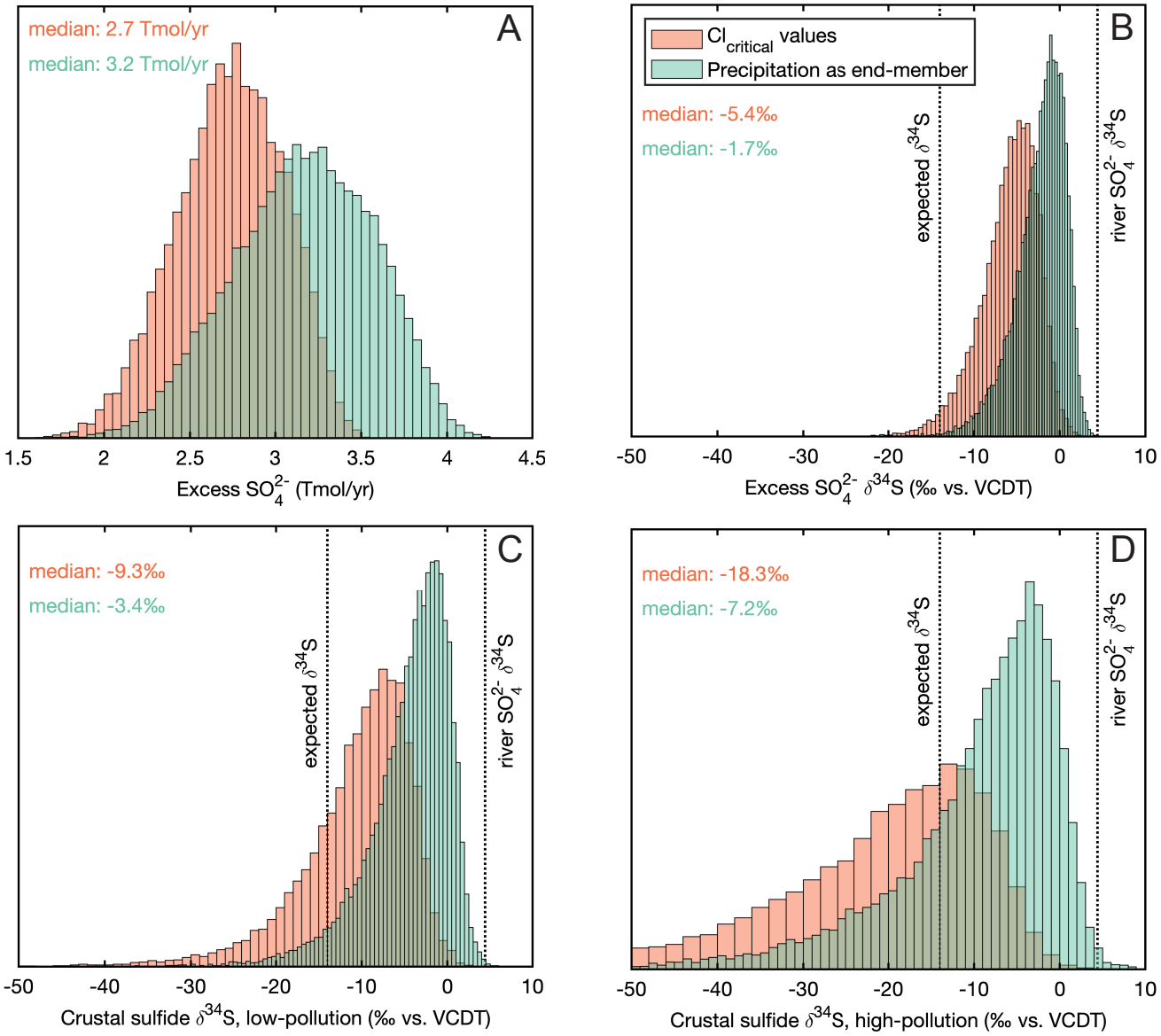

Fig. VI-S11: Model results for (A) the amount of excess SO_4^{2-}, (B) the $\delta^{34}S$ of excess SO_4^{2-}, (C) the $\delta^{34}S$ of crustal sulfide in the low-pollution case, and (D) the $\delta^{34}S$ of crustal sulfide in the high-pollution case for inversion results where precipitation is either treated as an end-member (green distributions) or constrained using Cl^- critical values (orange distributions). Constraining inputs from precipitation with Cl^- critical values results in lower $\delta^{34}S$ values for excess SO_4^2 and for crustal sulfide. The results shown in green differ from the results in blue in Fig. VI-S12 by including only samples with Cl^- critical values.

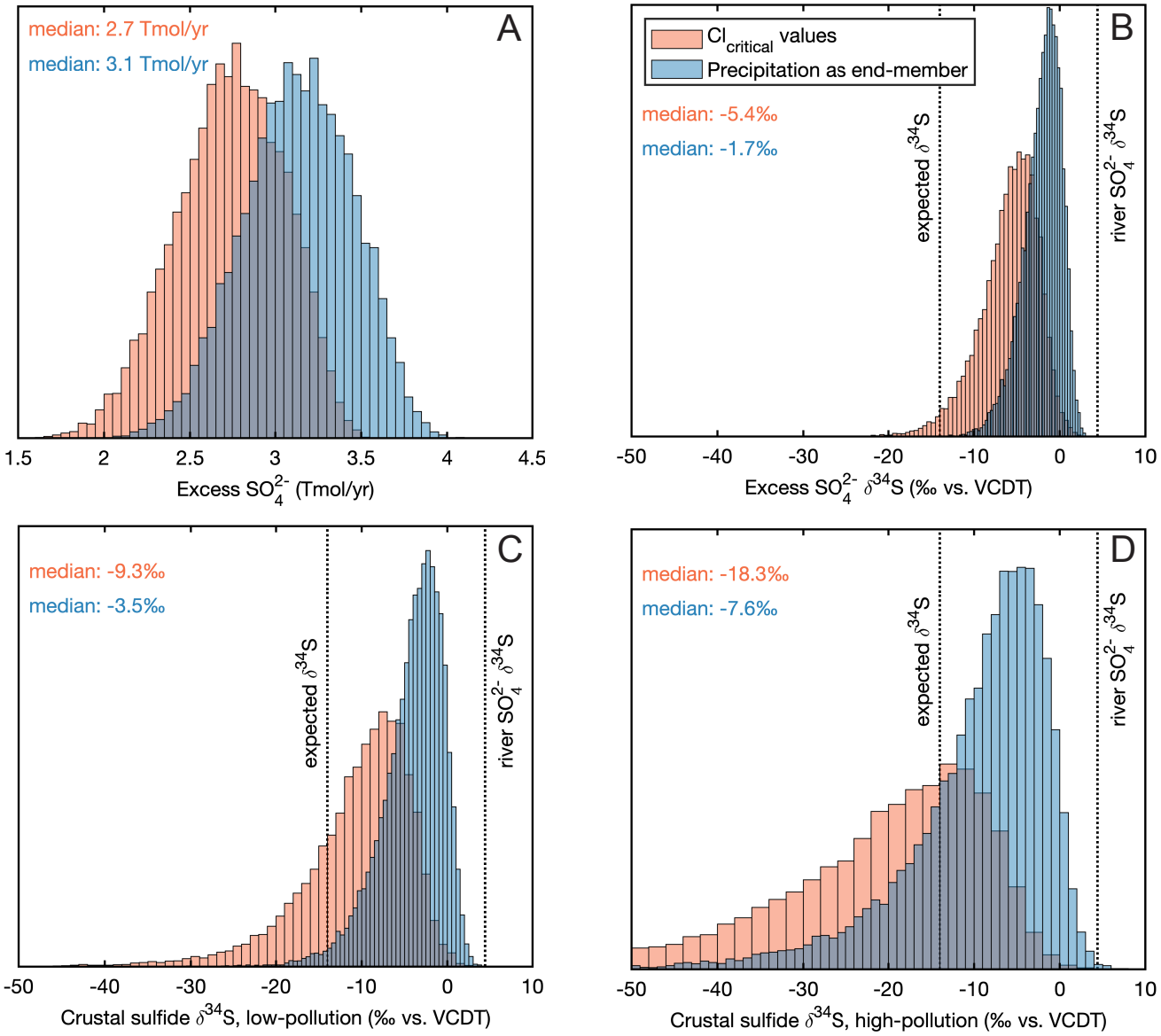

Fig. VI-S12: Model results for (A) the amount of excess SO_4^{2-}, (B) the $\delta^{34}S$ of excess SO_4^{2-}, (C) the $\delta^{34}S$ of crustal sulfide in the low-pollution case, and (D) the $\delta^{34}S$ of crustal sulfide in the high-pollution case for inversion results where precipitation is either treated as an end-member (blue distributions) or constrained using Cl^- critical values (orange distributions). Constraining inputs from precipitation with Cl^- critical values results in lower $\delta^{34}S$ values for excess SO_4^2 and for crustal sulfide. The results shown in blue differ from the results in green in Fig. VI-S11 by including all data, not just samples with Cl^- critical values.

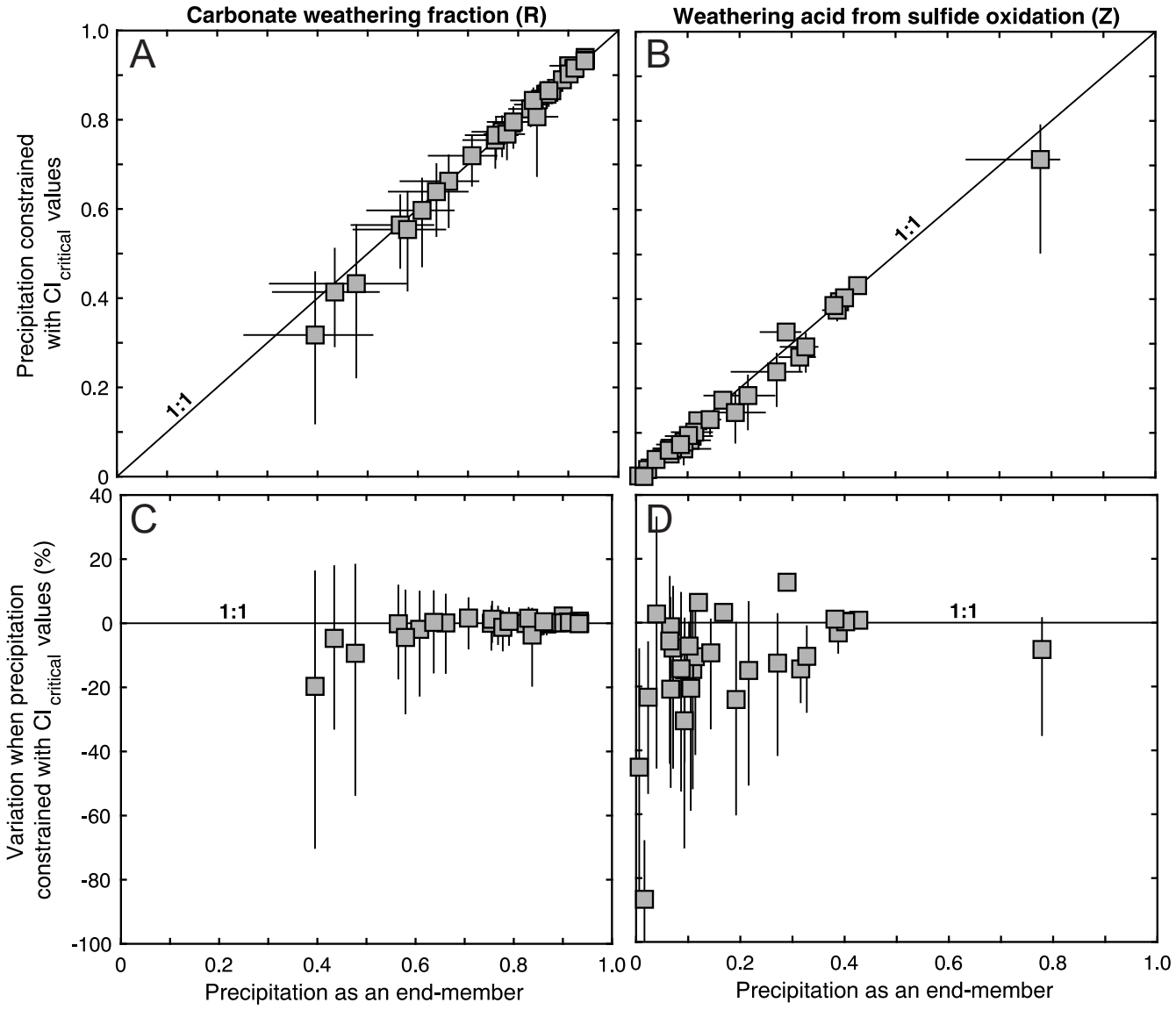

Fig. VI-S13: Model results for (A) the fraction and (C) the fractional difference in carbonate weathering fraction (R) and (B) the fraction and (D) the fractional difference in weathering acid sourced from sulfide oxidation (Z) for inversion results where precipitation is either treated as an end-member or constrained using Cl^- critical values. Most Z values are lower when the inversion uses Cl^- critical values, consistent with the lower amount of excess SO_4^{2-}. In all panels plotted points are the medians of accepted inversion results and error bars extend from the 25th to 75th percentiles of accepted results.

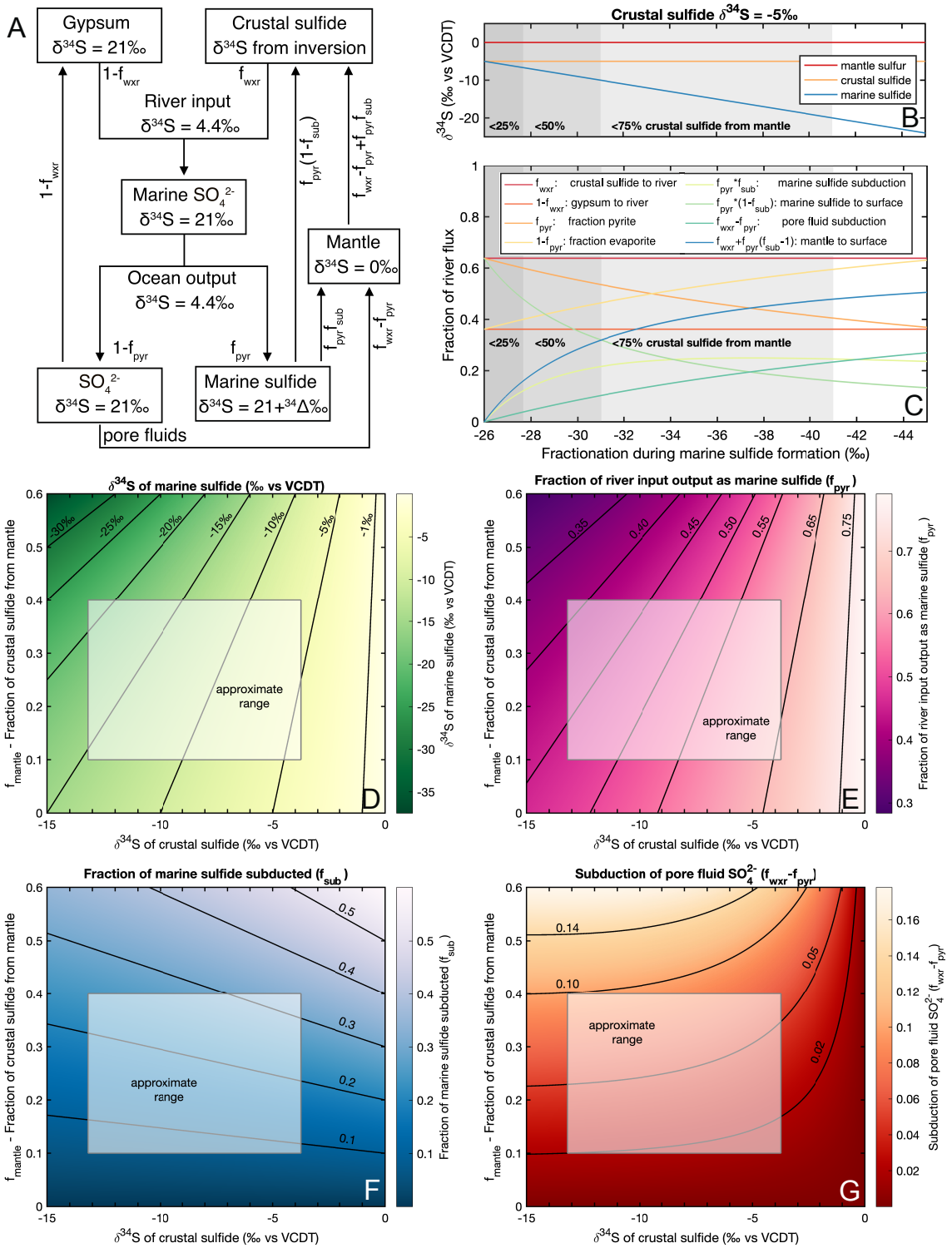
A
Gypsum
δ34S = 21‰
Crustal sulfide
δ34S from inversion
1-fwxr
fwxr
River input
δ34S = 4.4‰
Marine SO4 2-
δ34S = 21‰
Ocean output
δ34S = 4.4‰
Mantle
δ34S = 0‰
1-fpyr
fpyr
SO4 2-
δ34S = 21‰
Marine sulfide
δ34S = 21+34Δ‰
pore fluids
1-fwxr
fpyr(1-fsub)
fwxr-fpyr+fpyr fsub
fpyr fsub
fwxr-fpyr
Crustal sulfide δ34S = -5‰
δ34S (‰ vs VCDT)
mantle sulfur
crustal sulfide
marine sulfide
<25%
<50%
<75% crustal sulfide from mantle
B
fwxr: crustal sulfide to river
1-fwxr: gypsum to river
fpyr: fraction pyrite
1-fpyr: fraction evaporite
fpyr*fsub: marine sulfide subduction
fpyr*(1-fsub): marine sulfide to surface
fwxr-fpyr: pore fluid subduction
fwxr+fpyr(fsub-1): mantle to surface
Fraction of river flux
Fractionation during marine sulfide formation (‰)
C
δ34S of marine sulfide (‰ vs VCDT)
fmantle - Fraction of crustal sulfide from mantle
δ34S of crustal sulfide (‰ vs VCDT)
approximate range
D
Fraction of river input output as marine sulfide (fpyr)
E
Fraction of marine sulfide subducted (fsub)
F
Subduction of pore fluid SO4 2- (fwxr-fpyr)
G

Fig. VI-S14: A steady-state mass balance model of the global sulfur cycle is used to evaluate how mantle inputs alter the relative $\delta^{34}S$ values of crustal sulfide and marine sulfide. (A) Architecture of the model. (B) Steady-state $\delta^{34}S$ values for the mantle, crustal sulfide, and marine sulfide and (C) model variables against seawater-sulfide fractionation. (D) Model results for the $\delta^{34}S$ of marine sulfide against the $\delta^{34}S$ of crustal sulfide and the fraction of mantle-derived crustal sulfide. The steady-state $\delta^{34}S$ of crustal sulfide and marine sulfide are equal in the absence of mantle inputs ($f_{mantle} = 0$). In contrast, the input of mantle sulfur decouples the sulfur isotopic composition of crustal sulfide and marine sulfide. (E) f_{pyr}, (F) the fraction of deep marine sulfide subducted into the mantle, and (G) the fraction of evaporite subducted into the mantle against the $\delta^{34}S$ of crustal sulfide and the fraction of crustal sulfide derived from the mantle. From our inversion-constrained values for the $\delta^{34}S$ of crustal sulfide and the assumption that $10\% < f_{mantle} < 40\%$ (Dellinger et al., 2014), steady-state f_{pyr} is constrained between approximately 35% and 65%.

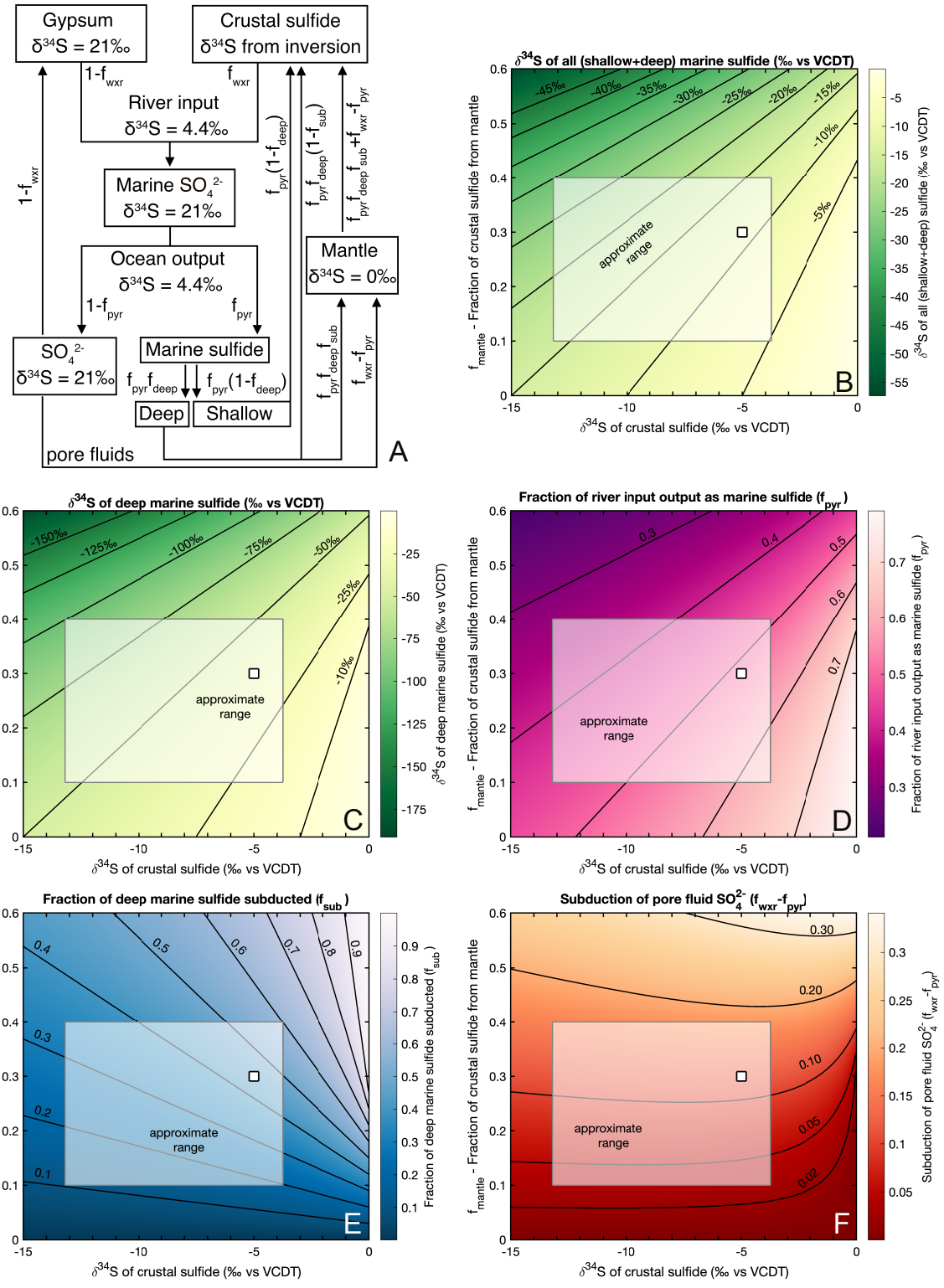
Gypsum
δ34S = 21‰
Crustal sulfide
δ34S from inversion
River input
δ34S = 4.4‰
Marine SO4 2-
δ34S = 21‰
Ocean output
δ34S = 4.4‰
Mantle
δ34S = 0‰
SO4 2-
δ34S = 21‰
Marine sulfide
Deep
Shallow
pore fluids
A
δ34S of all (shallow+deep) marine sulfide (‰ vs VCDT)
approximate range
B
δ34S of deep marine sulfide (‰ vs VCDT)
C
Fraction of river input output as marine sulfide (fpyr)
D
Fraction of deep marine sulfide subducted (fsub)
E
Subduction of pore fluid SO4 2- (fwxr-fpyr)
F
fmantle - Fraction of crustal sulfide from mantle
δ34S of crustal sulfide (‰ vs VCDT)

Fig. VI-S15: A steady-state mass balance model of the global sulfur cycle with two marine sulfide reservoirs, one shallow and one deep, is used to evaluate how mantle inputs alter the relative $\delta^{34}S$ values of crustal sulfide and marine sulfide. Model results are shown for f_{deep} = 30% and for fractionation between seawater and shallow sulfide equal to 21‰. (A) Architecture of the model. (B) Results for the $\delta^{34}S$ of total marine sulfide (shallow and deep sulfide reservoirs) against the $\delta^{34}S$ of crustal sulfide and the fraction of mantle-derived crustal sulfide. The steady-state $\delta^{34}S$ of crustal sulfide and total marine sulfide are equal in the absence of mantle inputs (f_{mantle}=0). Inputs of mantle sulfur decouple the sulfur isotopic composition of crustal sulfide and marine sulfide. (C) The $\delta^{34}S$ of deep marine sulfide, (D) f_{pyr}, (E) the fraction of deep marine sulfide subducted into the mantle, and (F) the amount of oxidized SO_4^{2-} subducted into the mantle within pore fluids against the $\delta^{34}S$ of crustal sulfide and the fraction of crustal sulfide derived from the mantle. From our inversion-constrained values for the $\delta^{34}S$ of crustal sulfide and the assumption that 10% < f_{mantle} < 40% (Dellinger et al., 2014), steady-state f_{pyr} is constrained between approximately 35% and 65%. White squares indicate the conditions plotted in Fig. VI-S16.

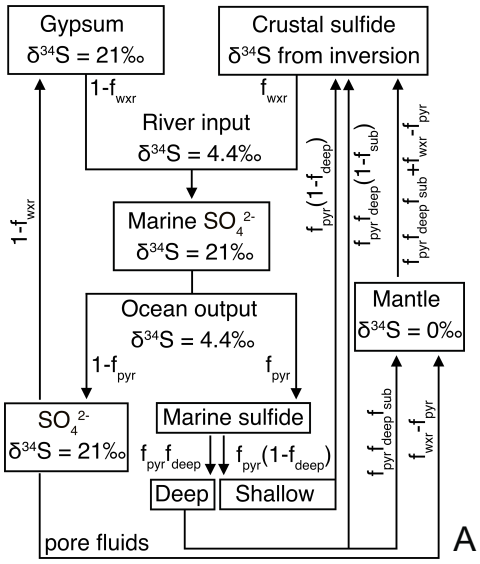
Gypsum
δ34S = 21‰
Crustal sulfide
δ34S from inversion
1-fwxr
fwxr
River input
δ34S = 4.4‰
Marine SO4 2-
δ34S = 21‰
Ocean output
δ34S = 4.4‰
1-fpyr
fpyr
Mantle
δ34S = 0‰
SO4 2-
δ34S = 21‰
Marine sulfide
fpyr fdeep
fpyr(1-fdeep)
Deep
Shallow
pore fluids
1-fwxr
fpyr(1-fdeep)
fpyr fdeep(1-fsub)
fpyr fdeep fsub+fwxr-fpyr
fpyr fdeep fsub
fwxr-fpyr
A

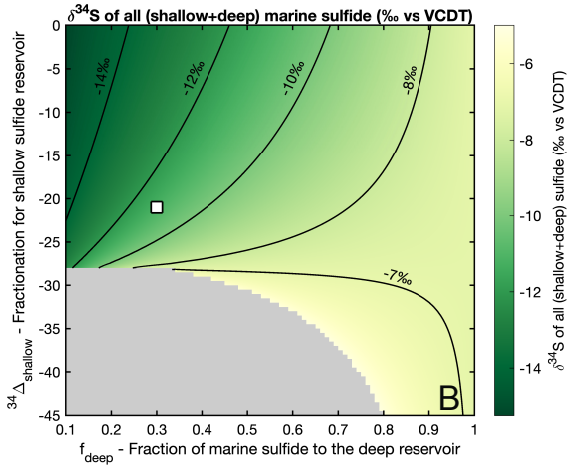
δ34S of all (shallow+deep) marine sulfide (‰ vs VCDT)
-14‰
-12‰
-10‰
-8‰
-7‰
B
34Δshallow - Fractionation for shallow sulfide reservoir
fdeep - Fraction of marine sulfide to the deep reservoir
δ34S of all (shallow+deep) sulfide (‰ vs VCDT)

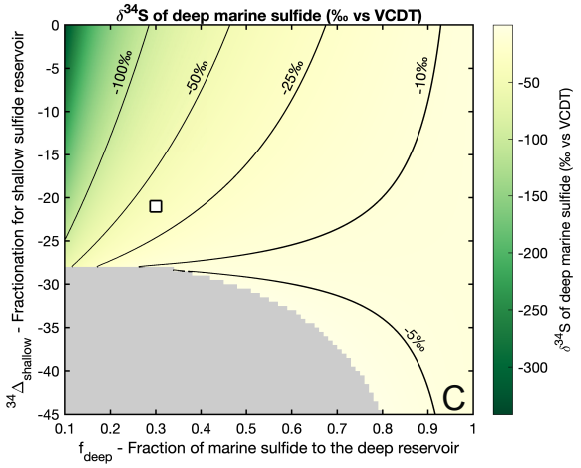
δ34S of deep marine sulfide (‰ vs VCDT)
-100‰
-50‰
-25‰
-10‰
-5‰
C
34Δshallow - Fractionation for shallow sulfide reservoir
fdeep - Fraction of marine sulfide to the deep reservoir
δ34S of deep marine sulfide (‰ vs VCDT)

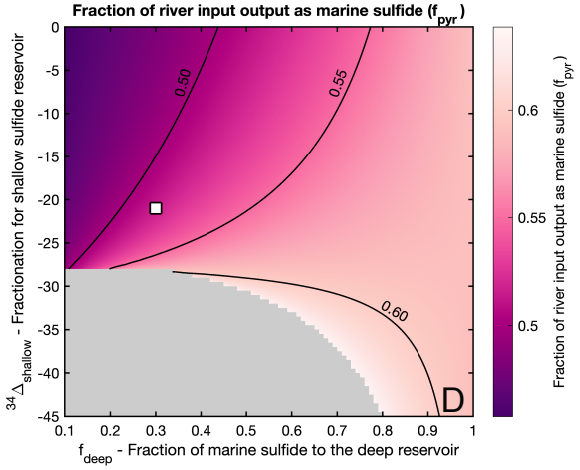
Fraction of river input output as marine sulfide (fpyr)
0.50
0.55
0.60
D
34Δshallow - Fractionation for shallow sulfide reservoir
fdeep - Fraction of marine sulfide to the deep reservoir
Fraction of river input output as marine sulfide (fpyr)

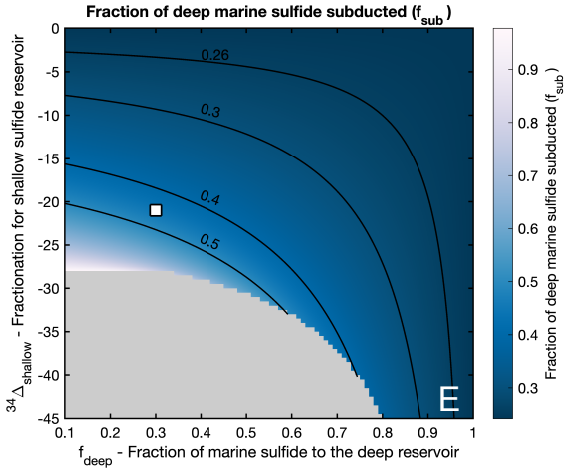
Fraction of deep marine sulfide subducted (fsub)
0.26
0.3
0.4
0.5
E
34Δshallow - Fractionation for shallow sulfide reservoir
fdeep - Fraction of marine sulfide to the deep reservoir
Fraction of deep marine sulfide subducted (fsub)

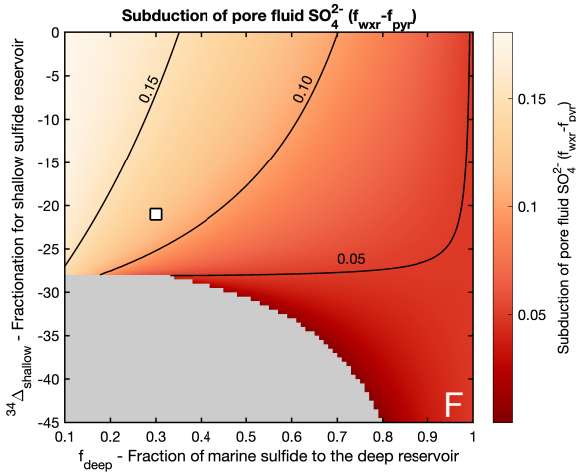
Subduction of pore fluid SO4 2- (fwxr-fpyr)
0.15
0.10
0.05
F
34Δshallow - Fractionation for shallow sulfide reservoir
fdeep - Fraction of marine sulfide to the deep reservoir
Subduction of pore fluid SO4 2- (fwxr-fpyr)

Fig. VI-S16: A steady-state mass balance model of the global sulfur cycle with two marine sulfide reservoirs, one shallow and one deep, is used to evaluate how mantle inputs alter the relative $\delta^{34}S$ values of crustal sulfide and marine sulfide. Model results are shown for f_{mantle} = 30% and for crustal sulfide $\delta^{34}S$ = -5‰. (A) Architecture of the model. (B) Results for the $\delta^{34}S$ of total marine sulfide (shallow and deep sulfide reservoirs). (C) The $\delta^{34}S$ of deep marine sulfide, (D) f_{pyr}, (E) the fraction of deep marine sulfide subducted into the mantle, and (F) the amount of oxidized SO_4^{2-} subducted into the mantle within pore fluids against f_{deep} and $^{34}\Delta_{shallow}$. Values of (D) f_{pyr} and (B) total sulfide $\delta^{34}S$ are minimally sensitive to f_{deep} and $^{34}\Delta_{shallow}$. White squares indicate the conditions plotted in Fig. VI-S15.